

JOURNAL OF SCIENCE



SAKARYA UNIVERSITY

Sakarya University Journal of Science



SAKARYA
UNIVERSITY

e-issn: 2147-835X

VOLUME: 24
ISSUE: 5
OCTOBER 2020

Sakarya University Journal of Science
Volume: 24 Issue: 5 October 2020
Editorial Boards

Editor-in-Chief

Davut Avcı, Pyhsics, Sakarya University (Turkey)

Editors

Alparslan Serhat Demir, Industrial Engineering, Sakarya University (Turkey)

Aysun Eğrisöğüt Tiryaki, Mechanical Engineering, Sakarya University (Turkey)

Ertan Bol, Civil Engineering, Sakarya University (Turkey)

Hüseyin Aksoy, Biology, Sakarya University (Turkey)

M. Hilmi Nişancı, Electrical and Electronics Engineering, Sakarya University (Turkey)

Mehmet İşleyen, Environmental Engineering, Bursa Technical University (Turkey)

Mehmet Nebioğlu, Chemistry, Sakarya University (Turkey)

Mehmet UYSAL, Metallurgical and Materials Engineering, Sakarya University (Turkey)

Mustafa Gülfen, Chemistry, Sakarya University (Turkey)

Muhammed Fatih Adak, Computer Engineering, Sakarya University (Turkey)

Murat Güzeltepe, Mathematics, Sakarya University (Turkey)

Nezaket Parlak, Mechanical Engineering, Sakarya University (Turkey)

Ömer Tamer, Physics, Sakarya University (Turkey)

Editorial Board

Aliye Suna Erses Yay, Environmental Engineering, Sakarya University (Turkey)

Aslı Uçar, Faculty of Health Sciences, Nutrition and dietetics, Ankara University (Turkey)

Aykut Astam, Physics, Erzincan Binali Yıldırım University (Turkey)

Burak Erkayman, Industrial Engineering, Atatürk University (Turkey)

Cansu Akbulut, Biology, Sakarya University (Turkey)

Caner Erden, Industrial Engineering, Sakarya University (Turkey)

Can Serkan Keskin, Chemistry, Sakarya University (Turkey)

Elif Büyük Öğüt, Mechanical and Metal Technologies, Kocaeli University (Turkey)

Emrah Bulut, Chemistry, Sakarya University (Turkey)

Emre Dil, Energy Systems Engineering, Beyket University (Turkey)

Emre Tabar, Physics, Sakarya University (Turkey)

Faruk Fırat Çalım, Civil Engineering, Alparslan Türkeş University (Turkey)

Gülner Arabacı, Chemistry, Sakarya University (Turkey)

İrfan Yazıcı, Electrical and Electronics Engineering, Sakarya University (Turkey)

İsmail Hakkı Demir, Architecture, Sakarya University (Turkey)
Latif Kelebekli, Chemistry, Ordu University (Turkey)
Mahmud Tokur, Metallurgical and Materials Engineering, Sakarya University (Turkey)
Mevlüt Sami Aköz, Civil Engineering, Çukurova University (Turkey)
Miraç Alaf, Metallurgical and Materials Engineering, Bilecik Şeyh Edebali University (Turkey)
Muhammed Maruf Öztürk, Computer Engineering, Süleyman Demirel University (Turkey)
Murat Sarduvan, Mathematics, Sakarya University (Turkey)
Murat Tuna, Chemistry, Sakarya University (Turkey)
Murat Utkucu, Geophysical Engineering , Sakarya University (Turkey)
Mustafa Akpınar, Software Engineering, Sakarya University (Turkey)
Nazan Deniz Yön Ertuğ, Biology, Sakarya University (Turkey)
Nükhet Sazak, Electrical and Electronics Engineering, Sakarya University (Turkey)
Osman Kırtel, Civil Engineering, Sakarya University of Applied Sciences (Turkey)
Özer Uygun, Industrial Engineering, Sakarya University (Turkey)
Öznur Özkan Kılıç, Mathematics, Başkent University (Turkey)
Rıfki Terzioğlu, Electrical and Electronics Engineering, Bolu Abant İzzet Baysal University, (Turkey)
Sibel Güneş, Mechanical Engineering, Erciyes University (Turkey)
Soley Ersoy, Mathematics, Sakarya University (Turkey)
Soydan Serttaş, Computer Engineering, Dumlupınar University (Turkey)
Tuğrul Çetinkaya, Metallurgical and Materials Engineering, Sakarya University (Turkey)
Turgay Şişman, Biology, Atatürk University (Turkey)

English Language Editor

Ömer Tamer, Physics, Sakarya University (Turkey)

SAKARYA UNIVERSITY JOURNAL OF SCIENCE
CONTENTS
Volume: 24 - Issue: 5 (OCTOBER 2020)

RESEARCH ARTICLES

Title	Authors	Pages
Classification of Breast Cancer Images Using Ensembles of Transfer Learning	Kadir GUZEL, Gokhan BILGIN	791-802
Ontology-based Instantaneous Route Suggestion of Enemy Warplanes with Unknown Mission Profile	Emre ÇINTAŞ, Barış ÖZYER, Y. Sinan HANAY	803-818
Investigation of Beam Width Shaping of a Ku-band Horn Antenna using a Diffractive Optic Element and an Electromagnetic Wave Absorber	Ahmet TEBER	819-831
Microcontroller-based Random Number Generator Implementation by Using Discrete Chaotic Maps	Serdar ÇİÇEK	832-844
Real-Time Obstacle Avoidance Based on Floor Detection for Mobile Robots	Adem HİÇDURMAZ, Adem TUNCER	845-853
Theoretical and Experimental Comparison of Micro-hardness and Bulk Modulus of Orthorhombic YBa ₂ Cu ₃ -xZnxO Superconductor Nanoparticles Manufactured using Sol-Gel Method	Elif AŞIKUZUN, Özgür ÖZTÜRK	854-864
Theta Point Calculation of a Polymer Chain with Electric Dipole Moments: Monte Carlo Simulation	Şahin UYAYER	865-871
Design of Heat Pipe Assisted Thermoelectric Generator and Experimental Investigation of the Power Performance	Yaşar İSLAMOĞLU, İmdat TAYMAZ, Cem PARMAKSIZOĞLU, Murat ÖZSOY, Erman ASLAN	872-881
Agile Methods in Game Programming based on Scrum	Şahin MERCAN, Yaşar BECERİKLİ	882-891
The Effect of Different Parameters on Shape Memory Alloys	İbrahim Nazem QADER, Mediha KÖK, Fethi DAĞDELEN, Shakhawan Salih ABDULLAH	892-913
Sustainable Maintenance Strategy for Wood Windows Defects	Özlem EREN, Emine Merve OKUMUŞ	914-935
CSK based on Priority Call Algorithm for Detection and Securing Platoon from Inside Attacks	Mohammed AL SHEIKHLY, Sefer KURNAZ	936-947
The Potential of the Karaman Wastewater Treatment Plant to Generate Electricity with MHP and Reduction of Electricity Bill Amounts by Adjusting Working Hours of the Facility	Ufuk SÜGÜRTİN, Türker Fedai ÇAVUŞ	948-955
The Replacement of Seashells with Calcite in White Ceramic Glaze Preparation	Levent KOROĞLU, Ceren PEKŞEN	956-964
Friction and Wear Properties of Glass Fiber Reinforced Polyphenylene Sulfide Composites	Mehmet İskender ÖZSOY, Levent ESATOĞLU	965-972
Determination of Coverage Oscillation for Inclined Communication Satellite	İbrahim ÖZ, Ümit Cezmi YILMAZ	973-983
Experimental Investigation on Effect to the Specific Strength of FDM Fabrication Parameters Using Taguchi Method	Sedat İRİÇ	984-990
The Geophytes of Sakarya City	Mehmet SAĞIROĞLU	991-1007

Groundwater Pollution Connected to Multiple Effect: A Case Study Kaman (Kırşehir, Turkey)	Tülay EKEMEN KESKİN, Bahadır SUBAŞI, Feyza GİRİŞEN, Zeynel BAŞIBÜYÜK	1008-1022
Synthesis And Characterization Of Maleic Anhydride Modified Poly (Ethylene Glycol) As Polymeric Solid-Solid Phase Change Materials	Tuğba GÜNGÖR ERTUĞRAL, Cemil ALKAN	1023-1028
Synthesis, Characterization and Photocatalytic Properties of Non-peripherally 3- (pyridin-4-yl) propane-1-oxy Groups Substituted Cu (II) Phthalocyanineand Water Soluble Derivative	Ece Tuğba SAKA	1029-1039
Investigation of the Frequency and Voltage Dependent Dielectric Properties of Au/n-SiC Metal Semiconductor (MS) and Au/Al ₂ O ₃ /n-SiC Metal-Insulator-Semiconductor (MIS) Structures	Gülçin ERSÖZ DEMİR, İbrahim YÜCEDAĞ	1040-1052
Phytochemical Screening of Bioactive Components of Medicinal Plant <i>Ajuga chamaepitys</i> subsp. <i>laevigata</i> (Banks & Sol.) P.H.Davis and <i>Ajuga bombycina</i> Boiss. by GC-MS Analysis	Alevcan KAPLAN	1053-1064
Neuro Sliding Mode Control for Exoskeletons with 7 DoF	Haci Mehmet GUZEY	1065-1073
The Role of Sodium Lauryl Sulfate on the Film Properties of Styrene-Butyl Acrylate-Acrylic Acid Copolymer Latex	Bilge EREN, Yasemin SOLMAZ	1074-1080
Removal of Maxilon Golden Yellow GL EC 400% from the Wastewater by Adsorption Method Using Different Clays	Sevgi GÜNEŞ DURAK	1081-1093
Determining the Factors that Influence the Effectiveness of the Health Sector in the OECD Countries	Selin Ceren TURAN, Mehmet Ali CENGİZ	1094-1104
On a Generalized Difference Sequence Spaces of Fractional Order associated with Multiplier Sequence Defined by A Modulus Function	Taja YAYING	1105-1114
Estimations of Cross-Sections for Photonuclear Reaction on Calcium Isotopes by Artificial Neural Networks	Serkan AKKOYUN, Hüseyin KAYA	1115-1120
Low Power-High Gain Bulk-Driven 3 Stages CMOS Miller OTA in 130nm technology	Engin AFACAN	1121-1134
Modelling of Remazol Black-B Adsorption on Chemically Modified Waste Orange Peel: pH Shifting Effect of Acidic Treatment	Ceren KARAMAN, Zümriye AKSU	1135-1150

JOURNAL OF SCIENCE



SAKARYA UNIVERSITY

Sakarya University Journal of Science

ISSN 1301-4048 | e-ISSN 2147-835X | Period Bimonthly | Founded: 1997 | Publisher Sakarya University |
<http://www.saujs.sakarya.edu.tr/en/>

Title: Classification of Breast Cancer Images Using Ensembles of Transfer Learning

Authors: Kadir GUZEL, Gokhan BILGIN

Received: 2020-04-15 09:52:30

Accepted: 2020-06-10 09:34:55

Article Type: Research Article

Volume: 24

Issue: 5

Month: October

Year: 2020

Pages: 791-802

How to cite

Kadir GUZEL, Gokhan BILGIN; (2020), Classification of Breast Cancer Images Using Ensembles of Transfer Learning. Sakarya University Journal of Science, 24(5), 791-802, DOI: <https://doi.org/10.16984/saufenbilder.720693>

Access link

<http://www.saujs.sakarya.edu.tr/en/pub/issue/56422/720693>

New submission to SAUJS

<http://dergipark.org.tr/en/journal/1115/submission/step/manuscript/new>

Classification of Breast Cancer Images Using Ensembles of Transfer Learning

Kadir GUZEL¹, Gokhan BILGIN^{*2}

Abstract

It is a challenging task to estimate the cancerous cells and tissues via computer-aided diagnosis systems on high-resolution histopathological images. In this study, it is suggested to use transfer learning and ensemble learning methods together in order to reduce the difficulty of this task and better diagnose cancer patients. In the studies, histopathological images with 40× and 100× magnification factors are analyzed. In order to prove the success of the study with experimental studies, firstly, the results provided by pre-modeled deep learning architectures trained by histopathological image dataset, then the results acquired by different transfer learning approaches and the results obtained with the ensembles of deeply learned features using transfer learning methods are presented comparatively. Three different approaches are applied for transfer learning by fine-tuning the pre-trained convolution neural networks. In the experimental section, results of single classifiers (i.e., support vector machines, logistic regression, k-nearest neighbor and bagging) are presented by employing features of CNN models obtained by defined transfer learning approaches. Then, decisions of each classifier model are combined separately by weighted decision fusion (WDF) and stacking decision fusion (SDF) ensemble learning methods that have proven to improve the classification performance of the proposed classification system.

Keywords: Histopathological images, breast cancer, deep learning, transfer learning, ensemble learning.

1. INTRODUCTION

Cancer remains one of the leading causes of human death causes worldwide. Only in 2018, 18.1 million new cancer cases and 9.6 million cancer-related deaths were reported in a total of 185 countries. Recent global cancer statistics

show that breast cancer is still the most common form of cancer among women with 24.2% (2.1 million) new cases and 626,679 deaths per year [1]. In all cancer types, early diagnosis and treatment process is very critical in the fight against cancer. In general approach, pathologists look for signs of cancer by analyzing histological descriptive features of tissue sections commonly

¹Yildiz Technical University, Dpt. of Computer Engineering, 34220 Istanbul, Turkey.

ORCID: <https://orcid.org/0000-0002-3664-6810>

*Corresponding Author: gbilgin@yildiz.edu.tr

²Yildiz Technical University, Dpt. of Computer Engineering, 34220 Istanbul, Turkey. ORCID: <https://orcid.org/0000-0002-5532-477X>

stained with hematoxylin and eosin (H&E), immunohistochemical (IHC) and some specific dyes in a microscopic environment with histopathological whole slides. In recent years, histopathological slides obtained from rapidly developing digital imaging devices are captured as digital high-resolution images and given to expert systems for evaluation. These medical images are an important research topic in the field of biomedical and machine learning to help clinicians and diagnose cancer patients. Computer-aided diagnostic systems gain importance especially in undecided diagnoses and in determining the regions where the doctor's attention should be concentrated.

Computer-aided diagnosis systems (CAD) have been implemented in different medical problems such as mammography and breast image analysis [2], mass detection [3], lung cancer [4], colorectal cancer classification [5], skin lesion classification [6]. Generally, histopathological image processing methods are based on approaches that recognizing patterns which are included local texture and extracting important features from images. In the recent machine learning literature, feature extraction methods can be divided into two parts: *i*) the first one is conventional feature extraction techniques commonly called as handcrafted methods and *ii*) the second one is the deep features extracted from images by deep learning networks [7].

Conventional feature extraction methods have been studied extensively in the biomedical pattern recognition literature; for example, local binary pattern (LBP) that evaluates the value of the center pixel according to neighboring the pixels [8]. A well-known method is the histogram of oriented gradients (HOG) that uses the orientation and magnitude values of the pixels in the image [9]. Gabor filtering is used to capture discriminative features aligned at specific angles on the image [10]. Speeded up robust features (SURF) rely on the determinant of the Hessian matrix for both scale and location [11]. On the other hand, deep features obtained from deep learning models can achieve higher recognition accuracies than handcrafted image features. Especially, the feature extraction from images by using convolution neural networks (CNN) has

made much progress in recent years [12]. Multi-layered forward computing and back-propagation artificial neural networks (ANN) have encountered intense interest by researchers with the use of graphics processors (GPU) and tensor processing unit (TPU). Deep neural models can code the raw pixels of histopathological images into feature vectors that represent high-level concepts for classification and segmentation problems [13].

Various learning methods have been applied to datasets in different medical fields in the literature. Transfer learning and ensemble learning are among the popular learning methods in the field of machine learning. In [14], it has been studied to build ensemble learning models that can achieve more robust results by combining the features or decisions in the classification of histopathological images. In another study, a community-based GoogLeNet architecture was proposed for breast cancer image classification [15]. In their study, the authors proposed a new ensemble scheme to fuse patch probabilities for image-wise classification. In another study, an ensemble of multi-scale CNN algorithm has been proposed to classify H&E stained breast histopathological microscopy images [16]. Transfer learning is a machine learning technique in which a model trained for a task is redesigned in a related second problem. In terms of deep learning, transfer learning involves reusing a pre-trained model on a new problem and fine-tuning stages to adapt to this problem. A deep learning technique based on the ensemble of CNN has been studied to differentiate adenocarcinomas from healthy tissues and benign lesions [17]. A bioimage classification system has been proposed for boosting the performance of trained CNNs by composing multiple CNN models into an ensemble and scores were combined by sum rule [18]. Deep learning based ResNet-50 and DenseNet-161 pre-trained models have been employed to classify histopathology images [19]. An ensemble transfer learning framework has been introduced to classify cervical histopathology images [20].

In this study, fine-tuned models, which ranked first in ImageNet competitions, are used to detect benign and malignant cells in breast cancer

images. The network is trained in three different approaches using pre-trained weights with the transfer learning method [21] and features are extracted using this fine-tuned model. The supervised learning methods used in the study are support vector machines (SVM), logistic regression (LR), k-nearest neighbor (KNN) and bagging (BG). A robust model was proposed to increase the collective success by using two different ensemble learning methods together with the decisions of the four best classifiers among these classifiers.

The proposed method for classifying breast cancer images is described in detail in Section 2. The properties of the experimental dataset are introduced in Section 3. After the experimental studies are discussed comparatively in Section 4, the results are concluded in Section 5.

2. METHODOLOGY

In the classification of breast cancer histopathological images, it is proposed to use transfer learning and ensemble learning methods together. To prove the success of the study with experimental studies; *i)* the results provided by pre-modeled deep learning architectures, *ii)* the results acquired by different transfer learning approaches and, ultimately *iii)* the results obtained with ensembles of deeply learned features using transfer learning methods are presented comparatively.

2.1. Classification via Pre-modeled CNN Models

Deep neural networks are capable of extracting low, medium and high level features in an end-to-end multi-layered manner. In addition, it can be seen that the number of stacked layers can enhance the levels of the features [13, 19]. Deep learning-based CNN architectures, which proved their efficiency in ImageNet competitions in image recognition problems, are used for breast cancer classification. Histopathological images in the dataset are evaluated by two different advanced CNN architectures, namely VGGNet16 [22] and ResNet50 [23].

- VGGNet16 deep learning algorithm is a 16-layer network consisting of 13 convolutions and 3 fully connected dense layers introduced in the ILSVRC-2014 competition. There are approximately 134 million parameters in this network total. The image placed on the input layer should be in the size of $224 \times 224 \times 3$. The last layer is the artificial neural network layer. It is a deep learning algorithm that achieves 92.7% accuracy in the ImageNet database which is a dataset of over 14 million images belonging to 1000 classes.
- ResNet50 architecture stands for residual networks and includes five stages each with a convolution and identity block. In this structure, each convolution block has three convolution layers and each identity block also has three convolution layers. The network model has 177 or more layers and there are approximately 23.5 million parameters in total. In addition, this layered structure provides information about how the connections between the layers will be and skip connection is applied before the ReLU (rectified linear unit) activation function. The input layer is in size of $224 \times 224 \times 3$. This network learns rich feature representations for a wide variety of images and presents a robust model that is used very frequently in many image processing tasks.

2.2. Classification with Employing Transfer Learning

Transfer learning is a deep learning methodology that allows the model, previously trained on a special problem, to use it in a new task. It is a promising methodology especially in the field of image processing because it makes it easy to create accurate and time-saving models. Sometimes, it may take days, weeks to train deep convolutional neural network models on very large datasets. One way to shorten this process is to reuse model weights from pre-trained convolutional models developed for standard computer vision benchmark datasets such as ImageNet. In this way, the models that are needed for our own problems can be created more easily

without starting from scratch by taking advantage of what the previous models have learned.

The pre-trained models that we employed in our study are architectures trained on a larger benchmark dataset (i.e. ImageNet containing 1.2 million images from 1000 categories) to solve a problem similar to the problem of finding distinctive features in histopathological images. It is common practice to use models that have proven their success in the machine learning literature to achieve more successful results with data sets containing a limited number of samples and classes, taking into account the computational cost of data. In parallel with these explanations, it is also supported by the results in our study that it is useful to use fine-tuned networks over the pre-trained network instead of training the entire network. There are three different approaches for transfer learning with the fine-tuning process of a convolution neural network. These approaches are summarized in Figure 1.

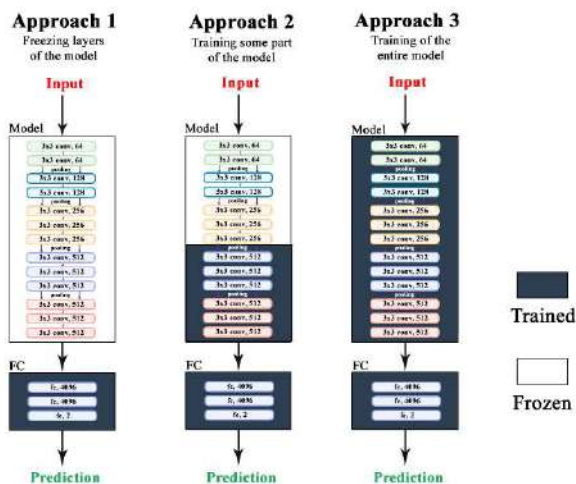


Figure 1. Transfer learning approaches

- **Approach 1 (A1):** The pre-trained deep model weights are loaded initially. The connections in the fully connected (FC) layers are retrained with our own data samples, whereas all other layers are frozen.
- **Approach 2 (A2):** The pre-trained deep model weights are loaded initially. A certain part of the network is retrained for fine-tuning with our own data samples, whereas other layers remain frozen.

- **Approach 3 (A3):** The pre-trained deep model weights are loaded initially. Then the entire network is retrained with our own data samples for fine-tuning.

2.3. Ensemble Learning with Deeply Learned Features

In the convolution layers of CNN networks, features are extracted using various sizes of kernels in the image; because discriminative features in the image are usually local and it is necessary to take into account several neighbor pixels [24]. The pre-trained deep learning models used in the experiments are handled by a method known as inductive learning, which is a kind of transfer learning. The main purpose of inductive learning algorithms is to extract a mapping from previous training samples.

Thus, thanks to transfer learning with the models used, deep features are extracted with three different approach types by using our own histopathology data. For this purpose, after the training is completed, the fully connected layers are removed for creating a model that could extract the discriminative features. In order for the feature vectors to have the same size, the flattened features are first normalized and then PCA is used for dimension reduction to obtain the principal components that contain 95% of the entire variance.

Ensemble learning can be defined as a process in which the decisions of the system consisting of more than one different classifier models are combined. Ensemble learning is primarily used to improve the classification performance of a total system model [20]. Therefore, instead of increasing the accuracy of a single classifier using some of the specified features, it is aimed to make a more accurate decision with the logic of the ensemble by combining different classification results.

In our study, weighted decision fusion (WDF) [25] and stacking decision fusion (SDF) [26] ensemble methods are used when combining decisions. The WDF method is utilized to combine weak learners using the weighting

strategy. Model weights are small positive values and the sum of all weights is equal to one. In the WDF method, weights are adjusted according to the percentage of confidence in each model or the expected performance. In regression problems, weights are multiplied and averaged while decisions for classification problems are multiplied in proportion to the weights of the classifiers. The weights used in the problem we discussed in our article are given according to the success of the learners as a result of the experiments. The method of SDF involves a combiner learning algorithm training to ensemble the predictions of many weak learning algorithms. In this approach, first, single/weak classifiers are trained using our own data. It is then trained to make a final prediction using all predictions of other algorithms through the combiner learning algorithm used. In this study, the logistic regression model, which is generally used as a combiner learning algorithm, is employed.

3. EXPERIMENTAL DATASET

Due to the difficulty of the data collection procedures, time consuming processing and the labeling costs, the high quality datasets in the scientific medical literature consist of limited numbers and limited samples. Therefore, accessing a good large-scale dataset with detailed explanations for researchers is quite laborious. In this study, the Breast Cancer Histopathological Image Classification (BreacKHis) dataset presented to the public by the Prognostic and Diagnostic (P&D) Laboratory in Brazil is used to perform our studies efficiently. The dataset contains microscopic biopsy images of benign and malignant breast tumors which were captured through a clinical study from January 2014 to December 2014 [27]. Breast tissue biopsy slides were stained with hematoxylin and eosin (H&E). The breast cancer dataset images were obtained by an Olympus BX-50 microscope with a 3.3 \times magnification relay lens combined with a Samsung digital color camera SCC-131AN. Histopathological images were taken in RGB color space true color format using magnification levels of 40 \times , 100 \times , 200 \times and 400 \times . The dataset totally is composed of 7909 microscopic biopsy breast cancer images collected from 82 patients.

The dataset consists of four different types of histological benign breast tumors (adenosis, fibroadenoma, phyllodes tumor, tubular adenoma) and four types of malignant tumors (ductal carcinoma, lobular carcinoma, mucinous carcinoma and papillary carcinoma). In this study, H&E images captured at 40 \times and 100 \times magnification levels from microscopic images at very different magnification levels are used. As can be seen from Table 1, the total number of benign images selected from the dataset is 1269 and the total number of malignant images is 2807. Examples of benign and malignant image samples taken at 40 \times and 100 \times magnification levels can be seen in Figure 2.

Table 1. The number of data samples according to magnification level and class label

Magnification	Benign	Malignant	Total
40x	625	1370	1995
100x	644	1437	2081

The magnification factor in digital microscopes plays an important role in the analysis of histology images [28]. In normal procedure, pathologists adjust the magnification factor on the slide so that the objects of interest can be easily seen. Histology images consist of different types of tissues and analysis of these tissues becomes difficult in low magnification levels. Besides that, background changes may occur in digitized images with different magnification levels. Therefore, different magnification factors make it difficult to obtain an accurate diagnosis in automated computer-aided diagnostic (CAD) systems [29].

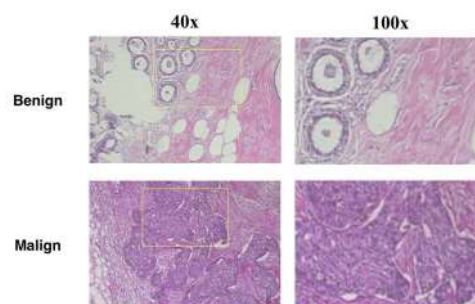


Figure 2. Examples of breast cancer histopathological image samples in different magnification levels [27]

4. EXPERIMENTAL RESULTS

In this study, experimental studies with histopathological images at 40× and 100× magnification levels are analyzed to observe the effects of different magnification factors. The experiments of this research have been developed by using Tensor Processing Units (TPU) with Keras [30], libraries with Scikit-learn [31] and TensorFlow [32] in the background.

In our study, firstly, the results are obtained by performing 10-fold cross-validation with pre-modeled deep learning architectures and presented in Table 2 with standard deviation values in parentheses to make comparative evaluations. The overall accuracy, recall, precision and F1-score metrics of the pre-modeled architectures are presented in Table 2. Note that, when using pre-modeled networks, results are obtained without using pre-trained weights in this table. Original VGGNet16 and ResNet50 network models are adopted and trained with breast cancer histopathological image classification dataset. As can be seen from Table 2, the results of VGGNet16 are better than ResNet50 in at 40× and 100× magnification levels. The results in Table 3 are obtained from experiments by applying 10-fold cross-validation with standard deviation values in parentheses using three different transfer learning approaches explained in previous sections, at 40× and 100× magnification levels of breast cancer histopathological image classification dataset. As can be seen from the Table 3, ResNet50 surpasses VGGNet16 by transfer learning approach 3 (A3) by retraining the entire network with our own data samples. With this fine-tuning approach, ResNet50 architecture reaches 95.09% and 94.62% for at 40× and 100× magnification levels respectively.

The flowchart of the proposed system is shown in Figure 3. In the third part of the experiments, SVM, LR, KNN and Bagging (BG) classifiers are employed for decision combining. The results of single classifiers and ensemble learning by employing features of CNN models obtained by defined transfer learning approaches are presented in Table 4. Table 4 presents the results

in the subsection structure for the transfer learning approaches used with each pre-modeled network architecture. For the first four rows in each subsection of Table 4, the results of single classifiers (SVM, LR, KNN and BG) are presented by employing features of CNN models obtained by defined transfer learning approaches. Then, in the lower part of each subsection of Table 4, decisions of the each single classifier models are combined by WDF and SDF ensemble learning methods which are used to improve the classification performance of a total system model. The results represented in Table 4 are also obtained by 10-fold cross-validation and standard deviation values are shown in parentheses. According to the Table 4, the results obtained at 40× magnification level are better than 100× magnification level for each deep model and defined transfer learning approach. In general, according to the results obtained with the single classifiers, the classification performances are increased with the use of the WDF and SDF ensemble learning methods. Between these two methods, it can be seen that SDF yields better results than WDF. When all of Table 4 is analyzed, it is seen that the best result of 97.01% is obtained with the ResNet50 deep network with transfer learning approach 3 (A3) via the SDF ensemble method. In addition, the results obtained in the experimental studies in the literature using the same data set are presented for comparison purposes in Table 5. It should be taken into account that different training and test sample numbers are used in these studies.

5. CONCLUSIONS

In this study, it is aimed to develop a framework that can be evaluated as the second reader that can help doctors aiming to automatically classify cancerous tissues in histopathological images. The proposed approach with ensemble learning by employing features of pre-modeled CNN architectures using transfer learning approaches show promising improvement. According to the results in the tables, it is concluded that using traditional machine learning algorithms such as SVM and LR instead of fully connected layers in deep learning architectures yielded better results in the breast cancer dataset. In addition, among

the three different for transfer learning methods, the third approach (A3) where the pre-modeled ResNet50 neural network is fine-tuned with initial weights and the proposal to combine single classifier decisions with the SDF method work

solidly than other methods. With this proposed framework structure, overall accuracies of 97.01% and 96.25% have been achieved at 40× and 100× magnification levels respectively.

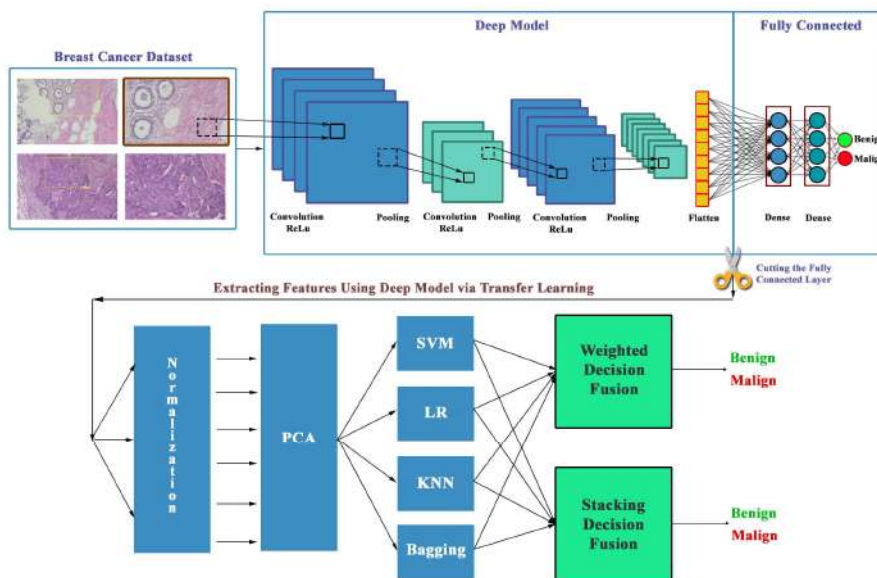


Figure 3. The flowchart of the proposed system

Table 2. The results obtained by pre-modeled networks without using pre-trained weights

Model	40×, 10-fold Cross-Validation				100×, 10-fold Cross-Validation			
	Accuracy	Recall	Precision	F1-Score	Accuracy	Recall	Precision	F1-Score
VGGNet16	86.50 (+/- 1.23)	0.86 (+/- 0.02)	0.81 (+/- 0.02)	0.83 (+/- 0.02)	87.12 (+/- 1.58)	0.85 (+/- 0.02)	0.84 (+/- 0.02)	0.84 (+/- 0.02)
ResNet50	77.50 (+/- 2.00)	0.76 (+/- 0.01)	0.79 (+/- 0.03)	0.76 (+/- 0.01)	64.75 (+/- 0.32)	0.65 (+/- 0.01)	0.74 (+/- 0.01)	0.71 (+/- 0.01)

Table 3. The results of three different transfer learning approaches using pre-trained weights

Model	App.	40×, 10-fold Cross-Validation				100×, 10-fold Cross-Validation			
		Accuracy	Recall	Precision	F1-Score	Accuracy	Recall	Precision	F1-Score
VGGNet16	A1	89.57 (± 2.54)	0.89 (± 0.01)	0.86 (± 0.04)	0.87 (± 0.04)	89.91 (± 1.51)	0.89 (± 0.02)	0.87 (± 0.03)	0.88 (± 0.02)
	A2	92.33 (± 1.66)	0.92 (± 0.02)	0.90 (± 0.02)	0.91 (± 0.02)	89.96 (± 1.77)	0.88 (± 0.03)	0.85 (± 0.01)	0.87 (± 0.02)
	A3	93.34 (± 2.38)	0.94 (± 0.04)	0.89 (± 0.05)	0.92 (± 0.05)	92.56 (± 3.85)	0.93 (± 0.02)	0.90 (± 0.07)	0.91 (± 0.06)
ResNet50	A1	70.12 (± 2.10)	0.65 (± 0.05)	0.58 (± 0.04)	0.59 (± 0.04)	71.35 (± 3.22)	0.66 (± 0.03)	0.60 (± 0.03)	0.61 (± 0.03)
	A2	64.75 (± 8.25)	0.68 (± 0.07)	0.63 (± 0.01)	0.61 (± 0.05)	70.23 (± 4.42)	0.60 (± 0.01)	0.64 (± 0.08)	0.60 (± 0.10)
	A3	95.09 (± 2.53)	0.96 (± 0.02)	0.93 (± 3.62)	0.94 (± 0.03)	94.62 (± 2.14)	0.96 (± 0.01)	0.92 (± 0.03)	0.93 (± 0.03)

Table 4. The results of single classifiers and ensemble learning by employing features of CNN models obtained by defined transfer learning approaches

		40×, 10-fold Cross-Validation				100×, 10-fold Cross-Validation			
Model	Alg.	Accuracy	Recall	Precision	F1-Score	Accuracy	Recall	Precision	F1-Score
VGGNet16+A1	SVM	89.82 (± 1.39)	0.90 (± 0.02)	0.86 (± 0.02)	0.88 (± 0.02)	89.48 (± 1.94)	0.89 (± 0.04)	0.86 (± 0.02)	0.87 (± 0.03)
	LR	90.27 (± 1.90)	0.89 (± 0.02)	0.87 (± 0.03)	0.88 (± 0.02)	89.62 (± 1.60)	0.89 (± 0.03)	0.87 (± 0.02)	0.88 (± 0.02)
	KNN	87.67 (± 1.68)	0.90 (± 0.02)	0.81 (± 0.02)	0.84 (± 0.02)	88.95 (± 1.87)	0.90 (± 0.02)	0.84 (± 0.02)	0.86 (± 0.02)
	BG	84.16 (± 1.63)	0.83 (± 0.02)	0.79 (± 0.02)	0.80 (± 0.02)	85.39 (± 1.79)	0.84 (± 0.03)	0.81 (± 0.02)	0.82 (± 0.02)
	WDF	89.92 (± 1.67)	0.90 (± 0.02)	0.86 (± 0.02)	0.88 (± 0.02)	89.96 (± 1.70)	0.90 (± 0.03)	0.86 (± 0.02)	0.88 (± 0.02)
	SDF	90.27 (± 1.90)	0.89 (± 0.02)	0.88 (± 0.03)	0.89 (± 0.02)	89.62 (± 1.60)	0.88 (± 0.03)	0.87 (± 0.02)	0.87 (± 0.02)
VGGNet16+A2	SVM	90.53 (± 1.10)	0.91 (± 0.02)	0.87 (± 0.02)	0.88 (± 0.01)	86.57 (± 2.96)	0.91 (± 0.02)	0.87 (± 0.02)	0.89 (± 0.02)
	LR	93.59 (± 1.47)	0.93 (± 0.02)	0.92 (± 0.02)	0.92 (± 0.02)	91.49 (± 1.14)	0.90 (± 0.01)	0.89 (± 0.02)	0.90 (± 0.01)
	KNN	89.72 (± 1.52)	0.91 (± 0.02)	0.85 (± 0.02)	0.87 (± 0.02)	90.54 (± 1.23)	0.91 (± 0.02)	0.86 (± 0.02)	0.88 (± 0.02)
	BG	86.21 (± 1.28)	0.85 (± 0.02)	0.81 (± 0.02)	0.83 (± 0.02)	87.36 (± 1.77)	0.87 (± 0.02)	0.83 (± 0.02)	0.84 (± 0.02)
	WDF	91.58 (± 0.89)	0.92 (± 0.02)	0.88 (± 0.01)	0.90 (± 0.01)	91.25 (± 2.03)	0.91 (± 0.03)	0.88 (± 0.03)	0.89 (± 0.03)
	SDF	93.62 (± 1.17)	0.92 (± 0.02)	0.92 (± 0.01)	0.92 (± 0.02)	91.49 (± 1.14)	0.90 (± 0.01)	0.89 (± 0.02)	0.90 (± 0.01)
VGGNet16+A3	SVM	94.29 (± 1.19)	0.95 (± 0.01)	0.92 (± 0.01)	0.93 (± 0.01)	93.51 (± 2.73)	0.94 (± 0.03)	0.91 (± 0.04)	0.92 (± 0.03)
	LR	95.54 (± 1.39)	0.95 (± 0.02)	0.94 (± 0.02)	0.95 (± 0.02)	94.14 (± 2.40)	0.94 (± 0.03)	0.93 (± 0.03)	0.93 (± 0.03)
	KNN	90.68 (± 2.12)	0.93 (± 0.02)	0.86 (± 0.03)	0.88 (± 0.02)	92.65 (± 2.39)	0.93 (± 0.02)	0.89 (± 0.03)	0.91 (± 0.03)
	BG	90.28 (± 1.58)	0.90 (± 0.02)	0.88 (± 0.02)	0.88 (± 0.02)	89.86 (± 1.81)	0.89 (± 0.02)	0.87 (± 0.02)	0.88 (± 0.02)
	WDF	94.59 (± 1.24)	0.95 (± 0.01)	0.92 (± 0.01)	0.94 (± 0.01)	93.56 (± 2.73)	0.94 (± 0.03)	0.91 (± 0.04)	0.92 (± 0.03)
	SDF	96.04 (± 1.42)	0.96 (± 0.02)	0.94 (± 0.02)	0.95 (± 0.02)	94.14 (± 2.40)	0.94 (± 0.02)	0.93 (± 0.03)	0.93 (± 0.03)
ResNet50+A1	SVM	92.67 (± 1.03)	0.93 (± 0.01)	0.91 (± 0.02)	0.91 (± 0.01)	91.91 (± 1.99)	0.91 (± 0.01)	0.90 (± 0.01)	0.90 (± 0.02)
	LR	89.83 (± 1.03)	0.88 (± 0.03)	0.89 (± 0.01)	0.88 (± 0.02)	90.08 (± 1.98)	0.89 (± 0.01)	0.88 (± 0.03)	0.89 (± 0.02)
	KNN	90.67 (± 0.24)	0.90 (± 0.02)	0.87 (± 0.01)	0.89 (± 0.01)	88.96 (± 2.42)	0.87 (± 0.02)	0.85 (± 0.02)	0.86 (± 0.02)
	BG	84.17 (± 1.43)	0.83 (± 0.01)	0.78 (± 0.01)	0.80 (± 0.01)	84.32 (± 2.73)	0.85 (± 0.01)	0.77 (± 0.03)	0.79 (± 0.04)
	WDF	93.83 (± 0.85)	0.94 (± 0.01)	0.92 (± 0.01)	0.92 (± 0.01)	92.32 (± 0.69)	0.92 (± 0.01)	0.90 (± 0.03)	0.91 (± 0.02)
	SDF	93.83 (± 0.85)	0.94 (± 0.01)	0.92 (± 0.01)	0.92 (± 0.01)	92.16 (± 1.98)	0.91 (± 0.02)	0.90 (± 0.03)	0.91 (± 0.02)
ResNet50+A2	SVM	89.25 (± 2.25)	0.92 (± 0.02)	0.85 (± 0.02)	0.87 (± 0.02)	87.52 (± 2.15)	0.88 (± 0.04)	0.81 (± 0.02)	0.84 (± 0.03)
	LR	94.25 (± 0.75)	0.95 (± 0.01)	0.93 (± 0.01)	0.93 (± 0.01)	91.00 (± 1.37)	0.89 (± 0.03)	0.90 (± 0.01)	0.90 (± 0.02)
	KNN	89.75 (± 0.75)	0.93 (± 0.01)	0.85 (± 0.02)	0.87 (± 0.01)	86.80 (± 2.91)	0.86 (± 0.01)	0.86 (± 0.01)	0.84 (± 0.03)
	BG	90.00 (± 3.50)	0.90 (± 0.03)	0.88 (± 0.04)	0.89 (± 0.04)	86.92 (± 3.48)	0.85 (± 0.03)	0.84 (± 0.05)	0.84 (± 0.04)
	WDF	92.75 (± 1.25)	0.94 (± 0.01)	0.90 (± 0.01)	0.91 (± 0.01)	90.76 (± 1.39)	0.91 (± 0.02)	0.87 (± 0.02)	0.88 (± 0.01)
	SDF	92.75 (± 1.25)	0.94 (± 0.01)	0.90 (± 0.01)	0.91 (± 0.01)	90.76 (± 1.39)	0.91 (± 0.02)	0.87 (± 0.02)	0.88 (± 0.01)
ResNet50+A3	SVM	96.84 (± 1.50)	0.97 (± 0.01)	0.96 (± 0.02)	0.96 (± 0.02)	96.25 (± 1.62)	0.96 (± 0.02)	0.95 (± 0.02)	0.95 (± 0.02)
	LR	96.04 (± 1.61)	0.96 (± 0.01)	0.95 (± 0.03)	0.95 (± 0.02)	95.39 (± 2.05)	0.95 (± 0.02)	0.94 (± 0.03)	0.94 (± 0.03)
	KNN	96.89 (± 1.77)	0.97 (± 0.02)	0.96 (± 0.03)	0.96 (± 0.02)	96.25 (± 2.05)	0.96 (± 0.02)	0.95 (± 0.03)	0.95 (± 0.03)
	BG	92.53 (± 1.75)	0.91 (± 0.02)	0.91 (± 0.02)	0.91 (± 0.02)	92.03 (± 1.68)	0.90 (± 0.02)	0.91 (± 0.02)	0.90 (± 0.02)
	WDF	96.94 (± 1.60)	0.97 (± 0.01)	0.96 (± 0.02)	0.96 (± 0.02)	96.25 (± 1.62)	0.96 (± 0.02)	0.95 (± 0.02)	0.95 (± 0.02)
	SDF	97.01 (± 1.56)	0.97 (± 0.01)	0.96 (± 0.02)	0.96 (± 0.02)	96.25 (± 1.62)	0.96 (± 0.02)	0.95 (± 0.02)	0.95 (± 0.02)

Table 5. Comparative analysis table of deep learning methods in the literature for the BreakHis dataset

Author [citation]	Methodology	Features / Application	Results (%)	
			40×	100×
Bayramoglu <i>et al.</i> [33]	Single Task CNN	<ul style="list-style-type: none"> Better accuracy than handcrafted methods Combined image data from many more resolution 	80.97	80.92
Kassani <i>et al.</i> [34]	VGG19, MobilNetV2, DenseNet201	<ul style="list-style-type: none"> A three-path ensemble architecture is used by transfer learning and fine-tuning with different number of training and test samples from our study Deep feature extraction and fused features 	98.13	
Vo <i>et al.</i> [35]	ResNetV1 + GBT, InceptionV3 + GBT	<ul style="list-style-type: none"> Fused model via Gradient Boosting Trees Fine-tuning deep learning models 	93.50	95.30
Alom <i>et al.</i> [36]	IRRCNN + Aug.	<ul style="list-style-type: none"> Better accuracy than similar studies Applied different data augmentation techniques with different number of training and test samples from our study 	97.95	97.57
Spanhol <i>et al.</i> [37]	AlexNet CNN	<ul style="list-style-type: none"> Used a deep learning approach to avoid hand-crafted features Proposed several strategies for training 	89.60	85.00
Han <i>et al.</i> [38]	CSDCNN + Aug.	<ul style="list-style-type: none"> A new deep learning model has been proposed 	92.80	93.90
Gandomkar <i>et al.</i> [39]	ResNet	<ul style="list-style-type: none"> A framework called ResNet based MuDeRN has been proposed with transfer learning Prediction with more class 	95.60	94.89
Mehra [40]	VGG16 + LR, VGG19 + LR, ResNet50 + LR	<ul style="list-style-type: none"> Used a fine-tuned model via logistic regression classifier Fine-tuned pre-trained network is more robust 	92.60	
Zhu <i>et al.</i> [41]	Hybrid CNN	<ul style="list-style-type: none"> Multiple hybrid models with the same architecture are fused. Used different subset with the voting 	85.7	84.2
Kumar <i>et al.</i> [42]	VGG16 + SVM, VGG16 + RF	<ul style="list-style-type: none"> Proposed a variant of VGGNet-16, a FC layer was removed and experimented with various classifiers 	94.11	95.12

Acknowledgements

The authors would like to thank the reviewers for all useful and instructive comments on our manuscript.

Funding

The authors received no specific funding for this study.

The Declaration of Conflict of Interest / Common Interest

No conflict of interest or common interest has been declared by the authors.

Authors' Contribution

All authors have contributed in experimental study and writing of the manuscript equally.

The Declaration of Ethics Committee Approval

The authors declare that this document does not require an ethics committee approval or any special permission.

The Declaration of Research and Publication Ethics

The authors of the paper declare that they comply with the scientific, ethical and quotation rules of SAUJS in all processes of the paper and that they do not make any falsification on the data collected. In addition, they declare that Sakarya University Journal of Science and its editorial board have no responsibility for any ethical violations that may be encountered, and that this study has not been evaluated in any academic publication environment other than Sakarya University Journal of Science.

REFERENCES

- [1] F. Bray, J. Ferlay, I. Soerjomataram, R. L. Siegel, L. A. Torre, and A. Jemal, "Global cancer statistics 2018: Globocan estimates of incidence and mortality worldwide for 36 cancers in 185 countries," *CA: A cancer Journal for Clinicians*, vol. 68, no. 6, pp. 394–424, 2018.
- [2] A. Hamidinekoo, E. Denton, A. Rampun, K. Honnor, and R. Zwiggelaar, "Deep learning in mammography and breast histology, An overview and future trends," *Medical Image Analysis*, vol. 47, pp. 45-67, 2018.
- [3] M. N. Gurcan, L. E. Boucheron, A. Can, A. Madabhushi, N. M. Rajpoot, and B. Yener, "Histopathological image analysis: A review," *IEEE Reviews in Biomedical Engineering*, vol. 2, pp. 147-171, 2009.
- [4] N. Coudray, P. S. Ocampo, T. Sakellaropoulos, N. Narula, M. Snuderl, D. Fenyö, and A. Tsirigos, "Classification and mutation prediction from non-small cell lung cancer histopathology images using deep learning," *Nature Medicine*, vol. 24, no. 10, pp. 1559-1567, 2018.
- [5] K. Sirinukunwattana, S. E. A. Raza, Y. W. Tsang, D. R. Snead, I. A. Cree, and N. M. Rajpoot, "Locality sensitive deep learning for detection and classification of nuclei in routine colon cancer histology images," *IEEE Transactions on Medical Imaging*, vol. 35, no. 5, pp. 1196-1206, 2016.
- [6] T. Majtner, S. Yildirim-Yayilgan, and J. Y. Hardeberg, "Combining deep learning and hand-crafted features for skin lesion classification," *IEEE 6th International Conference on Image Processing Theory, Tools and Applications, IPTA'16*, pp. 1-6, 2016.
- [7] N. Hatipoglu and G. Bilgin, "Cell segmentation in histopathological images with deep learning algorithms by utilizing spatial relationships," *Medical & Biological Engineering & Computing*, vol. 55, no. 10, pp. 1829-1848, 2017.
- [8] K. Guzel and G. Bilgin, "Textural feature extraction and ensemble of extreme learning machines for hyperspectral image classification," *IEEE 26th Signal Processing and Communications Applications Conference, SIU'18*, pp. 1-4, 2018.
- [9] N. Dalal and B. Triggs, "Histograms of oriented gradients for human detection," *International Conference on Computer Vision and Pattern Recognition, CVPR'15*, vol. 2, pp. 886–893, 2005.
- [10] D. A. Clausi and M. E. Jernigan, "Designing Gabor filters for optimal texture separability," *Pattern Recognition*, vol. 33, no. 11, pp. 1835–1849, 2000.
- [11] A. Abbas, T. Zehra, and F. Li, "Object detection in a cluttered scene using SURF for computer assisted histopathology," *International Conference on Electrical, Mechanical and Industrial Engineering*, Atlantis Press, 2016.

- [12] A. Albayrak and G. Bilgin, "Automatic cell segmentation in histopathological images via two-staged superpixel-based algorithms," *Medical & Biological Engineering & Computing*, vol. 57, no. 3, pp. 653–665, 2019.
- [13] A. F. Spanhol et al., "Deep features for breast cancer histopathological image classification," *IEEE International Conference on Systems, Man, and Cybernetics, SMC'17*, pp. 1868-1873, 2017.
- [14] K. Guzel and G. Bilgin, "Classification of nuclei in colon cancer images using ensemble of deep learned features," *IEEE Medical Technologies Congress, TipTekno'19*, pp. 1–4, 2019.
- [15] Y. S. Vang, Z. Chen, and X. Xie, "Deep learning framework for multi-class breast cancer histology image classification," *International Conference Image Analysis and Recognition, ICIAR'18*, pp. 914-922, 2018.
- [16] Z. Yang, L. Ran, S. Zhang, Y. Xia, and Y. Zhang, "EMS-Net: Ensemble of multiscale convolutional neural networks for classification of breast cancer histology images," *Neurocomputing*, pp. 46-53, 2019.
- [17] F. Ponzio, E. Macii, E. Ficarra and S. Di Cataldo, "Going deeper into colorectal cancer histopathology," *International Joint Conference on Biomedical Engineering Systems and Technologies, BIOSTEC'18*, pp. 114-131, 2018.
- [18] L. Nanni, S. Ghidoni, and S. Brahmam, "Ensemble of convolutional neural network for bioimage classification," *Applied Computing and Informatics*, 2018.
- [19] M. Talo, "Automated classification of histopathology images using transfer learning," *Artificial Intelligence in Medicine*, vol. 101, no. 101743, 2019.
- [20] C. Li et al., "Cervical histopathology image classification using ensembled transfer learning," *International Conference on Information Technologies in Biomedicine, ITIB'19*, pp. 26-37, Springer, Cham, 2019.
- [21] B. Harangi, "Skin lesion classification with ensembles of deep convolutional neural networks," *Journal of Biomedical Informatics*, vol. 86, pp. 25–32, 2018.
- [22] K. Simonyan and A. Zisserman, "Very deep convolutional networks for large-scale image recognition," *arXiv preprint arXiv:1409.1556*, 2014.
- [23] K. He, X. Zhang, S. Ren, and J. Sun, "Deep residual learning for image recognition," *IEEE Conference on Computer Vision and Pattern Recognition, CVPR'16*, pp. 770–778, 2016.
- [24] L. Liu, C. Shen, and A. van den Hengel, "The treasure beneath convolutional layers: Cross-convolutional-layer pooling for image classification," *IEEE Conference on Computer Vision and Pattern Recognition, CVPR'15*, pp. 4749–4757, 2015.
- [25] L. I. Kuncheva and J. J. Rodríguez, "A weighted voting framework for classifiers ensembles," *Knowledge and Information Systems*, vol. 38, no. 2, pp. 259–275, 2014.
- [26] J. Sill, G. Takács, L. Mackey, and D. Lin, "Feature-weighted linear stacking," *arXiv preprint arXiv:0911.0460*, 2009.
- [27] F. A. Spanhol, L. S. Oliveira, C. Petitjean, and L. Heutte, "A dataset for breast cancer histopathological image classification," *IEEE Transactions on Biomedical Engineering*, vol. 63, no. 7, pp. 1455–1462, 2015.
- [28] T. L. Sellaro, R. Filkins, C. Hoffman, J. L. Fine, J. Ho, A. V. Parwani, and M. Montalto, "Relationship between magnification and resolution in digital pathology systems," *Journal of Pathology Informatics*, vol. 4, 2013.

- [29] M. L. Giger and K. Suzuki, "Computer-aided diagnosis," *Biomedical Information Technology*, Academic Press, pp. 359-XXII, 2008.
- [30] F. Chollet, "Keras: The python deep learning library," *Astrophysics Source Code Library*, 2018.
- [31] F. Pedregosa, et al. "Scikit-learn: Machine learning in Python," *Journal of machine learning research*, vol.12, pp. 2825-2830, 2011.
- [32] M. Abadi, et al. "Tensorflow: A system for large-scale machine learning," *12th USENIX Symposium on Operating Systems Design and Implementation, OSDI'16*, pp. 265-283, 2016.
- [33] N. Bayramoglu, J. Kannala, and J. Heikkilä, "Deep learning for magnification independent breast cancer histopathology image classification," *IEEE 23rd International Conference on Pattern Recognition, ICPR'16*, pp. 2440-2445, 2016.
- [34] S. H. Kassani, P. H. Wesolowski, M. J. Schneider, and K. A. Deters, "Classification of histopathological biopsy images using ensemble of deep learning networks," *arXiv preprint arXiv:1909.11870*, 2019.
- [35] D. M. Vo, N. Q. Nguyen, and S. W. Lee, "Classification of breast cancer histology images using incremental boosting convolution networks," *Information Sciences*, vol. 482, pp. 123-138, 2019.
- [36] M. Z. Alom, C. Yakopcic, M. S. Nasrin, T. M. Taha, and V. K. Asari, "Breast cancer classification from histopathological images with inception recurrent residual convolutional neural network," *Journal of Digital Imaging*, vol. 32, no. 4, pp. 605-617, 2019.
- [37] F. A. Spanhol, L. S. Oliveira, C. Petitjean, and L. Heutte, "Breast cancer histopathological image classification using convolutional neural networks," *IEEE International Joint Conference on Neural Networks, IJCNN'16*, pp. 2560-2567, 2016.
- [38] Z. Han, B. Wei, Y. Zheng, Y. Yin, K. Li, and S. Li, "Breast cancer multi-classification from histopathological images with structured deep learning model," *Scientific Reports*, vol. 7, no. 1, pp. 1-10, 2017.
- [39] Z. Gandomkar, P. C. Brennan, and C. Mello-Thoms, "MuDeRN: Multi-category classification of breast histopathological image using deep residual networks," *Artificial Intelligence in Medicine*, vol. 88, pp. 14-24, 2018.
- [40] R. Mehra, "Breast cancer histology images classification: Training from scratch or transfer learning?," *ICT Express*, vol. 4, no. 4, pp. 247-254, 2018.
- [41] C. Zhu, F. Song, Y. Wang, H. Dong, Y. Guo, and J. Liu, "Breast cancer histopathology image classification through assembling multiple compact CNNs," *BMC Medical Informatics and Decision Making*, vol. 19, no. 1, pp. 198, 2019.
- [42] A. Kumar, S. K. Singh, S. Saxena, K. Lakshmanan, A. K. Sangaiah, H. Chauhan, and R. K. Singh, "Deep feature learning for histopathological image classification of canine mammary tumors and human breast cancer," *Information Sciences*, vol. 508, pp. 405-421, 2020.

JOURNAL OF SCIENCE



SAKARYA UNIVERSITY

Sakarya University Journal of Science

ISSN 1301-4048 | e-ISSN 2147-835X | Period Bimonthly | Founded: 1997 | Publisher Sakarya University |
<http://www.saujs.sakarya.edu.tr/en/>

Title: Ontology-based Instantaneous Route Suggestion of Enemy Warplanes with Unknown Mission Profile

Authors: Emre ÇİNTAŞ, Barış ÖZYER, Y. Sinan HANAY

Received: 2020-03-30 01:43:02

Accepted: 2020-06-16 10:19:27

Article Type: Research Article

Volume: 24

Issue: 5

Month: October

Year: 2020

Pages: 803-818

How to cite

Emre ÇİNTAŞ, Barış ÖZYER, Y. Sinan HANAY; (2020), Ontology-based Instantaneous Route Suggestion of Enemy Warplanes with Unknown Mission Profile. Sakarya University Journal of Science, 24(5), 803-818, DOI:

<https://doi.org/10.16984/saufenbilder.711109>

Access link

<http://www.saujs.sakarya.edu.tr/en/pub/issue/56422/711109>

New submission to SAUJS

<http://dergipark.org.tr/en/journal/1115/submission/step/manuscript/new>

Ontology-based Instantaneous Route Suggestion of Enemy Warplanes with Unknown Mission Profile

Emre ÇİNTAŞ^{*1,3}, Barış ÖZYER², Y. Sinan HANAY³

Abstract

The routes of warplanes are planned confidentially, and they are not shared with any organization in advance. In some cases, border violations may occur, and as a result, it increases the tension between two states. This situation puts many people at risk and impairs the prestige of the state both economically and socially. In this paper, Ontology-Based Instantaneous Route Suggestion System (SUARSIS) based on semantic approach is proposed to predict and plan routes of warplanes before they reach their target. In the proposed system, we developed an architecture called Ontology-based Route Suggestion by using the OWL (Web Ontology Language) language with realistic data. The aircraft model, aircraft fuel system, features of the military field, and the relations in the semantic context are logically defined through ontology. Synthetic scenarios were created to validate the accuracy of the proposed method. Experimental results show that the proposed system has a good performance on predicting warplane routes.

Keywords: Route suggestion system, semantic web, ontology, intelligent search engines, warplanes

1. INTRODUCTION

Aircraft follow predetermined routes in flight around the world. States share their airspace data with the International Civil Aviation Organization (ICAO) and the European Organization for the Safety of Air Navigation (EUROCONTROL). The headquarters of ICAO is in Montreal, Canada, and the headquarters of EUROCONTROL is located in Brussels, Belgium. Each country defines short, medium, and long-term flight strategies, developing the set

routes based on the intended use of the aircraft. Predetermined trajectories are registered in aircraft radar systems, allowing for individual users to track these predetermined aircraft routes via respective web applications [1]. However, it requires a completely different procedure for warplanes. Routes of warplanes are not shared with other countries, keeping them confidential to protect the political, social, and economic interests of individual countries and to ensure security.

*Corresponding Author: emrecintas@atauni.edu.tr

¹Atatürk University, Department of Computer Engineering, Erzurum, Turkey.

ORCID: <https://orcid.org/0000-0002-4954-5816>

²Atatürk University, Department of Computer Engineering, Erzurum, Turkey. E-Mail: baris.ozyer@atauni.edu.tr,

ORCID: <https://orcid.org/0000-0003-0117-6983>

³Erzurum Technical University, Department of Computer Engineering, Erzurum, Turkey. E-Mail: sinan.hanay@erzurum.edu.tr, ORCID: <https://orcid.org/0000-0002-3331-5936>

A warplane may change its regular and predetermined routes, violating the borders of neighboring countries even under conditions other than special ones like terror and war. A border violation may provoke international tension in countries sensitive to geopolitical fluctuations. A critical step in analyzing the tension to determine whether the act is intentional. In this paper, our goal is to estimate warplane routes based on semantic rules and ontology. In this context, very limited and irregular ontologies are developed in the military domain [2]. To the best of our knowledge, there is no research in the literature based on the ontology and semantic approach to estimate the routes of enemy warplanes according to aircraft propellant model and maximum range calculations and suggest routes. In this study, we have proposed a real warplane ontology database by using real-world military data. We have developed a platform-independent application; which predicts flight routes (PFR) and proposes flight routes (PRFR) by using the ontology data.

The main objective of a semantic web [3] study is to create ontologies specific to the field of study and to ensure their utilization in information systems. Ontologies allow the machines to interpret knowledge in a manner understandable to humans, facilitating communication among people. The basic objective of the ontology development is to create a common dictionary, serving for information sharing in a specific field. Much research on ontology in the healthcare domain has been studied in the literature during the last decades [4]. Ontologies developed in the healthcare field are used in making diagnoses, offering preventive measures, and recommending proper foodstuff relevant for particular diseases [5]. According to Çelik's research project on mobile safe food consumption system (FoodWiki) [5], it is discussed that it performs its inference semantic rules in its knowledge base. The developed rules examine the side effects that are causing some health risks: heart disease, diabetes, allergy, and asthma as initial. In another research [6] a semantic-based information extraction system was proposed to match resumes with business areas. The system planned to operate on several million free-format textual

resumes to convert them to a semantically enriched version.

On the other ontology research, Samperetal [7] use ontologies to associate traffic information, and support users with visualization and search tasks. They define a road traffic ontology, covering vehicle and road classifications, geography, location, people, events, and routes. Recently, the semantic web using for products such as Good Relation ontology [8], CEO (Consumer Electronics Ontology), and onto Product [9]. Product Types Ontology provides approximately 300,000 precise definitions for product types or services that extend the schema.org and Good Relations. Another large ontology knowledge bases have been created including DBpedia [10], Freebase [11], YAGO [12], Wikidata [13], NELL [14] and the Google Knowledge Graph [15]. Although they use different data formats to represent their data, most use an ontology graph structure.

Syntactic methods which do not have any semantic rules have been carried out in autonomous systems to estimate the route plans in the literature for several years. Tracking, estimation, and calculating the shortest route for aircraft or unmanned air vehicles are some popular studies interested by researchers [16-17-18]. In these studies, the well-known Potential Field Algorithm, Probabilistic Route Planning, Voronoi Diagrams, and Searching Algorithms have been implemented [19-20]. Coefficient rules and ant colony optimization algorithms were used to offer solutions for route planning problems [21-22] have combined genetic algorithms with local search heuristics in their study to determine the shortest route between two points in Turkey, covering destinations all over 81 provinces in the country [22]. Analyzing large data sets, Kasturi et al. (2016) [23] have determined key criteria for the aircraft and set new route plans. Data about the aircraft load, passengers, and airports were used for determining the key criteria. Bakhtyar and Holmgren (2015) [24] achieved to estimate new routes at a high level of precision based on the data of the previously used routes by mobile objects. Different from the studies in literature, we have utilized the semantic inference

techniques instead of syntactic methods in our study. In our approach, we tested our scenarios to estimate possible routes of virtual enemy warplanes before they reached their destination. The studies in the literature address the aircraft with fully or partially known mission profiles only. Furthermore, no studies utilizing a semantic approach have been found in the literature, studying how to estimate the routes and destinations of an enemy warplane (EW) with an unknown mission profile and no studies have examined the best methods to propose new routes to pilots in the decision-making process.

Being motivated with these issues in mind; we propose an ontology-based, platform-independent system, called “Instantaneous Route Suggestion System for Warplanes” (SUARSIS). The system is based on semantic search and semantic inference techniques [3]. This proposed system has the following contributions given as below:

- A new real aircraft ontology database based on semantic rules was developed. In this database, propellant forces, aerodynamic parameters, flight range equations, manufacture values, and arms capacity of warplanes were used to develop the ontology and SWRL (Semantic Web Rule Language) rules.
- We propose an algorithm that analyzes the data obtained from the ontology and then it finds the possible routes of enemy aircraft to stakeholders.
- We developed a unique platform-independent SUARSIS software application using the Secondo system to simulate the estimated routes.

The rest of the paper is organized as follows. The details of the proposed SUARSIS system, ontology methods, SWRL rules, and algorithms are described in Section 2. Section 3 shows the experimental results of the proposed approach. Lastly, we conclude and discuss potential future directions for our study.

2. PROPOSED SUARSIS DESIGN

In the proposed SUARSIS application system, at first, we developed an ontology to be used in the field of warplane and military to suggest possible routes of the plane from databases. Then, we combined the ontology with Semantic Web techniques using OWL 2.0. The proposed system includes three main phases given as below:

- 1. Aircraft Ontology Knowledge Base:** The system uses the ontology, to obtain all data about a selected EW in the selected scenario. Then, it searches the manufacturer specifications of that EW in the aircraft ontology. The ontology estimates and proposes the remaining amount of propellant in the aircraft along with its maximum flight range based on predefined semantic rules, concepts, and associations in the ontology. Proposed values are instantly transferred to the SUARSIS system.
- 2. Suggestion Algorithm:** The algorithm intelligently analyzes the data obtained from the ontology along with the proposed data. Then, it proposes the possible routes of the EW to the relevant stakeholders. This set of information provides guidance to the pilot, the navigation officer, and the security intelligence units in tracking the proposed routes, making a decision, and obtaining counter-intelligence.
- 3. Simulation with Secondo:** SUARSIS uses the platform-independent Secondo system to simulate proposed routes and provides them to stakeholders.

Synthetic scenarios for the ontology are generated in the proposed system to be used in a potential state of border violation. Manufacturer specifications of enemy warplanes (i.e. bomb mass, maximum loading capacity, the wing surface area, wingspan, and engine characteristics) and the propellant model of the aircraft system (i.e. propellant consumption) are used to define semantic rules with a logic-based approach. The average velocity and altitude of the aircraft, which are received from the radar, are added as a parameter in the semantic rule. We assume that the radar parameters including latitude, longitude, direction measurements are changed instantaneously.

The Semantic Web (Web 3.0) approach is used for determining the semantic rules and relations in the ontology. The flowchart of the proposed

system is shown in Figure 1. The detailed information about the proposed model is provided in the following sections.

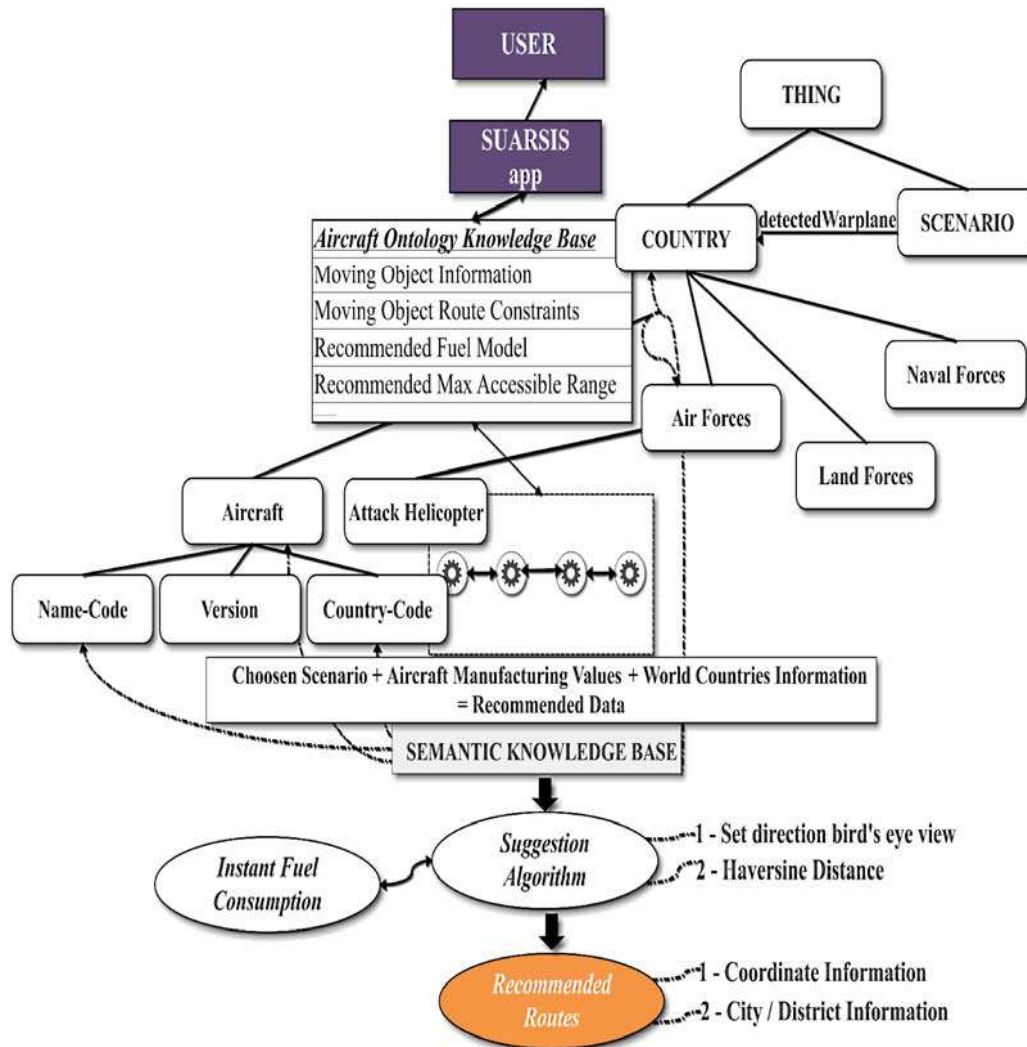


Figure 1 System working mechanism

2.1. Aircraft ontology knowledge-based and inference mechanism of the SUARSIS

Ontology is a new approach in information technologies to facilitate communication between people and allow interoperability computer systems. Also, ontologies aim to enable machines to understand the information in a manner interpreted by humans. In this context, we developed an authentic ontology database that comprises three main phases; semantic search, inference engine, and starting the engine as shown

in Figure 2. In the semantic search phase, manufacture information of detected warplane is specified. These data are then transferred to the inference engine. In the next inference engine phase which is the main contribution of the study, the semantic rules are created in the ontology. After running the inference engine, semantic information is obtained according to the semantic rules. These obtained rules are transferred into the starting engine. In the last phase, the suggestion algorithm suggests aircraft routes that are simulated with SECONDO.

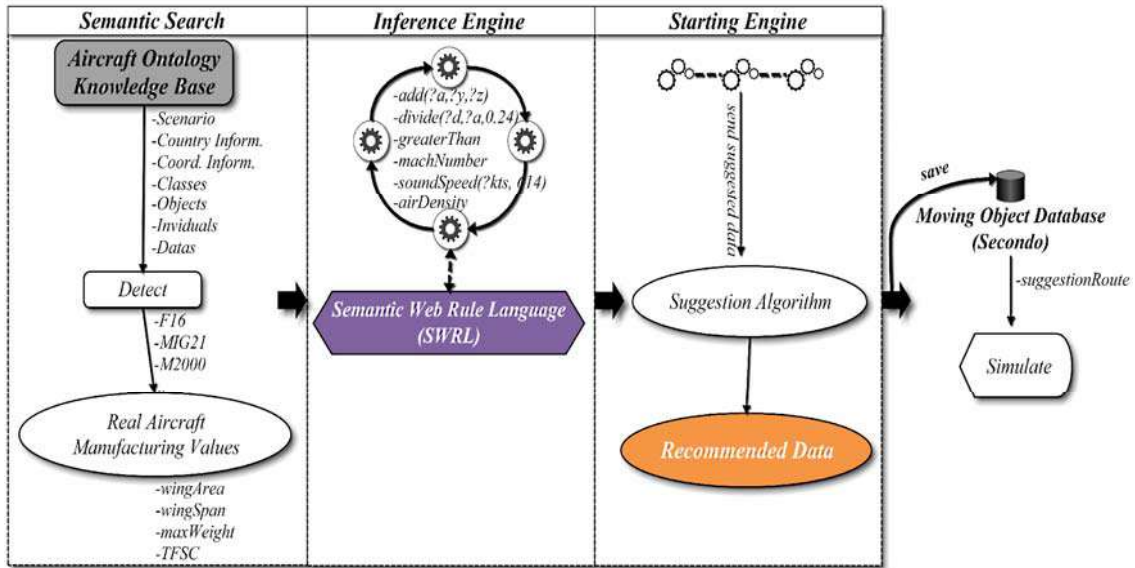


Figure 2 Semantic search, inference engine, and starting engine are the stages of developing an ontology knowledge base

The structure of the aircraft ontology and its respective semantic rules were developed in Semantic Web Rule Language (SWRL) which is a robust and deductive rule definition language [25] and Protégé (<https://protege.stanford.edu/download>) editor by using OWL2.0 web ontology language programming.

The semantic aircraft context are described in the aircraft ontology using OWL semantic tags such as <owl: class> <rdfs: subclassOf>, < owl: DatatypeProperty> and <owl: ObjectProperty> as semantic data contexts. Table 1 shows **80 concepts** and **246 components** in the aircraft ontology using OWL 2.0 web language such as "Country ", "City ", "Airforces", " Landforces", "Navalforces", "Airport". For each concepts include sub-classes and properties. For instance, "Airforces" concept includes "Version", "ActivePieces", and "CountryName" sub-classes and "hasownAircrafts", "specificfuelConsumptionofAircraft", "isenemyAircraft ", "requiredfuel forTakeoff" properties. The aircraft ontological data is comprised of the propellant model of EW such as air density, the speed of sound, maximum range etc. As an example of defining aircraft ontological rule is given by:

If(aircraftInstantAltitude>=34000.00 OR aircraftInstantAltitude<35000.00)}->Case:soundSpeed -> AIRCRAFT ONTOLOGY suggests the "579 kts"

where recommend "soundSpeed" is set to 579 kts in the case of instant aircraft altitude range is measured between 34000 and 35000 feet. The SWRL form of this rule is described as follows:

Name- Code(?kts),aircraftInstantAltitude(?kts, ?z), greaterThanOrEqual(?z,"34000"),lessThan(? z,"35000")->soundSpeed(?kts,"579" xsd:double)

Semantic search is a searching process extracting relevant values of interest in all classes, components, and rules created in the ontology. At first, the user selects a synthetic scenario in the ontology. According to the selected scenario, EW's official manufacturer informations are then searched and retrieved from the ontology to transfer the inference engine. At this point, the proposed SUARSIS system infers in line with the components and relationships defined in the aircraft ontology. For obtaining meaningful information from the aircraft manufacturer specifications during the operation of the inference engine, semantic rules are determined according to the aerodynamic forces affecting the

Table 1
A small portion of aircraft ontology in OWL

```

<Ontology xmlns="http://www.w3.org/2002/07/owl#" >
xml:base=".../ontologies/routeOntology"
<Class IRI="#Country"/>
<Class IRI="#City"/>
<Class IRI="#Airforces"/>
<Class IRI="#Landforces"/>
<ObjectProperty IRI="#detectedAircraft"/>
<ObjectProperty IRI="#hasownAircrafts"/>
<DataProperty IRI="#isenemyAircraft"/>
<SubClassOf>
<Class IRI="#ActivePieces"/>
<Class IRI="#Airforces"/>
</SubClassOf>
<SubClassOf>
<Class IRI="#CountryName"/>
<Class IRI="#Airforces"/>
</SubClassOf>
<SubClassOf>
<Class IRI="#Type"/>
<Class IRI="#Airforces"/>
</SubClassOf>
<SubClassOf>
<Class IRI="#Aircraft"/>
<DataProperty IRI="#isenemyAircraft"/>
<Class IRI="#Name-Code"/>
</SubClassOf>
</Ontology>
    
```

fuel consumption and flight range [26-27-28]. Figure 3 depicts the aerodynamic force components affecting an aircraft on a sample aircraft.

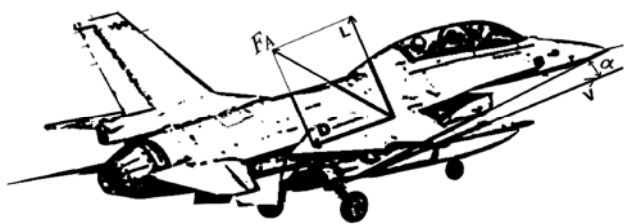


Figure 3 Aerodynamic force and components

F_A is the aerodynamic force resultant affecting a solid object calculated by,

$$F_A = q * S \tag{1}$$

where S refers to a reference surface area of the solid object and q refers to dynamic pressure and calculated with the below equation.

$$q = C_A \frac{P}{2} V^2 \tag{2}$$

where C_A is the dimensionless aerodynamic force coefficient comprising the effects of the angle of attack (α), the viscosity of air, the compressibility of the air, and the shape of the aircraft, P refers to the air density, V refers to the velocity of air flowing around the solid object. As seen in Figure 3, α is the angle of attack of the aircraft, L is the lift which is the component of the aerodynamic force perpendicular to the air velocity, D is the drag force of aerodynamic force that is the component parallel to the air velocity [26-27-28].

Accordingly, the magnitudes of the lift and drag forces are calculated with the equations below:

$$L = C_L \frac{P}{2} V^2 S \tag{3}$$

$$D = C_D \frac{P}{2} V^2 S \tag{4}$$

where C_L is the dimensionless carriage coefficient and C_D is the dimensionless drag coefficient. The inference engine takes all aerodynamic parameters and other drag parameters into consideration along with the fines parameter and the Oswald factor which is the wing efficiency factor. The estimated maximum flight distance is calculated by the information of the propellant system and the flight range that are specific to individual models of the warplane. Since the mission profile of an EW is not possible to be known in advance, we assume that three flight scenarios mainly adapted in real-world air transport are individually extracted with the semantic rule. These are extracted from the following three cases described as below;

1. Flight at a constant altitude with fixed lift coefficient,
2. Flight at constant velocity with fixed lift coefficient,
3. Flight at a constant altitude with a constant speed.

Algorithm 1 presents to calculate the maximum range of flight at a constant altitude with the fixed lift coefficient, defining the aerodynamic parameters and flight types in the ontology. Transactions regarding the motion of the aircraft at a constant velocity and fixed lift coefficient are shown in Algorithm 2. Pseudo-code of its flight at a constant speed and the constant altitude is shown in Algorithm 3. The calculation maximum range of multistage flights are shown in Algorithm 4. The Semantic rules based on the aerodynamic forces and algorithms are presented in Table 2.

In this stage, after obtaining information of all class hierarchy, data attributes, object attributes, and individually and semantically extracted data in the ontology are transferred to the starting engine using the OWL API [29] and Pellet API [30] libraries. For this purpose, we developed an interface developed in the Java environment to enable aircraft-related information retrieval from the ontology in SUARSIS.

2.2. Suggestion algorithm

The suggestion algorithm suggests aircraft routes by retrieving semantic associations between terms that enable the users to search semantically for any relevant information. Figure 4 depicts the flowchart of the suggestion algorithm. At first, semantic information is transferred from the starting engine. The aerial view of the aircraft is then determined in the direction of point coordinates in the world coordinate system. We assume that aircraft location is obtained in every 5 seconds. Fuel consumption and direction of aircraft are instantaneously obtained in the scenario. The next, instantaneous coordinates of EW are parametrically passed to the Haversine distance method [31], which is calculated by the following equation,

$$r = 2R \sin^{-1} \sqrt{\sin^2 \left(\frac{x_2 - x_1}{2} \right) + \cos(x_1) \cos(x_2) \sin^2 \left(\frac{y_2 - y_1}{2} \right)} \quad (5)$$

where, x_i and y_i refer to x and y coordinates of the point i, (x_1, y_1) is the starting point and (x_2, y_2) is the destination point in polar coordinate space. The world radius (R) is taken as 6,371 km. The distance between world coordinates and instantaneous coordinates of EW are then measured. At last, the algorithm suggests possible routes of the plane after comparing distance between the measured coordinates and the proposed flight range of EW.

3. EXPERIMENTAL RESULTS

The proposed SUARSIS system was developed with the Java programming language in Netbeans [32] editor. The proposed system initially requires the users (e.g. pilots etc.) to log in. Secondly, a synthetic scenario should be selected from the pilot. The system semantically searches the technical specifications of EW, radar data, the proposed fuel consumption, and flight range data in the aircraft ontology database. Finally, the SUARSIS system returns estimated route information based on inferential data. A synthetic scenario is given to describe the details of the proposed system

Algorithm 1. The maximum range of flight at a constant altitude with a fixed lift coefficient ($R_{max_{clcc}}$) pseudo-code

```

1:      entry Scenario, radar (routeAverageSpeeds, aircraftInstantAvgAltitude), ontology aircraft
manufacturing values
2:      output MaxRange
3:      rule set aircraftTotalAvgSpeed
4:      method
5:      define count=0
6:      while count<=1 do
7:      add(km/s, route1AvgSpeed)
8:      add(km/s, route2AvgSpeed)
9:      add(km/s, route3AvgSpeed)
10:     divide(aircraftTotalAvgSpeed, km/s,3)
11:     count++;
12:     endwhile
13:     rule set requiredFuelforTravel
14:     method
....    add(kg/requiredFuelforTakeoff, requiredFuelforLanding)
....    subtract(requiredFuelforTravel, kg, insideFuelVolume)
....    /*detect available fuel*/
17:     detect air density from standard atmosphere table
18:     method
....    if aircraftAverageAltitude greaterThanorEqual(20000ft) and lessThan(21000ft) then
airDensity, SET 0.5328 kg/m^3
46:     rule  $C_{D0}$  find dimensionless drag coefficient
47:     method
....    if M greaterThanOrEqual(0) and lessThan(0.8) then /*M (mach) number*/  $C_{D0}$ , SET;
48:     0.014
....    K find the drag coefficient
....     $K = \frac{1}{\pi A_{Re}}$  and  $A_{Re} = \frac{b^2}{S}$ , SET;
....    /*K CAL, S:wing area*/
....     $W_0 = 9.81 * (maxtakeoffMass - requiredFuelforTakeoff)$ ,
....    CAL; /*mass*/
....     $V_{md_0} = (\frac{K}{C_{D_0}})^{1/4} \sqrt{\frac{2W_0}{\rho S}}$ 
....    CAL; /* min drag speed */
....     $E_{max} = \frac{1}{2\sqrt{K C_{D_0}}}$ ,
....    CAL; /* aircraft's max fines */
....     $f = \frac{W_F}{W_0}$ , CAL; /* fuel ratio */
....     $R_{max_{clcc}} = \frac{3^4}{c} V_{md_0} E_{max} (1 - \sqrt{1-f})$ , CAL; /* max range*/
67:     END

```

Algorithm 2. The maximum range of flight at constant velocity with a fixed lift coefficient ($R_{max_{cvcc}}$) pseudo-code

```

1:      entry  $V_{md_0}, E_{max}$ 
2:      output MaxRange
3:      begin
4:      calculate
....     $R_{max_{cvcc}} = \frac{3^4}{2c} V_{md_0} E_{max} \ln(\frac{1}{1-f})$ , CAL;
5:      /* max range */
6:      END

```

Algorithm 3. The maximum range of Flight at a constant altitude with a constant speed ($R_{max_{crcl}}$) pseudo-code.

```

1:   entry  $Vmd_0, E_{max}$ 
2:   output MaxRange
3:   begin
4:   calculate
            $R_{max_{crcl}} = \frac{3^{\frac{3}{4}}}{2c} Vmd_0 E_{max} \left( \frac{f}{(1-f)^{1/4}} \right),$ 
5:   CAL; /* max range */
6:   END

```

Algorithm 4. The maximum range of flight cascade travel ($R_{max_{ct}}$) pseudo-code.

```

1:   entry  $Vmd_0, E_{max}$ 
2:   output MaxRange
3:   begin
4:   calculate
            $R_{max_{ct}} \cong \frac{R_{max_{clcc}} + R_{max_{cvcc}} + R_{max_{crcl}}}{3},$ 
5:   CAL;
6:   END

```

Table 2

A cross-section of the SWRL rules defined during the preparation of the semantic web rule base

-
- (1) Name-Code(?kg), requiredFuelForTakeoff(?kg, ?y1), requiredFuelForLanding (?kg, ?y2), insideFuelVolume (?kg, ?y3), add(?a, ?y1, ?y2), subtract(?s, ?y3, ?a) -> requiredFuelforTravel (?kg, ?s)
 - (2) Name-Code(?kgm3), aircraftInstantAltitude(?kgm3, ?z), greaterThanOrEqual(?z, "20000"^^xsd:double), lessThan (?z, "21000"^^xsd:double) -> airDensity(?kgm3, "0.5328"^^xsd:double)
 - ...
 - (11) Name- Code(?kts), aircraftInstantAltitude (?kts, ?z), greaterThanOrEqual(?z, "34000"^^xsd:double), lessThan(?z, "35000"^^xsd:double) -> soundSpeed(?kts, "579"^^xsd:double)
 - ...
 - (20) Name-Code(?m), AircraftTotalAvgSpeed (?m, ?z), divide(?d1, ?z, "1.852"^^xsd:double), soundSpeed(?m, ?sh), divide (?d2, ?d1, ?sh) -> machNumber(?m, ?d2)
 - ...
 - (35) Name-Code(?x), dragCoefficient (?x, ?k), dimensionlessDragCoefficient (?x, ?bs), aircraftWeightBeforeTakeoff (?x, ?sba), airDensity(?x, ?hy), aircraftWingArea(?x, ?uca), divide(?dvd, ?k, ?bs), multiply(?ml, ?sba, 2), multiply(?ml2, ?hy, ?uca), divide(?dvd2, ?ml, ?ml2), pow(?sq, ?dvd, "0.25"^^xsd:double), pow(?sq2, ?dvd2, "0.5"^^xsd:double), multiply(?ml3, ?sq, ?sq2, "3.6"^^xsd:double), divide(?dvd3, ?ml3, "1.852"^^xsd:double) -> mininumDragSpeed(?x, ?dvd3)
 - ...
 - (76) Name-Code(?x), maxRangeConstantLevelwithFixedCarriageCoefficientofAircraft (?x, ?rmax1), maxRangeConstantVelocitywithFixedCarriageCoefficientofAircraft (?x, ?rmax2), maxRangeConstantRatewithConstantLevel (?x, ?rmax3), add(?a, ?rmax1, ?rmax2, ?rmax3), divide(?dvd, ?a, 3) -> remainingRangeCascadingFlight(?x, ?dvd)
-

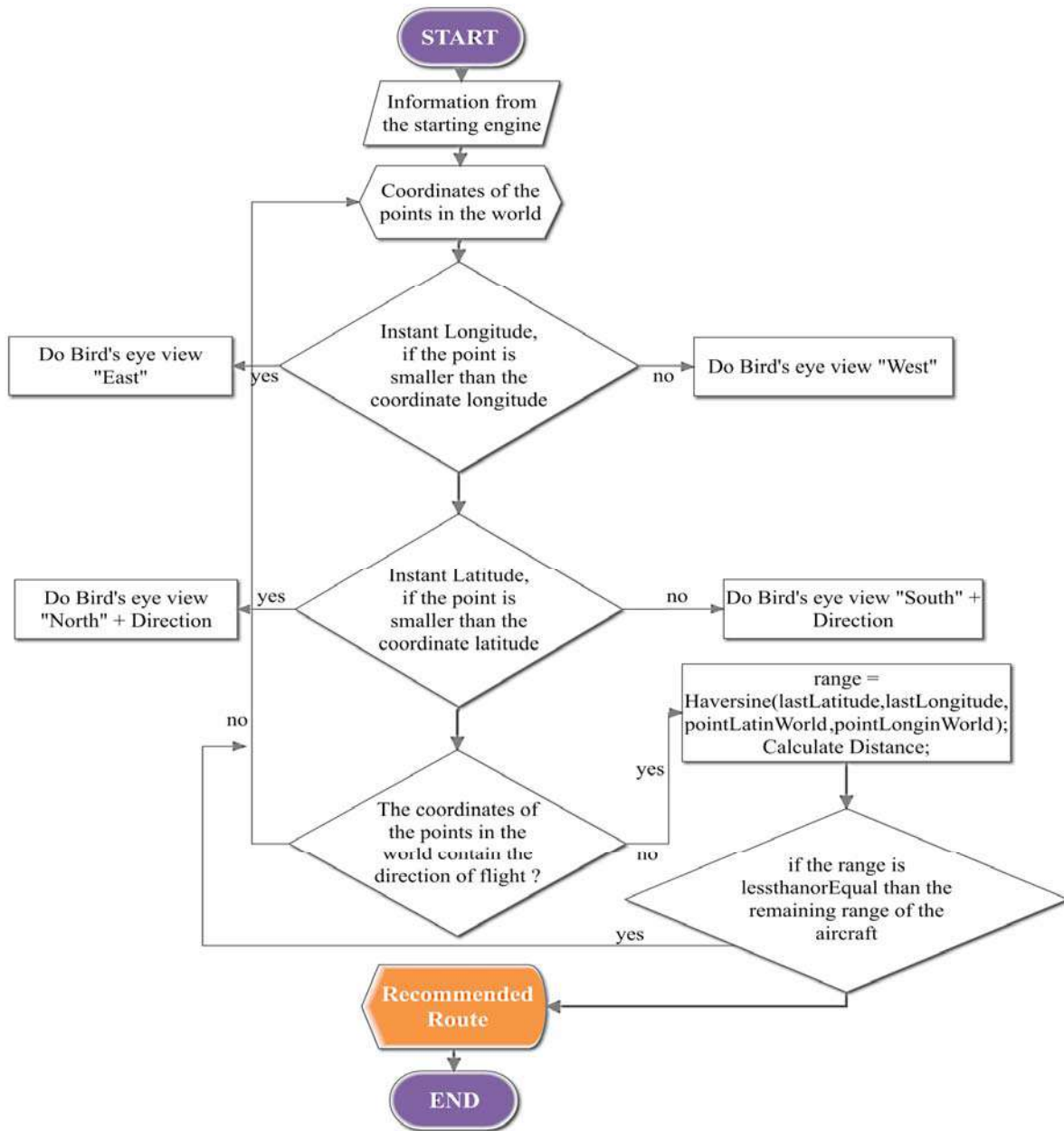


Figure 4 Flowchart of the suggestion algorithm

3.1. Scenario: Airspace Border violation between Syria and Turkey

We assume that the airspace border violation is noted between Syria and Turkey. The following assumptions are defined in the scenario:

1. A Syrian MIG-21/BIS model EW takes off near Aleppo starts and moves towards to Kilis without using the afterburner. The aircraft flies into the Turkey borders and violates Turkey airspace in a short period of time. Then, the

aircraft returns and lands to Aleppo without refueling.

2. The aircraft engines run during their stay on the runway. Then the aircraft takes off again, flying towards the Turkish border.

3. Weather conditions are suitable for the takeoff and landing of the aircraft.

The fighter pilot initially logs into his account, using his or her private password in the SUARSIS system. The SUARSIS system suddenly detects a Syrian MIG- 21/BIS heading towards ‘Northeast’

after taking off from Aleppo. The real-world manufacturer specifications of this warplane are semantically searched in the ontology as seen in Table 1. The extracted semantic data is inferred with SWRL. The rules are then instantaneously transferred to the SUARSIS system. The radar parameters are added to these rules. The SUARSIS system suggests possible routes of the aircraft considering the remaining fuel of the

aircraft when the “suggestion algorithm” runs. The maximum distance that the aircraft would fly with the remaining fuel is estimated based on SWRL rules and radar parameters. Since the result of the suggestion, the algorithm is dependent on the radar parameter, the accuracy of the suggestion algorithm is slightly decreased under the assumption that the radar data is immediately lost.

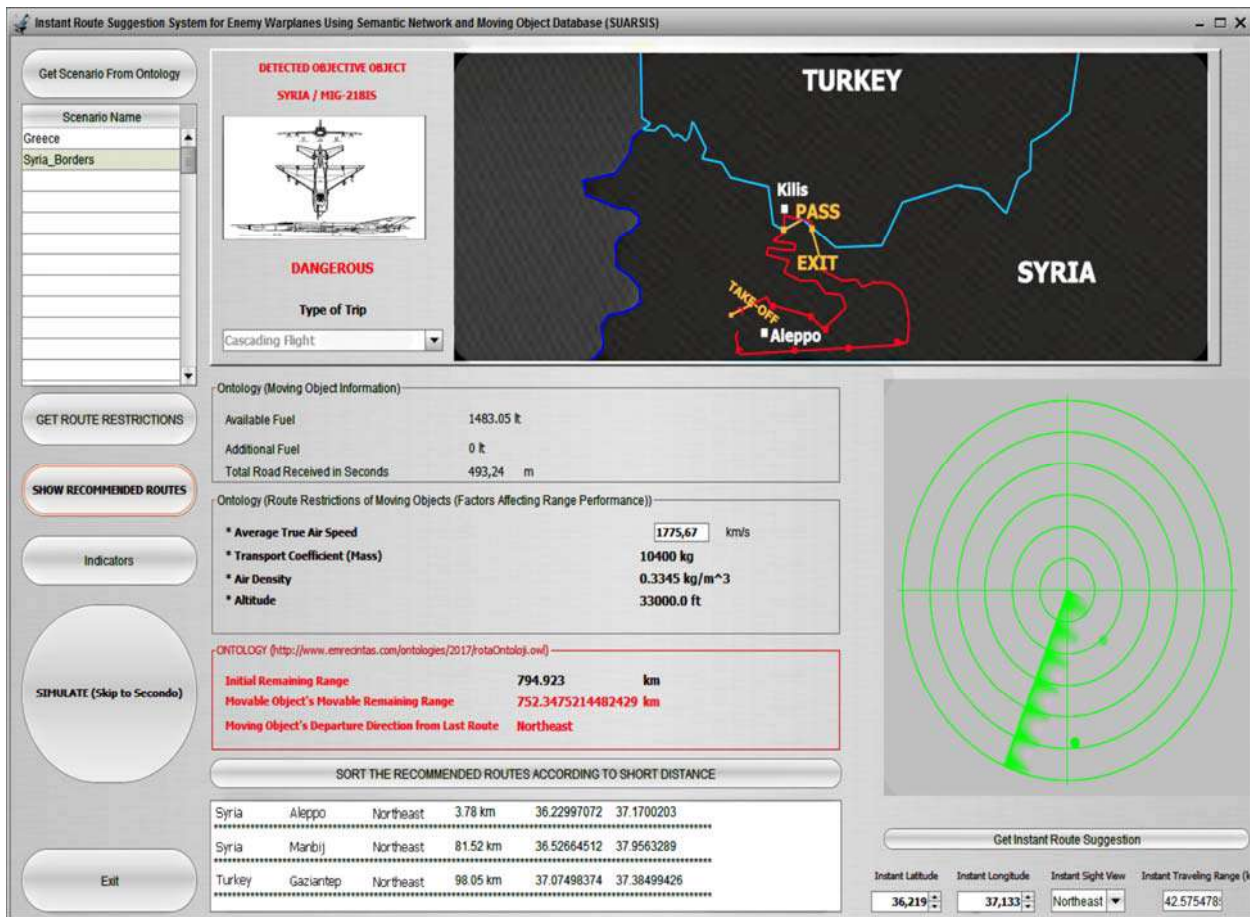


Figure 5 Estimated routes proposed to the pilot/navigation officer

Figure 5 depicts an example of a visualization of the proposed SUARSIS system. The route followed by aircraft is displayed on the screen.

The fighter pilot clicks the ‘Show Recommended Routes’ button, which will provide the estimations based on the technical data about EW. The inferential rules in Table 2 are used for finding the possible routes of MIG-21/BIS EW. The possible routes of EW are displayed on the screen of the SUARSIS system based on the

inferential data transferred to and analyzed by the suggestion algorithm Table 3. Using the data displayed on the screen, the pilot responds to the incident in coordination with his stakeholders. Consequently, necessary measures are taken via the counter-intelligence method before EW accomplishes the respective route. SUARSIS Node (0) represents the instant position of EW. SUARSIS Node (1), (2), (3) represents 3 different possible routes of EW.

Table 3
The results of the suggestion algorithm in the Syria boundaries scenario

SUARSIS Node	Country	Place	Direction	Remaining Distance (km)	Latitude	Longitude
(0)	Aircraft Instant Position	Aircraft Instant Position	Northeast	-----	36.21702201	37.1310420
(1)	Syria	Aleppo	Northeast	3.78	36.22997072	37.1700203
(2)	Syria	Manbij	Northeast	81.52	36.52664512	37.9563289
(3)	Turkey	Gaziantep	Northeast	98.05	37.07498374	37.3849942
Average Working Time 1.8 (ms)						

Table 4 represents the closest route retrieved from the nearest neighbor algorithm considering the instantaneous altitude, longitude, direction of the last aerial viewpoint, and the remaining flight range. As shown in Table 4, the average working time is calculated as 3 ms. Suggestion tour has been found that from SUARSIS Node (1) to KNode 0 and from SUARSIS Node (3) to KNode 2. Also node queue is obtained as 1-2-3. The total

tour cost is obtained as 2.568. When the results obtained from the suggestion algorithm and nearest neighbor algorithm are compared, it is observed that even if the suggestion algorithm processes more data such as world coordinates, Haversine distance, and remaining flight range, the performance of average working time is better than the closest neighboring algorithm.

Table 4
Comparison of the results of the proposed algorithm in the Syrian borders scenario with the nearest neighbor algorithm

SUARSIS Node	Nearest Neighbor	Nearest Neighbor Distance (km)
(0)	KNode 3	0.894
(1)	KNode 0	0.041
(2)	KNode 1	0.840
(3)	KNode 2	0.791
Average Working Time 3 (ms)		

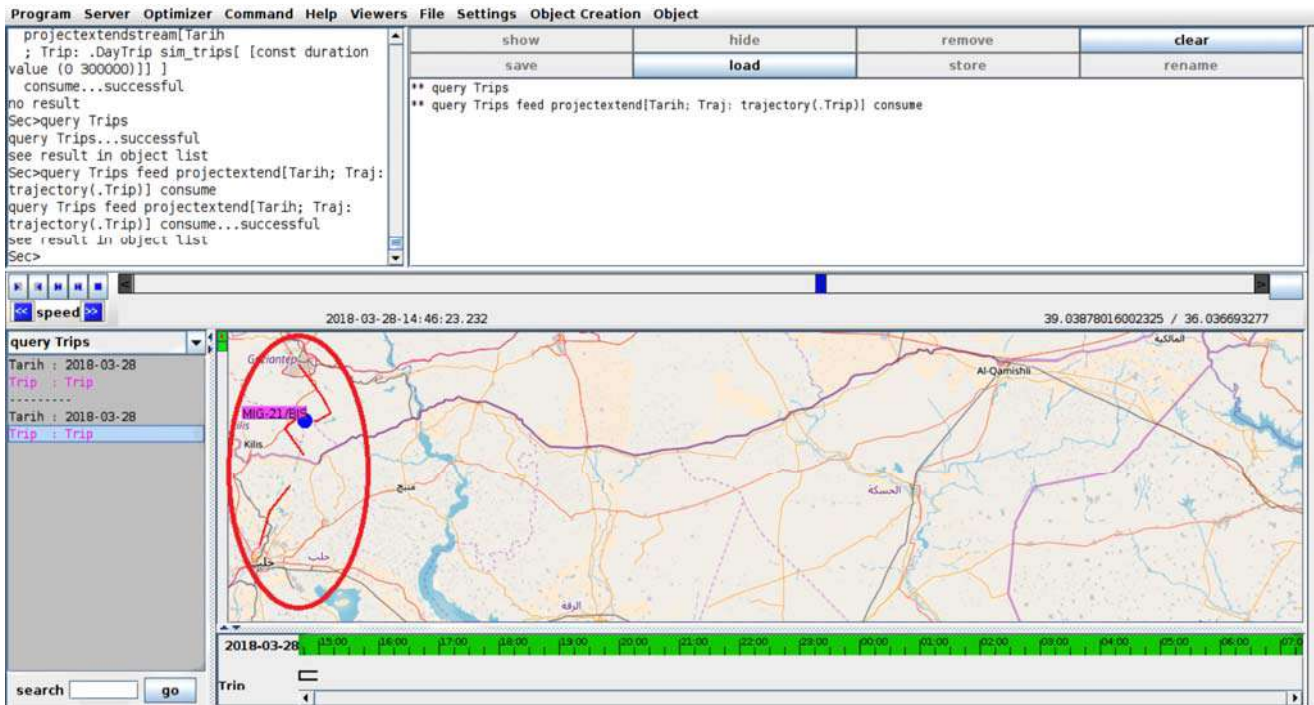


Figure 6 Simulation phase with Secondo

At the end, the routes suggested from the proposed SUARSIS system are simulated with Secondo shown in Figure 6.

4. CONCLUSION AND FUTURE WORK

In this study, we proposed a new platform-independent SUARSIS system that has been developed with the new generation Semantic Web Technology (Web 3.0). The main contribution of the system is to estimate possible routes for EW with an unknown mission profile based on the ontology and SWRL rules. The possible routes are estimated through the propellant model and the manufacturer specifications of EW along with radar data. The real data of aircraft such as the wing area, wingspan, engine type, reaction force of the engine, specific propellant consumption, the amount of propellant needed per flight, flight to propellant ratio, maximum take-off mass, propellant volume, bomb and arms mass, air density, gas constant, stall loss, and aerodynamic parameters are used to generate an authentic ontology and define SWRL rules. The proposed

system can distinguish the allying or enemy aircraft considering the country's information.

Synthetic scenarios are created to evaluate the performance of the proposed system. We assume that the airspace border violation has been noted on the southern border of Turkey. Semantic data of the aircraft based on the designed ontology are initially extracted. The proposed SUARSIS system produced synthetic radar parameters and observed its respective instantaneous changes. Possible routes of EW are then estimated after adding the radar measurements. In the case of the aircraft not detected in the radar and departure location is manually stored in the system, SUARSIS will automatically suggest the possible location of the aircraft through its path. It is observed that SUARSIS performs more accurately when the radar measurement can provide instant information to the system. The experimental results show that the proposed

system has satisfied the high success rate of the suggestion algorithm. In order to validate the accuracy of results, the proposed method is compared with the closest neighboring algorithm. We observed that while the success rate is similar in both algorithms, the operating time of the proposed method is better than the closest neighboring algorithm.

As a future work, real radar data is integrated into the SUARSIS system that provides to user enable the system dynamically in the real-world.

Funding

The authors received no financial support for the research, authorship, and/or publication of this paper.

The Declaration of Conflict of Interest/ Common Interest

No conflict of interest or common interest has been declared by the authors.

Authors' Contribution

EÇ: investigation, literature review, methodology, data analysis, simulation, writing-initial draft. BÖ: supervision, conceptualization, methodology, investigation, writing-revision and finalizing. YSH: supervision, conceptualization, methodology, design, writing-revision.

The Declaration of Ethics Committee Approval

The authors declare that this document does not require an ethics committee approval or any special permission.

The Declaration of Research and Publication Ethics

The authors of the paper declare that they comply with the scientific, ethical and quotation rules of SAUJS in all processes of the paper and that they do not make any falsification on the data collected. In addition, they declare that Sakarya University Journal of Science and its editorial

board have no responsibility for any ethical violations that may be encountered, and that this study has not been evaluated in any academic publication environment other than Sakarya University Journal of Science.

REFERENCES

- [1] Flightradar24 (2020). Live Flight Tracker [online]. Website <https://www.flightradar24.com> [accessed 09 January 2020].
- [2] Anonymous (2020). Military Ontology [online]. Website <http://rdf.muninn-project.org/ontologies/military.html> [accessed 02 February 2020].
- [3] T. Berners-Lee, J. Hendler and O. Lassila, "The Semantic Web," *Scientific American*, Vol. 284, No. 5, pp. 34-43, 2001.
- [4] J. Cantais, D. Dominguez, V. Gigante, L. Laera and V. Tamma, "An example of food ontology for diabetes control," In: *International Semantic Web Conference on Ontology Patterns for the Semantic Web*, Galway, Ireland, pp. 1-9, 2005.
- [5] D. Çelik Ertuğrul, "FoodWiki: A Mobile App Examines Side Effects of Food Additives via Semantic Web," *Journal of Medical Systems*, Vol. 40, No. 2, pp. 1-15, 2016.
- [6] D. Çelik, "Towards a semantic-based information extraction system for matching resumes to job openings," *Turkish Journal of Electrical Engineering & Computer Sciences*, Vol. 24, No. 1, pp. 141-159, 2016.
- [7] J. Samper, V. Tomas, J. Martinez and L. VandenBerg, "An ontological infrastructure for traveller information systems," In: *IEEE Intelligent Transportation Systems Conference (ITSC06)*, Toronto, Canada, pp. 1197-1202, 2006.

- [8] A. Gangemi and J. Euzenat, "GoodRelations: An ontology for describing products and services offers on the web," In: International Conference on Knowledge Engineering and Knowledge Management, Berlin, pp. 329-346, 2008.
- [9] J. Niderstigt, S.S. Aanen, D. Vandic and F. Frasincar, "Floppies: A framework for large-scale ontology population of product information from tabular data in E-commerce stores," Decision Support System, Vol. 59, No. 1, pp. 296-311, 2014.
- [10] C.B. Auer, G. Kobilarov, J. Lehmann, R. Cyganiak and Z. Ives, "DBpedia: A nucleus for a web of open data," In: 6th International Semantic Web Conference (ISWC), Berlin, pp. 722-735, 2007.
- [11] K. Bollacker, C. Evans, P. Paritosh, T. Sturge and J. Taylor, "Freebase: a collaboratively created graph database for structuring human knowledge," In: ACM SIGMOD International Conference on Management of Data, Canada, pp. 1247-1250, 2008.
- [12] G. W. F. M. Suchanek, "YAGO: a core of semantic knowledge," In: ACM 16th International Conference on World Wide Web, Banff, AB, Canada, pp. 697-706, 2007.
- [13] D. Vrandečić, "Wikidata: a new platform for collaborative data collection," In: ACM 21th International Conference on World Wide Web, Lyon, France, pp. 1063-1064, 2012.
- [14] J.B. Carlson, B. Kisiel, B. Settles, E.R. Hruschka and T. M. Mitchell, "Toward an architecture for never-ending language learning," In: Proceedings of the Twenty-Fourth AAAI Conference on Artificial Intelligence, Buenos Aires, Argentina, pp. 1306-1313, 2010.
- [15] M. Nickel, K. Murphy, V. Tresp and E. A. Gábrilovich, "A review of relational machine learning for knowledge graphs," In: Proceedings of the IEEE, pp. 11-33, 2016.
- [16] R. M. Nor, M. F. Ramli and M. H. Kharuddin, "Modeling and Simulation of Vehicle Routing Problem Based on Clustering Locations," Institute of Engineering Mathematics, Vol. 23, No. 5, pp. 4146-4148, 2017.
- [17] P. L. N. U. Cooray and T. D. Rupasinghe, "Machine Learning-Based Parameter Tuned Genetic Algorithm for Energy Minimizing Vehicle Routing Problem," Journal of Industrial Engineering, Vol. 2017, No. 2017, pp. 1-13, 2017.
- [18] M. A. Dramski, "Comparison between Dijkstra algorithm and simplified ant colony optimization in navigation," Scientific Journals, Vol. 29, No. 2012, pp. 25-29, 2012.
- [19] F. Scholer, "3D Path Planning for Autonomous Aerial Vehicles in Constrained Spaces," PhD, Aalborg University, Denmark, 2012.
- [20] X. Yang, M. Ding, C. Zhou and S. Shou, "Fast on-ship route planning using improved sparse A-star algorithm for UAVs," In: Proceedings of SPIE - The International Society for Optical Engineering, 2009.
- [21] G. Shang, Z. Lei, Z. Fengting and Z. Chunxian, "Solving Traveling Salesman Problem by Ant Colony Optimization Algorithm with Association Rule," In: Third International Conference on Natural Computation (ICNC2007), Haikou, China, pp. 693-698, 2007.
- [22] B. Özkan, U. Cevre and A. Uğur, "Melez Bir Eniyileme Yöntemi ile Rota Planlama," Akademik Bilişim Konferansı, Çanakkale, pp. 1-9 (in Turkish) 2008.
- [23] E. Kasturi, D. S. Prasanna, K. S. Vinu and S. Manivannan, "Airline Route profitability analysis and Optimization using BIG DATA analytics on aviation data sets under heuristic techniques," Procedia Computer Science, Vol. 87, No. 2016, pp. 86-92, 2016.
- [24] S. Bakhtyar and J. Holmgren, "A Data Mining Based Method for Route and

- Freight Estimation,” *Procedia Computer Science*, Vol. 52, No. 2015, pp. 396-403, 2015.
- [25] SWRL, “A Semantic Web Rule Language Combining OWL and RuleML,” W3C Member, Submission 21, 2004.
- [26] M. Cavcar, “Aerodinamik Kuvvetler Özet,” *Anadolu Üniversitesi*, (in Turkish) 2011.
- [27] M. Cavcar, “Seyahat Performansı - Menzil Özet,” *Anadolu Üniversitesi*, (in Turkish) 2014.
- [28] R.I. Martinez-Va and E. Perez, “Optimum cruise lift coefficient in initial design of jet aircraft,” *Journal of Aircraft*, Vol. 4, No. 1992, pp. 712-714, 1992.
- [29] M. Horridge and S. Bechhofer, “The OWL API: A Java API for OWL Ontologies,” *Semantic Web*, Vol. 1, No. 2011, pp. 11-21, 2011.
- [30] E. Sirin, B. Parsia, B. C. Grau, A. Kalyanpur and Y. Katz, “PELLET: A practical owl-dl reasoner, *Web Semantics: science, services and agents on the World Wide Web*,” *Journal of Web Semantics*, Vol. 5, No. 2007, pp. 51-53, 2007.
- [31] S. Hartanto, M. Furqan, U. P. A. Siahaan and W. Fitriani, “Haversine Method in Looking for the Nearest Masjid,” *International Journal of Engineering Research*, Vol. 3, No. 2017, pp. 187-195, 2017.
- [32] Netbeans (2020). Netbeans 8.2 IDE [online]. Website <https://netbeans.org/> [accessed 10 January 2020].

JOURNAL OF SCIENCE



SAKARYA UNIVERSITY

Sakarya University Journal of Science

ISSN 1301-4048 | e-ISSN 2147-835X | Period Bimonthly | Founded: 1997 | Publisher Sakarya University |
<http://www.saujs.sakarya.edu.tr/en/>

Title: Investigation of Beam Width Shaping of a Ku-band Horn Antenna using a Diffractive Optic Element and an Electromagnetic Wave Absorber

Authors: Ahmet TEBER

Received: 2020-04-25 21:21:40

Accepted: 2020-06-17 14:10:33

Article Type: Research Article

Volume: 24

Issue: 5

Month: October

Year: 2020

Pages: 819-831

How to cite

Ahmet TEBER; (2020), Investigation of Beam Width Shaping of a Ku-band Horn Antenna using a Diffractive Optic Element and an Electromagnetic Wave Absorber.

Sakarya University Journal of Science, 24(5), 819-831, DOI:

<https://doi.org/10.16984/saufenbilder.726905>

Access link

<http://www.saujs.sakarya.edu.tr/en/pub/issue/56422/726905>

New submission to SAUJS

<http://dergipark.org.tr/en/journal/1115/submission/step/manuscript/new>

Investigation of Beam Width Shaping of a Ku-band Horn Antenna using a Diffractive Optic Element and an Electromagnetic Wave Absorber

Ahmet TEBER ^{*1}

Abstract

The feasibility of beam-shaping of a Ku-Band horn as a transmitting (Tx) antenna by mounting two different versions of lenses which are kind of Fresnel Zone Plates (FZP) is studied. The designed and fabricated geometrical structures offer a simpler approach building Fresnel Zone Plates by using an electromagnetic wave absorber and diffractive optic material. The diffractive optic material, paraffin, forms a set of alternating open and opaque annular zones on a flat surface, based on the design principles of Fresnel Zone Plates. An electromagnetic wave absorber covers the top surface of the formed paraffin, but not including the grooves. Thereafter, the Fresnel Zone plates are suitably attached in front of the transmitter horn antenna, located in the far-field region of a receiving antenna. The half-power beam-widths for the horn antenna (unloaded) and with two types of lenses are investigated. The results indicate that Fresnel zone plate structures can play a role suppressing side lobes in H-plane so that the effective radiation is to be significantly concentrated.

Keywords: Beam-width, diffractive optic elements, electromagnetic wave absorber, Fresnel zone plates, horn antenna

1. INTRODUCTION

A Fresnel antenna incorporates a set of concentric annular zones called Fresnel zones [1-3]. Depending on the geometry and the fabrication material of Fresnel Zones, the Fresnel antenna can be classified as the Fresnel lens or Fresnel Zone Plates (FZPs). Unless the lens is very thin, a theoretical analysis of the Fresnel structure can complicate. Therefore, FZPs have been taking

place of the Fresnel lenses in recent years [4-8]. The applications of FZPs in millimeter/centimeter wave regions were uncommon in the past, because of their relatively low gain, controlling by shaping side/back lobes, in comparison with that of parabolic reflector antennas [2]. With advances in active devices, it is no longer a problem to increase the transmitted power and engineers have

* Corresponding Author: ahmetteber@bayburt.edu.tr

¹ Bayburt University, Department of Electricity and Energy, Bayburt, Turkey.
ORCID: <https://orcid.org/0000-0002-7361-2302>

been implementing different types of FZPs to deal with it.

Diffractive optic elements can be used for focusing (including focusing into an arbitrary area), filtration, polarization and formation, splitting and mixing of radiation beams in the GHz region [9-12]. In this work, paraffin wax is used as a diffractive optic material with low weight, high diffraction efficiency, high spatial resolution dictated by the diffraction limit, simple fabrication technology, and the feasibility of manufacturing FZPs on arbitrary surfaces. Other than that, Teflon which has a similar permittivity with paraffin, can be another diffractive optic material. But, it requires molding with a lathe workbench. Therefore, it is not preferred by us for this study. The other important part of the FZPs is electromagnetic wave absorbers (EMWAs), which have been used in various aerospace and defense applications [13-16]. In this study, manganese soft spinel ferrites blended with multi-walled carbon nanotubes as an EMWA were molded as toroid-shaped pellets with 1 mm thickness, suitable for the Ku-Band horn antenna aperture. The crystal structure, morphology, and magnetic nature of composites as well as the microwave absorption properties of the EMWA have been discussed in detail in our published works [14, 16]. The circular FZPs fit within the rectangular aperture of the antenna. According to the model of FZPs, either the odd-numbered zones or the even-numbered zones are covered with the absorbing material. When the even-numbered zones are covered with an absorbing material, there exists 180 degree phase correction. Odd-numbered zones are covered by the absorbing material in this study.

The horn antenna is utilized particularly at microwaves frequencies, yet straightforward antenna for many applications such as communication satellite antennas and radio telescopes etc. since they have no resonant elements. For a particular application of horn antenna, for example a ground-penetrating radar (GPR), antennas must achieve high gain, narrow beam, low side lobe and reflection characteristics over the wide band to attain the powerful and adequately shaped radiation [17]. In antenna

technologies, many claims about directivity of radar antennas, direction-finding equipment, indoor applications are for improving their side lobe performances [18]. The radiation patterns with the scenario of a far-field region on the horn antenna (unloaded) and the horn antenna with the absorbing material and diffractive optic element at the frequency of Ku-band are obtained. It was observed that there exists a reduction in both main lobe and side lobe levels due to the usage of absorber layer. This reduction was distributed as a portion in between the main lobe and side/rear lobes, causing the beam-width of antenna to be shaped. Another point that draws attention in this study is to attract attention to the fact that the beam-width of the antenna can be shaped with the help of absorber material. Therefore, the study suggests that absorbing material as thin layer can play a role on beamforming whereas controlling main and side/back lobes in Ku-band. In E-plane, the main lobe of the horn antenna loaded with the absorbing layer and a diffractive optic element is decreased whereas side lobes are increased when there are no significant changes on rear lobes at all frequencies that is measured. According to the angles of two orthogonal planes, the elevation angles of a horn antenna with the absorbing layer are obtained less than the transmitter (Tx) horn antenna (unloaded) in H-plane that means the suppressed side and back lobes are obtained. It has apparently lower side-lobes compared with the horn antenna (unloaded) in the H-plane, demonstrating that an absorbing material can effectively be used to reduction of side lobes and concentrating the main lobe in the forward direction. Moreover, beam-width shaping is quite important to enhance horn antenna gain for these applications. For that purpose, we claim that absorbing materials in the field of antennas can be used in a design of lens that is relatively new to concentrate the desired radiation without reducing distortion and bending with narrower beam width. Traditionally, using curved bends are used to avoid reflections by then antenna. In some of studies on beamforming antenna applications, the inside of antenna can be re-fabricated that causes sharp bends. It often results in increase reflections and mode distortions inherently reduce the transmitted power through the bend. In our design we did not make any changes of antenna structure,

which is one of the advantage of our work. In that way the losses by distortion and bending is prevented. In this experimental study, Fresnel Zone Plates serve how affects beam-shaping of a standard gain horn antenna. We investigated that the feasibility of two designs of Fresnel Zone Plates on beamforming in the GHz frequency range. For this purpose, first, an electromagnetic wave absorber was used from our previous work and the FZP Models were designed (using the design rules of the FZPs with absorbing / transparent zones) and fabricated.

Radiation pattern measurements obtained transmission parameters (S_{21}) were carried out and significant antenna parameter, namely Half-Power Beam-Widths (HPBW), were determined to understand how the HPBWs change. In order to plot radiation patterns in E- and H-plane S_{21} transfer parameters are used, which are obtained by vector network analyzer. All the measurements are done using quasi-anechoic chamber that we set up using pyramidal microwave absorbers. In that way, the reflections nearby objects which distort the radiation patterns are minimized. As known, S_{21} represents the power transferred from transmitter antenna to receiving antenna. It is also known that S_{21} is zero implies that all power delivered to receiving antenna. According to S_{21} measurement results, the radiation patterns in E-plane and H-plane are plotted with that aspect.

2. DESIGN OF FRESNEL ZONE PLATES

2.1. Design Procedure of Zone Plates

Fresnel zones composed of a set of concentric strips are arranged on a flat surface. The strips alternate between absorbing and transmitting layers. The geometrical configurations in Figure 1 are used throughout this work.

The FZP zones are annular for the considered normal incidence. The operating principle of the FZP has been described in detail at [1] and [17]. The FZP radiation characteristics are given by the more precise physical optics current method in [18].

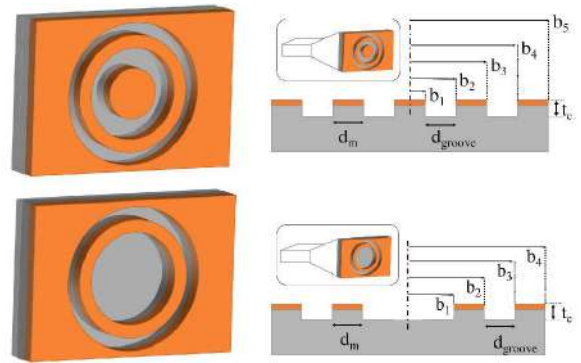


Figure 1 The design of Fresnel Zone Plates (a) Type 1 as shown on the top-left, (b) The side view of Type 1 as shown on the top-right, (c) Type 2 as shown on the bottom-left, (d) The side view of Type 2 as shown on the bottom-right

The transmission mode of FZP concentrates energy from the incident wave on one side to focus on the other side. The focusing effect is produced by the diffraction or the second radiation on the open and opaque ring surfaces. Depending on the material these zones are made of, we have two lens types of FZPs: lenses with absorbing/transparent (a/t) zones and lenses with phase-correcting (p/c) zones. Those lenses are designed below by using the Fresnel zone plate theory. The radii of the FZP rings are determined with the n -th radii, b_n , given by [1]:

$$b_n = \sqrt{\frac{2n\lambda}{P} \left(F + \frac{n\lambda}{2P} \right)} \quad (1)$$

where F , the focal length of the zone plates, equals to zero in this study and λ is the wavelength. According to the distances from a selected focal point, the consecutive radii of these zones are chosen on the central axis increase by a value of λ while going from the inner to the outer radius of any zone.

There exists a lower boundary limit for the difference between two consecutive radii: $d_{groove} = \lambda/P$ in Ref 1. P equals to two for the FZPA absorbing/transparent (a/t) zones, which means that if a plane wave is normally incident to the zone plate, the portions of the radiation, which pass through the various transparent zones, all reach by diffraction the focal point $z = -F$ with mutual phases that differ less than 180 degrees.

When a/t-zones are used, the odd-numbered zones are covered with absorbing material. We did not consider that the influence on the radiation pattern of Fresnel zones of which the width of zones $d_m = (b_{n+1} - b_n)/2$ is in the order of a few wavelength or even smaller in [1]. Therefore, d_m is constant value in this work. Reference [1] shows that not only the number of zones decreases with F but also d_m decreases with the radius of b_n . Nevertheless, the absorbing material with wider radii to keep them on the same dB level covers the last zone compatible with the dimensions on the horn antenna. The radius of zone plates for n values are listed in Table 1.

Table 1
The radius of the zones

n	2n	b_n	dgroove	d_m
1	2	0.83	0.83	0.415
2	4	1.66	0.83	0.415
3	6	2.49	0.83	0.415
4	8	3.32	0.83	0.415
5	10	4.29	0.97	0.415

The radius of zones for n values of selected absorbing/transparent zones by using focal length (F) equals to zero and P equals to two and λ , wavelength is 1.66 cm. According to the geometrical configuration of the Fresnel antenna [1], focal distance is assumed zero since the FZP lens in this study is mounted to the feed (transmitter (Tx) horn antenna) without any gap. Thus, the successive radius are calculated using the Equation 1 whereas F is zero as a lower limit for the differences between successive radii λ/P (F=0). The values of design parameters are calculated by using Equation 1. The depth of a groove can now be derived by calculating the phase delay of the wave in the dielectric or the paraffin as diffraction optic material with respect to the wave in free space. Then the following relation must be valid:

$$(k_x - k)t_c = \pi, \quad k_x = k\sqrt{\varepsilon_r} \quad (2)$$

the wave number (k) in the diffraction optic material, and the relative dielectric constant of the material ε_r , the latter equation can be written as

$$k(\sqrt{\varepsilon_r} - 1)t_c = \pi \quad (3)$$

The groove depth, t_c is defined by [12]:

$$t_c = \frac{\lambda_0}{2\sqrt{\varepsilon_r - 1}} \quad (4)$$

where $\varepsilon_r=2.5$ (the paraffin wax relative permittivity for paraffin wax) and the groove depth is 0.83 cm.

In this study, there are two type of zone plates as Type-1 and Type-2. The only difference in between them is absence of the section covered with the absorbing material at the center of the layer in Type-2. The zone radii are the same for Type-1 and -2 except the absence of center zone in Type-1.

2.2. Preparation of Electromagnetic Wave Absorbers (EMWAs)

The EMWA resulting from manganese soft spinel ferrite nano-particles (MF NPs) with multi-walled carbon nanotubes were prepared by a citric acid assisted sol-gel method whereas MWCNTs were purchased from US Research Nanomaterials, Inc., USA. The crystal structure, morphology, magnetic property and microwave absorption behavior were discussed in detail [13, 14]. According to the ring sizes mentioned above, the absorber rings are created with 1 mm thickness using the fabrication technique in [16]. The diffraction optic material of paraffin and the absorber with a toroidal-shape are attached to each other using epoxy glue with a very small thickness. Finally, the structures are mounted to the horn antenna in Figure 1.

3. EXPERIMENTAL SETUP OF RADIATION PATTERNS

The radiation pattern is a graphical representation of the strength of radiation of a horn antenna as a function of direction. The given antenna is located at the origin of a spherical polar coordinates system (r, θ , φ) and the variation in the field strength at different points on an imaginary concentric spherical surface of radius r is noted. For a sufficiently larger r, the radiation pattern is independent of r and the fields are tangential to the hypothetical spherical surface. In general, separate patterns are plotted for θ and φ

polarization [18-20]. The experimental setup of radiation pattern measurements is demonstrated in Figure 2. All directivity measurements were carried out in the laboratory environment with the experimental setup that is covered by pyramidal absorbers to reduce reflections from the walls, except on top of the measurement platform. The transmitting and the receiving antennas are set them up at an appropriate distance (approximately 2 meter) above the surface of the wooden table. A receiving antenna is considered to be from transmitter antenna with the material under test (MUT) in the far-field region. The distance with the transmitter and the receiving antennas is formulated on the condition of far-field region. r is the value of the distance a transmitting antenna from the receiving antenna, D (3.32 cm x 4.29 cm of inside dimensions of the horn antenna of WR62-15 dB) is the largest dimension of the receiver and transmitter horn antenna [20] and λ cm is the wavelength.

3.1. Measurement Procedure of E- and H-Plane Radiation Patterns

The antennas were positioned for the maximum meter reading and this position of the receiving antenna is marked as 0 degree. We kept the distance between the antennas constant and sufficiently large according to the distance (r) with the transmitter and the receiving antennas. We continually rotated the receiving horn clockwise, in steps of 2 degrees, to cover 360 degrees including the main, side and back lobes. At each position, we took care keeping the initial setup of the calibrated vector network analyzer (VNA) to restore the 2 degrees' scale deflection. We returned to the position 0 degree and repeated for the other plane in steps of 2-degree scale deflection on clockwise until completion of the 180 degree. Then we took into account the symmetry of all acquired data, which is field strength versus angle, so that the entire radiation pattern were obtained for E-plane on x-z plane as shown on Figure 2. The same procedure with E-Plane was repeated for y-z plane to obtain data of H-plane pattern. We finally plotted the radiation pattern in the above manner for both E- and H-planes after acquiring the data for H-Plane.

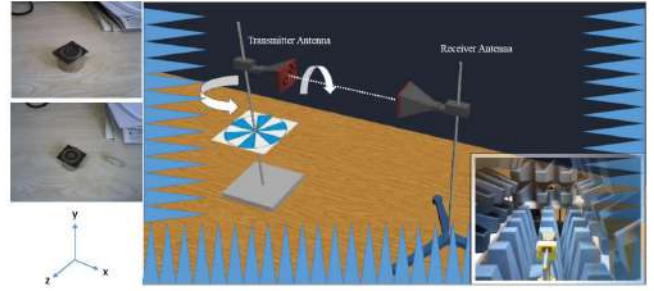


Figure 2 Fabricated Fresnel zone plates and the experimental setup: radiation field of a horn antenna with the Fresnel Zone Plates

4. RESULTS AND DISCUSSION

We have performed an experimental study of the beam-width forming with the scenario of a far-field radiation patterns on horn antenna (unloaded), a horn antenna with Types 1 and 2 at the seven frequencies (12.4, 13, 14,...,18 GHz) when the FZPs are attached to the transmitter antenna. Here, the azimuth and elevation half-power beam-width angles obtained are listed in Table 2.

Table 2
E- and H- Plane beam-widths

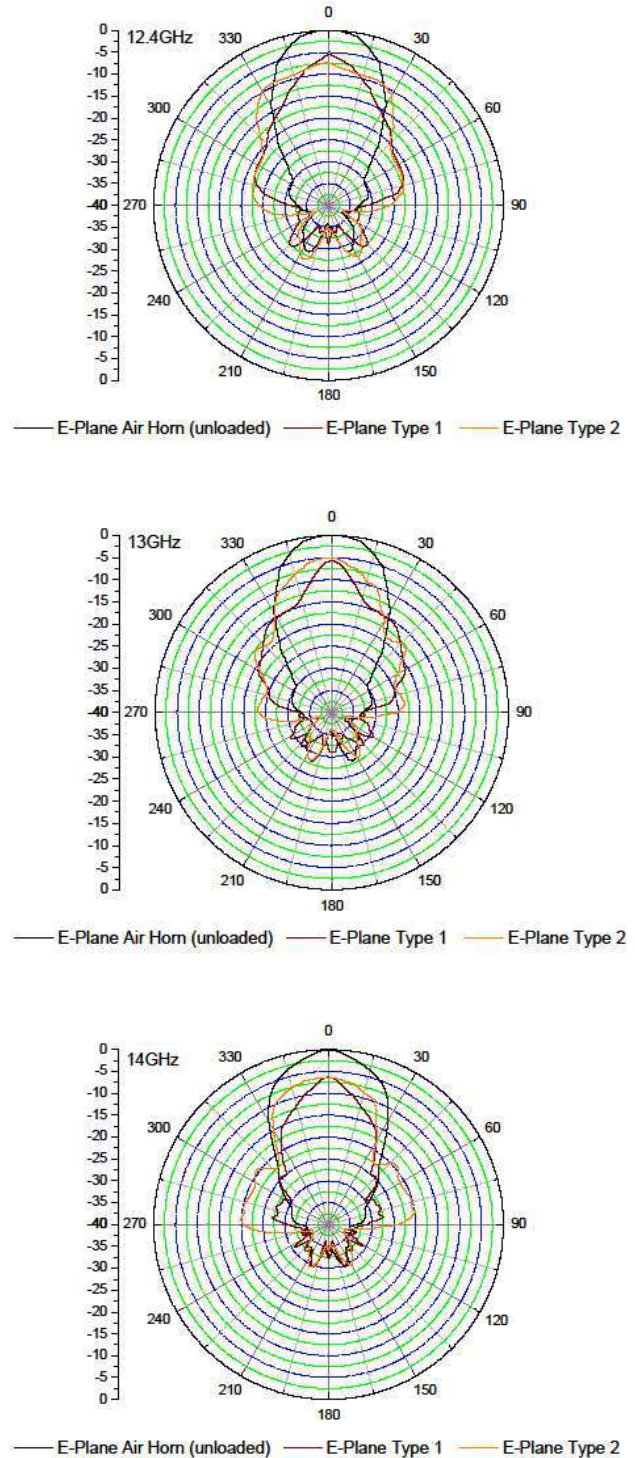
f (GHz)	E-PLANE (degree)			H-PLANE (degree)		
	Air Horn	Type 1	Type 2	Air Horn	Type 1	Type 2
12.4	30.48	18.94	65.08	33.74	25.20	28.80
13	30.48	13.18	33.36	31.92	17.50	23.26
14	27.58	17.50	47.78	30.48	15.68	22.64
15	20.38	11.74	34.80	30.18	17.40	21.32
16	23.26	14.62	34.80	29.86	15.52	19.62
17	23.26	17.50	36.66	25.16	13.46	18.08
18	22.82	16.24	43.66	19.82	13.72	15.74

We observed that the narrowest beam-width (BW) in both E- and H- Planes was obtained for a standard gain horn antenna with Type 1 of FZP. Depending on the beam-widths values, the narrower (smaller than the horn antenna with Type 1 of FZP) beam-widths in E-Plane was obtained for a standard gain horn antenna (unloaded) and horn antenna with Type 2 of FZP, respectively. In H-Plane, the beam-width of the horn antenna (unloaded) is larger than the beam-width of the horn antenna with Type 2 FZP. In addition, we found that the side lobe levels were

suppressed in H-Plane and the side-lobes in the E-Plane were higher than the side-lobes in the H-Plane. It has apparently lower side-lobes compared with the horn antenna (unloaded), demonstrating that one can effectively reduce side-lobes of the horn antenna by attaching the FZPs. According to the results, the horn antenna with Type 1 FZP shows that a good performance in the Ku-band whereas an absorbing material caused an effect on the side lobes because of that the absorbing materials on the zones are not infinitely thin, which caused a shadowing effect [21]. Note that FZP reduces the quadratic phase error at horn's aperture plane, however, the radiation efficiency, reflection loss and cross-pol performance due to FZP must be considered. In this study we have performed an experimental study using empirical data resulting from the measurement of transmission parameter S_{21} .

4.1. E-Plane Radiation Patterns (in Polar Coordinates) of Horn Antenna (unloaded), Horn Antenna with Type 1 and 2

The experimental far-field radiation patterns (E-Plane) of the scenario with the real structures of FZPs at seven sample frequencies (12.4 through 18 GHz) are shown in Figure 3. It is observed that the beam-widths of horn antenna with Type-1 at each frequency in E-plane have the smallest values. The beam-width values of horn antenna with Type-2 in E-plane are obtained higher than the beam-width values of horn antenna with Type-1 and smaller than the beam-width values of horn antenna (unloaded), respectively. Note that all directivity measurements are done in the scale of dB.



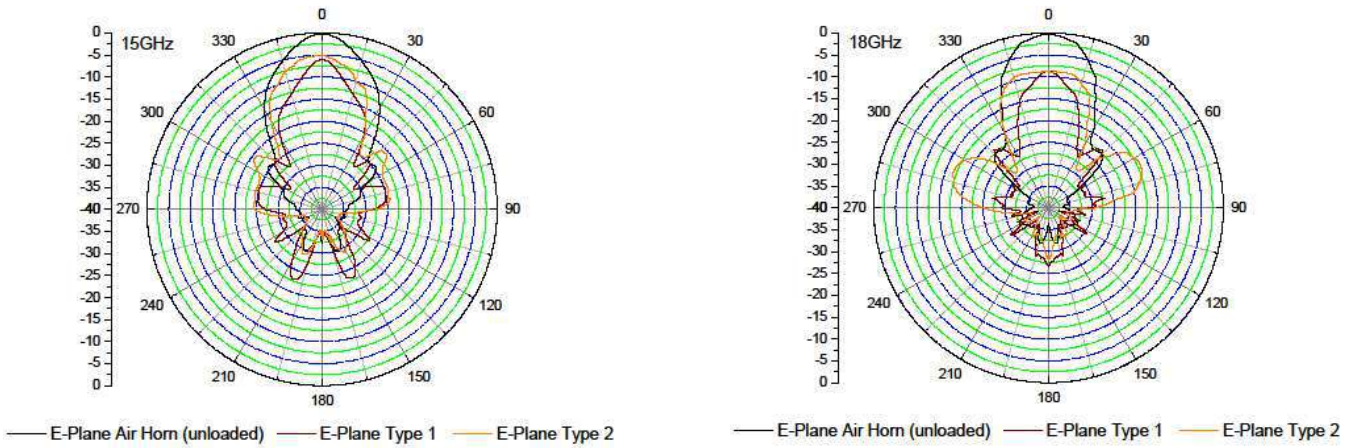
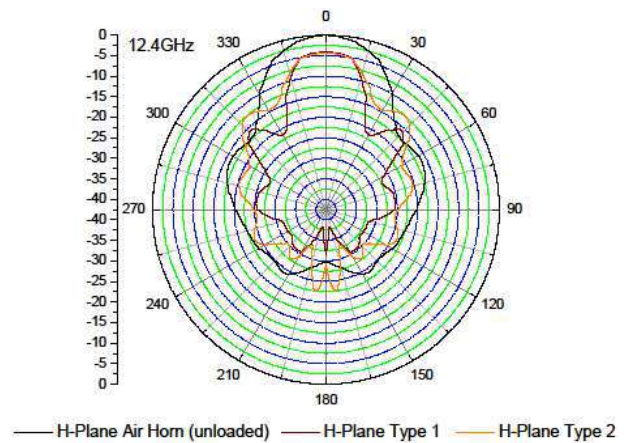
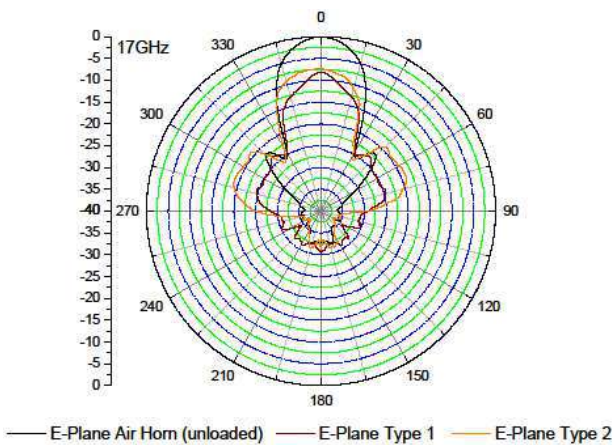
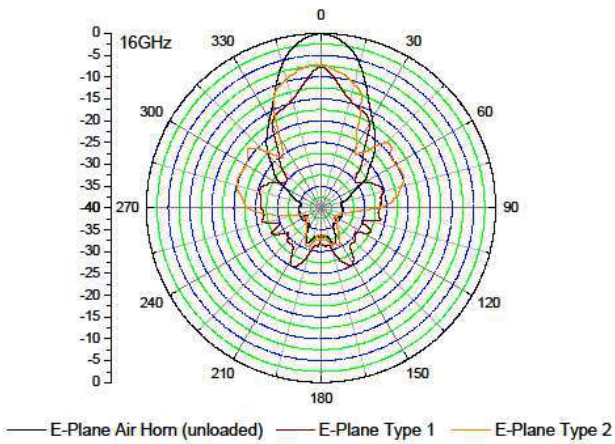


Figure 3 The comparison of the radiation patterns in E-Plane (12.4 GHz through 18 GHz) including the transmitter horn antenna (unloaded), the transmitter antenna with type 1 (wine color), and the transmitter antenna with type 2 (orange color) FZP

4.2. H-Plane Radiation Patterns (in Polar Coordinates) of Horn Antenna (unloaded), Horn Antenna with Type 1 and 2

The experimental far-field radiation patterns (H-Plane) of the scenario with the real structures of FZPs at seven sample frequencies (12.4 through 18 GHz) are shown in Figure 4. It is observed that the beam-widths of horn antenna with Type-1 at each frequency in H-plane have the smallest values. The beam-width values of horn antenna with Type-2 in H-plane are obtained higher than the beam-width values of horn antenna with Type-1 and smaller than the beam-width values of horn antenna (unloaded), respectively.



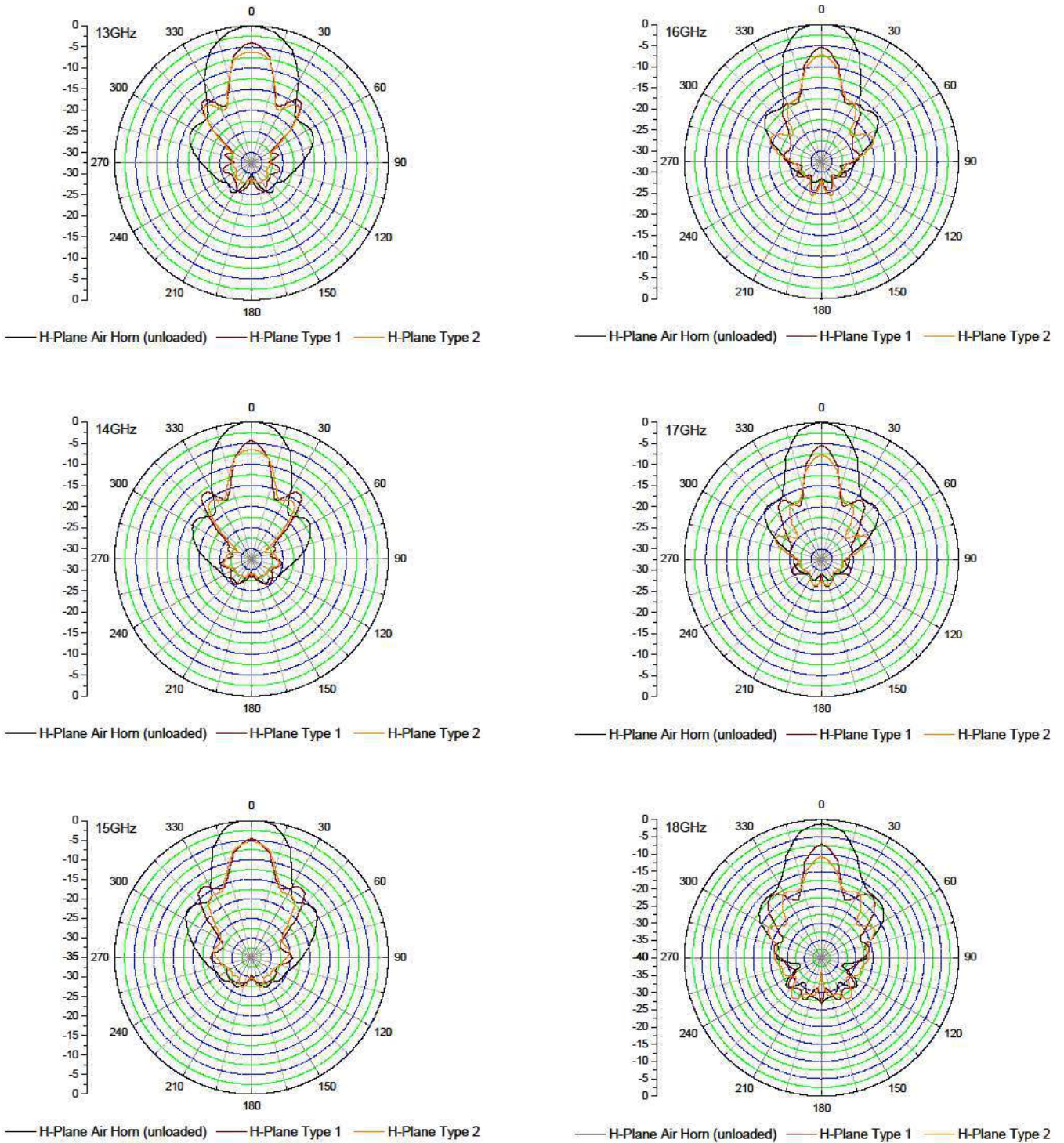
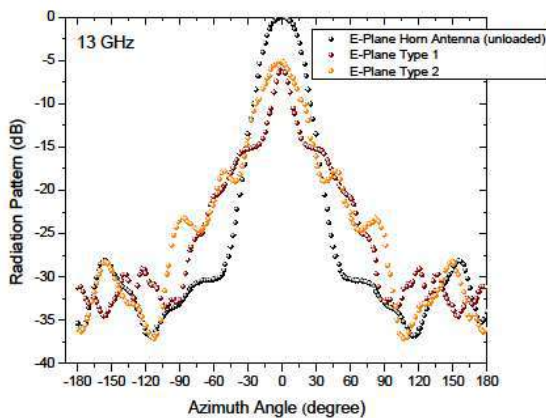
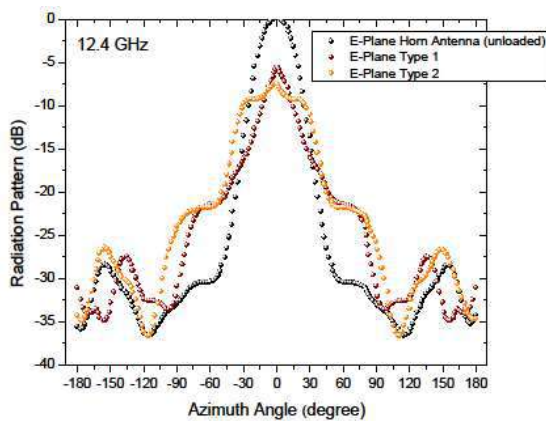
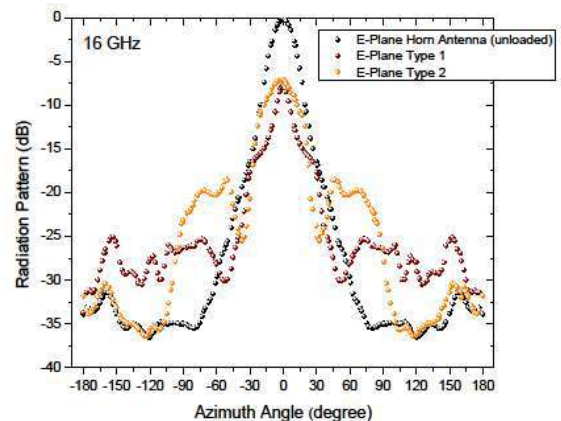
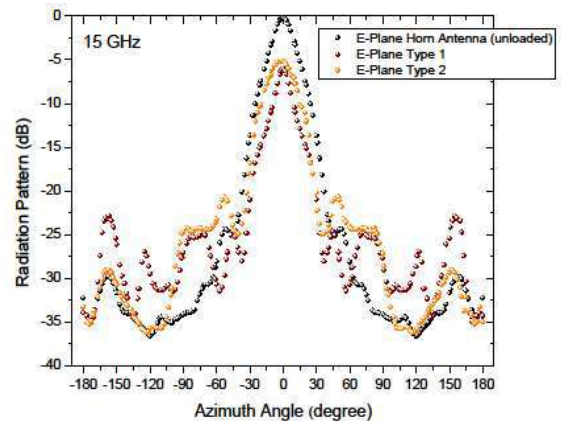
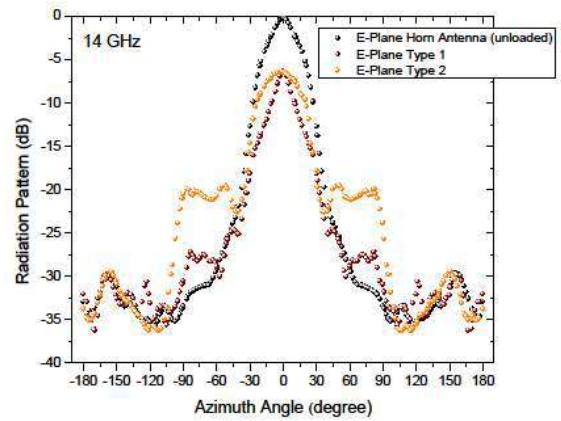


Figure 4 The comparison of the radiation patterns in H-Plane (12.4 GHz through 18 GHz) including the transmitter horn antenna (unloaded), the transmitter antenna with Type 1 (wine color), and the transmitter antenna with Type 2 (orange color) FZP

In E-plane, the main lobe of the horn antenna loaded with the absorbing layer and diffractive optic element is decreased whereas side lobes are increased when there are no significant changes on rear lobes at all frequencies that is measured. According to the angles of two orthogonal planes, the elevation angles of a horn antenna with the absorbing layer are obtained less than the transmitter (Tx) horn antenna (unloaded) in H-plane that means the suppressed side and back lobes are obtained. Horn antenna with Type-1 and Type-2 has apparently lower side-lobes compared with the horn antenna (unloaded) in the H-plane.

4.3. Measured Radiation Patterns (Diagonal Plane) in the E-Plane of Horn Antenna (unloaded), Horn Antenna with Type 1 and 2

The experimental far-field radiation patterns (E- and H-Plane) in diagonal plane are shown in Figure 5 and Figure 6.



4.4. Measured Radiation Patterns (Diagonal Plane) in the H-Plane of Horn Antenna (unloaded), Horn Antenna with Type 1 and 2

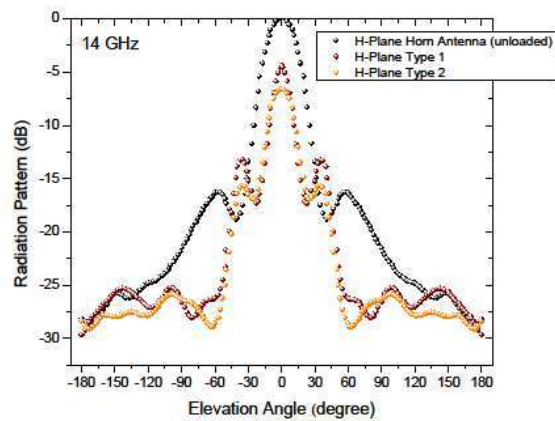
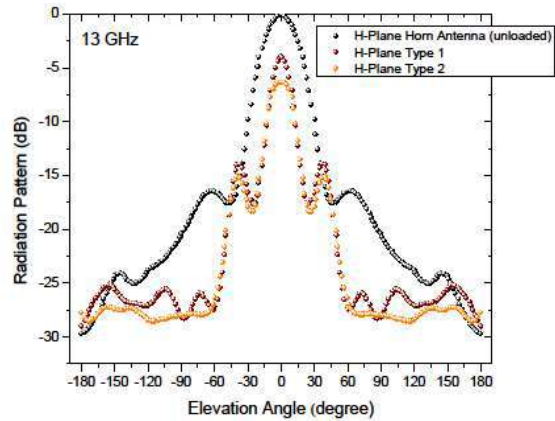
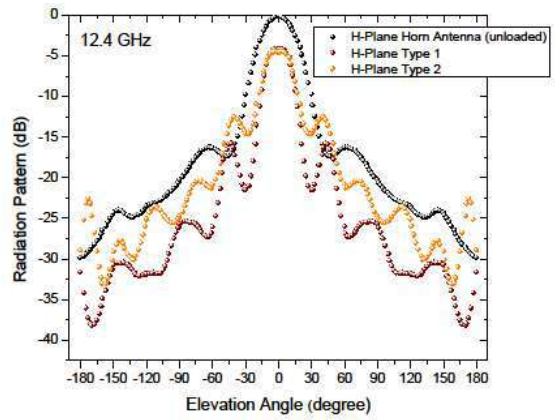
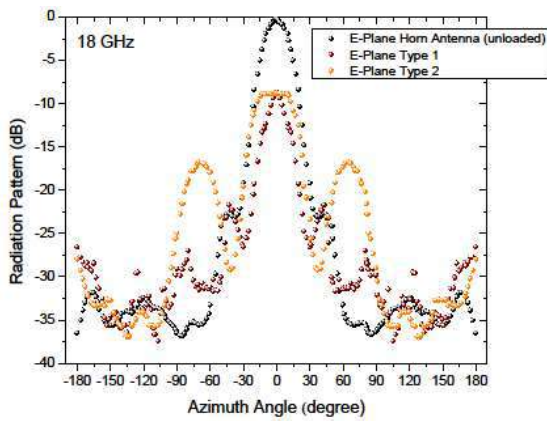
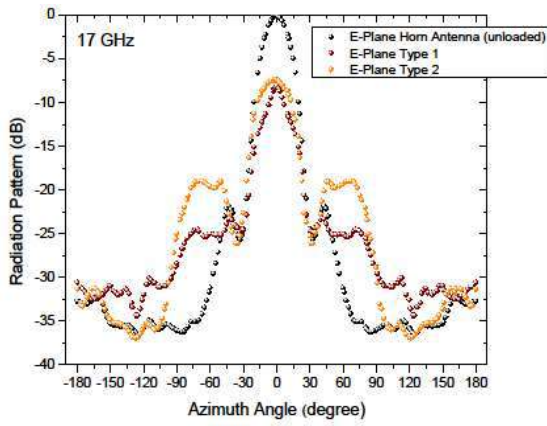


Figure 5 Measured far-field radiation patterns in E-Plane (12.4 GHz through 18 GHz) including the transmitter horn antenna (unloaded), the transmitter antenna with Type 1 (wine color), and the transmitter antenna with Type 2 (orange color) FZP

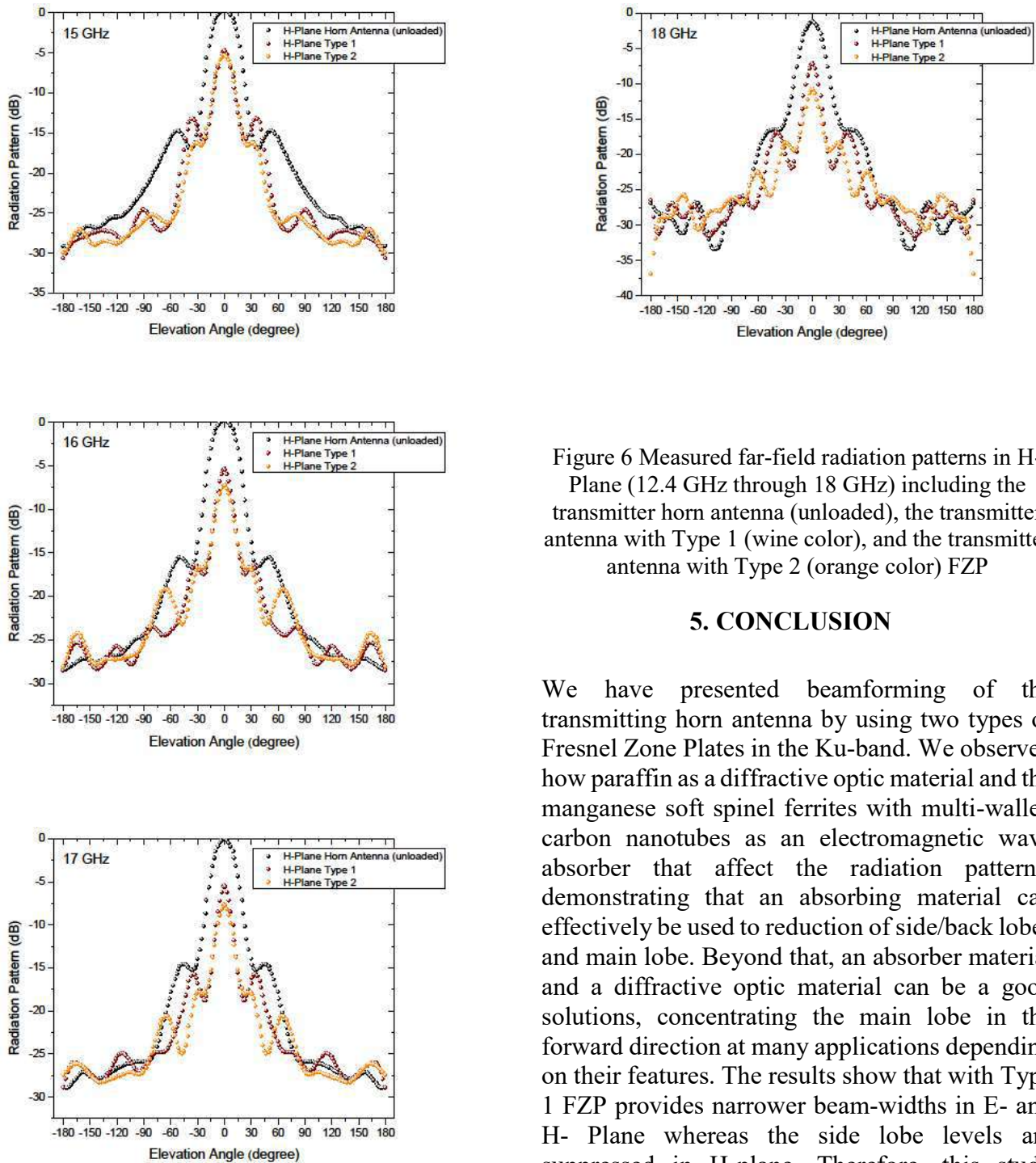


Figure 6 Measured far-field radiation patterns in H-Plane (12.4 GHz through 18 GHz) including the transmitter horn antenna (unloaded), the transmitter antenna with Type 1 (wine color), and the transmitter antenna with Type 2 (orange color) FZP

5. CONCLUSION

We have presented beamforming of the transmitting horn antenna by using two types of Fresnel Zone Plates in the Ku-band. We observed how paraffin as a diffractive optic material and the manganese soft spinel ferrites with multi-walled carbon nanotubes as an electromagnetic wave absorber that affect the radiation patterns, demonstrating that an absorbing material can effectively be used to reduction of side/back lobes and main lobe. Beyond that, an absorber material and a diffractive optic material can be a good solutions, concentrating the main lobe in the forward direction at many applications depending on their features. The results show that with Type 1 FZP provides narrower beam-widths in E- and H- Plane whereas the side lobe levels are suppressed in H-plane. Therefore, this study offers that electromagnetic wave absorbers as a thin layer structure and diffractive optic element of paraffin can play a role on beamforming that is controlled by side and back lobes. As it is known, the approximate antenna gain depends on the angle values at the points where the beam widths in E- and H- planes are reduced by 3dB. However, one of the Kraus and Tai & Pereira equations should be used in the antenna gain calculation depending on the 39.77 degree which is a critical value for these angle values. If the beam angles

are less than 39.77 degrees, antenna gain can be calculated using the Kraus and Tai & Pereira equations. It is obviously seen that suppressing side/back lobes are associate with the antenna gain. Therefore, it will be possible to increase the antenna gain in relation to suppress the beam widths of the side lobes and the rear lobe. By taking into consideration the relationship between beam width and antenna gain. This article has unique advantages to tune antenna gain. In this respect, this article is thought to make a significant contribution to the literature in terms of antenna gain increase. Therefore. This article will lead future studies on antenna gain, taking into account beam width results.

Funding

The author received no financial support for the research, authorship, and/or publication of this paper.

The Declaration of Conflict of Interest/ Common Interest

No conflict of interest or common interest has been declared by the author.

The Declaration of Ethics Committee Approval

The author declares that this document does not require an ethics committee approval or any special permission.

The Declaration of Research and Publication Ethics

The author of the paper declares that he complies with the scientific, ethical and quotation rules of SAUJS in all processes of the paper and that he does not make any falsification on the data collected. In addition, he declares that Sakarya University Journal of Science and its editorial board have no responsibility for any ethical violations that may be encountered, and that this study has not been evaluated in any academic publication environment other than Sakarya University Journal of Science.

REFERENCES

- [1] L. C. J. Baggen, "The Fresnel Zone Plate Antenna: design and analysis", Eindhoven Univ. of Tech., Eindhoven, Netherlands, 1992.
- [2] G. I. Greisukh, E. G. Ezhov, A. V. Kalashnikov, I.A. Levin and S.A. Stepanov, "The efficiency of relief-phase diffractive elements at a small number of Fresnel zones," Optics and Spectroscopy, vol. 113, no. 4, pp. 425-430, 2012.
- [3] J. C. Wiltse, "Recent developments in Fresnel zone plate antennas at microwave/millimeter-wave," In Optical Devices and Methods for Microwave/Millimeter-wave and Frontier Applications, vol. 3464, pp. 146-154, 1998.
- [4] H. D. Hristov, "Fresnel Zones in Wireless Links, Zone Plate Lenses and Antennas," Artech House, Inc., 2000.
- [5] J. Pourahmadazar, S. Sahebghalam, S.A. Aghdam, M.A. Nouri, "Millimeter-wave Fresnel zone plate lens design using perforated 3D printing material," In 2018 IEEE MTT-S International Microwave Workshop Series on Advanced Materials and Processes for RF and THz Applications (IMWS-AMP), pp. 1-3, 2018.
- [6] S. M. Stout-Grandy, A. Petosa, I. V. Minin, O. V. Minin, J. S. Wight, "Novel reflector-backed Fresnel zone plate antenna," Microwave and Optical Technology Letters, vol. 49, no. 12, pp. 3096-3098, 2007.
- [7] A. Jouade, J. Bor, M. Himdi, O. Lafond, "Millimeter-wave Fresnel zone plate lens with new technological process," International Journal of Microwave and Wireless Technologies, vol. 9, no. 4, pp. 939-944, 2017.
- [8] X. Liu, Y. Y. Chen, Y. Ge, "Wideband High-Efficiency Fresnel Zone Plate Reflector Antennas Using Compact

- Subwavelength Dual-Dipole Unit Cells,” *Progress in Electromagnetics Research*, vol. 86, pp. 29-39, 2018.
- [9] L. C. J. Baggen, M. H. A. J. Herben, “Design procedure for a Fresnel-zone plate antenna,” *Int. J. Infrared and Millimeter Waves*, vol. 14, no. 6, pp. 1341-1352, 1993.
- [10] J. C. Wiltse, “Millimeter-wave Fresnel zone plate antenna,” *Millimeter and Microwave Engineering for Communications and Radar: A Critical Review*, International Society for Optics and Photonics, vol. 10276, pp. 1027605, 1994.
- [11] I. Minin and O. Minin, “Diffractive optics and nanophotonics: Resolution below the diffraction limit,” Switzerland, Springer, 2015.
- [12] S. T. Bobrov, G. I. Greisukh and Y. G. Turkevich, “Design procedure for a Fresnel-zone plate antenna,” *Mashinostroenie*, pp. 223, 1986.
- [13] A. Teber, R. Bansal, I. S. Unver and Z. Mehmedi, “The measurement of microwave absorption characteristics of nanocomposites using a coaxial line technique,” *Int. J. High Speed Electronics and Systems*, vol. 27, no. 01n02, pp. 1840011, 2019.
- [14] A. Teber, K. Cil, T. Yilmaz, B. Eraslan, D. Uysal, G. Surucu, A. Baykal and R. Bansal, “Manganese and zinc spinel ferrites blended with multi-walled carbon nanotubes as microwave absorbing materials,” *Aerospace*, vol. 4, no. 1, pp. 2, 2017.
- [15] A. Teber, I.S. Unver, H. Kavas, B. Aktas and R. Bansal, “Knitted radar absorbing materials (RAM) based on nickel–cobalt magnetic materials,” *Journal of Magnetism and Magnetic Materials*, vol. 406, pp. 228-232, 2016.
- [16] A. Teber, “Development of radar absorbing materials (RAMs) based on nano-structured magnetic materials and applications,” Dept. Elect. Eng., Univ. of Connecticut, Storrs, Connecticut, Doctoral Dissertation, pp. 1532, 2017.
- [17] A. Mahmoudi and R. Afzalzadeh, “Analysis, design and fabrication of centimeter-wave dielectric Fresnel zone plate lens and reflector,” *The European Physical Journal-Applied Physics*, vol. 32, no. 2, 2005.
- [18] E. Pettinelli, P. M. Barone, E. Mattei, A. Di Matteo, F. Soldovieri, A. S. Turk, A. K. Hocaoglu and A. A. Vertiy, “Archaeology and cultural heritage,” *Subsurface Sensing*, pp. 644-667, 2011.
- [19] R. E. Collins, “Antennas and radiowave propagation,” New York: McGraw-Hill, 1985.
- [20] C. Balanis, “Antenna theory analysis and design,” New Jersey: John Wiley & Sons. Inc., 2005.
- [21] D. N. Black and J. C. Wiltse, “Millimeterwave characteristics of phase-correcting Fresnel zone plates,” *IEEE Transactions on Microwave Theory and Techniques*, vol. 35, no. 12, pp. 1122-1129, 1987.

JOURNAL OF SCIENCE



SAKARYA UNIVERSITY

Sakarya University Journal of Science

ISSN 1301-4048 | e-ISSN 2147-835X | Period Bimonthly | Founded: 1997 | Publisher Sakarya University |
<http://www.saujs.sakarya.edu.tr/en/>

Title: Microcontroller-based Random Number Generator Implementation by Using Discrete Chaotic Maps

Authors: Serdar ÇİÇEK

Received: 2020-04-27 03:59:56

Accepted: 2020-06-17 14:47:55

Article Type: Research Article

Volume: 24

Issue: 5

Month: October

Year: 2020

Pages: 832-844

How to cite

Serdar ÇİÇEK; (2020), Microcontroller-based Random Number Generator Implementation by Using Discrete Chaotic Maps. Sakarya University Journal of Science, 24(5), 832-844, DOI: <https://doi.org/10.16984/saufenbilder.727449>

Access link

<http://www.saujs.sakarya.edu.tr/en/pub/issue/56422/727449>

New submission to SAUJS

<http://dergipark.org.tr/en/journal/1115/submission/step/manuscript/new>

Microcontroller-based Random Number Generator Implementation by Using Discrete Chaotic Maps

Serdar ÇİÇEK*¹

Abstract

In recent decades, chaos theory has been used in different engineering applications of different disciplines. Discrete chaotic maps can be used in encryption applications for digital applications. In this study, firstly, Lozi, Tinkerbell and Barnsley Fern discrete chaotic maps are implemented based on microcontroller. Then, microcontroller based random number generator is implemented by using the three different two-dimensional discrete chaotic maps. The designed random number generator outputs are applied to NIST (National Institute of Standards and Technology) 800-22 and FIPS (Federal Information Processing Standard) tests for randomness validity. The random numbers are successful in all tests.

Keywords: Chaotic map, Random number generators, NIST 800-22, FIPS, Microcontroller

1. INTRODUCTION

Chaos theory and chaotic systems have typical features such as very much sensitivity to initial conditions, random-like behavior, ergodicity and broadband [1]. Chaotic systems have been used in different disciplines of science in the recent decades [2]. One of these fields is random number generator (RNG). RNG designs are very important because random numbers should be unpredictable in information security, encryption and cryptographic applications [3]. In the literature, various random number generators (RNGs) have been designed with different chaotic and hyperchaotic systems. Wang et al. designed RNG by using a single chaotic system [4]. Ergün et al. designed RNG by using non-autonomous

continuous-time chaotic oscillator [5]. Yalçın et al. designed RNG by using double-scroll chaotic system [6]. Vaidyanathan et al. [7] and Liu et al. [1] designed RNG by using 4D hyperchaotic systems. Akgul et al. designed RNG by using integer and fractional chaotic system based on microcomputer (Raspberry Pi) [8].

Besides chaotic and hyperchaotic systems, chaotic maps (CMs) are also used in chaos-based communication, encryption applications and RNG designs. There are two types of CMs: continuous and discrete. The continuous chaotic map (CM) function graph is in an unbroken structure [17]. Discrete CMs are generally obtained by iterations. In fact, discrete CMs are a special version of the continuous system with

* Corresponding Author: serdarcicek@gmail.com ; serdarcicek@nevsehir.edu.tr

¹ Nevşehir Hacı Bektaş Veli University, Vocational School of Hacıbektaş, Department of Electronic and Automation, Nevşehir, TURKEY. ORCID: <http://orcid.org/0000-0002-8738-3985>

instantaneous states depicted by continuous CM variables. Discrete CMs often have relatively simple algebraic equations than continuous CMs [9]. Also, the number of system state variables required for the hyperchaotic continuous time system is minimum four, but this situation is not necessary for discrete CMs [40]. Digital embedded systems cannot directly support the structure of continuous CMs. Therefore, the continuous signal needs to be discretization for digital embedded systems [10, 35].

Many CMs with different features have been introduced in the literature. Alzaidi et al. [11], Alpar [12], Hua et al. [13] and Liu et al. [14] introduced one-dimensional (1D) chaotic maps. In literature, Henon [15], Chen [16], Barnsley Fern [17], Tinkerbell, Lozi and other two-dimensional (2D) discrete CMs [18-21] and fractional CMs [22, 23] are also introduced.

Discrete chaotic maps are mostly used in chaotic maps based RNG, encryption and communication applications. Alghafis et al. designed encryption scheme based on quantum map and continuous chaotic system [24]. Fridrich designed symmetric ciphers based on continuous two-dimensional chaotic map [25]. Liao et al. designed secure image communication based on Chebyshev map [26]. Papadimitriou et al. proposed two new communication protocols by using CMs [27]. CMs have been widely used in encryption applications as well as communication applications. Zhang et al. presented image encryption design based chaotic map for different image formats [28]. Li et al. introduced a new encryption algorithm for image based on improved logistic map [29]. Pak et al. proposed an image steganography algorithm using a 1D chaotic map [30]. Naseer et al. introduced a new approach using 3D mixed CM to improve multimedia security [31]. Herbadji et al. introduced enhanced quadratic CM based color image encryption scheme [32].

RNGs are generally preferred on the basis of communication and encryption structures for information security. Chaos-based RNGs have also become popular in random number generation nowadays. For chaos-based RNG,

chaotic maps have been used such as chaotic and hyperchaotic systems. Dastgheib et al. designed a digital pseudo RNG based on discrete sawtooth CM [33]. Avaroğlu et al. designed a pseudo RNG by using Arnold cat map [34]. Lambic et al. designed a pseudo RNG by using discrete-space CM [35]. Tutueva et al. designed PRNG based on adaptive discrete CMs [36]. In addition to a single chaotic map based RNGs, RNGs are designed using multiple chaotic maps. Garasym et al. introduced new nonlinear chaotic PRNG based on discrete tent and logistic map [37]. Magfirawaty et al. introduced RNG design based on discrete Henon and logistic map [38]. Ergün and Tanrıseven implemented RNG based on discrete-time CM on FPAA (Field Programmable Analog Array) device [39].

The chaotic maps and chaotic map based applications in the literature are generally presented as simulations. The hardware implementation of these chaotic maps and applications is important for various real engineering applications. Hardware realizations can be performed as analog or embedded system designs (such as FPGA - Field Programmable Gate Array-, Microcontroller). In analog designs, the values of electronic devices can vary depending on the ambient conditions. This situation is much less in embedded systems. Additionally, updating analog designs is more difficult than embedded designs. Therefore, embedded system designs are more advantageous than analog designs. In the embedded system designs, microcontroller chips are much cheaper than FPGA chips. Also, updating the design is easy with the microcontroller than FPGA. It is advantageous to use microcontrollers in similar applications for the stated reasons.

In this study, first, microcontroller-based design is implemented of Lozi, Tinkerbell and Barnsley Fern discrete CMs and verified by numeric simulation results. Then, microcontroller-based RNG is implemented by using the CMs and test the design.

Other parts of the article are organized as follows: Section-2 presents the microcontroller-based implementation of the discrete CMs verified by

simulation results, Section-3 presents the implementation of microcontroller-based RNG design by using the discrete CMs, Section-4 provides NIST 800-22 and FIPS randomness tests results and Section 5 concludes the paper and mentions about future works.

2. MICROCONTROLLER-BASED IMPLEMENTATION OF THE DISCRETE CHAOTIC MAPS

In this section, Lozi, Tinkerbell and Barnsley Fern discrete CMs are introduced. Also the chaotic maps are implemented on microcontroller. In addition, the numerical simulation results with Matlab® program are compared the microcontroller outputs.

Arduino UNO board given in Figure 1 is used in Microcontroller design. Arduino boards and its software are open source. The board has an 8-bit ATmega328p microcontroller. The microcontroller software is programmed according to the flow chart given in Figure 2. In the microcontroller software, microcontroller input settings and CM parameter values are performed first. In the other step, the values of the state variables of the CM are sent to the output via the USB port. Then, the new values of the state variables are calculated and sent to the output. This process continues as long as the system is running.



Figure 1 Arduino UNO microcontroller board

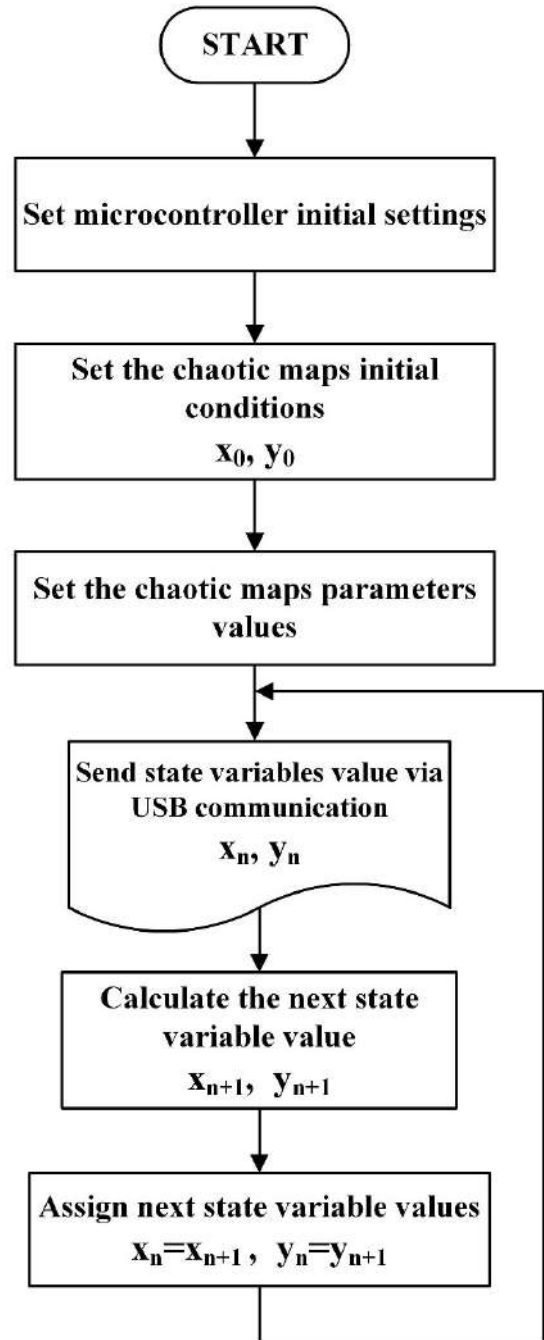


Figure 2 The flow chart of the microcontroller software

2.1. Lozi Discrete Chaotic Map

Lozi two-dimensional (2D) discrete-time CM introduced by Lozi in 1978 [19, 40]. The mathematical model of the Lozi CM is given in Eq. 1 [40]. Different outputs can be obtained by different values of a and b and initial conditions in the system. n is the discrete iteration step.

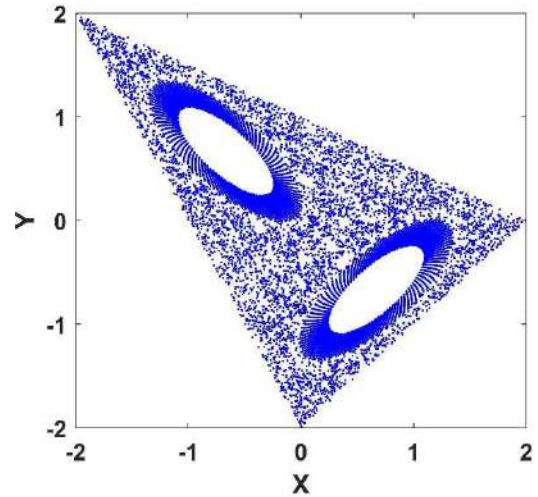
$$\begin{aligned}x_{n+1} &= 1 - a|x_n| + by_n \\ y_{n+1} &= bx_n\end{aligned}\quad (1)$$

In this study, $a = 1.5$, $b = 0.9999$ and $(x_0, y_0) = (0, 0)$ are taken in [40]. Data received via USB port from the microcontroller output are saved to the file with the computer. Data are received from the microcontroller as given in Figure 3.

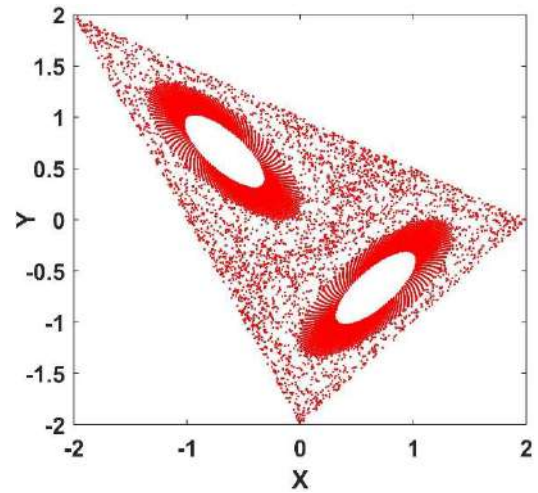
COM3	
x	y
0.0000000000	0.0000000000
1.0000000000	0.0000000000
-0.5000000000	0.9998999800
1.2498000000	-0.4999499900
-1.3745999000	1.2496749000
0.1876500800	-1.3744625000
-0.6558001600	0.1876313100
0.2039122700	-0.6557346000
0.0384625790	0.2038918700
1.1461776000	0.0384587310

Figure 3 Data received via USB port from the microcontroller output

The phase portraits (drawn in points) of the Lozi CM obtained from Matlab® numerical simulation and microcontroller output are given in Figure 4. As seen in Figure 4a and Figure 4b, the numerical calculation result and microcontroller based implementation results confirm each other.



(a)



(b)

Figure 4 The phase portraits of the Lozi discrete CM (a) Matlab simulation result (b) Microcontroller output result

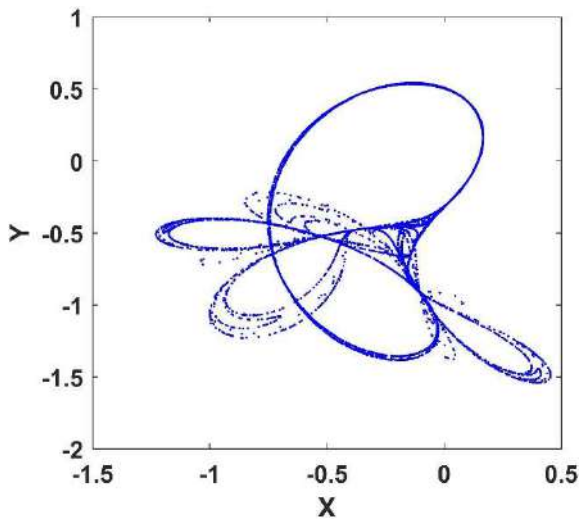
2.2. Tinkerbell Discrete Chaotic Map

Tinkerbell is a two dimensional discrete time CM. Tinkerbell CM is given in Eq. 2 [18]. In Eq. 2, α , β , γ , and δ are system parameters.

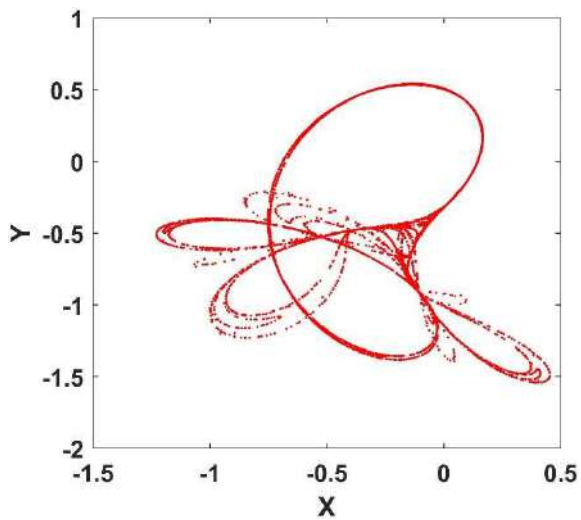
$$\begin{aligned}x_{n+1} &= x_n^2 - y_n^2 + \alpha x_n + \beta y_n \\ y_{n+1} &= 2x_n y_n + \gamma x_n + \delta y_n\end{aligned}\quad (2)$$

In this study, $\alpha = 0.9$, $\beta = -0.6013$, $\gamma = 2$, $\delta = 0.5$ and initial conditions $(x_0, y_0) = (-0.72, -0.64)$ are taken [18]. The phase portraits (drawn in points) of the Tinkerbell CM obtained from Matlab® numerical simulation and microcontroller output

are given in Figure 5. As seen in Figure 5 the numerical simulation result and microcontroller based implementation results confirm each other.



(a)



(b)

Figure 5 The phase portraits of the Tinkerbell discrete CM (a) Matlab simulation result (b) Microcontroller output result

2.3. Barnsley Fern Discrete Chaotic Map

Barnsley Fern two-dimensional (2D) discrete-time CM introduced by Michael F. Barnsley [17]. Phase portrait of this CM is similar to fern. The mathematical expression of the Barnsley Fern CM is given in Eq. 3. In Eq. 3, a , b , c , d , and e are parameters. In the calculation of the CM, the values to be taken by the parameters differ

according to the value taken by the random number p . In Eq. 4, the values of the parameters are given according to the value of the random number p which in range $[0, 1]$ [17]. Initial conditions of the CM are $(x_0, y_0) = (0.1, 0.9)$. In this study, p and the other parameters values are taken as given in Eq. 4.

$$\begin{aligned} x_{n+1} &= ax_n + by_n + e \\ y_{n+1} &= cx_n + dy_n + f \end{aligned} \quad (3)$$

$$\left\{ \begin{array}{ll} a, b, c, e, f = 0, d = 0.16 & p < 0.01 \\ a = 0.2, b = -0.26, c = 0.23, & p < 0.08 \\ d = 0.22, e = 0, f = 1.6 & \\ a = -0.15, b = 0.28, c = 0.26 & p < 0.15 \\ d = 0.24, e = 0, f = 0.44 & \\ a = 0.85, b = 0.04, c = -0.04 & \text{other } p \\ d = 0.85, e = 0, f = 1.6 & \text{values} \end{array} \right. \quad (4)$$

The phase portraits (drawn in points) of the Barnsley Fern CM obtained from Matlab[®] numerical simulation and microcontroller output are given in Figure 6. As seen Figure 6 the numerical simulation result and microcontroller based implementation results confirm each other.

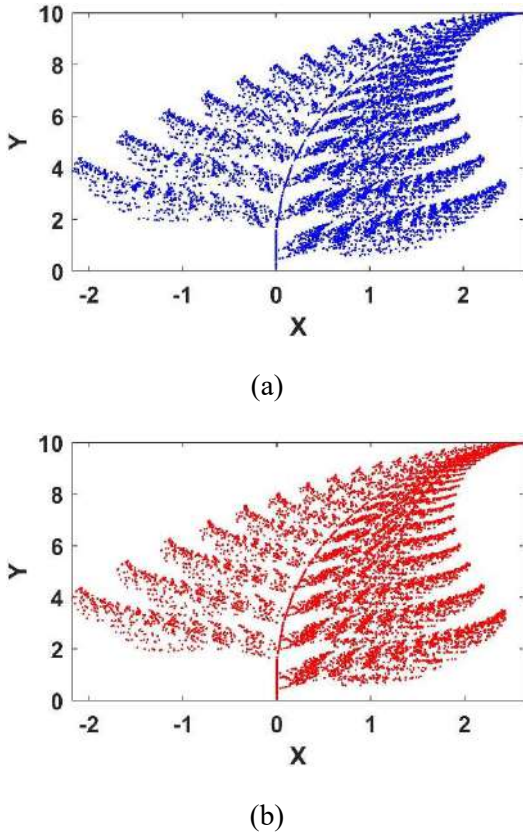


Figure 6 The phase portraits of the Barnsley Fern discrete CM (a) Matlab simulation result (b) Microcontroller output result

3. MICROCONTROLLER-BASED RNG IMPLEMENTATION BY USING THE DISCRETE CHAOTIC MAPS

Microcontroller-based RNG design is implemented by using the three different discrete two-dimensional CMs which are Lozi, Tinkerbell and Barnsley Fern in this part. For RNG design, the outputs of the x and y state variables of the CMs are first multiplied by 1000. Thus, the values of the variables are magnified. The output of the x and y state variables of the CMs are first converted to 32-bit single floating point binary number as in Figure 7.

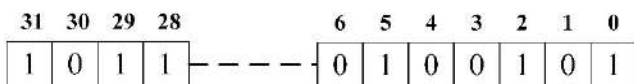


Figure 7 32-bit single floating-point binary format

In the RNG design, the first 24 bits (0,1,2, 3,..., 23) of the 32 bit floating point binary number obtained from CM outputs are used for pre-processing algorithm. The pre-processing algorithm is given schematically in Figure 8 and Figure 9. In the first case, the EXOR operation is performed mutually from the 0th bit of the x state variable of Lozi CM and the 23th bit of the x state variable of Tinkerbell CM (0 \rightarrow 23, 1 \rightarrow 22, 2 \rightarrow 21, ...). The result obtained here is applied to EXOR processing with the 0st bit of the x of the Barnsley CM. The other bits are also applied to the same processing in order. In this way, the first 24-bit RNG output is obtained.

Then, used the similar algorithm, as given in Figure 9 for second 24-bit RNG output. For the second 24-bit RNG output, y state variables of the CMs are used this time. First, the EXOR operation is performed mutually from the 23th bit of the y state variable of Lozi CM and the 0th bit of the y state variable of Tinkerbell CM (23 \rightarrow 0, 22 \rightarrow 1, 21 \rightarrow 2, ...). The result obtained here is applied to EXOR processing with the 23st bit of the y state variable of the Barnsley CM. The other bits are also applied to the same processing in order. In this way, the second 24 bit RNG output is obtained. With the algorithm given in Figure 8 and Figure 9, 48-bit RNG output is obtained.

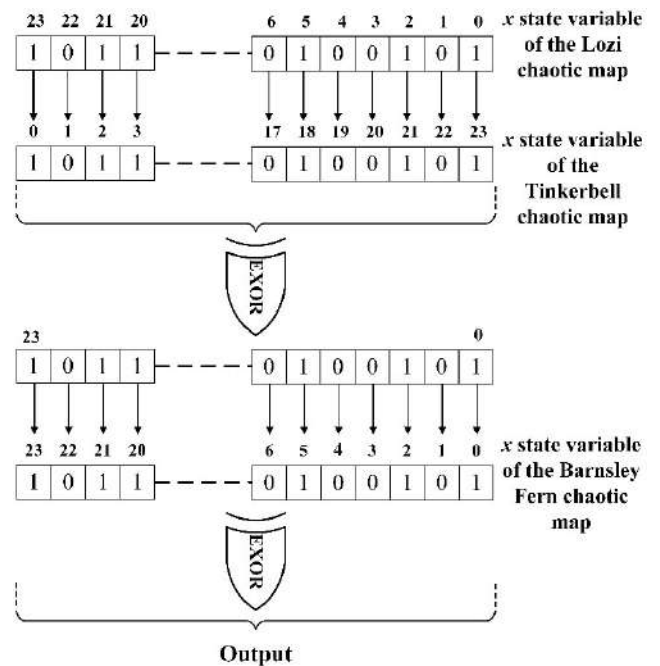


Figure 8 First 24-bit algorithm of the RNG output

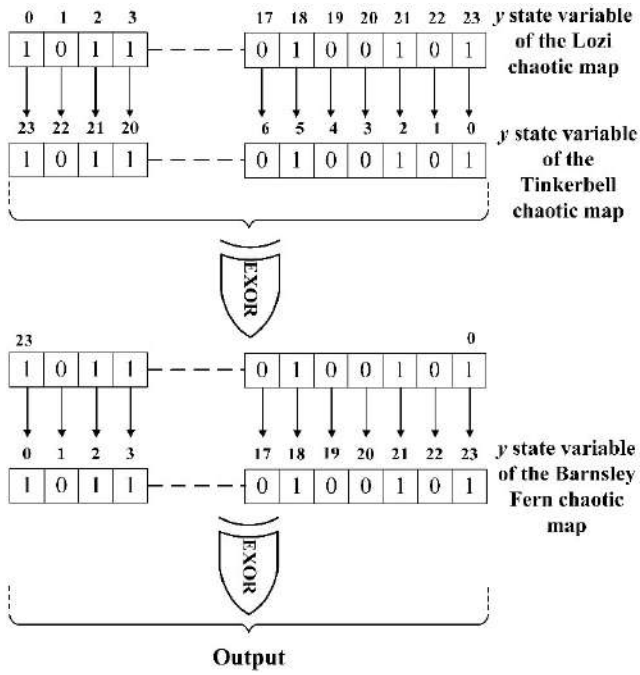


Figure 9 Second 24-bit algorithm of the RNG output

The subsequent 48-bit sequences are obtained from the chaotic maps output values obtained after every 95 iteration calculations. In this way, different values are obtained instead of close numbers that are produced consecutively.

The implemented RNG design is run on the microcontroller and obtained random numbers are tested for validity. Figure 10 shows the measurement set-up of microcontroller based RNG output signals with a computer-based oscilloscope. Signal sample of the random numbers obtained from the microcontroller output is given in Figure 11.

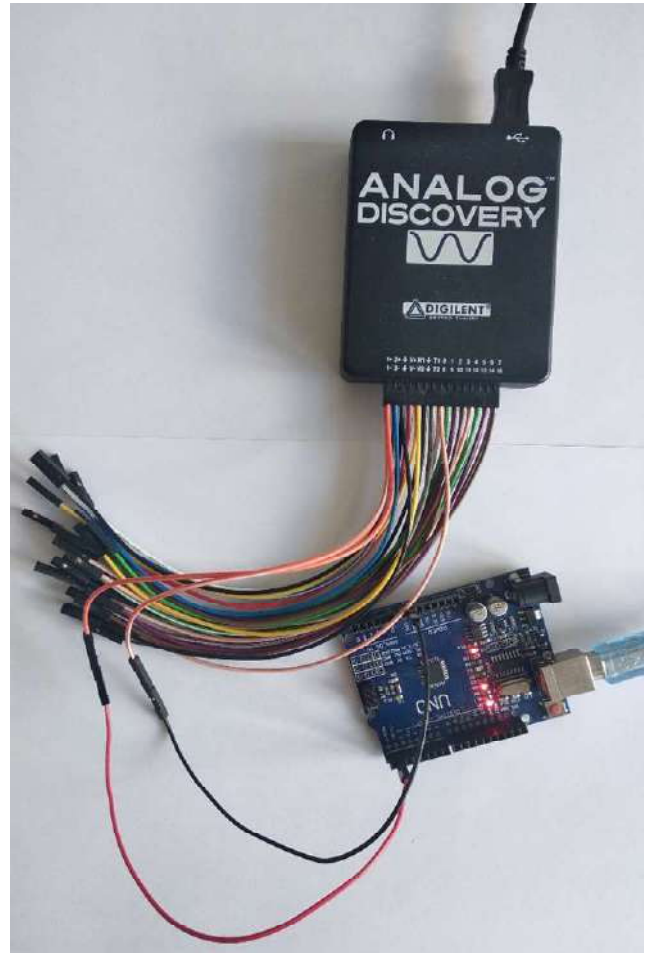


Figure 10 Measurement set-up of microcontroller based RNG output signal with a computer-based oscilloscope

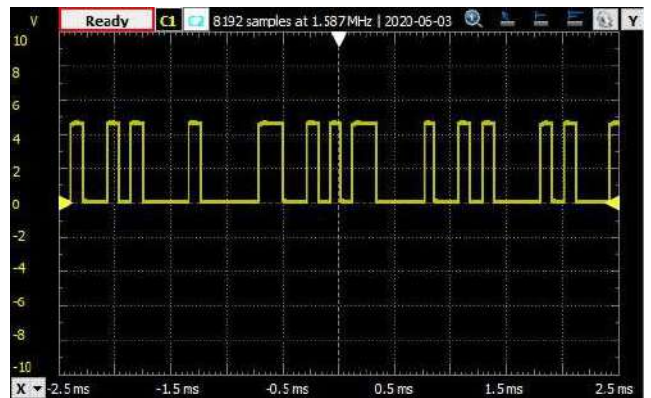


Figure 11 Signal sample of the random numbers obtained from the microcontroller

4. RANDOMNESS TESTS OF THE MICROCONTROLLER-BASED RNG

Various statistical tests are available to determine RNG success. Diehard, TestU01, AIS 31, FIPS and NIST 800-22 tests can be used to determine RNG performance. Diehard test package was introduced in 1996 by George Marsaglia. Diehard includes 15 statistical tests, but it has drawbacks and limitations, such as the sample sizes are not too large and the numbers to be tested must be in the form of 32-bit integers in the binary file [42]. AIS 31 test consists of 8 statistical tests. Today, this test is not very common in the literature to determine RNG performance [43]. TestU01 is empirical test package to determine randomness for RNGs. The TestU01 test also has a limitation that accepts only 32-bit entries [42].

Instead of Diehard, TestU01 and AIS 31 tests, the NIST 800-22 test is commonly used to determine RNG success in the literature. The NIST test suite covers many tests in other test packages. Besides the NIST test, FIPS test is also used in the literature. Therefore, in this study, NIST and FIPS tests were preferred to determine the random success rate of the implemented microcontroller-based RNG outputs.

4.1. NIST 800-22 Test

NIST SP800-22 is a commonly used statistical test package that measures the randomness of sequences produced by RNGs. The NIST 800-22 test consists of a total of 15 statistical randomness tests [44, 45]. The NIST 800-22 statistical test is a procedure that generates two hypotheses, H_0 (data random) or H_a (data not random). The significance level of the test is indicated by α . In the test, α is the probability that the test is not random when the sequence is really random [45]. The value of α is selected between [0.001 - 0.01]. In the NIST tests, the p value points out the degree of randomness and must be greater than the specified α parameter value in the NIST test. If $p \geq \alpha$ the sequence is random, if $p < \alpha$ the sequence is not random. The p takes a value between 0 and 1. If p is closer to 1, the degree of randomness of the sequence is better [41, 45]. NIST tests are

perform with standard normal and chi-square (χ^2) distribution reference. The standard normal distribution is used to compare the test statistic value obtained from RNG with the expected value. The chi-square (χ^2) distribution is used to compare the value of observed frequencies of a sample sequence measure to the expected frequencies of distribution [45]. The calculation formulas of all these tests can be found in detail in Ref [45]. For some of the NIST 800-22 tests, the number of sequences obtained from the RNG output should be sufficient. The number of sequences to be tested must be between 10^3 and 10^7 [41, 45].

NIST 800-22 test was applied to the implemented RNG. In the test, α value is taken as 0,01. For the test, 1,000,000 bits are taken from the RNG output. The NIST test results are given in Table 1. When Table 1 is examined, it is seen that the RNG outputs are successful in all NIST tests. Because p value was obtained greater than 0,01 in all tests. In the "Random-excursions" and "Random-excursions-variant" tests, only the results of at $x = -4$ and $x = -9$ are given in Table 1, in order for the table to not too long. But in all the tests, the results were successful in all values of x .

Table 1

NIST tests result of implemented microcontroller-based RNG by using the discrete chaotic maps

Test name	p value	Result
Frequency	0,9729	Valid
Block frequency	0,7410	Valid
Runs	0,9077	Valid
Longest run	0,6196	Valid
Rank	0,9686	Valid
Discrete Fourier transform	0,2402	Valid
Nonoverlapping template matching (B=001111111)	0,2040	Valid
Overlapping template matching	0,5170	Valid
Universal statistical	0,0668	Valid
Linear complexity	0,7258	Valid
Serial	0,7412	Valid
	0,9191	Valid
Approximate entropy	0,9163	Valid
Cumulative sums	0,6718	Valid
Random-excursions-test (x= -4)	0,8830	Valid
Random-excursions-variant test (x = -9)	0,4597	Valid

4.2. FIPS Test

In addition to the NIST 800-22 test, the FIPS test was also applied for the RNG success determine. The FIPS test consists of four separate tests: Monobit test, Poker test, Run test and Long Run test. For every FIPS test, 20,000 bits (1 and 0) are required. If any of the four tests fail, the RNG does not pass the FIPS test. Each test result has a required range to succeed [46]. The purpose of the "monobit" test is to determine the distribution of '0' and '1' in the bit sequence. The purpose of the "poker" test is to determine if the number of repetitions of the specified block pieces is within the required range. The purpose of the "run" test is to determine if all consecutive bit sequences of all '1' or '0' values that are part of the 20,000 bits stream are within the desired range. The purpose of the "long run" test is to determine if there are more than 34 consecutive bits in the "run" test [46, 47].

For the FIPS test, 20,000 bits are taken from the implemented RNG output. The FIPS test requirements and results are given in Table 2. When Table 2 is examined, it is seen that the RNG outputs are successful in all FIPS tests.

Table 2

FIPS tests result of implemented microcontroller-based RNG by using the discrete chaotic maps

Test name	Required condition	Test result value	Result
Monobit	$9654 < X < 10346$	9963	Valid
Poker	$1.03 < X < 57.4$	51	Valid
Run	Consecutive 1 and 0 block length = 1	2479	Valid
	$2267 < X < 2733$		
Run	Consecutive 1 and 0 block length = 2	1190	Valid
	$1079 < X < 1421$		
Run	Consecutive 1 and 0 block length = 3	681	Valid
	$502 < X < 748$		
Run	Consecutive 1 and 0 block length = 4	314	Valid
	$223 < X < 402$		

	Consecutive 1 and 0 block length = 5	156	Valid
	$90 < X < 223$		
	Consecutive 1 and 0 block length = 6 and more	144	Valid
	$90 < X < 223$		
Long Run	All consecutive blocks of "1" and "0" must be less than 34.	No consecutive blocks greater than 34 were found.	Valid

5. CONCLUSIONS AND FUTURE WORK

In this study, firstly, two-dimensional (2D) Lozi, Tinkerbell and Barnsley Fern discrete CMs are implemented based on microcontroller. When Figure 4, Figure 5 and Figure 6 are examined, the numerical simulation results performed in the Matlab® program and microcontroller output results confirm each other. Then, microcontroller based random number generator with the pre-processing algorithm given in Figure 8 and Figure 9 is implemented by using the three different discrete CMs. The RNG outputs are applied to the NIST 800-22 and FIPS tests and passed the all tests.

Consequently, implemented microcontroller-based RNG by using CMs can be used in a variety of engineering applications. In future works, chaos based encryption and communication applications can be realized with the RNG outputs obtained in this study. Similarly, the RNG outputs can be used for random number needs in various optimization algorithms. In this way, optimization success can be increased.

Acknowledgements

The author would like to thank the SAUJS editors and reviewers who reviewed the study.

Funding

The author received no financial support for the research, authorship, and/or publication of this paper.

The Declaration of Conflict of Interest/ Common Interest

No conflict of interest or common interest has been declared by the author.

The Declaration of Ethics Committee Approval

The author declares that this document does not require an ethics committee approval or any special permission.

The Declaration of Research and Publication Ethics

The author of the paper declares that he complies with the scientific, ethical and quotation rules of SAUJS in all processes of the paper and that he does not make any falsification on the data collected. In addition, he declares that Sakarya University Journal of Science and its editorial board have no responsibility for any ethical violations that may be encountered, and that this study has not been evaluated in any academic publication environment other than Sakarya University Journal of Science.

REFERENCES

- [1] Y. Liu and X. Tong, "Hyperchaotic system-based pseudorandom number generator", *IET Information Security*, vol. 10, no. 6, pp. 433-441, 2016.
- [2] İ. Koyuncu and A.T. Özcerit, "The design and realization of a new high speed FPGA-based chaotic true random number generator", *Computers and Electrical Engineering*, Vol. 58, pp. 203-214, 2017.
- [3] F. Yu, L. Li, Q. Tang, S. Cai, Y. Song and Q. Xu, "A survey on true random number generators based on chaos", *Discrete Dynamics in Nature and Society*, Vol. 2019, Article ID: 2545123, 2019.
- [4] X.Y. Wang and Y.X. Xie, "A design of pseudo-random bit generator based on single chaotic system", *International Journal of Modern Physics C*, Vol. 23, no. 3, pp.1250024-1 – 1250024-11, 2012.
- [5] S. Ergün and S. Özoğuz, "Truly random number generators based on non-autonomous continuous-time chaos", *International Journal of Circuit Theory and Applications*, Vol. 38, pp. 1-24, 2010.
- [6] M.E. Yalçın, J.A.K. Suykens and J. Vandewalle, "True random bit generation from a double-scroll attractor", *IEEE Transactions on Circuit and Systems-I: Regular Papers*, Vol. 51, no. 7, pp. 1395-1404, 2004.
- [7] S. Vaidyanathan, A. Akgul, S. Kaçar and U. Çavuşoğlu, "A new 4-D chaotic hyperjerk system, its synchronization, circuit design and applications in RNG, image encryption and chaos-based steganography", *The European Physical Journal Plus*, Vol. 133, Article number: 46, 2018.
- [8] A. Akgul, C. Arslan and B. Arıcıoğlu, "Design of an interface for random number generators based on integer and fractional order chaotic systems", *Chaos Theory and Applications*, Vol. 01, no. 1, pp. 1-18, 2019.
- [9] B.C. Bao, H.Z. Li, X. Zhang and M. Chen, "Initial-switched boosting bifurcations in 2D hyperchaotic map", *Chaos*, Vol. 30, no. 3, 033107, 2020.
- [10] D. Lambic, "A novel method of S-box design based on discrete chaotic map", *Nonlinear Dynamics*, Vol. 87, pp. 2407-2413, 2017.
- [11] A.A. Alzaidi, M. Ahmad, M.N. Doja, E.A. Solami and M.M.S. Beg, "A new 1D chaotic map and β -hill climbing for generating substitution-boxes", *IEEE Access*, Vol. 6, pp. 55405-55418, 2018.
- [12] O. Alpar, "Analysis of a new simple one dimensional chaotic map", *Nonlinear*

- Dynamics, vol. 78, no. 2, pp. 771-778, 2014.
- [13] Z. Hua and Y. Zhou, "One-dimensional nonlinear model for producing chaos", *IEEE Transactions on Circuit and Systems-I: Regular Papers*, Vol. 65, no. 1, pp. 235-246, 2018.
- [14] L. Liu and S. Miao, "A new simple one-dimensional chaotic map and its application for image encryption", *Multimedia Tools and Applications*, Vol. 77, pp. 21445-21462, 2018.
- [15] M. Hènon, "A two-dimensional mapping with a strange attractor", *Communications in Mathematical Physics*, Vol. 50, pp. 69-77, 1976.
- [16] L.Q. Chen, "An open-plus-closed-loop control for discrete chaos and hyperchaos", *Physics Letters A*, Vol. 281, pp. 327-333, 2001.
- [17] M.F. Barnsley, "Fractals Everywhere", Academic Press, USA, pp. 85-91, 1993.
- [18] A. Ouannas, A.A. Khennaoui, S. Bendoukha, T.P. Vo, V.T. Pham and V.V. Huynh, "The fractional form of the Tinkerbell map is chaotic", *Applied Sciences*, Vol. 8, Article ID: 2640, 2018.
- [19] R. Lozi, "Un attracteur étrange (?) du type attracteur de hènnon", *Journal De Physique*, Vol. 39, no. 8, pp. C5-9, 1978.
- [20] Y. Xiao, K. Sun and S. He, "Constructing chaotic map with multi-cavity", *The European Physical Journal Plus*, Vol. 135, Article number: 21, 2020.
- [21] Z. Hua, Y. Zhou, C.M. Pun and C.L.P. Chen, "2D sine logistic modulation map for image encryption", *Information Sciences*, Vol. 297, pp. 80-94, 2015.
- [22] Z. Liu, T. Xia and J. Wang, "Fractional two-dimensional discrete chaotic map its applications to the information security with elliptic-curve public key cryptography", *Journal of Vibration and Control*, Vol. 24, no. 20, pp. 4797-4824, 2018.
- [23] Y. Peng, K. Sun, D. Peng and W. Ai, "Dynamics of a higher dimensional fractional-order chaotic map", *Physica A*, Vol. 525, pp. 96-107, 2019.
- [24] A. Alghafis, N. Munir, M. Khan and I. Hussain, "An encryption scheme based on discrete quantum map and continuous chaotic system", *International Journal of Theoretical Physics*, Vol. 59, pp. 1227-1240, 2020.
- [25] J. Fridrich, "Symmetric ciphers based on two-dimensional chaotic maps", *International Journal of Bifurcation and Chaos*, Vol. 8, no. 6, pp. 1259-1284, 1998.
- [26] X. Liao, X. Li, J. Pen and G. Chen, "A digital secure image communication scheme based on the chaotic Chebyshev map", *International Journal of Communication Systems*, Vol. 17, pp. 437-445, 2004.
- [27] S. Papadimitriou, A. Bezerianos, T. Bountis and G. Pavlides, "Secure communication protocols with discrete nonlinear chaotic maps", *Journal of Systems Architecture*, Vol. 47, pp. 61-72, 2001.
- [28] M. Zhang and X. Tong, "A new chaotic map based image encryption schemes for several image formats", *The Journal of Systems and Software*, Vol. 98, pp. 140-154, 2014.
- [29] R. Li, Q. Liu and L. Liu, "Novel image encryption algorithm based on improved logistic map", *IET Image Processing*, Vol. 13, no. 1, pp. 125-134, 2019.
- [30] C. Pak, J. Kim, K. An, C. Kim, K. Kim and C. Pak, "A novel color image LSB steganography using improved 1D chaotic map", *Multimedia Tools and*

- Applications, Vol. 79, pp. 1409-1425, 2020.
- [31] Y. Naseer, D. Shah and T. Shah, "A novel approach to improve multimedia security utilizing 3D mixed chaotic map", *Microprocessors and Microsystems*, Vol. 65, pp. 1-6, 2019.
- [32] D. Herbadji, A. Belmeguenai, N. Derouiche and H. Liu, "Colour image encryption scheme based on enhanced quadratic map", *IET Image Processing*, Vol. 14, no. 1, pp. 40-52, 2019.
- [33] M.A. Dastgheib and M. Farhang, "A digital pseudo-random number generator based on sawtooth chaotic map with a guaranteed enhanced period", *Nonlinear Dynamics*, Vol. 89, pp. 2957-2966, 2017.
- [34] E. Avaroğlu, "Pseudorandom number generator based on Arnold cat map and statistical analysis", *Turkish Journal of Electrical Engineering & Computer Sciences*, Vol. 25, pp. 633-643, 2017.
- [35] D. Lambic, M. Nikolic, "Pseudo-random number generator based on discrete-space chaotic map", *Nonlinear Dynamics*, Vol. 90, pp. 223-232, 2017.
- [36] A.V. Tutueva, E.G. Nepomuceno, A.I. Karimov, V.S. Andreev and D.N. Butusov, "Adaptive chaotic maps and their application to pseudo-random numbers generation", *Chaos, Solitons and Fractals*, Vol. 133, 109615, 2020.
- [37] O. Garasym, I. Taralova and R. Lozi, "New Nonlinear CPRNG Based on Tent and Logistic Maps". In: J. Lü, X. Yu, G. Chen, W. Yu (eds) *Complex Systems and Networks. Understanding Complex Systems*, Springer, Berlin, Heidelberg, pp.131-161, 2016.
- [38] Magfirawaty, M.T. Suryadi, K. Ramli, "On the design of henon and logistic map-based random number generator", *IOP Conference Series: Journal of Physics: Conference Series*, Vol. 893, 012060, 2017.
- [39] S. Ergün, S. Tanrıseven, "Random number generators based on discrete-time chaotic maps", *IEEE EUROCON 18th International Conference on Smart Technologies*, pp. 1-4, 2019.
- [40] L. Moysis and A.T. Azar, "New discrete time 2D chaotic maps", *International Journal of System Dynamics Applications*, Vol. 6, no. 1, pp.77-104, 2017.
- [41] A.M. Garipcan, E. Erdem, "Implementation and performance analysis of true random number generator on FPGA environment by using non-periodic chaotic signals obtained from chaotic maps", *Arabian Journal for Science and Engineering*, Vol. 44, pp. 9427-9441, 2019.
- [42] P. L'ecuyer, R. Simard, "TestU01: A C library for empirical testing of random number generators", *ACM Transactions on Mathematical Software*, Vol. 33, no. 4, 22, 2007.
- [43] R. Santoro, O. Sentieys and S. Roy, "On-line monitoring of random number generators for embedded security", *IEEE International Symposium on Circuit and Systems*, pp. 3050-3053, 2009.
- [44] D. Lihua, Z. Yong, J. Ligang and H. Xucang, "Study on the pass rate of NIST SP800-22 statistical test suite", *IEEE Tenth International Conference on Computational Intelligence and Security*, pp. 402-404, 2014.
- [45] A. Rukhin, J. Soto, J. Nechvatal, M. Smid, E. Barker, S. Leigh, M. Levenson, M. Vangel, D. Banks, A. Heckert, J. Dray and S. Vo, "A Statistical Test Suite for Random and Pseudorandom Number Generators for Cryptographic Applications", *National Institute of Standards and Technology (NIST)*, 2010.

- [46] L. Min, T. Chen and H. Zang, “Analysis of FIPS 140-2 test and chaos-based pseudorandom number generators”, *Chaotic Modeling and Simulation*, Vol. 2, pp. 273-280, 2013.
- [47] İ. Koyuncu, “Kriptolojik uygulamalar için FPGA tabanlı yeni kaotik osilatörlerin ve gerçek rastgele sayı üreticilerinin tasarımı ve gerçekleştirilmesi”, PhD Thesis, Sakarya University, Institute of Science, Sakarya, 2014.

JOURNAL OF SCIENCE



SAKARYA UNIVERSITY

Sakarya University Journal of Science

ISSN 1301-4048 | e-ISSN 2147-835X | Period Bimonthly | Founded: 1997 | Publisher Sakarya University |
<http://www.saujs.sakarya.edu.tr/en/>

Title: Real-Time Obstacle Avoidance Based on Floor Detection for Mobile Robots

Authors: Adem HİÇDURMAZ, Adem TUNCER

Received: 2020-01-13 13:39:02

Accepted: 2020-06-18 18:32:25

Article Type: Research Article

Volume: 24

Issue: 5

Month: October

Year: 2020

Pages: 845-853

How to cite

Adem HİÇDURMAZ, Adem TUNCER; (2020), Real-Time Obstacle Avoidance Based on Floor Detection for Mobile Robots. Sakarya University Journal of Science, 24(5), 845-853, DOI: <https://doi.org/10.16984/saufenbilder.674122>

Access link

<http://www.saujs.sakarya.edu.tr/en/pub/issue/56422/674122>

New submission to SAUJS

<http://dergipark.org.tr/en/journal/1115/submission/step/manuscript/new>

Real-Time Obstacle Avoidance Based on Floor Detection for Mobile Robots

Adem HIÇDURMAZ^{*1}, Adem TUNCER²

Abstract

Obstacle detection and avoidance are two main problems that demand solutions in the autonomous movement of mobile robots. To this end, the robots have been equipped with sensors and cameras. This study proposes a new method that allows mobile robots to move freely without any collision in an uncertain (i.e., both static and dynamic) workspace by processing images taken using a real-time webcam. In the study, a robot was allowed to move depending on the visibility and suitability of the floor in the images. These steps were repeated for each new image and, furthermore, the images were segmented based on an adaptive threshold obtained by calculating the statistical parameters. This segmentation was aimed to separate the floor from other areas in the study. Experimental results demonstrate that the proposed method is extremely successful to separate the floor from other regions and has a low cost and flexible method for obstacle avoidance.

Keywords: Mobile robot, Obstacle avoidance, Floor detection, Image segmentation, Adaptive threshold

1. INTRODUCTION

It is critical for a mobile robot to be able to move freely in a known or unknown environment by avoiding obstacles. Detecting and avoiding obstacles are among the most important and challenging issues to be considered in safe navigation. Various methods have been proposed to solve the obstacle avoidance problem. Some approaches use laser sensors [1], and some use ultrasonic sensors [2]. In addition to sensors,

vision-based methods are also used to avoid obstacles.

Various studies have been conducted on vision-based approaches using monocular [3, 4] or stereo [5] cameras. Vision-based systems provide significant information about the environment with a wide perspective [6]. An autonomous mobile robot using a camera can map an unknown environment with no prior information. Images taken with cameras can provide abundant

* Corresponding Author: ademhicdurmaz@gmail.com

¹ Yalova University, Department of Computer Engineering, Institute of Science, Yalova, Turkey.
ORCID: <https://orcid.org/0000-0001-7765-4529>

² Yalova University, Department of Computer Engineering, Engineering Faculty, Yalova, Turkey.
E-mail: adem.tuncer@yalova.edu.tr ORCID: <https://orcid.org/0000-0001-7305-1886>

information about the environment, including brightness, color, and texture. In vision-based systems, images must be processed in real-time. The acquired images may contain various noises due to factors such as the amount of light, the brightness of the objects, and the angle of the camera, which cause deterioration in image quality. During image processing, segmentation and threshold techniques are applied to eliminate these negative effects and achieve successful results [7, 8]. Image segmentation, one of the most fundamental issues in image processing, subdivides a digital image into various parts of pixels [9].

Several past studies have focused on floor detection. Instead of detecting the obstacles, the areas where the robot can move freely are obtained by processing the floor images. Processing floor images for navigation without collision is practical and effective, especially for robots used in indoor environments. The floor-detection method establishes the separation of the floor and the obstacles at a low cost by processing the images obtained by the camera on the robot. No additional processing cost is required to determine the characteristics of the obstacles, such as location and dimensions.

In this study, we propose a novel floor-based detection approach for autonomous robots to effectively avoid obstacles, based on monocular vision. The major drawback to floor-based detection is that objects close to the floor, such as walls, cannot be detected. The motivation in this study was to perform segmentation by simple and fast filtering on images obtained simultaneously to distinguish between the floor and obstacles in the images taken and to determine the areas where the robot can move freely.

Classical segmentation methods can achieve very good results when the colors in the image are significantly different from each other [10]. While the obstacles have certain edge characteristics, the areas described as floor are variable, and it is very difficult to obtain features of the floor from the images. In our study, a statistical method was applied to the images to determine the floor areas. The image segmentation technique of thresholding was used. Thresholding is of great

importance in the detection process [11], and it is one of the most common and simple methods [12]. Since the effects of negative factors (light, shade, etc.) and colors in each image will vary, segmentation was performed with an adaptive threshold value. Comparisons between the segments were made according to the percentage change of the arithmetic mean (PCAM). The proposed method can be used effectively in static and dynamic environments.

The main contributions of this study are summarized as follows:

- An effective method based on a monocular camera that can be used to avoid collision has been proposed.
- The mobile robot is capable of navigating by avoiding obstacles in a known and unknown environment.
- Since obstacles are not detected separately, obstacle avoidance is achieved quickly and easily without the need for additional filters (e.g. Canny, Sobel, and Laplacian). Thus, the calculations are performed at a lower cost.
- To our best knowledge, this is the first study that uses the PCAM to find similarities or differences between segments.

2. LITERATURE REVIEW

Obstacle detection and avoidance have key roles in mobile robot navigation systems. To solve these challenging processes, numerous studies have been carried out, especially with vision-based systems. Li et al. [13] proposed image-based obstacle avoidance. They combined the dynamic window approach (DWA) and artificial potential field algorithm to determine the path of motion and to avoid obstacles. Kalogeiton et al. [14] used a stereo camera for mapping the environment for both obstacles and free space. After mapping the environment, the cognitive-based adaptive optimization (CAO) approach was used for the next optimum motion. Dönmez et al. [15] proposed a Gaussian controller method that would allow the robot to be advanced from an

initial position to the target position by determining the least costly path between the starting and target position on the images obtained from a camera mounted on the ceiling. Tuncer and Yildirim also [16] proposed a whole system for mobile robots including a vision-based path planning system using a camera mounted to the ceiling for locating the robot and obstacles. Mishra and Panda [17] proposed a multilevel color image segmentation method using entropy-based thresholding and bat algorithm. In the study, to measure the performance of the method, several objective functions, such as RMSE, PSNR, Jaccard similarity coefficient were used.

Some of the vision-based navigation studies include floor detection approaches. Benn and Lauria [12] proposed a two-stage method that can be used in dynamic environments, using a combination of image color segmentation and edge detection. Their study focused on separating the floor and obstacles from traversable space. The first stage uses segmentation for color images and the second stage uses the Canny filter and Hough transform to clarify the edges of the floor. However, since pixel-based evaluation and edge filters were emphasized in the study, objects that were very similar to the floor, such as the wall could be indistinguishable. Bhowmick et al. [18] relied on floor detection using a conventional breadth-first search-based region-growing technique to detect obstacles. However, they stated that the process was slow because of the many conditions in the study. Chun et al. [19] proposed detecting the floor candidate regions by exploiting the nonlinear diffusion method and detecting floor regions using the image segmentation technique. Li and Birchfield [20] proposed a combination of vertical edges, thresholding, and segmentation to approximate a wall-floor boundary. Their technique combined three visual cues for calculating the likelihood of horizontal intensity edge line segments defining the wall-floor boundary. Ling et al. [21] proposed a combination of k-means clustering and improved principal component analysis (PCA) methods for vision-based floor segmentation in indoor robot navigation, with a camera that was fixed on the ceiling. However, because the camera

was on the ceiling, objects that the robot could pass under could also be perceived as the floor.

3. METHOD OVERVIEW

Since the variety and shape of obstacles in an indoor environment can be unlimited, the detection of the floor instead of the obstacles is the focal point of the proposed method. Various filters are available for detecting the edges of objects in an image. The most used filters are Canny, Sobel, and Laplacian. In the proposed approach, floor detection can be performed quickly and easily without the use of these filters. Image segmentation is one of the first and most important steps in image processing; in this process, an image is partitioned into multiple segments. Since light, shadow, and patterns are factors that have a significant impact on the pixel-based approach to floor detection, in this study, the image is divided into segments and then processed.

In the study, all the images were resized to the 300×535. Grid-based segmentation was applied to the images, as shown in Figure 1. As seen in the figure, the image is segmented to 37×5 which performs well for images of the size 300×535 in the experiments. The number of segments can be changed depending on the size of the image or robot.

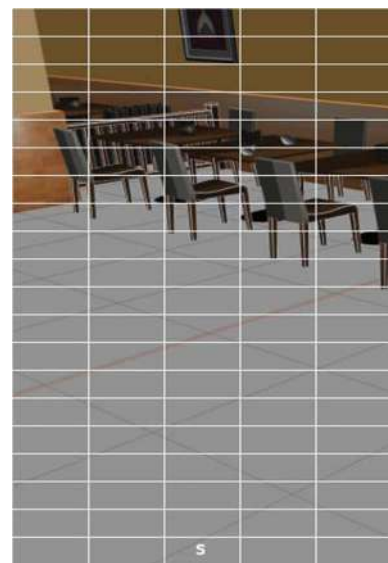


Figure 1 An example of image segmentation

The floor is always located in the lower half of the images. To reduce the possibility of errors and avoid unnecessary operations, the bottom half of the image is processed. The edges of the floor and the parts where the obstacles begin are important for the movement of the robot. Areas that are upper the obstacles in the images are not considered because they are not be related to robot movement. Even if there are errors in the detection of floor segments that are far from the robot, the image becomes clearer when the robot moves, when these segments are approached. Therefore, the floor segments which are close to the robot are notable, others are negligible. For all these reasons, ground detection is carried out by considering the segments close to the robot, not the entire image in the movement of the robot.

The sample segment, which is indicated by s , is selected from the bottom of the image because this will very likely be the floor. The arithmetic means of all the segments are calculated and compared with the segment s , which is detected as the floor. Values lower than the predefined threshold value are considered to be the floor. After comparing the segments, the floor segments are assigned a value of '0' and the other segments are assigned a value of '1' to obtain a filtered matrix. This study uses an adaptive threshold value instead of a fixed value. The PCAM is taken as the threshold value. For indoor images, the floor images may be similar to the images of other objects (wall, curtains, sofa, etc.). In this case, the threshold value must be changed dynamically to be effective. In this study, the threshold value is updated at the end of each new image captured by the camera. If the standard deviation of the filtered matrix is low, the threshold value is increased by one unit as a percentage, otherwise, it is decreased by one unit.

$$A = \frac{1}{n} \sum_{i=1}^n a_i \quad (1)$$

where A is the arithmetic mean of any segment, a is the pixel values, and n is the number of pixels, which is given by Equation 1. The PCAM is found by Equation 2.

$$p = |A - s(A)|/s(A) \times 100 \quad (2)$$

where p is the PCAM of two segments and $s(A)$ is the arithmetic mean of the s segment. The filtered matrix is obtained by Equation 3.

$$FM_{ij} = \begin{cases} 0, & \text{if } t > p \\ 1, & \text{otherwise} \end{cases} \quad (3)$$

where FM is the filtered matrix, i and j are the dimensions of the matrix, and t is an adaptive threshold value.

Then, the standard deviation of the filtered matrix is calculated. The low standard deviation makes it difficult to distinguish between the floor and other things, such as a wall or curtains. This status indicates that the segments are close to each other in terms of the arithmetic mean value. In this case, the threshold value is reduced, otherwise, this value is increased. Thus, robust results are obtained for close segments. The filtered matrix provides effective floor information for robot navigation. Since the size of the filtered matrix is much smaller than the size of the original image, the trajectory planning on this filtered image can be done quickly.

Algorithm 1. Pseudo-code of floor detection

Input : Current frame as a matrix M
Output : Filtered matrix FM
 $s \leftarrow \text{getMatrixSampleAreaMean}(M)$
 $t \leftarrow \text{threshold acceptable rate of changes}$
 $v \leftarrow \text{reference variance value}$
 $\text{row} \leftarrow \text{getRowByImageSize}(M)$
 $\text{col} \leftarrow \text{getColByImageSize}(M)$
foreach $i=0$ to gridrow **do**
 foreach $j=0$ to gridcol **do**
 $m = \text{getCurrentGridPartMean}()$
 $p = \text{getPercentageofChange}(s,m)$
 if t is greater than p **then**
 $FM[i][j]$ is 0
 else
 $FM[i][j]$ is 1
 end
end
if ($FM.\text{variance} \leq v$)
 update threshold value ($t=t+t \times 0.1$)
return FM

Algorithm 1 shows the pseudo-code of the floor detection used in the study. PCAM is calculated

using the steps followed in the algorithm. How many parts the image will be horizontally and vertically divided into is dynamically determined; then, the threshold in which the arithmetic mean change will be most effective is identified. The ν value which is the reference variance value used in the algorithm is used to decide whether the threshold value should be updated. The threshold value is updated if the variance of the image is smaller than ν , otherwise not update.

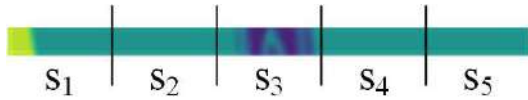


Figure 2 A horizontal part of the image consisting of 5 segments

Figure 2 shows the top row of the segmented image seen in Figure 1. A comparison of the variance, standard deviation, and arithmetic mean values of the sample segment s and five segments are shown in Table 1.

Table 1

Variance, mean and standard deviation values for sample s segment and 5 segments

Method	s	s_1	s_2	s_3	s_4	s_5
Variance	0.22	416.01	0	388.38	0	0
Arithmetic mean	121.66	81.63	68	40.45	68	68
Standard deviation	0.47	20	0	20	0	0

As shown Table 1, the variance of segment s is 0.22, the arithmetic mean is 121.66, and the standard deviation is 0.47. Moreover, although the variance and standard deviation values are very close to the s segment, s_2 , s_4 , and s_5 have very different arithmetic means. In this respect, the variance and standard deviation values used in image processing will be insufficient for distinguishing between the floor and the other objects. Therefore, PCAM has been proposed in the study.

4. EXPERIMENTS

In this study, image segmentation was performed in a simple and fast way with the proposed method, and the effect of the PCAM was

determined to find the similarities between the segments. Experiments were performed on a machine with i7 1.8 GHz CPU and coded in Python programming language. The proposed algorithm is able to process an image in about 40 milliseconds. The method also works effectively in environments with dynamic obstacles.

Firstly, simulation studies with different images were carried out on the Robot Operating System (ROS) [22] framework to demonstrate the performance of the proposed algorithm. The Kinect cam was used to obtain the images in the ROS. The images were captured at 20 frames per second. The robot which used for simulations moves at 0.25 m/s when there is no obstacle, but slowdowns its speed when detected any obstacle.

After the successful results from the simulation studies, floor detection was performed on the real images, and these were presented here. Figure 3 shows: (a) the image taken from a real environment, (b) the filtered image according to the variance, (c) the filtered image according to the standard deviation, and (d) the filtered image according to the PCAM. The noise, which is a light, shadow, and a floor with a pattern, makes it difficult to detect the floor. For example, as seen in the image, there is a carpet with patterns. However, with the proposed method, as shown in Figure 3(d), the floor in the actual environment image can be easily detected.

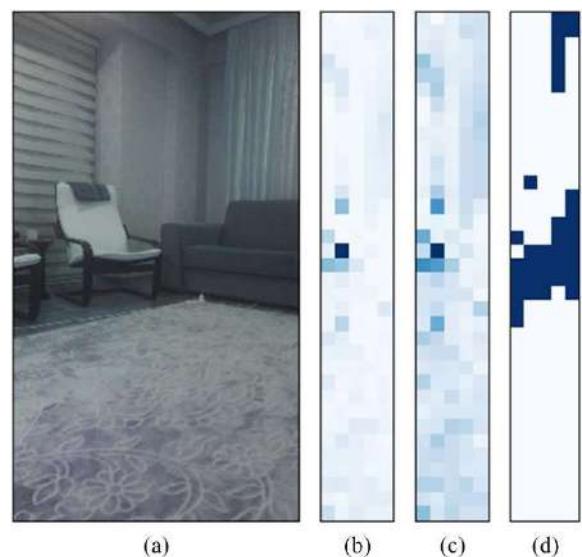


Figure 3 (a) Original image (b) variance (c) standard deviation (d) PCAM

Since the threshold value may vary depending on the complexity and size of the images, it has no fixed value. Experiments were carried out with different initial threshold values for the same image, and the appropriate value was determined according to the similarity ratio of the sample floor segment and other segments in the image. Therefore, the initial threshold value for the images given in the study was considered as 40, and at each step, the threshold value is updated according to the variance value of the filtered image. The arithmetic means of the sample segment and other segments were compared and the segments with at least the same threshold value were marked as “1” and the others as “0”.

In Figure 4, an obstacle is placed in the environment, and the effect of the method is observed when the environment is dynamic. It is clear that the proposed method can better detect the obstacle and distinguish it from the floor. This allows the mobile robot to easily distinguish between the floor and the obstacles in dynamic environments during autonomous navigation.

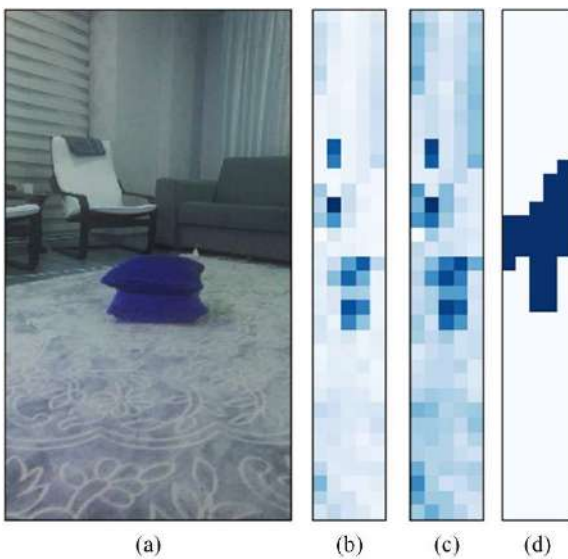


Figure 4 (a) Original image (b) variance (c) standard deviation (d) PCAM

Even if the floor and objects can be distinguished, it is a little more difficult to distinguish objects that are similar to the floor. For example, in general, the floor and wall have similar features. As can be seen in the Figure 5, although the distinction between floor and wall is difficult, the

difference between the proposed approach can be clearly determined.

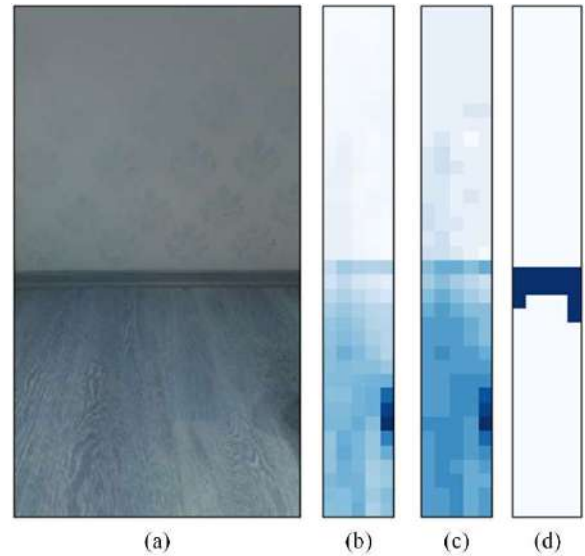


Figure 5 (a) Original image (b) variance (c) standard deviation (d) PCAM

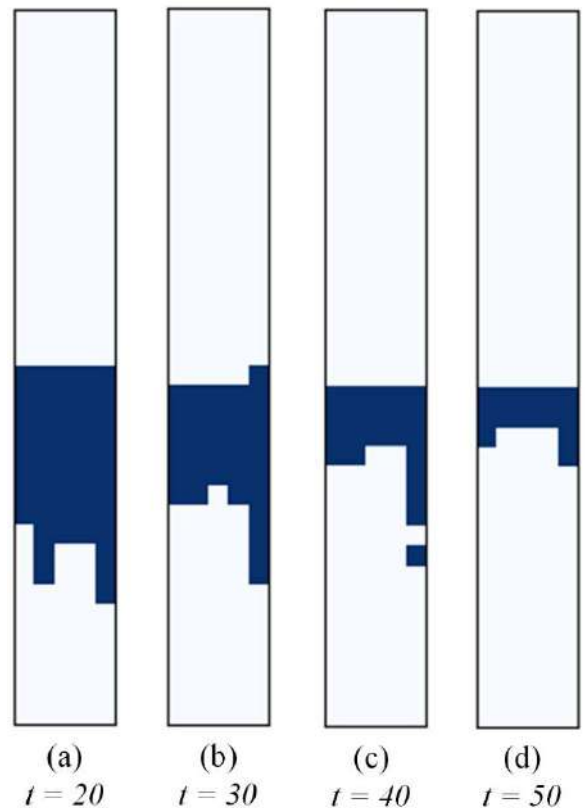


Figure 6 Effect of different threshold values

In addition, experiments in which the threshold values for the image of Figure 5 are applied as 20, 30, 40, and 50 are shown in Figure 6 to show the

effect of the initial threshold values. The appropriate threshold value for this image appears to be 50. The effect of adaptive threshold value on the separation of floor and wall is quite effective and, in this respect, the threshold value is used adaptively in the study.

5. CONCLUSION

This study proposed a new image-based floor detection approach in an indoor environment for autonomous mobile robots. The floor was detected using image segmentation and an adaptive threshold. Then, the segments were compared according to PCAM to determine which segments constitute the floor. To the best of our knowledge, the present study is the first to use the PCAM for the identification of the similarities or differences between the segments. However, it should be noted that even if the floor and the wall are similar, the floor can easily be separated from the wall. Additionally, as the proposed method does not require any prior knowledge of the environment, it can be applied to real-time problems.

The experimental results show that the proposed algorithm reaches 92% accuracy, which shows successful in separating the floor from other regions making it a highly flexible method for obstacle avoidance. Hence, it can be concluded that the proposed provides successful results at a low cost without the need for additional filters that are used in image processing.

Funding

The authors received no financial support for the research, authorship, and/or publication of this paper.

The Declaration of Conflict of Interest/ Common Interest

No conflict of interest or common interest has been declared by the authors.

Authors' Contribution

AH: Literature review, research, methodology, simulation, writing the initial draft.

AT: Supervision, research, methodology, interpretation, writing-revision, and finalizing.

The Declaration of Ethics Committee Approval

The authors declare that this document does not require an ethics committee approval or any special permission.

The Declaration of Research and Publication Ethics

The authors of the paper declare that they comply with the scientific, ethical and quotation rules of SAUJS in all processes of the paper and that they do not make any falsification on the data collected. In addition, they declare that Sakarya University Journal of Science and its editorial board have no responsibility for any ethical violations that may be encountered, and that this study has not been evaluated in any academic publication environment other than Sakarya University Journal of Science.

REFERENCES

- [1] H. Surmann, A. Nüchter, and J. Hertzberg, "An autonomous mobile robot with a 3D laser range finder for 3D exploration and digitalization of indoor environments," *Robotics and Autonomous Systems*, vol. 45, no. 3–4, pp. 181–198, 2003.
- [2] S. Kim and H. Kim, "Optimally overlapped ultrasonic sensor ring design for minimal positional uncertainty in obstacle detection," *International Journal of Control, Automation and Systems*, vol. 8, no. 6, pp. 1280–1287, 2010.
- [3] A. Al-Kaff, F. García, D. Martín, A. De La Escalera, and J. M. Armingol, "Obstacle detection and avoidance system based on

- monocular camera and size expansion algorithm for UAVs,” *Sensors*, vol. 17, no. 5, pp. 1061, 2017.
- [4] H. Alvarez, L. M. Paz, J. Sturm, and D. Cremers, “Collision avoidance for quadrotors with a monocular camera,” In *Experimental Robotics*, Springer, Cham., pp. 195–209, 2016.
- [5] K. McGuire, G. De Croon, C. De Wagter, K. Tuyls, and H. Kappen, “Efficient optical flow and stereo vision for velocity estimation and obstacle avoidance on an autonomous pocket drone,” *IEEE Robotics and Automation Letters*, vol. 2, no. 2, pp. 1070–1076, 2017.
- [6] H. Zhang, D. E. Hernandez, Z. Su, and B. Su, “A low cost vision-based road-following system for mobile robots,” *Applied Sciences*, vol. 8, no. 9, pp. 1635, 2018.
- [7] N. Otsu, “A threshold selection method from gray-level histograms,” *IEEE transactions on systems, man, and cybernetics*, vol. 9, no. 1, pp. 62–66, 1979.
- [8] N. M. Zaitoun and M. J. Aqel, “Survey on image segmentation techniques,” *Procedia Computer Science*, vol. 65, pp. 797–806, 2015.
- [9] N. Ikonomakis, K. N. Plataniotis, and A. N. Venetsanopoulos, “Color image segmentation for multimedia applications,” *Journal of Intelligent and Robotic Systems*, vol. 28, no. 1–2, pp. 5–20, 2000.
- [10] H. Zhang, X. Wang, Y. Chen, G. Jiang, and S. Lin, “Research on Vision-Based Navigation for Plant Protection UAV under the Near Color Background,” *Symmetry*, vol. 11, no. 4, pp. 533, 2019.
- [11] S. J. Dumble and P. W. Gibbens, “Horizon profile detection for attitude determination,” *Journal of Intelligent & Robotic Systems*, vol. 68, no. 3–4, pp. 339–357, 2012.
- [12] W. Benn and S. Lauria, “Robot navigation control based on monocular images: an image processing algorithm for obstacle avoidance decisions,” *Mathematical Problems in Engineering*, 14 pages, 2012.
- [13] S. A. Li, L. H. Chou, T. H. Chang, C. H. Yang, and Y. C. Chang, “Obstacle Avoidance of Mobile Robot Based on HyperOmni Vision,” *Sensors and Materials*, vol. 31, no. 3, pp. 1021–1036, 2019.
- [14] V. S. Kalogeiton, K. Ioannidis, G. C. Sirakoulis, and E. B. Kosmatopoulos, “Real-Time Active SLAM and Obstacle Avoidance for an Autonomous Robot Based on Stereo Vision,” *Cybernetics and Systems*, vol. 50, no. 3, pp. 239–260, 2019.
- [15] E. Dönmez, A. F. Kocamaz, and M. Dirik, “A Vision-Based Real-Time Mobile Robot Controller Design Based on Gaussian Function for Indoor Environment,” *Arabian Journal for Science and Engineering*, vol. 43, no. 12, pp. 7127–7142, 2018.
- [16] A. Tuncer and M. Yildirim, “Design and implementation of a genetic algorithm IP core on an FPGA for path planning of mobile robots,” *Turkish Journal of Electrical Engineering and Computer Sciences*, vol. 24, no. 6, pp. 5055–5067, 2016.
- [17] S. Mishra and M. Panda, “Bat algorithm for multilevel colour image segmentation using entropy-based thresholding,” *Arabian Journal for Science and Engineering*, vol. 43, no. 12, pp. 7285–7314, 2018.
- [18] S. Bhowmick, A. Pant, J. Mukherjee, and A. K. Deb, “A novel floor segmentation algorithm for mobile robot navigation,” In *2015 Fifth National Conference on Computer Vision, Pattern Recognition, Image Processing and Graphics (NCVPRIPG)*, IEEE, pp. 1–4, 2015.
- [19] C. Chun, D. Park, W. Kim, and C. Kim, “Floor detection based depth estimation from a single indoor scene,” In *2013 IEEE International Conference on Image Processing*, pp. 3358–3362, 2013.

- [20] Y. Li and S. T. Birchfield, "Image-based segmentation of indoor corridor floors for a mobile robot," In 2010 IEEE/RSJ International Conference on Intelligent Robots and Systems, pp. 837–843, 2010.
- [21] M. Ling, W. Jianming, Z. Bo, and W. Shengbei, "Automatic floor segmentation for indoor robot navigation," In 2nd International Conference on Signal Processing Systems, vol. 1, pp. 684–689, 2010.
- [22] "About ROS." [Online]. Available: <https://www.ros.org/about-ros/>. [Accessed: 10-Nov-2019].

JOURNAL OF SCIENCE



SAKARYA UNIVERSITY

Sakarya University Journal of Science

ISSN 1301-4048 | e-ISSN 2147-835X | Period Bimonthly | Founded: 1997 | Publisher Sakarya University |
<http://www.saujs.sakarya.edu.tr/en/>

Title: Theoretical and Experimental Comparison of Micro-hardness and Bulk Modulus of Orthorhombic $\text{YBa}_2\text{Cu}_3\text{-xZnxO}$ Superconductor Nanoparticles Manufactured using Sol-Gel Method

Authors: Elif AŞIKUZUN, Özgür ÖZTÜRK

Received: 2020-01-16 14:51:33

Accepted: 2020-06-20 17:02:42

Article Type: Research Article

Volume: 24

Issue: 5

Month: October

Year: 2020

Pages: 854-864

How to cite

Elif AŞIKUZUN, Özgür ÖZTÜRK; (2020), Theoretical and Experimental Comparison of Micro-hardness and Bulk Modulus of Orthorhombic $\text{YBa}_2\text{Cu}_3\text{-xZnxO}$ Superconductor Nanoparticles Manufactured using Sol-Gel Method. Sakarya University Journal of Science, 24(5), 854-864, DOI: <https://doi.org/10.16984/saufenbilder.676028>

Access link

<http://www.saujs.sakarya.edu.tr/en/pub/issue/56422/676028>

New submission to SAUJS

<http://dergipark.org.tr/en/journal/1115/submission/step/manuscript/new>



Theoretical and Experimental Comparison of Micro-hardness and Bulk Modulus of Orthorhombic $YBa_2Cu_{3-x}Zn_xO$ Superconductor Nanoparticles Manufactured using Sol-Gel Method

Elif AŞIKUZUN^{*1}, Özgür ÖZTÜRK²

Abstract

In the present study, the sol-gel method was preferred for the production of superconductor materials since it is known that the sol-gel method is useful in producing nanoparticles. The Zn (Zinc) doped *YBCO*-123 superconductor samples ($YBa_2Cu_{3-x}Zn_xO$) were produced. The main objective in the present study was to examine the effects of both of Zn doping and sol-gel method, which was chosen as the production method, on the structural, electrical, and mechanical properties of Y-123 superconductor materials. Especially, the effects of the nanoparticles and doping on the mechanical properties of materials were discussed over the bulk modulus. It was aimed to obtain information about the mechanical properties by comparing the bulk modules calculated theoretically and experimentally. Besides that, the XRD, SEM, and resistivity measurements were performed in order to characterize the structural and electrical properties.

Keywords: Sol-gel, vickers, bulk modulu, micro-hardness

1. INTRODUCTION

The mechanical behavior of the materials reflects the deformation or resistance of material against the force or load applied. Depending on the force applied to the material, two types of deformation occur; i) elastic (non-permanent change) and ii) plastic (permanent change). The elastic deformation refers to the change of distance between the atoms of material, on which the force is applied, without any separation between the adjacent atoms. When the applied force is

removed, then the object gains its previous form. If the stress created on the material by the force applied exceeds beyond the elasticity limit of the material, then the permanent deformation called plastic deformation occurs. In other words, the materials deform under the external forces. When the applied forces are removed, the deformation is called “elastic” (reversible) if the material gained its previous size and

*Corresponding Author: easikuzun@kastamonu.edu.tr

¹Kastamonu University, ORCID: <https://orcid.org/0000-0003-1850-7080>

²Kastamonu University, E-Mail: oozturk@kastamonu.edu.tr

ORCID: <https://orcid.org/0000-0002-0391-5551>

shape, it is called “plastic” (permanent) if the previous form was not gained.

The hardness is defined as the material's resistance to the friction, scratch, cutting, and plastic deformation. The value obtained from the hardness measurements performed in the laboratories using special devices is the resistance of material against to the plastic deformation.

The most common and effective experiment carried out in order to determine the mechanical properties of the materials is the hardness measurement. The main reasons for this are that the procedure is simple and that it damages the sample less than the other procedures do. The other advantage is that the hardness of a material is directly proportionate to the other mechanical properties [1-4]. For instance; the tensile strength of steels is directly proportionate to the hardness. Thus, it is possible to have an idea about the strength of the material by measuring the hardness.

In the present study, the mechanical properties of the Zn doped YBCO-123 superconductor nanoparticles ($\text{YBa}_2\text{Cu}_3\text{-xZn}_x\text{O}$) which were produced using sol-gel method, are reported by making use of both experimental and theoretical data. The microhardness and bulk module values obtained experimentally were compared with the theoretically obtained results. Moreover, in order to determine the crystal structure and lattice parameters of the superconductors, the X-ray diffraction (XRD) measurements were performed, whereas ρ -T measurements were performed in order to examine the superconductor characteristics.

2. EXPERIMENTAL DETAILS

In the present study, the sol-gel method that is one of the methods most widely used for obtaining nano-sized samples was used. $\text{YBa}_2\text{Cu}_3\text{-xZn}_x\text{O}$ samples were prepared by

using yttrium (III) acetate hydrate, barium acetate, copper (II) acetate, and zinc acetate dihydrate powders, as well as the acetic acid and methanol as solvents. 3 g powder mixtures (Y, Ba, Cu and Zn) were prepared for each sample and the zinc acetate dihydrate powder was added by 1%, 5%, 10%, 20%, and 50%. The solutions that were prepared were stirred using a heated magnetic stirrer for 8 hours with closed cover until obtaining a transparent solution. Then, the stirring process was continued for approx. 12 hours until the solution gelled. Then, the samples were dried in muffle furnace at 300° for 30 minutes. The powder samples were calcined for three times at 850° for 24 hours. The produced powder samples containing Zn were named $\text{Zn}_{0.01}$, $\text{Zn}_{0.05}$, $\text{Zn}_{0.10}$, $\text{Zn}_{0.20}$, and $\text{Zn}_{0.50}$, whereas the undoped sample was named $\text{Zn}_{0.00}$.

3. RESULTS

3.1. XRD and SEM Measurements

X-ray diffraction method was used to determine the crystal structures and lattice parameters of the materials. XRD measurements were performed by Bruker D8 Advance X-ray powder diffractometer using $\text{CuK}\alpha$ ($\lambda = 1,541\text{\AA}$) radiation in the range of $3^\circ \leq 2\theta \leq 90^\circ$ at a scan speed of $4^\circ/\text{min}$. When XRD graph was examined, it was seen that the dominant phase in all samples was the Y-123 phase (Figure 1). There were no peaks of Zn ion doped instead of Cu ion. This result was shown that Zn ions entered into the YBCO structure [5, 6]. In addition, the ionic radius (0.73\AA) of the Cu (+2) ion was comparable with the ionic radius of the doped Zn (+2) ion (0.74\AA).

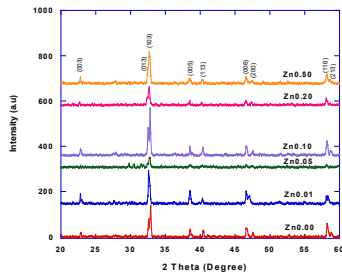


Figure 1 XRD patterns for all samples

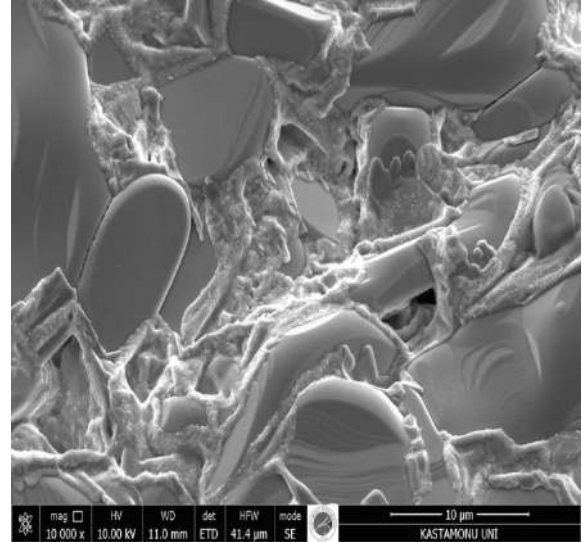
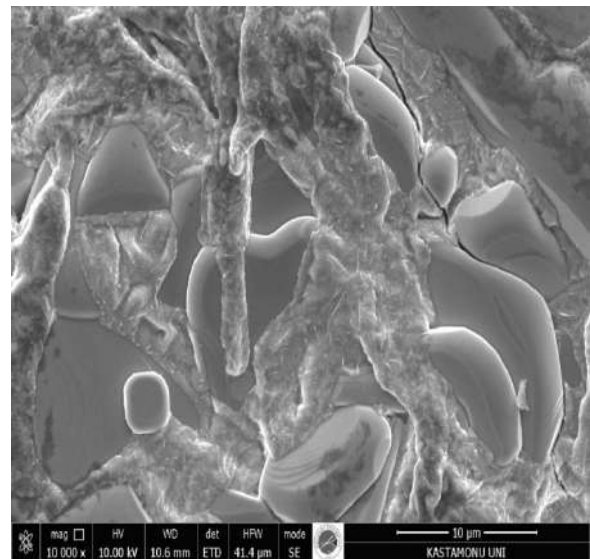
In the literature, the lattice constants of the Y-123 system which has orthorhombic symmetry ($a \neq b \neq c$) are $a = 3.82 \text{ \AA}$, $b = 3.89 \text{ \AA}$ ve $c = 11.7 \text{ \AA}$. In this study, it was seen that the lattice parameters and crystal structure obtained for the Zn doped Y-123 system conformed with the literature (Table 1). In addition, grain sizes of the samples were calculated using the Warren-Scherrer equation [7]. As can be seen from Table 1, the Zn doping was decreased the grain size compared with the undoped sample.

Table 1
 a , b , c lattice parameters and grain size values of samples

Samples	Lattice Parameters			Grain Size (nm)
	a (Å)	b (Å)	c (Å)	
Zn_{0.00}	3.81	3.89	11.65	92.39
Zn_{0.01}	3.85	3.83	11.02	77.96
Zn_{0.05}	3.88	3.87	10.77	72.06
Zn_{0.10}	3.81	3.80	10.98	63.67
Zn_{0.20}	3.83	3.83	10.54	60.93
Zn_{0.50}	3.82	3.79	10.99	60.71

The surface morphology of the samples was examined by using FEI brand QUANTA FEG 250 model scanning electron microscopy (SEM). The surface images obtained at 10000 magnifications were given in Figure 2.

According to SEM results, we can say that grain size decreased and inter-particle pores increased with increasing the Zn doping.

a) Zn_{0.00}b) Zn_{0.05}

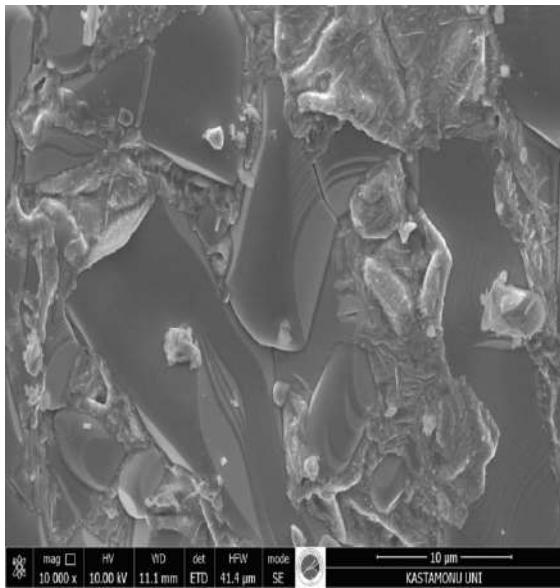
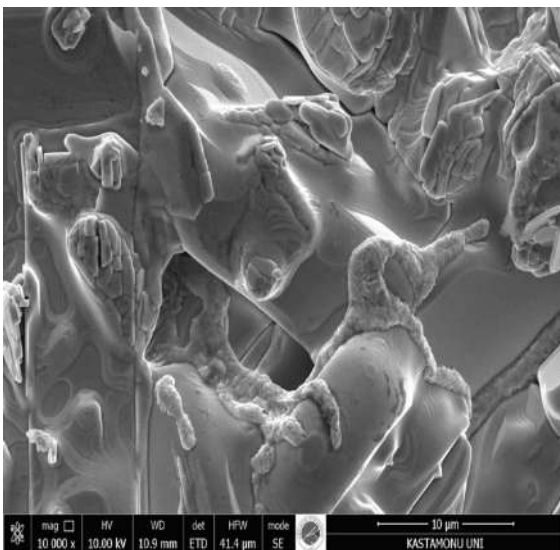
c) Zn_{0.10}d) Zn_{0.20}

Figure 2 SEM images for all samples

3.2. Resistivity Measurements

For electrical measurements, contacts were performed by a standard four-point method using a silver paste on the surface of samples. The He cooled closed-circuit cryostat system, the Lakeshore 336 temperature controller, the Keitley 2400 current source and the Keithley 2182 A Nanovoltmeter devices were used.

Above the onset transition temperatures (T_c^{onset}) of the samples were determined as the transition temperature from normal state to superconducting state were shown metallic behavior (Fig. 3). T_c^{onset} were 89K, 84K, 75K, 56K and 54K for undoped, Zn_{0.01}, Zn_{0.05}, Zn_{0.10} and Zn_{0.20} samples, respectively. Zn_{0.50} sample showed insulating behavior. Zn doping negatively affected to T_c^{onset} . However, the effect of nanoparticles on the electrical properties of materials was not determined.

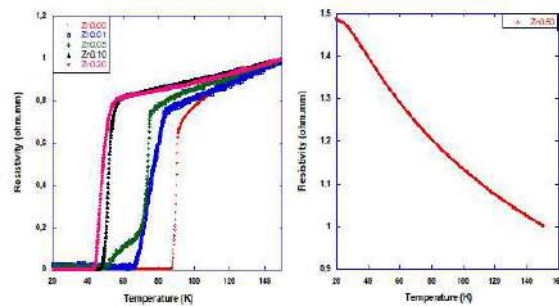


Figure 3 Normalized resistivity as a function of temperature curves for all samples

3.3. Microhardness measurements

The mechanical characterizations of samples were carried out using Shimadzu brand HMV-2 model digital static microhardness tester. The hardness is generally determined by measuring the resistance of material against a standard conic or spherical tip. The tip that is chosen appropriately leaves a trace on the material when it is pushed on the material under a constant load. In general, the hardness of the material is inversely proportional to the size of this trace [8-10]. The hardness measurements, which are performed in laboratories by using special devices, are classified based on the tip being used, the force being applied, the size of trace, and the method of measurement. The most widely used microhardness measurement methods are Brinell, Rockwell, Knoop, and Vickers methods.

In the present study, the Vickers microhardness measurement method, in which a diamond tip is used in order to prevent the negative consequences of the change of the geometrical shape of trace observed in Brinell experiment, was preferred. In the Vickers method, the pyramid stinging tip with 136° of apex angle between the counter-surfaces of the pyramid having square base is stung onto the sample for 10 seconds under force (F). Five different levels of force (0.245, 0.490, 0.980, 1.960, and 2.940 N) were applied to the superconductor samples during the procedures. After removing the load, two diagonal length of the trace (d_1 and d_2) on the material are measured using a microscope and the arithmetic mean (d) is calculated. This procedure is repeated for minimum 10 times for each load and the mean value is calculated. Vickers hardness value is the proportion of load expressed in gram to the area of trace expressed in μm^2 . Vickers microhardness value is calculated using the formula below,

$$H_V = 1854.4 \frac{F}{d^2} \quad (1)$$

The microhardness values obtained experimentally are presented in Table 2. Moreover, the diagram of the change in microhardness depending on the force applied (H_V -F) is presented in Figure 4. As seen in the figure, the microhardness values increased in parallel with the load applied. This behavior is defined as RISE (Reverse Indentation Size Effect) in the literature. These materials exhibit only the plastic deformation. No elastic deformation is observed or it is at much lower levels when compared to the plastic deformation. Furthermore, as it can be seen in Figure 3, the hardness values did not change when the loads higher than 1N were applied. In and after this region that is called the saturation region, there would be no significant change in the hardness value even if the load applied

is increased [11-14]. While calculating the microhardness values, the bulk modulus of the material were calculated by using Equation (2).

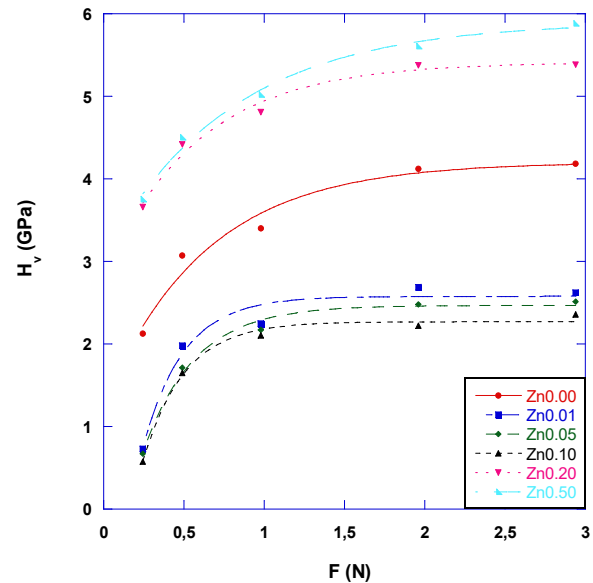


Figure 4 Vickers microindention hardness variation as a function of indentation test load for all samples

$$B = 81.9635 H_V \quad (2)$$

The bulk module is an elastic characteristic that defines the decrease in a material exposed to a applied force. The results obtained are presented in Table 2. As it can be seen in the table, the microhardness value of the material did not change in parallel with the Zn doping when compared to the undoped sample. The microhardness values decreased in $Zn_{0.01}$, $Zn_{0.05}$, and $Zn_{0.10}$ samples and decreased in $Zn_{0.20}$ and $Zn_{0.50}$ samples. The decrease observed here is related with the status of impurity phases and irregularity. These factors lead the strong bonds to weaken and, thus, the microhardness to decrease. Moreover, the decrease in value of H_V causes increase in resistivity between the particles,

reduction in the interparticular transmission surface, and weakening in the borders of particles. Here, the material behavior did not

change but the microhardness values were observed to change in parallel with the Zn doping.

Table 2

The experimental values of H_v and B weakening in the borders of particles.

Samples	F (N)	Exp. H_v (GPa)	Exp. B (GPa)
Zn_{0.00}	0.245	2.126	174.27
	0.490	3.073	251.92
	0.980	3.401	278.78
	1.960	4.121	337.84
	2.940	4.186	343.11
Zn_{0.01}	0.245	0.728	59.72
	0.490	1.979	162.23
	0.980	2.245	184.08
	1.960	2.687	220.30
	2.940	2.621	214.87
Zn_{0.05}	0.245	0.672	55.10
	0.490	1.715	140.56
	0.980	2.173	178.14
	1.960	2.478	203.12
	2.940	2.513	205.99
Zn_{0.10}	0.245	0.576	47.21
	0.490	1.651	135.32
	0.980	2.105	172.54
	1.960	2.224	182.28
	2.940	2.360	193.43
Zn_{0.20}	0.245	3.658	299.85
	0.490	4.416	362.02
	0.980	4.808	394.10
	1.960	5.377	440.72
	2.940	5.385	441.38
Zn_{0.50}	0.245	3.753	307.64
	0.490	4.503	369.09
	0.980	5.019	411.44
	1.960	5.608	459.69
	2.940	5.882	482.16

In order to be able to compare the experimental results that we obtained to the theoretical results, an empirical approach was developed for the bulk module [15]. In this approach, it is possible to obtain a projectable

value in examining the bulk modules of all the compounds consisting of elements between I and VII [15]. Given the results, there is an approx. scale for these materials.

$$B=550d^{-3} \quad (3)$$

The d here refers to the bond length of the crystal structure. The doping applied to the materials may cause local planar defects on the samples. These defects cause extra reflections arising from n different planes differing from the XRD patterns. These changes create changes in the mean length of bond.

As known, different crystal structures have different lengths of bond. The lengths of these bonds vary depending on the lattice parameters of the crystal. The YBCO superconducting materials have body-centered orthorhombic crystal structure. Some of the important characteristics of orthorhombic structure are provided below;

Lattice parameters $a \neq b \neq c$

Bond angles $\alpha = \beta = \gamma = 90$

$$\text{Bond length } d = \sqrt{\frac{a^2}{9} + c^2 \left(\frac{1}{4} - u\right)^2} \quad (4)$$

u is related with c/a .

$$u = 0.24 \sqrt{1 - a^2/c^2} \quad (5)$$

Using the theoretical B values calculated with Equation 3, the theoretical microhardness values were calculated (Eqn.2). All of the calculated values are presented in Table 3. The calculated values are different from the experimental values. This can be explained with the difference of samples' porosity from the estimated values. Moreover, the theoretically calculated B value depends on the bond length. The bond length depends on the lattice parameters. Since the crystal structure of examined materials did not change with the doping, no significant change was observed in the lattice parameters and consequently the bond lengths. The crystal structures of samples with and without

doping are body-centered orthorhombic. This crystal structure is also seen in data cards obtained from the XRD measurement. Besides that, the bulk module values obtained experimentally are calculated with a force applied on the surface of sample. The possible accumulation at the particle borders or porosity changing with the doping directly affects the hardness measurements. Detecting this difference is almost impossible in theoretical calculations. Thus, the difference between the theoretically calculated values and the experimentally obtained ones can be explained.

Moreover, in the literature, there are the mathematical models used in microhardness analysis. As specified in previous studies, these are Meyer's law, proportional sample resistance (PSR) model, elastic/plastic deformation (EPD) model, Hays-Kendall (HK) approach, and indentation-induced cracking (IIC) model [16, 17]. The main purpose of applying these models is to achieve the theoretical model that is closest to the experimentally obtained microhardness values. Among these models, the model that is most appropriate for the materials exhibiting RISE behavior is generally reported to be the IIC model [18, 19]. In the present study, only the IIC model is explained in supporting the theoretical calculations.

• *Mechanic Analysis according to the Indentation Induced Cracking (IIC) Model*

This model is a model developed to explain RISE behavior [20]. It is about the reaction of the sample at maximum depth against the load applied to the surface of the material. There are different reasons of the reaction of the material. The most important of these are the shift of the tip or sample on the interface, the elastic and plastic deformation or the cracks formed in the sample. According to Li and Bradt, the cracks cause to exhibiting RISE behavior of the sample [18]. The cracks prevent to exhibiting elastic deformation of

the sample and the material only shows plastic deformation. That is, elastic recovery is either absent or very small in samples exhibiting RISE behavior. The theoretical hardness value calculated by this model is given by Eqn. (7).

$$H_v = K(F^{5/3}/d^3)^m \quad (7)$$

The values K and m obtained from the $\ln H_v - \ln(F^{5/3}/d^3)$ graph are load-

independent constants (Figure 5). If m value obtained from the slope of the graph is greater than 0.6, the material exhibits RISE behavior. The microhardness values calculated according to the model were given in Table 4. As seen clearly from the table, the microhardness values were quite close to the values in the plateau region. This result is also in agreement with the theoretical results obtained using Eqn. (6).

Table 3

Calculated theoretical values

Samples	Bond Length	u	Theoretical B	Theoretical H	Experimental B (Average)	Experimental H (Average)
Zn_{0.00}	1.274	0.285	265.72	3.242	277.18	3.381
Zn_{0.01}	1.297	0.290	251.84	3.072	137.29	2.052
Zn_{0.05}	1.312	0.293	243.28	2.968	130.54	1.910
Zn_{0.10}	1.282	0.290	260.49	3.178	120.32	1.783
Zn_{0.20}	1.296	0.294	252.10	3.075	370.61	4.728
Zn_{0.50}	1.286	0.290	258.29	3.151	394.90	4.953

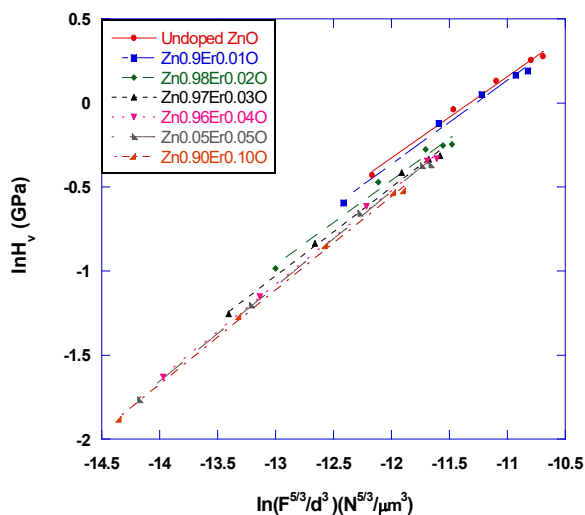


Figure 5 Variation of $\ln(H_v)$ with $\ln(F^{5/3}/d^3)$ according to IIC model for all samples

Table 4

Experimental microhardness values

Samples	m	ln K	H _{IIC}
Zn_{0.00}	0.47	5.72	3.581
Zn_{0.01}	0.56	6.43	1.547
Zn_{0.05}	0.56	6.42	2.944
Zn_{0.10}	0.56	6.49	3.732
Zn_{0.20}	0.39	5.08	4.883
Zn_{0.50}	0.41	5.25	4.981

4. CONCLUSIONS

In the present study, the Zn doped YBCO-based high-temperature superconducting samples were produced using sol-gel method and their structural, electrical, and mechanical properties were analyzed. The

superconductivity characteristics of the samples were determined by using dc resistivity, the mechanical properties were determined using Vickers microhardness, and the surface morphology, crystal structure characteristics, and lattice parameters were determined using *XRD* and *SEM* measurements. The results obtained are summarized below.

- In diffraction patterns obtained from XRD analyses, no remarkable second phase or peak related with Zn ion was observed. All of the phases obtained here are the characteristic phases of YBCO.
- It can be seen that the *a* lattice parameters of the samples increased up to Zn_{0.05} and then decreased. *c* lattice parameter, however, decreased until Zn_{0.05} and then showed increase. This finding indicates that the doping ratio of 0.05 is a threshold and the structure changed in all the doping ratios beyond this level.
- According to SEM results, we can say that grain size decreased and inter-particle pores increased with increasing the Zn doping.
- It can be said that room temperature resistance increased with increasing Zn doping using R-T measurements.
- The microhardness values increased with increasing the applied load on the surface. That is, the material exhibited RISE behavior.
- The microhardness results were experimentally and theoretically calculated. When the obtained results were compared, it was determined that the theoretical values are lower. This difference can be explained with the difference of samples' porosity from the estimations and the result that the crystal structure did not change with the Zn doping.

Acknowledgements

We thank the Kastamonu University Research and Application Center and Kastamonu University Scientific Research Projects Coordination Department for the supports.

Funding

This study was supported by the Kastamonu University Scientific Research Projects Coordination Department under the Grant No. KÜ-BAP01/2016-21.

The Declaration of Conflict of Interest/ Common Interest

No conflict of interest or common interest has been declared by the authors.

Authors' Contribution

All authors of the paper contributed actively to the parts of study such as experiments, analysis, writing and submission of article.

The Declaration of Ethics Committee Approval

The authors declare that this document does not require an ethics committee approval or any special permission.

The Declaration of Research and Publication Ethics

The authors of the paper declare that they comply with the scientific, ethical and quotation rules of SAUJS in all processes of the paper and that they do not make any falsification on the data collected. In addition, they declare that Sakarya University Journal of Science and its editorial board have no responsibility for any ethical violations that may be encountered, and that this study has not been evaluated in any academic publication environment other than Sakarya University Journal of Science.

REFERENCES

- [1] R.L. Smith and G.E. Sandland, "An Accurate Method of Determining the Hardness of Metals, with Particular Reference to Those of a High Degree of Hardness," *Proceedings of the Institution of Mechanical Engineers*, 1, pp. 623-641, 1922.
- [2] S.M. Khalil, "Enhancement of superconducting and mechanical properties in BSCCO with Pb additions," *J. Phys. and Chem. Solids*, 62, pp. 457-466, 2001.
- [3] E. Asikuzun, O. Ozturk, H.A. Cetinkara, G. Yildirim, A. Varilci, M. Yilmazlar, and C. Terzioglu, "Vickers hardness measurements and some physical properties of Pr₂O₃ doped Bi-2212 superconductors," *J. Mat. Sci. Mater. in Elect.*, 23, pp. 1001-1010, 2012.
- [4] S.M. Khalil, "Role of rare-earth Ba²⁺ doping in governing the superconducting and mechanical characteristics of Bi-Sr-Ca-Cu-O," *Smart Mater. and Structure*, 14, 804, 2005.
- [5] H. Koralay, O. Hicyilmaz, S. Cavdar, E. Asikuzun, A.T. Tasci, and O. Ozturk, "Effect of Zn content on microstructure and mechanical performance in Bi_{1.8}Sr₂Ca₂Cu_{3.22-x}Zn_xO_{10+δ} glass ceramic," *J. Mat. Sci. Mater. in Elect.* 25, pp. 3116-3126, 2014.
- [6] H. Koralay, O. Hicyilmaz, S. Cavdar, E. Asikuzun, A.T. Tasci, and O. Ozturk, "Effect of Zn content on microstructure and mechanical performance in Bi_{1.8}Sr₂Ca₂Cu_{3.22-x}Zn_xO_{10+δ} glass ceramic," *Journal of Materials Science: Materials in Electronics*, 25, pp. 3116-3126, 2014.
- [7] E. Asikuzun, A. Donmez, L. Arda, O. Cakiroglu, O. Ozturk, D. Akcan, and C. Terzioglu, "Structural and mechanical properties of (Co/Mg) co-doped nano ZnO," *Ceramics International*, 41, pp. 6326-6334, 2015.
- [8] U. Kölemen, O. Uzun, M. Yilmazlar, N. Güçlü, and E. Yanmaz, "Hardness and microstructural analysis of Bi_{1.6}Pb_{0.4}Sr₂Ca_{2-x}Sm_xCu₃O_y polycrystalline superconductors," *J. Alloys and Compounds*, 415, pp. 300-306, 2006.
- [9] R. Awad, A.A. Aly, M. Kamal, and M. Anas, "Mechanical Properties of (Cu_{0.5}Tl_{0.5})-1223 Substituted by Pr," *J. Supercond. and Novel Magn.*, 24, pp. 1947-1956, 2011.
- [10] K. Sangwal, "On the reverse indentation size effect and microhardness measurement of solids," *Mater. Chem. and Phys.*, 63, pp. 145-152, 2000.
- [11] L. Arda, O. Ozturk, E. Asikuzun, and S. Ataoglu, "Structural and mechanical properties of transition metals doped ZnMgO nanoparticles," *Powder Technology*, 235, pp. 479-484, 2013.
- [12] A.A. Elmustafa and D.S. Stone, "Nanoindentation and the indentation size effect: Kinetics of deformation and strain gradient plasticity," *J. Mech. and Phy. Solids*, 51, pp. 357-381, 2003.
- [13] O. Ozturk, E. Asikuzun, and G. Yildirim, "The role of Lu doping on microstructural and superconducting properties of Bi₂Sr₂CaLu_xCu₂O_y superconducting system," *J. Mat. Sci. Mater. in Elect.*, 24, pp. 1274-1281, 2013.
- [14] H. Koralay, A. Arslan, S. Cavdar, O. Ozturk, E. Asikuzun, A. Gunen, and A.T. Tasci, "Structural and Mechanical Characterizations of Bi_{1.75}Pb_{0.25}Sr₂Ca₂Cu_{3-x}Sn_xO_{10+δ} Superconductor Ceramics Using Vickers Microhardness Test," *J. Mat. Sci. Mater. in Elect.*, 24, pp. 4270-4278, 2013.
- [15] L. Martin Cohen, "Calculation of bulk moduli of diamond and zinc-blende solids," *Phys. Rev. B*, 32, pp. 7988-7991, 1985.

- [16] O. Ozturk, H.A. Cetinkara, E. Asikuzun, M. Akdogan, M. Yilmazlar, and C. Terzioglu, "Investigation of mechanical and superconducting properties of iron diffusion-doped Bi-2223 superconductors," *J. Mat. Sci. Mater.in Elect.*, 22, pp. 1501-1508, 2011.
- [17] M. Tosun, S. Ataoglu, L. Arda, O. Ozturk, E. Asikuzun, D. Akcan, and O. Cakiroglu, "Structural and mechanical properties of ZnMgO nanoparticles," *J. Mater. Sci. Eng. A.*, 590, pp. 416-422, 2014.
- [18] E. Asikuzun, O. Ozturk, L. Arda, D. Akcan, S.D. Senol, and C. Terzioglu, "Preparation, structural and micromechanical properties of (Al/Mg) co-doped ZnO nanoparticles by sol-gel process," *J. Mat. Sci.: in Elect.*, 26, pp. 8147-8159, 2015.
- [19] O. Ozturk, E. Asikuzun, S. Kaya, M. Erdem, S. Safran, A. Kilic, and C. Terzioglu, "Ac Susceptibility Measurements and Mechanical Performance of Bulk MgB₂," *J. Supercond. Nov. Magn.*, 28, pp. 1943-1952, 2015.
- [20] H. Li and R.C. Bradt, "The microhardness indentation load/size effect in rutile and cassiterite single crystals," *J. Mater. Sci.*, 28, pp. 917-926, 1993.

JOURNAL OF SCIENCE



SAKARYA UNIVERSITY

Sakarya University Journal of Science

ISSN 1301-4048 | e-ISSN 2147-835X | Period Bimonthly | Founded: 1997 | Publisher Sakarya University |
<http://www.saujs.sakarya.edu.tr/en/>

Title: Theta Point Calculation of a Polymer Chain with Electric Dipole Moments: Monte Carlo Simulation

Authors: Şahin UYAVER

Received: 2020-03-29 03:11:15

Accepted: 2020-06-20 17:07:26

Article Type: Research Article

Volume: 24

Issue: 5

Month: October

Year: 2020

Pages: 865-871

How to cite

Şahin UYAVER; (2020), Theta Point Calculation of a Polymer Chain with Electric Dipole Moments: Monte Carlo Simulation. Sakarya University Journal of Science, 24(5), 865-871, DOI: <https://doi.org/10.16984/saufenbilder.710797>

Access link

<http://www.saujs.sakarya.edu.tr/en/pub/issue/56422/710797>

New submission to SAUJS

<http://dergipark.org.tr/en/journal/1115/submission/step/manuscript/new>

Theta Point Calculation of a Polymer Chain with Electric Dipole Moments: Monte Carlo Simulation

Şahin UYAYER*¹

Abstract

Monte Carlo simulations are used to simulate a single polymer chain in a more generalized model. The more generalized model differs from the simpler models by including dipole-dipole interactions. The polymer chain is modeled as a freely rotating chain where the neighboring beads are connected by harmonic spring. Excluded volume effects are included employing modified Lennard-Jones potential. As the extension in this work, each monomer unit carries permanently a freely-rotating electric dipole moment. After getting the system equilibrated the average values are measured and Θ -temperature of the system is determined. The effects of the presence of the dipole moments to the Θ -temperature of the system are investigated. The results are analyzed in comparison with a bare model.

Keywords: Polymer Chain, Theta Temperature, Monte Carlo, Dipole-dipole interaction

1. INTRODUCTION

Polymers are large molecules and composed of many repeating units and very complex systems. Polymers play many important roles in our daily life. Both synthetic and natural polymers are of high interest [1, 2]. For polymeric systems many theoretical approximations have been developed and also many experiments have been carried out. Despite many outgoing pieces of research of today, frequently it is not easy to have a direct comparison between theory and experiments.

Therefore, computer simulations are very common way to perceive the details of polymeric systems [3]. In a polymeric system, the chains are essentially very long. Especially polymeric systems carrying electric charges, which are called polyelectrolytes (PELs), are of high interest in science and technology. PELs are so important in technology because they are seen in many modern applications. In PELs one examines the clash between different interactions, on the one hand, the interactions emerging from the presence of electric charges, while on the other hand the

*Corresponding Author: uyaver@tau.edu.tr

¹Department of Energy Science and Technologies, Faculty of Science, Turkish-German University, Şahinkaya Cad. No 106 34820 Beykoz, Istanbul, Turkey.

ORCID: <https://orcid.org/0000-0001-8776-3032>

ones emerging from solvent effects [4-6]. In a polymeric or polyelectrolyte system, the solvent is allocated as good, poor (or bad) and theta (Θ) solvent. The general behavior of a polymer chain or a charged one is quite different in these different solvent regimes. The critical solvent regime can be seen as the theta (Θ) solvent because it splits the good solvent regime and poor solvent regime. The determination of the Θ solvent could be very crucial when one needs to understand the solvent effects. The determination of Θ point for polymeric systems is widely worked essentially, but in this current work the polymer system is modeled in a more generalized way: That is, each unit along polymer chain carries one freely-rotating electric dipole. Utilizing Monte Carlo (MC) simulations, the effects of the presence of electric dipoles to the Θ point of the system are investigated. The paper is outlined: In the next section we give the details of the solvent effects for polymeric systems, next we describe our model and method to distinguish the effects of having permanent dipole moments. Afterward we display our results and finally make our conclusion.

1.1. Solvent Effects in Polymeric Systems

In a dilute solution, the interaction between polymer chains can be neglected, because the chains are far apart from each other. This fact enables us to start with a single polymer chain. However, monomer units along the same chain can interact with each other. The simplest model in polymer physics is "ideal chain", where no interaction is considered between the monomer units. But the interactions between monomers are so important because they determine if the polymer dissolves in the solution. Because of this fact real polymers are modeled as a self-avoiding walk, opposite to a random walk of an ideal chain. It means that one physical space can be occupied by only one polymer subunit. This is called "excluded-volume effect". This makes the chain more expanded.

In a simple mean-field approach due to Flory [7], the size of polymer chain can be calculated at different solvent qualities. In a "good" solvent case, effective interaction between monomer

subunits is repulsive; that is, interactions between solvent molecules and polymer molecules are more important than interactions between the polymer molecules. As a result, polymer chain is found in an expanded form. This repulsive effect makes the polymer chain swollen. In a poor (or bad) solvent, interactions between monomer subunits are more important than interactions between solvent and polymer subunits. In this case, polymer collapses into a compact globular structure. At very poor solvents polymer chain can be even separated from the solution.

Between these solvent regimes, Θ solvent regime lies. In this regime, both competing attractive and repulsive interactions are equal and cancel each other and the chain is said to be at the Θ point. Θ chains are amazing because it is a transition structure. The change of polymer structure as the solvent quality changes is called "coil-globule" transition. At Θ point the chain is found as exhibiting the characteristics of an ideal polymer chain. This is interesting because it is the case of an imaginary chain where monomer subunits are allowed to overlap each other. That is, there is no interaction between monomers or solvent molecules. These kinds of polymers are not present in reality. Θ chains are very important concerning the fact that they are often used as starting steps in understanding the properties of real polymers (neutral or charged). Coil-globule transition has been worked extensively because of its importance. For instance, protein is found in a globular structure (biologically active). But when heated it forms into a looser coil (stopping its activity). In the scaling theory [5], the end-to-end distance R for an ideal and Θ polymer chain is written as

$$R \cong bN^{1/2} \quad (1)$$

in the case of a neutral polymer chain with excluded volume effect,

$$R \cong bN^{3/5} \quad (2)$$

but in a poor solvent case,

$$R \cong b(N/\tau)^{1/2} \quad (3)$$

where b is the typical segment length and N is the total number of the segments. τ is the scaled temperature from the Θ temperature as given by

$$\tau = \frac{\Theta - T}{\Theta} \quad (4)$$

where T is the temperature of the solvent. The solvent effects mentioned above can be also schematically drawn like in Figure 1.

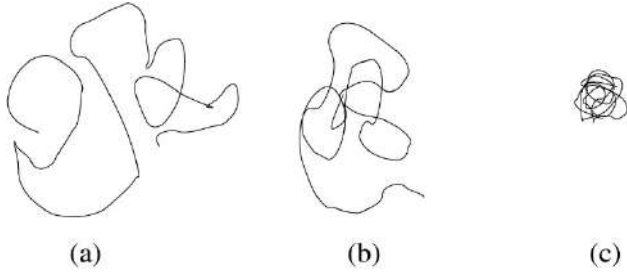


Figure 1 A single polymer chain in different solvents: (a) in a good solvent, (b) in a Θ solvent and, (c) in a poor solvent

In many simulation works the Θ point of the system to be investigated is required to be known [see 8, 9]. In many of these studies, only the basic interactions are included. In [10] the authors studied the effects of residual interactions on polymer properties near its Θ point. In that work, the physical measurables of the system are obtained by perturbation calculations. This theoretical work has shown that through including binary and ternary excluded volume interactions experimental and simulation data could be explained and the conflicts of mean-field and perturbation theories could be removed. Further to this work, Cherayil *et al.* investigated the effects including higher moments and also compared the results with the results of Monte Carlo simulations [11]. In another relatively old work [12] for various solvents, Θ temperatures were studied. This analytical work included first-order calculations in the density of vacancies and showed the changes in Θ temperatures. A molecular dynamics work by Zhou and Davis [13] simulates polymer chains versus solvent quality. The coarse-grained simulation approach, model and the determination of Θ of the system are similar to our Monte Carlo simulation. But our work aims to investigate the effects of higher interactions to Θ point of the system. Apart from these works, our current work presents a clear

picture of the effects of these higher interactions to the Θ point of the polymer system and the work aims to investigate the changes in the Θ point of the system.

2. MODEL AND METHOD

The polymer chain is of freely jointed beads, harmonic springs between neighboring monomers, so that the interaction potential between neighboring monomers is

$$U_{bond}(r) = \frac{3}{2} k_B T \frac{r^2}{b_0^2}, \quad (5)$$

where $r_{nm} = |\mathbf{r}_m - \mathbf{r}_n|$ is the distance between beads n and m and b_0 being the (bare) average bond length. Furthermore, monomer-monomer and monomer-solvent interactions are taken into account by a modified Lennard-Jones potential

$$U_{LJ}(r) = \begin{cases} 4\epsilon\{m(r) + s(r)\} & , \text{if } r \leq r_c \\ 0 & , \text{if } r > r_c \end{cases} \quad (6)$$

where

$$m(r) = \left[\left(\frac{\sigma}{r} \right)^{12} - \left(\frac{\sigma}{r} \right)^6 + \frac{1}{4} \right], \quad (7)$$

and

$$s(r) = \beta \left[\cos \frac{2\pi r}{r_c} - 1 \right]. \quad (8)$$

The cut-off distance in this interaction potential can be taken as $r_c = 2^{1/6} \sigma$ [13]. This cut-off distance is shorter than the one of the standard Lennard-Jones potential, so that the simulation has an advantage over the simulation time. The solvent effects are taken into account by the second term, $s(r)$, where β parameter tunes the solvent quality, namely from good solvent to poor solvent through Θ point. The solvent quality is being hidden in the parameter of β . A sketch of this potential for a few β values is given in Figure 2.

Besides, the monomer units are modeled as having electric dipoles. The interaction between two electric dipoles (that is, between any monomers pairs here), while they are rotating freely when they are separated and shielded in a medium with high dielectric constant follows as [15]

$$U_{d-d}(r) = - \frac{u_1^2 u_2^2}{3k_B T r^6} \quad (9)$$

where the orientation between two dipoles is not constant, freely rotating by the random thermal

motions of molecules, so that thermal averaging can be taken implementing Boltzmann distribution to compute the averages over all possible orientations.

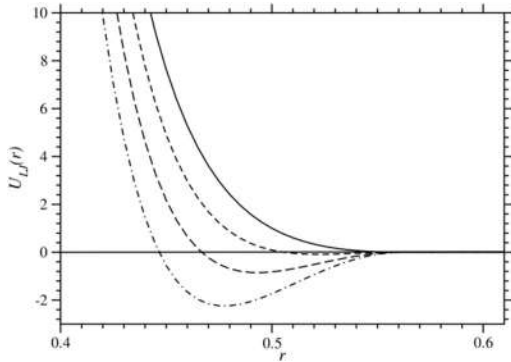


Figure 2 Modified Lennard-Jones potential at various β 's: solid line for $\beta=0.0$, the dashed line for 1.0, the long-dashed line for 2.0 and the dot-dashed line for 3.0

Modeling the system with identical electric dipole moments $u_1 = u_2 = ed$ (e being the elementary electric charge and d the distance between two charges), this equation can be reduced to the following:

$$U_{d-d}(r) = -\frac{\lambda_B^2 d^4 k_B T}{3r^6}, \quad (10)$$

where λ_B is the Bjerrum length.

In the work, b_0 is used as the unit of length, ϵ as the unit of energy and the monomer mass m as the unit of mass. The simulations are carried out at $k_B T = 1.2$. σ is set to $1/2$, to ensure that the length distribution will be only weakly perturbed by the short-range interaction, but remains almost Gaussian. ϵ is set to unity and λ_B is set to b_0 .

This polymer chain is simulated by applying the standard Metropolis Monte Carlo (MC) method [16]. Three different MC moves are done in the simulations, which are local move, pivot move, and reptation move. The local move means that one single monomer unit is selected randomly and then given a random displacement. In the pivot move, one monomer unit is again selected randomly and then one hand of the chain is rotated as a rigid body at a random orientation. The reptation move selects randomly one end of the chain and then attaches it to the opposite end at a random orientation. During the simulations the

acceptance rates of these moves are monitored, a tuning in the frequency of these moves can be needed, especially for the maximum displacement amount of the local move. As mentioned already in some works [17, 18], depending on the type of starting configuration different mixing of the elementary MC moves is necessary. In particular, the acceptance rate of the pivot one becomes very low for compact structures. After assuring equilibrated structures we measure the averages of physical quantities on the system. The ergodicity of the simulation is confirmed by running the simulations with different starting configurations.

2. RESULTS AND DISCUSSION

The Θ point of the system is resolved at various d values in Eq. 10. As d raises, the side effects of dipole-dipole interaction increase, making the comprehensive interaction more attractive. The case where no dipole-dipole interaction exists was given in the literature [18]. In this current paper, the determination of the Θ point will be given in detail for various d values. To determine the Θ point of the modeled system, the parameter β in Eq.8 is varied, since this parameter indicates varying the solvent quality. At $d = 0.05\lambda_B$, the short-ranged attractive interactions compensate the repulsive interactions, therefore the chain evinces the features of an ideal chain, $R \cong N^{1/2}b$. For $\beta < \beta_\Theta$, resembling a good solvent case, the chain turns into a swollen coil, $R \cong N^{3/2}b$, while in the poor solvent regime $\beta > \beta_\Theta$ the chain collapses into a globule, $R \cong N^{1/3}b$. The determination of the Θ point was done through the simulations of the neutral chains of length $N=4, 8, 16, 32, 64, 128, 256$ at different β 's. In Figure 3 $\langle R^2 \rangle / (Nb^2)$ versus $1/N$ is plotted. At $\beta = \beta_\Theta$ the curve straightens at larger N 's. The determined $\beta = \beta_\Theta$ can be confirmed in several ways. One way can be to plot the scaled end-to-end distance (R^2/bN) versus β . For larger lengths of the chains, the curves merge at the value of $\beta = \beta_\Theta$ [19]. For this d value, the determination of θ value is confirmed in Figure 4.

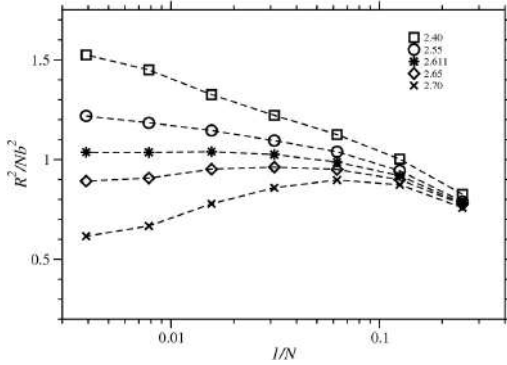


Figure 3 For $d = 0.05\lambda_B$, the chain length dependence of the normalized mean square end-to-end distance of an uncharged chain at different values of the parameter β of the modified Lennard-Jones potential: $\beta=2.40$ (squares), 2.55 (circles), 2.611 (stars), 2.65 (diamonds), 2.70 (crosses). Error bars are less than symbol size

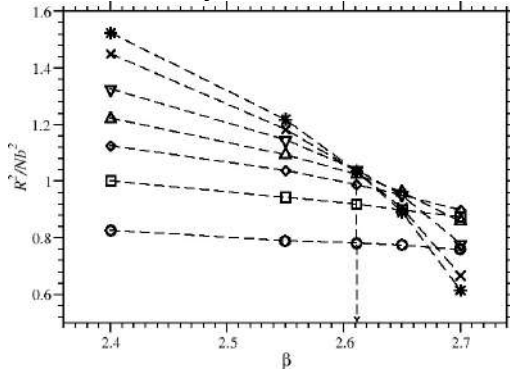


Figure 4 For $d = 0.05\lambda_B$, the scaled end-to-end distance versus β . $N=4$ (circles), 8 (squares), 16 (diamonds), 32 (triangle-ups), 64 (triangle-downs), 128 (crosses) and 256 (stars). The arrow points the $\beta = \beta_\Theta$ point. Error bars are less than symbol size

For a more detailed examination of the structure at all length scales, the spherically averaged form factor $S(q)$ can be measured;

$$S(q) = \left\langle \left\langle \frac{1}{N+1} \left| \sum_{j=0}^N \exp(i\vec{q}\cdot\vec{r}_j) \right|^2 \right\rangle \right\rangle_{|q|}, \quad (7)$$

where r_j is the position vector of monomer j [20, 21]. In Figure 5, for $d = 0.05\lambda_B$, this single chain structure factors calculated at three different β values are plotted. In this plot, one sees that the asymptotic behavior of the chain at the $\beta_\Theta = 2.611$ is identical to an ideal polymer chain.

The other β_Θ points determined at the different d values are displayed in Table 1. The second row of the

table is the β_Θ value determined for the case without dipole moments [18].

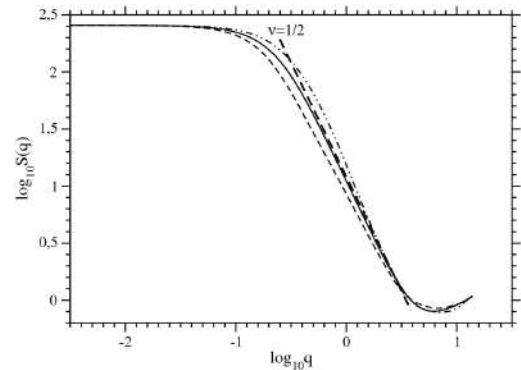


Figure 5 For $d = 0.05\lambda_B$, the spherically averaged structure factors are shown for $\beta=2.40$ (dashed), 2.611 (solid) and 2.70 (dot-dashed curve). The dashed line shows the asymptotic behavior for an ideal chain

Table 1

The determined β_Θ values at various d values

d	β_Θ
No dipole	2.615
$0.05\lambda_B$	2.611
$0.10\lambda_B$	2.606
$0.20\lambda_B$	2.600
$0.30\lambda_B$	2.520
$0.40\lambda_B$	2.454
$0.50\lambda_B$	1.973

Looking at the table, we observe that the presence of the dipole moments increases the overall attraction inside the system. This effect lets the Θ point of the system appear at lower values. The shift in β_Θ value for the very small d values is quite small, especially for the first two ones. To understand it, we can look at the contribution of the dipole-dipole interaction potential to the overall potential of the system. In Table 2, the average (absolute) proportions of dipole-dipole interaction potential to the total energy are given at $\tau=0.0$. Also in the same table, the average bond lengths are given. In this table, we see that the average bond lengths are almost the same at these $\tau=0.0$ cases. But we see that the contribution is (almost) zero at small d values. When the contribution increases, the shift in β_Θ (or Θ) points becomes larger.

Table 2

At various d values and $\tau=0.0$, the average absolute portion of the dipole-dipole energy to the total energy (second row) and the average bond length values (third row)

d	$\frac{ E_{d-d} }{E_{total}}$	$\langle b \rangle$
$0.05\lambda_B$	0.0000	1.040
$0.10\lambda_B$	0.0000	1.038
$0.20\lambda_B$	0.0007	1.032
$0.30\lambda_B$	0.0065	1.032
$0.40\lambda_B$	0.0411	1.038
$0.50\lambda_B$	0.1351	1.030

3. CONCLUSIONS AND OUTLOOK

Performing standard Metropolis Monte Carlo simulations of a polymer chain whose monomers carrying freely rotating electric dipole moments, in agreement with the theoretical expression [15], it has been shown that the effect of the presence of electric dipole moments decreases the overall interaction potential energy of the system. This effect is figured out by determining Θ point of the system into consideration. Comparing the determined corresponding Θ point for the system with the one determined previously [18], the shift to the smaller values is presented. The results are also analyzed by the structure factors of the system. On the other hand, due to the small contribution of this dipole-dipole interaction, the shift is in small quantity, as can be predicted theoretically. When the contribution of the dipole-dipole interactions to the total energy grows, the effect is seen more clearly.

Acknowledgements

The simulations and data analysis of the paper were carried out at TUBITAK ULAKBIM High Performance and Grid Computing Center (TRUBA resources). Special thanks must be sent to Dr. Christian Seidel and Prof. Dr. Idris Adnan Gümüş for the very fruitful discussions.

Funding

This work was supported by TUBITAK 1001 Project 101M459.

The Declaration of Conflict of Interest/ Common Interest

No conflict of interest or common interest has been declared by the author.

The Declaration of Ethics Committee Approval

The author declares that this document does not require an ethics committee approval or any special permission.

The Declaration of Research And Publication Ethics

The author of the paper declares that he complies with the scientific, ethical and quotation rules of SAUJS in all processes of the article and that he does not make any falsification on the data collected. In addition, he declares that Sakarya University Journal of Science and its editorial board have no responsibility for any ethical violations that may be encountered, and that this study has not been evaluated in any academic publication environment other than Sakarya University Journal of Science.

REFERENCES

- [1] P. C. Painter and M. M. Coleman, "Fundamentals of polymer science: an introductory text", Lancaster, Pa.: Technomic Pub. Co., 1997.
- [2] N. G. McCrum, C. P. Buckley and C. B. Bucknall, "Principles of polymer engineering", Exord, New York, Oxford University Press, 1997.
- [3] K. Binder and A. Milchev, "Off-lattice Monte Carlo methods for coarse-grained models of polymeric materials and selected applications", J. Comput. Aided Mater. Des., vol. 9, pp. 33-74, 2000.
- [4] P. Hiemenz and L. Timothy, "Polymer Chemistry", Boca Raton, Florida: CRC Press. ISBN 1-57444-779-3, 2007.

- [5] H. Elias, "Theta Solvents", Wiley Database of Polymer Properties, John Wiley & Sons, 2003.
- [6] P. Sundararajan, "Physical Properties of Polymers Handbook", Ed. James Mark (New York, New York: Springer, 2006.
- [7] P. Flory, "Principles of Polymer Chemistry", Cornell Univ.: Ithaca, ISBN 0-8014-0134-8, 1971.
- [8] S. Uyayer and C. Seidel, "Pearl-necklace structures in annealed polyelectrolytes", *The Journal of Physical Chemistry B*, vol. 108, no. 49, pp. 18804-18814, 2004.
- [9] S. Uyayer and C. Seidel, "Effect of varying salt concentration on the behavior of weak polyelectrolytes in a poor solvent", *Macromolecules*, vol. 42, no. 4, pp.1352-1361, 2009.
- [10] B. J. Cherayil, J. F. Douglas and K. F. Freed, "Effect of residual interactions on polymer properties near the theta point", *The Journal of Chemical Physics*, vol. 83, pp. 5293-5310, 1985.
- [11] B. J. Cherayil, J. F. Douglas and K. F. Freed, "Effect of residual interactions on polymer properties near the theta point. II. Higher moments and comparison with Monte Carlo calculations", *The Journal of Chemical Physics*, vol. 87, pp. 3089-3098, 1987.
- [12] M. K. Kosmas, "Solvent effects on the theta temperature of polymers of various architectures", *J. Chem. Soc., Faraday Trans. 2*, vol. 84, no. 6, pp. 633-642, 1988.
- [13] Z. Zhou and P. J. Daivis, "Molecular dynamics study of polymer conformation as a function of concentration and solvent quality", *Journal of Chemical Physics*, vol. 130, no. 22, pp. 224904:1-10, 2009.
- [14] A. V. Lyulin, B. Dünweg, O. V. Borisov, and A. A. Darinskii, "Computer simulation studies of a single polyelectrolyte chain in poor solvent", *Macromolecules*, vol. 32, pp. 3264-3278, 1999.
- [15] J. N. Israelachvili, "Intermolecular and Surface Forces: With Application to Colloidal and Biological Systems", 2nd Edition, Academic Press, 1992.
- [16] D. P. Landau and K. Binder, "A Guide to Monte Carlo Simulations in Statistical Physics", Cambridge University Press, New York, NY, ISBN 0-521-65366-5, 2000.
- [17] P. Chodanowski and S. Stoll, "Monte Carlo simulations of hydrophobic polyelectrolytes: Evidence of complex configurational transitions", *J. Chem. Phys.*, vol. 111, pp. 6069-6081, 1999.
- [18] S. Uyayer and C. Seidel, "First-order conformational transition of annealed polyelectrolytes in a poor solvent", *Europhysics Letter*, vol. 64, no. 4, pp. 536-542, 2003.
- [19] D. I. Dimitrov, A. Milchev and K. Binder, "Polymer brushes in solvents of variable quality: Molecular dynamics simulations using explicit solvent", *The Journal of Chemical Physics*, 127, pp. 084905:1-9, 2007.
- [20] S. W. Lovesey and W. Marshall, "Theory of Thermal Neutron Scattering", Oxford University Press, 1971.
- [21] R. Pecora ed., "Dynamic Light Scattering", Plenum Press: New York., 1985.

JOURNAL OF SCIENCE



SAKARYA UNIVERSITY

Sakarya University Journal of Science

ISSN 1301-4048 | e-ISSN 2147-835X | Period Bimonthly | Founded: 1997 | Publisher Sakarya University |
<http://www.saujs.sakarya.edu.tr/en/>

Title: Design of Heat Pipe Assisted Thermoelectric Generator and Experimental
Investigation of the Power Performance

Authors: Yaşar İSLAMOĞLU, İmdat TAYMAZ, Cem PARMAKSIZOĞLU, Murat ÖZSOY, Erman ASLAN
Received: 2020-03-05 16:49:16

Accepted: 2020-06-23 18:19:54

Article Type: Research Article

Volume: 24

Issue: 5

Month: October

Year: 2020

Pages: 872-881

How to cite

Yaşar İSLAMOĞLU, İmdat TAYMAZ, Cem PARMAKSIZOĞLU, Murat ÖZSOY, Erman ASLAN;
(2020), Design of Heat Pipe Assisted Thermoelectric Generator and Experimental
Investigation of the Power Performance. Sakarya University Journal of Science,
24(5), 872-881, DOI: <https://doi.org/10.16984/saufenbilder.699176>

Access link

<http://www.saujs.sakarya.edu.tr/en/pub/issue/56422/699176>

New submission to SAUJS

<http://dergipark.org.tr/en/journal/1115/submission/step/manuscript/new>



Design of Heat Pipe Assisted Thermoelectric Generator and Experimental Investigaton of the Power Performance

Yaşar İSLAMOĞLU^{*1}, Cem PARMAKSIZOĞLU², İmdat TAYMAZ³,
Murat ÖZSOY⁴, Erman ASLAN⁵

Abstract

A thermoelectric generator system has a potential to transform waste heat into electricity. Equate to other technologies of waste heat recover, usage of thermoelectric generators (TEGs) in a waste heat recovery system has many attractive features, for example quite operation, no moving parts, small size and endurance In addition to, thermoelectric generators are environmentally friendly materials that convert thermal energy directly into electricity by Seebeck effect.

In work presented, a heat pipe assisted thermoelectric generator system is designed to generate electricity from the waste heat. Usage of heat pipes can latently decrease the thermal resistance and pressure losses in the system as well as temperature regulation of the TEGs and enhanced design flexibility. The designed system is suitable for the heat recovery from the piped systems such as the exhaust and the cylindrical chimney systems.

The power performance of the designed thermoelectric generator system has been determined both theoretically and experimentally.

Keywords: thermoelectric generator, seebeck effect, heat pipe, experimental methods

* Corresponding Author: yasari@sakarya.edu.tr

¹Sakarya University, Faculty of Engineering, Department of Mechanical Engineering, Esentepe Campus, Serdivan-Sakarya and Heat Transfer Laboratory in Thermoelectric Systems, Sakarya University, Serdivan-Sakarya. ORCID: <https://orcid.org/0000-0003-3856-7240>

²İstanbul Technical University, Faculty of Mechanical Engineering, Gümüşsuyu, İstanbul and İstanbul Gedik University, Kartal-İstanbul. E-Mail: parmaksizo@itu.edu.tr ORCID: <https://orcid.org/0000-0003-0789-9840>

³Sakarya University, Faculty of Engineering, Department of Mechanical Engineering, Esentepe Campus, Serdivan-Sakarya. E-Mail: taymaz@sakarya.edu.tr ORCID: <https://orcid.org/0000-0001-5025-5480>

⁴Sakarya University, Faculty of Engineering, Department of Mechanical Engineering, Esentepe Campus, Serdivan-Sakarya. E-Mail: ozsoy@sakarya.edu.tr ORCID: <https://orcid.org/0000-0003-2400-5212>

⁵İstanbul University, Cerrahpaşa Avcılar Campus Engineering Faculty, Avcılar-İstanbul. E-Mail: erman.aslan@istanbul.edu.tr ORCID: <https://orcid.org/0000-0001-8595-6092>

1. INTRODUCTION

Due to the increase in energy consumption, new investments have to be made to produce energy. In order to meet the ascending demand of energy, intensive studies are being made especially in the field of clean energy technologies in order to generate energy by alternative methods because of the harm that fossil fuels give to the environment.

Considering that the most used fossil fuels will be consumed nowadays, renewable energy sources will be preferred more in meeting the increasing energy demand [1-4].

In the past 30 years, there has been growing relevance in applying thermoelectric technology to recovery waste heat [1]. A direct thermal-to-electrical energy transformation of the waste heat can also be realized by using a thermoelectric generator [4]. The thermoelectric generator (TEG) module can also be described as thermal battery. When the gradient of the temperature in the TEG module occur, electric power (DC) is directly produced by heat energy as a result of Seebeck effect. Thermoelectric power systems are environmentally friendly power generating and cooling systems [1,5].

Compare to other technologies of waste heat recovery, usage of TEGs in a waste heat recovery system has many attractive features such as silence, small size, scalability and durability. Heat pipes and TEGs could be used in conjunction for use in a waste heat recovery system [6]. There are examples of exhaust heat recovery using both heat pipes and thermoelectric generator modules: Orry et al. [7-9] has proposed an exhaust heat recovery system with the potential of decreasing the fuel consumption, emission of CO₂ and running costs of a car. Remeli et al. [4, 10-12] designed and produces a prototype of thermoelectric waste heat recovery system. The system come out of Bismuth Telluride (Bi₂Te₃) based TEG sandwiched between two heat pipes. The first and second pipe were connected to hot and cold side, respectively. A new type of heat pipe assisted thermoelectric generator for automobile exhaust waste heat recovery has been suggested by Cao et

al. [13]. In order to verify the optimized configurations of the thermoelectric device, an experimental test set up was built for attaining the best heat pipes insertion depth and the optimum angle between the heat pipe row and the gas flow direction.

Both thermoelectric generator modules and heat pipes have quite promising property for their usage in exhaust heat recovery system [8,9]. Heat pipes are not active heat transfer devices, in other words, heat pipes are passive heat transfer devices. In passive heat transfer devices like heat pipes, thermal conductivity values are much greater than copper, it does not need large temperature gradient between heat source and heat sinks for efficient heat transfer [14,15]

It is understood for the literature review that there are many publications for thermoelectric systems both using heat sink and heat pipes. However, the heat sink considered for condenser block is designed as tower type heat sink, which is rarely known in the literature. Therefore, it is expected that the design will provide original contribution when the ease of production and cost are obtained.

In the work presented, heat pipe assists designing of thermoelectric generator system in order to transform waste heat from piping systems such as exhaust and chimney systems. Thanks to the thermoelectric generator module used in the designed system, the thermal energy is directly transformed into electric energy (DC). The designed new system is compact, modular and both easy to manufacture and install.

2. THEORETICAL PRINCIPLES

Thermoelectric devices are able to transform thermal energy from a gradient of a temperature into electrical energy. This phenomenon was found out in 1821 and is named as "Seebeck effect". Thermoelectric generators (TEG) are comprised of p and n type semiconductor materials [2,5]. Thermoelectric generator (TEG) modules are formed by series and thermally parallel connection of pairs of leg made of p and n type semiconductor materials [16]. Figure 1. below shows the form of both the thermoelectric

generator leg pair ($N=1$) and the thermoelectric generator module ($N>1$). As represented in the figures, p and n type semiconductor materials are electrically connected serially to each other with a conductive material. The semiconducting materials are also placed between the insulating plates to provide electrical insulation. The electric current I (A) in the circuit occurs when heat input is provided in Q_H amount from a heat source to a surface of the leg, because of a temperature difference ΔT (K) between two surfaces of thermoelectric legs.

The performance of thermoelectric material, "Figure of Merit", FoM ie Z is calculated by the following formula

$$Z = \frac{S^2 \sigma}{k} \quad (1)$$

The material performance Z , which is the unit (1 / K), is usually determined by a dimensionless formula multiplied by the average absolute temperature.

$$Z \cdot T = \frac{S^2 \sigma T}{k} \quad (2)$$

The performance of thermoelectric materials is also expressed as follows.

$$Z = \frac{S^2}{KR} \quad [1/K] \quad (3)$$

Today, the ZT value of thermoelectric materials is even lower than 1. The $Z.T$ value of Bismuth Tellurium (BiTe) thermoelectric material widely used in the industry ranges from 0.5 to 0.8 [16-18].

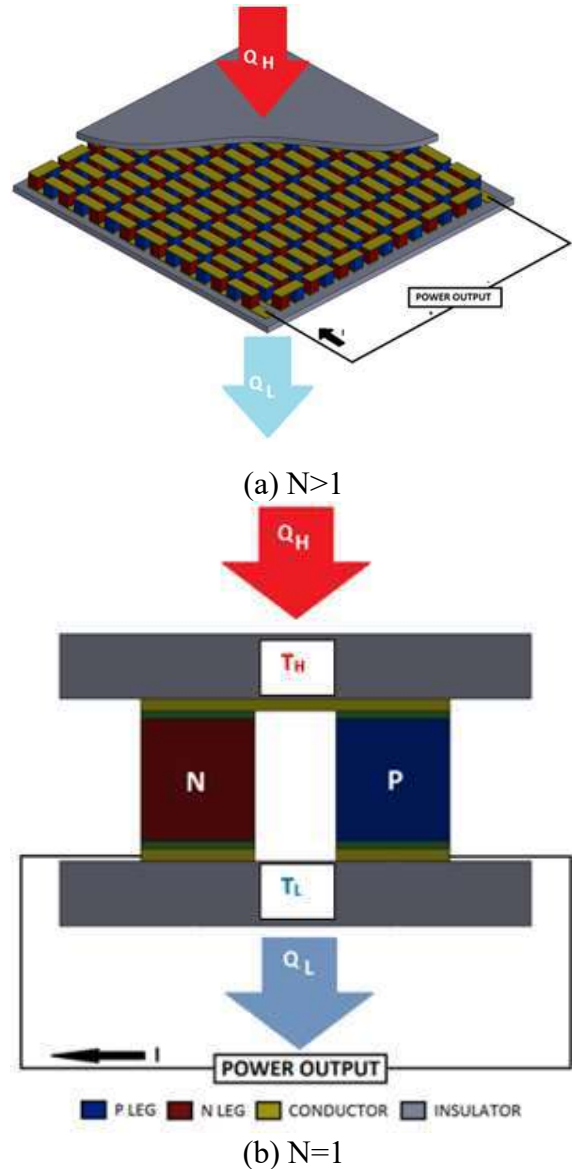


Figure 1 (a) Thermoelectric generator (TEG) module ($N > 1$) and (b) thermoelectric pair of leg ($N = 1$)

The ideal thermoelectric equations which are widely used in the analysis of thermoelectric energy systems are given below [19-21]. These equations depend on the Seebeck effect, the heat transmitted and the Joule heat. The following assumptions are made in the derivation of ideal equations:

- Thermal and electrical contact resistances are neglected.
- Thomson heat is neglected because the materials properties are assumed not to change with temperature.

- The convection and radiation heat transfer from or to thermoelectric leg are neglected.

The conduction heat transfer:

$$Q=K\Delta T=K(T_H-T_L) \quad [W] \quad (4)$$

Where K is the total heat transfer coefficient of a pair of legs ($N = 1$), T_H and T_L are the hot and cold surfaces temperatures of the thermoelectric legs consisting of p and n type leg, respectively.

$$K=k_p \frac{A_p}{L_p} + k_n \frac{A_n}{L_n} \quad [W/K] \quad (5)$$

The Joule heat, which flows when the current flows from thermoelectric leg, can be calculated by the following equation, where R [Ω] is the internal resistance of the module.

$$Q_J=I^2R \quad [W] \quad (6)$$

It is assumed that the amount of Joule heat is equal to both surfaces of the thermoelectric leg. In this case, the amount of heat incoming to each surface will be $Q_J/2$.

The internal resistance of the module is calculated as follows.

$$R=\rho_p \frac{L_p}{A_p} + \rho_n \frac{L_n}{A_n} \quad (\Omega) \quad (7)$$

where $\Omega.m$ and $\Omega.m$ are the electrical resistances of the p and n type legs, respectively.

The heat from the hot surface,

$$Q_H=N[(S_p-S_n).I.T_H+K.(T_H-T_L)-I^2R/2] \quad [W] \quad (8)$$

Heat from cold surface:

$$Q_L=N[(S_p-S_n).I.T_L+K.(T_H-T_L)+I^2R/2] \quad [W] \quad (9)$$

Electrical power generation,

$$P=Q_H-Q_L =N.[S.I.(T_H-T_L)-I^2R]=V.I \quad [W] \quad (10)$$

Efficiency:

$$\eta = \frac{P}{Q_H} = \frac{Q_H-Q_L}{Q_H} = \frac{P}{Q_L+P} \quad (11)$$

Voltage and current are calculated in the following formulas respectively.

$$V=N[S(T_H-T_L)-I.R] \quad [Volt] \quad (12)$$

$$I=\frac{S(T_H-T_L)}{R} \quad (A) \quad (13)$$

3. EXPERIMENTAL STUDY

The shape of the designed and prototype thermoelectric heat recovery system, turning into the energy of waste heat into electricity is shown in Figure 2. All the components except the Peltier module and heat pipe which are used "reversible" in order to produce thermoelectric power in the mentioned system have been manufactured at the CAD / CAM center in the laboratory of Sakarya University Department of Mechanical Engineering.

In our experimental studies, a commercial thermoelectric module (Marlow, SP1848-27154SA) made of Bismuth Telluride (BiTe) semiconducting material and having $N = 127$ leg pairs of p and n type was used. The module has equal edge lengths of 40 mm and a height of 3.4 mm. The thermophysical properties of thermoelectric materials are given in Table 2.

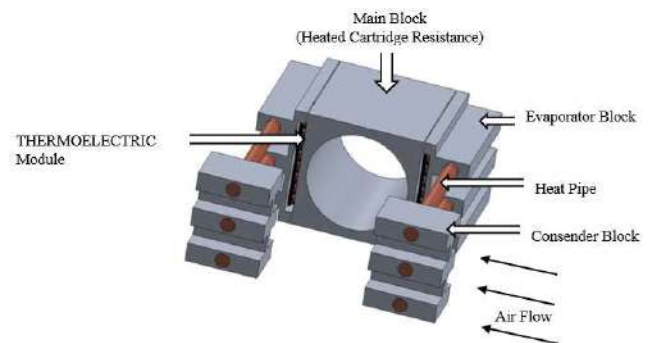


Figure 2 (a) Thermoelectric heat recovery system (a) and developed for experimental operation (b)

Table 1
Thermophysical properties and geometrical properties of thermoelectric materials [22,23]

	Seebeck coefficient S (μV/K)	Electrical resistivity ρ (μΩ m)	Thermal conductivity k (W/m K)
P P type leg	210	18	1,32
N N type leg	-210	12	1,78

The cross-sectional area of thermoelectric feet is
A = 1x1 = 1 mm² and height L = 1 mm

Main Block				Condenser Block					
W	L1	H1	D1	W	L1	L2	H1	H2	D1
50	48	50	42	30	8	8	20	8	6
Evaporator Block									
W	L1	L2	L3	L4	H1	H2	D1		
50	8	8	8	40	14,5	5	6		

Figure 3 The shape and dimensions of the heat transfer elements in the thermoelectric heat recovery system

The performance tests of the prototype thermoelectric power generator were carried out in the Heat Transfer Laboratory in Thermoelectric Energy Systems at Sakarya University. The test setup is shown in Fig 4.

The designed generator system is provided with cartridge heaters (Euroheat) which produces 900 W of power at 230 V, which is operated by trasformer (Varatran 36 Y) to supply heat source

of Q_H to the newly designed generator for experiment. The size of the cartridge is 130 mm and the diameter is 20 mm. Q_L heat transfer from the system is provided by ambient air. With a valve connected to the duct where the air flow is, the air flow has been changed and it is now possible to work at different air velocities. The speed of the air was measured both by the anemometer connected to the inlet of the test section (Airflow TA2 Anemometer / Thermometer) and by the turbine type flow sensors (Dwyer VT-200 Anemometer) connected to the fan outlet. Air temperature, hot side and cold side temperature of the thermoelectric legs respectively, T_H and T_L measurements were made with digital temperature sensors (Dwyer TC-20 Thermometer).

The DC electrical quantities of the thermoelectric power generator such as current and voltage are measured by a multimeter capable of reading AC / DC (Keithley 197 Autoranging Microvolt DMM). The thermoelectric heat recovery system under test has two thermoelectric modules (n = 2). Table 3 below sets forth the data obtained for one module (n = 1).

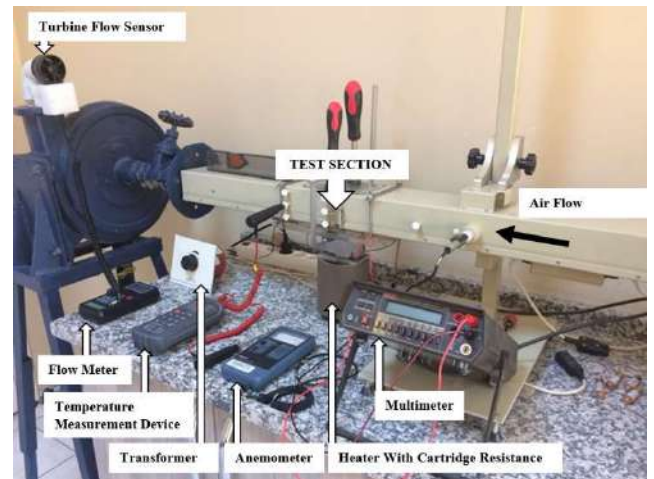


Figure 4 Experimental setup

4. RESULTS

In present study, heat recovery performance of heat pipe assisted thermoelectric generator designed to recover waste heat from piping systems was determined experimentally in Heat

Transfer Laboratory for Thermoelectric Systems at Sakarya University.

The power generation characteristic of the thermoelectric generator was examined by varying the air flow velocity and temperature during the experimental studies. The results are given in Figure 5 and Figure 6.

It is understood from the Figure 5 and 6 that the output power values increase as both increasing of the hot side legs temperature T_H and cold side air velocity. The cold side legs temperature T_L decreases with increasing air velocity.

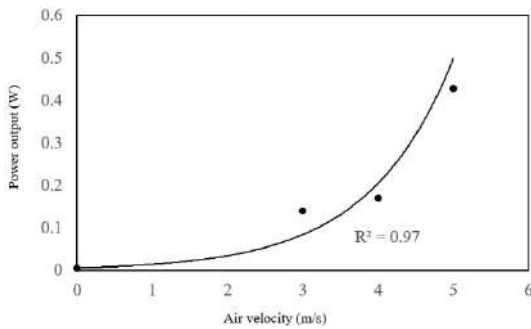


Figure 5 The power output versus air velocity

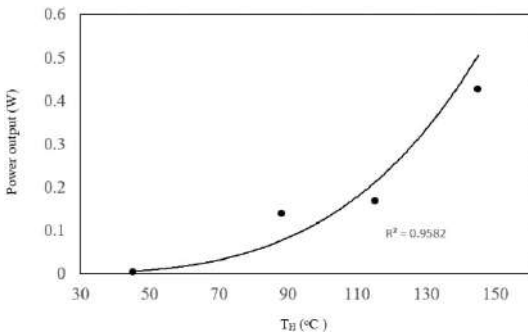


Figure 6 The power output versus the hot side temperature of the legs (air velocity $v=4$ m/s)

The thermal energy conversion efficiency of the thermoelectric heat recovery system according to the differences of temperature between the hot and cold surfaces of the module is shown in Figure 7 below.

Experimental results are also compared with the theoretical results determined by ideal thermoelectric equations for one generator module ($n = 1$) in Figure 7. When the figure is examined, it is seen that experimental and theoretical results are not as compatible as

expected. Because the equations used in the analysis of thermoelectric energy systems depend on the Seebeck coefficient. Therefore, in determining the thermal-electrical performance of the system, the Seebeck coefficient of the thermoelectric module used in the system must be determined correctly. However, since the Seebeck coefficient of the module is not given by the module manufacturer, the Seebeck coefficient which is widely calculated theoretically is used while the thermoelectric modules and energy systems are designed. Since the theoretical and experimental Seebeck coefficients are incompatible [20], the experimental and theoretical performance data of the system are different as can be seen in the figure.

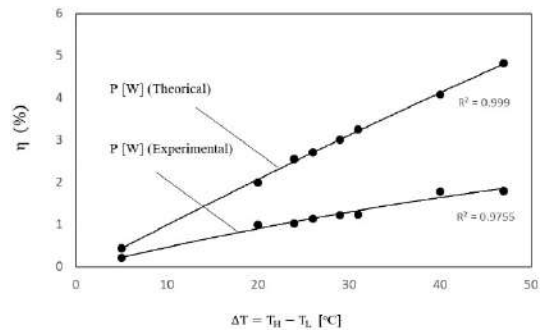


Figure 7 The thermal efficiency (η) of the system according to temperature difference ($\Delta T = T_H - T_L$)

As shown in Figure 7, the thermal efficiency (η) of the thermoelectric heat recovery system is small. For this reason, it is not possible to compete with existing power plants yet. However, since there are no moving parts in the thermoelectric systems, they are preferred for generator and cooler in the military, space and medical industry because of their quiet and vibration-free operation and small size.

The calculated ZT value for thermoelectric module used our experimental studies ($Z = S^2 / KR$ and $T = 300$ K) is 0.588. The $Z.T$ value for commercial Bismuth Tellurium (Bi_2Te_3) material commonly used today is approximately 1. Z value depends upon the Seebeck coefficient, the electrical resistivity and the conductive heat transfer coefficient. For developing the performance of the thermoelectric power system,

the Z value of the thermoelectric material must be high. For Z to be high, the Seebeck coefficient should be improved, low resistivity, and low thermoelectric materials with low heat transfer coefficient.

5. CONCLUSION

An thermoelectric generator system has been designed to product electricity using hermoelectric modules and heat pipes. This design is completely solid state and passive. The maximum power generated during testing from one thermoelectric module was about 0,5 W while theoretically of 1 W.

In the theoretical calculation of the thermoelectric effects with the ideal equations, electrical and thermal contact resistance, properties of the material depending on the temperature, concective and radiative heat transfer form or to the thermoelectric legs are neglected. In practice or during experimental work, the changing contact resistance between the module and the heat transfer devices, depending on the mounting style of the module and the pressure on it, also changes the effective Seebeck coefficient. Therefore, while thermoelectric power systems are being designed using commercial thermoelectric modules, the use of the "effective" Seebeck coefficient determined by the experimental method will contribute to the correct determination of the thermoelectric performance of the thermoelectric system.

The thermal-electrical performance of thermoelectric power systems depends on both the thermoelectric module and the thermal performance of the heat transfer devices that provide heat transfer from the modulo or to modulo. For the development of thermoelectric power systems with improved performance, thermal resistance must be small or total heat transfer coefficient of devices must be large. Particularly in this context, convective heat transfer improvement studies should be regarded as important. The development of efficient and compact heat transfer devices for thermoelectric power systems will contribute to the design and development of efficient thermoelectric energy

systems. These studies will contribute to the much wider use of thermoelectric systems, whose utility is higher environmental friendly clean energy systems. The widespread use of these systems will also contribute to reducing fossil fuel consumption and preventing global warming.

6. NOMENCLATURE

A	Cross-sectional area of a thermoelectric leg [m ²]
H	Height of a thermoelectric leg [m]
I	Electric current [A]
J	Electric current density [A/m ²]
k	Thermal conductivity [W/mK]
N	Number of thermoelectric element or couples
n	Number of thermoelectric module
P	Generated power [W]
Q _H	Heat input [W]
Q _L	Heat rejected [W]
R	Electrical resistance [Ω]
S,	Seebeck coefficient [V/K]
T	Absolute mean temperature ($T = \frac{T_H + T_L}{2}$) [K]
T _H	Hot side temperature [K]
T _L	Cold side temperature [K]
V	Voltage [V]
Z	Figure of merit [1/K]
Z.T	Figure of merit
ρ	Electrical resistivity [Ω.m], [m/S]
σ	Electrical conductivity [1/Ω.m], [S/m]
η	Efficiency

Subscripts

n n-type

p p-type

Funding

The authors received no financial support for the research, authorship, and/or publication of this paper.

The Declaration of Conflict of Interest/ Common Interest

The authors declare that they have no known competing financial interests or personal relationships that could have appeared to influence the work reported in this paper.

Authors' Contribution

Yİ: Conceptualization, methodology, writing, experimental design, experimental studies, investigation, original draft, supervision.

CP: Review, editing, supervision.

İT: Review, editing.

MÖ: Experimental design, investigation.

EA: Review, writing, editing, investigation.

The Declaration of Ethics Committee Approval

The authors declare that this document does not require an ethics committee approval or any special permission.

The Declaration of Research and Publication Ethics

The authors of the paper declare that they comply with the scientific, ethical and quotation rules of SAUJS in all processes of the paper and that they do not make any falsification on the data collected. In addition, they declare that Sakarya University Journal of Science and its editorial board have no responsibility for any ethical violations that may be encountered, and that this study has not been evaluated in any academic publication environment other than Sakarya University Journal of Science.

REFERENCES

- [1] X. Liu, C. Li., Y.D. Deng. and C.Q. Su., “An energy-harvesting system using thermoelectric power generation for automotive application”, *Electrical Power and Energy Systems*, vol. 67 pp.510–516, 2015.
- [2] M.A. Elsheikh., D.A., Shnawah., M.F.M. Sabri, B.M. Said, M.H. Hassan, M.B.A. Bashir and M. Mohamad, “A review on thermoelectric renewable energy: Principle parameters that affect their performance”. *Renewable and Sustainable Energy Reviews*, vol. 30, pp. 337–355, 2014.
- [3] D. Champier, “Thermoelectric generators: A review of applications”, *Energy Conversion and Management* vol. 140, pp. 167–181, 2017.
- [4] M.F. Remeli, A. Date, B. Orr, L.C. Ding, B. Singh, N.D.N. Affandi and A. Akbarzadeh, “Experimental investigation of combined heat recovery and power generation using a heat pipe assisted thermoelectric generator system”, *Energy Conversion and Management*, vol. 111, pp.147–157, 2017.
- [5] Z. Tian, S. Lee and G. Chen, “Heat transfer in thermoelectric materials and devices”, *Journal of Heat Transfer*, vol. 135, pp. 1-14, 2013.
- [6] B. Orr, A. Akbarzadeh, M. Mochizuki and L. Singh, “A review of car waste heat recovery systems utilising thermoelectric generators and heat pipes”, *Applied Thermal Engineering*, vol. 101, pp. 490–495, 2016.
- [7] B. Orr, A. Akbarzadeh. and P. Lappas, “An exhaust heat recovery system utilising thermoelectric generators and heat pipes”, *Applied Thermal Engineering*, vol. 126, pp. 1185–1190, 2017.

- [8] B. Orr, B. Singh, L. Tan and A. Kbarzadeh, "Electricity generation from an exhaust heat recovery system utilising thermoelectric cells and heat pipes", *Applied Thermal Engineering*, vol. 73, pp. 588-597, 2014.
- [9] B. Orr and A. Akbarzadeh A, "Prospects of waste heat recovery and power generation using thermoelectric generators", *Energy Procedia*, vol. 110, pp. 250 – 255, 2017.
- [10] M.F. Remeli, K. Verojporn, B. Singh, L. Kiatbodin L, A. Date and A. Akbarzadeh, "Passive heat recovery system using combination of heat pipe and thermoelectric generator", *Energy Procedia*, vol. 75, pp. 608 – 614, 2015.
- [11] M.F. Remeli, L. Kiatbodin, B. Singh, K. Verojporn, A. Date and A. Akbarzadeh, "Power generation from waste heat using heat pipe and thermoelectric generator", *Energy Procedia*, vol. 75, pp. 645 – 650, 2015.
- [12] M.F. Remeli, L. Tan, A. Date, B. Singh and A. Akbarzadeh, "Simultaneous power generation and heat recovery using a heat pipe assisted thermoelectric generator system", *Energy Conversion and Management*, vol. 91, pp. 110–119, 2015.
- [13] Q. Cao, W. Luan. and T. Wang, "Performance enhancement of heat pipes assisted thermoelectric generator for automobile exhaust heat recovery", *Applied Thermal Engineering*, vol. 130, pp. 1472–1479, 2017.
- [14] H. Jouhara, A. Chauhan, T. Nannou, S. Almahmoud, B. Delpech and L.C. Wrobel, "Heat pipe based systems - Advances and applications", *Energy*, vol. 128, pp. 729-754, 2017.
- [15] C.W. Chan, E. Siqueiros, J. Ling-Chin, M. Royapoor, A.P. and A.P. Roskilly, "Heat utilisation technologies: A critical review of heat pipes", *Renewable and Sustainable Energy Reviews*, vol. 50, pp. 615–627, 2015.
- [16] S. Manikandan. and C.S. Kaushik, "Thermodynamics studies and maximum power point tracking in thermoelectric generator-thermoelectric cooler combined system". *Cryogenics*, vol. 67, pp. 52-62, 2015.
- [17] D.K. Aswal, R. Basu and A. Singh, "Key issues in development of thermoelectric power generators: High figure-of-merit materials and their highly conducting interfaces with metallic interconnects", *Energy Conversion and Management*, vol. 114, pp. 50–67, 2016.
- [16] J. Meng, X. Zhang and X. Wang, "Characteristics analysis and parametric study of a thermoelectric generator by considering variable material properties and heat losses" *International Journal of Heat and Mass Transfer*, vol. 80, pp. 227–235, 2015.
- [18] Zhang, X. and Zhao, L-D, Thermoelectric materials: Energy conversion between heat and electricity, *Journal of Materiomics*, 2015; 1: 92-105.
- [19] S. Twaha, J. Jie Zhu, Y. Yan and B. Li B, "A comprehensive review of thermoelectric technology: Materials, applications, modelling and performance improvement", *Renewable and Sustainable Energy Reviews*, vol 65, pp, 698–726, 2016.
- [20] C.T. Hsu, G.Y. Huang, H.S. Chu, B. Yu, and D.J. Yao, An effective seebeck coefficient obtained by experimental results of a thermoelectric generator module, *Applied Energy*, vol. 88, pp. 5173–5179, 2011.
- [21] S.-C. Tzeng, T.-M. Jeng, and Y.-L. Lin, "Parametric study of heat-transfer design on the thermoelectric generator system", *International Communications in Heat and Mass Transfer*, vol. 52, pp. 97–105, 2014.

- [22] U. Erturun, K. Erermis and K. Mossi K, “Effect of various leg geometries on thermo-mechanical and power generation performance of thermoelectric devices” *Applied Thermal Engineering*, vol. 73, pp. 128-141, 2014.
- [23] U. Erturun, K. Erermis and K. Mossi, “Influence of leg sizing and spacing on power generation and thermal stresses of thermoelectric devices” *Applied Energy*, vol. 159, pp. 19–27, 2015.

JOURNAL OF SCIENCE



SAKARYA UNIVERSITY

Sakarya University Journal of Science

ISSN 1301-4048 | e-ISSN 2147-835X | Period Bimonthly | Founded: 1997 | Publisher Sakarya University |
<http://www.saujs.sakarya.edu.tr/en/>

Title: Agile Methods in Game Programming based on Scrum

Authors: Şahin MERCAN, Yaşar BECERİKLİ

Received: 2019-12-12 20:42:54

Accepted: 2020-07-02 10:35:58

Article Type: Research Article

Volume: 24

Issue: 5

Month: October

Year: 2020

Pages: 882-891

How to cite

Şahin MERCAN, Yaşar BECERİKLİ; (2020), Agile Methods in Game Programming based on Scrum. Sakarya University Journal of Science, 24(5), 882-891, DOI:

<https://doi.org/10.16984/saufenbilder.658752>

Access link

<http://www.saujs.sakarya.edu.tr/en/pub/issue/56422/658752>

New submission to SAUJS

<http://dergipark.org.tr/en/journal/1115/submission/step/manuscript/new>

Agile Methods in Game Programming based on Scrum

Şahin MERCAN^{*1}, Yaşar BECERİKLİ²

Abstract

Game programming requirements, which is one of the problems of game programming in recent times, is constantly changing. Therefore, the process we are conducting while programming the game does not keep up with this change leads to the failure of the product we develop or the result of higher costs. Therefore, the use of agile programming, which brings a more dynamic and modern solution to changing environment conditions, is increasing day by day and the project teams are transitioning to these processes. In this thesis, firstly historical development, content, rules and methods of Agile methods are presented with literature researches. In the next section, Grumpy Ball is applied by using Scrum method which is agile programming method. Since the agile methods provide dynamic solutions, an end date cannot be determined Therefore, the aim of this article is to determine the exact date of a game application using agile method. For this reason, our project is divided into specific parts and the last periods given to these parts were compared according to certain criteria. In the light of the results, determinations were made.

Keywords: agile methods, game programming process, game project management, scrum

1. INTRODUCTION

It is foreseen that there will be changes that may occur in the progressing stages of the software processes. For this reason, traditional methods are based on a comprehensive study at the very beginning of the software processes to determine all the requirements that may occur and to prevent any changes that may occur in the future stages.

However, despite the rapidly changing, evolving environment and market conditions, project requirements are changing more and more quickly.

Therefore, it is almost impossible to determine all the needs at the beginning of the project.

*Corresponding Author: sahinmrcn@gmail.com

¹Kocaeli University, Graduate School of Natural and Applied Sciences, Kocaeli, Turkey.

ORCID: <https://orcid.org/0000-0002-8646-6834>

²Kocaeli University, Department of Computer Engineering, Kocaeli, Turkey, ybecerikli@kocaeli.edu.tr,

ORCID: <https://orcid.org/0000-0002-2951-7287>

Therefore, it is expected that the software development process will have the features that will meet these changes in less time and with less cost. Therefore, agile software development methods have emerged as an alternative to traditional software development methods [2, 7]. If agile methods cannot be applied to the whole project, it can only be agile where necessary or

- Interpersonal and interpersonal relationships in place of process and development tools [3].
- Detailed documentation instead of running software [3].
- Contract negotiations instead of customer cooperation [3].
- Instead of following the plan to keep up with changes [3].

The above common opinion is included in the Agile Alliance Development Agenda and supported by the Agile Alliance and is considered the key to effective software development [7, 3].

1.1. Agile Software Development Features

- Focus and perspective: Agile methods have a project perspective. The focus of the agile methods is the project and project team [12].
- Management: Agile methods are also traditionally made in the form of coaching (command control) and not management. In order for the team to advance, the coach assists the team in eliminating the barriers [12].
- Planning: Agile methods can be planned on more than one level. Project planning at the top level and sprint planning at the detail level are carried out. This brings about flexibility and re-planning [12].
- Learning: Agile methods also occur during learning, project or sprint and activities [12].
- Evaluation: Agile methods are also made through evaluation, results and product (customer satisfaction, project returns) [12].

agile approaches can be tailored to the project and the structure of the development team [11, 10, 6].

In 2001, after the creation of the Agile Software Development Manifesto, agile software principles were introduced. These principles are given below [5].

- Personal development: Agile methods are team and individual oriented (human is above the process). The team is created by selecting people who are good at their work [12].
- Project lifecycle activities: Agile Methods support simultaneous development, test sprints and peer reviews as needed. What is important is that the product is not working as early as possible. With the assumption that the cost of delay and error will be low, incremental delivery method is adopted [12].
- Estimation: In order to accelerate development activities, the development phase is divided into conditions, design and solutions evolve; thus, an attempt is made to achieve a predictable development speed. The aim here is to avoid the need to narrow down the scope of sprint by examining the time and calendar limit at the end of the sprint at the end of the sprint [12].

1.2. Agile Software Development Methods

Although different agile methods share many features, there are important differences between them. Some are committed to working in project management and collaboration (Adaptive Software Development, Scrum, and Dynamic System Development), while others have focused on Extreme Programming software development work [7].

The most important agile methods are Adaptable Software Development, Scrum, Extreme Programming, Crystal Methods, Feature-Guided Development, Open Source Development and Dynamic System Development [7]. We used the Scrum method in this article, we just examined the Scrum method.

In 1986, Hirotaka Takeuchi and Ikujiro Nonaka defined a new approach in product development where all process phases overlap and the team could work together at different stages. The basis of this new approach is based on case studies of automotive, computer, copier, printer manufacturers, and basically aimed to bring speed and flexibility to production. They gave this approach the name of holistic and rugby, the whole process being carried out by a team that was cross-tasked and working for a single purpose [19].

In the early 1990s, Ken Schwaber applied this approach to Easel in its own company and named it Scrum [15]. In 1995, Sutherland and Schwaber jointly presented the first public presentation of the Scrum methodology in a study in Texas [16]. Scrum is a methodology that has been applied extensively in recent years and produces successful results [2].

The Scrum approach was developed to manage the system development process. Scrum is an empirical approach that implements the ideas of industrial process control theory for the system development process, resulting in an approach that redefines ideas of flexibility, harmony and efficiency [1]. The software deals with how to manage rather than how to develop it [12]. This method facilitates management in small-scale projects, directs teams to small pieces in large-scale projects and requires constant reviews [12]. Through these reviews, teamwork is clearly seen, which increases collaboration and communication within the team [12]. It can be applied at the beginning of the project or in the middle of production or when the production is problematic. It is used not only in software development but also in the production of financial and medical products [4].

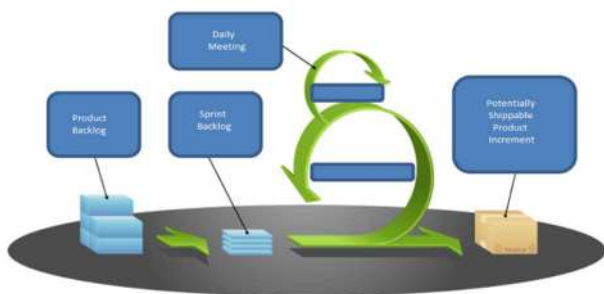


Figure 1 Scrum method

In the Scrum method, planning, job descriptions and documentation spend less time focusing on how the project team can develop a flexible system that is compatible with changing conditions [18]. This method includes sprint planning, sprint backlog identification and Scrum meetings [18]. The loop is restarted by testing the intermediate product customer (job / product owner) as a result of the flag delivery (sprint), and the cycle is restarted and all process steps are reapplied. Figure 1. A second sprint is not started before a sprint is complete (9).

2. SCRUM METHODOLOGY

Scrum initial product requirements will be created and used in architecture, technical details, contracts and so on. It is a project management methodology that starts with the preparation phase, the software is developed with iterative sprints, the product is presented to the customer with intermediate distributions and the product is presented to the customer with the tests and documentation after the final sprint.

In Scrum, organizations perform iterative and incremental development between start and end stages as in Figure 2.

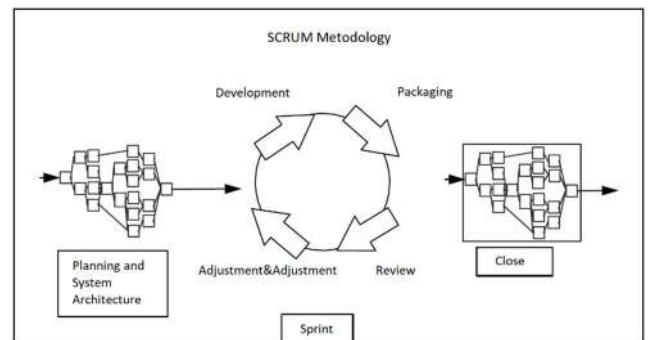


Figure 2 Scrum stages

The start and end stages (planning and closure) consist of defined processes. All process steps and input outputs are defined. With some iterations, the flow at the planning stage is linear [13].

Any changes in the intermediate product after each sprint are re-planned according to the severity of the next conditions. By doing this, it provides the desired product to be produced by providing the desired requirements instead of the

requirements with less value in the product increments [17].

The detailed diagram of Scrum is as in Figure 3. below;

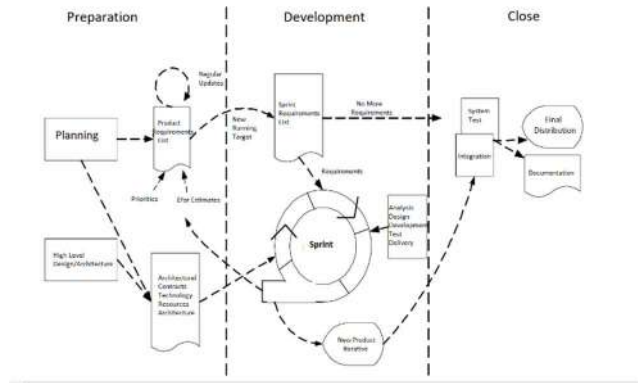


Figure 3 Overview of process in scrum

The development phase consists of iterative development steps as shown in Figure 4. Management deals with time, competition, quality, functionality, completed steps and shutdown phase. This approach is also known as simultaneous engineering [13].

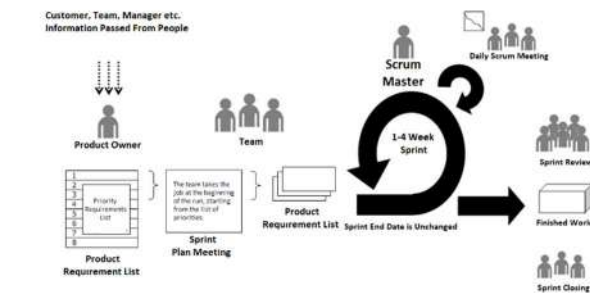


Figure 4 Scrum methodology development phase [17]

In each project there is a time required to understand whether the project is good or not. This period should not be too long. If it is too long, the risks are greater. The project's predictability should be checked at least once a month, except that the project may be out of control or unpredictable [14]. The day starts with a sprint planning meeting and a daily Scrum meeting is held every day.

3. APPLICATION

In this section, game programming is done using Scrum method.

The game basically consists of a ball and rings. Sky and clouds are as background. The speed of the clouds determines the speed of the game. The game progresses faster. Because the game is in the sky, the ball tends to fall down constantly. When you click on the screen, the ball bounces. The rings move from left to right. There are 3 rings in red, green and blue. If the color of the ball is the same as the color of the ring, the user will try to pass the ball through that ring.

The user is given 3 lives at the beginning of the game. There are stars in the right ring every 10 rings. If the user receives this star, one more can will be added.

In addition, our game consists of 4 main sections. In the first part the color of the ball is changed randomly from the colors of fixed rings. In the second part the color of the ball is fixed, the color of the rings is changing randomly. In the third part, the color of both the ball and the rings changes randomly. In the last part, the rings move in addition to the third part.

The screen shows how many rings the user has left.

This is the scenario of our game.

One of the advantages of the agile method has been the flexibility, as it progresses continuously. However, this flexibility constantly changes the existing properties and even adds new features. Therefore, it is not possible to determine an end date of the application. In this application, we are working to determine the end date by using agile method. For this purpose, we will try to make an inference by separating the time estimates at the planning stage and the time elapsed at the end time according to the items. Below we explain the stages of our application. And then we analyzed the results according to the data.

3.1. Pre-Production

The main features of the game were determined at this stage. These are composed of rings and a wholesale in our game. There will be 3 rings of different colors each time. If the ball is the same color as the ball will be tried to pass through the ring. The game will end at a constant speed and a total of 100 rings. The basic principles of our game are determined in this way.

Our game is coded in c # using Unity platform. Desktop, Android and IOS platforms can be played. There is no prototype production. The construction of the pole was started. In order to better test the success of the agile method, the changes in the place where it is necessary in the game have been realized and changed after being realized.

In the later stages of the game, the structure of the game changed a bit as the game was made. The changes were as follows.

What is considered in the changes made here is that the game is more verifiable. For this reason, 3 user rights are given to the user in the game. However, this game has not been easy to finish. Therefore, one user is given a life in every 10 rings. In addition, the game speed is increased as the game progresses to save the game from being monotonized. In order to be able to play the game for a longer period of time, the game was partitioned.

A total of 4 sections. The color of the ball in these sections by changing the color of the ring has become increasingly difficult.

The above changes were related to the game scenario. As a design, the rings in the game were redesigned in 3D.

3.2. Game design documentation

This is a very important issue. Because if something is omitted or neglected in the design, it can lead to the loss of some features in our game. And this leads to a decrease in the "entertainment"

factor, which is the most important feature of the game.

3.3. Product requirement list

This is the section where a list of objects will be prepared according to the game scenario. According to the scenario of our game objects are planned as follows.

Sky and cloud are thought as background elements. These are the main factors that determine the speed of the game while the user is playing.

Secondly, it is considered as game information items, game status, life, playing conditions and main menu.

Finally, the game is considered as the main elements of the ball, ring and star.

3.4. Preparatory Stage

Calculations related to the duration of the game will be made at this stage. The priorities of the improvements to be made during this planning are determined. Then the necessary times for these improvements were determined. These levels were determined as high, medium and low 3 levels. In addition, the works that affect each other have been done consecutively.

3.5. Sprint requirement list

The Sprint Requirement List is the physical presentation of the requirements that the current team is committed to doing, such as a task schedule [8].

It serves to the team and other people to show the work they are planning, the sprint and the situation [8].

This is the part of the development time of the items that we have determined in the product requirement list. In this section, you can create a running requirement list to determine the scenario of our game and determine the duration of the game.

The game is expected to be completed after a period of 55 hours in total when the running requirement list is created and the appropriate periods are given. After this list is determined, the items in the list will be started according to the priorities.

This period can be updated in times when some problems are encountered in the evaluation of the daily Scrum.

3.6. Development

At this stage, the game is being developed. These periods are updated every day according to the rate of completion of the items removed from the running requirement list.

The project was initially set up for the game. To do this, the screen rates are first started. Screen ratios have been adjusted so that the screen can be played both mobile and desktop.

Then the sky and cloud designs in the background of the game were made and the clouds were moved according to the speed of the game.

After these works, ball and ring designs were made. Then the ball jump motion was made. This move is the most important point of our game. Because the bouncing motion of the ball must be natural, that is, as in real life. If this is not the case, we will not be able to include the user in the game and the game's fluency will be gone. After the movement of the ball was completed, the movement of the ring was made. The rings were moved from left to right according to this game speed. Now, according to the scenario of the game, the ball passes through the ring of the correct color, that is, its own color.

Tests after this stage revealed that the game was very monotonous and it was very difficult to finish the game. Therefore, some scenario changes have been made in the game.

Firstly there are 3 can fixed in the game. In these conditions, it is understood that it is very difficult for the user to switch to 100 people. For this reason, a star is added in every 10 rings. And if

the user passes through this ring, he will gain another life.

Then the game is monotonous and the game is too short to be partitioned. In these sections, the color of the ball changes first as it passes through each ring. In the following sections, the colors of the rings are variable and the rings are moving to make the game more difficult. Thus, the game has become increasingly difficult.

The rings were originally planned in two dimensions. However, it was difficult to understand that the ball passed through the ring fully. Therefore, the rings were then redesigned in 3D. And so our game has become more fun.

Lastly, when the user burns or when he finishes the game, the game menus are displayed and the game status indicators are displayed so that he can see his status in the game.

It is planned to be completed in 55 hours in total. However, due to the flexibility of Agile software, several features have been added to make the game more fun and playable at the end of the 5th and 12th days. And then the sprint was re-planned according to the severity of the added features. The time graph of the application is shown in Figure 5 below.

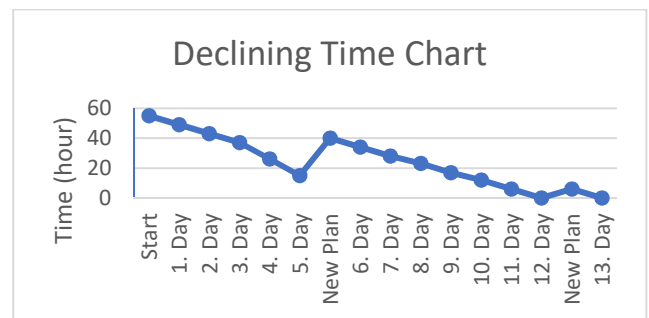


Figure 5 Time schedule of game planning

4. CONCLUSION

A screenshot of the resulting game is shown after the development is completed.



Figure 6 Game screenshot

The game starts when the user clicks on the screen shown in Figure 6. In the upper left corner there is the total number of rings and the number of rings passed. The upper right corner shows the number of lives remaining.

Each time the screen is clicked, the ball bounces. The rings move from right to left. The ball must pass through the ring of its own color. If it passes through the wrong ring, the number of lives remaining decreases by 1. After passing 100 rings, it moves to the next section.

The project is planned to be completed after a period of 55 hours in total. However, as the product was developed later, as the product was examined, some changes were made to make the game better, fun and playable and ended at the end of 86 hours. In our project, due to the flexibility principle of the agile method, a deviation of about 31 hours occurred at the end time. This deviation value is quite a while based on the total time.

Let us examine the causes of this deviation:

When we generalize the game made here, we can say that it consists of 4 main parts. These sections consist of:

- Design of game visuals.
- The menus in the game and the game information.
- Visuals and scenarios created by the more trivial side characters of the game on the game screen.

- Images and scenarios created by the main characters of the game on the game screen.

4.1. Design of Game Visuals

In the game planning phase, a total of 14 hours was calculated for this section. As the game progresses, new features are added in the game, but these added features are generally based on the development of existing scenarios. Star design was needed since the game was added to the 10 rings. In addition, the 3-dimensional redesign of the rings was needed. They have caused a total of 6 hours. In other words, 14 hours of the 20-hour period were determined during the game planning phase. That is, a time deviation of 43% was experienced.

4.2. Game Menus and Information

A total of 16 hours has been calculated for this section when planning the game. As new features are added to the game, it is necessary to display these features on the screen. And so, we had to prepare new menus and texts. In this game, the user had to start all over again. This was becoming very frustrating. Reducing the entertainment aspect of the game. Therefore, the game has been added to the feature. A total of 2 hours has been detected in excess of the time since the visualization of this image and the addition of the can, the need for updates such as cancellation when the user is lit. In total, 16 hours of the 18-hour period were determined during the game planning phase. That is, a time deviation of 13% was experienced.

4.3. Making Game Side Characters

A time period of 10 hours was calculated for the game planning. As the game develops, a star image has been added to the ring of the correct color in every 10 rings to improve the game. When the player passes through this ring, the star disappears, and another player is added to the player. In addition, the time needed for this section in the 3-dimensional construction of rings. A total of 3 hours was spent to make these properties. In total, 10 hours of the 13-hour period

were determined during the game planning phase. That is, a time deviation of 30% was experienced.

4.4. Making Game Main Characters

In this game, a period of 11 hours was calculated for this section. As the game evolves, there are some problems. These games have been very monotonous. The rings are stationary. The color of the ball is fixed and it is thought to be a game that consists of only one part, making the game quite tedious. For this reason, the game has been converted into 4 sections in total. In these sections, the changes of the color of the ball randomly changed, such as the movement of the rings to make the game more monotonous and more fun are planned. A total of 20 hours of additional time was needed to make these features. As a result, a total of 11 hours of the 31-hour period were planned at the start of the game. That is, a time deviation of 182% was experienced.

4.5. Results and Suggestions

The graph of time deviation according to the above-mentioned starting and subsequently changing conditions is shown in Figure 7 below.

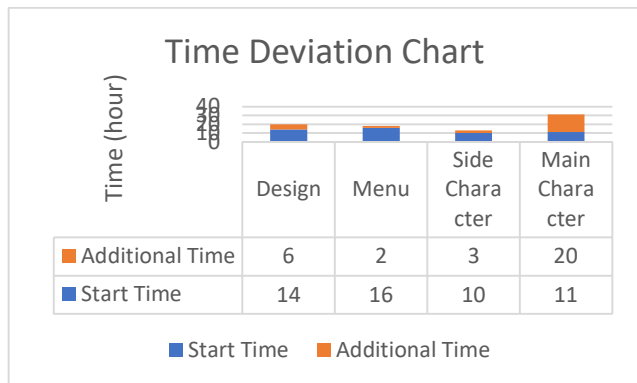


Figure 7 Time deviation graph

As an alternative, a 4-hour period is planned for project initial settings. The reason we don't take this time is due to the speed of the code developers in the background. Therefore, since there will not be any deviation in this period, this part is only added to the end of the project planning in the time calculation.

When the above 4 main sections are examined, this ratio is quite high in the sections that directly affect the game's scenario, fiction and playing situations while the game design, game menus design and game side characters section change in a very limited ratio. As a result, an end date for the project can be calculated if time is added to the planned times at the beginning of the game. However, due to the flexibility principle of agile methods, a definite date cannot be predicted. Just predictable. As these examples are reproduced, a more accurate result will be increased.

The most important part that will negatively affect the removal of this period is the correct identification of the 4 main sections mentioned above. In particular, the game's main characters and the less significant side and back characters must be separated from each other by the total time determination of the section. People who make this distinction must understand the scenario of the game very well.

In a matter that adversely affects this proposition:

Sometimes the side characters of the game are so popular that the effect on the game can be increased and become the main characters of the game. This may adversely affect the time estimate. For this reason, it is important to pay attention to this aspect when deciding the game side characters.

5. FUTURE WORK

In order for a better end date determination to be carried out in further studies, the 4 main sections we use in this article can be further elaborated. The more detailed these sections, the more accurate deviation can be determined.

While we were making the game, we went directly to the development stage without prototyping. Therefore, as the game develops, there have been more locations changed. In particular, changes in the design may have been more because prototyping was not performed. Therefore, if such an application is prototyped without directly developing, the results will be examined.

In addition, the game can be compared with other agile methods or traditional methods and the results can be compared.

Funding

Financial support wasn't received for the production of this paper.

The Declaration of Conflict of Interest/ Common Interest

No conflict of interest or common interest has been declared by the authors.

Authors' Contribution

Ş.M: literature, project construction, writing

Y.B: project construction, writing

The Declaration of Ethics Committee Approval

The authors declare that this document does not require an ethics committee approval or any special permission.

The Declaration of Research and Publication Ethics

The authors of the paper declare that they comply with the scientific, ethical and quotation rules of SAUJS in all processes of the paper and that they do not make any falsification on the data collected. In addition, they declares that Sakarya University Journal of Science and its editorial board have no responsibility for any ethical violations that may be encountered, and that this study has not been evaluated in any academic publication environment other than Sakarya University Journal of Science.

REFERENCES

[1] P. Abrahamsson, O. Salo, J. Ronkainen, and J. Warsta, 2017. Agile software development methods: Review and analysis. arXiv preprint arXiv:1709.08439.

[2] V. Baytam, O. Kalıpsız, Scrum Software Development Model Management Tool ScrumMAp. Fifth National Software Engineering Symposium, September (in Turkey), 2011.

[3] K. Beck, M. Beedle, A. V. Bennekum, A. Cockburn, W. Cunningham, M. Fowler, and J. Kern, Manifesto for agile software development, 2001.

[4] B. Boehm, Get ready for agile methods, with care. Computer, 1, pp. 64-69, 2002.

[5] İ. Duru, Design and implementation of mobile applications in agile methods (in Turkey), 2014.

[6] J. Grenning, Launching extreme programming at a process-intensive company. IEEE Software, vol. 18, no. 6, pp. 27-33, 2001.

[7] J. Highsmith and C. Alistair, What is agile software development?. crosstalk, vol. 15, no. 10, pp. 4-10, 2002.

[8] P. Hundermark, Do better scrum. ScrumSense: <http://www.scrumsense.com/wp-content/uploads/2009/12/DoBetterScrum-v2.Pdf>, 2009.

[9] R. E. Landaeta, V. S. Viscardi, and A. Tolks, 2011. Strategic management of scrum projects: An organizational learning perspective. In First International Technology Management Conference, pp. 651-656, IEEE.

[10] M. Lippert, P. Becker-Pecbau, H. Breitling, J. Koch, A. Kornstadt, S. Roock, H. Zullighoven, Developing complex projects using XP with extensions. Computer, vol. 36, no. 6, pp. 67-73, 2003.

[11] D. J. Reifer, F. Maurer, and H. Erdogmus, Scaling agile methods. IEEE software, vol. 20, no. 4, pp. 12-14, 2003.

[12] E. Şahin, İ. Keskin Kaynak, and H. Koç, Implementation of SCRUM Agile Software Development Method in Software Development Works in an Organization with CMMI-DEV

Level-3 Certification. In UYMS (in Turkey), 2013.

[13] K. Schwaber, Scrum development process. In Business object design and implementation, pp. 117-134, Springer, London, 1997.

[14] K. Schwaber and J. Sutherland, Scrum guide: developed and sustained. Scrum. org., 2009.

[15] J. Sutherland, Agile development: Lessons learned from the first scrum. Cutter Agile Project Management Advisory Service: Executive Update, vol. 5, no. 20, pp. 1-4, 2004.

[16] J. V. Sutherland and K. Schwaber, The SCRUM methodology. In Business object design and implementation: OOPSLA workshop, 1995.

[17] J. Sutherland and K. Schwaber, The Scrum Papers: Nuts, Bolts and Origins of an Agile Process (2007), 2010.

[18] S. Süloğlu, When the method is agile (in Turkey), 2005.

[19] H. Takeuchi and I. Nonaka, The new new product development game. Harvard business review, vol. 64, no. 1, pp.137-146, 1986.

JOURNAL OF SCIENCE



SAKARYA UNIVERSITY

Sakarya University Journal of Science

ISSN 1301-4048 | e-ISSN 2147-835X | Period Bimonthly | Founded: 1997 | Publisher Sakarya University |
<http://www.saujs.sakarya.edu.tr/en/>

Title: The Effect of Different Parameters on Shape Memory Alloys

Authors: İbrahim Nazem QADER, Mediha KÖK, Fethi DAĞDELEN, Shakhawan Salih ABDULLAH

Received: 2020-05-07 13:00:41

Accepted: 2020-07-03 15:43:01

Article Type: Research Article

Volume: 24

Issue: 5

Month: October

Year: 2020

Pages: 892-913

How to cite

İbrahim Nazem QADER, Mediha KÖK, Fethi DAĞDELEN, Shakhawan Salih ABDULLAH;
(2020), The Effect of Different Parameters on Shape Memory Alloys. Sakarya

University Journal of Science, 24(5), 892-913, DOI:

<https://doi.org/10.16984/saufenbilder.733645>

Access link

<http://www.saujs.sakarya.edu.tr/en/pub/issue/56422/733645>

New submission to SAUJS

<http://dergipark.org.tr/en/journal/1115/submission/step/manuscript/new>

The Effect of Different Parameters on Shape Memory Alloys

İbrahim Nazem QADER^{1*}, Mediha KÖK², Fethi DAĞDELEN³, Shakhawan Salih ABDULLAH⁴

Abstract

Shape memory alloys' characteristics are different from ordinary materials because they can memorize their pre-determined shape, thus they are excellent candidates for different applications. In this review article, the most interesting parameters that researchers are using in their investigation have been highlighted. Also, the popular techniques used for the characterization of shape memory alloys have been described. The diagrams and sketches can show a clear view of metallurgies and related research areas.

Keywords: Shape memory alloys, diagrams, sketches, characterization process

1. INTRODUCTION

Shape memory alloys (SMAs) have been found in the 20th century and they merged with technology whenever NiTi (nitinol) was discovered in Naval Ordnance Laboratory [1]. Nowadays, various SMA's families are known and for different applications, their properties have been changed. Several parameters are involved to change SMA's characteristics, such as compositional rate, type of constituents, and microstructure. The effect of different parameters on mechanical, thermal, and other physical properties of SMA can be determined using some specific measurements.

Different techniques have been developed for fabricating and characterizing different properties of SMAs. Figure 1 showed the most important techniques utilized for producing NiTi SMAs. The different methods, including VAR, VIM, EBM, CS, SHS, HIP, SPS, MIM, SLS, SLM, and LENS, which are Vacuum Arc Remelting [2], Vacuum Induction Melting, Electron Beam Melting, Conventional Sintering, Self-propagating High-Temperature Synthesis (combustion) Synthesis, Hot Isostatic Pressing [3], Spark Plasma Sintering [4], Metal Injection Molding, Selective Laser Sintering [5], Selective Laser Melting [6], and Laser Engineered Net Shaping [7], respectively.

*Corresponding author: inqader@gmail.com

¹ University of Raparin, College of Science, Department of Physics, Sulaymaniyah, Iraq
ORCID: <http://orcid.org/0000-0003-1167-3799>

² Firat University, Faculty of Science, Department of Physics, Elazığ, Turkey
ORCID: <http://orcid.org/0000-0001-7404-4311>

³ Firat University, Faculty of Science, Department of Physics, Elazığ, Turkey
ORCID: <http://orcid.org/0000-0001-9849-590X>

⁴ Erbil Polytechnic University, IT Department, Erbil, Iraq
ORCID: <http://orcid.org/0000-0001-6468-3793>

There are many review articles that have detailed about various applications and important results. Jani et al. [9] described a general view of SMA, some applications, and opening research gates for investigation. Nespoli et al. [10] overviewed the potential of SMAs to develop miniature mechanical devices. Cisse et al. reviewed the

modeling methods for modeling complex bearing in SMAs [11]. Follador and colleagues discussed the general technique for fabricating SMA-based actuator springs [12]. However, there are few studies that mentioned different influenced parameters on SMAs and the main ideas about characterization.

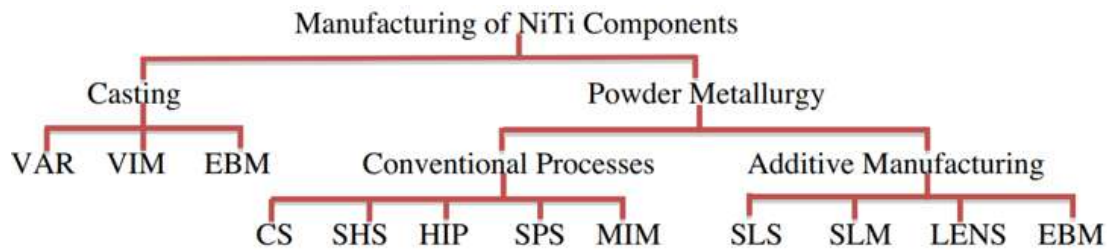


Figure 1 Importance methods used for fabrication NiTi SMA [8]

In this review, SMA has been defined and the superior characteristic has been specified. Some related information about SMA has been described. Also, some application has been given to show the importance of SMAs for technology. In addition, the influence of different studied parameters has been highlighted with some literature review. Finally, the measurement techniques and some important instruments have been clarified in terms of clear sketches with important basics about their operation.

2. SHAPE MEMORY ALLOYS

Some fundamental information needs to understand the shape memory alloys (SMAs), i.e. the alloy should be well defined and also the prefix (shape memory) should be explained through some diagrams.

2.1. Metals

Metals are a group of materials that have some unique characteristics compared with the other materials. One of the significant parameters in the electrical nature of the metals. Since the metal elements have an ocean of free electrons, so this group of elements can transfer electricity via the

electrical carrier extremely more than the other groups.

2.2. Metal Alloys

Alloy is a combination of two or more chemical elements to share their physical characteristics. Mostly, the materials are alloyed with other elements to change the properties of the materials for different applications. When a material is alloyed with another element, the dopant elements distribute all over the materials in either substitute, interstitial, and/or cluster form. It should be kept in mind that the two different constituents do not chemically bond but they only share their physical properties, i.e. melting temperature, heat capacity, electrical and thermal conductivity.

2.3. Shape Memory Alloys

Sometimes by doping the material with a particular amount of dopant element, the alloy may achieve a new property, which existed previously in neither host nor dopant material. A characteristic that a shape memory material is based on their new formation of a superlattice crystal structure. Like other metals, a shape

memory alloy (SMA) has a parent solid phase, is called austenite phase, which is a high similarity, and normally it has a cubic crystal structure. Furthermore, the SMA has another crystal structure, which is a non-cubic crystal structure and is stable at lower temperatures. The lower temperature is so-called martensite phase [13, 14]. Martensite has twinned crystals that can transform into detwinned martensite whenever an external load is applied. Thus the induced strain can be saved in the detwinned martensite variants and can be recovered through heating to the austenite temperature region. Therefore, the aforementioned characteristic can give a shape memory property to the SMA, which is known as a shape memory effect (SME). In addition, superelasticity (pseudoelasticity) is another shape recovery feature that can occur in the austenite phase without the heating process [15].

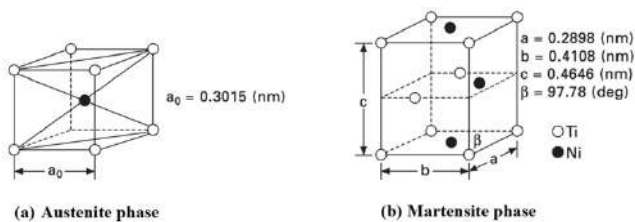


Figure 2 (a) Austenite and (b) martensite phase of NiTi shape memory alloy [16]

Figure 2 shows the austenite and martensite crystal structure of a particular SMA. They have various site arrangements and different lattice parameters. The phase transformation in point of view of the crystal structure is shown in the schematic diagram (Figure 3). The phase transformation temperatures are austenite start, austenite finish, martensite start, martensite finish and martensite transformation temperature by deformation (i.e. maximum temperature at which martensite transformation occurs) Temperatures that are symbolized as A_s , A_f , M_s , M_f , and M_d , respectively [17-29].

2.4. Phase diagrams

In thermodynamics, the state of materials is defined with several parameters. Likewise, there are some parameters in metallurgy that should be controlled to monitor the physical characteristics of an alloy. Based on these parameters, three

different phase diagrams are introduced in this review.

2.4.1. Temperature-Composition diagram

In this kind of diagram, the temperature and composition of the constituents are play the rule. A binary phase diagram is more popular, however in some cases the binary alloy doped by a third element with a constant ratio. There is a boundary line between liquid and solid-state of the alloy which can be different by changing the composition. The liquid-solid boundary has less important in the metallurgy of shape memory alloys.

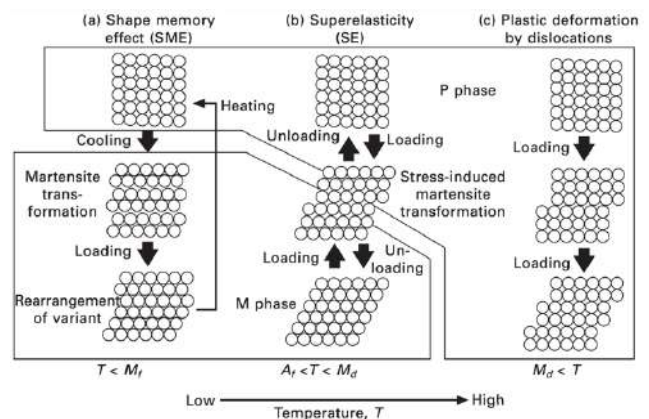


Figure 3 shape memory effect, (b) superelasticity, and (c) plastic deformation by dislocations [16]

Figure 4 shows two important SMA families. The binary NiTi SMA was found by William J. Buehler in the Naval Ordnance Laboratory [30]. In the NiTi phase diagram, it can be seen that there are many different regions with different solid phases. However, only the areas that occurred around eutectoids are important in shape memory studying point of view. For example, in Figure 4a there are just two regions, one in the high composition of titanium (Ti) and the second can be found in the nearly equiatomic composition of nickel and titanium. Although Ti-rich NiTi SMAs and nearly equiatomic NiTi SMAs have different characteristics, the Ti-rich NiTi SMAs are used comparably less than equiatomic NiTi SMAs because titanium is an expensive element in the markets.

CuAlNi shape memory alloys are also an important family that can be alloyed with other

elements and/or can be treated to be used in different application areas. The composition change and treatments can play with the existing phases shown in Figure 4. The austenite phase of CuAlNi SMA is called β -phase and martensite phase can be γ' phase with coarse martensite plates and/or β' phase with narrow (needle-shape) martensite plates. Figure 5 illustrates a Cu-Al-Ni SMA that showed the martensite phase. Although the microstructure of the martensitic phases is different, the crystal structure can be either twin or detwinned. It is also known that some precipitation phases can be obtained in the austenite and martensite phase which produced through a diffusion process and make a compound. The type, amount and shape of these precipitations can directly effect on the physical properties of the shape memory alloys.

2.4.2. TTT diagram

Isothermal transformation diagram or time-temperature-transformation (TTT) diagram shows how the cooling time can influence on the microstructure of the alloy. The diagram is essential for designing and making a decision about the production process. The temperature is kept constant (isothermal) during the measuring process. Figure 6 is a simple TTT diagram for $Ti_{48.7}Ni_{51.3}$ (at.%) SMA which is found for experimental results and theoretical calculation [31]. The TTT diagram for some alloys, e.g. Fe-C, is more complicated.

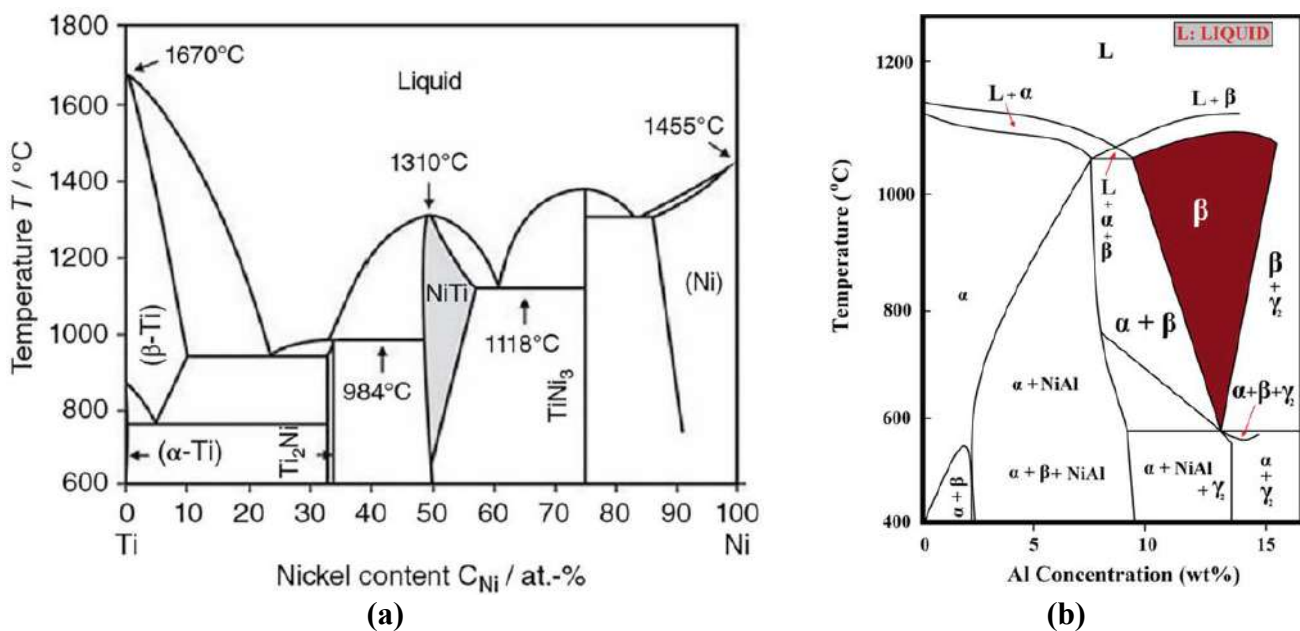


Figure 4 (a) Binary Ni-Ti alloy and (b) Ternary Cu-Al-3.0 wt. % Ni [32, 33]

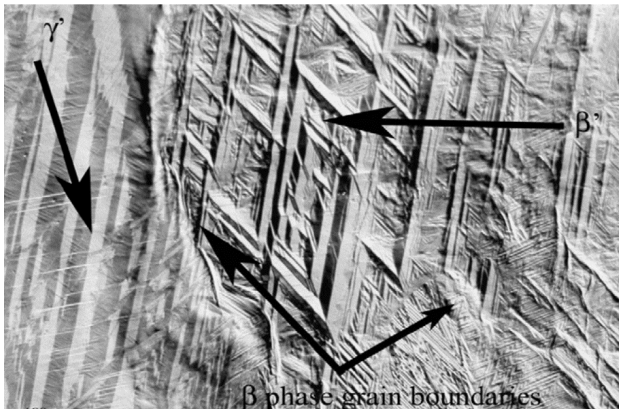


Figure 5 A combination of two different martensite phase in a Cu-Al-Ni shape memory alloy [34]

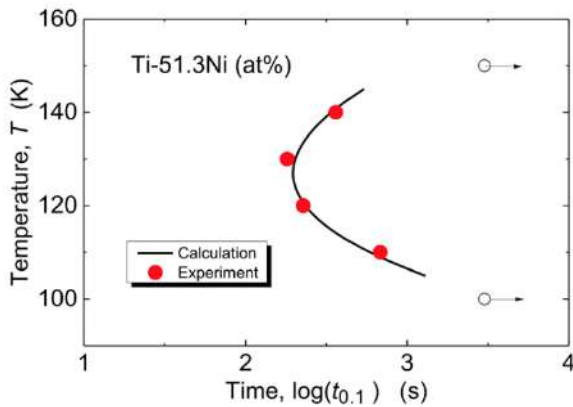


Figure 6 TTT diagram of $Ti_{48.7}-Ni_{51.3}$ (at.%) alloy [31]

For a duration of time at a specific temperature, the microstructures undergo changes because of a diffusion process of the constituents. Thus, the microstructure of an alloy, such as steel, can be monitored to obtain a desired feature for a specific application. However, the operation of an SMA, which is a phase transformation between austenite, and martensite, is supposed to be a diffusionless process. The properties of an ideal SMA should be constant, especially the phase transformation temperatures. Therefore, the microstructure should not be changed during phase transformation. Nevertheless, a real SMA is not thermally stable, because the process of heating and cooling take time, which provides the opportunity for the diffusion process and change the grain size of the SMA. The differential scanning calorimetry (DSC) results showed that

there is no thermal stability during the cycling process [35-38].

2.4.3. Stress-strain diagram

Metal alloys are classified into ferrous and non-ferrous alloys [39]. In all cases, the metals showing a different stress-strain property. Figure 7 shows the stress-strain test for a brass specimen, whereby applying stress on the brass, it starts to deform. The deformation started with an elastic deformation which has a linear relationship between applying stress and the induced strain. In this stage, materials can recover their induced strain when the applying load is removed. Metals can be further deformed by increasing the applying load, however, when the deformation passed a critical point (yield point) it cannot recover the all induced strain. Thus the predetermined shape cannot be recovered through external treatments, such as hot or cold working. Also, some residual stress can release through heat treatments [40, 41]. Shape memory materials, on the other hand, can recover their original shape spontaneously [42-44].

Figure 8 shows the schematic representation of traditional material and two superior behavior of an SMA. In all cases, there is an elastic behavior, where the materials can recover almost all the induced strain. However, when the applying stress is increased, the material deformed and finally is broken in a maximum applying force. After a material deformed it cannot recover the induced strain, while in SMA the material can recover its predetermined shape through shape memory SME or pseudoelasticity (superelasticity) [16, 45].

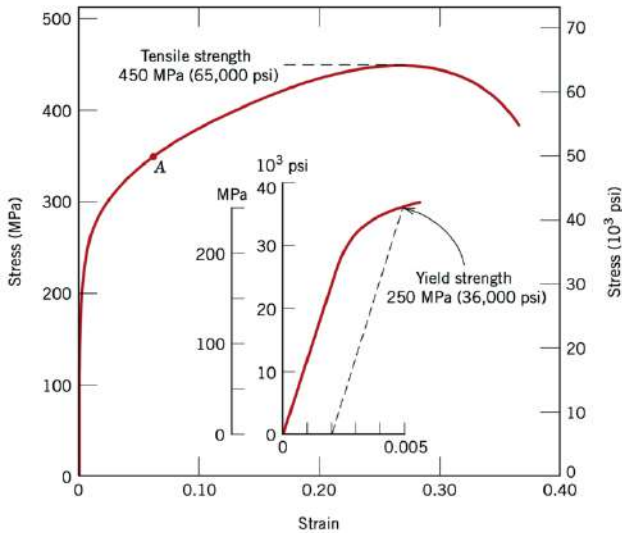


Figure 7 The stress-strain property of brass [39]

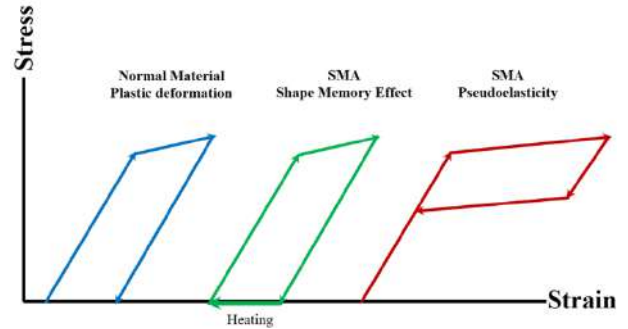


Figure 8 Schematic diagram of stress-strain behavior of a normal material and a SMA that can show SME and pseudoelasticity

2.5. Characteristics

SMA similar to the other types of materials have physical properties, such as electrical conductivity, heat capacity, and thermal expansion. Also, there are some chemical properties such as corrosivity. Additionally, they have some superior properties that distinguish them from other counterparts. Shape memory effect and pseudoelasticity are two important characteristic that only belongs to SMAs.

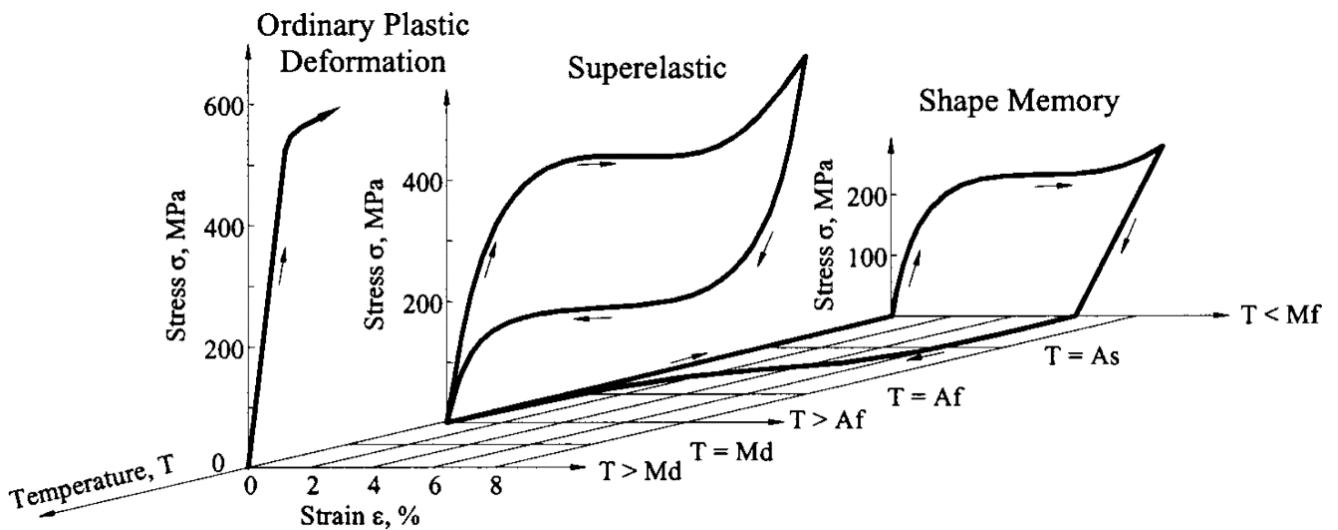


Figure 9 The diagram of an ordinary deformation above M_d temperature, superelasticity in the temperature range ($A_f - M_d$), and SME by heating the NiTi alloy to temperature up to A_f [46]

2.5.1. Shape memory effect

The shape memory effect (SME) is a shape memory recovering process. A deformed SMA in

the martensite phase can be heated up to austenite phase to recover the original form, however, the shape cannot precisely be returned to its original. An equiatomic NiTi alloy can recover about 8%

of the induced strain [43, 9]. Figure 9 shows the process of shape recovery for an approximately equiatomic NiTi SMA. The SMA directly responded to the external stress and the deformation can stretch the atomic bonds, thus the energy can release whenever the external force was removed. When the magnitude of the external load exceeded, the SMA deformed like other ordinary materials, however, the slip did not occur for the applying load. The twinned martensite has only been detwinned, so by heating the SMA, the crystal structure of the alloy started to transform from martensite (twinned or detwinned martensite) to the austenite phase. This transformation started from A_s and it finished at A_f . Lastly, the shape-recovered SMA was cooled to the martensite phase in an extremely short time. In reality, some residual phases can remain, and austenite \leftrightarrow martensite transformation cannot completely be dissolved through the transformation process. Also, creating precipitation made of a compound can noticeably be detected using XRD measurements [47-49].

2.5.2. Pseudoelasticity

Pseudoelasticity or superelasticity (SE) is another potential shape memory ability of SMAs that the alloy can restore the strain through an isothermal process and without an additional stimulus process. It can be seen in Figure 9 that the characteristic occurred between A_f and M_d temperatures. The Pseudoelasticity is such that in the prior loading the SMA showed elasticity, like other ordinary materials, and by increasing the load the strain can increase with constant stress.

In this stage, the austenite phase transformed into a detwinned meta-stable martensite phase, which absorbed a huge amount of loading. If the loading is not exceeded its limit, the SMA can return back to its original shape. Indeed some energy consumed during internal energy through the phase transformation process, which appeared as a different path of *austenite* \leftrightarrow *metastable-martensite* and *metastable-martensite* \leftrightarrow *austenite* transformation.

2.6. Some Applications

Nowadays, several applications based on SMAs. Mostly, SMA is used as an actuator form. Fast response to stimulus and no need for external control are advantages of SMAs. Some applications in three main categories are shortly mentioned.

2.6.1. Medical applications

The first popular utilization is in the Orthodontic field. NiTi SMA, artificial known as NiTiNOL, is the best candidate which is better than the ordinary materials. Table 1 represents some selected mechanical properties of three different materials. It is obviously can be seen that NiTi alloy has bigger ultimate tensile stress and smaller ultimate tensile strain compared with stainless steel (316L), non-magnetic Cobalt-Chromium-Nickel-Molybdenum alloy (ELGILOY). In addition, the NiTi alloy has a comparably lower elastic modulus. These properties made the alloy to be chosen as the best candidate for orthodontic purposes.

Table 1

Some mechanical properties of stainless steel (316L), non-magnetic Cobalt-Chromium-Nickel-Molybdenum alloy (ELGILOY), and nitinol (NiTi) alloys. UTS and UTE are ultimate tensile stress and strain, respectively [50]

Alloys	Elastic Modulus (GPa)	Yield stress (MPa)	Yield strain (%)	UTS (MPa)	UTE (%)
316L	193	340	0.17	670	48
ELGILOY	221	450	0.20	950	45
NiTi	$E_A = 53.5, E_M = 29.2$	$\sigma^{AS} = 400$	$\epsilon_y^S = 9.0$	1355	14.3

Figure 10a shows a schematic comparison for undeformed stainless steel and nitinol shape memory alloy. The arc wire should be chosen such that it has sufficient stiffness and it should exert optimal stress on the displaced teeth. Thus, the induced stress, by the arc-wire, is classified to subthreshold (has no effect), suboptimal (has a low effect), optimal (the sufficient effect), and excessive (the undesired effect). It can be seen that the effective strain of nitinol is comparably more than stainless steel. Figure 10b showed the

stress-strain characteristics of NiTi and stainless steel, where the stainless steel permanently deformed while the NiTi SMA instantly deformed and the induced strain is stored in terms of phase transformation from austenite to detwinned-metastable-martensite phase. The overall effective strain of NiTi SMA is several times bigger than stainless steel due to the pseudoelasticity effect. Therefore the SMAs are a selective candidate for orthodontic purposes [51].

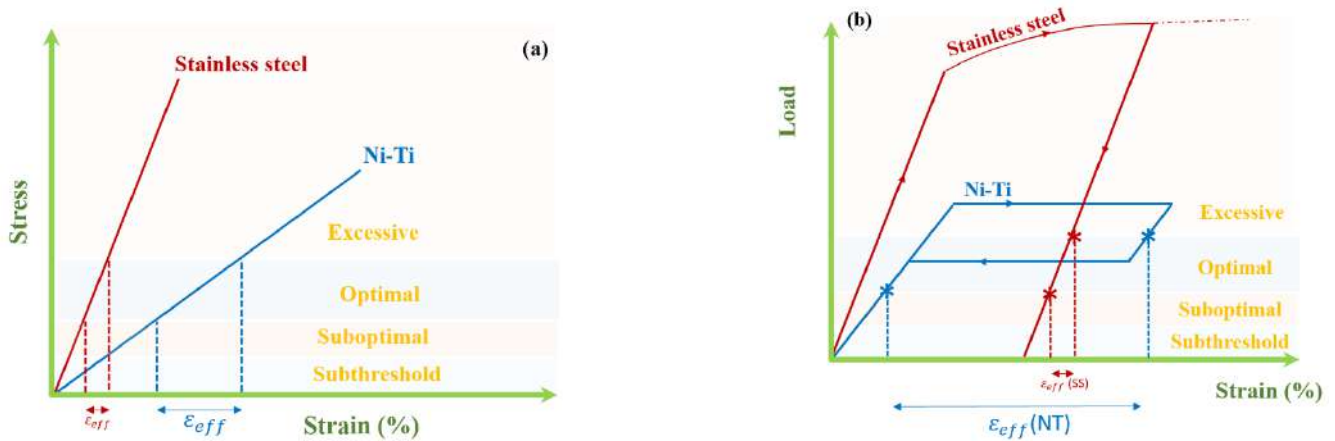


Figure 10 (a) A comparison of elasticity between stainless steel and NiTi SMA (as an ordinary material); (b) compare the strain recovery after deforming stainless steel and NiTi alloy [13]

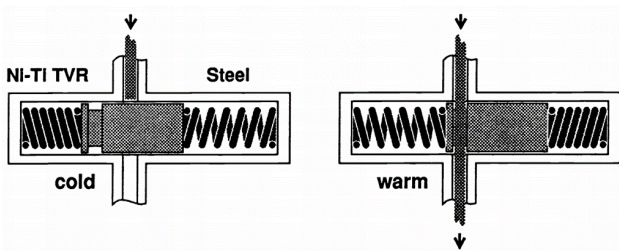


Figure 11 A steel-SMA system [52]

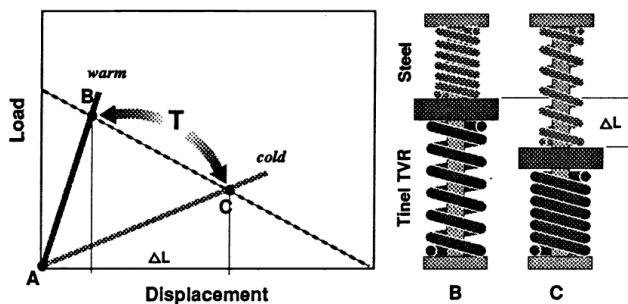


Figure 12 Ni-Ti spring properties for biasing forces

2.6.2. Engines and Aerospace

There is numerous application in this area, such as Smart Aircraft and Marine Project System Demonstration SAMPSON [53, 54], Rotor blade system [55], reconfigurable rotor blade [56], and nozzle configuration [56]. The most SMA-applications is used in term of the actuator. For example for making a cooling system based on temperature, a combination of steel and a SMA, such as NiTi alloy, can make a smart independent valve system (Figure 11). In low temperature, the steel-spring has more stiffness compared to the NiTi alloy, so the valve is closed and coolant does not flow into the engine. When the temperature increases the NiTi transforms from martensite to austenite phase, and therefore its stiffness becomes bigger than the steel. In such condition, the NiTi-based spring pushes the steel-based spring and consequently the valve is opened for

passing the coolant into the engine. Figure 12 displays the austenite and martensite response of a NiTi alloy to a biasing load. The austenite phase has bigger stiffness compared to the martensite phase.

2.1. Heat treatments

Some physical properties of a SMAs, such as phase transformation hardness, stiffness, electrical resistivity and magnetization, can be influenced through heating (or cooling) process. Since, the type and size of microstructure is one of important factors to give different characteristic to a SMAs, so by controlling these parameters their physical properties can be monitored in a specific range. There are also isothermal process, which depend one time and temperature called aging. On the other hand the process of cooling is one of key point to determine the microstructure and hence to change the SMAs' characteristics.

3. DIFFERENT STUDIED PARAMETERS

SMAs response to different physical stimuli and phenomena, such as heating, electrical and magnetic fields, oxidation, and mechanical stress. In following sections some parameters are explained with a recent literature review for each.

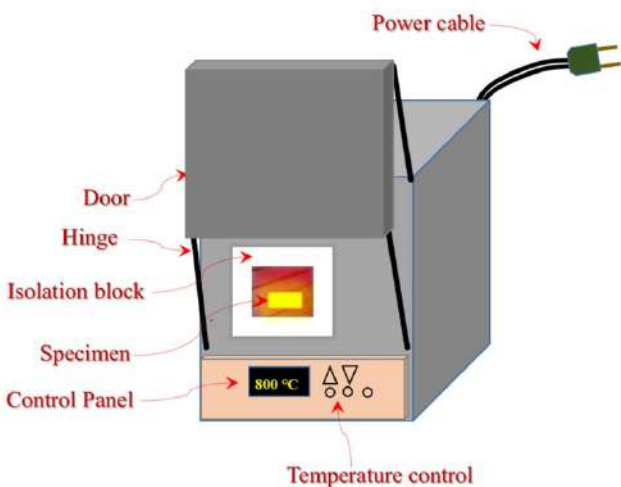


Figure 13 A sketch of furnace for aging SMA

3.1.1. Aging

Aging is a thermal process, where a specimen is taken in a particular temperature for a determined time [28]. A convenient furnace need for heating up a SMA. The furnace should be designed with some particular features. The temperature and the sample atmosphere should be under control. Generally, lab furnace uses an electrical heater to heat up and they have a panel to set the temperature and time of operation. Figure 13 illustrates a sketch of a furnace used for aging SMAs. It has an isolation block that is passive and can tolerate high temperatures. The atmosphere should be controlled to enhance the efficiency of the aging process. In addition, vacuolization avoids the specimen from oxidation in high temperatures. However, the capsulation of the sample is another way for those furnaces that have no atmosphere control facilities.

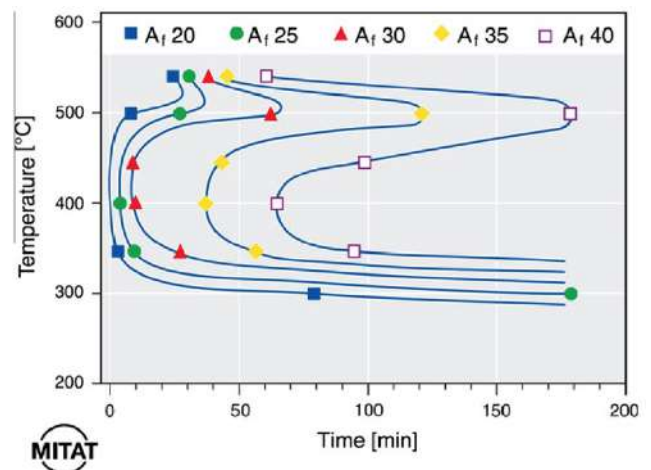


Figure 14 Aging and cooling process as a function of time for austenite finish temperature (A_f) [57]

The temperature of aging can be changed to investigate its influence on some physical properties of SMAs. There is a temperature-composition-phase diagram for most binary SMAs, where the melting temperature, eutectoid temperature as a function of composition is determined. The metallurgists can choose the effective temperature of aging, however, for some SMAs with more than two constituents, the researchers should investigate different temperatures using trial and error. Figure 2 shows the effect of aging and cooling process on

austenite finish temperature. The TTT diagram has obtained for Ni_{49.2}Ti_{50.8} (at.%). The alloy has been aged at 300 and 500 °C for 2-180 min with initial $A_f = 11^\circ\text{C}$. The best-obtained aging temperature is nearly 400 °C because the most precipitation occurs in this temperature and there is a balance was achieved between the driving force and diffusion rate needed for phase transformation. It is found that to obtain a full martensite phase in the lower temperature, the alloy should have a high austenite finish temperature. However, for the temperature <500°C, a higher diffusion rate happens and consequently the time needed for transformation to be ended diminished [8].

Sari et al. [58] studied the effect of aging on a Cu-Al-Ni-Mn SMA in three different temperatures (300, 400 and 500 °C). They realized that some precipitation, including bainite, α , and γ_2 phases, were obtained. The phase transformation temperatures were decreased with increasing time and temperature of aging, while the hardness values were increased. On the other hand, the time of aging can impact on a SMAs characteristic. Shamimi et al. [59] reported that increasing the time of aging in different temperatures increased the forward and reverse phase transformation temperatures.

3.1.2. Quenching

One of the aforementioned phase diagrams is the TTT diagram (temperature-time-transformation) which showed how the time of cooling can affect the obtained phase in the lower temperature. Generally, the time of cooling is taken in a fraction of second, in order to achieve a martensitic microstructure in SMAs. Moreover, the phase transformation from austenite to the martensite phase is a diffusionless phase transformation process, thus the time of cooling should be as short as possible. Fast cooling, or quenching, depends on the medium where a high-temperature SMA in the austenite phase immediately loses a huge amount of heat energy. Two of the important parameters, which should be kept in mind, are the temperature difference and heat capacity of the medium. In this process, the temperature of cooling-medium is supposed to be

constant, therefore its amount should be comparably more than the SMA.

Dagdelen et al. [60] studied some physical properties of Cu-13Al-4.5Ni-1.5Ti (wt. %) SMA, where subjected to heat treatment at 930 °C for 30 min. They used liquid nitrogen, alcohol, and iced-brine mediums that had -196, 0, and 6 °C, respectively. They reported that alcohol and iced brine increased phase transformation temperatures about 100 K. Also, grain boundaries were more identifiable for the alloy in which quenched into the alcohol and iced brine. Likewise, Saud et al. [61] found that the quenched Cu-Al-Ni-Fe SMA into the oil had the best grain refinement because it has a higher cooling rate compared to ice-brined water.

3.2. Changing Compositions

Materials with pure elements have particular properties, which may not be used for all applications, thus alloying with different amounts of other elements can give novel features to the materials. SMAs are also can obtain new characteristics by alloying with different elements [62, 22]. Khalil-Allaf et al. [63] studied the different composition of NiTi alloy. They found that the enthalpy and entropy changes of martensitic transformation, elastic energy, and chemical forces were diminished with increasing Ni content in the SMA. On the other hand, Buytoz et al. [21] reported that enthalpy and entropy changes of NiTi-Hf alloy decreased with increasing Hf content, while PTTs the alloy increased. Also, they found that the alloy with different composition showed different oxidation behavior. Mehrabi et al. [64] added tungsten (W) into nitinol (Ni-Ti) SMA to investigate some physical behavior, such as hardness, through changing the composition. They reported that the hardness of the alloy significantly increased by increasing tungsten content. Zheng et al. [65] alloyed NiTi with Ag for medical investigation. They found that the strength and bacteria adhesion was improved by adding Ag into the NiTi SMA, whereas, the corrosion resistance and cyto-biocompatibility had not been significantly affected.

3.3. Mechanical treatments

The mechanical treatment does not affect the microstructural types in a SMA, but it can grain refinement and, thus, these treatments can influence the SMA characteristics. There are two popular methods of rolling, cold and hot rolling. Sometimes, the rolling process makes some micro-cracks which is one of the disadvantages of the method. It may be followed by annealing at a particular higher temperature. Sharifi et al. [66] studied the effect of cold rolling on an equiatomic-NiTi SMA. Some samples with different thicknesses were produced at room temperature, where the stiffness was increased by reducing the thickness. They realized that the dislocation of the alloys was increased by applying a rolling process. The obtained amorphous alloys were completely crystallized by annealing at 400°C for 1h. The plateau region in the stress-strain test was obtained only for those alloys that annealed after cold rolling.

3.4. Coating

The coating is one of the attractive processes to improve some properties of a SMA, e.g. corrosion resistance and biocompatibility. Hu and colleagues [67] produced an ultrafine grain layer on NiTi SMA consisting of nanocrystallites. They improved the hardness and wear resistance of the alloy by grain refinement of the surface. Furthermore, the coated alloy had lower friction coefficients compared with uncoated coarse grain NiTi alloy. Cheng et al. [68] coated NiTi with biocompatible-Ti. The corrosion resistance obtained by the electrochemical method showed that the alloy achieved an excellent corrosion resistance property due to obtaining a thin oxide film on the NiTi alloy, which is a passivated material. Maleki-Ghaleh et al. [69] electrophoretically deposited hydroxyapatite on a NiTi SMA with various electrical potential differences. The in-vitro study results showed that the samples coated at 60 V had comparably better protection against Ni (toxic element) release into simulated body fluid (SBF).

4. CHARACTERIZATIONS

All aforementioned effective parameters are characterized through some advance types of equipment. The common and important devices includes Differential scanning calorimetry (DSC), thermogravimetry / differential thermal analysis (TG/DTA), x-ray diffraction (XRD), scanning electron microscope (SEM)- energy dispersive x-ray spectroscopy (EDS), metallurgical microscope or optical microscope (OM), Vickers microhardness, and the stress-strain measurements; also, there are different in vitro (or in vivo) studies to investigate the biocompatibility of materials.

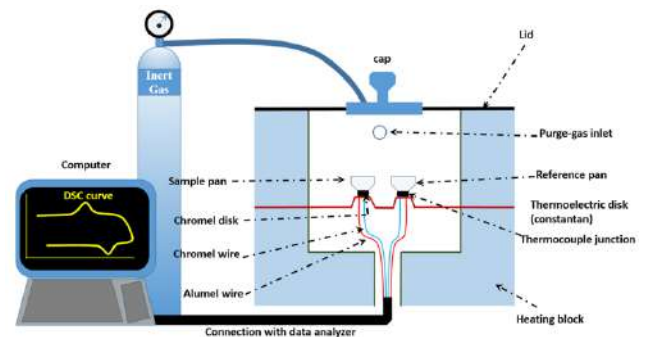


Figure 15 Sketch of a Differential Scanning Calorimetry (DSC) connected with a data analyzer

4.1. Thermal Characteristics

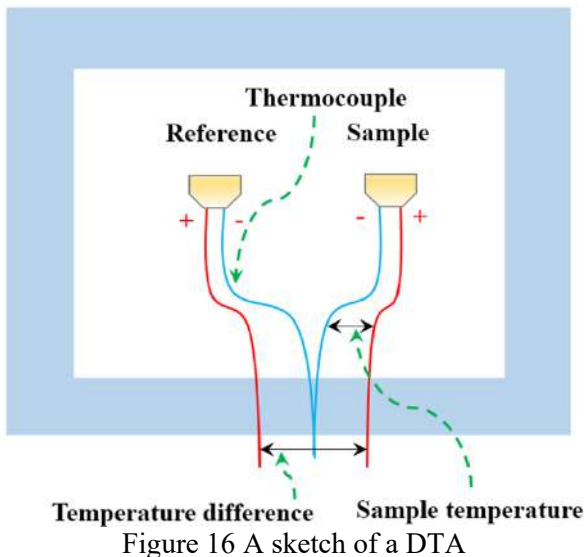
4.1.1. DSC

Differential scanning calorimetry (DSC) is one of the fundamental tests for measuring phase transformation and obtaining some thermodynamics properties of a SMA. Figure 15 shows a sketch of a DSC measuring system with a DSC, inert gas, and a data analyzer (computer). The inert gas flowed into the DSC chamber to minimize the oxidation. There are two unique crucibles put on the sensitive thermocouple. The reference pan is left empty and the specimen is taken inside the Sample pan. The heat flow recorded as a function of temperature, thus and change in heat flow gives information about a physical (or chemical) reaction, which the phase transformation between austenite and martensite is what a researcher is looking for in a SMA. The computer utilizes a special software program to analyze the DSC measurement data. The phase

transformation temperatures and enthalpy changes of the transformation are the main DSC results of a SMA.

4.1.1. TG/DTA

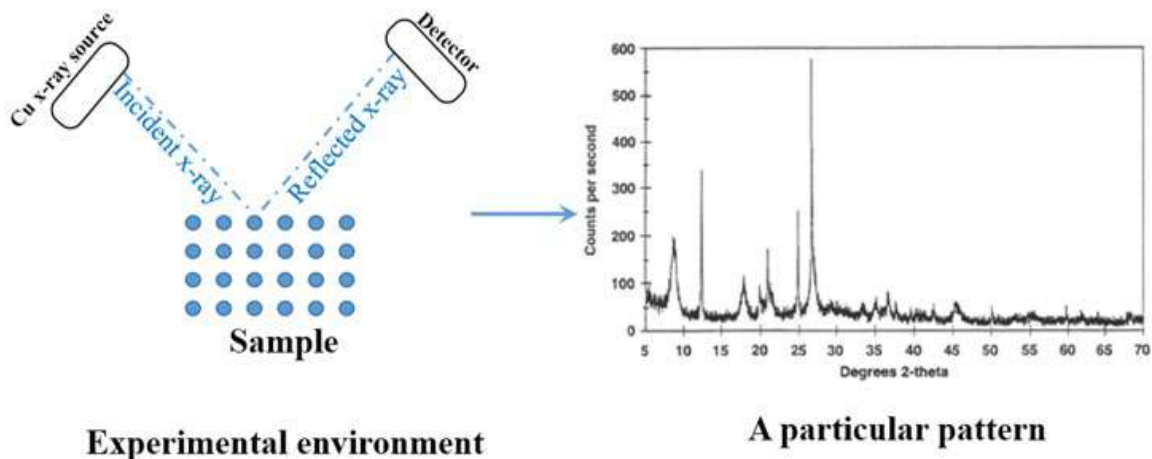
Thermogravimetric/differential thermal analysis (TG/DTA) is another tool that can be used for obtaining some physical properties, such as phase transformation of heating, oxidation, obtaining an oxide layer in an isothermal process. Similar to DSC, TG/DTA device includes two unique crucibles, one for the sample and the other is the reference. Mass gain/loss as a function of temperature and temperature change as a function of time are two important results that can be achieved with this device. The atmosphere can be controlled by injecting inert gas or maybe left naturally. Normally, TG/DTA is used for phase transformation in high temperatures [70].



4.2. Crystal and Microstructural Analysis

4.2.1. XRD

X-ray diffraction is one of the effective techniques that is used by many material Scientists. Basically, an x-ray source is needed which is generally obtained from the first electron transition of the Cu element, known as k_{α} (with a wavelength of 1.5406 Å [21]). The incident x-ray reflects from different atoms. The atoms work as a plan, where the interplanar distance can be found in the XRD result (Figure 17). The wavelength of reflecting x-ray is not changed and the collision between x-ray and atoms is an elastic collision. The diffracted x-rays detected by a special detector and finally, the pattern is analyzed by some calculations so by using some database the obtained peaks can be indexed. Since metals have a crystalline structure, so the pattern consists of peaks, where the angle of detection, wideness, and intensity of the peaks give valuable information about the crystal structure of the material. The XRD is not for a single atom crystal structure, but it can be used for complicated molecules and to find different compounds [71]. Some phases after phase transformation will not completely transformed, such as austenite \leftrightarrow martensite phase, and the DSC results cannot give any information about the residual phases and other precipitations that can influence the physical properties of a SMA.



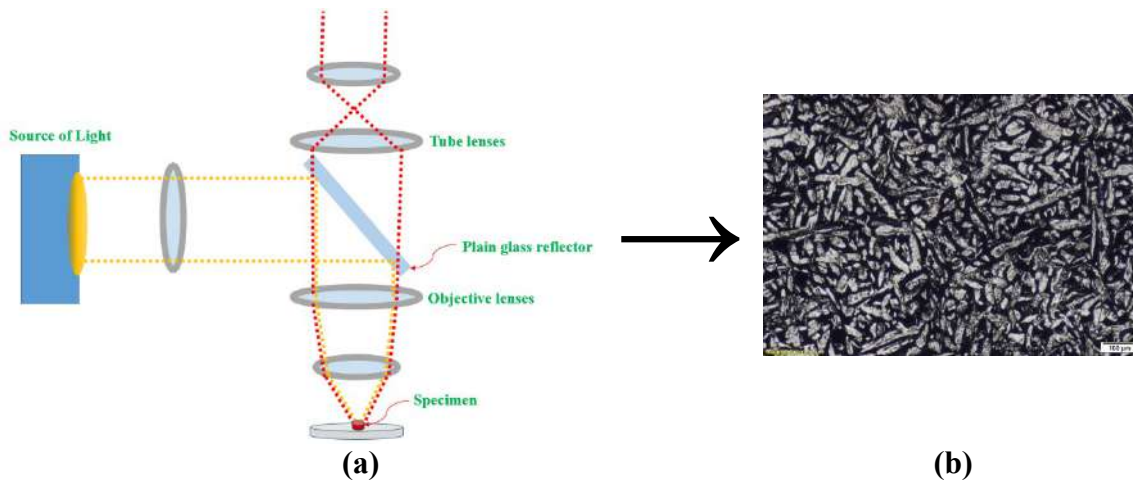


Figure 18 (a) Schematic representation of an optical microscope, (b) a particular CuAlNi-based SMA [72]

4.2.2. Optical Microscope

An optical microscope (OM) is one of the pre-examining microstructures of SMAs. An OM consist of a source of visible light that illuminated on the specimen's surface. The scattered light is collected with objective lenses and partially transmitted through plain glass reflector. A clear image can be achieved with magnification about 1000x.

Figure 18 represents a schematic diagram of an OM and a specific image obtained for a CuAlNi-based SMA. The microstructure can be investigated for the selective range of magnification. However, most professional researchers used to use a scanning electron microscope, which can give more crystal images, moreover using the EDS facility the compositional rate also can be obtained.

4.2.3. SEM-EDS

A scanning electron microscope (SEM) is a type of electron microscope that frequently is used by many researchers. Its magnification is thousands as more as an optical microscope. Electrons are produced by a tungsten filament (electron gun), then the electrons are arranged and accelerated with an anode (has a positive charge). The electrons passing through a magnetic lens and then using a scanning coil the concentrated-high speed-electrons are directed to the different

position of the specimen's surface. A part of electrons are scattered from the surface, which is known as a backscatter electron, and they detected by a detector to obtain an image (SEM image). Another part of the incident electrons can penetrate into the specimens and since they have high energy, so they can kick and eject a core electron. The electrons in the upper energy levels transmitted into the lower energy level that produce an electromagnetic wave (EM). Then the EM is analyzed to obtain the type of elements in the specimens. The concentration of most metallic elements can be determined by energy dispersive x-ray spectroscopy (EDX or EDS) [73-75].

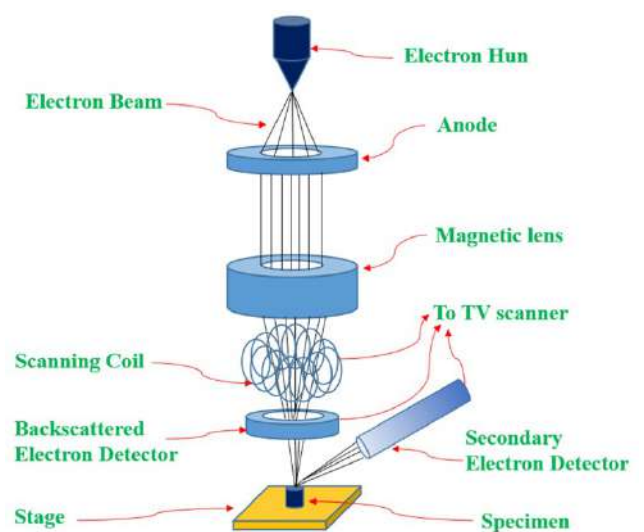


Figure 19 Schematic diagram of a scanning electron microscope

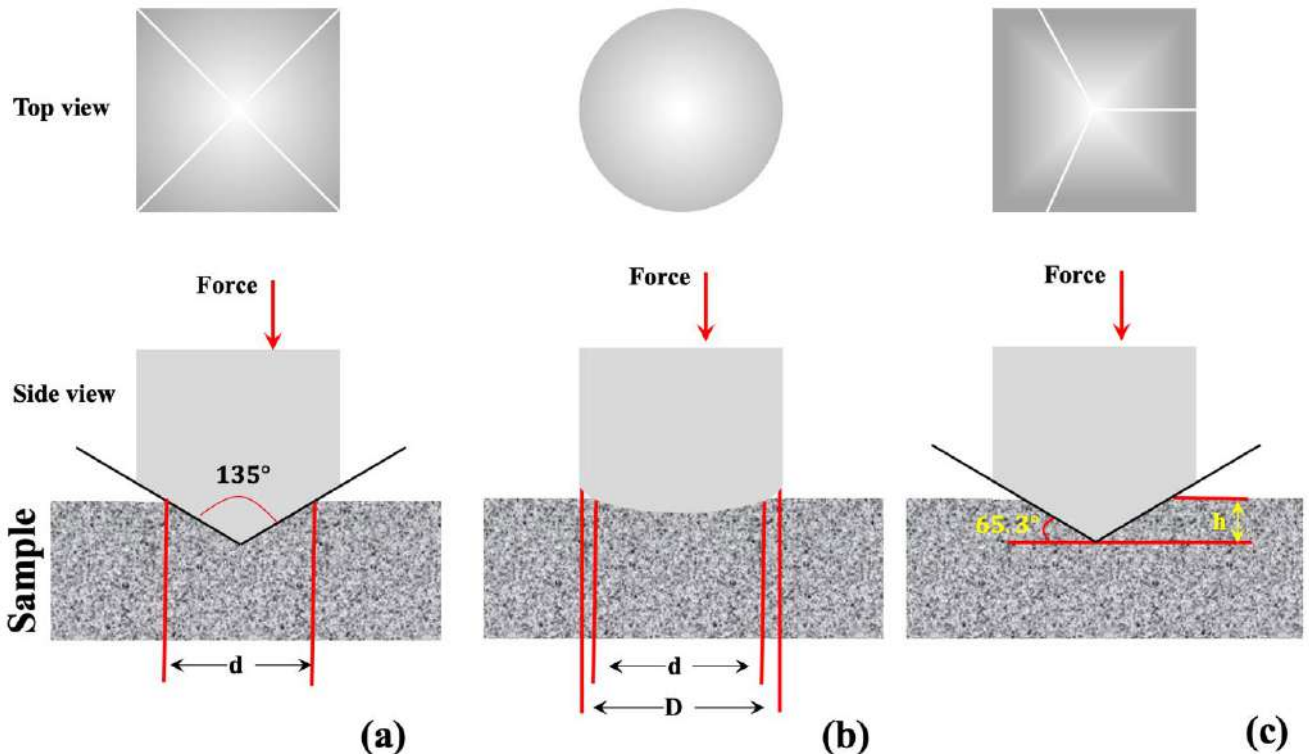


Figure 20 Schematic diagrams of different types of microhardness testing instruments, (a) Vickers microhardness (four-sided pyramid tip), (b) Brinell microhardness (spherical tip) and (c) Nanoindentation (Berkovich tip) [82]

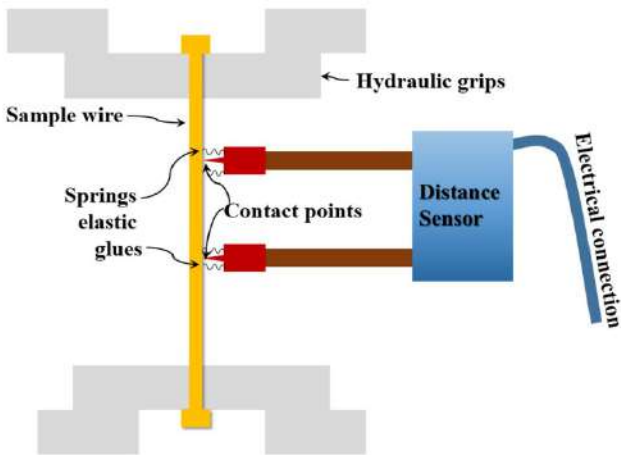


Figure 21 Schematic set-up of tensile testing [83]

4.1. Mechanical testing

4.1.1. Microhardness

There are various types of measurements for testing hardness of a sample, including Vickers hardness (HV), Brinell hardness (HB), Knoop

hardness (HK), Janka hardness, Meyer hardness, Rockwell hardness (HR), Shore durometer hardness, Nanoindentation, and Barcol hardness testing. Figure 20 represents Vickers microhardness, Brinell hardness, and Nanoindentation indentation testing. The aforementioned techniques depend on different indentation and different calculations. There are defined standards for each technique [76-78].

Vickers microhardness is one of popular testing because its calculation does not depend on the size of the indenter. The units of Vickers microhardness are Vickers Pyramid Number (HV) or Diamond Pyramid Hardness (DPH), and sometimes it can be converted to SI unit (Pascal) [79-81].

4.1.2. Tensile test

In this mechanical test, the samples should be prepared in a standard form (Figure 21). When the sample is pulled from its ends it will firstly be

elongated elastically, then it reached yield point. By. On the other hand, the compression test is another popular test for ceramic materials, such as concretes.

Figure 22a and Figure 22b shows the schematic diagram of a stress-strain test for an ordinary metallic material and for a SMA that showed pseudoelasticity. The real experimental data for aluminum and steel (ordinary material) and an approximately equiatomic NiTi SMA is given in Figure 4.8c and Figure 4.8d, respectively. The tensile test gives information about many mechanical properties of materials, such as modulus of elasticity, ductility, stiffness, superelasticity behavior (in SMAs).

4.1. Biocompatible tests

There are several applications of SMAs that need to be biocompatible, thus the SMAs should be checked out some tests, including carcinogenic,

genotoxic, mutagenic, cytotoxic, allergic, and corrosion behavior [84]. For example, corrosion tests can give information about the reactivity of a SMA with different environmental conditions.

The specimens, in the implanted SMAs, should be put inside a simulated body fluid (in-vitro study) or, their behavior can be investigated inside a real medium (in-vivo study). Figure 23 shows a schematic comparison between the in-vitro and in-vivo studies. Since the in-vitro study is easier to control parameters, so it is used more frequently in this research area. Although there are many passive elements that have high biocompatibility, some functional materials are beyond this scope. Therefore material scientists should treat them through some techniques, e.g. coating is one of a practical method to reduce the toxic release into the alive tissues [87-90].

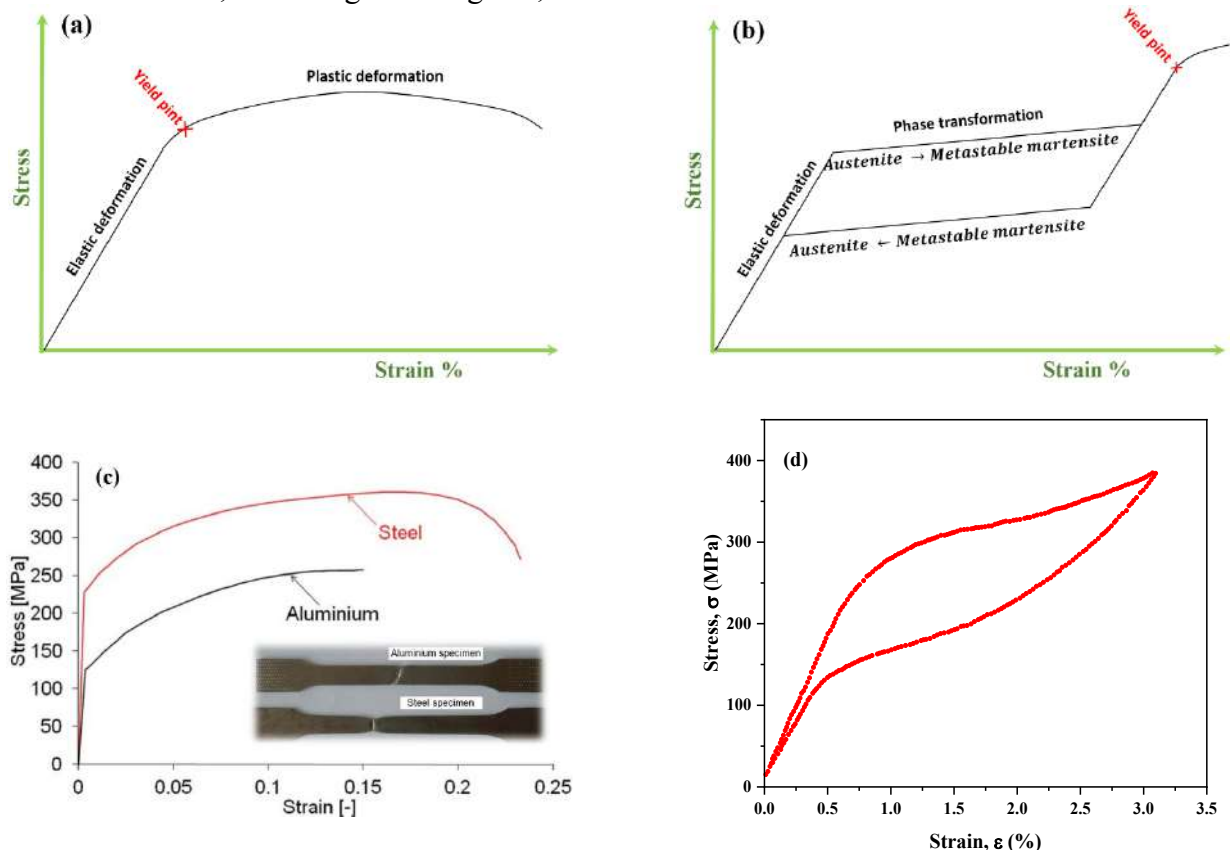


Figure 22 Stress-strain test for (a) an ordinary metallic material and (b) for a SMA. (c) Experimental result for a particular aluminum and steel [85], and hysteretic behavior of Ni₅₁Ti₄₉ (at.%) SMA obtained at 303K [86]

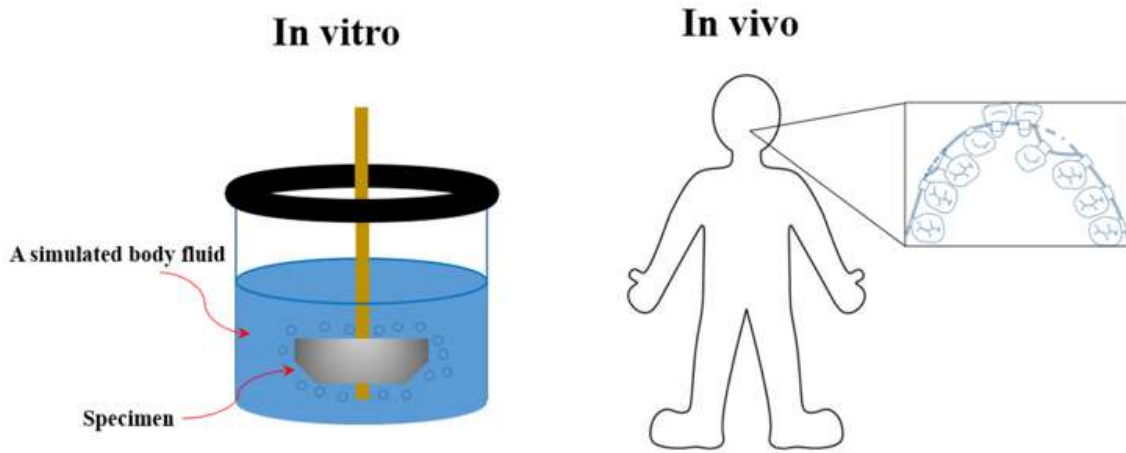


Figure 23 A comparison between in-vitro and in vivo study

5. CONCLUSION

In this review, different shape memory alloys' characteristics were explained. Also, the most extended effective parameters on shape memory alloy were reviewed. In addition, the techniques used for the characterization of SMAs were defined with some related devices. The basics of the device operation were explained through some sketches. This review can open a gate for new researchers, who have not enough information in this field.

Funding

The authors received no financial support for the research, authorship, and/or publication of this paper.

The Declaration of Conflict of Interest/ Common Interest

No conflict of interest or common interest has been declared by the authors.

Authors' Contribution

Conception: INQ-SSA, Design: MK-FD, Supervision: FD-MK, Materials: INQ, Data Collection and/or Processing: INQ-SSA, Analysis and/or Interpretation: INQ-MK-FD Literature Review: SSA, Writer: INQ, Critical Review: INQ-MK-FD-SSA

The Declaration of Ethics Committee Approval

The authors declare that this document does not require an ethics committee approval or any special permission.

The Declaration of Research and Publication Ethics

The authors of the paper declare that they comply with the scientific, ethical and quotation rules of SAUJS in all processes of the paper and that they do not make any falsification on the data collected. In addition, they declare that Sakarya University Journal of Science and its editorial board have no responsibility for any ethical violations that may be encountered, and that this study has not been evaluated in any academic publication environment other than Sakarya University Journal of Science.

REFERENCES

- [1] W. J. Buehler, F. E. Wang, "A summary of recent research on the nitinol alloys and their potential application in ocean engineering," *Ocean Engineering*, vol. 1, no. 1, pp. 105-20, 1968.

- [2] F. J. Zanner, L. A. Bertram, "Vacuum arc remelting: An overview," *STIN*, vol. 86, no., pp. 16417, 1985.
- [3] F. Swinkels, D. Wilkinson, E. Arzt, M. F. Ashby, "Mechanisms of hot-isostatic pressing," vol., no., pp., 1983.
- [4] V. Mamedov, "Spark plasma sintering as advanced PM sintering method," *Powder Metall*, vol. 45, no. 4, pp. 322-8, 2002.
- [5] D. L. Bourell, H. L. Marcus, J. W. Barlow, J. J. Beaman, "Selective laser sintering of metals and ceramics," *International Journal of Powder Metallurgy (Princeton, New Jersey)*, vol. 28, no. 4, pp. 369-81, 1992.
- [6] X. Chen, K. Liu, W. Guo, N. Gangil, A. N. Siddiquee, S. Konovalov, "The fabrication of NiTi shape memory alloy by selective laser melting: a review," *Rapid Prototyping Journal*, vol., no., pp., 2019.
- [7] K. Chang. Chapter 14-Rapid Prototyping. e-Design. Boston: Academic Press; 2015.
- [8] M. H. Elahinia, M. Hashemi, M. Tabesh, S. B. Bhaduri, "Manufacturing and processing of NiTi implants: a review," *Prog Mater Sci*, vol. 57, no. 5, pp. 911-46, 2012.
- [9] J. M. Jani, M. Leary, A. Subic, M. A. Gibson, "A review of shape memory alloy research, applications and opportunities," *Materials & Design (1980-2015)*, vol. 56, no., pp. 1078-113, 2014.
- [10] A. Nespoli, S. Besseghini, S. Pittaccio, E. Villa, S. Viscuso, "The high potential of shape memory alloys in developing miniature mechanical devices: A review on shape memory alloy mini-actuators," *Sensors and Actuators A: Physical*, vol. 158, no. 1, pp. 149-60, 2010.
- [11] C. Cisse, W. Zaki, T. B. Zineb, "A review of modeling techniques for advanced effects in shape memory alloy behavior," *Smart Mater Struct*, vol. 25, no. 10, pp. 103001, 2016.
- [12] M. Follador, M. Cianchetti, A. Arienti, C. Laschi, "A general method for the design and fabrication of shape memory alloy active spring actuators," *Smart Mater Struct*, vol. 21, no. 11, pp. 115029, 2012.
- [13] I. N. Qader, M. Kök, F. Dağdelen, Y. Aydogdu, "A Review of Smart Materials: Researches and Applications," *El-Cezeri Journal of Science and Engineering*, vol. 6, no. 3, pp. 755-88, 2019.
- [14] S. S. Mohammed, K. Mediha, I. N. Qader, F. Dağdelen, "The Developments of piezoelectric Materials and Shape Memory Alloys in Robotic Actuator Systems," *Avrupa Bilim ve Teknoloji Dergisi*, vol., no. 17, pp. 1014-30, 2019.
- [15] K. Otsuka, C. M. Wayman. Shape memory materials. Cambridge university press; 1999.
- [16] M. Niinomi, "Shape memory, superelastic and low Young's modulus alloys," *Biomaterials for Spinal Surgery*. Elsevier; 2012. p. 462-90.
- [17] E. Ercan, F. Dagdelen, I. Qader, "Effect of tantalum contents on transformation temperatures, thermal behaviors and microstructure of CuAlTa HTSMAs," *J Therm Anal Calorim*, vol. 139, no. 1, pp. 29-36, 2020.
- [18] M. Kök, I. N. Qader, S. S. Mohammed, E. ÖNER, F. Dağdelen, Y. Aydogdu, "Thermal Stability and Some Thermodynamics Analysis of Heat Treated Quaternary CuAlNiTa Shape Memory Alloy," *Materials Research Express*, vol. 7, no., pp., 2020.
- [19] E. Acar, M. Kok, I. Qader, "Exploring surface oxidation behavior of NiTi-V alloys," *The European Physical Journal Plus*, vol. 135, no. 1, pp. 58, 2020.
- [20] F. Dagdelen, B. Esra, I. N. Qader, E. Ozen, M. Kok, M. S. Kanca et al., "Influence of the Nb Content on the Microstructure and Phase Transformation Properties of NiTiNb Shape Memory Alloys," *JOM*, vol. 72, no., pp. 1664-72, 2020.
- [21] S. Buytoz, F. Dagdelen, I. Qader, M. Kok, B. Tanyildizi, "Microstructure Analysis and Thermal Characteristics of NiTiHf Shape

- Memory Alloy with Different Composition," *Metals and Materials International*, vol., no., pp. 1-12, 2019.
- [22] M. Kök, H. S. A. Zardawi, I. N. Qader, M. S. Kanca, "The effects of cobalt elements addition on Ti₂Ni phases, thermodynamics parameters, crystal structure and transformation temperature of NiTi shape memory alloys," *The European Physical Journal Plus*, vol. 134, no. 5, pp. 197, 2019.
- [23] F. Dagdelen, M. Kok, I. Qader, "Effects of Ta Content on Thermodynamic Properties and Transformation Temperatures of Shape Memory NiTi Alloy," *Metals and Materials International*, vol., no., pp. 1420–7, 2019.
- [24] F. Dagdelen, M. A. K. Aldalawi, M. Kok, I. N. Qader, "Influence of Ni addition and heat treatment on phase transformation temperatures and microstructures of a ternary CuAlCr alloy," *The European Physical Journal Plus*, vol. 134, no. 2, pp. 66, 2019.
- [25] I. N. Qader, M. Kök, F. Dağdelen, "Effect of heat treatment on thermodynamics parameters, crystal and microstructure of (Cu-Al-Ni-Hf) shape memory alloy," *Physica B: Condensed Matter*, vol. 553, no., pp. 1-5, 2019.
- [26] M. Kok, A. O. A. Al-Jaf, Z. D. Çirak, I. N. Qader, E. Özen, "Effects of heat treatment temperatures on phase transformation, thermodynamical parameters, crystal microstructure, and electrical resistivity of NiTiV shape memory alloy," *J Therm Anal Calorim*, vol., no., pp., 2019.
- [27] I. N. Qader, M. Kok, Z. D. Çirak, "The effects of substituting Sn for Ni on the thermal and some other characteristics of NiTiSn shape memory alloys," *J Therm Anal Calorim*, vol., no., pp., 2020.
- [28] I. N. Qader, E. Ercan, B. A. M. Faraj, M. Kok, F. Dagdelen, Y. Aydogdu, "The Influence of Time-Dependent Aging Process on the Thermodynamic Parameters and Microstructures of Quaternary Cu₇₉–Al₁₂–Ni₄–Nb₅ (wt%) Shape Memory Alloy," *Iranian Journal of Science and Technology, Transactions A: Science*, vol., no., pp., 2020.
- [29] S. S. Mohammed, M. Kok, I. N. Qader, M. S. Kanca, E. Ercan, F. Dagdelen et al., "Influence of Ta Additive into Cu₈₄–xAl₁₃Ni₃ (wt%) Shape Memory Alloy Produced by Induction Melting," *Iranian Journal of Science and Technology, Transactions A: Science*, vol., no., pp., 2020.
- [30] W. J. Buehler, J. Gilfrich, R. Wiley, "Effect of low-temperature phase changes on the mechanical properties of alloys near composition TiNi," *J Appl Phys*, vol. 34, no. 5, pp. 1475-7, 1963.
- [31] T. Fukuda, T. Kawamura, T. Kakeshita, "Time-temperature-transformation diagram for the martensitic transformation in a titanium-nickel shape memory alloy," *J Alloys Compd*, vol. 683, no., pp. 481-4, 2016.
- [32] S. N. S. Al-Humairi, "Cu-Based Shape Memory Alloys: Modified Structures and Their Related Properties," *Recent Advances in Engineering Materials and Metallurgy*. IntechOpen; 2019.
- [33] M. Mehrpouya, "Laser welding of NiTi shape memory sheets: experimental analysis and numerical modeling," *Department of Mechanical and Aerospace Engineering, Sapienza University of Rome*, vol., no., pp. 134, 2017.
- [34] A. Ibarra, J. San Juan, E. Bocanegra, M. Nó, "Thermo-mechanical characterization of Cu–Al–Ni shape memory alloys elaborated by powder metallurgy," *Materials Science and Engineering: A*, vol. 438, no., pp. 782-6, 2006.
- [35] E. Acar, M. Çalışkan, H. E. Karaca, "Differential scanning calorimetry response of aged NiTiHfPd shape memory alloys," *Appl Phys A*, vol. 125, no. 4, pp. 239, 2019.
- [36] C. H. Gonzalez, C. A. d. N. Oliveira, E. A. C. d. Pina, S. L. Urtiga Filho, O. O. d. Araújo Filho, C. J. d. Araújo, "Heat treatments and thermomechanical cycling influences on the R-phase in Ti-Ni shape

- memory alloys," *Materials Research*, vol. 13, no. 3, pp. 325-31, 2010.
- [37] T. Tadaki, Y. Nakata, K. i. Shimizu, "Thermal cycling effects in an aged Ni-rich Ti–Ni shape memory alloy," *Transactions of the Japan institute of metals*, vol. 28, no. 11, pp. 883-90, 1987.
- [38] A. Ahadi, E. Rezaei, "Microstructure and phase transformation behavior of a stress-assisted heat-treated Ti-rich NiTi shape memory alloy," *J Mater Eng Perform*, vol. 21, no. 8, pp. 1806-12, 2012.
- [39] W. D. Callister, "An introduction to materials science and engineering," John Wiley and Sons Inc, vol., no., pp., 2007.
- [40] Y. Sun, F. Jiang, H. Zhang, J. Su, W. Yuan, "Residual stress relief in Al–Zn–Mg–Cu alloy by a new multistage interrupted artificial aging treatment," *Materials & Design*, vol. 92, no., pp. 281-7, 2016.
- [41] P. Dong, S. Song, J. Zhang, "Analysis of residual stress relief mechanisms in post-weld heat treatment," *International Journal of Pressure Vessels and Piping*, vol. 122, no., pp. 6-14, 2014.
- [42] J. Uchil, K. Mahesh, K. G. Kumara, "Electrical resistivity and strain recovery studies on the effect of thermal cycling under constant stress on R-phase in NiTi shape memory alloy," *Physica B: Condensed Matter*, vol. 324, no. 1-4, pp. 419-28, 2002.
- [43] K. Wada, Y. Liu, "Shape recovery of NiTi shape memory alloy under various pre-strain and constraint conditions," *Smart Mater Struct*, vol. 14, no. 5, pp. S273, 2005.
- [44] D. Song, G. Kang, Q. Kan, C. Yu, C. Zhang, "The effect of martensite plasticity on the cyclic deformation of super-elastic NiTi shape memory alloy," *Smart Mater Struct*, vol. 23, no. 1, pp. 015008, 2013.
- [45] M. S. Alam, M. A. Youssef, M. L. Nehdi, "Exploratory investigation on mechanical anchors for connecting SMA bars to steel or FRP bars," *Mater Struct*, vol. 43, no. 1, pp. 91-107, 2010.
- [46] R. DesRoches, J. McCormick, M. Delemont, "Cyclic properties of superelastic shape memory alloy wires and bars," *Journal of Structural Engineering*, vol. 130, no. 1, pp. 38-46, 2004.
- [47] B. Bertheville, J.-E. Bidaux, "Alternative powder metallurgical processing of Ti-rich NiTi shape-memory alloys," *Scripta Mater*, vol. 52, no. 6, pp. 507-12, 2005.
- [48] H. Jiang, S. Cao, C. Ke, X. Ma, X. Zhang, "Fine-grained bulk NiTi shape memory alloy fabricated by rapid solidification process and its mechanical properties and damping performance," *Journal of Materials Science & Technology*, vol. 29, no. 9, pp. 855-62, 2013.
- [49] E. M. Sharifi, A. Kermanpur, F. Karimzadeh, A. Esmaili, "Formation of the nanocrystalline structure in an equiatomic NiTi shape-memory alloy by thermomechanical processing," *J Mater Eng Perform*, vol. 23, no. 4, pp. 1408-14, 2014.
- [50] L. Petrini, F. Migliavacca, "Biomedical applications of shape memory alloys," *Journal of Metallurgy*, vol. 2011, no., pp., 2011.
- [51] S. Miyazaki, R. Sachdeva, "Shape memory effect and superelasticity in Ti—Ni alloys," *Shape memory alloys for biomedical applications*. Elsevier; 2009. p. 3-19.
- [52] D. Stoeckel, T. Waram, editors. *Use of Ni-Ti shape memory alloys for thermal sensor-actuators. Active and adaptive optical components*; 1992: International Society for Optics and Photonics.
- [53] D. Pitt, J. Dunne, E. White, E. Garcia, editors. *SAMPSON smart inlet SMA powered adaptive lip design and static test*. 19th AIAA Applied Aerodynamics Conference; 2001.
- [54] D. M. Pitt, J. P. Dunne, E. V. White, editors. *SAMPSON smart inlet design overview and wind tunnel test: Part I: design overview*. *Smart Structures and Materials 2002: Industrial and Commercial Applications of Smart Structures*

- Technologies; 2002: International Society for Optics and Photonics.
- [55] J. Mabe, F. Calkins, G. Butler, editors. Boeing's variable geometry chevron, morphing aerostructure for jet noise reduction. 47th AIAA/ASME/ASCE/AHS/ASC Structures, Structural Dynamics, and Materials Conference 14th AIAA/ASME/AHS Adaptive Structures Conference 7th; 2006.
- [56] D. J. Arbogast, R. T. Ruggeri, R. C. Bussom, editors. Development of a 1/4-scale NiTiNol actuator for reconfigurable structures. Industrial and Commercial Applications of Smart Structures Technologies 2008; 2008: International Society for Optics and Photonics.
- [57] A. R. Pelton, J. Dicello, S. Miyazaki, "Optimisation of processing and properties of medical grade Nitinol wire," *Minim Invasive Ther Allied Technol*, vol. 9, no. 2, pp. 107-18, 2000.
- [58] U. Sari, T. Kirindi, F. Ozcan, M. Dikici, "Effects of aging on the microstructure of a Cu-Al-Ni-Mn shape memory alloy," *International Journal of Minerals, Metallurgy, and Materials*, vol. 18, no. 4, pp. 430, 2011.
- [59] A. Shamimi, B. Amin-Ahmadi, A. Stebner, T. Duerig, "The effect of low temperature aging and the evolution of R-phase in Ni-rich NiTi," *Shape Memory and Superelasticity*, vol. 4, no. 4, pp. 417-27, 2018.
- [60] F. Dagdelen, M. Kanca, M. Kok, "Effects of Different Quenching Treatments on Thermal Properties and Microstructure in Quaternary Cu-Based HTSMA," *Physics of Metals and Metallography*, vol. 120, no. 13, pp. 1378-83, 2019.
- [61] S. N. Saud, E. Hamzah, T. Abubakar, S. Farahany, "Structure-property relationship of Cu-Al-Ni-Fe shape memory alloys in different quenching media," *J Mater Eng Perform*, vol. 23, no. 1, pp. 255-61, 2014.
- [62] C. Tatar, R. Acar, I. N. Qader, "Investigation of thermodynamic and microstructural characteristics of NiTiCu shape memory alloys produced by arc-melting method," *The European Physical Journal Plus*, vol. 135, no., pp. 311, 2020.
- [63] J. Khalil-Allafi, B. Amin-Ahmadi, "The effect of chemical composition on enthalpy and entropy changes of martensitic transformations in binary NiTi shape memory alloys," *J Alloys Compd*, vol. 487, no. 1-2, pp. 363-6, 2009.
- [64] K. Mehrabi, H. Bahmanpour, A. Shokuhfar, A. Kneissl, "Influence of chemical composition and manufacturing conditions on properties of NiTi shape memory alloys," *Materials Science and Engineering: A*, vol. 481, no., pp. 693-6, 2008.
- [65] Y. Zheng, B. Zhang, B. Wang, Y. Wang, L. Li, Q. Yang et al., "Introduction of antibacterial function into biomedical TiNi shape memory alloy by the addition of element Ag," *Acta biomaterialia*, vol. 7, no. 6, pp. 2758-67, 2011.
- [66] E. M. Sharifi, F. Karimzadeh, A. Kermanpur, "The effect of cold rolling and annealing on microstructure and tensile properties of the nanostructured Ni₅₀Ti₅₀ shape memory alloy," *Materials Science and Engineering: A*, vol. 607, no., pp. 33-7, 2014.
- [67] T. Hu, C. Wen, G. Sun, S. Wu, C. Chu, Z. Wu et al., "Wear resistance of NiTi alloy after surface mechanical attrition treatment," *Surf Coat Technol*, vol. 205, no. 2, pp. 506-10, 2010.
- [68] Y. Cheng, W. Cai, H. Li, Y. Zheng, L. Zhao, "Surface characteristics and corrosion resistance properties of TiNi shape memory alloy coated with Ta," *Surf Coat Technol*, vol. 186, no. 3, pp. 346-52, 2004.
- [69] H. Maleki-Ghaleh, V. Khalili, J. Khalil-Allafi, M. Javidi, "Hydroxyapatite coating on NiTi shape memory alloy by electrophoretic deposition process," *Surf Coat Technol*, vol. 208, no., pp. 57-63, 2012.
- [70] M. E. Brown, P. K. Gallagher. *Handbook of thermal analysis and calorimetry: recent*

- advances, techniques and applications. Elsevier; 2011.
- [71] T. Sattar, T. Manzoor, F. A. Khalid, M. Akmal, G. Saeed, "Improved in vitro bioactivity and electrochemical behavior of hydroxyapatite-coated NiTi shape memory alloy," *Journal of materials science*, vol. 54, no. 9, pp. 7300-6, 2019.
- [72] K. K. Alaneme, E. A. Okotete, N. Maledi, "Phase characterisation and mechanical behaviour of Fe-B modified Cu-Zn-Al shape memory alloys," *Journal of materials research and technology*, vol. 6, no. 2, pp. 136-46, 2017.
- [73] S. Green, D. Grant, N. Kelly, "Powder metallurgical processing of Ni-Ti shape memory alloy," *Powder Metall*, vol. 40, no. 1, pp. 43-7, 1997.
- [74] X. Wang, Y. Bellouard, J. Vlassak, "Laser annealing of amorphous NiTi shape memory alloy thin films to locally induce shape memory properties," *Acta Mater*, vol. 53, no. 18, pp. 4955-61, 2005.
- [75] F. Dagdelen, E. Ercan, "The surface oxidation behavior of Ni-45.16% Ti shape memory alloys at different temperatures," *J Therm Anal Calorim*, vol. 115, no. 1, pp. 561-5, 2014.
- [76] K. Herrmann. *Hardness testing: principles and applications*. ASM international; 2011.
- [77] H. Chandler. *Hardness testing*. ASM international; 1999.
- [78] W. F. Gale, T. C. Totemeier. *Smithells metals reference book*. Elsevier; 2003.
- [79] Y. Uematsu, T. Kakiuchi, Y. Tozaki, editors. *Fatigue behavior of dissimilar friction stir spot welds between A6061 and AZ31 fabricated by a scroll grooved tool without probe*. Proceedings of the 1st International Joint Symposium on Joining and Welding; 2013: Elsevier.
- [80] M. Mathew, K. Shenoy, K. Ravishankar, "Vickers hardness and specific wear rate of poly propylene reinforced PMMA," *International journal of scientific study*, vol. 2, no. 3, pp. 71-5, 2014.
- [81] H. Wu, S. Wen, K. Gao, H. Huang, W. Wang, Z. Nie, "Effect of Er additions on the precipitation strengthening of Al-Hf alloys," *Scripta Mater*, vol. 87, no., pp. 5-8, 2014.
- [82] M. Z. Yahaya, A. A. Mohamad, "Hardness testing of lead-free solders: a review," *Soldering & Surface Mount Technology*, vol., no., pp., 2017.
- [83] A. Michael, Y. Zhou, M. Khan, "Novel method to analyse tensile properties of ultra-fine NiTi wires with a visual extensometer," *Mater Lett*, vol. 182, no., pp. 177-80, 2016.
- [84] A. Biesiekierski, J. Wang, M. A.-H. Gepreel, C. Wen, "A new look at biomedical Ti-based shape memory alloys," *Acta biomaterialia*, vol. 8, no. 5, pp. 1661-9, 2012.
- [85] B. Liu, R. Villavicencio, C. G. Soares, "Failure characteristics of strength-equivalent aluminium and steel plates in impact conditions," *Analysis and Design of Marine Structures*, vol., no., pp. 167, 2013.
- [86] C. Maletta, A. Falvo, F. Furgiuele, J. Reddy, "A phenomenological model for superelasticity in NiTi alloys," *Smart Mater Struct*, vol. 18, no. 2, pp. 025005, 2009.
- [87] Q. Li, Y.-Y. Xia, J.-C. Tang, R.-Y. Wang, C.-Y. Bei, Y. Zeng, "In vitro and in vivo biocompatibility investigation of diamond-like carbon coated nickel-titanium shape memory alloy," *Artificial Cells, Blood Substitutes, and Biotechnology*, vol. 39, no. 3, pp. 137-42, 2011.
- [88] S. Jin, Y. Zhang, Q. Wang, D. Zhang, S. Zhang, "Influence of TiN coating on the biocompatibility of medical NiTi alloy," *Colloids and Surfaces B: Biointerfaces*, vol. 101, no., pp. 343-9, 2013.
- [89] P. Dong, W. Hao, X. Wang, T. Wang, "Fabrication and biocompatibility of polyethyleneimine/heparin self-assembly coating on NiTi alloy," *Thin Solid Films*, vol. 516, no. 16, pp. 5168-71, 2008.

- [90] T. Sun, L.-P. Wang, M. Wang, H.-W. Tong, W. W. Lu, "PIIID-formed (Ti, O)/Ti,(Ti, N)/Ti and (Ti, O, N)/Ti coatings on NiTi shape memory alloy for medical applications," *Materials Science and Engineering: C*, vol. 32, no. 6, pp. 1469-79, 2012.

JOURNAL OF SCIENCE



SAKARYA UNIVERSITY

Sakarya University Journal of Science

ISSN 1301-4048 | e-ISSN 2147-835X | Period Bimonthly | Founded: 1997 | Publisher Sakarya University |
<http://www.saujs.sakarya.edu.tr/en/>

Title: Sustainable Maintenance Strategy for Wood Windows Defects

Authors: Özlem EREN, Emine Merve OKUMUŞ

Received: 2020-02-11 12:27:49

Accepted: 2020-07-05 12:43:00

Article Type: Research Article

Volume: 24

Issue: 5

Month: October

Year: 2020

Pages: 914-935

How to cite

Özlem EREN, Emine Merve OKUMUŞ; (2020), Sustainable Maintenance Strategy for Wood Windows Defects. Sakarya University Journal of Science, 24(5), 914-935,

DOI: <https://doi.org/10.16984/saufenbilder.687722>

Access link

<http://www.saujs.sakarya.edu.tr/en/pub/issue/56422/687722>

New submission to SAUJS

<http://dergipark.org.tr/en/journal/1115/submission/step/manuscript/new>



Sustainable Maintenance Strategy for Wood Windows Defects

Özlem EREN^{*1}, Emine Merve OKUMUŞ²

Abstract

Regular maintenance and repair of window systems in the existing building stock provide both resource and energy savings. While planning the maintenance strategy of window systems that offer benefit in terms of two different aspects, first of all, the possible damage types should be known. Then, what is the damage to the scope of this study? The question was investigated, and the causes and types of defects in the wooden windows were listed. The proposed maintenance planning method is based on 5 tools. The tools that can be used for maintenance planning are listed in the literature. First, the defect levels of the wood windows were specified and then the AHP method was used to select among the alternative maintenance according to the severity of the defect. The study was planned according to the 6 Sigma tool. Firstly, the causes of the defects were investigated and then these defects were evaluated by assigning numbers to each defect by experts. Finally, the AHP method was used to select the right alternative among proposed maintenance alternatives according to the level of defects. By using this simple method while choosing the window maintenance strategy according to the demands, wrong decision-making will be prevented.

Keywords: maintenance, wood window, defect

* Corresponding Author: ozlem.eren@msgsu.edu.tr

¹ Mimar Sinan Fine Arts University, Department of Architecture, Istanbul, Turkey.
ORCID: <https://orcid.org/0000-0002-7675-6483>

² Fatih Sultan Mehmet Vakıf University, Department of Architecture and Design, , Istanbul, Turkey.
ORCID: <https://orcid.org/0000-0003-2899-6631>

1. INTRODUCTION

Defects in window systems can be diagnosed not only by complex tools, tests, etc. but also by observation-based inspections with simple-to-use hand tools. The accuracy of this method can be proved by different research tools. According to the results, the defects can be rehabilitated with maintenance actions that will increase the comfort of the user and meet the expectations, and the possible damages can be prevented or postponed. The questions asked in this study were as follows: Are the defects in the components of the window systems related to each other? What are the most common defects in wooden window systems? At what stages were they occur?

Windows are exposed to deterioration from the date they are built. However, the sustainability of building conditions is the main purpose of providing services to the users [1, 2]. Windows are openings on the building facade that have to meet multiple performance requirements. The window provides natural light and ventilation while protecting the inside from outside conditions. The window system is constantly exposed to both climatic influences and daily use that accelerates deterioration, leading to premature damage that affects the window's durability, appearance, and value. Therefore, it is necessary to classify damages to diagnose anomalies correctly and find the appropriate solution [3]. Appropriate maintenance should be performed to control irreversible defects in window systems and to extend the physical life of the building [2].

The method was applied to the historical education building. Defects have been detected in the windows of the building by observation-based and non-destructive inspection methods, and the detected damages have been matched with the maintenance recommendations corresponding to the defects in the previously created database.

2. DEFECTS AND MAINTENANCE METHODS IN WOOD WINDOW SYSTEMS

In the building sector, there are words with different meanings that are thought to have the same meaning concerning building defects. It is necessary to know the equivalents of these words in defining the problem well. The words which are thought to have the same meaning in the literature but they are different as follows:

- “Error” wrong human action - wrong choice or decision,
- “Fault”, an element fails to perform the intended action,
- “Defect”, in which one or more elements are not performing”,
- “Snag ”, obstacle,
- “Anomaly”, Probable defect that is anomaly-directly visible or measurable,
- “Degradation”, something is destroyed
- “Damage”-It is defined by the words deterioration expressed in terms of cost.

Atkinson (1987) has made a very clear definition of differentiating defects from failure. Failure means formations that may or may not be corrected before the building is delivered, on the other hand, the defect is the decrease in performance after the building is started to be used [27,4]. While error and failure terms are very close to each other due to their meaning, the error is usually related to human movements while defect occurs in elements [4]. According to Flores and Brito (2010), maintenance rehabilitations are actions taken during operation of a building to secure minimum performance levels without any deterioration of the elements of the building and to maintain the commercial value of the building and ensure sustainability [5, 6, 9].

2.1. Defects in Wooden Systems

Degradation of wood materials occurs in the form of mold, blight, cavity formation, breakage, cracking and so on since microorganisms and pests live within these materials. Components made with wooden material that is susceptible to such degradation due to the damp internal structure may deteriorate very quickly and become irreparable if necessary, precautions are not taken according to the places where they are used. It is possible to extend the service life by regular maintenance of the window systems made of wood materials that are directly exposed to external climatic conditions.

Defects occur in windows due to the following reasons [11],

- Incorrect design
- Incorrect construction
- Improper maintenance
- Faulty material
- Improper use
- Lack of information
- Poor communication

The reasons for the transition of windows from performing to the non-performing condition must be identified. Degradation may not be attributed to only one reason. Natural degradation begins with the aging of materials and components/elements. On the other hand, failures depend on design or construction. The degradation process takes time to evolve, and the performance of the components does not immediately pass from to another. This is crucial for the planning of preventive maintenance strategies. Degradations often occur before the final damage/defect occurs [28]. The type or severity of the defect affects the performance of the construction components. Most condition assessment methods classify the defect type of different building components as unimportant, important and critical. Critical defects significantly affect the function of the structural component. Serious defects show symptoms by causing deterioration in performance. The intensity of defects has a strong impact on the condition of the building components. Straub

(2014), prepared a table that lists the defects threaten the function in the windows by referring to Damen et al. [12], [10]. (Table 1-2)

Table 1. Classification of defects in windows (Developed from [10])

Critical defects	Serious defects	Minor defects
Distortion and leakage,	Aging of sealing materials	Deterioration of surface finishes
Frame breakage and cracking,	Wear of gaskets	Discoloration-fading
Mushroom formation	Loss of protective layer	Color change on glass surface
Cracking	Having mist on double glazing units	Pollution
Insect Attack	Moisture retention of window frames	
Track loss	Partial spaces	
Strain	Water leakage	
Rupture	Corrosion on fasteners	
	Degradation in fasteners	

2.2. Methods Used in Diagnosis of Defects

Please be sure to check your document for spelling and grammar before submitting it electronically. Observation-based, simple instruments and more complex instruments are used to diagnose degradation in window systems. According to Masters (1985), what should be known in the estimation of service life are as follows [13, 14].

- A systematic approach to treating/solving the problem,
- In-service performance of the material,
- Knowledge about environmental factors causing degradation,
- Knowledge of mathematical models that define material behaviors with specific applications and environment,
- Number of factors causing degradation,
- Geographical location and the importance of factors changing with the available material,

Knowledge of the range of factors needed for the development of test methods to estimate the service life.

Table 2. Classification of defects in wooden frames (Developed from [3])

DEFECTS GROUP	DEFECTS NAME
A-DEFECTS IN DESIGN	A1-Wrong window type selection
	A2-Failure to place the casing in the right place (inside, center, outside)
	A3-Unprotected window (eaves etc.)
	A4-Faulty design of sills
	A5-Lack of water drainage system / failure
	A6-Overlap number is not selected correctly
	A7-Incorrect section selection
	A8-Missing connection due to through-opening
	A9-Inadequate selection of fittings
	A10-Not selecting the appropriate glass type / thickness
	A11-Designing / detailing the wrong water discharge system
	A12-Designing / detailing the wrong window sill
	A13-Insufficient number of fasteners during design
	A14-No incorrect design / ventilation elements
	A15-Failure support design
	A16- Incorrect selection of frame section and sash
	A17- Incorrect selection of frame profiles
	A18-Excessive frame angle (deflection problem)
	A19-Failure sealing material selection
B-DEFECTS IN CONSTRUCTION	B1.Faulty fixing of the case to the wall
	B2-Improper insulation of the casing and wall
	B3-Incorrect detection of the sash to the frame
	B4-Incorrect detection of sealing elements
	B5-Incorrect fixation of glass strip
	B6-Incorrect application of water drainage system
	B7-Poor workmanship
	B8-Use of inexperienced or inadequately qualified workforce
	B9-Use of inadequate, poor quality and / or non-approved materials
	B10-Fixation with missing fasteners
C-DEFECTS IN USE	C1-Number of users
	C2-Poor maintenance
	C3-Incorrect using of mobile parts
	C4-Improper use of the closing mechanism
	C5-Lack of maintenance

2.3. Methods Used in Diagnosis of Defects

Please be sure to check your document for spelling and grammar before submitting it electronically. Observation-based, simple instruments and more complex instruments are used to diagnose degradation in window systems. According to Masters (1985), what should be known in the estimation of service life are as follows [13, 14].

- A systematic approach to treating/solving the problem,
- In-service performance of the material,
- Knowledge about environmental factors causing degradation,
- Knowledge of mathematical models that define material behaviors with specific applications and environment,
- Number of factors causing degradation,
- Geographical location and the importance of factors changing with the available material,
- Knowledge of the range of factors needed for the development of test methods to estimate the service life.

Visual inspection of degradation of the windows (Table 3) can be carried out with simple on-site measurements (thermographic instruments). The complex process of deterioration in windows occurs due to several factors. Understanding the pathological methods and knowing these factors are important for controlling the appropriate maintenance method [15]. In this study, defects in wood window systems were determined based on observation.

Table 3. Diagnostic Method

Table 3. Diagnostic Method	
Based on Observation	Crack and gap sizes
	Angle measurement
	Alignment

2.4. Maintenance Methods

When the necessary precautions are taken against the defects that occurred or may occur in the window systems, the expected performance level of the window can be kept at the desired

level. To achieve this, it is necessary to plan the process well and to plan maintenance with a systematic approach. The consequences of an inefficient maintenance policy go far beyond the cost of maintenance [5, 8]. In the literature, maintenance methods are widely examined in three stages.

1. *Predictive maintenance*: this type of maintenance is suitable for elements whose performance and condition can be observable. Inspections are planned and the maintenance actions are performed according to the inspection results under the degradation conditions of the element. Predictive strategies are based on a large number of technical and statistical knowledge of the building element's behavior [7].

2. *Preventive maintenance*: is performed at predetermined intervals to prevent defects. Preventive maintenance planning requires extensive knowledge of service time, service performance, deterioration models, effective maintenance operations and costs for each staff member [15].

3. *Corrective maintenance*: In cases where the effect of the fault is very small, corrective maintenance is applied. According to corrective maintenance, inconvenience caused by unplanned errors can be solved with very small costs [15].

4. *Time-based maintenance*: after the 2000s, there has been a transition to state-based maintenance [7].

3. METHODOLOGY OF THE STUDY

The research aims to determine the causes of defects in the wooden window systems of the existing structures and to select the most appropriate maintenance alternative for these defects according to the demands of the user. For this purpose, extensive literature review and standards and regulations were examined. The possible defect types and diagnostic methods that can be encountered by these investigations have been determined, and then maintenance alternatives have been listed. In the methodology

of the study, the problem will be solved by using 4 steps with 5 tools (Table 4,5; Figure 1). In this study, to have multiple criteria affecting the deterioration of the window system, Multi-Criteria Decision-Making Methods (MCDMM) were investigated. The study was structured based on the 4 Stages of the 6 Sigma (Table 4) research method. The method consists of identification, measurement, analysis, improvement, and control. The control phase could not be performed in the study. Because the proposed maintenance and repair proposal has not been implemented but remained as a proposal.

Data is collected and recorded in the control list based on the observation of the expert diagnosing the defects in the windows.

The expert must have all the necessary information, such as the location of the building, the year of construction, the functional characteristics, the previous maintenance of the window. All this information should be stored in a standard database [15]. The following steps were followed according to 6 Sigma Research Method.

3.1. Description

In this stage defects in window systems are explained. Root causes of defects are tried to be determined by using cause-effect analysis in determining the defects in the windows. The path to be followed is determined by the workflow chart (Figure 1).

3.2. Measurement

The expert records the current status of the structure and the window as well as the historical information in the template specified in Table 6. The status of the window is determined by this table which we will call as a checklist. The aesthetic and physical damage levels of the window systems divided into 5 sections in the checklists are graded between 1-5. In this way, the damage that can be corrected, monitored and/or done can be determined. The process continues by following the workflow chart. In

the second stage, the damage is scored for prioritization. In the third stage, the procedure is completed by selecting the appropriate maintenance from the archive of the previously created maintenance proposals by the AHP method.

3.3. Analysis Stage

The reason for the same defect types in the window systems is investigated. The matrix in Tables 7 and 8 and the checklist in Table 6 will be filled according to where the aesthetic and physical defects occur, the reasons for their occurrence and the stages. Knowing the causes of damages is important in terms of protecting the window, not making the same failure again and making maintenance planning by taking these reasons into consideration.

3.4. Improvement Stage

The maintenance plan is applied according to the score obtained for the selected window. After inspection, the criteria for maintenance prioritization are analyzed, and the most

appropriate criteria are identified based on the relative weight. Depending on the type of physical performance or construction solution, it is possible to determine an index that reflects the priority of intervention, urgent actions (up to six months), short-term (up to two years) and medium-term actions by combining certain factors related to risk (critical type of the affected area and maintenance cost). Heat, sound and water problems occur due to the defects in window systems. In order to eliminate these problems, alternative maintenance plans are developed according to the data obtained from the window types which are examined, and the most suitable one is selected and applied (Table 9).

3.5. Control Stage

At this stage, the recommended maintenance planning for window systems could not be carried out. Therefore, this stage is not applicable within the scope of our research (we could not have a sponsor for this purpose).

Table 4. Sigma Improvement Tools- Management and Quality Tools

Table 4: Sigma Improvement Tools- Management and Quality Tools				
Method	Purpose of Usage	Benefits	Source	
Customer's Requests	The objectives of the project are set out and the customer's wishes are fully understood so that the problems that arise after are eliminated.	The contract with employees for the realization of the objectives of the project reduces the likelihood of problems because the obligations are determined.		
Brainstorming	Idea development	It is a process in which different ideas are freely expressed by everyone. Ideas are ranked from 1 to 5 according to their	Munro, 2007 [16]	
Gantt chart	Making the job program	Completing the project steps in the desired time and order to prevent possible disruptions	Pande et. al, 2001 [17]	
Work Flow Charts and Process Mapping	Observing, identifying and improving problems are important in deciding the processes	Observing, identifying and improving problems are important in deciding the processes		
Prioritization Matrix	Choosing between options	Choosing between options	Munro, 2007 [16]	
Hypothesis Testing and ANOVA	Propose to special situations	Used to propose solutions to special situations with statistical data		
Regression Analysis	Used to explain how the dependent variable is changed by the argument			
Benchmarking	It is used to apply a system process to another system.	Organizations benefit from each other's positive aspects		
Control Chart	Used to distinguish process variations	Used to control the process.	Sönmez, 2013 [19]	
Process adequacy index	Process adequacy is the ability of the process to meet the expected specifications.			
Failure Types and Effects Analysis-HTEA FMEA-Fault	FMEA	It is used to track all failures in the process step by step.	The frequency of failures is listed according to their causes and severity.	Pahl et.al, 1996 [23]; Tooley and Knovel, 2010 [24]
	Root cause analysis	It is a step-by-step method used to analyze problems based on root causes.	It is a step-by-step method used to analyze problems based on root causes.	Ben-Daya et. Al, 2009 [18]
	Pareto Diyagram	Used to see the frequency of failure types.		
	Cause and Effect Diagram Fishbone Method	This tool helps to identify the underlying causes of the problem in Six Sigma.	It is easy to use and generally gives remarkable results.	Munro, 2007 [16]
	Fault Tree Analysis	Top-down sequence of possible failure events after a significant failure.		Pahl et.al, 1996 [23]; Tomiya et al,2009 [25] Shetty, 2016 [26]
	Fuzzy Logic and Fuzzy Clustering Method - FDM	The fuzzy set can be defined mathematically as assigning a value to any entity in the discourse universe to the degree of membership within the fuzzy set.	Fuzzy logic is an appropriate methodology to investigate many problems characterized by unreliable data, incomplete measurements, and ambiguous definitions.	Zadeh, 1975 [20]
Control Sheets	Data collecting	Provides more organized data collection process.		

Table 5. Methodology of the study; tools and steps that used in this study

Tools	Steps	Method
Cause and Effect Analysis Brainstorming Checklist (Figure 1) Workflow chart	Identification of defects	-
	Identifying defects in components	Based on observation method
Scoring	Scoring of defects	-
AHP	Selecting appropriate maintenance Response severity / urgency level	-

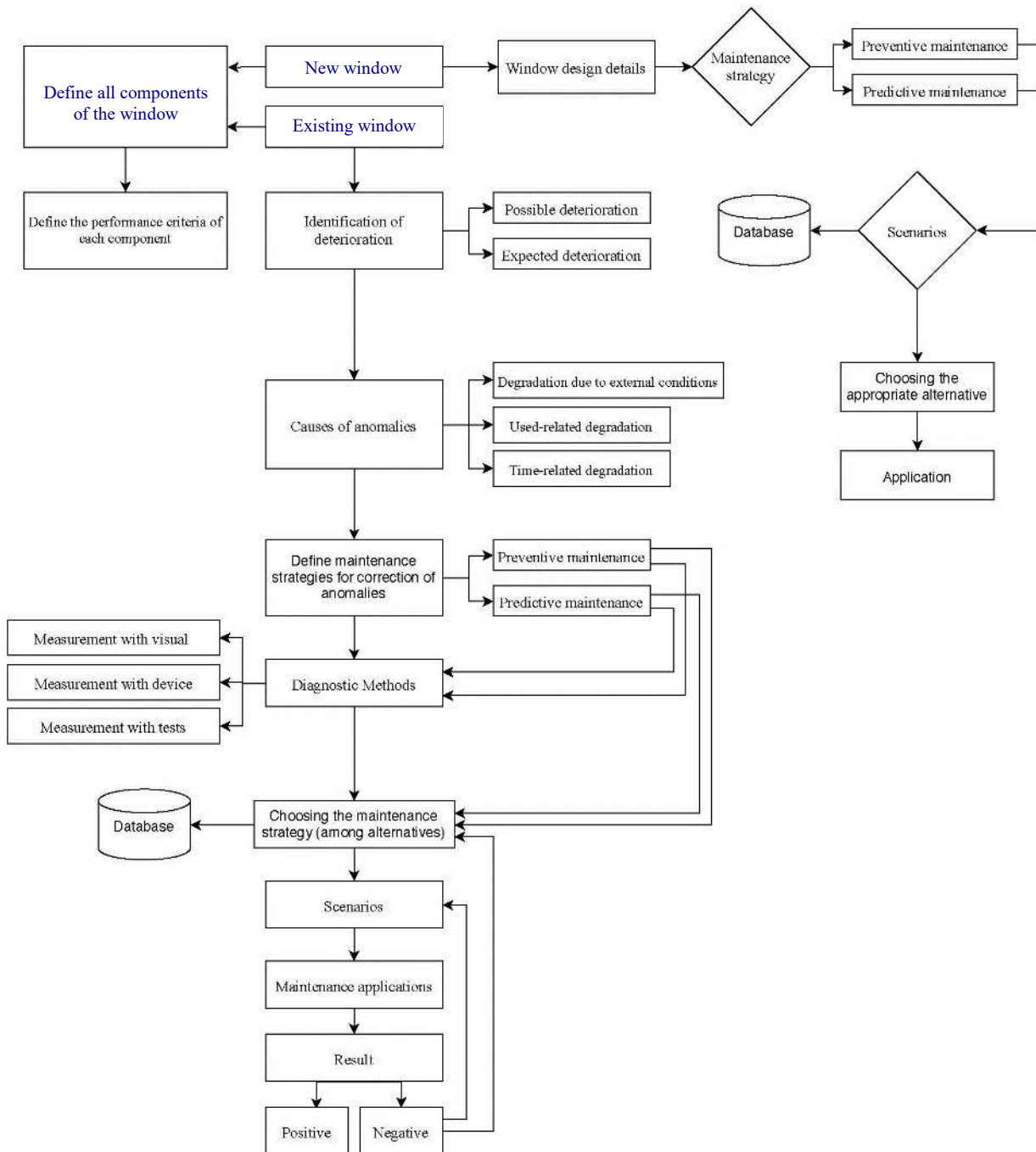


Figure 1 Workflow Chart for Window Maintenance Planning

Table 6. Checklist

Table 6: Checklist							
General Information about Building	Code:		Name of the Building:				
			Function of Structure:				
			Function of Space:				
			Supporting System of the Building:				
			Floor location:				
			Distance to Sea:				
			Distance to Road:				
General Information about the Window			Direction:				
			Wall Type:				
			Position of the window on the wall:				
			Protective element on the wall: (wiping, eaves, etc.)				
			Lintel:				
			Sills:				
			Window Size:				
		Material of the window:					
		Glass Type:					
		DEFFECTS TYPE		Score	DEFFECTS TYPE		
DEFECTS IN WINDOW SYSTEM COMPONENTS	SASH -GLASS	Aesthetic Defects	E1. Rupture		Physical Damages	F1. Distortion-Breaking of Fasteners	
			E2. Smooth Pollution			F2. Corrosion in Fasteners	
			E3. Color Change			F3. Water Leakage	
			E4. Mold fungus			F4. Partial Blanks	
			E5. Cracking			F5. Sealing Deterioration	
			E6. Swelling			F6. Shattered Glass	
			F7. Heat problem			
	Failures in Design		Installation Failure		Failures in Use		
	FRAME-SASH	Aesthetic Defects	E1. Rupture		Physical Damages	F1. Distortion-Breaking of Fasteners	
			E2. Smooth Pollution			F2. Corrosion in Fasteners	
			E3. Color Change			F3. Water Leakage	
			E4. Mold fungus			F4. Partial Blanks	
			E5. Cracking			F5. Sealing Deterioration	
			E6. Swelling			F6. Shattered Glass	
			F7. Heat problem			
	Failures in Design		Installation Fail.		Failures in Use		
	SASH*SASH	Aesthetic Defects	E1. Rupture		Physical Damages	F1. Distortion-Breaking of Fasteners	
			E2. Smooth Pollution			F2. Corrosion in Fasteners	
			E3. Color Change			F3. Water Leakage	
			E4. Mold fungus			F4. Partial Blanks	
E5. Cracking				F5. Sealing Deterioration			
E6. Swelling				F6. Shattered Glass			
.....			F7. Heat problem				
Failures in Design		Installation Fail.		Failures in Use			
WALL-FRAME	Estetik Hasarlar	E1. Rupture		Physical Damages	F1. Distortion-Breaking of Fasteners		
		E2. Smooth Pollution			F2. Corrosion in Fasteners		
		E3. Color Change			F3. Water Leakage		
		E4. Mold fungus			F4. Partial Blanks		
		E5. Cracking			F5. Sealing Deterioration		
		E6. Swelling			F6. Shattered Glass		
		F7. Heat problem				
Failures in Design		Installation Fail.		Failures in Use			
LINTEL-FRAME	Aesthetic Defects	E1. Rupture		Physical Damages	F1. Distortion-Breaking of Fasteners		
		E2. Smooth Pollution			F2. Corrosion in Fasteners		
		E3. Color Change			F3. Water Leakage		
		E4. Mold fungus			F4. Partial Blanks		
		E5. Cracking			F5. Sealing Deterioration		
		E6. Swelling			F6. Shattered Glass		
		F7. Heat problem				
Failures in Design		Installation Fail.		Failures in Use			
SILLS-FRAME	Aesthetic Defects	E1. Rupture		Physical Damages	F1. Distortion-Breaking of Fasteners		
		E2. Smooth Pollution			F2. Corrosion in Fasteners		
		E3. Color Change			F3. Water Leakage		
		E4. Mold fungus			F4. Partial Blanks		
		E5. Cracking			F5. Sealing Deterioration		
		E6. Swelling			F6. Shattered Glass		
		F7. Heat problem				
Failures in Design		Installation Failure		Failures in Use			

Photos of window

Scoring System: 1: Excellent (no damage) 2: Good (damage that can be easily corrected) 3: Moderate (usable - maintenance required) 4: Bad (parts replacement required) 5: Very bad (parts cannot be replaced, cannot be used See Table: List of design, construction, usage failure

Table 7. Matrix related to defects and possible causes of windows

Defects Code	Region of Origin			Possible Reasons						Stages			
	Y1	Y2	Y3	N1	N2	N3	N4	N5	N6	T	Y	K	Ç
Aesthetic Defects	E1												
	E2												
	E3												
	E4												
	E5												
	E6												
	E7												
Total													
Physical Defects	F1												
	F2												
	F3												
	F4												
	F5												
	F6												
Total													
Total													

* Y1: Sash-frame, Y2: Sash-sash, Y3: Sash-glass, Y4: Between wall-frame, Y5: Between Lintel-frame, Y6: Between sill-frame;
 * Phases: T (design); Y (construction); K / B (use / maintenance); O (environment)
 * Causes: N1- Small sash-frame section, N2-Incorrect installation, N3-

Table 8. Matrix of possible causes of defects in windows

Defects Code	Region of Origin			Possible Reasons						Stages			
	Y1	Y2	Y3	N1	N2	N3	N4	N5	N6	T	Y	K	Ç
Aesthetic Defects	E1												
	E2												
	E3												
	E4												
	E5												
	E6												
	E7												
Total													
Physical Defects	F1												
	F2												
	F3												
	F4												
	F5												
	F6												
Total													
Total													

Invalid use, N4-Incorrect maintenance-repair, N5-Incorrect positioning, N6-Incorrect selection
 * Defects; The E and F codes are the codes of the defects given in the checklist in Table 11.

Table 9. Maintenance (Developed from [3])

Defect Locations	Maintenance Recommendations
HY1.Frame Components Maintenance	A1- Repair or replacement of EPDM, silicone, strip, etc. sealing materials A2- Repair / replacement of fasteners such as nail screws A3- Replacing the glazing bead A4- Repair / replacement of hinges, opening / closing mechanisms
HY2. Frame Maintenance	B1- General cleaning of the frame B2- Repairing damaged areas according to the material of the frame B3- Repair of drains and drainage B4- Removal of damaged parts of glass
HY3.Glass Maintenance	C1-Glass replacement C2-Glass repair C3-Installation of ventilation system
HY4. Frame-Lintel Maintenance	L1- Silicone squeezing between frame-lintel L2- Insulation if thinner than lintel wall L3- Strengthening frame fixings L4- Placing raincoats / profiles to remove rainwater etc.
HY5.Frame-Sills Maintenance	D1-Silicone squeezing between case-windowsill D2- Installation of profile / raincoat to reduce water leakage between frame (case) and windowsill

Table 10. Recommended maintenance for scoring from Table 9

	1 Point	2 Point	3 Point	4 Point	5 Point
Recommended maintenance	HY2-B1.	HY2-B1, HY1, HY2, HY4, HY5	HY2-B1, HY1, HY2, HY4, HY5	HY2-B1, HY1, HY2, HY3, HY4, HY5	HY2-B6

According to the score obtained as a result of the visual evaluations, the selection is made by applying the AHP method while planning maintenance for the relevant window. The AHP method is used in the selection of maintenance alternatives. The AHP method is one of the most widely used multi-criteria decision-making methods where the decision (selection and prioritization of alternatives) is based on a variety of tangible and intangible criteria (sub-criteria). The complex problem-solving process is divided into a hierarchical structure consisting of the purpose of the problem, criteria, sub-criteria, and alternatives. When designing the AHP hierarchical tree, the objective is to develop a general framework that meets the needs of analysts to solve the problem of selecting the best maintenance policy. AHP begins by dividing the complex multi-criteria problem into a hierarchy where each level contains several manageable elements that can be divided into another group of elements [22]. The AHP hierarchy developed in this study is based on the selection of the performance characteristics in the window system and the appropriate maintenance alternatives. Tables 9, 10 and 11 are used for selection of the best alternative.

4. APPLICATION of METHODOLOGY

4.1. Description Phase

The model is applied to a historical educational building which is near the sea. The examined defects are classified under the title of aesthetic and physical defects. The reasons for the defects were small frame-sash section, incorrect installation, incorrect use, incorrect maintenance, incorrect positioning, and incorrect selection, and it was decided to investigate whether all these faults occurred during the design, application or usage stages or environmental condition. At this stage, a workflow chart

(Figure 1) was made to decide which stages to follow.

Table 11. Criteria to be used in the evaluation









Evaluation Criteria-Main Criteria and Sub-Criteria	
Structural performance	Structural stability
Durability	Security
Physical performance Ecological performance	Health
	Air impermeability
	Water impermeability
	Heat performance
	Sound impermeability
Cost	Noise control
	Natural ventilation
	Solar Control
Structural performance	Use of recyclable materials
Durability	Selection of materials and details suitable to the historical building
	Material in suitable color-texture

4.2. Measurement Phase

62 wooden window systems of the building were examined according to the checklist in Table 11. One of the long façades of the building is close to the sea and the other façade is parallel to the main street. The defects in the windows were investigated by observation, the data obtained from the investigation were recorded in the checklist and the defects were documented and archived with photographs (Tables 12- 13).

After completing the checklists, the data was converted to numerical values using Tables 14 and 15. It was found that 100% of the aesthetic damages occurred in the frame and sash and 15% in the glass.

Table 12. Defects in the windows













Defects in Window P2 Code	Defects in Glass Bead P56 Code window	Defects in Sash P3 Code window	Defects in Frame P7 Code window
 window Defect type: Glass contamination	 Defect type: Deformation of lath	 Defect type: Spill in paints	 Defect type: Clogging of water discharge pipes
 Defect type: Glass misting	 Defect type: Decay, crack formation, spill	 Defect type: Breaking, cracking, surface contamination	 Defect type: Decay, spill, spill between sill-frame

4.3. Analysis Phase

The wooden windows investigated in this stage were separated as wall-frame, window components, glass component, and places where defects occurred were examined in terms of aesthetic and physical defects. The reasons for the defects were evaluated under the headings of the small case-sash section, incorrect installation, incorrect usage, incorrect maintenance, incorrect positioning, and incorrect selection. Finally, it was investigated whether the defects occurred due to design, construction, usage and/or environmental conditions. The data are recorded in Table 14-15. According to Table 14, most of the defects are seen in the frame. It is determined that the cause of these defects is due to improper maintenance.

According to the data in Tables 14 and 15, defects in the window system investigated were assigned as follows. Aesthetic damages were seen in the frame and sash as smooth contamination, color change, mold fungus formation, cracking and blistering. On the other hand, only fouling was detected on the glass. It has been determined that these defects occurred due to incorrect maintenance and incorrect positioning. Decisions given according to the design and environmental factors were found to be important in the formation of these defects. It was further detected that partial cavities in the sash and the frame, decay, mold, and fungus were available, and the strip in the sash was completely removed, wherein heat problems occurred.

Table 13. Photographs for information on the status of windows according to defects

	2nd Degree Damaged Windows (P37 Code Window)	3rd Degree Damaged Windows (P5 Code Window)	4th Degree Damaged Windows (Window P13 Code)	5th Degree Damaged Windows (Window P26 Code)
There is no 1 st degree damaged window				
				
				

There was also heat loss on the glass surface. It was also found that there was a gap, mold, and wear of the silicones between the frame-wall, the frame-lintel, and the frame-windowsill. 90% of these damages occurred due to design and environmental conditions. In the design, placing the window frames on the outer surface of the wall caused them to remain unprotected and hence, be exposed to severe environmental conditions directly.

4.4. Improvement Stage

All components are subject to loss of performance due to aging, handling and external reasons. Hermans 1995 [13] showed that the relationship between deterioration and

performance loss could develop in three different ways (Figure 1).

1. While performance loss decreases continuously, distortion increases continuously.
2. No deterioration occurs when the performance is constantly at the same level, the performance suddenly disappears/diminishes.
3. Performance loss and defects are independent.

Tables 14 and 15 indicate scores assigned to the levels of defect, which were identified as an outcome of on-site observations. Table 14 shows in which stage or stages including design, application, construction and usage phases the deterioration of window components (frame, sash, glass, and their junction points) occurs by

summing up the scores. Table 15 shows the deterioration score between the wall and the windowsill and whether it occurs due to the

Table 14. Matrix of possible causes of defects in the window system

Defects Code	Region of Origin			Possible Reasons						Stages			
	Y1	Y2	Y3	N1	N2	N3	N4	N5	N6	T	Y	K	Ç
Aesthetic Defects	E1	X	X				X		X			X	X
	E2	X	X	X						X		X	X
	E3	X	X							X		X	X
	E4	X	X										X
	E5	X	X										X
	E6	X	X										X
	Total	6	6	1				1		1	2		3
Physical Defects	F1												
	F2					X	X						X
	F3	X	X							X			X
	F4	X	X				X						X
	F5		X				X						
	F6	X	X				X						X
	F7	X	X	X			X			X	X		X
Total	4	5	1		1		5			2	1		5
Total	10	11	2		1		6		1	4	1	3	11

Table 15. Matrix of possible causes of defects between wall and window

Defects Code	Region of Origin			Possible Reasons						Stages			
	Y1	Y2	Y3	N1	N2	N3	N4	N5	N6	T	Y	K	Ç
Aesthetic Defects	E1						X	X		X			X
	E2	X	X	X			X			X			X
	E3	X	X	X			X			X			X
	E4	X	X	X			X	X		X			X
	E5	X	X	X			X	X		X			X
	E6	X	X	X				X					X
	Total	5	5	5				5	4		5		
Physical Defects	F1											X	
	F2							X					X
	F3							X		X			
	F4			X				X		X			
	F5									X			
	F6			X			X		X	X			X
	F7	X	X	X				X	X	X			X
Total	1	1	3			1		5	1	5		1	3
Total	6	6	8			1	5	9	1	10		1	9

* Y1: in the casing-frame, Y2: in the sash, Y3: in the glass; Y4: Between wall-frame, Y5: Between Lintel-frame, Y6: Between sill-frame;

* Phases: T (design; Y (construction); K / B (use / maintenance); O (environment)

* Causes; N1- Small frame-sash section, N2-Incorrect installation, N3. Failure use, N4-Incorrect maintenance-repair, N5-Incorrect positioning, N6-Incorrect selection


* Defects; The E and F codes are the codes of the defects given in the checklist in Table 11.

With the previous scoring system, maintenance alternatives were selected for the windows

design, construction and usage stages. The information obtained here is used in the selection of the maintenance method. having scores of 2.3 and 4. A selection is to be made among the options to upgrade the score of window systems from 2 to 1 point or to protect their current status and to improve the condition of window systems scored 3 and 4. Maintenance plans are created and selected for each grade.

In the study, the most appropriate maintenance and repair planning were made for the window system with the damage degree code of P13 among the 62 window systems examined. The most important damage detected in this window system is the presence of decay in the casing and cracks in the sash. The criteria were determined according to the rate of deterioration of the window. Maintenance planning has been subjected to general preliminary assessment in terms of heat impermeability, water impermeability, durability aesthetics, and cost criteria. In terms of heat impermeability, it was observed that there were leaks from these points where the strip on the edges of the window sash were worn. Heat transitions have been detected on the areas where the frame and sash connect, which caused swelling of the plaster and paint between the wall and the frame. When the water impermeability was examined, it was observed that the gutters made to prevent the ingress of water into the frame were blocked, and the frame was found to be rotting from the cracks caused by both water and sun rays. In terms of aesthetics, there is intense visual deterioration especially on the exterior surface with the rotting of the frame and sash. Decay was seen as critical damage in the examined window systems, and it was found that the sub-head of the sash was broken, and the sash could not perform its function. The second critical defect that occurred due to decay was spillage and cracking of the wooden frame, sash and glass laths. The common defect observed in almost all windows was the application of very thick paint on the surface, and swelling, as well as spilling of this thick paint layer depending on the environmental conditions, which means that the wood remained unprotected.

Table 16. Control List

Kod: P13	Name of Building: Historical Education Building						
General Information about Building	Function: Education						
	Function of room: Office						
	Supporting System: Concrete+Masonry						
	Floor Level: First floor						
	Distance to Sea: 4m						
General Information about the Window	Distance to Road: -						
	Direction: North-east						
	Wall Type: Stone						
	Position of the window on the wall: Outside						
	Protective element on the wall: (wiping, eaves, etc.) Wiping, eaves						
	Lintel: Arch						
	Sills: no exist						
	Window Size:						
Material of the window: Wood							
Glass Type: Two layered glass							
DEFECTS IN WINDOW SYSTEM COMPONENTS	Defect Location and Type		Yes-no	Defect Location and Type		Yes/No	
	SASH-GLASS	Aesthetic Defects	E1. Rupture	-	Physical Defects	F1. Distortion-Breaking of Fasteners	-
			E2. Smooth Pollution	X		F2. Corrosion in Fasteners	X
			E3. Color Change	X		F3. Water Leakage	-
			E4. Mold fungus	X		F4. Partial Blanks	X
			E5. Cracking	X		F5. Sealing Deterioration	X
			E6. Swelling	X		F6. Shattered Glass	-
					F7. Heat problem	X
	Failures in Design	X	Installation Failure		Using Failure	X	
	FRAME-SASH	Aesthetic Defects	E1. Rupture	X	Physical Defects	F1. Distortion-Breaking of Fasteners	-
			E2. Smooth Pollution	X		F2. Corrosion in Fasteners	-
			E3. Color Change	X		F3. Water Leakage	-
			E4. Mold fungus	X		F4. Partial Blanks	-
			E5. Cracking	X		F5. Sealing Deterioration	X
			E6. Swelling	X		F6. Shattered Glass	X
					F7. Heat problem	X
	Failures in Design	X	Installation Failure		Using Failure	X	
	SASH-SASH	Aesthetic Defects	E1. Rupture	-	Physical Defects	F1. Distortion-Breaking of Fasteners	-
			E2. Smooth Pollution	X		F2. Corrosion in Fasteners	-
			E3. Color Change	X		F3. Water Leakage	-
			E4. Mold fungus	X		F4. Partial Blanks	-
			E5. Cracking	X		F5. Sealing Deterioration	X
			E6. Swelling	X		F6. Shattered Glass	X
					F7. Heat problem	X
	Failures in Design	X	Installation Failure		Using Failure	X	
	WALL-FRAME	Aesthetic Defects	E1. Rupture	-	Physical Defects	F1. Distortion-Breaking of Fasteners	-
			E2. Smooth Pollution	X		F2. Corrosion in Fasteners	X
			E3. Color Change	X		F3. Water Leakage	-
			E4. Mold fungus	X		F4. Partial Blanks	X
			E5. Cracking	X		F5. Sealing Deterioration	X
E6. Swelling			X	F6. Shattered Glass		X	
.....				F7. Heat problem		X	
Failures in Design	X	Installation Failure		Using Failure	X		
LINTEL-FRAME	Aesthetic Defects	E1. Rupture	-	Physical Defects	F1. Distortion-Breaking of Fasteners	-	
		E2. Smooth Pollution	X		F2. Corrosion in Fasteners	-	
		E3. Color Change	X		F3. Water Leakage	-	
		E4. Mold fungus	X		F4. Partial Blanks	-	
		E5. Cracking	X		F5. Sealing Deterioration	X	
		E6. Swelling	X		F6. Shattered Glass	-	
				F7. Heat problem	X	
Failures in Design	X	Installation Failure		Using Failure	X		
SILLS-FRAME	Aesthetic Defects	E1. Rupture	X	Physical Defects	F1. Distortion-Breaking of Fasteners	-	
		E2. Smooth Pollution	X		F2. Corrosion in Fasteners	-	
		E3. Color Change	X		F3. Water Leakage	-	
		E4. Mold fungus	X		F4. Partial Blanks	X	
		E5. Cracking	X		F5. Sealing Deterioration	X	
		E6. Swelling	X		F6. Shattered Glass	X	
				F7. Heat problem	X	
Failures in Design	X	Installation Failure		Using Failure	X		

Scoring System: 1: Excellent (no damage) 2: Good (damage that can be easily corrected) 3: Moderate (usable - maintenance required) 4: Bad (parts replacement required) 5: Very bad (parts cannot be replaced, cannot be used See Table: List of design, construction, usage failure

Table 17. Scoring examined windows

Window Code	Direction	Defect Degree					Total	
		1	2	3	4	5		
P1	Southeast				X			
P2					X			
P3				X				
P4				X				
P5					X			
P6					X			
P7				X				
P8				X				
P9				X				
P10				X				
P11				X				
P15						X		
P16						X		
P17				X				
P18				X				
P19				X				
P20						X		
P21				X				
P22				X				
P23				X				
P24				X				
P25				X				
Total			0	0	15	7	0	22
P32		Northwest			X			
P33					X			
P34				X				
P36				X				
P37				X				
P38				X				
P39				X				
P40				X				
P41			X					
P42			X					
P43			X					
P44			X					
P45			X					
P46			X					
P47				X				
P48				X				
P49				X				
P50			X					
P51			X					
P52				X				
P53							X	
P54				X				
P55				X				
P56				X				
P57						X		
P58				X				
P59				X				
P61			X					
P62						X		
Total			0	7	18	2	1	28
P28	South west					X		
P29						X		
P30					X			
P12				X				
P14				X				
Total		0	0	3	2	0	5	
P13	Northeast					X		
P31				X				
P26							X	
P27						X		
P35							X	
P60					X			

Consequently, partial gaps and loss of aesthetic value have been experienced. It has been found that most of the strip between the casing and the sash have been removed or never used, due to the demand of the user and construction failure. Therefore, heat losses occur. Corrosion was detected by invisible fasteners. In particular, protrusion of glass nails over the fixing lath presents both fixing problem and aesthetically unfavorable situation. Due to improper maintenance and environmental conditions, the level of contamination on the frame and sash was determined as 90%. Condensation has been detected on the glass of a window.

All of the aforementioned aesthetic damages were observed on the frame and sash. Smooth and intense contamination was observed on glass surfaces where there was no continuous cleaning (P2). Only one window glass showed condensation (P61). As a result of the inspections, the main reason for the damage is the lack of continuous maintenance depending on the environmental conditions or the defective/inadequate maintenance.

Table 18. Criteria for evaluation

Evaluation Criteria- Main Criteria and Sub-Criteria	
Structural Performance	Structural stability
Durability	Security
Physical performance	Health
	Air impermeability
	Water impermeability
	Heat performance
	Sound impermeability
Ecological performance	Noise control
	Natural ventilation
	Solar Control
Cost	Use of recyclable materials
Aesthetic	Appropriate materials and details for the historical building
	Suitable color and textured material

It was found that the deteriorations on the façade of the building facing the sea were more severe and the deteriorations were observed on the lower frame and planted drip. As for the level of deterioration where decay was observed, the lower part of the sash fell and the window

became unusable (Table 12-13). The sash must be replaced. Again, 95% of the windows in this direction showed intense blistering on the outer surfaces. For this reason, the amount of deterioration was high. Intense cracking and crevices were found on the exterior. Breaks and disintegration were also observed in glass laths. Depending on the cross-section, the heat permeability level was quite high. The glass cannot be changed as the cross section cannot be increased.

Basic and sub-criteria have been determined to be used within the scope of the evaluation by using Table 18. The maintenance plan was chosen to evaluate the criteria of heat impermeability, cost, aesthetics, and durability, as it did not impair the originality of the historical building. Since the building is a historical building, each maintenance process should be effective in the preservation of the original value of the building. Particular attention has been paid to the fact that maintenance of each component of the window system, which is part of this, should be taken into account. It is thought that the energy consumption of the building would be reduced by preventing heat escape within the windows, which affects the energy performance of the building to a great extent, especially during the winter months and hence, causes intensive use of heating systems. The cost criterion is important for the selection of the most effective and necessary solution in the long term with the most appropriate budget.

With the completion of information collection and determination of evaluation criteria steps, the maintenance phase for the window being studied and the selection of the alternative can be started.

Maintenance alternatives based on selected criteria are as follows:

1. Cleaning, sanding, puttying and painting the frame,
2. Placing insulation strips on the edges of the frame to increase the heat impermeability; replacement of fixing elements such as nails; replacement of

the necessary glass laths; sanding, pasting and painting the whole window; repairing the drainages,

3. General cleaning of the frame; removing the damaged parts and replacing them; removing all window slats; closing the connection points between the frame and the rough structure with silicon; installing the planted drip on the frame for removal of the water from the frame; renewing the opening and closing mechanism, and applying weather-strip to ensure impermeability.
4. General cleaning of the frame, removing damaged parts and replacing them, removing all window laths, closing the connection points between the casing and the rough structure with silicon, installing the planted drip on the casing to remove water from the casing, renewing the opening and closing mechanism, and increasing the thickness of the glass by replacing the available one with the thicker glass to increase heat insulation, and replacing the lath due to the increase in glass thickness. As the area where the lath will be fixed will be narrower, the lath detail will be changed and a different lath section will be required by turning over the sash.
5. Completely changing the window for heat, sound, water, durability, aesthetic criteria to make the most ideal window system.

Table 19 shows the comparison of 5 maintenance options recommended for the window system analyzed. These 5 alternatives were examined according to the criteria, and the A1, A2, A3 alternatives were evaluated. Option A4 proposing replacement of the glass was eliminated during the preliminary evaluation stage due to the fact that this option increases cost, and the thickness of the cross-section of the sash cannot support the load of this glass, which creates security problem, The option A5 was also eliminated due to the cost increase (Table 19). As a result of the elimination, alternatives A1, A2, A3 satisfying most of the criteria were chosen for evaluation purposes.

After creating the hierarchy table in Figure 2, alternatives were questioned according to the criteria with the help of Super Decisions program. Cross-queries generated by the program was answered by relevant experts.

Table 19. Evaluation of alternatives in terms of selected criteria

Alternatives	K1. Heat performance	K2. Water impermeability	K3. Durability	K4. Aesthetic	K5. Cost effective
A1				X	X
A2	X	X	X	X	X
A3	X	X	X	X	X
A4	X	X	X	X	
A5	X	X	X		

Saaty (2006) scored the criteria as follows. Support was obtained from experts in weighting the criteria [21]. Points to be given to the criteria are as specified below:

- 1 point=equally important
- 3 points = moderately significant
- 5 points = strongly important
- 7 points = very important
- 9 points - absolutely significant
- 2,4,6 points = intermediate values (used when there are small values between two elements)

According to hierarchy in Figure 2, each criterion for Aim was compared in pairs. At the end of the comparison, a paired comparison matrix was formed on the basis of the scores obtained from the expert views.

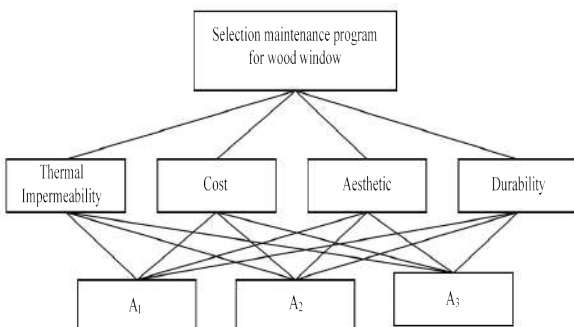


Figure 2. A hierarchical tree selection maintenance program for wood window

Table 20. Binary comparison matrix of criteria for selected window

Aim	Heat Impermeability	Cost	Aesthetic	Durability / Security
Heat Impermeability	1	5	3	5
Cost	1/5	1	2	3
Aesthetic	1/3	1/2	1	3
Durability/ Security	1/5	1/3	1/3	1

Table 20 shows the criteria to be identified by the expert and their pairwise comparison. Table 21 shows the result of Super Decision program. All values were evaluated with the answers given to cross-questions comparing the two criteria of the Super Decision program. Then the alternatives were evaluated with cross-questions considering the aforementioned criteria, and the final result was reached. Since heat impermeability is a very important factor in terms of criteria, it is concluded that the 3rd alternative should be selected as a maintenance and repair method.

Table 21. Comparison of alternatives for selected window in Super Decision program

Icon	Name	Normalized by Cluster	Limiting
No Icon	Maintenance of wooden windows	0.00000	0.000000
No Icon	Thermal Impermeability	0.56021	0.280104
No Icon	Cost	0.14280	0.071398
No Icon	Aesthetic	0.22235	0.111174
No Icon	Durability	0.07465	0.037324
No Icon	Alternative-1	0.23430	0.117148
No Icon	Alternative-2	0.29822	0.149109
No Icon	Alternative-3	0.46749	0.233743

5. RESULT

70% of the energy losses in buildings occur due to the faulty design of the facade or performance losses over time. Window systems covering the gaps on the facade are the areas where these losses are most intense. Determination of design, construction, usage and time-related failure in existing wooden window systems and preparing a maintenance plan for this will reduce energy consumption and provide resource efficiency instead of demolishing and destroy.

In this study, the possible defects on the wooden window systems were listed with a wide literature review and the data obtained from the observations made by the expert for the detection of these defects were recorded in the control lists. In the study, a method was developed based on the maintenance alternatives listed before and according to the degree of defects. This method has been applied to the window systems of a building with historical value and used for educational purposes. According to the data obtained from 62 wooden window systems examined, it was concluded that defects occurred due to environmental conditions, improper use and maintenance.

In these window systems, which have been used for more than 20 years, there is a big difference between the deterioration rates between the façade facing the sea and the façade facing the road. It was observed that the decay, swelling and rupture rates were higher on the sea-facing façade and that the lower part of the sash of the window P26 was broken and became unusable due to decay. In other windows, the application of a thick paint layer and swelling of the thick paint layer on surfaces exposed to strong wind caused damage on the unprotected surfaces. Due to the lack of regular maintenance, this damage has increased the effect level and has reached a level requiring serious interventions. The proposed maintenance was evaluated according to the criteria of heat incompatibility, cost, aesthetics, and durability. The arrangement of the windows differs according to the usage of the examined places as offices and classrooms. While the lower and upper sashes of the classrooms are arranged as fixed and openable

respectively, windows of the office spaces are designed as an openable sash on the top section and fixed window at the upper part.

Due to the extreme height, cleaning problems are experienced in both cases. There is no windowsill in the original windows and inside there is a marble window board. The original window frame-sash sections of the building are thin so the space between the double glazing cannot provide sufficient thermal insulation. The heat impermeability criterion has been prioritized within the scope of alternative selection criteria. The cost has been considered as the second most important issue wherein it is aimed to satisfy all desired conditions economically. The aesthetic criterion is considered as 3rd most significant issue where the objective is to apply the maintenance process without disturbing the originality of the historical structure. The durability criterion means ensuring safety in a building with a high number of students. All of these criteria were determined by comparing them with each other via the computer-based Super Decision program of AHP, after which the significance of the obtained criteria was compared with alternatives to choose the most suitable option.

The method is simple and practical. With this method, the best option can be chosen among the maintenance alternatives developed by taking the requests of the users and operators into consideration. Storing the data in the checklist will also be a guide for future maintenance and repair work.

6. CONCLUSION

Making proper maintenance and repair plans for the window systems of existing buildings reduces energy consumption and ensures resource protection. The largest energy consumption in existing building occurs in the building façade, windows and doors. In this respect, window systems are evaluated from very different aspects such as energy consumption, resource, aesthetic value etc.

Maintenance and repair decisions must be related by providing information about energy losses,

safety, aesthetics, etc., especially by minimizing the energy consumption, by providing information to the user with the guide created by the local authorities, in certain periods. This method when used by local authority have many advantages such as reducing energy consumption, and do not change character of the building (by choosing different colors, choosing different size windows, etc.).

The study starts with recording the current state of the building via preliminary examination. Several information about windows are written on prepared tables such as material, dimensions, on which floor and in which direction they are placed, etc. This preliminary information is important in finding the rate of impact on the severity of the defects. All of them will affect the selection among the maintenance alternatives to be determined later. For this reason, preliminary assessment should be made accurately and completely. Then the preliminary information phase of the database is completed with visuals showing the deterioration status of the current window. According to the information obtained, the defects are scored, and after the analysis is made in accordance with the determined criteria, a selection is made among the maintenance alternatives according to the total score.

In the study, the defects in 60 wooden windows of a historical educational building were investigated. As a result of the negotiations with the directors of the building, the main reason of the defects in the windows is identified as the size of the building and the high floor heights and environmental conditions of the building located at the seaside. A method has been proposed for the selection of the appropriate alternative depending on the degree of deterioration among the maintenance alternatives for the windows by prioritizing with all these criteria, and this proposed method has been applied on a selected window system. It was seen that the obtained result coincides exactly with the desired one. This proved the correctness of the proposed method.

As a result of the study, it was seen that wrong maintenance applications increased the deterioration rates in the examined window

systems. Accurate determination of the maintenance planning periods according to the environmental impacts may extend the service times of the existing windows. Prioritizing the criteria needed to be satisfied by the windows in the existing building stock and the maintenance methods to be selected can both increase the comfort conditions, extend the service time and provide energy and resource efficiency.

Funding

The authors received no financial support for the research, authorship, and/or publication of this paper.

The Declaration of Conflict of Interest/ Common Interest

No conflict of interest or common interest has been declared by the authors.

Authors' Contribution

ÖE: investigation, literature review, methodology, data analysis, writing and finalizing.

MO: investigation, literature review, drawings, finalizing

The Declaration of Ethics Committee Approval

The authors declare that this document does not require an ethics committee approval or any special permission.

The Declaration of Research and Publication Ethics

The authors of the paper declare that they comply with the scientific, ethical and quotation rules of SAUJS in all processes of the paper and that they do not make any falsification on the data collected. In addition, they declare that Sakarya University Journal of Science and its editorial board have no responsibility for any ethical violations that may be encountered, and that this study has not been evaluated in any

academic publication environment other than Sakarya University Journal of Science.

REFERENCES

- [1] S. S. Liu and G. Ramadhan, "Conditioned –Based Building Maintenance Strategy Selection Using Constraint Programming," *Facility Maintenance and Management*, pp. 345-351, 2017.
- [2] M. Y. L. Chew, S. S. Tan, and K. H. Kong, "Building Maintainability-Review of State of the Art," *Journal of Architectural Engineering*, pp 80-87, 2004.
- [3] A. Santos, M. Vicente, J. de Brito, I. Flores-Colen, and A. Castelo, "Inspection, Diagnosis, and Rehabilitation System of Door and Window Frames," *Journal of Performance of Constructed Facilities*, vol. 31, no. 3, pp 04016118-1-12, 2017.
- [4] M. Macarulla, N. Forcada, M. Casals, M. Gangoells, A. Fuertes, and X. Roca, "Standardizing housing defects: classification, validation, and benefits," *Journal of Construction Engineering and Management*, vol. 139, no. 8, pp. 968-976, 2013.
- [5] J. Morgado, "Inspection and maintenance plan for roofs in current buildings," Ph.D. thesis, Instituto Superior Técnico, Universidade Técnica de Lisboa, Lisboa, Portugal (in Portuguese), 2012.
- [6] I. Flores-Colen, and J. de Brito, "Plan of inspection and maintenance of a school building—A case study." *Proc., QIC, National Meeting on Quality and Innovation in Construction*, LNEC, Lisbon, Portugal, 569–580, 2006.
- [7] H. Lind, and H. Muyingo, H, "Building maintenance strategies: planning under uncertainty," *Property Management*, Vol. 30, no. 1, pp. 14-28, 2012.
- [8] Lopes J.N.P., Morgado V., 2012, *Inspection and Maintenance Plan for Roofs in Current Buildings*, Instituto Superior Tecnico.
- [9] I. Flores-Colen, and J. de Brito, "A systematic approach for maintenance budgeting of buildings façades based on predictive and preventive strategies," *Construction and Building Materials*, vol. 24, no. 9, pp. 1718-1729, 2010.
- [10] A. Straub, "Using a condition-dependent approach to maintenance to control costs and performances," *Journal of Facilities Management*, vol 1, no. 4, pp. 380-395, 2002.
- [11] M. Riley, A. Cotgrave, "The Technology of refurbishment and Maintenance," Palgrave Macmillan. Basingstoke, 2005
- [12] T. Damen, L K. Quah, and H. C. M. van Egmond, "Improving the art and science of condition-based maintenance systems", in Quah, L.K. (Ed.), *Proceedings of the CIB W070 Symposium, The Way Ahead into the Millennium*, Singapore, McGraw-Hill, Singapore, pp. 141-8, 1998.
- [13] M. H. Hermans, "Deterioration characteristics of building components: a data collecting model to support performance management," Technische Universiteit Eindhoven, 1995.
- [14] L.W. Masters, (Ed.), "Problems in service life prediction of building and construction materials" vol. 95, Springer Science and Business Media, 2012.
- [15] S. Madureira, I. Flores-Colen, J. de Brito, and C. Pereira, C, "Maintenance planning of facades in current buildings," *Construction and Building Materials*, no 147, pp. 790-802, 2017.
- [16] R. A. Munro, M. J. Maio, M. B. Nawaz, G. Ramu, D. J. Zrymiak, "The Six Sigma Green Belt Handbook," Wisconsin: ASQ, 2007.

- [17] P. Pande, and L. Holpp, "What is six sigma?," New York: McGraw-Hill, 2001.
- [18] M. Ben-Daya, S. O. Duffuaa, A. Raouf, J. Knezevic and D. Ait-Kadi, "Handbook of maintenance Management and Engineering," Springer, London, 2009.
- [19] Z. Sönmez, "Six Sima methodology process improvement and an application in service sector," Istanbul Kultur University, Master thesis, İstanbul, 2013.
- [20] L. A. Zadeh, "The concept of a linguistic variable and its application to approximate reasoning—I," *Information sciences*, vol. 8, no.4, pp. 301-357, 1975.
- [21] T. L. Saaty, and L. G. Vargas, L. G, "Decision making with the analytic network proceses Economic, Political, Social and Technological Applications with Benefits, Opportunities, Costs and Risks, Springer Science+Business Media, LLC, New York, USA, 2006.
- [22] T. L. Saaty, "How to make a decision: the analytic hierarchy process," *Interfaces*, vol. 24, no. 6, pp. 19-43, 1994.
- [23] G. Pahl, W. Beitz, and K. Wallace, "Engineering Design: A Systematic Approach," London: Springer, 1996.
- [24] M. H. Tooley, and Knovel, "Design Engineering Manual (1st ed)," Amsterdam; London; Boston: Butterworth-Heinemann, 2010.
- [25] T. Tomiyama, P. Gu, Y. Jin, D. Lutters, C. Kind, and F. Kimura, "Design Methodologies: Industrial and Educational Applications," *CIRP Annals - Manufacturing Technology*, vol 58, no.2, pp. 543-565, 2009.
- [26] D. Shetty, "Product Design for Engineers," Boston: Cengage Learning, 2016.
- [27] G. Atkinson, "A century of defects." *Building*, 54–55, 1987.
- [28] CIB Working Commission W86, "Building Pathology: A State-ofthe Art Rep, International Council for Building Research Studies and Documentation," Rotterdam, The Netherlands, 1993.

JOURNAL OF SCIENCE



SAKARYA UNIVERSITY

Sakarya University Journal of Science

ISSN 1301-4048 | e-ISSN 2147-835X | Period Bimonthly | Founded: 1997 | Publisher Sakarya University |
<http://www.saujs.sakarya.edu.tr/en/>

Title: CSK based on Priority Call Algorithm for Detection and Securing Platoon from Inside Attacks

Authors: Mohammed AL SHEIKHLY, Sefer KURNAZ

Received: 2020-01-04 17:30:13

Accepted: 2020-07-08 02:35:10

Article Type: Research Article

Volume: 24

Issue: 5

Month: October

Year: 2020

Pages: 936-947

How to cite

Mohammed AL SHEIKHLY, Sefer KURNAZ; (2020), CSK based on Priority Call Algorithm for Detection and Securing Platoon from Inside Attacks. Sakarya University

Journal of Science, 24(5), 936-947, DOI:

<https://doi.org/10.16984/saufenbilder.670273>

Access link

<http://www.saujs.sakarya.edu.tr/en/pub/issue/56422/670273>

New submission to SAUJS

<http://dergipark.org.tr/en/journal/1115/submission/step/manuscript/new>

CSK based on Priority Call Algorithm for Detection and Securing Platoon from Inside Attacks

Mohammed AL-SHEIKHLY*¹, Sefer KURNAZ²,

Abstract

The platooning is an emerging concept in VANETS that involves a group of vehicles behaving as a single unit via the coordination of movement. The emergence of autonomous vehicles has bolstered the evolution of platooning as a trend in mobility and transportation. The autonomous vehicles and the elimination of individual and manual capabilities introduces new risks. The safety of the cargos, passenger and the advanced technology had increased the complication of the security concerns in platooning as it may attract malicious actors. In improving the security of the platoon, the threat and their potential impacts on the vehicular systems should be identified to ensure the development of security features that will secure against the identified risks. In this paper, two critical types of security breaches were identified those are Sybil attack and Delay attacks. Those security attacks can be somewhat disruptive and dangerous to the regular operation of the platoon leading to severe injuries, increased fuel consumption and delay the performance of the network. The research in this paper focuses on design, detection and the mitigation of attacks in a vehicle platoon. priority call algorithm in combination with color-shift keying modulation is used to protect the platoon alleviating the undesirable impacts such as collisions, oscillations and disintegration in the platoon caused by the attacks.

Keywords: VAENT, Priority call, Color-shift keying, Inside and Outside Attacks.

1. INTRODUCTION

With the increasing of traffic accident caused by human error that take millions of lives, recent studies showed that 60% of these accidents could be avoided if the driver had been warned half a second before the accident occur, for that it

become essential to implement intelligent transportation system to reduce not only the accident that caused by human error but also to reduce pollution and traffic congestion for more safety and road efficiency [1]. Autonomous vehicles consider the future of the transportation system, where vehicles will be able to take

* Corresponding Author: mohbar.isl@gmail.com

¹ Altinbas University, Electrical and Electronic Engineering, İstanbul, Turkey.

ORCID: <https://orcid.org/0000-0003-4694-152X>

² Altinbas University, Computer Engineering, İstanbul, Turkey. E-mail: sefer.kurnaz@altinbas.edu.tr

ORCID: <https://orcid.org/0000-0002-7666-2639>

decision and communicate with each other to share sensitive information such as accident warning, intersection warning and blind spot warning etc, even in bad weather without human intervention. Autonomous vehicles depend on the real time exchange of sensory data for decision making, for that communication system is a major part to achieve autonomous vehicles (self-driving vehicles). vehicular ad-hoc network (VANET) which is a network design to meet the requirement of autonomous vehicles by allowing vehicles approximately 300 meters from each other to communicate and share different kind of information for instance when accident is detected, vehicle will send this information to other vehicles in the same roads to avoid it [2]. In VANET there are sub network called platoon that consist of platoon leader any many other followers for more reliability and road safety in which all the vehicles in the platoon will have same speed, acceleration, inter vehicles distance and same destination, etc. In the same platoon vehicles will share its own information with other members but the platoon leader only has the ability to take decisions in the platoon. In each platoon there are two communication (internal and external), in which internal communication called vehicle to vehicle communication (V2V) where vehicles communicate with each other in the road and external communication with road side unit known as vehicle to infrastructure communication (V2I), in which the infrastructure will provide the vehicles with road condition and weather condition, etc [2]. The most important issue that facing such a network is its security, where it's essential that this network safe from different types of attacks, whether these attacks where passive or active attacks [4]. Currently, technologies such as IEEE 802.11p suffer from many weaknesses for its latency and wide coverage area that make it vulnerable to attacks [5]. to overcome this problem visible light communication (VLC) consider proper solution due to the directionality of the communication that this technology provides which make it difficult to interrupt by an outsider malicious actor and for much higher data rate that required by vehicular system [6]. In vehicular system there are two types of attacks inside attacks and outside attacks. In term of inside attacks which count the

most significant and critical attacks for such a network since one of the platoon members is the malicious actor meaning that this attacker able to send fake message from a trust member. In term of outside attacks, the attacker is an outsider meaning that the malicious actor is a vehicle near the platoon but not part of the platoon.

VANETs purpose of improving the protection of the highways, stopping collisions, supporting the passengers and help vehicles to interact with other vehicles [7]. VLC is a new technology that can overcome these attacks. problem of collaborative driving for vehicles platoon in the existence of message falsification vulnerability and communication weakness on wireless vehicular networks is investigated [8]. To secure the communication between vehicles new technology called VLC was proposed, to carry the digital information in wireless manner it will use modify light radiation in the visible light spectrum. VLC transceiver use LED to send the information and CMOS or diode image for the receiver. Improving safety performance and its long service, LED become common in automotive lighting. Similarly, many vehicles use CMOS for tracking purposes and parking assist. Previous studies have focused on VLC vehicle connections on derivation of channel characteristics [9], requirements [10][11], advanced modification schemes [6][12]. Few studies focus only on VLC security, but for non-vehicle scenarios [13].

Other studies focus on making independent vehicles more reliable and support decision-making by referring to the confidence system while integrating the maneuver scenario into the platoon. Vehicles that want to join the platoon and the relationship between platoon members have been described in the case of priority and speed adjustment but not in the security situation [14].

In [15] proposed a scheme not for eliminate the sybil attack but only to suppress the attack based on signal strength distribution. This study shows that verification error rate significantly reduced. In [16] proposed detection scenario for sybil attack based only on road side unit. This study shows that this method enormously decreases the effect of Sybil attacks. This study did not take in consideration the inside attack where the

malicious actor is not an outsider vehicle but as a vehicle part of the platoon.

Delay attack is one of the most serious attack that reduce the stability of the platoon due to the necessity of real time exchange of sensory data by adding extra time slot to the message. In [17] proposed delay attack detection based on intrusion detection system (IDS), in which sensors will observe the network by illegal listening to the transmission of its neighbors. But this detection system designed for a specific topology and their appropriate reconfiguration for various purposes or topologies is not discussed. In [18] a misdirection attack and topologies analysis were investigated where the attacker (malicious actor) will misdirect the packet to another vehicle to affect the stability and reduce efficiency due to the high delay caused by this attack. The study shows that wireless sensor network (WSN) performance in tree topology better than mesh topology.

This paper aim to detect and secure the platoon from inside attacks in particular (sybil and delay) attacks. To design secure platoon, we introduced the possible instances of attacks which can be implemented by malicious actors to exploit the weaknesses in the visible light communication algorithm used in the platoon. In securing the platoon, we explored the ability of the attacker to disrupt the traditional performance of the platoon via the control of the vehicles and modification of the control law. Further, a detection algorithm is proposed to isolate the attacker in the platoon as the first step towards mitigation of the control law. Ultimately, a priority call algorithm in combination with color-shift keying modulation is used to protect the platoon alleviating the undesirable impacts such as collisions, oscillations and disintegration in the platoon caused by the attacks.

The rest of this paper is organized as follows. Section II describes the system model in term of the platoon and attacker formation. Section III presents our result in term of detecting and securing the platoon from those attacks. Finally, concluding remarks given in Section IV.

2. SYSTEM MODEL

This section will evaluate the two internal integrity attacks i.e. Sybil and delay attack. The two attacks have been evaluated in the previous section and they tend to affect the vehicular ad hoc networks (VANET) especially in the platooning of vehicles. The design will provide the structure and communication of the platoon and the simulation design of the attacks and the solution.

2.1. Platoon Model

The structure of the platoon will be based on the following spatial position and functionalities where the vehicles can be classified into the following important roles as illustrated in the “Fig. 1”. The behavior of vehicles in the Platoon in this model will not only rely on their driver’s objectives but also consider the management and constraint from the Platoon control center i.e., the leader vehicle [19]. Remember vehicles will transmit request messages in case the driver wants to alter the driving behavior to match up with its own need such as arrest or destination. This characteristic will be vital in case of attacks especially internal breaches [20]. Upon reception of the request the leader will make judgement based on the condition of the traffic at the time of request. In case the leader vehicle responds to the request then all the vehicles in the Platoon will have to adjust their behavior to align with the new instructions to maintain stability in the platoon. Thus, considering the dynamics of the vehicle in the platoon then the control law may be used to describe the relationship in the platoon using the following equations;

$$\dot{x}_1 = v_1 \quad (1)$$

Then the vehicle dynamics for the first vehicle can be expressed as;

$$\dot{v}_1 = -k_p^1 x_1 + k_p^1 x_2 + k_p^1 d + k_p^1 v_1 + k_p^1 v_2 \quad (2)$$

For the second vehicle

$$\dot{x}_2 = v_2 \quad (3)$$

Vehicle dynamics for the second vehicle can be expressed as

$$\dot{v}_2 = k_p^2 x_1 + k_p^2 x_2 + k_p^2 d + k_p^2 x_3 + k_p^2 x_3 - k_p^2 d + k_d^2 v_1 + 2k_d^2 v_2 + k_d^2 v_3 \quad (4)$$

For the n-1th vehicle

$$\dot{x}_{n-1} = v_{n-1} \quad (5)$$

Vehicle dynamics for the n-1 vehicle can be expressed as

$$\dot{v}_{n-1} = k_p^{n-1} x_{n-2} + k_p^{n-1} x_{n-1} + k_p^{n-1} d + k_p^{n-1} x_3 + k_p^2 x_n - k_p^{n-1} x_{n-1} + k_p^{n-1} d + k_d^{n-1} v_{n-2} - 2k_d^{n-1} v_{n-1} + k_d^{n-1} v_n \quad (6)$$

For the nth vehicle

$$\dot{x}_n = v_n$$

Vehicle dynamics for the n-1 vehicle can be expressed as

$$\dot{v}_{n-1} = k_p^n x_{n-1} + k_p^n x_n + k_p^n d + k_d^n v_{n-1} - k_d^n v_n + u \quad (7)$$

Where

v_i is the velocity of the i th vehicle

x_i is the position of the i th vehicle

k_p^i is the proportional gain

k_d^i is the derivate gain

u is the control unit i.e., the leader.

From the above model equation the value for k_p is constant whereas the value for the k_d is a variable based on the size of the platoon.

1) Leader vehicle: This is conventionally the first vehicle in the platoon. The vehicle is tasked with the roles of establishing and furnishing the platoon with coordinates using the advanced traffic management system [21]. The advanced traffic management system utilized by the platoon leader is vital for the controlling of driving behavior of the other platoon vehicles, the

collection of data from the other vehicle and the roadside units, broadcasting of information to the platoon [19]. The movement of the platoon leader forms the reference for all the other platoon vehicles.

2) Member vehicle: These are the vehicles within the platoon that follow the platoon leader and are located neither at the front door at the back [22]. These vehicles receive specified control messages from the leader and the preceding member vehicles.

3) Relay vehicle: This can be any member of the platoon charged with assisting the leader vehicle in conveyance of messages to all the other respective member vehicles.

4) Free vehicle: These are the vehicles that do not belong to any platoon [20]. In the event that they want to join a platoon they will send a request to the leader who will grant permission and that it can perform the join operation.

5) Tail vehicle: This the vehicle located at the tail end of the platoon. it is essential for the inter-platoon communication [19]. The vehicle is vital and responsible for establishment of connection with the next platoon.

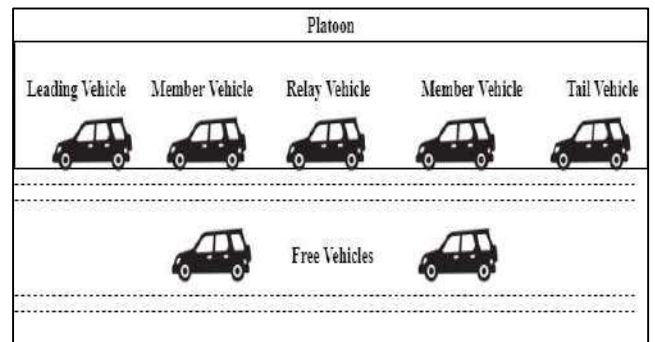


Figure 1 The Model of the platoon

2.2. Communication Model

The intra-vehicle communication is vital in achieving the platoon stability. The stability is maintained by constant and reliable exchange of information between the vehicles in the platoon as illustrated in “Fig. 2”. The call mechanism of platoon communication is the V2V scheme. The visible light communication (VLC) system will

be used for the vehicle to vehicle communication in the platoon [23]. The transmission will be such that the flow of the information will be from the leader to the second vehicle to the succeeding vehicle in a consecutive manner. Additionally, there will be no broadcasting the VLC system so that malicious actors can be detected easily. The broadcast mode in this model will be different from the traditional schemes as not all the vehicles in the platoon will be required to transmit an acknowledgement (ACK) to prevent the occurrence of an acknowledgements storm. In case that the transmission fails in broadcast mode, the source vehicle will not retransmit the lost packets. The Request To Send / Clear To Send (RTS/CTS) access mode will not be applied as it will lower performance in the broadcast mode due to the mobility in the platoon and the increased overhead [23]. The longitudinal movement of the vehicles in a Platoon will be affected by the leader therefore the communication framework should ensure that the leader receives information from each vehicle in the platform. Thus, it is assumed that the length of the platform will not exceed the communication range R of the leaders hence restricting the communication range [19]. The vehicle in the platoon will be fixed with a transceiver for communication. In this model, the leader can send information to any member of the platoon while all the other vehicles can only send information to the following member vehicle. The leader will transmit the control information which dictate the behavior of the vehicles such as accident warning, driving behavior and traffic conditions [24]. The non-control information will entail application data such as media, office services and entertainment. The movement of the control information affect the stability and safety of the platoon therefore in this research we will consider the flow of control data.

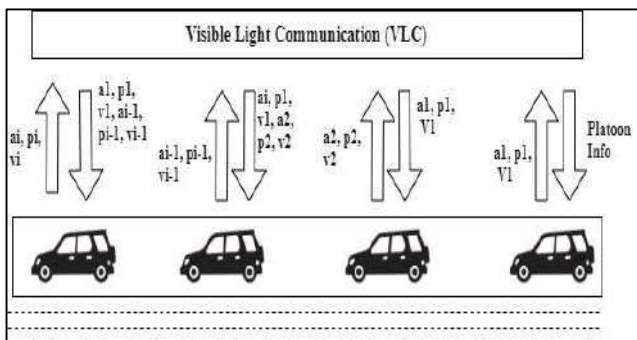


Figure 2 The visible light communication framework for the platoon

2.3. VEHICLE CONTROL MODEL

The dynamics of the platoon vehicle is non-linear but they can be linearized when certain assumptions and feedbacks are applied. Therefore, a simple model is applied for the dynamic model for the longitudinal motion in the platoon. The communication will be based on the leader-predecessor scheme as demonstrated in “Fig. 3”. The spacing error can be defined using the following system equations.

$$\epsilon_i = p_{i-1} - p_i - l_{i-1} - \mathcal{G}_{i-des} \quad (6)$$

Where

p_i is the position of the i th vehicle

p_{i-1} is the position of the preceding vehicle

l_{i-1} is the length of the preceding vehicle

\mathcal{G}_{i-a} is the desired gap between the two

At $t = 0$ at initial condition $\epsilon_i(0)$ is the geared towards the objective of attaining convergence at

$$\epsilon_i(t) \rightarrow 0, \text{ where } t \rightarrow \infty$$

Taking the initial condition of $\epsilon_i = 0$ the desired position of the i th vehicle can be calculated as

$$p_{i-des} = p_{i-1} - l_{i-1} - \mathcal{G}_{i-des} \quad (7)$$

The desired acceleration can be compute considering the feedback messages such as the speed, acceleration and the position of the preceding vehicle and the position desired by the leader vehicle thus the acceleration will be expressed as;

$$u_{i-des} = (1 - q_1)a_{i-1} + q_1a_l - q_2(v_i - v_{i-1}) - q_3(v_i - v_l) - q_4 \epsilon_i \quad (8)$$

Where

q_1, q_2, q_3 and q_4 are the design parameters

l denotes the leader

Further, in this model a first-order filter will be utilized to model the signal processing delay and actuator lag in the platoon as demonstrated below.

$$u_{i-des} = (1 + \mu s)u_i \quad (9)$$

Where μ is the collective delay such as actuator delay (which is a constant), sensor detection, processing delays and control delay.

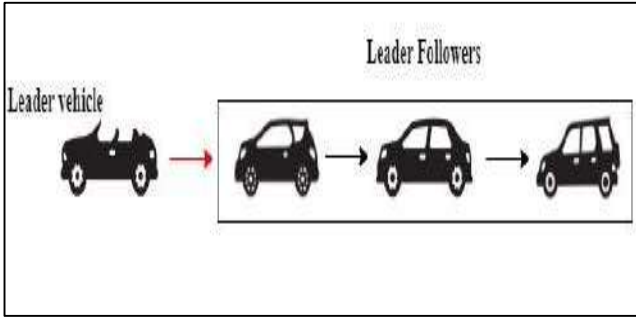


Figure 3 The leader-predecessor flow of information

2.4. Threat Model

In this research we will consider a case of a single actor in control of a vehicle that is in an already established platoon. The vehicle will be travelling at a constant speed as the rest of the members of the platoon and will attempt to destabilize or take control of the platoon [21]. The attacker in this may attain its objective by causing the vehicle under control to subvert or ignore the control information does leading to follower separation. The vehicle under the controller will not obey any laws regarding modification or change in direction of the movement [24]. The attacker’s vehicle possesses the same ability as all the vehicles in the platoon. To illustrate that the attacker is capable of destabilizing the platoon operations without possessing nominal control then it will be assumed that the vehicle under control is not the leader of the platoon. The state-space representation of the linear time-invariant (LTI) system when a vehicle is under the control of an attacker will be represented as

$$\dot{x} = Ax + Bu \tag{12}$$

$$y = Cx \tag{10}$$

Where x is the state of all the vehicles in the platoon and can be expressed as;

$$x = [x_1, v_1, x_2, v_2 \dots, x_n, v_n]^T \in \mathbb{R}^{2n} \tag{14}$$

$$A \in \mathbb{R}^{2nx2n}$$

$B \in \mathbb{R}^{2nx2}$, has non-zero entries for both the leader and the attacker

C is the identity matrix

$$u = [u_l u_a]^T$$

u_l is the state of the leader

$u_a = a \sin \omega t$ is the state of the attacker where a is the amplitude of attacker’s input and ω is the frequency.

The primary goal of the attacker will be to cause instability in the network through the modifications of the entries of A . The attacker will attain the $a \sin \omega t$ point so as to convey messages and cause instability.

2.5. Priority Scheduling for Attack Detection

This is a non-preemptive algorithm that is commonly used in batch systems. This algorithm will be modified to conform to the commands send by the leader. The control commands from the leader have more precedence that all other commands. All the member vehicles in the platoons will scan for control commands before acting to any other form of instruction. Therefore, during an attack especially Sybil attack the member vehicles will scan for control instructions from the leader. In case of conflicting commands, the vehicle will act on the information with the highest level of precedence. The priority call algorithm will be implemented as demonstrated in “Fig. 4”;

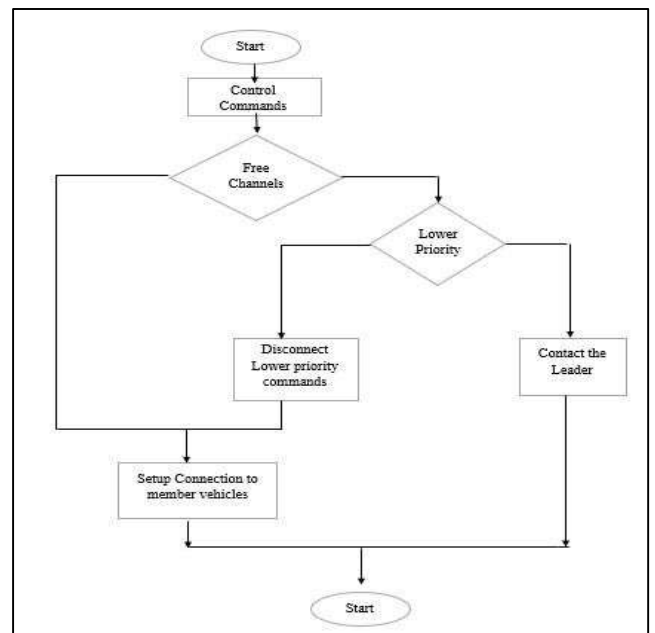


Figure 4 priority call algorithm

3. RESULT

This section talks about the effects, detection and the mitigation of sybil and delay attacks by using priority call algorithm in combination with color-shift keying modulation to protect the platoon alleviating the undesirable impacts such as collisions, oscillations and disintegration in the platoon caused by the attacks.

3.1. Visible Light Communication

The leader is fixed with VLC sensors which uses light to send control communication to the succeeding vehicles in the platoon. The communication from the leader to the second vehicle is dependent on the luminous intensity of the light in the VLC as illustrated in “Fig. 5”.

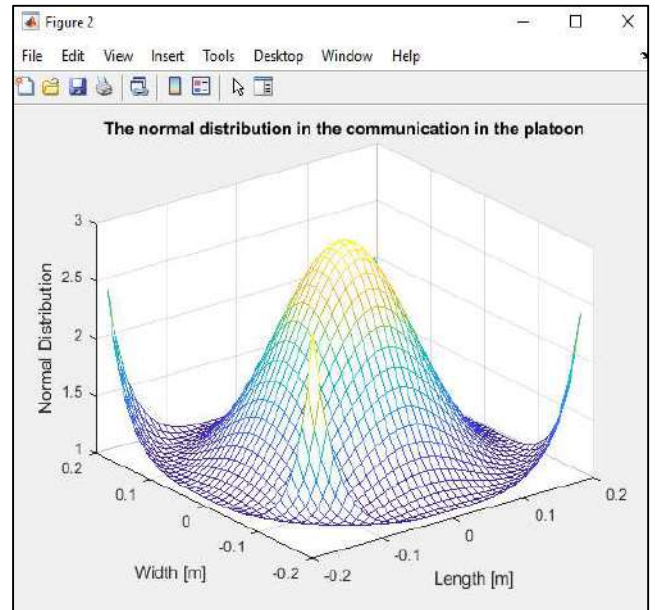


Figure 6 The normal distribution leader and the vehicles in the platoon [25]

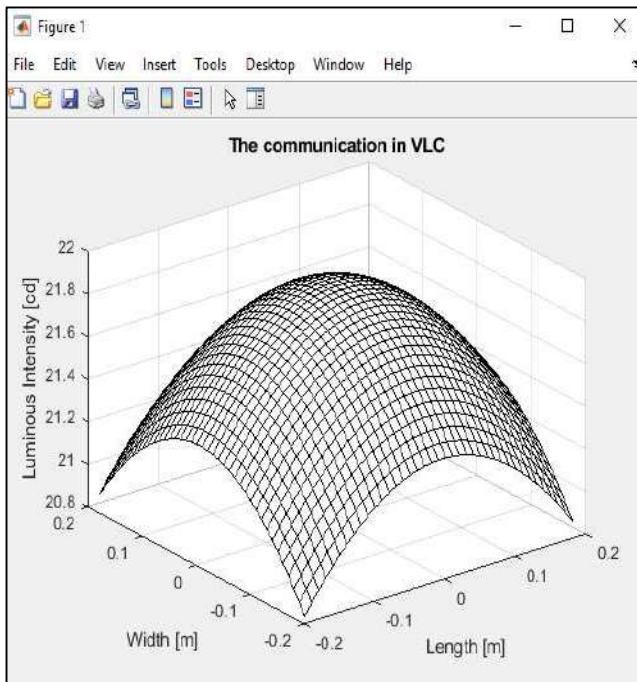


Figure 5 The visible light communication scheme between the platoon vehicles [25]

Thus, using the VLC scheme the normal distribution can be completed as illustrated below for the communication from one vehicle to the next in the platoon.

Further, the leader uses the flow of communication in the VLC scheme to detect any break in communication caused by a malicious actor. The malicious actor in the platoon will be detected as a break in the light communication between the leader and the rest of the platoon vehicle. The simulation for this proposed framework commenced with the creation of the ideal scenario where the communication of the platoon vehicles via VLC will be greatly impaired by the malicious actor. in “Fig. 6” above illustrate that the connectivity of the vehicles for VLC will increase exponentially with increase in the luminous intensity of the light. The changes in the traffic will not significantly affect VLC communication, therefore, for ideal case we expect the communication between the member vehicles and the leader vehicle to behavior in a similar manner unlike IEEE 802.11p as shown in “Fig. 7”, where duration time increase with the increasing of traffic density.

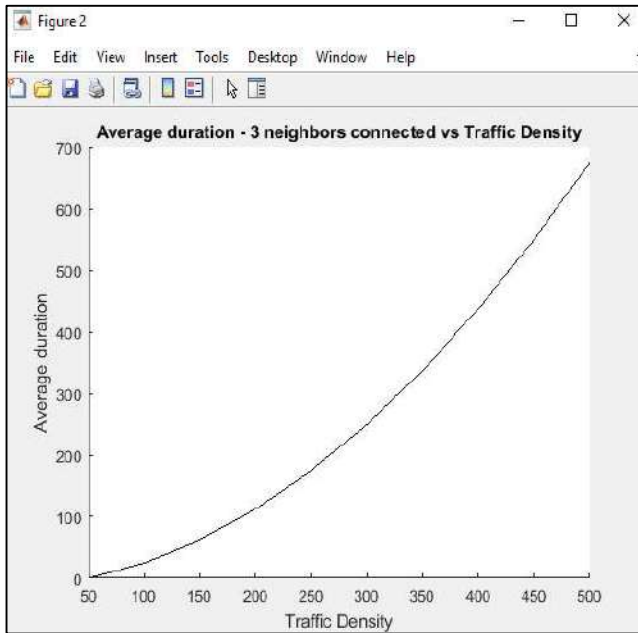


Figure 7 The duration of V2V communication for the normal communication of platoon vehicles. The graph illustrates the time taken for communication between the vehicles in the platoon as the vehicle increases [25]

The average duration describes the delay in the system. The delay behaves in a similar fashion as the VLC communication as rate of communication determine the waiting time for acknowledgement in the system. The average waiting time increases in the system with the increase in the number of vehicles in the traffic as well as the platoon.

3.2 Sybil Attack

The simulation was based on a real scenario where the vehicles in the platoon are expected to negotiate an intersection and take the forward route. In the model the leader will communicate the dynamics of the road to detect the behavior of the vehicles as they negotiate the intersection. The rate of communication of the control information will be based on the VLC communication where the malicious actor will hinder information moving to the vehicle.

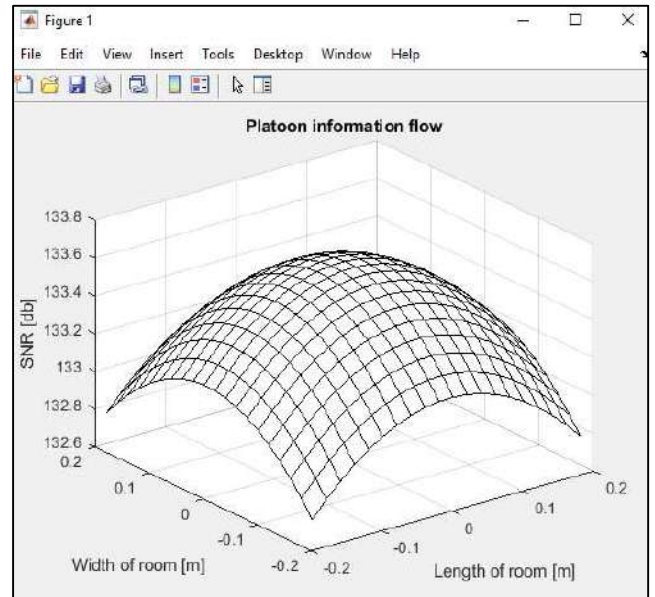


Figure 8 The normal flow of information in the platoon [25]

In the normal scenario the vehicles will communicate the control information between each other through VLC. Alternatively, the attacker will be an impediment to the traditional communication between the vehicles in the platoon. Considering the attacker is located within the platoon vehicles then the VLC scheme integrity will decay rapidly until it become non-existent in cases of longer distances from the leader.

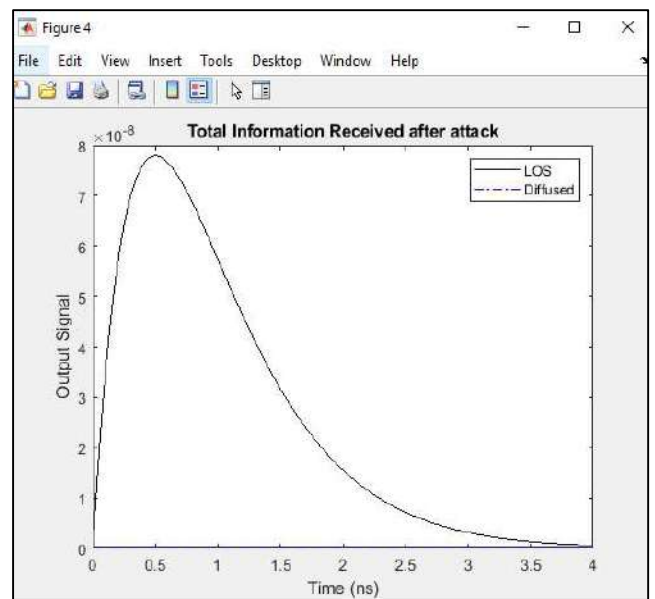


Figure 9 The change in the VLC communication received during the attack in the platoon [25]

The VLC will enable the conveyance of the control information from the leader to the tail vehicle. The proportion of VLC communication should increase to a certain point of integrity where it cannot be affected by the number of vehicles in the platoon provided they are within the range of each platoon member. In the event of an attack the proportion of VLC communication will be compromised thus decrease rapidly hindering the transmission of the control information from the leader to the tail vehicle as illustrated in “Fig. 9”. The attack will diminish the efficiency of the diffused VLC hence it will appear nonexistent compared to the LOS.

3.3 Delay Attack

The delay attack will occur in a similar fashion as the Sybil attack in which the attacker will try to take control of the vehicle as well as the follower. “Fig. 10” illustrate the delay leading to the loss of communication in the platoon. The attacker will lead to reduced flow of information via VLC scheme.

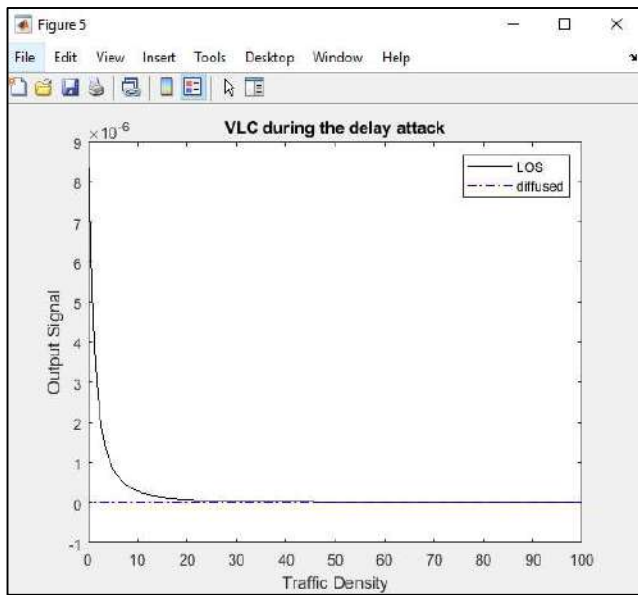


Figure 10 The delay in the communication in the system [25]

3.4 Detection and Mitigation

The second simulation was to detect the attacker where the parameter for the gains and the estimated alterations are identified. The system incorporated a detection and mitigation mechanism. The method was applied to the data

used in the attack simulation. “Fig. 11” illustrate that the information flow will build exponentially in the VLC communication as each vehicle waiting for its turn to transmit. Whereas “Fig. 12” illustrate the time taken to detect the attacks with the increase in the traffic density in the platoon.

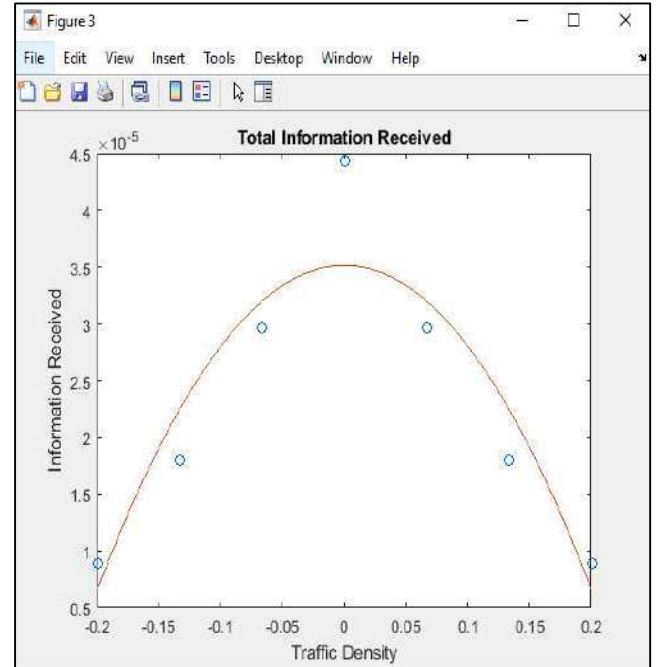


Figure 11 The detection of the attackers and subsequent mitigation. The graph illustrates the communication between the members of the vehicles after mitigation of the attack [25]

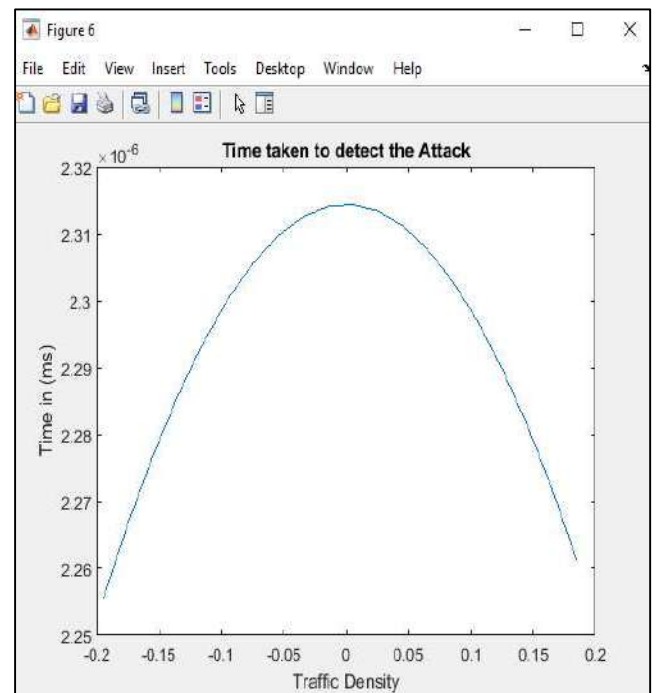


Figure 12 The time taken for the detection of the attacks [25]

To address the attacks, the vehicles should always fetch the control information before acting to other commands. The priority of the control information will prevent splitting at the intersection. For instance, when a vehicle receives a split or turn command which will affect its dynamics such as position and velocity will have to search and check for commands from the leader before acting on the information.

3.5 Color Shift Keying

After detection platoon security will be implemented using the color-shift keying (CSK). CSK is a VLC modulation scheme used to transmit information by altering the light intensity. In this research we recommend a light-to-frequency (LTF) converter. In this system the receiver will decode the symbols with regards to the frequency of transmission. Once there is a drop in the intensity of the light transmitted in the platoon the CSK will be implemented to alter the intensity of the RGB coupling with radio frequency to ensure security of the communication. The CSK will use coded symbols to transmit the control information from the leader.

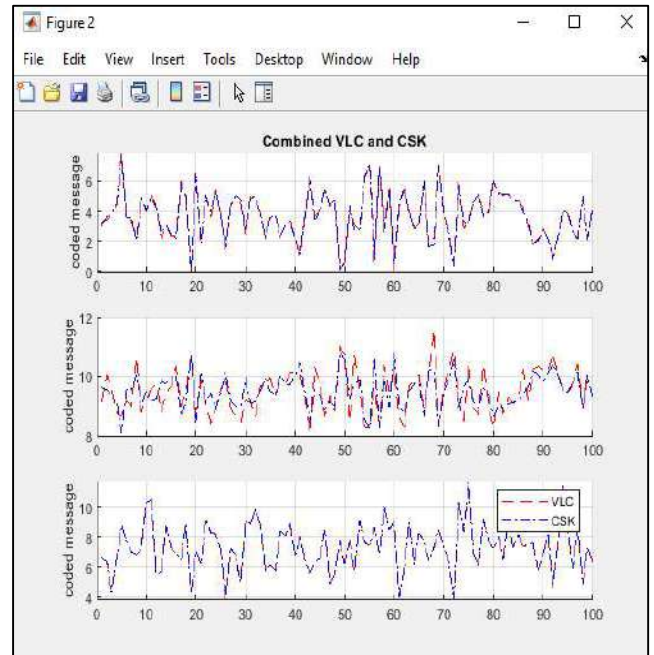


Figure 14 VLC communication coded using CSK [25]

4. CONCLUSION

This research has shown that the vehicular networks have the potential of becoming a vital application of the Ad hoc networks. Platooning is a special application of these networks being applied in autonomous vehicles presenting several security challenges in communication. The security challenges in VANETs and vehicle platoon need to be addressed using new communication perspectives. In vehicle platoon, security consideration is considered as paramount over all other networking elements. The application of a robust security system will ensure the resilience of the vehicle platoon in the presence of interference and other communication problems that can induce an error in VANETs. This research has shown that security for vehicle platoon can be achieved through the application of two techniques to detect and mitigate interruption in the visible light communication algorithm used in the network. The network and the attack scenarios were simulated in MATLAB [25] to create a simplified detection and mitigation system to counter the effects of the breaches and guarantee security thereafter. The results of the research illustrated that a vehicle in the platoon that is under a modified control system and being operated by a malicious actor would interrupt and destabilize the normal operation of the platoon.

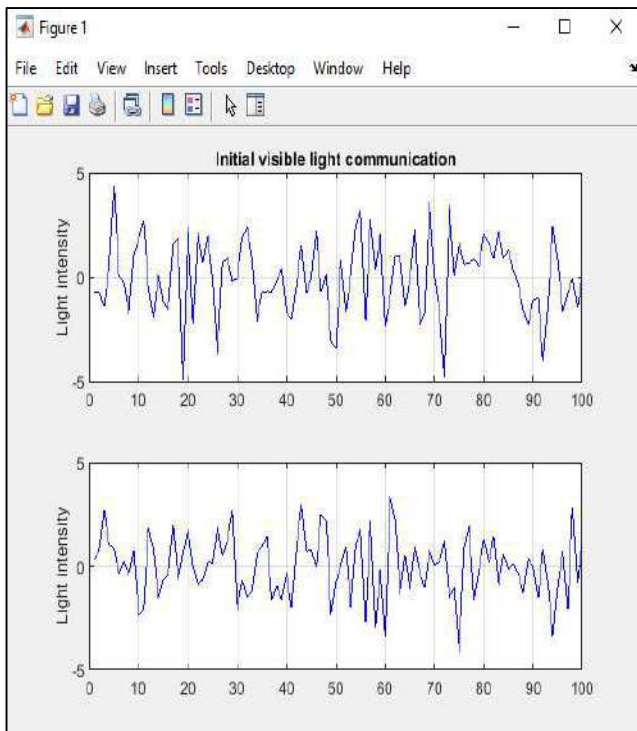


Figure 13 The initial VLC communication after attack [25]

The communication of the vehicles in the platoon will provide the first incites on the attacks in the system.

Using MATLAB [25], a model was created to simulate the multiple scenarios of attack. The model created several aspects of the vehicle platoon; the physical operation of the platoon, the communication in the Ad hoc network via visible light communication (VLC), possible security breaches and the effect of attacks on the platoon and the Ad hoc network. The scenarios were created based on the underlying knowledge collected during the literature review. The information gathered led to the decision to incorporate the physical and the network aspect of the vehicle platoon in the simulations. The network design was independent of the vehicles; thus, different communication protocols can be implemented. The defenses were tested using attack scenarios. The behavior of the network was used to identify the different types of attacks. The attacks were mitigated using a variant of the priority call algorithm and the system secured using the color-shift keying algorithm.

Funding

The authors received no financial support for the research, authorship, and/or publication of this paper.

The Declaration of Conflict of Interest / Common Interest

No conflict of interest or common interest has been declared by the authors.

Authors' Contribution

Both authors contributed equally to the design and implementation of the research, to the analysis of the results and to the writing of the manuscript.

The Declaration of Ethics Committee Approval

The authors declare that this document does not require an ethics committee approval or any special permission.

The Declaration of Research and Publication Ethics

The authors of the paper declare that they comply with the scientific, ethical and quotation rules of SAUJS in all processes of the article and that they do not make any falsification on the data collected. In addition, they declare that Sakarya University Journal of Science and its editorial board have no responsibility for any ethical violations that may be encountered, and that this study has not been evaluated in any academic publication environment other than Sakarya University Journal of Science.

REFERENCES

- [1] B. Chen, "A cooperative control method for platoon and intelligent vehicles management," pp. 1–5, 2017.
- [2] F. Sakiz and S. Sen, "A survey of attacks and detection mechanisms on intelligent transportation systems: VANETs and IoV," *Ad Hoc Networks*, vol. 61, pp. 33–50, 2017.
- [3] S. Zhao, T. Zhang, N. Wu, H. Ogai, and S. Tateno, "Vehicle to Vehicle Communication and Platooning for EV with Wireless Sensor Network," pp. 1435–1440, 2015.
- [4] S. Rehman, M. A. Khan, T. A. Zia, and L. Zheng, "Vehicular Ad-Hoc Networks (VANETs) - An Overview and Challenges," vol. 3, no. 3, pp. 29–38, 2013.
- [5] V. L. Hybrid, "IEEE 802.11p and Visible Light Hybrid Communication Based Secure Autonomous Platoon," *IEEE Trans. Veh. Technol.*, vol. 67, no. 9, pp. 8667–8681, 2018.
- [6] S. Ucar, S. C. Ergen, and O. Ozkasap, "Visible light communication in vehicular ad-hoc networks," in *2016 24th Signal Processing and Communication Application Conference (SIU)*, 2016, pp. 881–884.
- [7] S. Ucar, B. Turan, S. Colen, O. Ozkasap, and M. Ergen, "Dimming Support for Visible Light Communication in Intelligent Transportation and Traffic System," pp. 1193–1196, 2016.

- [8] A. Petrillo, A. Pescap, and S. Santini, "A collaborative control strategy for platoons of autonomous vehicles in the presence of message falsification attacks," pp. 110–115, 2017.
- [9] H. Menouar, "Visible Light Communication," no. december, pp. 45–53, 2015.
- [10] Tseng, Y. Wei, A. Chen, H. Wu, H. Hsu, and H. Tsai, "Characterizing Link Asymmetry in Vehicle-to-Vehicle Visible Light Communications," pp. 88–95, 2015.
- [11] P. Luo, Z. Ghassemlooy, H. Le Minh, and E. Bentley, "Performance analysis of a car-to-car visible light communication system," no. March, 2015.
- [12] M. Y. Abualhoul, M. Marouf, O. Shagdar, and F. Nashashibi, "Platooning Control Using Visible Light Communications: A Feasibility Study," no. Itsc, pp. 1535–1540, 2013.
- [13] W. Whyte, A. Weimerskirch, V. Kumar, and T. Hehn, "A Security Credential Management System for V2V Communications," pp. 1–8, 2013.
- [14] X. U. S. H. S. Hen and U. N. O. F. W. Aterloo, "Complementing Public Key Infrastructure To Secure Vehicular AD HOC Networks Albert Wasef And Rongxing L U , University Of Waterloo," no. October, pp. 22–28, 2010.
- [15] X. Bin, Y. Bo, and G. Chuanshan, "Detection and localization of sybil nodes in VANETs," DIWANS 2006 - Proc. 2006 Work. Dependability Issues Wirel. Ad Hoc Networks Sens. Networks (part MobiCom 2006), vol. 2006, pp. 1–8, 2006.
- [16] S. Chang, Y. Qi, H. Zhu, J. Zhao, and X. Shen, "Footprint: Detecting Sybil attacks in urban vehicular networks," *IEEE Trans. Parallel Distrib. Syst.*, vol. 23, no. 6, pp. 1103–1114, 2012.
- [17] M. Stehlik, V. Matyas and A. Stetsko "Towards Better Selective Forwarding And Delay Attacks Detection in Wireless Sensor Networks," no. April, 2016.
- [18] R. S. Sachan, M. Wazid, and R. H. Goudar, "Misdirection Attack in WSN: Topological Analysis and an Algorithm for Delay and Throughput Prediction." *Proceedings of 7th International Conference on Intelligent Systems and Control (ISCO 2013)*
- [19] Y. Zhang and G. Cao, "V-PADA: Vehicle-Platoon-Aware Data Access in VANETs," *IEEE Transactions on Vehicular Technology*, vol. 60, no. 5, pp. 2326–2339, 2011.
- [20] M. Su. and S. Ahn, "Autonomous platoon formation for VANET-enabled vehicles," in 2016 International Conference on Information and Communication Technology Convergence (ICTC), Jeju Island, Korea, 2016.
- [21] H. Hexmoor, S. Alsamarace and M. Almaghshi, "BlockChain for Improved Platoon Security," *International Journal of Information Systems and Computer Sciences*, vol. 7, no. 2, pp. 1-6, 2018.
- [22] M El-Zaher, B. Dafflon, F. Gechter, and J.-M. Contet, "Vehicle platoon control with multi-configuration ability," *Procedia Computer Science*, vol. 9, pp. 1503 – 1512, 2012.
- [23] M. Amoozadeh, A. Raghuramu, C.-N. Chuah, D. Ghosal, M. H. Zhang, J. Rowe, and K. Levitt, "Security vulnerabilities of connected vehicle streams and their impact on cooperative," *IEEE Communications Magazine*, vol. 53, no. 6, pp. 126-132, 2015.
- [24] J. Liu, D. Ma, A. Weimerskirch and H. Zhu, "Secure and Safe Automated Vehicle Platooning," *IEEE Reliability Society*, Detroit, 2016.
- [25] MATLAB, R2019a (9.6.0.1072779), 64-bit(win 64), March 8, 2019, License Number 968398. Professional License.

JOURNAL OF SCIENCE



SAKARYA UNIVERSITY

Sakarya University Journal of Science

ISSN 1301-4048 | e-ISSN 2147-835X | Period Bimonthly | Founded: 1997 | Publisher Sakarya University |
<http://www.saujs.sakarya.edu.tr/en/>

Title: The Potential of the Karaman Wastewater Treatment Plant to Generate Electricity with MHP and Reduction of Electricity Bill Amounts by Adjusting Working Hours of the Facility

Authors: Ufuk SÜGÜRTİN, Türker Fedai ÇAVUŞ

Received: 2020-03-20 09:06:45

Accepted: 2020-07-13 01:02:16

Article Type: Research Article

Volume: 24

Issue: 5

Month: October

Year: 2020

Pages: 948-955

How to cite

Ufuk SÜGÜRTİN, Türker Fedai ÇAVUŞ; (2020), The Potential of the Karaman Wastewater Treatment Plant to Generate Electricity with MHP and Reduction of Electricity Bill Amounts by Adjusting Working Hours of the Facility. Sakarya University Journal of Science, 24(5), 948-955, DOI:

<https://doi.org/10.16984/saufenbilder.706169>

Access link

<http://www.saujs.sakarya.edu.tr/en/pub/issue/56422/706169>

New submission to SAUJS

<http://dergipark.org.tr/en/journal/1115/submission/step/manuscript/new>



The Potential of the Karaman Wastewater Treatment Plant to Generate Electricity with MHP and Reduction of Electricity Bill Amounts by Adjusting Working Hours of the Facility

Ufuk SÜĞÜRTİN^{*1}, Türker Fedai ÇAVUŞ²

Abstract

In this study, in order to reduce the electricity consumption / cost of the Karaman Wastewater Treatment plant, which has the highest flow and electricity consumption in Sakarya, the arrangements that can be made during the working hours of the treatment plant and the generation of electricity by the MHP that can be installed between the outlet of the facility and the discharge point of the wastewater are examined. A change of 17% in the electricity bill costs and up to 50% in the flow rates were observed. Wastewater treatment plant projects keep their capacities high, considering the needs of the next 20-30 years. Based on these results, it is determined that if the electricity consumption amounts in the peak time interval where the unit price of electricity is high is shifted to day and night time zones, the electricity costs of the facilities will decrease. In addition, it has been shown that a part of its own electricity consumption will be met by the micro hydro power plant to be installed between the outlet of the facility and the discharge point.

Keywords: Micro hydro power plant, electricity, wastewater treatment plant,

1. INTRODUCTION

According to the water pollution control regulation, wastewater is defined as contaminated or partially or completely altered waters as a result

of domestic, industrial, agricultural and other uses [1]. The wastewater infrastructure facility is defined as the systems and facilities in which wastewater is treated and the final disposal of treated wastewater is achieved through the entire

*Corresponding Author: ufuk.sugurtin@gmail.com

¹Sakarya University, Electrical Electronics Engineering Department, Turkey.

ORCID: <https://orcid.org/0000-0002-0889-5684>

²Sakarya University, Electrical Electronics Engineering Department, Turkey. E-Mail: tfcavus@sakarya.edu.tr

ORCID: <https://orcid.org/0000-0003-1399-8044>

sewage system that collects domestic and industrial wastewater. Turkey is an energy dependent country. In 2018, electricity consumption in Turkey was 304.2 TWh and electricity generation was 304.8 TWh. Electricity consumption is estimated to reach 375.8 TWh in 2023. The installed capacity of Turkey was 90.72 GW as of September 2019 [2].

As of September 2019, according to the sources where energy is produced, the installed power distribution in Turkey; 28.6% natural gas, 31.4% hydraulic energy, 8.1% wind, 6.2% solar, 22.4% coal, 1.6% geothermal and 1.7% is in the form of other sources. Turkey's electricity generation according to sources in 2018 are given in Table 1.

Table 1
Electricity Generation of Turkey In 2018 [2]

Electricity Generation of Turkey In 2018	
Coal	% 37.3
Natural Gas	% 29.8
Hydraulic Energy	% 19.8
Wind	% 6.6
Sun	% 2.6
Geothermal energy	% 2.5
Other Source	% 1.4

In Turkey, there are 597 hydroelectric plants and their total installed power capacity is 26.7 GW [3]. Aimed at reducing greenhouse gas emissions, the Kyoto Protocol was signed in Turkey. [4].

In 2017, 86.3% of total CO₂ emissions are caused by energy. 34.6% of this constitutes electricity and heat generation. [5]. A large part of the carbon dioxide emission that causes greenhouse effect results from the use of fossil fuels in energy generation and consumption [6]. Therefore, increasing electricity production from renewable power is important. Turkey is a country rich in water resources, but this potential of Turkey cannot be utilized sufficiently.

In this article, a study was made to draw attention to the operation of wastewater treatment plants in an optimized way to reduce the electricity costs, in the Karaman wastewater treatment plant in Sakarya, and the earnings were calculated. Secondly, it is predicted that part of the electricity consumption of the facility will be met by the micro hydroelectric power plant to be installed between the outlet of the Karaman Wastewater

Treatment plant and the discharge point. There are two peak flows in one day. The first happens in the morning, when daily life begins, and the second happens in the evening. Minimum consumption during the day generally occurs around 4.00 AM [7].

2. WASTEWATER AND TREATMENT PLANTS

These are the facilities that ensure the treatment of wastewater coming through the sewage system that collects domestic and / or industrial wastewater, by subjecting them to processes that will not harm the environment and the receiving environment. Apart from rainwater, we can examine the wastewater in three groups as domestic, industrial wastewater and leachate [8]. While industrial water consumption is 5 billion m³, it is predicted that it will be 22 billion m³ in 2023 [9]. Wastewater treatment plants consume large amounts of electricity due to the devices / engines used in their processes during cleaning these contaminated waters. Considering of Turkey dependence on imported energy, it is very important to take measures to reduce the electricity consumption and costs of wastewater treatment plants. There are almost 250000 water service facilities in the world. Nearly 90% of these facilities are from municipalities. 8% of these facilities are almost privately operated.

Municipalities discharged 4.8 billion m³ of wastewater according to the results of the waste water statistics survey announced by TÜİK in 2018 and organized for municipalities. The average daily amount of wastewater per person discharged by municipalities by sewerage network was calculated as 188 liters [10].

2.1. Wastewater Treatment Electricity Consumption

Electricity consumption of wastewater purification facility varies depending on the methods selected for wastewater quantity, concentration, treatment processes, topography of the facility area, energy efficiency of the equipment used in treatment and the level of automation at the facility. In a study conducted in

Norway, 0.8 kWh of energy was consumed to treat 1 cubic meter of wastewater, which is twice the energy required to provide the same amount of drinking water [11].

2 to 3 % of the electricity generated in the world is used in the production, distribution and treatment of water [12]. An average of 0.4 kWh electricity is consumed for 1 m³ of wastewater treatment in Germany, and it is stated to be 0.29 kWh in China, 0.20 kWh / m³ in the USA and 0.26 kWh / m³ in Japan [13]. The amount of electricity consumed for purifying wastewater in Turkey ranges from 0.08 to 0.5 kWh/m³. In Karaman Wastewater Treatment Plant, this value is 0.3 kWh/m³.

2.2. Karaman Wastewater Treatment Plant

Domestic wastewater from Adapazarı, Erenler, Serdivan, Arifiye, Sapanca districts is treated at the Karaman Wastewater Treatment Plant. Stage 1; It has the capacity to serve an equivalent population of 750000 people until 2015. 2nd stage; It will be able to serve a population of 1625767 people by 2035.

2.3. Karaman Wastewater Treatment Plant Electricity Consumption Times and Investigation of Paid Prices

When the electricity bills of the facility are examined, 12 month electricity consumption average of Karaman wastewater treatment plant for the last 4 years (2015-2016-2017-2018) is shown in figure 1.

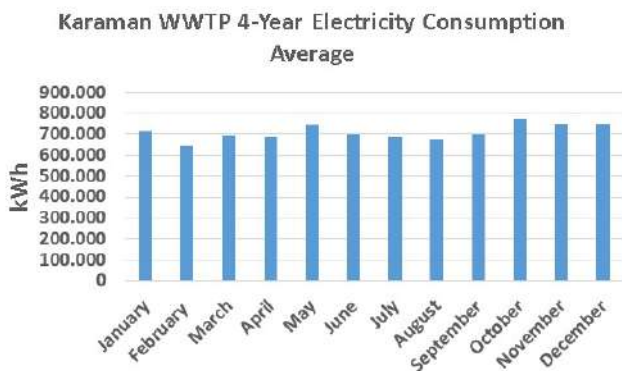


Figure 1 Karaman WWTP Electricity Consumption

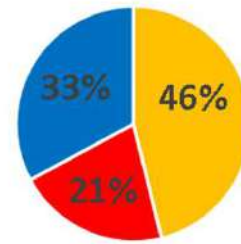


Figure 2 Karaman WWTP Electricity Consumption Distribution According to Daily Tariff

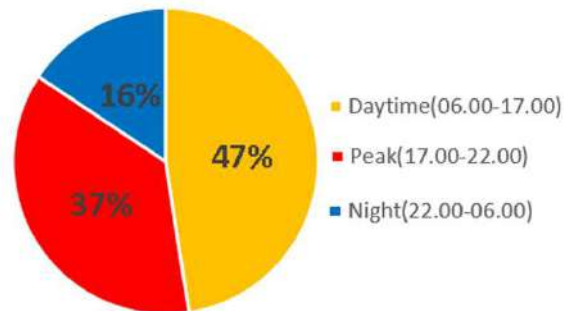


Figure 3 Karaman WWTP Electricity Consumption Prices

Karaman WWTP electricity consumption distribution (kWh) according to daily tariff is shown in Figure 2. Karaman WWTP Electricity Consumption distribution (TL) according to daily tariff is shown in Figure 3.

While the distribution of the electricity consumption amounts of the Karaman Waste Water Treatment Plant during the day according to time periods is shown in figure 2, the figure 3 shows the prices paid according to these consumption amounts (the most expensive time period (17.00-22.00))

Unit prices of electricity approximately are 0.39 TL for the daytime, 0.63 TL for the peakttime, 0.19 TL for the nighttime in 2018

2.4. Evaluation of Wastewater Treatment Plant Electricity Consumption Data

When the electricity consumption of the Karaman Wastewater Treatment Plant is analyzed, up to 17 % change in electricity consumption (between the highest electricity consumption and the lowest

consumption on a monthly basis) was observed. The flow rate of the facility also varies up to a maximum of 50%. These kinds of investments are planned for 20-30 years, considering the wastewater formations in the coming years [14].

Based on these findings and information, we can assume that the wastewater treatment plant does not operate at the same capacity throughout the year.

It is considered that the amount to be paid for the electricity consumption of the facilities will decrease if the amount of work in the peak time interval where the cost of electricity consumption of the Wastewater Treatment Plants is shifted before (day) or after (night) in line with the facility facilities. Current electricity consumption and improved values of the facility are given in table 2.

Table 2
Karaman WWTP current and improved consumption amounts

	Current	Improved
Daytime	% 46	%47
Peak	%21	%19
Night	%33	%34

2.5. Calculation

The current electricity consumption costs of the Karaman wastewater treatment plant and the improved electricity consumption cost are shown in figure 4.

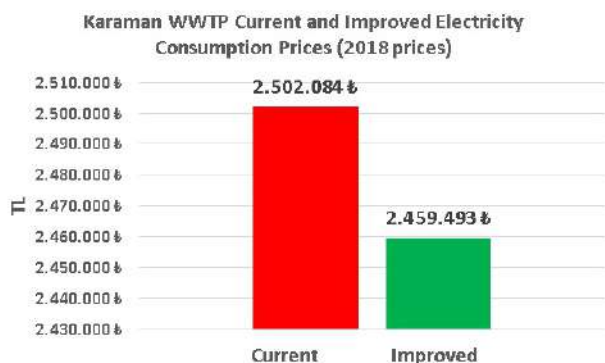


Figure 4 Karaman WWTP Current and Improved Electricity Consumption Costs

3. MICRO HDYROELECTRIC POWER PLANTS

Studies are carried out to produce electrical energy from large water resources in Turkey. It is important to do the same studies in the evaluation of small water resources.

With the regulation that came into force on 12/05/2019, an incentive was provided for micro energy production. Real or legal persons engaged in production activities in production facilities based on renewable energy sources with a maximum installed capacity of 1 MW are exempt from the obligation to obtain licenses and set up companies [15].

The study on micro-hydro power plants used for the recovery of energy in water pipelines by Williams are some of the earliest research records in this area [16]. Valves are used to control the downward flow pressure in water mains lines. The plants that generate electricity at the micro level will be integrated into the water network lines, while reducing the downward pressure made by the valves and generating electricity[17].

The service offered to consumers by water service providers will be offered at lower costs as energy costs are reduced.

There are similar facilities in Germany [18] and Scotland [16] that provide energy recovery. A micro hydro power plant was established in 1947 to gain energy from the flow between an upper storage reservoir and the treatment plant located at its lower level in Ireland.

In the study on the Applicability of Micro Scale Hydroelectric Power Plants for Energy Recovery in Wastewater Treatment Plants in Harran University in 2018, theoretically calculated the amount of electrical energy that can be produced through the wastewater flow [19].

In the UK, a micro hydro power plant was installed, which works with an archimedes screw system to generate energy from the outlet of a wastewater treatment plant.

The facility has two turbines with a total power of 180 kW. The facility provides € 160000 savings in annual electricity costs [20].

In Turkey, projects for the construction of micro hydro power plant accounts are being carried out and implemented in order to evaluate the water potential of wastewater treatment plants.

An example of this type of micro hydro power plant is installed at the outlet of the central waste water treatment plant of Gaziantep Water and Sewerage Works, and 1 million 500 thousand kilowatts / hour of energy can be generated annually [21].

Another similar study will be able to generate 8000000 kilowatts / hour of electricity per year, established in the wastewater plant of the Ankara Metropolitan Municipality Aski General Directorate [22].

3.1. Investigation of Energy Production with Micro Hydro Power Plant from Karaman Wastewater Treatment Plant

The most important parameters for the recovery of energy from the water infrastructure are the flow of water and the height at which water falls[23]. Special conditions such as the pH value of water, high pressure pipe networks may affect the turbines that can be used in some plants, affecting energy recovery [24].

The potential to generate energy with micro hydro power plant from Karaman Wastewater Treatment Plant was examined.

3.1.1. Flow Detection

The data of the flow rate of Karaman Wastewater Treatment Plant were learned by means of the devices measuring 24/7 in the facility (Table 3).

Table 3
Karaman WWTP Flow Quantities

Karaman WWTP Flow Rates (m ³ /day)	
Max	93720
Average	82353
Min	52560

3.1.2. Detection of Level Difference

The height difference between the exit point and the discharge point of the Karaman Wastewater Treatment Plant was determined through the wastewater treatment project and has a drop of 2.86 meters.

3.1.3. Turbine Selection

Turbines are produced according to the specific flow values of each facility. If the flow values change, the energy produced will also affect the turbine efficiency, which will cause changes. PATs (Pumb as Turbine) have been assumed to be the most suitable turbines to be used for energy recovery from water pipelines in various studies [25].

For example; for PAT, which is designed according to certain values, a 50% increase or decrease in water flow will result in a 30% to 80% reduction in energy conversion efficiency.

It has been determined that the most suitable turbine will be the archimedes auger turbine according to the height and flow rates, the various turbine types according to the flow and the pressure according to the working areas(Figure 5)

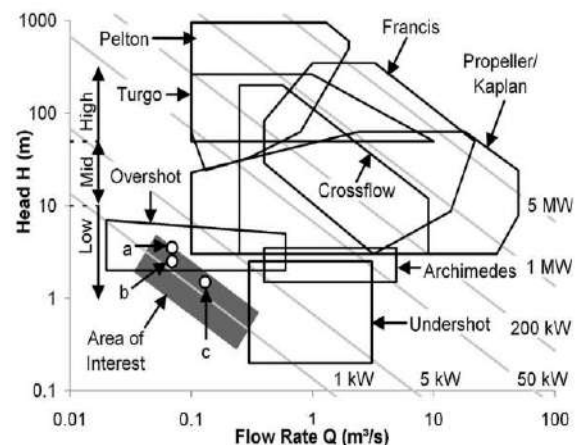


Figure 5 Turbine selection according to flow rate and pressure [26]

3.1.4. Installation Costs

Micro hydro power plant investment cost ranges from \$ 1300-8000 / kW (€ 1000-6200 / kW).The

operating cost varies between approximately 1-4% of the investment value [26]. Investment cost per kW of micro hydro power plants varies between € 3000 and 6000 [27].

In the market research conducted for the Karaman wastewater treatment plant, the investment cost was determined as 300000 TL.

3.1.5. Operating Costs

The maintenance / operation costs of the archimedes augers to be installed are very low. The operating cost varies between approximately 1-4% of the investment value [26]. 3000 TL is assumed annually.

4. RESULTS

If the wastewater treatment plant's flow rate is 1 m³ / sec, gravity acceleration is 9.81, efficiency is 70%, and the dream is 2.86, the installed power is calculated as 20 kW

Q =flow (m³/sec)

P =Power (Watt)

ρ = density of water (kg/m³)

g =gravity acceleration (9,81 m/sec²)

H =current water height (m)

ϵ = productivity

$P=Q \cdot \rho \cdot g \cdot H \cdot \epsilon$

$P=1 \cdot 1000 \cdot 9,81 \cdot 2,86 \cdot 0,7=20 \text{ kW}$

The wastewater treatment plant operates 365 days a year, with minimum flow rate of 0.6, m³/sec, maximum flow of 1.08 m³/sec, and average flow rate of 0.95 m³/sec.

The amount of electricity produced with flow rates will vary proportionally. There are 8760 hours in a year. It is assumed to be 7700 hours considering the flow rates as the working period of the facility.

Annual electricity amount to be produced is calculated as 154.000 kWh / year. Operating Income = 7700 * 20 * 0.59 = 90.860 TL / Year (It is assumed that the unit price of electricity is 0.59 TL).

From the interoperability calculation methods, the repayment period of the facility was analyzed according to the management's economical feasibility and it was calculated that the investment cost was equal to net income after 3 years and 11 months (Figure 6).

With this study, in the wastewater treatment plants with suitable facility capacity, it has been observed that the amount to be paid for electricity consumption will decrease when necessary arrangements are made for shifting some of the electricity consumption corresponding to the evening hours (17.00-22.00) to day and night time zones.

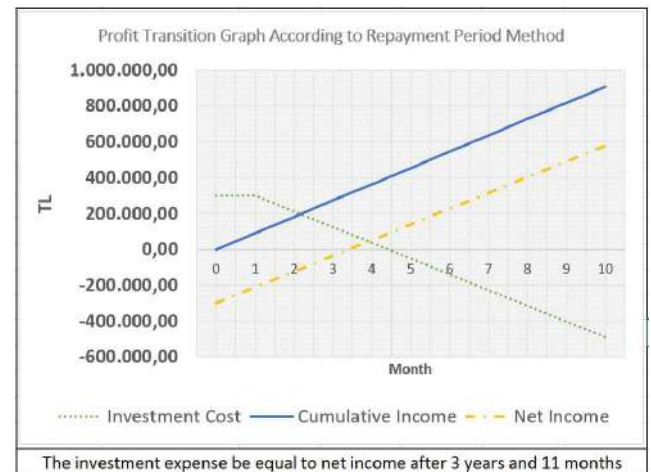


Figure 6 Profit Transition Graph According to Repayment Period Method

It was concluded that the potential water energy of the Karaman wastewater treatment plant, which has a flow rate and appropriate consideration, is converted into electrical energy and some of the electricity consumption amounts of the facilities will be met and this project to be invested is economically feasible.

Moreover, if wastewater treatment plants comply with the requirements of the legislation in Turkey, since up to 50 % of the electricity costs of wastewater treatment facilities are covered by the government [28].

Therefore, it is economically feasible to implement micro hydro power plant investments immediately for institutions that receive incentives from the state for electricity costs.

Acknowledgements

The authors would like to thank the valuable managers and employees of SASKI General Directorate for their assistance in obtaining and using the data used in the paper.

Funding

The authors received no financial support for the research, authorship, and/or publication of this paper.

The Declaration of Conflict of Interest/ Common Interest

No conflict of interest or common interest has been declared by the authors.

The Declaration of Ethics Committee Approval

The authors declare that this document does not require an ethics committee approval or any special permission.

The Declaration of Research and Publication Ethics

The authors of the paper declare that they comply with the scientific, ethical and quotation rules of SAUJS in all processes of the paper and that they do not make any falsification on the data collected. In addition, they declare that Sakarya University Journal of Science and its editorial board have no responsibility for any ethical violations that may be encountered, and that this study has not been evaluated in any academic publication environment other than Sakarya University Journal of Science.

REFERENCES

- [1] Resmi Gazete (31.12.2004 tarih ve 25687 sayılı). Su Kirliliği Kontrolü Yönetmeliği
- [2] <https://www.enerji.gov.tr/tr-TR/Sayfalar/Elektrik> [Accessed-12-Jan- 2020]
- [3] <https://www.enerjiatlas.com/hidroelektrik/> [Accessed-14-Jan- 2020]
- [4] http://iklim.cob.gov.tr/iklim/Files/Mevzuat/kyoto_protokol.pdf [Accessed-14-Jan-2020]
- [5] <https://www.haberturk.com/seragazi-emisyonlari-2429941-ekonomi> [Accessed-15-Jan- 2020]
- [6] O. Çoban and N. Şahbaz Kılınç, The Relationship Between Renewable Energy Consumption and Carbon Emission: The Case of TR- Journal of Social Sciences Institute vol. 38, no.1, pp. 195-208,2015
- [7] İ. Öztürk, Atık su mühendisliği. Teknik Kitaplar Serisi (İSKİ), 2017
<http://www.iski.gov.tr/web/assets/SayfalarDocs/e-kutuphane/kultur/docs/at%C4%B1ksu-m%C3%BChendisli%C4%9Fi.pdf> [Accessed-12-Jan- 2020]
- [8] A. Samsunlu, Atık suların arıtılması. Birsen Yayınevi, 2011.
- [9] E. Özcan, Türkiye kıyılarında yüzme suyu profillerinin belirlenmesi ve turizmde atık su yönetimi, 2014.
<https://webdosya.csb.gov.tr/db/tay/webmenu/webmenu13378.pdf> [Accessed-04-Jan- 2020]
- [10] Tüik 2018, Belediye atık su istatistikleri. <http://www.tuik.gov.tr>. [Accessed-09-Jan- 2020]
- [11] G. Venkatesh, and H. Brattebø, Energy consumption, costs and environmental impacts for urban water cycle services: case study of Oslo (Norway). Energy vol. 36, no. 2, pp. 792–800, 2011.
- [12] S. C. Kwok, H. Lang, P. O’Callaghan, and M. Stiff, Water Technology Markets 2010, Key Opportunities and

- Emerging Trends. Media Analytics Ltd, Oxford, 2010.
- [13] http://www.emo.org.tr/ekler/38a62084d5b1ff_ek.pdf [Accessed-12-Jan- 2020]
- [14] [https://www.tarimorman.gov.tr/SYGM/Belgeler/ar%C4%B1tma%20norm%20rehberi/AAT%20Tasar%C4%B1m%20Rehberi%20\(1\).pdf](https://www.tarimorman.gov.tr/SYGM/Belgeler/ar%C4%B1tma%20norm%20rehberi/AAT%20Tasar%C4%B1m%20Rehberi%20(1).pdf) .[Accessed-19-Jan-2020]
- [15] Resmi Gazete(12.05.2019 tarih ve 30772 sayılı). Elektrik Piyasasında Lisanssız Elektrik Üretim Yönetmeliği
- [16] A. A. Williams, Pumps as Turbines for Low Cost Micro Hydro Power. World Renewable Energy Congress, Denver, USA, 1996.
- [17] A. A. Williams, N. P. A. Smith, C. Bird, and M. Howard, Pumps as turbines and induction motors as generators for energy recovery in water supply systems. Journal of the Chartered Institute of Water and Environmental Management vol. 12, pp. 175–178, 1998.
- [18] K. Mikus, Erfahrungen mit Kreiselpumpenanlagen zur Energierückgewinnung aus dem Trinkwassersystem. Das Gasund Wasserfach – Wasser/Abwasser vol. 124, no. 4, pp. 159–163, 1984.
- [19] D. Erkan, T. Yılmaz, A. Yücel, A. Yılmaz, A. Tel, and D. Uçar, Applicability of Micro Scale Hydroelectric Power Plants for Energy Recovery in Wastewater Treatment Plants. Harran University Journal of Engineering vol. 2, pp.1-6, 2018.
- [20] Engineering & Technology Magazine Power generation by Archimedes screw, 2010.
- [21] <https://www.hurriyet.com.tr/gaski-atik-su-ile-enerji-uretecek-40215041> .[Accessed-18-Jan- 2020]
- [22] <http://www.yekenergy.com/referanslar/aski-arsimet-burgulu-elektrik-uretim-santrali/> [Accessed-12-Jan- 2020]
- [23] A. McNabola, A.P. Williams, and P. Coughlan, Energy recovery in water supply networks: an assessment of the potential of micro hydropower. Water and Environment Journal vol. 27, pp. 435–436, 2013.
- [24] M. O. Engelhardt, P. J. Skipworth, D. A. Savic, A. J. Saul, and G. A. Walters, Rehabilitation strategies for water distribution networks – a literature review with a UK perspective. Urban Water vol. 2, no. 2, pp. 153–170, 2000.
- [25] M. Giugni, N. Fontana, and D. Portolano, Energy Savings policy in water distribution networks. Proceedings of the International Conference on Renewable Energies & Power Quality, Valencia, Spain, 2009.
- [26] http://www.mneproje.com/public/websi te/news/atiksu-aritma-hes_20200131070151.pdf-[Accessed-12-Jan-2020]
- [27] Gaius-obaseki, T. Hydropower opportunities in the water industry. International Journal of Environmental Sciences vol.1, no. 3, pp. 392–402, 2010.
- [28] Resmi Gazete (01.10.2010 tarih ve 27716 sayılı).Çevre Kanununun 29. Maddesi Uyarınca Atık Su Arıtma Tesislerinin Teşvik Tedbirlerinden Faydalanmasında Uyulacak Usul Ve Esaslara Dair Yönetmelik

JOURNAL OF SCIENCE



SAKARYA UNIVERSITY

Sakarya University Journal of Science

ISSN 1301-4048 | e-ISSN 2147-835X | Period Bimonthly | Founded: 1997 | Publisher Sakarya University |
<http://www.saujs.sakarya.edu.tr/en/>

Title: The Replacement of Seashells with Calcite in White Ceramic Glaze Preparation

Authors: Levent KOROĞLU, Ceren PEKŞEN

Received: 2020-04-28 12:45:20

Accepted: 2020-07-15 15:04:21

Article Type: Research Article

Volume: 24

Issue: 5

Month: October

Year: 2020

Pages: 956-964

How to cite

Levent KOROĞLU, Ceren PEKŞEN; (2020), The Replacement of Seashells with Calcite in White Ceramic Glaze Preparation. Sakarya University Journal of Science, 24(5), 956-964, DOI: <https://doi.org/10.16984/saufenbilder.728340>

Access link

<http://www.saujs.sakarya.edu.tr/en/pub/issue/56422/728340>

New submission to SAUJS

<http://dergipark.org.tr/en/journal/1115/submission/step/manuscript/new>



The Replacement of Seashells with Calcite in White Ceramic Glaze Preparation

Levent KOROGLU¹, Ceren PEKŞEN*²

Abstract

In this study, the effect of seashell utilization as a replacement for calcite on the surface features and optical properties of white ceramic glazes was investigated. As received seashells collected from Black Sea beaches of Samsun, Turkey and purified seashells at 700°C for 1 h were used as calcite replacement by 15 wt.%. Seashell powders were incorporated to white glaze compositions which are applied on the surface of different fired clay bodies such as red clay, chamotte, white and porcelain by dipping technique. Next, the glazed green bodies were sintered at 1100°C for 8 h. Following to TG-DTA, heating microscope, XRD and optical analysis, the obtained results exhibited that as received seashell powder (SP-1) was composed of calcite (CaCO₃), whereas purified seashell powder (SP-2) comprised aragonite (CaCO₃) and calcium oxide (CaO). The iron (hematite) content in red clay and the impurities in seashells composition caused specks and crawlings on the surface of glazed red clay bodies and of some glazes containing seashell, respectively. In generally, the higher CaO content in SP-2 enhanced gloss (60°) values, and whiteness values of most glazed surfaces were closed to each other. The color of chamotte bodies increased redness-greenness values. The variations in optical parameters were mainly associated with the difference in body compositions. SP-1 contained glaze, applied on porcelain body, was selected as optimal because that had 33 gloss value, high whiteness (87) and no surface defect. Therefore, the utilization of as received seashells by 15 wt.% as calcite replacement allows eco-friendly and cost-effective production of white ceramic glazes without any additional heat treatment.

Keywords: White Ceramic Glazes, Seashells, Calcite, Optical Properties, Clay Products

* Corresponding Author: cpeksen@omu.edu.tr

¹ Eskisehir Technical University, Department of Materials Science and Engineering, Eskisehir, Turkey.

ORCID: <http://orcid.org/0000-0003-4696-1459>

² Ondokuz Mayıs University, Department of Ceramic and Glass, Samsun, Turkey.

ORCID: <http://orcid.org/0000-0002-3378-4804>

1. INTRODUCTION

Glazes are stable glassy coatings applied to on ceramic surfaces in order to supply a protective layer to the ceramic body. Also, glazing provides the product with a range of technical properties such as waterproof, cleanability, chemically and mechanically resistance and aesthetic features like gloss, color and texture. These features generally vary depending on the chemical composition and firing parameters. The ceramic glazes can be classified according to production process, application area, composition and the optical properties of the finished surface. Optical properties (e.g., brightness, color and texture) of the product are the important criteria for the classification of finished surfaces [1,2].

Glazes consist of several oxides. Silicon dioxide is the glass former of a glaze composition, while alkaline and alkaline earth oxides act as fluxers, opacifiers or dyes. CaO is an inexpensive raw material, widely used in glaze compositions, that reduces the viscosity of glaze. Also, CaO provides hardness and durability to glazes [2-4]. In glaze compositions, CaO is obtained from calcium carbonate which has two polymorphs: calcite and aragonite. Although the crystal structures of calcite and aragonite are different from each other, both the strength and the density of aragonite is higher than calcite [5].

Seashells are natural materials that consist of calcium carbonate compressed between biopolymers. Calcium carbonate provides strength, hardness and toughness to the shell structures [6,7]. They are used as raw materials in ceramic glaze compositions due to the calcium carbonate content. Seashells collected from the beaches are composed of calcite phase.

The aim of the study was to investigate the surface features and optical properties of white ceramic glazes prepared with as received seashells and purified seashells as a replacement for calcite by 15 wt.%. The seashells were collected from Black Sea beaches of Samsun, Turkey. Next, the collected seashells were heat-treated at 700°C for 1 h to remove organics in their composition. Seashell powders were incorporated to white

glaze composition, and the prepared glaze compositions were applied on the surface of different fired clay bodies. Gloss values and coloring parameters of finished products were determined.

2. EXPERIMENTAL PROCEDURE

2.1. Body Preparation

For the preparation of fired bodies (25x25 mm), slurries were hand-pressed, dried and heat-treated at 800°C for 7 h under atmospheric conditions. Four different plastic slurry were used which contain red mud, chamotte mud, white mud and porcelain mud.

2.2. Preparation of Seashell Powders

The collected seashells from Black Sea beaches of Samsun, Turkey were firstly washed. Secondly, a part of as received seashell powders were subjected to heat-treatment at 700°C for 1 h in an electrically-heated furnace to remove organics in the composition. While the collected and washed (as received) seashell powders were called as SP-1, the heat treated (purified) seashell powders were called as SP-2. Finally, both SP-1 and SP-2 were crushed and ball-milled for 90 s. Differential Thermal Analysis (DTA) and Thermogravimetry (TG) of SP-1 and SP-2 were carried out using Simultaneous Thermal Analyzer (STA, 409 PC/PG, Netzsch) between 25°C-1200°C. The critical temperatures of compacted SP-1 and SP-2 (2x2x3 mm) were determined using a heating microscope (Misura, TA Instruments) between 400°C-1550°C. The thermal analysis were conducted under oxygen atmosphere.

2.3. Preparation of Glazes

In order to obtain glazes, SP-1 and SP-2 were incorporated to glaze composition. Seashell powders were used as calcium carbonate source. The recipes of glazes are given in Table 1. After ball-milling of glaze compositions for 30 min in alumina media, they were applied on the surface of different fired bodies such as red clay body (B1), chamotte body (B2), white body (B3) and

porcelain body (B4) by dipping technique [10]. After glaze application, the sintering of glazed bodies was performed at 1100°C for 8 h under atmospheric conditions.

Table 1

Recipes of the glazes (wt.%)

Raw material / glaze code	G1	G2	G3
K-Feldspar	37	37	37
Calcite	15	-	-
Kaolin	8	8	8
Flint	37	37	37
Bentonite	3	3	3
SP-1	-	15	-
SP-2	-	-	15

The qualitative phase analysis of non-glazed bodies was carried out using X-Ray Diffractometer (XRD, Miniflex 600, Rigaku). The optical parameters of the glazed bodies were determined using a chromometer (CM-2300d, Konica Minolta) between wavelength range of 360 nm - 740 nm. During the study, "G" referred to glazing code and "B" referred to fired body code.

3. RESULTS AND DISCUSSION

3.1. Characterization of Seashell Powders

Chemical composition and the qualitative phase analysis results of SP-1 and SP-2 were reported in prior study [8]. In still, the chemical composition (wt.%) of SP-1 and SP-2 are given again in Table 2. Both SP-1 and SP-2 were comprised mainly CaO and some trace elements. While SP-1 comprised only calcite (CaCO₃; ICDD 05-0586), SP-2 included aragonite (CaCO₃; ICDD 41-1475) and calcium oxide (CaO; ICDD 28-0775) crystalline phases. The polymorphic transition of calcite into aragonite occurred during purification (at 700°C for 1 h) [9]. The presence of CaO as a minor phase caused by the partial decomposition of calcium carbonate during the purification (organic removal) of SP-2 [10]. For this reason, loss on ignition (L.O.I) value below 1000°C of SP-2 was found 2 % less.

Table 2

Chemical composition (wt.%) of SP-1 and SP-2

Comp.	SP-1	SP-2
CaO	54.32	56.22
Na₂O	0.59	0.32
SiO₂	0.23	0.17
Fe₂O₃	0.03	0.05
SO₃	0.06	0.05
P₂O₅	0.01	0.01
Al₂O₃	0.23	-
BaO	-	0.30
SrO	-	0.19
L.O.I.	44.52	42.69

TG-DTA curves of SP-1 are given in Figure 1. According to DTA and TG/DTG curves of SP-1, endothermic peak at 854.0°C were related with thermal decomposition of calcite [10]. A high mass loss (44.2 wt. %) occurred between room temperature and 900°C was related with the removal of moisture and CO₂ gas. TG-DTA curves of SP-2 are given in Figure 2. The endothermic peak at 842.5°C were related with the decomposition of aragonite. A high mass loss (43.5 wt. %) occurred again until the finishing of decomposition (900°C). The endothermic peak and total mass loss of SP-2 (842.5°C, 43.5 wt. %) was found lower than these of SP-1 (854.0°C, 44.2 wt. %) because of the reduced content of calcium carbonate during purification and the absence of the organics. Heating microscope curve of SP-1 is given in Figure 3. The sintering, softening and melting points were determined as 1052°C, 1394°C and 1440°C, respectively. Heating microscope curve of SP-2 is given in Figure 4. The sintering, softening and melting points were specified as 1358°C, 1414°C and 1440°C, respectively. The higher sintering temperature of SP-2 could be related with the presence of CaO which has significantly higher melting point (2572°C) than calcium carbonates (calcite:1339°C and aragonite:825°C) [11,12].

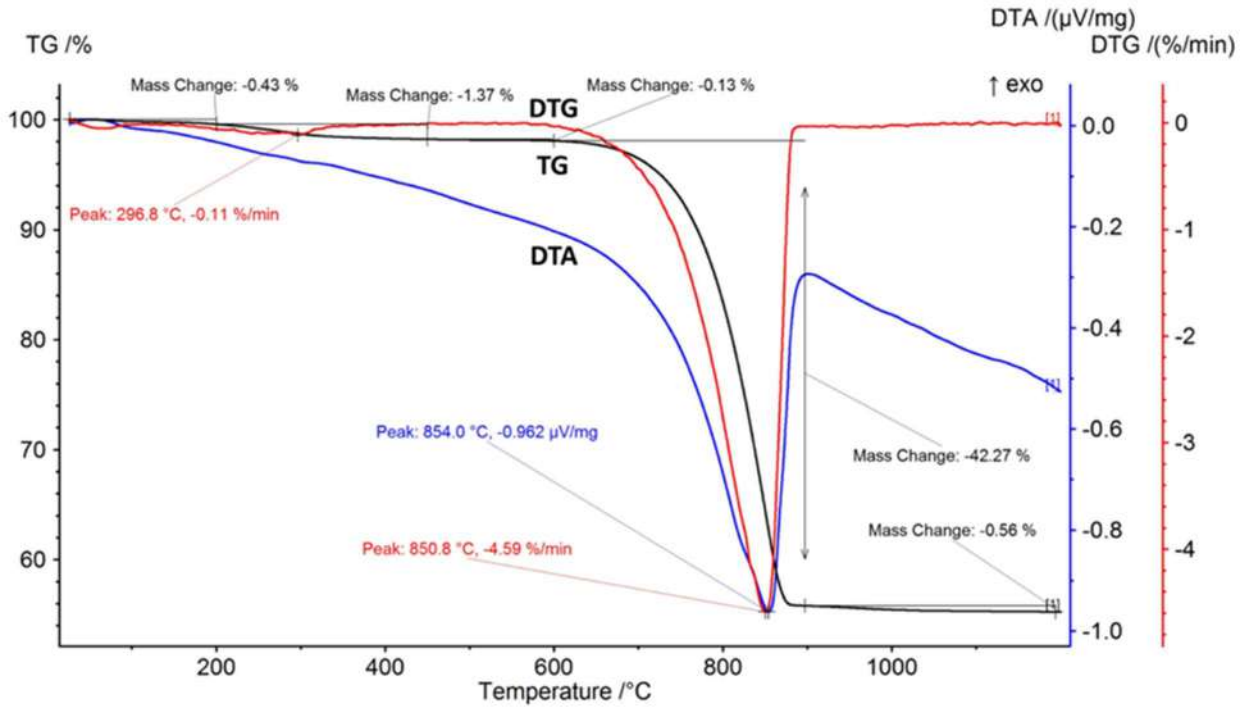


Figure 1 TG-DTA curves of SP-1

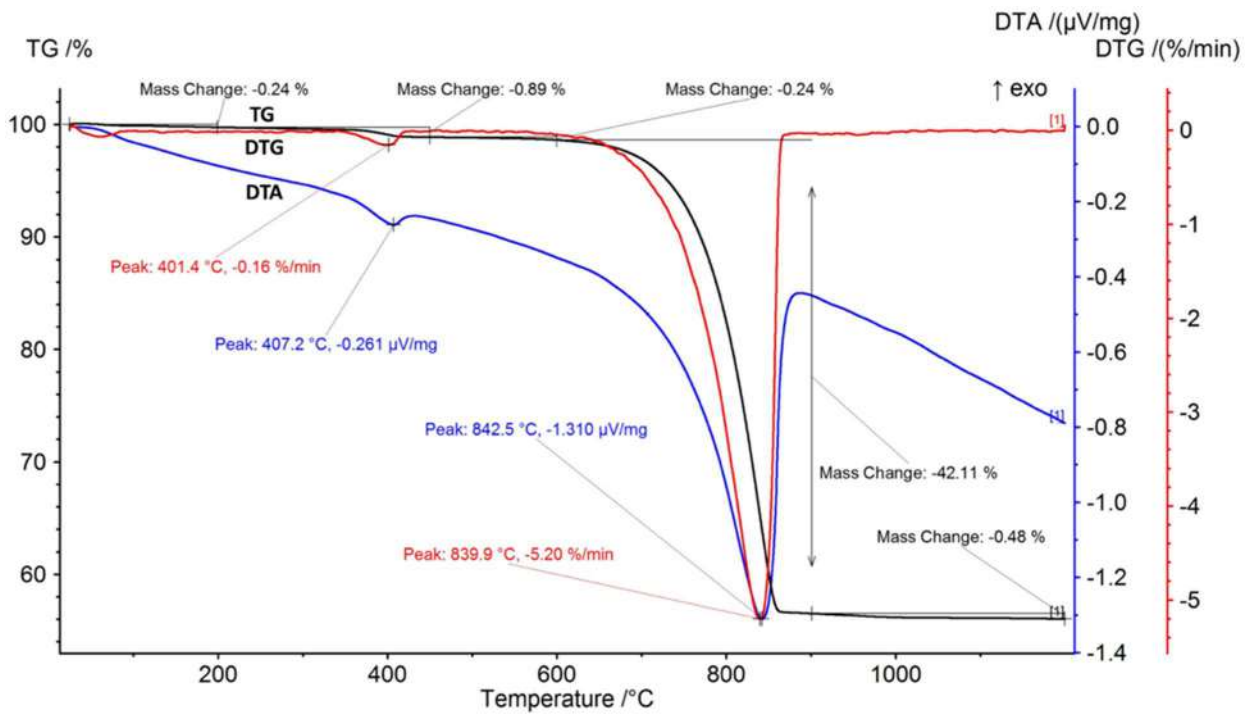


Figure 2 TG-DTA curves of SP-2

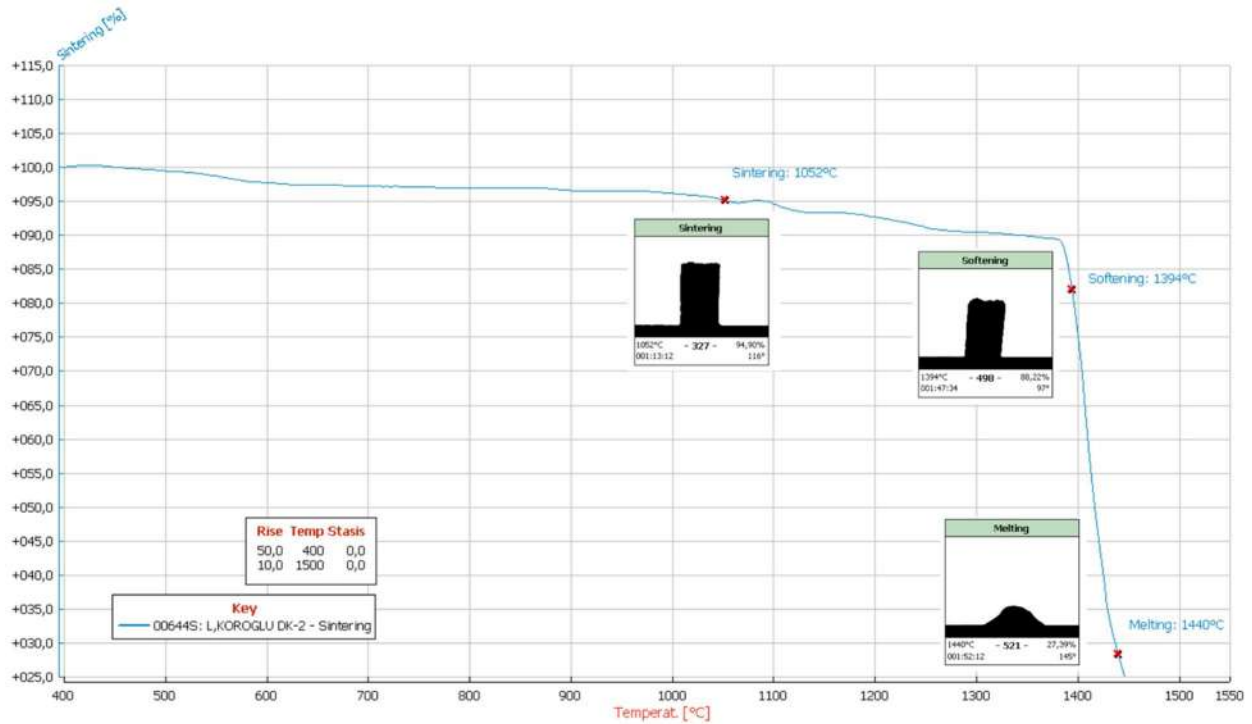


Figure 3 Heating microscope curve of SP-1

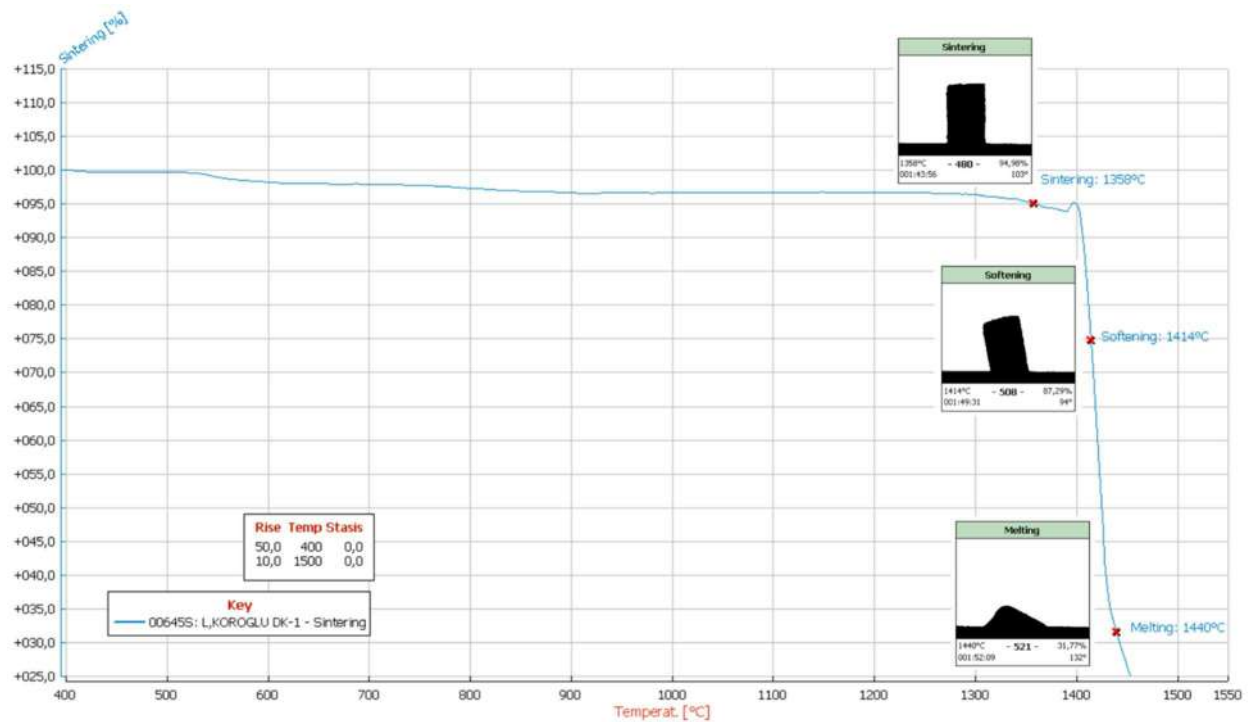


Figure 4 Heating microscope curve of SP-2

3.2. Characterization of Sintered Bodies

XRD patterns of sintered bodies are given in Figure 5. The phase analysis of bulk samples caused a shift in the patterns. Red clay body (B1) included quartz (SiO_2), hematite (Fe_2O_3) and albite ($\text{NaCa}(\text{Si},\text{Al})_4\text{O}_8$) crystalline phases.

Chamotte body (B2) contained of quartz and mullite ($\text{Al}_6\text{Si}_2\text{O}_{13}$). Both white body (B3) and porcelain body (B4) comprised quartz, albite and mullite. In contrast to other sintered bodies, red clay body contained Fe_2O_3 as a minor phase besides the quartz and albite.

According to XRD patterns, all sintered bodies mainly contained quartz whereas aluminum silicate phases such as mullite and albite were

presented as minor crystalline phases. It caused by the higher peak intensity of quartz due to its higher structural factor [13].

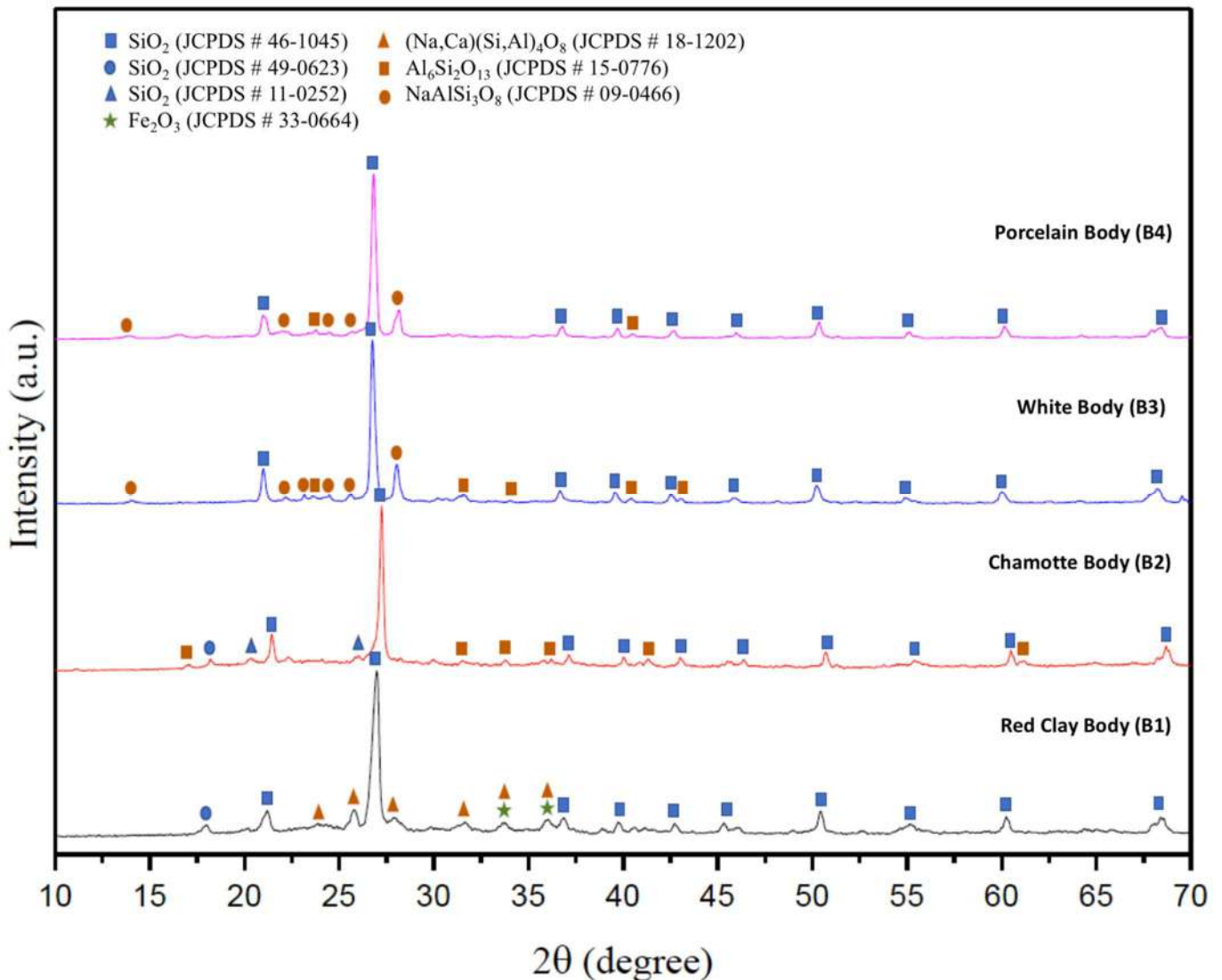


Figure 5 XRD patterns of sintered bodies

3.3. Characterization of Glazes

Digital images of sintered bodies are given in Figure 6. All glazes applied on B1 and B2 bodies provided non-homogenous opacity whereas, the dispersal of the glaze on B3 and B4 bodies were homogenous. The white color of these bodies could have inevitably affected the appearance. Some specks were observed on the surface of all B1 bodies. It was associated with the presence of iron (hematite) in B1 composition because it can pass into the glaze and cause a surface defect like that [3]. Also, the surface of G2-B2, G2-B3, G3-B3 and G3-B4 included crawling which is

unglazed or partially glazed area with irregularly shape, and breaks the uniformity of the fired glaze. The main factors causing crawling are glaze surface tension, the bond strength between the green glaze and the substrate, the shrinkage of the green glaze during drying, the lack of wetting of the body by the glaze and the presence of soluble salts which can lift the glaze away from the body in single-fire operations [3]. The crawling is seen only on seashell added glazes (G2 and G3). Even though the composition of all glazes was same (they contain same amount of calcium carbonate), the impurities were existed in G2 and G3 compositions (Table 2). Hence, the

reason of crawling could be the presence of impurities in seashells which alter surface tension and the bond strength between the glaze and body. Nevertheless, the surface of G2-B4 has not any defects.

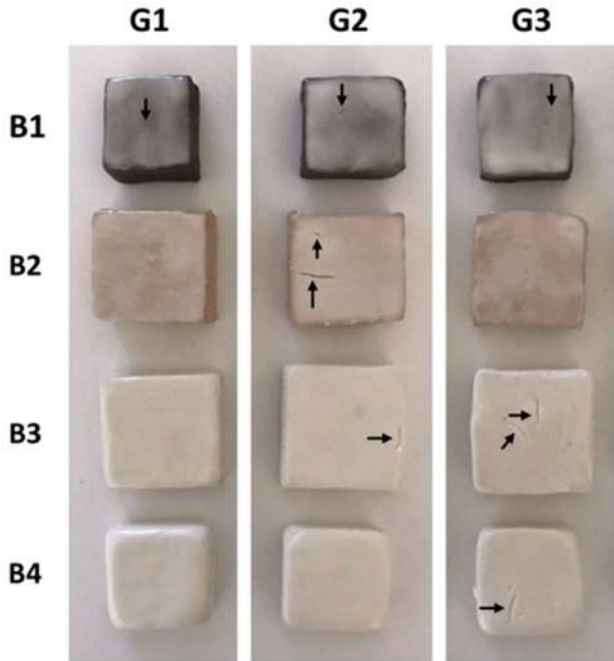


Figure 6 Digital images of sintered bodies

The color and gloss values of sintered bodies are given in Table 3, where L^* indicates whiteness, a^* redness-greenness and b^* yellowness-blueness. In generally, G3 glazed bodies had the highest gloss (60°) values. The maximum gloss value (45) was found for G3 glazed B2 body. It is known that a high gloss value is obtained from a smooth surface where the high percentage of the light is reflected off the surface at the same angle to the surface as the incident beam (specular reflection). On the contrary, some of the light is reflected at angles other than the incident angle (diffuse reflection) on a matte (opaque) surface. Hence, lower gloss values are obtained due to higher refractive index of the glaze resulting of surface roughness, crystals or phase separation [14]. Also, CaCO_3 and CaO have white and grayish white color, diminish viscosity and retard crystallization during sintering [3,15,16]. Considering that, the higher gloss values of G3 glazed bodies were associated with the relatively higher CaO content in G3 composition. CaO as a fluxing agent could decrease the crystallinity degree of glaze and consequently, the diffuse

reflection was reduced. Moreover, the existence of Na_2O in G2 and G3 compositions as a fluxing agent could contributed to the increasing of glassy phase content in the glaze. L^* values of all glazed surfaces except G1-B1 were found closed to each other because G1 and G2 compositions included same calcite content even though G3 composition had $\sim 2\%$ higher CaO content compared to G1 and G2, where the even small content of CaO has a dominant effect on the viscosity compared to whitening. a^* values of glazed B2 bodies were found remarkably higher. It showed the effect of red color of these bodies on coloring parameters. In this case, the thickness of the glazes could be lower due to the porous microstructure of chamotte bodies (B2) at sintering temperature (1100°C) [17] which have different composition (absence of albite phase) compare to other bodies. In addition, some variations in gloss, L^* , a^* and b^* values were observed. It was thought that the reactions between the phases of green glazes and different bodies took place inevitably during sintering (at 1100°C for 8 h), and the composition, crystallinity degree and distribution of formed phases affected all optical parameters.

Table 3

Color and gloss values of sintered bodies

Sample Code	Gloss (60°)	L^*	a^*	b^*
G1-B1	35.8	86.68	1.50	8.13
G1-B2	30.9	73.82	7.25	11.44
G1-B3	24.1	86.84	1.46	8.25
G1-B4	18.4	88.45	0.65	6.92
G2-B1	21.5	64.11	1.02	0.36
G2-B2	23.9	78.53	4.88	7.65
G2-B3	27.2	83.84	1.55	8.57
G2-B4	33.5	87.02	0.77	7.21
G3-B1	29.0	68.45	0.66	0.47
G3-B2	45.2	75.12	5.49	6.88
G3-B3	30.6	85.9	1.65	8.87
G3-B4	29.9	88.48	0.85	6.53

4. CONCLUSION

In the present study, the effect of seashell utilization as a replacement for calcite on the surface features and optical properties of white ceramic glazes was investigated. As received seashells collected from Black Sea beaches of Samsun, Turkey and purified seashells at 700°C

for 1 h was used as calcite replacement in powder form by 15 wt. % during white glaze preparation. Seashell powders were incorporated to white glaze compositions which are applied on the surface of different fired bodies such as red clay, chamotte, white and porcelain by dipping technique. Then, the glazed green bodies were sintered at 1100°C for 8 h under atmospheric conditions. The obtained results showed that as received seashell powder (SP-1) comprised calcite (CaCO_3), whereas purified seashell powder (SP-2) included aragonite (CaCO_3) and calcium oxide (CaO). The specks were observed on the surface of glazed red clay bodies, and the crawlings were detected on the surface of some glazes containing seashell. These were associated with the presence of iron (hematite) in red clay composition and the existence of impurities in seashell's composition. In generally, the gloss (60°) values were higher for SP-2 incorporated glazes, and whiteness (L^*) values of most glazed surfaces were closed to each other. The main reason for gloss enhancement was higher CaO content as a fluxing agent. The color of chamotte bodies increased redness-greenness (a^*) values. The variations in optical parameters were mainly associated with the difference in body compositions. SP-1 added glaze, applied on porcelain body, was selected as optimal because it had 33 gloss value, high whiteness (87) and no surface defect. The utilization of as received seashells by 15 wt.% as calcite replacement made white ceramic glaze production eco-friendly and cost-effective without any additional heat treatment.

Funding

This research did not receive any specific grant from funding agencies in the public, commercial, or not-for-profit sectors.

The Declaration of Conflict of Interest/ Common Interest

No conflict of interest or common interest has been declared by the authors.

Authors' Contribution

Conception:CP-LK, Supervision:CP, Materials:CP, Data Collection and/or Processing:CP-LK, Analysis:LK, Literature Review:CP-LK, Writer:CP-LK

The Declaration of Ethics Committee Approval

The authors declare that this document does not require an ethics committee approval or any special permission.

The Declaration of Research and Publication Ethics

The authors of the paper declare that they comply with the scientific, ethical and quotation rules of SAUJS in all processes of the paper and that they do not make any falsification on the data collected. In addition, they declare that Sakarya University Journal of Science and its editorial board have no responsibility for any ethical violations that may be encountered, and that this study has not been evaluated in any academic publication environment other than Sakarya University Journal of Science.

REFERENCES

- [1] D.W. Richerson, The magic of ceramics, John Wiley & Sons, New Jersey, 2012.
- [2] R. Casasola, J.M. Rincónand, M. Romero, "Glass-ceramic glazes for ceramic tiles: a review", J. Mater. Sci., vol. 47, pp. 553-582, 2012.
- [3] R.A. Eppler and D.R. Eppler, Glazes and glass coatings, The American Ceramic Society, Ohio, 2000.
- [4] M. Burlison, The Ceramic Glaze Handbook: Materials, Techniques, Formulas, Lark Books, New York, 2003.

- [5] W.F. Tegethoff, *Calcium Carbonate: From the Cretaceous Period into the 21st Century*, Springer, Basel, 2001.
- [6] N.M. Neves and J.F. Mano, "Structure/mechanical behavior relationships in crossed-lamellar sea shells", *Materials Science and Engineering: C*, vol. 25, no. 2, pp. 113-118, 2005.
- [7] S. Chowdhury and P. Saha, "Sea shell powder as a new adsorbent to remove Basic Green 4 (Malachite Green) from aqueous solutions: Equilibrium, kinetic and thermodynamic studies", *Chemical Engineering Journal*, vol. 164, no. 1, pp. 168-177, 2010.
- [8] C. Peksen, L. Koroglu, and H. Kartal, "Utilization of Seashells in Matte Glaze Preparation", *International Journal of Applied Ceramic Technology*, pp. 1-8, 2020.
- [9] M. Ryu, H. Kim, M. Lim, K. You and J. Ahn, "Comparison of dissolution and surface reactions between calcite and aragonite in l-glutamic and l-aspartic acid solutions", *Molecules*, vol. 15, pp. 258-269, 2010.
- [10] K.S.P. Karunadasa, C.H. Manoratne, H.M.T.G.A. Pitawala and R.M.G. Rajapakse, "Thermal decomposition of calcium carbonate (calcite polymorph) as examined by in-situ high-temperature X-ray powder diffraction", *Journal of Physics and Chemistry of Solids*, vol. 134, pp. 21-28, 2019.
- [11] R.C. Ropp, *Encyclopedia of the Alkaline Earth Compounds*, Elsevier, Oxford, 2013.
- [12] R.J. Lewis, *Food Additives Handbook*, Springer, New York, 1990.
- [13] B.D. Cullity and S.R. Stock, *Elements of X-Ray Diffraction*, Addison-Wesley Publishing, Massachusetts, 1956.
- [14] R.A. Eppler and D.R. Eppler, "Controlling the Gloss of Leadless Glazes," *Ceram. Eng. Sci. Proc.*, vol. 16, no. 1, pp. 40-5, 1995.
- [15] A.R. Jamaludin, S.R. Kasim and Z.A. Ahmad, "The effect of CaCO₃ addition on the crystallization behavior of zno crystal glaze fired at different gloss firing and crystallization temperatures", *Science of Sintering*, vol. 42, pp. 345-355, 2010.
- [16] F. Cardelli, *Materials Handbook: A Concise Desktop Reference*, Springer-Verlag, London, 2008.
- [17] C.N. Djangang, A. Elimbi, U.C. Melo, G.L. Lecomte, C. Nkoumbou, J. Soro, J.P. Bonnet, P. Blanchart and D. Njopwouo, "Sintering of clay-chamotte ceramic composites for refractory bricks", *Ceramics International*, vol. 34, pp. 1207-1213, 2000.

JOURNAL OF SCIENCE



SAKARYA UNIVERSITY

Sakarya University Journal of Science

ISSN 1301-4048 | e-ISSN 2147-835X | Period Bimonthly | Founded: 1997 | Publisher Sakarya University |
<http://www.saujs.sakarya.edu.tr/en/>

Title: Friction and Wear Properties of Glass Fiber Reinforced Polyphenylene Sulfide Composites

Authors: Mehmet İskender ÖZSOY, Levent ESATOĞLU

Received: 2020-05-04 16:00:06

Accepted: 2020-07-21 18:59:40

Article Type: Research Article

Volume: 24

Issue: 5

Month: October

Year: 2020

Pages: 965-972

How to cite

Mehmet İskender ÖZSOY, Levent ESATOĞLU; (2020), Friction and Wear Properties of Glass Fiber Reinforced Polyphenylene Sulfide Composites. Sakarya University

Journal of Science, 24(5), 965-972, DOI:

<https://doi.org/10.16984/saufenbilder.731914>

Access link

<http://www.saujs.sakarya.edu.tr/en/pub/issue/56422/731914>

New submission to SAUJS

<http://dergipark.org.tr/en/journal/1115/submission/step/manuscript/new>

Friction and Wear Properties of Glass Fiber Reinforced Polyphenylene Sulfide Composites

Mehmet İskender ÖZSOY*¹, Levent ESATOĞLU²

Abstract

The aim of this study is the experimental investigate of wear and friction properties of polyphenylene sulfide polymer (PPS) and 20%, 30% and 40% by weight glass fiber reinforced polyphenylene sulfide composites. Tribological tests were done by pin-on-disc test configuration. The disc material is AISI 1040 steel. 50, 100, 200 N normal loads and 1, 2, 3 m/s speeds were applied to the test specimens. Adding fiber decreased the friction values and specific wear rates. Furthermore, increasing load decreased the friction coefficient but increased the specific wear rate, although increasing sliding speed increased both friction and specific wear rate.

Keywords: Friction, wear, polyphenylene sulfide, glass fiber

1. INTRODUCTION

Polymer materials have been used widely in engineering applications. In use generally, polymers have been reinforced with various fibers. Fibers improved the tribological performance of the materials and gained the high wear resistance [1-9]. Mens et al. [1], investigated the tribological properties of different polymer materials and concluded that the increasing load increased the wear amount but decreased the friction coefficient. Yilmaz et al. [2], studied the pomza powder/carbon fiber hybrid composites and stated that the reinforcement and fillers enhanced the wear properties of PPS. Sumer et al.

[3], studied the 30 wt% glass fiber (GF) reinforced PEEK composite and concluded that the increasing load increased the friction coefficient and wear. Friedrich et al. [4], studied PTFE with glass fiber composites. They found that adding glass fiber enhanced the wear properties of PTFE polymer. Tewari et al. [5], studied the polyetherimidin with glass fiber composites. They stated that increasing wt % glass fiber ratios decreased the friction coefficient. They also showed that increasing load decreased the friction coefficient. Yousif et al. [6], studied the polyester composites with glass fiber mat. They investigated the wear surfaces and observed the cracks in the matrix, breakage in glass fibers at the major load. Reinicke et al. [7],

* Corresponding Author: jozsoy@sakarya.edu.tr

¹ Sakarya University, ORCID: <https://orcid.org/0000-0001-6777-4818>

² Sakarya University, E-Mail: levent.ing2405@gmail.com, ORCID: <https://orcid.org/0000-0002-4890-8013>

studied different fiber reinforced thermoplastic materials. They used the glass fiber as a reinforcement material in the PA46, PP, PPS and PEI polymers. Cai et al. [8], tested the PEI composites reinforcing with glass and carbon fiber. They stated that both increasing fiber ratios and increasing load decreased the friction coefficient. Voss et al. [9], studied the glass and carbon fiber-PEEK composites. They showed that adding fiber into the matrix enhanced the wear resistance of polymer.

Polyphenylene Sulfide (PPS) polymer has a widespread usage area such as automotive, electrical and electronical. It has high heat, chemical resistance and high mechanical properties. Its melting point is 285 °C. These properties make the PPS an alternative of thermosets and metals [10]. Researchers have been using different reinforcements in the PPS polymer to gain the wear resistance [11-15]. Guo et al. [11], studied the molybdenum concentrate and PTFE filled PPS composites. They stated that thickening of transfer film layer on the disc decreased the friction. Uniform location of transfer film layer and less detachment of materials from the surface, ensured the increasing of wear resistance. Jiang et al. [12], studied the carbon fiber reinforced sub micro TiO₂ filled PPS composites. For this composite increasing sliding speed increased the friction coefficient, but increasing carbon fiber ratios improved the tribological behaviour. Lhymn et al. [13], studied the fiber reinforced PPS composites. They stated that increasing of glass and carbon fiber ratios, decreased the wear amount. Unal et al. [14], studied the glass fiber reinforced PPS composites. They found that increasing speed worsen the tribological behavior, while increasing load increased the wear and decreased the friction. Besnea et al. [15], tested the 40 wt % glass fiber + PPS and 10 wt % PTFE+ 20 wt % carbon fiber reinforced PPS composites.

In the light of these literatures it is seen that the studies for PPS polymer composites have been being rarely and more detailed studies are needed such as different fiber ratios, influence of load and speed parameters. The aim of this study is to experimental investigate of friction and wear

behavior of chopped glass fiber reinforced polyphenylene sulfide composites with glass fiber reinforcements in 20%, 30% and 40% weight ratios. Tests were carried 50, 100, 200 N normal loads and 1, 2, 3 m/s sliding speed values at room temperatures. In these tests, the counterface disc material is AISI 1040 steel used.

2. MATERIALS AND EXPERIMENTAL WORK

In this study, the materials used were PPS polymer and chopped glass fiber reinforcements. Mechanical and physical properties of PPS and chopped glass fiber were given in Table 1. Specimens were prepared using an extruder. Firstly, the composite materials were produced in granular form in an extruder which temperature ranges from 210 °C to 240 °C. Then the test specimens were obtained as cylindrical forms with a 5 mm diameter and 40 mm length by an injection mold. The molding temperature varied from 200 °C to 240 °C. Tests were done with pin-on-disc test configuration. ASTM G99 test standard was used in wear tests. Experimental and schematic images of the wear test rigs were given in Figure 1a and 1b respectively.

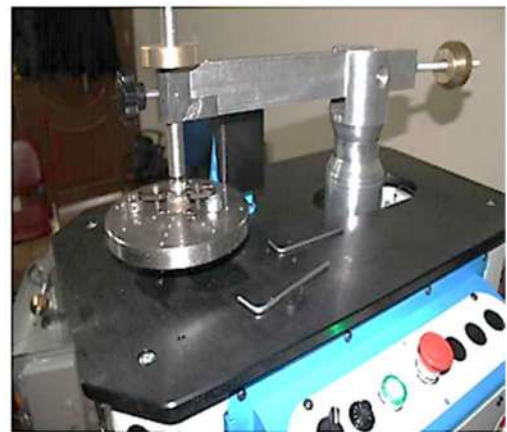


Figure 1a Experimental image of the wear test rig

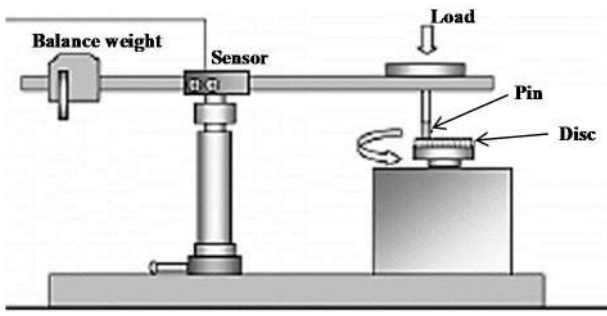


Figure 1b Schematic representation of the wear test rig [16]

Table 1
Mechanical and physical properties of PPS [17] and chopped glass fiber [18]

Properties	PPS	Chopped GF
Tensile strength (MPa)	80	520
Elongation at break (%)	10	4.8
Elasticity modulus (GPa)	2.9	75
Thermal conductivity (W/m.K)	0.2	1.35

Before and after each test, pin specimens and AISI 4140 counterface steel disc with surface roughness (R_a) is $0.29 \mu\text{m}$ were cleaned with alcohol. Friction force was calculated with a load cell sensor and data were transferred to the computer. A software calculated the friction forces according to equation (1).

$$\mu = F_F / F_N \quad (1)$$

where F_F is the frictional force and F_N is the normal load. Wear amount was obtained by weight differences which obtained before and after the tests. Applied loads were 50, 100, 200 N and sliding speeds were 1, 2, 3 m/s. Tests were repeated three times at room temperature conditions. At the end of the tests, the specific wear rates were calculated, compared and evaluated. Eq. (2) gives the specific wear rate.

$$\text{Wear rate} = \frac{\text{Wear loss}}{\text{Density} \cdot \text{Load} \cdot \text{Sliding distance}} \quad [\text{mm}^3/\text{Nm}] \quad (2)$$

3. RESULTS AND DISCUSSIONS

Figure 2 shows the friction coefficient and sliding distance relationship of PPS polymer and glass fiber reinforced PPS composites at 2m/s sliding

speed and 50N applied load conditions. It is clear from this figure that PPS polymer showed a small increasing trend up to 1200 m travelling distance and then showed a sharp decreasing behavior and then it continued a steady state behavior. There are some weavings on the PPS line. It is thought that polymer pin could be melt during the rubbing process and detachment particles could make a roughness effect. 20 wt% glass fiber reinforced PPS composites have more waving behavior than the other reinforced composites. Increasing fiber ratio showed more steady state trend and adding of glass fiber decreased the friction coefficient. PPS polymer showed the maximum friction value and 40 wt% glass fiber PPS composite showed the minimum friction with very little waving trend.

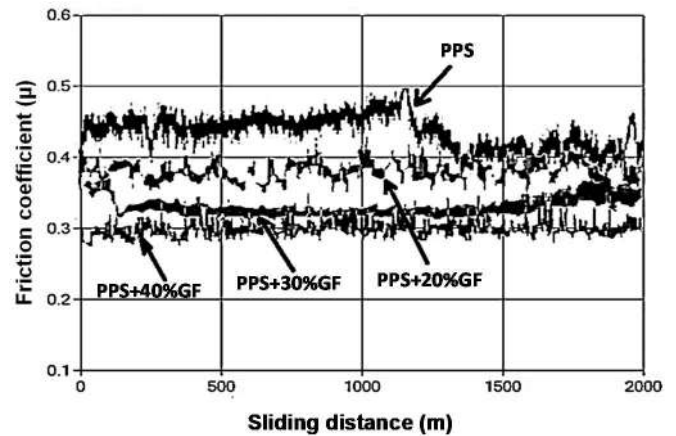


Figure 2 Friction coefficient and sliding distance relationship of pure PPS and PPS composites (speed 2 m/s, load:50N)

Figures 3 and 4 show the friction coefficients of PPS polymer and glass fiber reinforced PPS composites with load and speed, respectively. In the Figure 3 that, adding fiber decreased the friction coefficient and increasing load decreased the friction. Similar situation is seen in the literature [5, 8, 12, and 14]. It is thought that increasing load could shear the surface asperities between pin and disc and it made the pin surface smooth. Therefore, the friction coefficients were decreased. Sarkar et al. [19], explained that as a result of increasing load, it could be a transfer film because of heat generation of rubbing process, thus the friction coefficient decreases because of the increasing load. In the Figure 4, increasing sliding speed caused an increase of friction coefficient. Similar behavior was observed in the

literature [13, 14]. It is thought that increasing speed could increase the surface temperature and it could melt and deform the pin surfaces. This could cause the roughness of pin surfaces. And increasing roughness could increase the friction coefficient. It is seen that in the figures 3 and 4, increasing fiber ratio decreased the friction coefficients of PPS polymer. It is thought that adding fiber could decrease the adhesion forces between pin and disc. Also, fibers could decrease the shear forces and thus it could ensure the decreasing of friction forces. Thus, the movement of rotating disc against the pin could be easily. It is seen that in the figures, 40 wt% glass fiber PPS composites have the lowest friction coefficient all the load and velocity conditions.

During the rubbing process, adhesive bonds occurred at the polymer metal contact surfaces and adhesion transfer of polymer material to counterface occurred by molecular and electrostatics forces [20]. Contact region is subjected to shear forces during the rubbing and the forces which effect the contact asperities defined by $F_T = \tau_s \cdot A_r$ equation. A_r is the contact area, τ_s is the shear stress and F_T is the shear force which cuts the adhesive joints at the interface [21, 22]. Polymer – metal adhesion is greater than composite materials. So the F_T tangential forces which necessary to shear the junction points are higher and friction forces are higher than reinforced materials. Adding fiber decreased the adhesion bonds between the contact surfaces and ensured the composites slide easily on the disc so the tangential friction forces decreased as it is seen in the Figures 2-4.

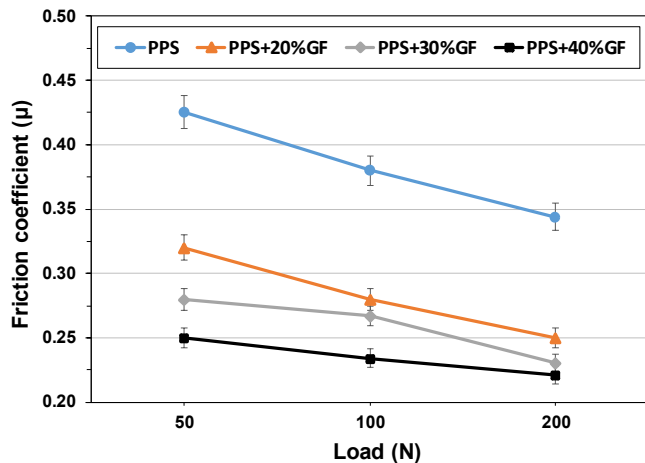


Figure 3 Friction coefficients of materials with load at 1 m/s sliding speed

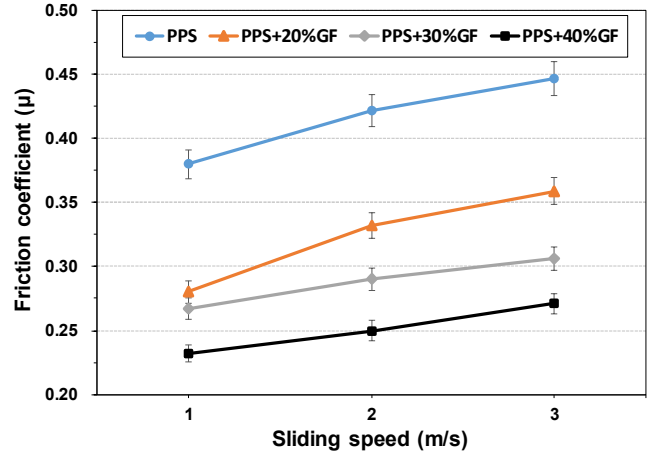


Figure 4 Friction coefficients of materials with speed at 100N load

Figures 5 and 6 show the specific wear rates of PPS polymer and glass fiber reinforced PPS composites with load and speed, respectively. In the Figure 5, it is shown that increasing load increased the wear rates of PPS and glass fiber PPS composites. These results are agreement with the literature [1,3,14]. Increasing fiber ratios strengthened and made the polymer surface harder and so fibers decreased the deformations on the polymer surface and amount of detachment particles decreased. Thus the wear rates of composites decreased. It is seen in Figure 5 that specific wear rate of 40 wt% PPS composite is higher than that of 30 wt% PPS composite at 200N load condition. It is stated in the literature, glass fibers were broken at the high loads [6, 23]. It is thought that it could be a fiber breakage in the PPS polymer at high fiber ratios and higher load. It is seen in the Figure 5 that increasing normal load caused an increase of wear amount and increase of specific wear rate, according to the formula given by equation (2).

Figure 6 shows increasing speed increased the wear rate. This is in a good agreement with the literature [14,19,24,25]. PPS polymer showed the highest wear rate, while 40 wt% reinforced PPS composite showed the minimum specific wear rate. In the literature, increasing speed increased the contact surface heat [19]. It is thought that increasing speed could cause the increasing of surface temperature of pin specimens due to the frictional heating and it could be result of melting the pin contact surfaces and it could increase the

wear amount. Furthermore, the work which performed by friction force is given by equation (3) at below,

$$Q(t) = \mu(t) \cdot W \cdot v \quad (3)$$

where the $Q(t)$ is the work which generated by friction force by over time, μ is the friction coefficient, W is the load and v is the speed [26]. It is clear in this formula, load and speed are effective on the friction force. Increasing sliding speed increased surface temperature and it caused a high adhesion between the contact surfaces [14,19,24]. High adhesion caused an increase of friction force, thus, increasing friction forces increased the wear rates as it is seen in Figures 4 and 5.

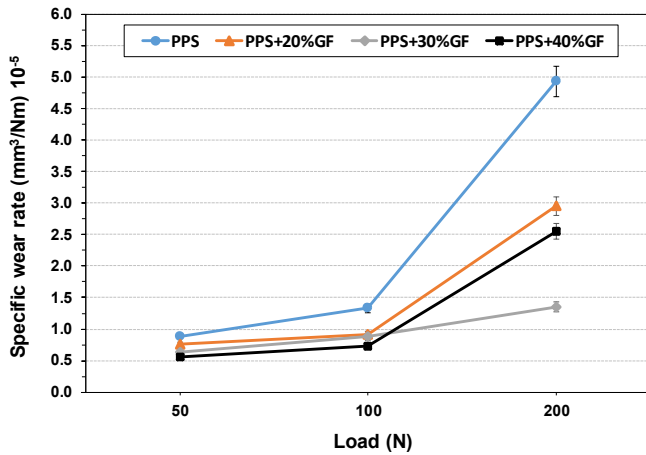


Figure 5 Specific wear rates of materials with load at 1 m/s speed

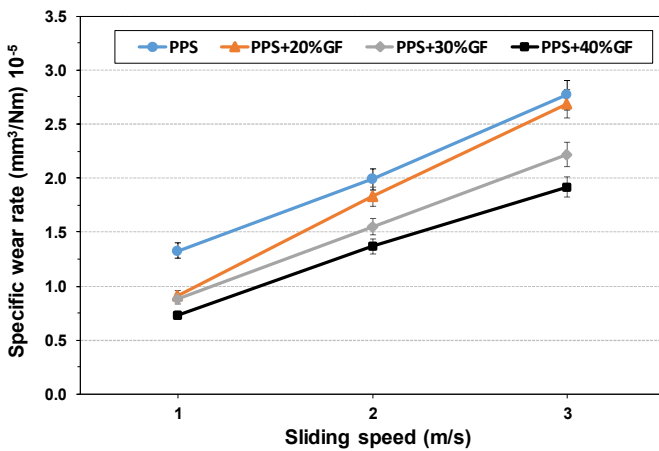


Figure 6 Specific wear rates of materials with speed at 100N load

Figure 7 shows the scanning electron microscopy (SEM) images of disc and pin worn surfaces at 1m/s speed and 100 N applied load value. In Figure 7a, PPS polymer caused the transfer film on the disc surface and is not regular on the disc surface. It caused the waving in friction coefficient values as it is seen in the Figure 1 (friction coefficient vs. sliding distance diagram). In Figure 7b (PPS polymer), micro ploughing lines are more than composite materials. Applied load and sliding speed were caused the softening of PPS contact surface. Besides the shear forces which applied by the disc caused the detachment of particles. In Figures 7c-d-e, it is seen that fibers were broken towards the sliding direction by protecting matrix to the shearing failure. Existing of overlapping layers because of fiber breakage on the material surfaces show the plastic deformation and material losses. Also, 40 wt% ratio of fiber content caused the increase in wear rate at the higher load. It is thought that polymer matrix does not sufficient to bond the fibers at the higher fiber ratios. Some researchers concluded that higher load caused the breakage of the fibers [23, 27]. Wear debris adhered to disc and it makes an abrasive effect on the pin contact surface. Hence, PPS polymer and glass fiber reinforced PPS composites were subjected to adhesive and abrasive wear mechanisms and deformations were seen on the pin surfaces.

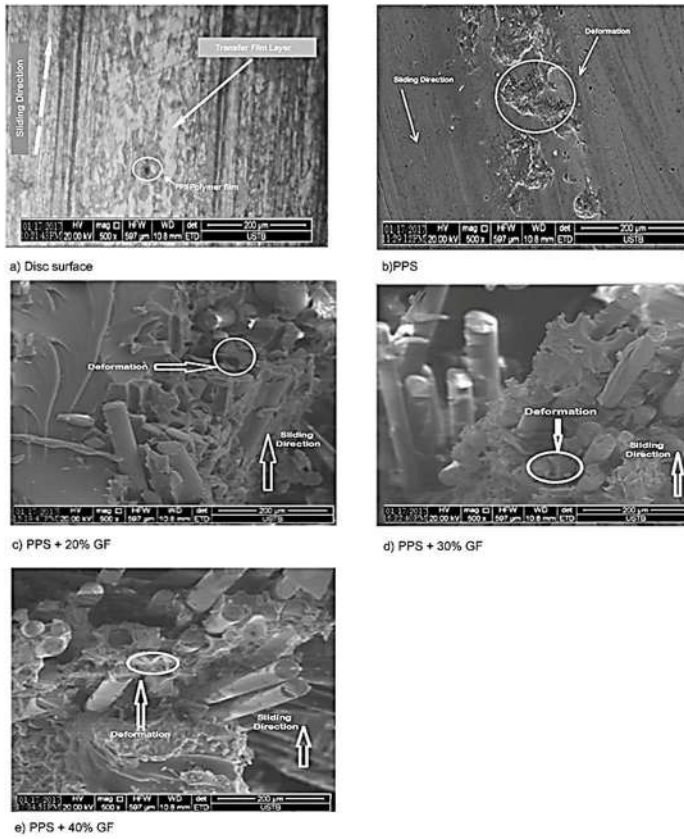


Figure 7 Scanning electron microscopy images of disc and pin worn surfaces at 1m/s sliding speed and 100 N applied load. a) Disc surface, b) PPS, c) PPS+20%GF, d) PPS+30%GF, e) PPS +40%GF

4. CONCLUSIONS

In this study, the following conclusions are reached:

Increasing load from 50N to 200N, decreased the friction values of PPS and glass fiber reinforced PPS composites.

Increasing speed increased the friction value of PPS and glass fiber-PPS composites.

Friction coefficients of glass fiber-PPS composites decreased with increasing fiber ratio.

Increasing sliding speed and load increased the wear rate. Adding glass fiber ratio decreased the wear rates of PPS composites. PPS polymer showed the maximum increment of wear rate with increment of speed and load.

Acknowledgements

We would like to thank the dear editor and reviewers for their contribution to our work.

Funding

This study is supported by Sakarya University Scientific Research Projects Coordination Unit. Project Number: 2017-50-01-083.

The Declaration of Conflict of Interest/ Common Interest

No conflict of interest or common interest has been declared by the authors.

The Declaration of Ethics Committee Approval

The authors declare that this document does not require an ethics committee approval or any special permission.

The Declaration of Research and Publication Ethics

The authors of the paper declare that they comply with the scientific, ethical and quotation rules of SAUJS in all processes of the paper and that they do not make any falsification on the data collected. In addition, they declare that Sakarya University Journal of Science and its editorial board have no responsibility for any ethical violations that may be encountered, and that this study has not been evaluated in any academic publication environment other than Sakarya University Journal of Science.

REFERENCES

- [1] J. Mens and Jee. De A., "Friction and wear behavior of 18 polymers in contact with steel in environments of air and water," *Wear*, vol. 149, pp. 255-268, 1991.
- [2] S. Yılmaz, A. E. Şahin, T. Yılmaz, and T. Sınmazçelik., "Pomza tozu ve karbon elyaf takviyeli polifenilen sülfid (PPS) kompozitlerin adhezif aşınma davranışının incelenmesi," *International*

- Participation III. Ege Composite Materials Symposium, pp.34-36, Turkey, Kuşadası, 2015.
- [3] M. Sumer, H. Unal, and A. Mimaroglu, "Evaluation of tribological behaviour of peek composite under dry sliding and water lubricated conditions," *Wear*, vol. 265, pp. 1061-1065, 2008.
- [4] K. Friedrich and A. Voss, "Sliding and abrasive wear of short glass fibre reinforced PTFE composites," *Journal of materials science letters*, vol. 5, pp. 1111-1114, 1986.
- [5] U.S. Tewari and J. Bijwe, "Tribological Behavior of Polyimides, Polyimides: Fundamentals and Applications," M.K. Ghosh and K.L. Mittal, Ed., Marcel Dekker Inc., p 533–586, 1996.
- [6] N.S.M. El-Tayeb, F. Yousif, and T.C. Yap, "An investigation on worn surfaces of chopped glass fibre reinforced polyester through SEM observations," *Tribology International*, vol. 41, pp. 331-340, 2008.
- [7] R. Reinicke, K. Friedrich, W. Beier and C. Liebold, "Tribological properties of SiC and G-fiber reinforced glass matrix composites," *Wear*, vol. 225-229, pp. 1315-1321, 1999.
- [8] C. Cai, "Evaluation of the friction and wear properties of PEI composites filled with glass and carbon fiber," *Advanced Materials Research*, Vols. 299-300, pp 21-24, 2011
- [9] H. Voss and K. Friedrich, "On the Wear Behaviour of Short Fibre Reinforced Peek Composites," *Wear*, vol. 116, pp. 1- 18, 1987.
- [10] *Engineering plastics handbook* / [edited by] James M. Margolis. McGraw-Hill Education: New York, Chicago, San Francisco, Athens, London, Madrid, Mexico City, Milan, New Delhi, Singapore, Sydney, Toronto, 2006 McGraw-Hill Education
- [11] L. Guo, H.Q. Zhu, and Y.B. Sun, "Friction and wear studies on polyphenylene sulfide filled with a complex mixture," *Applied Mechanics and Materials*, vol. 184-185, pp.1400-1403, 2012.
- [12] Z. Jiang, A. Schlarb, K. Friedrich, and Z. Zhang, "Study on friction and wear behavior of PPS composites reinforced by short carbon fibers," *Article in composites science and technology*, vol. 68, pp.124, 2009.
- [13] C. Lhymn, "Friction and wear of fiber reinforced PPS composites," *Advances in polymer technology*, Vol. 7, No. 4, pp. 451-461, 1987.
- [14] H. Ünal, U. Şen, and A. Mimaroglu, "Dry sliding wear characteristics of some industrial polymers against steel counterface," *Tribology International*, vol. 37, pp. 727-732, 2004.
- [15] A. Besnea, D. Trufasu, G. Andrei, and L. Deleanu, "Wear behavior of polyphenylene sulfide composites during dry sliding tests," *Mechanical Testing and Diagnosis*, vol. 2, pp. 15-20, 2012.
- [16] N.A. Emira, H.T. Mohamad, and M. S. Tahat, "Stick-slip detection through measurement of near fieldnoise", *Journal of Mechanical Engineering Research* Vol. 3(3), pp. 96-102, 2011.
- [17] D.I. Chukov, A.A. Stepashkin, V.V. Tcherdyntsev, L.K. Olifirov, and S.D. Kaloshkin, "Structure and properties of composites based on polyphenylene sulfide reinforced with Al-Cu-Fe quasicrystalline particles", *Journal of Thermoplastic Composite Materials*, Vol. 31, no. 7, pp. 882–895, 2018.
- [18] M.A. Abdulrehman, I.I. Marhoon, and A.K AlKamal, "Studying the Effect of Reinforcement with Random Short Fibers and Temperature on the Impact Strength of an Epoxy/Polyurethane Blend Matrix", *International Conference on Materials Engineering and Science*, IOP Conf. Series: Materials Science and Engineering, vol. 454, pp.1-6, 2018.
- [19] P. Sarkar, N. Modak, and P. Sahoo, "Effect of Normal Load and Velocity on

- Continuous Sliding Friction and Wear Behavior of Woven Glass Fiber Reinforced Epoxy Composite,” *Materials Today: Proceedings*, vol. 4, pp. 3082–3092, 2017.
- [20] W. Wieleba, “The Mechanism of Tribological Wear of Thermoplastic Materials,” *Archives of Civil and Mechanical Engineering*, Vol: VII, No:4, pp. 185-199, 2007.
- [21] V. Quaglioni and P. Dubini, “Friction of Polymers Sliding on Smooth Surfaces,” *Advances in Tribology*, Volume 2011, pp. 1-8, 2011.
- [22] K.V. Shooter and D. Tabor, “The Frictional Properties of Plastics,” *Proceedings of the Physical Society. Section B*, Volume: 65, Number: 9, Pages: 661–671, 1952.
- [23] Kishore, P. Sampathkumaran, S. Seetharamu, S. Vynatheya, A. Murali, R.K. Kumar, SEM observations of the effects of velocity and load on the sliding wear characteristics of glass fabric–epoxy composites with different fillers, *Wear*, vol. 237, pp. 20–27, 2000.
- [24] A. Mimaroglu, H. Unal, and T. Arda, “Friction and Wear Performance of Pure and Glass Fiber Reinforced Poly-Ether-Imide on Polymer and Steel Counter face Materials,” *Wear*, vol. 262, pp.1407–1413, 2007.
- [25] B. Suresha, G. Chandramohan, P. Sampathkumaran, S. Seetharamu, and S. Vynatheya, “Friction and Wear Characteristics of Carbon Epoxy and Glass-Epoxy Woven Roving Fiber Composites,” *J. of Rein. Plast. and Comp.* vol. 25, pp. 771-782, 2006.
- [26] *Surface Effects and Contact Mechanics X: Computational Methods and Experiments*, WIT Transactions on Engineering Sciences, Vol 71, 2011 WIT Press, UK, page 223, Edited By: J.T.M. DE HOSSON, C.A. Brebbia, ISSN 1743-3533 (on-line)
- [27] H. Pıhtılı and N. Tosun, “Effect of load and speed on the wear behaviour of woven glass fabrics and aramid fibre-reinforced composites,” *Wear*, vol. 252, pp. 979–984, 2002.

JOURNAL OF SCIENCE



SAKARYA UNIVERSITY

Sakarya University Journal of Science

ISSN 1301-4048 | e-ISSN 2147-835X | Period Bimonthly | Founded: 1997 | Publisher Sakarya University |
<http://www.saujs.sakarya.edu.tr/en/>

Title: Determination of Coverage Oscillation for Inclined Communication Satellite

Authors: İbrahim ÖZ, Ümit Cezmi YILMAZ

Received: 2020-03-11 11:42:47

Accepted: 2020-07-21 21:12:03

Article Type: Research Article

Volume: 24

Issue: 5

Month: October

Year: 2020

Pages: 973-983

How to cite

İbrahim ÖZ, Ümit Cezmi YILMAZ; (2020), Determination of Coverage Oscillation for Inclined Communication Satellite. Sakarya University Journal of Science, 24(5), 973-983, DOI: <https://doi.org/10.16984/saufenbilder.702190>

Access link

<http://www.saujs.sakarya.edu.tr/en/pub/issue/56422/702190>

New submission to SAUJS

<http://dergipark.org.tr/en/journal/1115/submission/step/manuscript/new>

Determination of Coverage Oscillation for Inclined Communication Satellite

İbrahim ÖZ^{*1}, Ümit Cezmi YILMAZ²

Abstract

The communication engineers need to evaluate footprint movement to deploy a ground station. Geostationary communication satellite's inclination angle causes the movement of a satellite footprint. The calculation of the inclination angle requires complex astronomical knowledge and mathematical calculations. On the other hand, a satellite communication engineer does not need a very accurate inclination angle value to design a ground station for required service availability. We propose a practical method called trigonometric curve fitting for the inclination to solve the problem. The past and the future value of inclination can be evaluated by using the curve-fitting method. It is a simplified practical method and does not need advanced orbital dynamics knowledge. The orbit geometry and evaluated inclination angle are used for estimation of a coverage area movement. A satellite communication engineer can evaluate coverage area oscillation quickly and design a better link for an inclined orbit satellite by using the proposed method. We have evaluated the inclination angle of the communication satellite Sat-1 with the proposed method. Sat-1 spot beam movements and wide beam coverage area movements are estimated to obtain EIRP and G/T fluctuation for link budget purposes. The proposed method provides the results that are consistent with the results of measurements and the results of satellite operators' professional tools.

Keywords: coverage oscillation, geo satellite, communication, inclination, curve fitting

1. INTRODUCTION

Geostationary (GEO) satellites are placed into the orbit with 35786 km altitude above the equator. This orbit is called Clarke belt, and the satellites on this orbit have the same revolution period with the earth rotation. GEO satellites seem to be fixed from the earth [1]. The users can have full time transmit/receive ability with a satellite by using

simple non-tracking, fixed antenna. GEO satellites called communication satellites' primary services are television broadcasting, internet, telephone, and military applications. GEO communication satellites, although they are named as "geostationary," they are not entirely stable in space. The perturbing forces that cause the satellite orbit motion to deviate from an ideal theoretical orbital motion. The sun and the moon gravitational forces, non-uniform mass

* Corresponding Author: ibrahim1loz@gmail.com

¹ Turksat AS, Cevizliler Cad. No:31, Ankara, Turkey, ORCID: <https://orcid.org/0000-0003-4593-917X>

² Turksat AS, Satellite Control Center Ankara, Turkey, E-Mail: cylimaz@turksat.com.tr
ORCID: <https://orcid.org/0000-0001-5886-9743>

distribution of earth, solar pressure, and electromagnetic are primary perturbing forces act on a GEO satellite [2-5]. GEO satellites have two types of movements under the external forces. The first is north-south (N/S) oscillation and the second is to drift east or west (E/W) direction to the closest stable longitude.

Maneuver compensates perturbing forces acted on a satellite. North-south station keeping (NSSK) and east-west station-keeping (EWSK) maneuvers are performed periodically to keep a communication satellite within a defined control window. NSSK maneuver controls the inclination angle and consumes much more propellant than EWSK maneuvers. It is about 20-24 times more propellant consumption than EWSK maneuvers [6-8]. EWSK maneuver controls longitudinal drift and eccentricity.

GEO satellite lifetime is calculated by taking available fuel disregarding equipment and subsystems' lifetime. Aging GEO satellite lifetime can be extended by performing only the EWSK maneuver to use the remaining limited amount of fuel more efficiently. The satellite operators decide to stop the NSSK maneuvers to extend the lifetime of a communication satellite for several years. In this case, satellites become operated in an inclined orbit. A geosynchronous orbit with a non-zero inclination is defined as inclined geosynchronous orbit (IGSO). Fixed ground stations cannot track IGSO satellites all day. Ground stations that have tracking system can track the IGSO satellites all day [9,10]. The operators offer special services via IGSO satellites. The IGSO satellites provide services to stations that have tracking capability. Customers or users access special services such as short time satellite newsgathering, point-to-point data transmission.

The IGSO satellite's inclination increases gradually by time but communication payload continues to operate, with some loss of performance at some parts of the coverage beams. Another issue satellite no longer always point accurately because of inclination at the boresight on the ground all of the time. IGSO satellite coverage beams movement follow the satellite inclination angle. This movement is basically in

the north-south direction and sinusoidal. Its period is equal to the satellite period which is 24 hours. Oscillating coverage beams cause signal degradation even service interruption at certain time interval and some parts of coverages [1,8-10].

The footprint or coverage area of a communications satellite is the ground area that a satellite transmits and or receives signals within that area. Each satellite transponders or group of transponders offers different footprint maps to provide services to the desired customer area. Wide coverage area is ideal for transmitting signals over a vast geographical area while spot beam provides high power signals over small size area.

The product of transmit antenna gain and the maximum RF power per transponder defines the most important technical parameters of a communication satellite, effective isotropic radiated power (EIRP). The relative gain to noise temperature ratio (G/T) defines the receive performance of a communication satellite. These two main parameters contour values inside coverage map identify signal levels and provide information about requirements of ground system. Unfortunately, coverage contour follows satellite movement, and EIRP and G/T values are subject to change at earth fixed ground station point.

This paper aims to determine a coverage beam movement of IGSO satellite to support satellite communication engineers about EIRP and G/T margins. EIRP and G/T level vary due to inclination. The variation must be considered to have a successful transmission of signals. Satellite communication engineers can design better satellite links by having signal fluctuation levels and related link budget margins. On the other hand, the calculation of the Keplerian parameters, including the inclination angle, requires complex astronomical knowledge and mathematical calculations. The development of a new method simplifies the estimation of the inclination. A new method proposed to evaluate the inclination angle and related coverages oscillation to achieve the goal. The trigonometric curve fitting method (CFM) applied to the inclination data, and we

obtain the inclination as a function of time. The method simplifies the calculation for the prediction of the inclination angle and related coverage movement.

ITU-R requirement is to operate a communication satellite within a $\pm 0.1^\circ$ control window in N/S and E/W direction. This $\pm 0.1^\circ$ control window allows the operator about 11 km daily oscillation on satellite beams. That is why, for the proposed method presented in this work, 11 km has been chosen as success criteria.

2. INCLINATION ANGLE and COVERAGE OSCILLATION RELATION

The inclination angle is one of the six Keplerian orbital parameters, which defines the angle between the equatorial plane and satellite orbital plane. Figure 1 below shows an illustrative image of earth equatorial plane and satellite orbital plane with inclination. Satellite inclination causes to move satellite in N/S direction. The period of that sinusoidal oscillation is the same as the satellite revolution period 24 hours (1436,7 minutes). We assume a satellite at zero latitude at time T_0 , and then it reaches maximum inclination value at T_0+6h and T_0+18h . A satellite crosses the earth equator twice a day. Satellite completes its' 12 hours' revolution over the northern hemisphere and another 12 hours over the southern hemisphere due to the inclination angle [8,11-13]. Figure 3 shows satellite inclination angle instantaneous values for 1° , 3° , and 5° inclination over one revolution period. IGSO satellite ground track is the path followed by the sub-satellite points.

The altitude and the latitude of a satellites influence the ground track figure8-shape. IGSO satellite ground track shape is like figure-8 shape. The typical figure-8 shape of the GEO circular orbit (zero eccentricity) is shown in Figure 2 Increased eccentricity distorts the figure-8 shape. The view of figure-8 shape depends on earth station latitude. If figure-8 shape midpoint is on the higher or lower altitude instead of being on the equator then, the view of figure-8 shape is distorted. The slender and very long or

asymmetric figure-8 shape can be observed at higher latitudes.

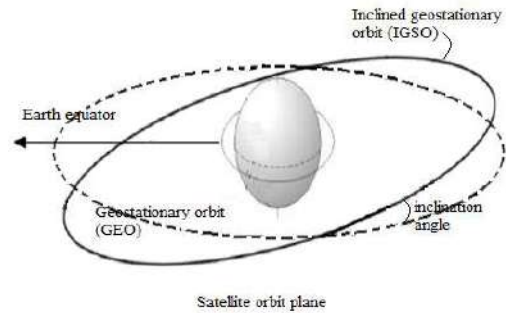


Figure 1 GEO inclination angle (the angle between the earth equator plane and satellite orbit plane)

The sub-satellite point over the earth follows the deviation in the longitude and latitude values of a communication satellite. The coverage pattern moves with the satellite inclination in both N/S and E/W direction, as shown in Figure 2. Satellite and coverages draw a figure-8 shape over a day, as shown in Figure 4. The width of the figure-8 shape depends upon E/W oscillation, while the height of the figure-8 shape depends upon N/S oscillation. The sub-satellite points of an IGSO satellite N/S oscillation exactly follow the inclination angle. Sub-satellite points E/W oscillation due to inclination is negligibly small for the eccentricity close to zero [4,14]. That's why in this study, E/W oscillation is not considered.

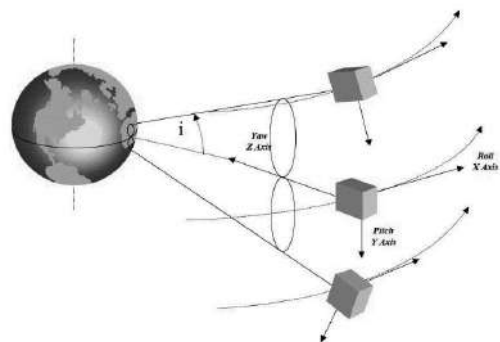


Figure 2 Satellite pointing in inclined orbit configuration, sub-satellite points over the earth, and daily figure-8 shape due to inclination

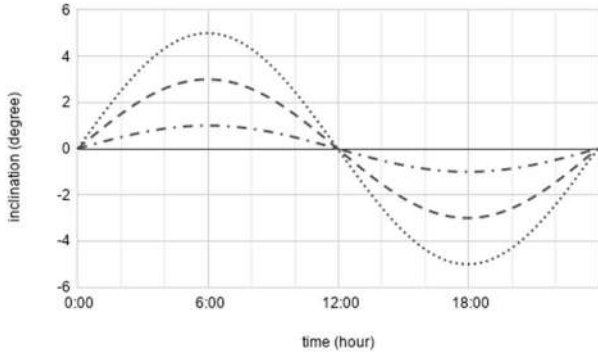


Figure 3 Satellite GEO satellite variation of inclination angle for 1°, 3° and 5° over one revolution period (one sidereal day)

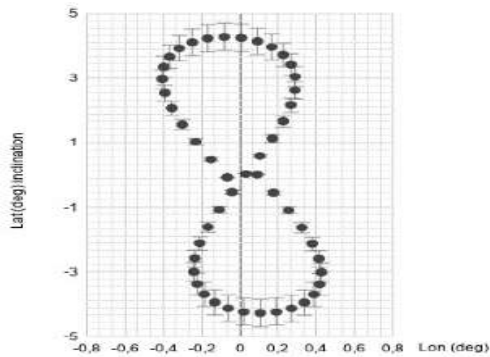


Figure 4. Diurnal movement of an inclined orbit satellite figure-8 shape over one sidereal day (ground track of IGSO), not to scale

Satellites ground stations have many types according to ITU-R regulations. Satellite ground stations may have satellite tracking capability or may have fixed antenna dishes according to the regulations. Fixed ground stations (antenna has no satellite tracking capability) have antenna mechanical misalignment due to inclination. Those misalignments are out of our study. So we neglect the signal change due to antenna misalignment. We assume the ground station's antenna has satellite tracking capability, and the antenna can track the satellite correctly. In this case, the only movement of the coverages is considered due to the inclination and neglecting other effects. The movements cause a signal change in both uplink and downlink for the ground station. Now, we can consider only uplink and downlink signals fluctuation due to the inclination angle. This oscillation affects satellite EIRP and G/T performance. The effect can be assessed as a loss in satellite performances at the

Centre of Coverage (CoC) and the Edge of Coverage (EoC) as shown in the following (Equation 1) to (Equation 4):

$$\Delta G_c = \text{EIRP}_{\text{initial}} - \text{EIRP}_{\text{final}} \quad (1)$$

$$\Delta G_E = \text{EIRP}_{\text{initial}} - \text{EIRP}_{\text{final}} \quad (2)$$

$$\Delta G_c = G/T_{\text{initial}} - G/T_{\text{final}} \quad (3)$$

$$\Delta G_E = G/T_{\text{initial}} - G/T_{\text{final}} \quad (4)$$

where;

ΔG_c : Gain Loss at the center of coverage (CoC) due to a coverage movement

ΔG_E : Gain Loss at the edge of coverage (EoC) due to a coverage movement

Satellite coverage areas follow the sub-satellite point's sinusoidal movement. The fluctuation in EIRP and G/T effect ground station sizing and availability of transmission. The primary ground station sizing contains antenna diameter and high power amplifier size. A communication engineer must consider other ground station devices such as up or down converters, low noise amplifiers, waveguides, couplers, attenuators, and their losses to perform accurate and optimized link budget.

3. TRIGONOMETRIC CURVE FITTING METHOD (CFM) AND INCLINATION

The GEO satellites are under the perturbing forces such as the sun and the moon gravitational forces, non-uniform mass distribution of the earth, solar pressure, electromagnetic forces, planets, and other stars gravitational forces, etc. The sun and the moon and earth gravitational forces have large magnitude and primary contributors to the satellite orbit perturbations. The remaining perturbing forces have small effects. When all contributors are taken into account the calculation of the inclination angle becomes very complex. There are many approaches to evaluate the inclination angle accurately [1]. However, if the inclination angle is not used for satellite control purposes such as maneuver planning, conjunction analysis, etc., the evaluation may be simplified and customized for new purposes.

The inclination angle of a GEO satellite depends on time. It's main characteristics are; it has annual increment between 0.75° and 0.95° depending on the year, it has a magnitude up to 15 degrees [1,9,14] depending on the high area to mass ratio, and it has 18.6 years period because of the moon and the sun orbits and their gravity forces [9].

The periodic motions that have sinusoidal characteristics have been used for most of the approximations in astronomy and orbital motions. The trigonometric curve fitting method (CFM) expresses the periodic oscillation phenomena and movements effectively. The trigonometric curve fitting is a new method to evaluate the inclination angle. The CFM is the process of constructing a curve or mathematical function that has the best fit to a data set. In numerical trigonometric curve fitting technique, the sum of sines models fits periodic functions and given by,

$$f = \sum_{j=1}^n a_j \sin(b_j x + c_j) \quad (5)$$

In this study, we applied the CFM to inclination angle data sets, and we determine the inclination angle behavior of communication satellites. We obtained data sets from actual measurements of the inclination angle of the satellite and theoretical propagated results of the tool. These propagated values are taken from the focusgeo program, which is the software provided by GMV and commonly being used among the satellite operators, including TURKSAT. This professional tool determines the orbit of the satellite by using a series of numeric integrations and plans the control maneuvers and their firing durations as well as directions. The measured and propagated data sets have been processed, and the inclination equation and its correlation coefficient were obtained. Among different curves, the following (Equation 6) has been obtained;

$$i_{annual} = 0.097 \sin(0.3378t + 2.538) + 0.856 \quad (6)$$

where i : inclination angle in degree/year,
 t : the yearly inclination angle variation to be calculated (like 2020, 2021 etc).

The (Equation 6) correlation coefficient is 0.9963 compared to the theoretical inclination results. Figure 5 shows the behavior of the inclination for each year from 1970 to 2040 and the relationship between theoretical values and the curve fitting results.

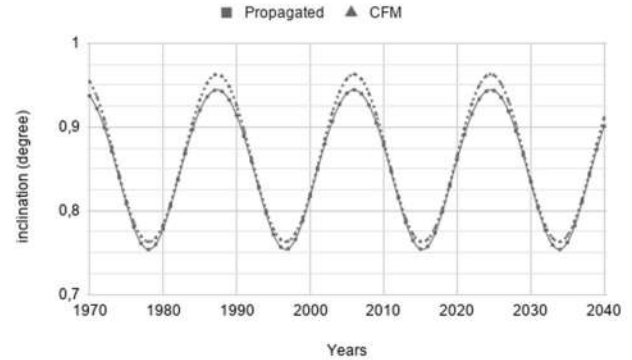


Figure 5 Comparison of proposed calculation and theoretical inclination

The formula is given in (Equation 7) starts with January 1st of each year. Accumulated inclination angle can be calculated by integrating the (Equation 6) and, as shown in (Equation 7);

$$\Delta i = \frac{\partial i}{\partial Y} \int_{T_0}^{T_1} i_{annual} dt + i_{initial} \quad (7)$$

where: T_0 and T_1 are the dates in decimal (for example 30 June 2020 = 2020.5).

T_0 : the date of the final inclination control maneuver,

T_1 : the day of inclination angle calculated,

$i_{initial}$: the initial inclination at T_0 .

(Equation 8) can be derived from the geometry, which takes into account the radius of the earth, R_e , as 6378.1 km to calculate the final oscillation of the spot beam in N/S direction.

$$n_{S_{osc}} = i R_e \frac{\pi}{180} \quad (8)$$

where: $n_{S_{osc}}$ beam movement of a satellite in km.

The inclination not only causes oscillations in N/S direction, but it also causes footprint movement in E/W direction due to conservation of the angular momentum as per Kepler's Second Law and due to the Earth oblateness. Considering the earth radius seen from GEO orbit is 8.6708 degrees (which is about 0.151 rad) and by using the polar radius of the earth (R_p), which is about 6356.8 km. Similarly, from the geometry, the oscillation at E/W longitude sinusoidal

half width oscillation due to inclination and for zero eccentricity can be calculated, as shown in (Equation 9).

$$ew_{osc} = \left(\operatorname{atan}\left(\frac{1}{2}\sqrt{\sec(i)} - \sqrt{\cos(i)}\right) R_p \frac{\pi}{180} \right) \quad (9)$$

E/W oscillation due to 1°, 3° and 5° inclinations are 0.004°, 0,039°, 0.109° respectively. Circular orbit (eccentricity very close to zero) IGSO satellites E/W oscillation due to inclination is negligibly small and has minor effect on EIRP and G/T. That is why in this study, E/W oscillation effects on signals level are not considered. The N/S oscillation caused by the inclination moves the coverages from its zero inclination position. Figure 6 shows the boresight movement in terms of km for 3° inclination. Its maximum displacement is around 334 km when the satellite is at the north and the south peak latitude. Larger inclination causes more displacement and more magnitude of oscillation.

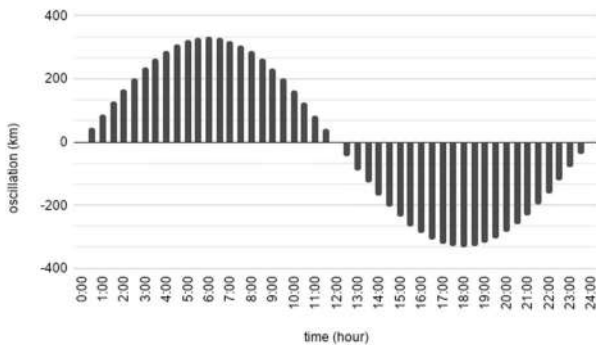


Figure 6 GEO satellite at 3-degree inclination, coverage movement in km for 24 hours' period

3.1. Sat-1 Communication Satellite at IGSO

We have selected Sat-1 communication satellite as an illustrative example. Sat-1 wide area coverage and spot beam are examined to verify signal fluctuation. A satellite spot beam and wide beam have different oscillations in terms of signal fluctuation level. Similarly, coverages at the equator and coverages at the higher altitude have different behavior in terms of E/W oscillation. However, the oscillation in the E/W direction was not considered because of explained reasons. We selected two ground stations as a reference. The

first CoC site is in the middle of the spot beam at 32.00° E longitude and 40.00° N latitude while the second reference is EoC site, and it is at 32.00° E longitude and 35.00° N latitude. Figure 7 below shows the spot beam examples on Sat-1 satellite at 42.00° East longitude and in 0°, 1°, 5°, -3°, -1°, and -5° inclinations. The “+” sign shows the antenna boresight, and the contours show the center of coverage, mid of coverage, and the edge of coverage from inner contour to outer contour, respectively. The boresight has peak EIRP and G/T values while the outer contour has 20 dB gain loss compared to the peak value. Outside of the outer contour is assumed to be out of service area. The movement due to inclination is shown in Figure 7 for the Turkey spot beam of Sat-1. Figure 7 shows inclination maximum and minimum values i.e Sat-1 at T₀+6 and T₀+18 hour. The coverages are in between those two places and draw the sinusoidal figure, as shown in Figure 2.

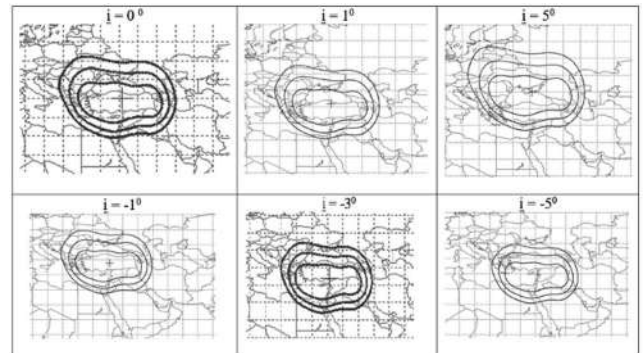


Figure 7 Sat-1 spot beam movement for 0°, 1°, 5°, -3°, -1° and -5° inclination, from satellite @42° East

Figure 8 below shows the wide beam examples on a Sat-1 satellite at 42.00° East longitude and in 0°, 1°, 5°, -3°, -1°, and -5° inclination. We selected two ground sites as a reference to calculate signal level fluctuation. The CoC site is in the middle of the wide beam at 32.00° E longitude and 40.00° N latitude while the second reference is EoC site, and it is at 38.00° E longitude and 24.00° N latitude. Similarly, “+” shows boresight of the satellite antenna, and the contours show the center of the coverage, mid of the coverage, and the edge of the coverage from closed inner to outer line, respectively. The boresight has peak EIRP and G/T values. The outer contour has 20 dB gain loss. We assume inside of the outer contour is the service area of the Sat-1. The inclinations 1° and 5° show Sat-1 at time T₀+6 hour while the inclination -1°, -3°, and -5° show Sat-1 at time T₀+18 hour.

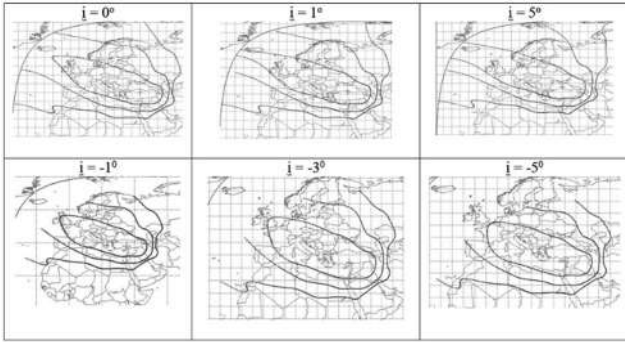


Figure 8 Sat-1 wide beam movement for 0° , 1° , 5° , -1° , -3° and -5° inclination, from satellite @ 42° East

The Figure 7 and Figure 8 coverage contours are taken from actual Sat-1 antenna pattern data. The measured and propagated inclination angle effects on the Sat-1 spot beam (small size coverage) and wide beam (large size coverage) show coverages movement at north peak and south peak inclination compared to reference zero inclination. Those figures show 1 cycle oscillation. The beam's complete cycle oscillation is fully interpreted by combining Figure 3 with Figure 7 and Figure 8.

4. RESULTS AND DISCUSSION

We have obtained the inclination values with the CFM for future and past. Those results first compared with the measured data of in orbit satellite. The actual measured data has been taken from the TURKSAT Sat-1 satellite. This satellite last N/S maneuver was performed on July 18th, 2008, and then the satellite was left in inclined orbit operation. The second column of Table 1, shows the measured inclination angle of Sat-1 at different times. The measured inclination angle of the satellite data was acquired from the Sat-1 orbit measurement's value from the satellite control center. The CFM column shows the results evaluated with the proposed method. The comparison of measured and CFM results are very close to each other. As can be seen in the last column, the differences are always less than 9 km. The measured data of the inclination and the evaluated data of the inclination mean difference is 0.038° , which is about 4.23 km. So the results

obtained from the CFM are in very good agreement with the results of measurements.

Table 1

Comparison with Sat-1 measured and proposed CFM inclination values, T_0 : 19.05.2008, initial inclination 0.153°

T	Inclination		Δi	ns _{osc} (in km)		Δns_{osc} km
	M.	CF		M.	CF	
25.09.2008	0.49	0.48	0.018	55.3	53.3	1.98
18.12.2008	0.72	0.69	0.026	79.7	76.8	2.91
26.02.2009	0.91	0.87	0.044	100.9	95.9	4.92
24.09.2009	1.40	1.38	0.024	156.2	153.5	2.71
03.12.2009	1.58	1.55	0.034	176.2	172.5	3.82
11.03.2010	1.83	1.79	0.049	204.1	198.7	5.49
29.07.2010	2.19	2.12	0.074	244.0	235.8	8.25

Table 2 shows the theoretical propagated inclination angle of Sat-1 for the past. The past years propagated inclination data are obtained from the tool by running the software backward in time. The CFM column shows the results evaluated with the proposed method in a backward direction in time. The comparison of theoretical propagated and CFM results are very close to each other. As the results can be seen in the last column, the differences are always less than 9 km. The propagated data of the inclination and the evaluated data of the inclination average difference is 0.038° that is about 4.23 km.

Table 2

Comparisons with propagated (p) and curve fitting (CF) method in backward direction, $T_0=01.01.2000$ and initial inclination 0.001°

T	Inclination		Δi	ns _{osc}		Δns_{osc} (km)
	P.	CF		P.	CFM	
19.07.2000	0.46	0.45	0.0063	51.3	50.61	0.70
04.02.2001	0.92	0.92	0.0036	102.3	101.89	0.40
23.08.2001	1.38	1.39	0.0066	153.8	154.51	0.73
11.03.2002	1.85	1.87	0.0174	206.3	208.23	1.94
27.09.2002	2.31	2.36	0.0503	257.4	262.99	5.59
15.04.2003	2.80	2.86	0.0665	311.3	318.72	7.40
01.11.2003	3.29	3.37	0.0807	366.3	375.30	8.98

Table 3 shows the future theoretical propagated inclination angle of Sat-1. Those data are obtained from the focusgeo tool by running the software forward in time, and we get the next year's estimated inclination angle values. The CFM column shows the results evaluated with the proposed method in the forward direction in time. The comparison of the theoretical propagated and

CFM results are very close to each other. As the results can be seen in the last column, the differences are always less than 9 km. The propagated data of the inclination and the evaluated data of the inclination average difference is 0.032^0 that is about 3.56 km. The differences between the results of CFM and other methods are all less than 0.10 and less than 11 km, which is the success criteria.

Table 3

Comparisons with propagated and proposed method in forward direction, $T_0=01.01.2020$ and initial inclination 0.001^0

T	Inclination		Δi	nsosc (in km)		$\Delta nsosc$ (km)
	P.	CF		P.	CF	
19.07.2020	0.48	0.48	0.001	53.2	53.3	0.09
04.02.2021	0.97	0.97	0.001	107.5	107.3	0.14
23.08.2021	1.46	1.46	0.004	162.2	162.6	0.47
11.03.2022	1.94	1.97	0.025	216.1	218.8	2.74
27.09.2022	2.43	2.48	0.052	270.1	275.9	5.73
15.04.2023	2.93	2.99	0.063	326.5	333.5	6.97
01.11.2023	3.43	3.52	0.085	382.2	391.6	9.41

We can study the inclination angle effects on satellite communication performance. To analyze the effects, we have a communication satellite illustrative examples that are for inclination 1^0 , 3^0 , and 5^0 cases.

The IGSO satellites are generally multi-beam satellites. When a satellite moves due to inclination, all coverages move together with satellite. Coverage movement due to N/S oscillations influences satellite communication performances. We assume the sub-satellite point is on the equator at T_0 in this case satellite operates like in geostationary operation. However, at the $T_0 +6$ h satellite reaches maximum inclination value on the northern hemisphere, the coverages move the north, and maximum displacement occurs with respect to zero inclination nominal operation status. Satellite continues its movement and T_0+18 hour; it reaches maximum inclination value in the southern hemisphere, again the maximum coverages displacement occurs with respect to zero inclination but in the opposite direction in this case. Satellite coverages movement follows

the sinusoidal movement, as shown in Figure 2. Consequently, the satellite's EIRP and G/T fluctuate due to the inclination. These oscillations influence satellite transmit EIRP and satellites receive G/T.

We assume the edge of coverage ground station is at the southern part of the contour. In this case, EIRP and G/T values first increase and then decrease for negative inclination values. Table 4 shows spot beam EIRP and G/T fluctuation for Sat-1 IGSO satellite. Center of the coverages EIRP and G/T changes due to 3^0 inclination is about 1.5 dB. Edge of coverages EIRP and G/T fluctuation due for 3^0 inclination is about 4.5 dB.

Table 4

Sat-1 Spot beam EIRP G/T variation due to the given inclination angles

i	EIRP CoC	EIRP EoC	G/T CoC	G/T EoC	Δ EIRP CoC	Δ EIRP EoC	Δ G/T CoC	Δ G/T EoC
0^0	53.53	43.03	11.28	-7.77	0.00	0.00	0.00	0.00
1^0	52.99	40.98	11.28	-8.77	-0.54	-2.05	0.00	-1.00
3^0	51.41	36.31	9.73	-12.77	-1.58	-4.67	-1.55	-4.00
5^0	49.66	30.66	9.23	-18.82	-1.75	-5.65	-0.50	-6.05
-1^0	52.67	36.67	11.01	-6.71	3.01	6.01	1.78	12.11
-3^0	51.31	41.82	9.79	-8.59	-1.36	5.15	-1.22	-1.88
-5^0	49.44	29.35	9.41	-12.91	-1.87	-12.47	-0.38	-4.32

Similarly, Table 5 shows wide beam EIRP and G/T fluctuation for Sat-1 IGSO satellite. CoC EIRP and G/T changes due to 3^0 inclination is about 1.5 dB. This value is very good. Edge of coverages EIRP and G/T fluctuation due to 3^0 inclination is about 3 dB.

Table 5

Sat-1 Wide beam EIRP G/T variation due to the given inclination angles

i	EIRP CoC	EIRP EoC	G/T CoC	G/T EoC	Δ EIRP CoC	Δ EIRP EoC	Δ G/T CoC	Δ G/T EoC
0^0	51.14	37.59	4.84	-9.54	0.00	0.00	0.00	0.00
1^0	50.60	35.62	4.56	-11.51	-0.54	-1.97	-0.28	-1.97
3^0	49.01	32.01	3.35	-15.12	-1.59	-3.61	-1.21	-3.61
5^0	47.27	28.61	2.83	-18.52	-1.74	-3.40	-0.52	-3.40
-1^0	50.28	36.51	4.59	-10.62	3.01	7.90	1.76	7.90
-3^0	48.92	41.61	4.51	-13.52	-1.36	5.10	-0.08	-2.90
-5^0	47.05	37.57	3.12	-17.56	-1.87	-4.04	-1.39	-4.04

The daily coverages oscillation of an IGSO satellite can be determined practically to understand the EIRP and G/T fluctuation at the earth station at CoC and EoC. The earth stations at EoC, are more affected than the stations at the CoC. Additional power requirement of 3 dB due to coverage movement implies to have double HPA size or implies to have larger size antenna. The users may not request 24 hours uninterrupted transmission; in this case, the communication engineers may prepare a part-time transmission plan by using daily EIRP and G/T fluctuation.

EIRP and G/T values evaluated with the CFM and other method are shown in Table 6. Referring EIRP and G/T change to compare the methods, it is about 10^{-4} or 10^{-3} dB. These values have no practical meaning in terms of antenna diameter and HPA size.

Table 6

The difference of inclination angle average and standard deviation values for the CFM vs

Measurements and the CFM vs Forward propagation

	Δi CFM- Measurement	Δi CFM- Propagated	$\Delta EIRP$ dB	$\Delta G/T$ dB/K
Avg	0.0386°	0.0328°	$\sim 10^{-4}$	$\sim 10^{-4}$
Stdev	0.0192°	0.0337°	$\sim 10^{-3}$	$\sim 10^{-3}$

These small differences in the inclination angle of the CFM and the other methods have no effect on parameters of the link budgets. Therefore, the related earth station sizing is the same for all methods.

The communication engineers check link margins before the start of services. Satellite EIRP, G/T fluctuation due to inclination depends on coverage size and shape. Spot beams i.e., small size coverages, have more degradation in signal level and quality. The wide beams have less fluctuation and hence more degradation in signal level and quality. The edge of coverages has considerable fluctuation. Signals may not be received at the edge of the coverages in some period of day, even if ground stations entirely operated.

5. CONCLUSION

A practical simplified method was developed to estimate the coverage movements of an IGSO communication satellites. The inclination angle of a communication satellite depends many astronomical factors such as, the sun and the moon gravitational forces and the earth obsolescence. The satellite communication engineers evaluate the coverage oscillations quickly by using the CFM. Comparisons of the CFM with real data and propagated data show that the footprint variation can be predicted better than 10 km accuracy, and this value is below the nominal daily oscillation of any GEO satellite which is controlled in $\pm 0.1^\circ$. However, the CFM is not suitable for satellite control purposes, such as maneuver planning or conjunction analysis. The method is valid to use for a maximum duration of 27 consequential years, which means up to 15° inclination.

Acknowledgements

We would like to thank Turksat Uydu Haberlesme ve Kablo TV AS for its invaluable support.

Funding

The authors received no financial support for the research, authorship, and/or publication of this paper.

The Declaration of Conflict of Interest/ Common Interest

No conflict of interest or common interest has been declared by the authors.

Authors' Contribution

İ.Ö. and C.Y. conceived a new method to calculate inclination and to evaluate the relevant footprint movement. C.Y. developed the CFM and performed the inclination angle computations. İ.Ö. and C.Y. verified the analytical methods with practical measurements. İ.Ö. performed calculation of footprint movement and EIP and G/T fluctuation. İ.Ö. wrote the

manuscript. Both İ.Ö and C.Y. contributed to the final version of the manuscript.

The Declaration of Ethics Committee Approval

The authors declare that this document does not require an ethics committee approval or any special permission.

The Declaration of Research and Publication Ethics

The authors of the paper declare that they comply with the scientific, ethical and quotation rules of SAUJS in all processes of the paper and that they do not make any falsification on the data collected. In addition, they declare that Sakarya University Journal of Science and its editorial board have no responsibility for any ethical violations that may be encountered, and that this study has not been evaluated in any academic publication environment other than Sakarya University Journal of Science.

REFERENCES

- [1] E. M. Soop, "Introduction to Geostationary Orbits", ESA, pp. 232-235, 1983.
- [2] B. Gurol, S. Gulgonul, G. Gokay, A. Okan, and I. Oz., "Optical monitoring of inter satellite distance between Turksat-2A And Turksat-3A. In Proceedings of 5th International Conference on Recent Advances in Space Technologies- RAST2011, pp. 337-340, 2011.
- [3] S. Hu-Li, H Yan-Ben, M. Li-Hua, P. Jun, Y. Zhi- Qiang, and J. Hai-Fu, "Beyond life-cycle utilization of geostationary communication satellites in end-of-life", Satellite Communications, Nazzareno Diodato(Ed), Intech, ISBN: 978-953-307-135-0, pp. 323-365, 2010.
- [4] L. Ma, "The Benefits of Inclined-Orbit Operations for Geostationary Orbit Communication Satellites", Artificial Satellite, Vol.46, DOI: 10.2478/v10018-011-0007-1, 2011 .
- [5] I. Oz, "Evaluation of station location for orbit determination of geo satellites at different slots", 8th International Conference on Recent Advances in Space Technologies (RAST), pp. 375-379, 2017.
- [6] Z. Chang-Yin, Z. Ming-Jiang, W. Hong-Bo, X. Jian-Ning, Z. Ting-Lei, and Z. Wei, "Analysis on the long-term dynamical evolution of the inclined geosynchronous orbits in the Chinese BeiDou navigation system, Advances in Space Research, 56 pp. 377–387, 2015.
- [7] Y. Han, L. Ma, Q. Qiao., Z.Yin, H.Shi, and G. Ai, "Functions of retired GEO communication satellites in improving the PDOP value of CAPS", Sci China Ser G-Phys Mech Astron, Vol. 52, No. 3, pp. 423-433, 2009.
- [8] G.Dai, X.Chen, M.Zuo, L. Peng, M. Wang, and Z. Song, "The Influence of Orbital Element Error on Satellite Coverage Calculation". International Journal of Aerospace Engineering, 2018.
- [9] S. Y. Fu, Z. R. Wang, H. L. Shi, and L. H. Ma, "The application of decommissioned GEO satellites to CAPS", In IOP Conference Series: Materials Science and Engineering, Vol. 372, No. 1, pp. 012033, IOP Publishing, 2018.
- [10] C.Sun, H. Jiang, J. Zhang, Y. Tao, B. Li, and C. Zhao, "Modeling and Calibrating the Ground-Surface Beam Pointing of GEO Satellite", IEEE Access, 7, 121897-121906, 2019.
- [11] S. Lee, "GEO Satellite Collision Avoidance Maneuver Strategy Against Inclied GSO Satellite", In SpaceOps :1294441, 2012.
- [12] A. F. Yagli, M. Gokten, S. Gulgonul, I. Oz, and O. Dalbay, "Regional positioning system using Turksat satellites", In 6th International Conference on Recent

Advances in Space Technologies
RAST:2013: pp.237-240, 2013.

- [13] A. E. Emam, J. Victor, and M. A. Elghany, “Performance Assessment of GSO Satellite before and after Enhancing Pointing Effect”, World Academy of Science, Engineering and Technology, International Journal of Electrical, Computer, Energetic, Electronic and Communication Engineering, 12, pp. 1434-1440, 2015.
- [14] A. E. Emam and M. A. Elghany, “Collocation Assessment between GEO and GSO Satellites”, International Journal of Aerospace and Mechanical Engineering, vol. 9, no. 12, pp. 2124-2132, 2015.

JOURNAL OF SCIENCE



SAKARYA UNIVERSITY

Sakarya University Journal of Science

ISSN 1301-4048 | e-ISSN 2147-835X | Period Bimonthly | Founded: 1997 | Publisher Sakarya University |
<http://www.saujs.sakarya.edu.tr/en/>

Title: Experimental Investigation on Effect to the Specific Strength of FDM Fabrication Parameters Using Taguchi Method

Authors: Sedat İRİÇ

Received: 2020-07-19 05:57:02

Accepted: 2020-07-27 13:31:15

Article Type: Research Article

Volume: 24

Issue: 5

Month: October

Year: 2020

Pages: 984-990

How to cite

Sedat İRİÇ; (2020), Experimental Investigation on Effect to the Specific Strength of FDM Fabrication Parameters Using Taguchi Method. Sakarya University Journal of Science, 24(5), 984-990, DOI:

<https://doi.org/10.16984/saufenbilder.771389>

Access link

<http://www.saujs.sakarya.edu.tr/en/pub/issue/56422/771389>

New submission to SAUJS

<http://dergipark.org.tr/en/journal/1115/submission/step/manuscript/new>

Experimental Investigation on Effect to the Specific Strength of FDM Fabrication Parameters Using Taguchi Method

Sedat İRİÇ*¹

Abstract

The Fused Deposition Modeling (FDM) fabrication is commonly used printing technique, the reasons behind this are low consumable cost, simplicity of workflow and more reliable. The quality of the printed parts depends on various process variables such as part orientation, layer thickness, hotend and bed temperature, fabricating speed, infill pattern and infill density, number of top-bottom solid layers, number of shells etc. Literature suggests that infill density, number of shells and number of top-bottom solid layers are variables that changing the tensile strength under tension of 3D fabricated parts and also have effect on weight of the parts. This study focuses on effect of infill density (ID), number of shells (NS) and top-bottom solid layers (TBSL) on specific strength (strength/weight ratio). Taguchi L18 Orthogonal Array (OA) design is used to perform the experiments. 18 runs with 3 repeated specimens were printed according to the ASTM D638 Type I standard using different printing variables. According to the results, parameters increase of ID, NS and TBSL were seen to effect significant improvement in the specific strength increase. However, between 40-60% ID has negative effect to specific strength while NS and TBSL increase.

Keywords: Fused Deposition Modelling, Specific Strength, 3D printing, Taguchi Method

1. INTRODUCTION

3D printing technology is used by defence and aviation, medical, automotive, logistics, food and other related industry due to its physical size, easy definition of workflow and cost effective fabrication of conceptual design, prototypes and functional components [1]. The usage of 3d printed components are increased day by day because of lower assembly and material expense of 3d printers. 3d printers using different production technologies and materials are

commercially available such as Stereolithography (SLA), Fused Deposition Modeling (FDM), Binder Jetting (BJ), Digital Light Processing (DLP). Working conditions, mechanical properties of parts, number of products and product quality etc. are played an important role in the selection of 3d printer. FDM type 3d printers are the most used printer type after resin based printers (SLA) due to their ease of production, low operating cost and different material usage options [2]. In this type of printers, the continuous filament fed from the reel is

* Corresponding Author: siric@sakarya.edu.tr

¹ Sakarya University, ORCID: <https://orcid.org/0000-0001-8477-7906>

extruded from the heated nozzle and laid according to the layer prepared in the slicing program and this process continues layer by layer until the part is produced. Schematic model of FDM process is shown in Figure 1 [3]. The part fabricated with FDM has 85% of the strength of the part that conventional manufacturing techniques used [4]. However, many variables such as layer height, printing speed, hot end and bed temperature, infill pattern, ID, NS and TBSL etc. should be optimized to produce part that has good mechanical properties. [5].

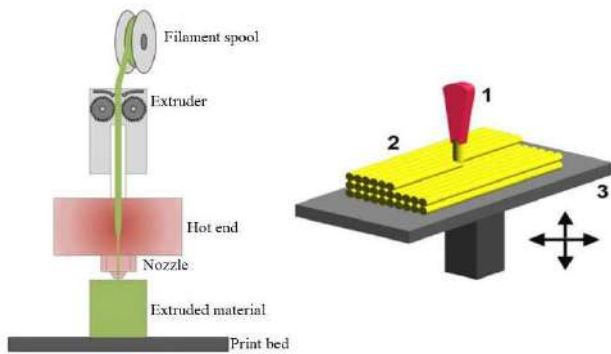


Figure 1 Schematic model of FDM printing (1-nozzle, 2-building material, 3-print bed) [3]

Nowadays, experimental research on FDM technology is still a novel technology and many researchers is investigated the influence of process variables on tensile properties of fabricated parts, for example, Tontowi et al. examined the effects of nozzle temperature, layer thickness and raster angles on tensile properties of build parts using Taguchi method [6]. Alafaghani et al. worked on the effect of some fabrication variables on tensile and geometric properties [7]. Monterol et al. studied the process parameters of FDM, using the design of experiment (DOE) approach [8]. Cristian et al. worked on influence of different infill rates, infill patterns and printing direction on mechanical properties of printed specimens [9]. Gebisa et al. investigated on the flexural strength of FDM fabricated samples that have different process parameters. [10]. Wang et al. studied the influence of various printing variables, including layer thickness, printing temperature and speed on the tensile properties [11]. Alafaghani et al. examined the selected four fabricating variables using Taguchi [12]. Christian et al. inspected the effect of printing

parameters on the tensile and flexural strength of ABS composite parts [13]. Mostafa et al. worked on to find out the maximization model for the strength to cost ratio using Taguchi prediction model [14]. The motivation of this work is to examine influence of ID, NS, TBSL on the specific strength (strength/weight ratio) of fabricated specimens using PLA (Polylactic acid) according to the ASTM 638 Type I standard.

2. METHODOLOGY

2.1. Taguchi Method

Taguchi technique is the most commonly used method to make design optimization efficiently. This method uses orthogonal array to reduce the number of test to a reasonable one, in terms of cost and time. [15]. Taguchi L18 OA was used to investigate the effect of the ID, NS and TBSL. An OA means the design is well balanced so that factor levels are weighted equally. Therefore, each factor can be analyzed independently of all the other factors, so the effect of one factor does not effect the estimation of other factor [16]. The ID has 6 levels, and the NS and TBSL have 3 levels as shown in Table 1.

Table 1

Level values for each variable

Variable	Level Values					
ID (Infill density) %	0	20	40	60	80	100
NS (No. of shells)	1	2	3			
TBSL (Top-bottom solid layer)	2	3	4			

Table 2 show that the value of printing variables with different levels used to fabricate tensile samples for each run. Each run was printed 3 times to control for repeatability of the obtained results and 54 specimens were fabricated for this study. During the fabrication some printing specification were remained constant like layer thickness at 0.2mm, the printing speed at 45.0 mm/s, the infill pattern at rectilinear, the nozzle and bed temperature at 195°C and 60°C, respectively.

Table 2
L-18 Orthogonal array

Run	ID (%)	NS	TBSL	No. of Specimen
1	0	1	2	3
2	0	2	3	3
3	0	3	4	3
4	20	1	2	3
5	20	2	3	3
6	20	3	4	3
7	40	1	3	3
8	40	2	4	3
9	40	3	2	3
10	60	1	4	3
11	60	2	2	3
12	60	3	3	3
13	80	1	3	3
14	80	2	4	3
15	80	3	2	3
16	100	1	4	3
17	100	2	2	3
18	100	3	3	3

2.2. Specimens Preparation

ASTM D638 Type I specimen was chosen due to fabrication time and repeatability. The specimen's shape and dimensions are shown in Figure 2. Solid model of specimen was designed in PTC Creo and converted to STL format with the same software and then the STL file were converted to G-code files with PrusaSlicer software and made ready for fabrication.

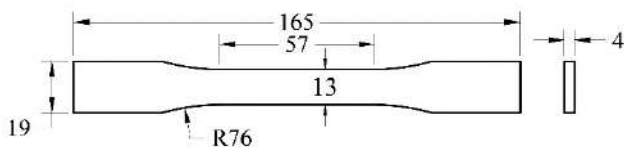


Figure 2 Dimensions of the ASTM D638 Type I tensile specimen, dimensions in mm

All samples were printed using the same spool and fabricated by a custom design Cartesian type FDM printer (Figure 3a) with 0.4 mm nozzle.

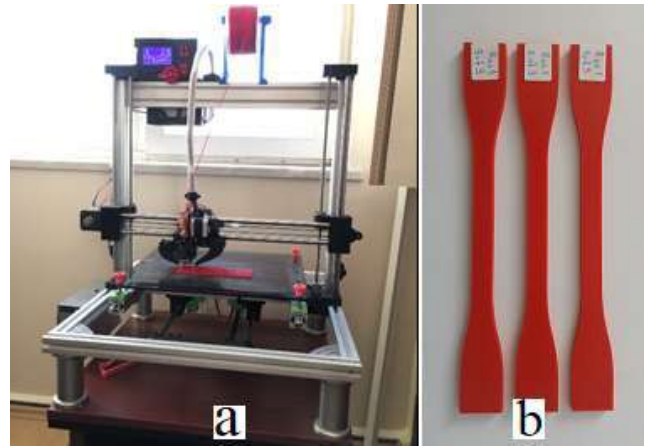


Figure 3 (a) Custom designed printer and (b) fabricated specimens

The filament used in the study has a diameter of 1.75 mm produced by UZARAS under the trade name PLA+. A total of 54 samples were produced and labeled for tensile tests, 3 samples were produced for each run (Figure 3b).

2.3. Weight Measurement and Tensile Testing

Before to examine the tensile properties of the printed specimens, the mass of the samples were measured using precision scales (resolution: 0.001 g) (Figure 4).



Figure 4 Desis NHB+ used in weighing of the specimens

All the samples were tested according to ASTM D638 standards on Zwick testing machine with a capacity of 50 kN (Figure 5). Tensile tests were conducted with a speed of 5 mm/min, following the standard and the test was stopped once the sample broken.



Figure 5 Zwick/Roell Z050 testing machine

Three test specimens were measured and tested for each run (Figure 6) and the evaluations were made by taking the arithmetic average of the weight values, peak load and specific strength values obtained in Table 3.



Figure 6 Tested tensile specimens

Table 3
L-18 Orthogonal array

Run	ID	NS	TBSL	Mean Weight (N)	Mean Peak Load (N)	Mean Specific Strength (N/N)
1	0	1	2	48,667	318	6,5
2	0	2	3	60,175	640	10,6
3	0	3	4	69,494	901	13,0
4	20	1	2	62,084	443	7,1
5	20	2	3	69,125	719	10,4
6	20	3	4	77,486	967	12,5
7	40	1	3	77,149	709	9,2
8	40	2	4	82,881	946	11,4
9	40	3	2	78,205	856	10,9
10	60	1	4	87,924	956	10,9
11	60	2	2	84,513	855	10,1
12	60	3	3	89,480	1086	12,1
13	80	1	3	96,288	1105	11,5
14	80	2	4	98,826	1264	12,8
15	80	3	2	97,269	1245	12,8
16	100	1	4	105,386	1562	14,8
17	100	2	2	105,255	1592	15,1
18	100	3	3	104,650	1609	15,4

3. RESULT AND DISCUSSIONS

The force vs elongation curves of 54 specimen were plotted and shown in Figure 7. The results of tensile test clearly demonstrated that noticeable difference has been found in all the values of test such as max. force and elongation.

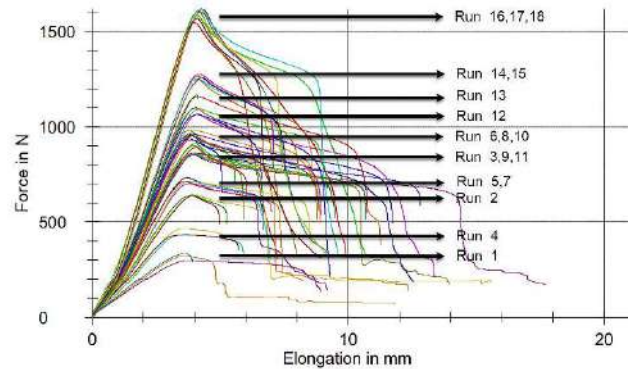


Figure 7 The results of tensile test (load-displacement) for all condition

The maximum peak load (1609 N) has been observed in case of run 18, which was printed at 100% ID, 3 NS and 3 TBSL. This indicates that the highest ID, NS and TBSL reinforce the inner form of specimen which under tensile loading. Using Taguchi design L18 OA analysis, the main effects plots graph Figure 8 were created. The test results were analyzed using the Minitab 19 software.

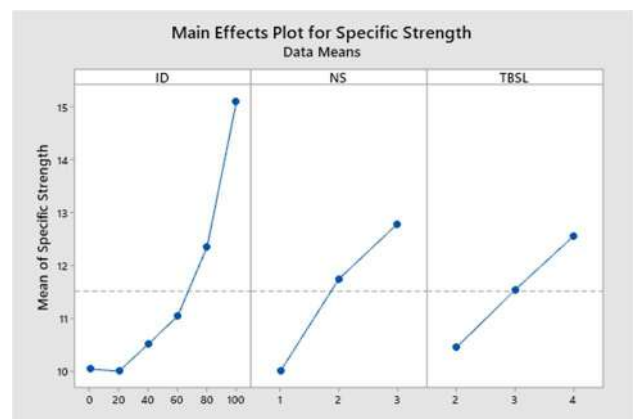


Figure 8 Main effects plot for Specific strength

From the Figure 8 between ID and mean specific strength, it is observed that the sample with 100% ID has the highest specific strength value of 15.4 N/N. Similarly, the specimen with 3 NS and 3 TBSL have the highest specific strength value of

12.78 N/N and 12.55 N/N respectively. However, the specimens with 0-20% ID have approximately the lowest specific strength value of 10 N/N. The lowest values of the NS and TBSL have the lowest specific strength as well (10 N/N and 10.4 N/N respectively). The specific strength increases linearly with increasing NS and TBSL. However, between 0-20% change of the ID does not cause a certain specific strength change. The reason for this is that as the ID increases, the peak load and the weight of the part also increase at a similar rate. Between 20-60% changes of the ID causes to increase specific strength. Furthermore, between 60-100% changes of the ID shows the most significant effect in the specific strength increase. Specific strength changes of test specimen fabricated using different ID, NS and TBSL are given as interaction graphs in Figures 9.

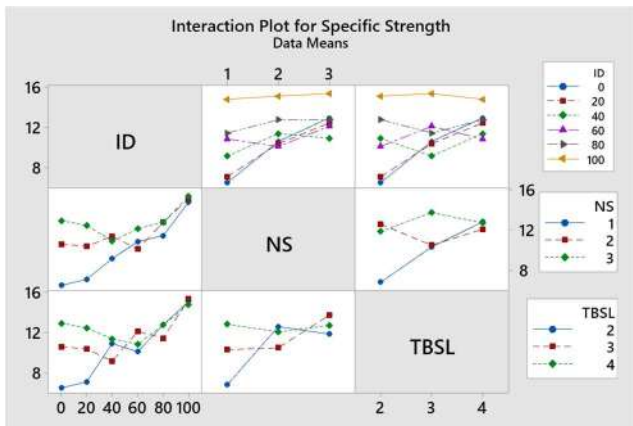


Figure 9 Specific strength changes according to fabrication parameters

When considering the Figure 9, it is seen that ID, NS and TBSL have a positive effect at most scenarios on the specific strength. However, NS and TBSL has no a noticeable effect of specific strength on specimen fabricated with 100% ID. Because of the specific strength was increased due to the high load-carrying capacity per unit area depending on the higher infill density. In addition, while one parameter has the lowest value, increasing the other parameters has a positive effect on specific strength.

4. CONCLUSIONS

In this study, both the effect of parameter levels and their interactions with each other were

investigated using Taguchi method. Taguchi L18 Orthogonal Array was used to examine the influence of ID, NS and TBSL on the specific strength (Peak load/weight) of FDM specimens. 54 samples were tested, because of each of the 18 runs had 3 repeated samples. The results presented that the ID has the most remarkable influence on the specific strength of the FDM specimen as expected. However, between 40-60% ID have negative effect to specific strength while NS and TBSL increase. Considering estimated printing time and the optimal level of fabrication parameters are achieved 40% ID, 2 NS and 3 TBSL, resulting in specific strength of 10.5 N/N, which means 60% of the best result. Overall, it is clear that the set process parameters will have noticeable effect to the tensile properties of 3D fabricated parts. In the future work, the interactions of the specific strength with the fabrication time, part orientation and the other parameters can be investigated.

Funding

The author received no financial support for the research, authorship, and/or publication of this paper.

The Declaration of Conflict of Interest/Common Interest

No conflict of interest or common interest has been declared by the author.

The Declaration of Ethics Committee Approval

The author declares that this document does not require an ethics committee approval or any special permission.

The Declaration of Research and Publication Ethics

The author of the paper declares that he complies with the scientific, ethical and quotation rules of SAUJS in all processes of the paper and that he does not make any falsification on the data collected. In addition, he declares that Sakarya University Journal of Science and its editorial board have no responsibility for any ethical

violations that may be encountered, and that this study has not been evaluated in any academic publication environment other than Sakarya University Journal of Science.

REFERENCES

- [1] A. J. Sheoran and H. Kumar, "Fused Deposition modeling process parameters optimization and effect on mechanical properties and part quality: Review and reflection on present research," *Materials Today: Proceedings*, vol. 21, pp. 1659–1672, 2020.
- [2] H. Vardhan, R. Kumar and J. S. Chohan, "Investigation of tensile properties of sprayed aluminium based PLA composites fabricated by FDM technology," *Materials Today: Proceedings*, Article in Press, 2020.
- [3] A. Pandzic, D. Hodzic, and A. Milovanovic, "Effect of infill type and density on tensile properties of pla material for fdm process," *30th Daaam International Symposium on Intelligent Manufacturing and Automation*, pp. 545–554, 2019.
- [4] R. Srinivasan, R. Srinivasan, Asrith Raj, S. A. Kannan and V. Deepak, "Influence of fused deposition modeling process parameters on the mechanical properties of PETG parts," *Materials Today: Proceedings*, vol. 27, pp. 1877–1883, 2020.
- [5] P. Wang, B. Zou, S. Ding, L. Li, and C. Huang, "Effects of FDM-3D printing parameters on mechanical properties and microstructure of CF/PEEK and GF/PEEK," *Chinese Journal of Aeronautics*, Article in Press, 2020.
- [6] A. E. Tontowi, L. Ramdani, R. V. Erdizon and D. K. Baroroh, "Optimization of 3D-printer process parameters for improving quality of polylactic acid printed part," *International Journal of Engineering and Technology*, vol. 9, no. 2, pp. 589–600, 2017.
- [7] A. Alafaghani, A. Qattawi, B. Alrawi, and A. Guzman, "experimental optimization of fused deposition modelling processing parameters: a design-for-manufacturing approach," *Procedia Manufacturing*, vol. 10, pp. 791–803, 2017.
- [8] M. Montero, S. Roundy, D. Odell, S.-H. Ahn and P. K. Wright, "Material characterization of fused deposition modeling (FDM) abs by designed experiments," *Society of Manufacturing Engineers*, 2001.
- [9] C. Dudescu, and L. Racz, "Effects of raster orientation, infill rate and infill pattern on the mechanical properties of 3D printed materials," *Acta Universitatis Cibiniensis – Technical Series*, vol. 69, 2017.
- [10] A. W. Gebisa, R. Kumar and H. G. Lemu, "Investigating Effects of Fused-Deposition Modeling (FDM) processing parameters on flexural properties of ULTEM 9085 using designed experiment," *Materials*, 11, 500 (article number: 19), 2018.
- [11] P. Wang, B. Zou, H. Xiao, S. Ding and C. Huang, "Effects of printing parameters of fused deposition modeling on mechanical properties, surface quality, and microstructure of PEEK," *Journal of Materials Processing Tech.*, vol. 271, pp. 62–74, 2019.
- [12] A. Alafaghani, and A. Qattawi, "Investigating the effect of fused deposition modeling processing parameters using Taguchi design of experiment method," *Journal of Manufacturing Processes*, vol. 36, pp. 164–174, 2018.
- [13] K. G. J. Christiyan, U. Chandrasekhar and K. Venkateswarlu, "A study on the influence of process parameters on the Mechanical Properties of 3D printed ABS composite," *Materials Science and Engineering*, vol. 114, 2015.
- [14] K. G. Mostafa, C. Montemagno and A. J. Qureshi, "Strength to cost ratio analysis of

FDM Nylon 12 3D printed parts,” *Procedia Manufacturing*, vol. 26, pp. 753–762, 2018.

- [15] V. Wankhede, D. Jagetiya, A. Joshi and R. Chaudhari, “Experimental investigation of FDM process parameters using Taguchi analysis,” *Materials Today: Proceedings*, vol. 27, pp. 2117–2120, 2020.
- [16] Y. Magdum, D. Pandey, A. Bankar, S. Harshe, V. Parab and M: S. Kadam, “Process parameter optimization for FDM 3D printer,” *International Research Journal of Engineering and Technology*, vol. 6, pp. 1472–1477, 2019.

JOURNAL OF SCIENCE



SAKARYA UNIVERSITY

Sakarya University Journal of Science

ISSN 1301-4048 | e-ISSN 2147-835X | Period Bimonthly | Founded: 1997 | Publisher Sakarya University |
<http://www.saujs.sakarya.edu.tr/en/>

Title: The Geophytes of Sakarya City

Authors: Mehmet SAĞIROĞLU

Received: 2020-04-10 12:55:52

Accepted: 2020-07-27 19:59:44

Article Type: Research Article

Volume: 24

Issue: 5

Month: October

Year: 2020

Pages: 991-1007

How to cite

Mehmet SAĞIROĞLU; (2020), The Geophytes of Sakarya City. Sakarya University Journal of Science, 24(5), 991-1007, DOI:

<https://doi.org/10.16984/saufenbilder.717563>

Access link

<http://www.saujs.sakarya.edu.tr/en/pub/issue/56422/717563>

New submission to SAUJS

<http://dergipark.org.tr/en/journal/1115/submission/step/manuscript/new>



The Geophytes of Sakarya City

Mehmet SAĞIROĞLU*¹

Abstract

Sakarya city is within the Europe-Siberia phytogeographic region in Turkey. The effect of the Black Sea climate is usually seen in the study area. Black sea climate is effective in the northern part, while the Mediterranean climate is generally dominant in the South. In the area under the influence of the Mediterranean climate, there is a vegetation where the maquis-pseudomaquis communities are seen. The main research area of this study is chosen to be the geophyte plants collected in the city of Sakarya, Turkey. 1051 plant specimens were collected during field studies between 2009-2020. From the plant collection, 220 taxa and 80 genus belonging to 29 families have been identified. 18 of these taxa, are endemic. Of the total taxa in the area are 40 elements Euro-Siberian, 41 widespread, 79 Mediterranean, 7 Iranian-Turan, 16 Euxine, 34 phytogeographically unknown, 1 Hyrcano, 1 Hyrcano-Euxine, 1 North Americana elements.

Keywords: Geophyte, Endemic, Sakarya, Turkey

*Corresponding Author: msagioglu@sakarya.edu.tr

¹Sakarya University, ORCID: <http://orcid.org/0000-0001-8654-3361>

1. INTRODUCTION

The term of Geophyte means ground plants. They are commonly known as onion, tuber, rhizome, corm plants. Turkey stays in mild climate zone in the World. From the plant variety point of view, it appears in the first rank. In Turkey there are exists about 12 000 plant taxa.

Geophyte plants are of importance within this wealth flora. About 2500 geophyte plants grow in Turkey [1]. These plants are attractive for their alluring flowers. Geophytes are accepted to be the herald of the spring and the source of inspiration of arts and love. With this biodiversity in Turkey, the flora becomes privileged and the works carried upon these flora may thus have the potential to obtain different results. The geophyte species are the main part in the flora of Sakarya. In this study it is aimed to determine the geophyte taxa growing the city of Sakarya.

Sakarya city stays within the Europe-Siberia phytogeographic region (Figure 1). The effect of the Black Sea climate is mostly seen in the study area. While the black sea climate has a prominent effect in the northern part of the province, the Mediterranean climate is seen in the south. In the area under the influence of the Mediterranean climate, there is a vegetation where the maquis-pseudomaquis communities are seen.



Figure 1 Study area map

There are various habitats in Sakarya province such as mountainous areas, hills, valleys, wide sands, lakes, rivers, floodplain ranging from 0 to 1600 m.

There are many and different species in these particular habitat types. In this study geophyte species in Sakarya are given.

2. MATERIALS AND METHODS

The main materials for that study were geophyte plants spread in the city of Sakarya. The plants were collected between the years 2009 and 2020.

For the identification process of the taxa we used the books titled “Flora of Turkey and the East Aegean Islands [2-4]. The names of the detected species were organized according to the book “Türkiye Bitkileri Listesi (Damarlı Bitkiler)” [5]. The threat categories of these endemic and rare taxa were determined using the criteria described in the books “Türkiye Bitkileri Kırmızı Kitabı [6]” and IUCN [7]. Plants were made Herbarium materials and conserved at the herbarium of Biology Department, Sakarya University.

Some geofit taxa given in Geyve flora could not be found in the specified localities [8]. It has been observed that most of these localities have turned into agricultural lands or settlements. Taxa that we believe can be in the area but cannot be found by us are given with their records in this list.

Taxons collected in this study are given together with their localities, phytogeographic elements and endemism states.

2.1 Abbreviations

Sakarya University: **SAU**, Iranian Turanian Element: **Ir.-Tur.** Widespread: **Widesp.**, -Siberian Element: **Euro-Sib.**, Element: Mediterranean; **Medit.**, Euxine Element: **Eux.**, Hyrcano Element: **Hyrc.**, Hyrcano-Euxine Element: **Hyrc.-Eux.**, North America Element: **N.Ame.**, Unknown: **Unk.**, Critically endangered: **CR**, Endangered: **EN**, Vulnerable: **VU**, Near Threatened: **NT**, Least concern: **LC**.

3.RESULTS

Geophyte Flora of Research Area

ALISMATACEAE

*Alisma plantago-aquatica*L.

Sapanca lake, 10.06.2012, M.Sağiroğlu
3421. **Euro.-Sib.**

Alisma lanceolatum With.

Acarlar longozu, 15.06.2020, M.Sağiroğlu
6766. **Widesp.**

Alisma gramineum Lej.

Acarlar longozu, 15.06.2020, M.Sağiroğlu
6767. **Unk.**

AMARYLLIDACEAE

*Allium rubellum*M. Bieb

SAU- Aşağıdereköy way 100 m,
20.06.2012, M. Sağiroğlu 3544. **Ir.-Tur.**

Allium paniculatum L.subsp. *paniculatum*

SAU, surroundings of Engineering
Faculty 180 m, 14.06.2012 M. Sağiroğlu
3541. **Medit.**

Allium paniculatum L.subsp. *fuscum* (Waldst. & Kit) Soó

Pamukova Hayrettin village, 400 m,
15.07.2013, M.Sağiroğlu 3948. **Medit.**

Allium pallens L. subsp. *pallens*

Karasu-Akkum village, 40 m, 15.06.2012,
M.Sağiroğlu 3848. **Medit.**

*Allium rupestre*Steven

Geyve, Kışlaçay-Doğançay, 2nd Km, 100
m, 14.11.2016, M. Sağiroğlu 5485. **Eux.**

Allium hirtovaginatatum Kunth

Pamukova-Kırca upland, 850 m,
05.06.2013, M.Sağiroğlu 3940. **Medit.**

Allium sativum L.

Pamukova-Hüseyinli village way, 3rd km,
200 m, 17.06.2012, M. Sağiroğlu 3524.
Widesp.

Allium atroviolaceum Boiss.

Kaynarca-Oflak Mountain, Around
Taşoluk village, 170 m, M.Sağiroğlu
3954. **Widesp.**

Allium scorodoprasum L.subsp. *rotundum*(L.) Stearn

Geyve, Doğançıl village, 1340 m,
18.05.2017, M. Sağiroğlu 6065. **Widesp.**

Allium ampeloprasum L.

Kaynarca-Karasu way, 3rd km, 60 m,
15.06.2012, M.Sağiroğlu 3993. **Widesp.**

Allium sphaerocephalon L. subsp. *sphaerocephalon*

Hendek-Çamlıca village, 700 m,
M.Sağiroğlu 5032. **Euro.-Sib.**

*Allium amethystinum*Tausch

Geyve, Doğançıl village, 1350 m,
18.05.2017, M. Sağiroğlu 6065. **Medit.**

Allium guttatum Steven subsp. *sardoum* (Moris) Stearn

Pamukova-Hüseyinli village way, 450 m,
17.06.2012, M. Sağiroğlu 3521. **Medit.**

Allium guttatum Steven subsp. *guttatum*

Akyazı-Şerefiye village, 750 m,
15.08.2009, M.Sağiroğlu 2781. **Euro.-Sib.**

Allium lycaonicum Siehe ex Hayek

Geyve, kulfalar-kamışlı road, 647 m,
20.04.2008, OUF 15878 [8] **Unk.**

Leucojum aestivum L subsp. *aestivum*

Karasu, around Karapınar village, 11 m,
05.04.2017, M. Sağıroğlu 5738. **Euro.Sib.**

Sternbergia lutea (L.) Ker Gawl. ex Spreng.

Serdivan-Kazımpaşa way, 2nd km,
09.10.2016, M. Sağıroğlu 5341. **Widesp.**

Panocratium maritimum L.

Karasu, Denizköy coast, 5 m, 18.09.2016,
M. Sağıroğlu 5095. **Medit.**

Narcissus poeticus L. subsp. *poeticus*

Arifiye-Akçay stream, roadside, 50 m,
01.06.2011, M. Sağıroğlu 3096. **Medit.**

Narcissus jonquilla L.

Kaynarca-Kefken way, 2nd km, 120 m,
15.06.2012, M. Sağıroğlu 3489. **Medit.**

Narcissus pseudonarcissus L.

Karasu-Denizköy, roadside, 16.03.2020,
M. Sağıroğlu 6628. **Unk.**

ARACEAE

Arum italicum Mill

Sapanca, İkramiye valley, 170 m,
01.06.2011, M. Sağıroğlu 3051. **Unk.**

Arum byzantinum Blume

Kaynarca, Uğurlu vilage, clearings forest,
170 m, 27.04.2017, M. Sağıroğlu 5893.
Eux.

Arum maculatum L.

Geyve, Epçeler village, 250 m, 13.06.2017,
M. Sağıroğlu 5771. **Unk.**

Arum orientale M.Bieb.

Pamukova, Şahmelek village, 350 m,
02.04.2017, M. Sağıroğlu 5701. **Eux.**

Arum higraphilum Boiss. subsp. *euxinum*
(R.R.Mill.) Alpınar. **Endemic**

Akyazı, Keremali mountain, 980 m,
09.03.2017, M. Sağıroğlu 5587. **Eux.**

Arum elongatum Steven

Sapanca, İkramiye valley, 250 m,
01.06.2011, M. Sağıroğlu 3091. **Unk.**

Dracunculus vulgaris Schott

Geyve, Hacılar village, 300 m, 25.05.2017,
M. Sağıroğlu 6228. **Medit.**

ARISTOLOCHIACEAE

Asarum europaeum L.

Hendek-Kocaali road, Kırızlı village, 350
m, 25.04.2017, M. Sağıroğlu 5864. **Euro.-
Sib.**

Aristolochia clematitis L.

Kaynarca-Oflak mountain, 150 m,
24.07.2013, M. Sağıroğlu 3955. **Euro.-Sib.**

Aristolochia pallida Willd.

Pamukova, Kazımiye, Kırca upland, 1000
m, 01.05.2017, M. Sağıroğlu 5931. **Euro.-
Sib.**

Aristolochia bodamae Dingler

Akyazı, Sultanpınar upland, 1230 m,
08.06.201, M. Sağıroğlu 6247. **Unk.**

Aristolochia pontica Lam.

Geyve, Akıncı village, 570 m, 04.05.2016,
M. Sağıroğlu 5000. **Eux.**

ASPARAGACEAE

Agave americana L. subsp. *americana*

Serdivan mountain, roadside, 210
m, 02.07.2011, M. Sağıroğlu 3148.
Widesp.

Asparagus acutifolius L.

Geyve, between Kışlaçay-Doğançay, 150 m, 14.11.2016, M. Sağıroğlu 5487. **Medit.**

Asparagus aphyllus L.subsp. *orientalis* (Baker) P.H. Davis

Kaynarca, between Şeyhtımarı-Yenice, 180 m, 16.10.2016, M. Sağıroğlu 5344. **Medit.**

Asparagus tenuifolius Lam.

Pamukova, West of Kemaliye village, 732 m, 28.09.2016, M. Sağıroğlu 5266. **Euro.-Sib.**

Asparagus officinalis L. subsp. *officinalis*

Kaynarca, around Karaboğaz village, 120 m, 09.05.2017, M. Sağıroğlu 5964. **Widesp.**

Prospero autumnale (L.) Speta

Karasu, Denizköy coast, 5 m, 18.09.2016, M. Sağıroğlu 5101. **Medit.**

Bellevalia clusiana Griseb. **Endemic**

Sakarya, around Poyrazlar Lake, 30 m, 02.05.2017, M. Sağıroğlu 5954. **Ir.-Tur.**

Hyacinthella lineata (Steud. ex Schult. &Schult.f.) Chouard **Endemic.**

Geyve-Akıncı village, Beşiktaş stream, 525 m, 13.04.2013, M. Sağıroğlu 3815. **Medit.**

Hyacinthella micrantha (Boiss.) Chouard. **Endemic**

Taraklı-Karagöl upland, 1122 m, 26.03.2017, M.Sağıroğlu 5659. **Medit.**

Galanthus plicatus M.Bieb.subsp. *byzantinus* (Baker) D.A. Webb

Taraklı, east of Karagöl, 1153 m, 26.03.2017, M. Sağıroğlu 5668. **Eux.**

Galanthus elwesii Hokk.f. subsp. *elwesii*

Akyazı, Keremali mountain, 550 m, 09.03.2017, M. Sağıroğlu 5585. **Medit.**

Galanthus gracilis Čelak.

Geyve, Kışlaçay village, 133 m, 13.11.2016, M. Sağıroğlu 5476. **Medit.**

Galanthus nivalis L.subsp. *nivalis*

Kaynarca- Acarlar longozu, 20, m, 14.03.2020, M. Sağıroğlu 6635, **Euro.-Sib.**

Scilla bithynica Boiss.

Sakarya, Sinanoğlu village, open Quercus, 60 m, 28.02.2017, M. Sağıroğlu 5557. **Eux.**

Scilla bifolia L.

Akyazı. Dokurcun, Davlumbaz upland, 1000 m, M. Sağıroğlu 06.04.2017. **Medit.**

Muscari comosum (L.) Mill.

Pamukova, Şahmelek village, 300 m, 01.05.2017, M. Sağıroğlu 5905. **Widesp.**

Muscari armeniacum Leichtlin ex Baker

Kaynarca, around Karaboğaz village, 110m, 09.05.2017, M. Sağıroğlu 5963. **Widesp**

Muscari tenuiflorum Tausch.

Geyve, around Akıncı village, 140 m, 24.05.2017, M. Sağıroğlu 6186. **Widesp.**

Muscari bourgaei Baker

Akyazı, Dokurcun-Davlumbaz upland, 1450 m, 06.04.2017, M. Sağıroğlu 5749. **Medit. Endemic**

Muscari neglectum Guss. ex Ten.

Karasu, Sakarya riverside, 15, m, 09.05.2017, M. Sağıroğlu 5987. **Medit.**

***Muscari aucheri* (Boiss.) Baker Endemic.**

Pamukova-Kazımiye-Kırca upland, 1020 m, 01.05.2017, M. Sağırođlu 5932. **Ir.-Tur.**

***Ornithogalum pyrenaicum* L.**

Pamulova, Hüseyinli way, 3rd km, 11.05.2019, M. Sağırođlu 6520. **Euro.-Sib.**

***Ornithogalum sphaerocarpum* Kerner**

SAU campus, 170 m, 18.05.2010, M.Sađırođlu 2897. **Widesp.**

***Ornithogalum narbonense* L.**

Akyazı-Mudurnu, Taşkesti-Bakdemirler, 550 m, 08.05.2014, M.Sađırođlu 4975. **Widesp.**

***Ornithogalum oligophyllum* E.D.Clarke**

Pamukova, Kırca upland, 950 m, 02.04.2017, M. Sağırođlu 5688. **Eux.**

***Ornithogalum montanum* Cirillo.**

Karasu-Karapınar village, 40 m, 05.04.2017, M. Sağırođlu 5740. **Medit.**

***Ornithogalum fimbriatum* Willd.**

Pamukova, Çilekli village, 700 m, 23.06.2019, M. Sağırođlu 6487. **Medit.**

Ornithogalum wiedemannii* Boiss. var. *wiedemannii

Karasu, Camitepe village, 20 m, 06.03.2017, M.Sađırođlu 5578. **Widesp.**

***Ornithogalum sigmoideum* Freyn & Sint.**

Taraklı-Şehren way, 300 m, 13.06.2017, M. Sağırođlu 5783. **Euro.-Sib.**

***Ornithogalum comosum* L.**

Taraklı-Şehren way, 410 m, 13.04.2017, M. Sağırođlu 5788. **Medit.**

***Ornithogalum umbellatum* L.**

Hendek-karadere way 8. Km, 640 m, 20.03.2017, M. Sağırođlu 5652. **Medit.**

***Ornithogalum orthophyllum* Ten.**

Hendek-Düzce border, left hand, 300 m, 20.03.2017, M. Sağırođlu 5657. **Widesp.**

***Ornithogalum nutans* L.**

Geyve-Akıncı village, 536 m, 15.04.2013, M.Sađırođlu 3818. **Medit.**

***Polygonatum orientale* Desf.**

Geyve-Akıncı village, Beşiktaş stream, 370 m, 07.05.2013, M.Sađırođlu 3887. **Eux.**

***Polygonatum multiflorum* (L.) All.**

Geyve, Dođancıl, 1352 m, 18.05.2017, M. Sağırođlu 6078. **Widesp.**

***Ruscus aculeatus* L.**

Geyve-Akıncı vilage, Beşiktaş stream, 105 m, 19.11.2016, M. Sağırođlu 5503. **Medit.**

***Ruscus hypoglossum* L.**

Geyve-Akıncı village, Beşiktaş stream, 105 m, 19.11.2016, M. Sağırođlu 5502, **Euro.-Sib.**

ASTERACEAE

***Helianthus tuberosus* L.**

Kaynarca-Şeyhtımarı village, 180 m, 16.10.2016, M. Sağırođlu 5353. **N. Ame.**

***Leontodon tuberosus* L.**

Hendek-Kocaali, 17th km, 800 m, 25.04.2017, M. Sağırođlu 5873. **Medit.**

***Lactuca tuberosa* Jacq.**

Geyve-Setçe, 340 m, 10.05.2017, M. Sağırođlu 6016. **Widesp.**

BRASSICACEAE

Cardamine bulbifera (L.) Crantz

Sapanca-İstanbulderesi, 300 m,
15.06.2011, M.Sağiroğlu 3119. **Euro.-Sib.**

Cardamine quinquefolia (M.Bieb.)
Schmalh.

Karasu, Sinanoğlu köyü, under forest, 60
m, 14.03.2020, M. Sağiroğlu 6616. **Euro.-Sib.**

BORAGINACEAE

Symphytum bulbosum K.F.Schimp.

Karasu-Başoğlu- 15 m, 07.04.2013, D.
Karaduman 1748,[9] **Medit.**

Symphytum tuberosum L.subsp.
nodosum (Schur) Soó

Karasu-Manavpınar village, 20 m,
06.04.2017, M.Sağiroğlu 5706. **Euro.-Sib.**

BUTOMACEAE

Butomus umbellatus L.

Sapanca Lake, 30 m, 14.06.2012, M.
Sağiroğlu 3515. **Euro.-Sib.**

COLCHICACEAE

Colchicum umbrosum Steven

Akyazı, Açelya upland, 1218 m,
08.08.2018, M. Sağiroğlu 6437. **Medit.**

Colchicum turcicum Janka

Pamukova, Çilekli village, 700 m,
16.10.2018, M. Sağiroğlu 6452. **Medit.**

Colchicum speciosum Steven

Geyve, Şehren-Gündüzler villages, 3rd km,
09.10.2016, M. Sağiroğlu 5332. **Eux.**

Colchicum atticum Spruner ex Tommas

Pamukova-Mekece village, 600 m,
25.10.2017, M.Sağiroğlu 6417. **Medit.**

CYPERACEAE

Carex flacca Schreb. subsp.
erythrostachys (Hoppe) Holub

Sapanca Lake, 30 m, 18.05.2010,
M.Sağiroğlu 2900. **Medit.**

DIOSCOREACEAE

Dioscorea communis (L.) Caddick &
Wilkin

Geyve, Akıncı village, Beşiktaş stream,
170 m, 07.05.2013, M.Sağiroğlu 3891.
Unk.

GERANIACEAE

Geranium tuberosum L.

Arifiye, E5 Motorway, 70 m, 21.04.2010,
M.Sağiroğlu 2830. **Ir.-Tur.**

Geranium sylvaticum L.

West of Sapanca Lake, 23.05.2011,
M.Sağiroğlu 3038. **Euro.-Sib.**

Geranium asphodeloides Burm.subsp.
asphodeloides

Serdivan mountain, 315 m, 28.04.2012,
M.Sağiroğlu 3227. **Euro.-Sib.**

Geranium sanguineum L.

Pamukova, Kazımiye-Kırca upland way,
560 m, 01.05.2017, M. Sağiroğlu 5929.
Euro.-Sib.

Geranium pyrenaicum Burm.f.

SAU, around guesthouse, 90 m,
24.05.2009, M.Sağiroğlu 2686. **Unk.**

Erodium acaule (L.) Becherer & Thell.

SAU campus, 110 m, 08.05.2011,
M.Sağiroğlu 3029. **Medit.**

IRIDACEAE

Crocus abantensis T. Baytop & B. Mathew **Endemic**

Sakarya-Akyazı, Sülüklü Lake, 1450 m, 26.03.2017, M. Sağıroğlu 5671. **Euro.-Sib.**

Crocus chrysanthus(Herb.) Herb.

Pamukova-Kırca upland, 992 m, 02.04.2016, M. Sağıroğlu 5686. **Unk.**

Crocus danfordiae Maw subsp. *danfordiae***Endemic**

Pamukova, Çilekli village, 750 m, 12.02.2019, M. Sağıroğlu 6465. **Unk.**

Crocus pestalozzae Boiss. **Endemic**

Pamukova, Şahmelek-Kırca upland, 992 m, 02.04.2017, M. Sağıroğlu 5687. **Medit.**

Crocus flavus Weston subsp. *flavus*

Sakarya Taşkısığı Lake, clearings forest, 100 m, 27.02.2017, M. Sağıroğlu 5523. **Euro.-Sib.**

Crocus flavus Weston subsp. *dissectus* T. Baytop & B. Mathew **Endemic**

Akyazı-Dokurcun, Davlumbaz upland, 1450 m, 06.04.2017, M. Sağıroğlu 5748. **Unk.**

*Crocus antalyensis*B. Mathew subsp. *antalyensis* **Endemic**

Pamukova, Mesruriye way, 740 m, 22.02.2019, M. Sağıroğlu 6467. **Medit.**

*Crocus olivieri*J.Gay subsp. *istanbulensis* B. Mathew **Endemic**

Pamukova, Çilekli village, 755 m, 19.03.2017, M. Sağıroğlu 6544, **Euro.-Sib.**

*Crocus olivieri*J. Gay subsp. *olivieri*

Pamukova-Kadıköy, Pamukova, 2nd km, 653 m, 02.03.2017, M.Sağıroğlu 5566. **Euro.-Sib.**

Crocus pallasii Goldb. subsp. *pallasii*

Doğançay-karaçam road, 90 m, 10.04.2007, OUFE 15888 [8]. **Unk.**

*Crocus speciosus*M.Biebsubsp. *speciosus*

Akyazı, Açelya upland, 1157 m, 23.10.2016, M. Sağıroğlu 5425. **Euro.-Sib.**

*Crocus speciosus*M.Bieb subsp. *sakariensis* Rukšāns **Endemic**

Akyazı, Keremali mountain, 1300 m, 06.11.2016, M. Sağıroğlu 5454. **Euro.-Sib.**

Crocus pulchellus Herb.

Pamukova- Hüseyinli upland, 1140 m,16.9.2018, M.Sağıroğlu 6454. **Medit.**

Romulea columnae Sebast. & Mauri subsp. *columnae*

Sakarya, Aşağıdere -Eşme way, 1st km, 40 m, 18.03.2012, M. Sağıroğlu 3212. **Medit.**

Romulea linaresii Parl.subsp. *graeca* Bég.

Geyve-Akıncı village, Beşiktaş stream, 540 m, 13.02.2013, M. Sağıroğlu 3812. **Medit.**

Gladiolus italicus Mill.

Geyve, Akıncı village, Hacılar station, 570 m, 04.05.2016, M. Sağıroğlu 4998. **Medit.**

Gladiolus atroviolaceus Boiss.

Geyve, Akıncı village, 400 m, roadside, 05.07.2016, M. Sağıroğlu 5012. **Ir.-Tur.**

JUNCACEAE

Juncus acutus L. subsp. *acutus*

Kaynarca, Ortaköy, 30 m, 06.05.2012, D. Karaduman 1232 [9]. **Widespr.**

Juncus heldreichianus Marssonsubsp.
heldreichianus

Geyve-Pamukova yolu, 50 m, 10.05.2017,
M.Sağiroğlu 6010. **Medit.**

Juncus compressus Jacq.

Sapanca lake, 30 m, 01.06.2012, M.
Sağiroğlu 3374. **Unk.**

Juncus articulatus L. subsp. *articularis*

Geyve-Sakarya Nehri kenarı, 40 m,
10.05.2017, M. Sağiroğlu 6013. **Widespr.**

LILIACEAE

Lilium martagon L.

Hendek-Kocaali way, 22 km, 680 m,
14.06.2012, M. Sağiroğlu 3490. **Euro.-Sib.**

Fritillaria pontica Wahlenb.

Geyve, between Doğançay-Boğazköy, 560
m, 20.04.2017, , M. Sağiroğlu 5794.
Euro.-Sib.

Fritillaria bithynica Baker

Pamukova, Kazımiye, Kırca upland, 1000
m, 01.05.2017, , M. Sağiroğlu 5930.
Medit.

Gagea bithynica Pasch. **Endemic.**

Sakarya, west of Taşkısığı lake, 220 m,
27.02.2017, M. Sağiroğlu 5531. **Medit.**

Gagea bohemica (Zauschn.) Schult.
&Schult.f.

Pamukova, Şahmelek village, 690 m,
02.03.2017, M. Sağiroğlu 5562. **Medit.**

Gagea granatelli (Parl.) Parl.

Akyazı-Dokurcun davlumbaz upland, 1400
m, 06.04.2017, M. Sağiroğlu 5751. **Medit.**

Gagea villosa (M.Bieb.) Sweet var. *villosa*

Geyve-Akıncı village, 520 m, 07.05.2013,
M. Sağiroğlu 3902. **Widespr.**

NYMPHAEACEAE

Nuphar lutea (L.) Sm.

Sapanca lake, 30 m, 14.04.2009,
M.Sağiroğlu 2733. **Unk.**

Nymphaea alba L.

Sapanca lake, 30 m, 24.05.2007,
M.Sağiroğlu 2677. **Unk.**

ORCHIDACEAE

Cephalanthera rubra (L.) Rich.

Geyve, Akıncı village, 450 m, 05.06.2016,
M. Sağiroğlu 5011. **Widespr.**

Cephalanthera longifolia (L.) Fritsch

Geyve, Akıncı village, Beşiktaş stream,
340 m, 07.05.2013, M. Sağiroğlu 3883.
Medit.

Cephalanthera damosonium (Mill.) Druce

Geyve, Akıncı village, 500 m, 10.05.2017,
M. Sağiroğlu 6008. **Widespr.**

Cephalanthera epipactoides Fisch. &
C.A.Mey

Geyve, Akıncı village, Beşiktaş stream,
290 m, M. Sağiroğlu 5002-B, **Unk.**

Dactylorhiza romana (Seb.) Soó subsp.
romana

Geyve-Akıncı village, 350 m, 09.04.2016,
M. Sağiroğlu 4989. **Medit.**

Dactylorhiza saccifera (Brongn.)
Soó subsp. *saccifera*

SAU campus, near 190 m, 21.04.2010, M.
Sağiroğlu 2862-A. **Medit.**

Dactylorhiza saccifera (Brongn.)
Soósubsp. *bithynica*(H.Baumann) Kreutz
Endemic.

Geyve-Burhaniye village, 380
m,10.05.2017, M. Sağıroğlu 6002. **Medit.**

Dactylorhiza nieschalkiorum H.Baumann
& Künkele **Endemic.**

Pamukova-Kırca upland, 1000 m,
05.06.2013, M. Sağıroğlu 3942. **Unk.**

Dactylorhiza incarnata (L.) Soó subsp.
incarnata

SAU campus, near cafetaria, 190 m,
21.04.2010, M. Sağıroğlu 2862-B. **Medit.**

Epipactis helleborine(L.) Crantz subsp.
helleborine

Geyve-Akıncı village, 800 m, 25.07.2013,
M. Sağıroğlu 3959. **Widespr.**

Epipactis pontica Taubenheim

Geyve-Akıncı village, 450 m, 15.07.2013,
M. Sağıroğlu 3946. **Eux.**

Limodorum abortivum (L.) Schwartz
subsp. *abortivum*

Geyve, Akıncı village, Beşiktaş stream,
250 m, 07.05.2013, M. Sağıroğlu 3884.
Widespr.

Spiranthes spiralis (L.) Chevall.

Geyve, Akıncı village, Beşiktaş stream,
290 m, 07.05.2013, M. Sağıroğlu 3890.
Medit.

Platanthera bifolia (L.) Rich.

Sapanca-İstanbul stream, 370 m,
10.06.2011, M. Sağıroğlu 3395. **Euro.-Sib.**

Platanthera chlorantha (Cruster) Rchb.

Pamukova-Kırca upland, 990 m,
05.06.2013, M. Sağıroğlu 3944. **Widesp.**

Coeloglossum viride (L.) Hartman

Pamukova-upland of Hüseyinli village,
800 m, 17.06.2012, M. Sağıroğlu 3522.
Widespr.

Himantoglossum caprinum (M.Bieb.)
Spreng.

Kaynarca-Oflak mountain, 200 m,
24.07.2013, M. Sağıroğlu3952. **Eux.**

Himantoglossum comperianum (Steven)
P.Delforge

Geyve-Doğançay village, 560 m,
01.06.2013, M. Sağıroğlu 3938. **Ir.-Tur.**

Anacamptis pyramidalis(L.) Rich.

SAU campus, near cafetaria, 180 m,
14.05.2010, M. Sağıroğlu 2880. **Widespr.**

Listera ovata (L.)R.Br.

Serdivan mountain, 140 m, 02.07.2011. M.
Sağıroğlu 3150. **Euro.-Sib.**

Neottia nidus-avis (L.) Rich.

Serdivan-Meşelik village, Fagus forest,
191 m, 02.07.2011, M. Sağıroğlu 3137.
Medit.

Neotinea maculata(Desf.) Stearn

SAU campus, 140 m, 05.05.2019, M.
Sağıroğlu 6497. **Medit.**

Stenisiella satyroides (Spreng.) Schlrt.

Hendek, Kocaeli-Kirazlı 1st km, 285 m,
15.06.2012, M. Sağıroğlu 3492. **Hyc.**

*Ophrys speculum*Link subsp. *speculum*

SAU campus, 164 m, 06.04.2019, M.
Sağıroğlu 6608. **Medit.**

*Ophrys speculum*Linksubsp. *regis-*
ferdinandii(Acht. & Kellerer ex Renz)Soó

Taraklı-Şehren junction, 2nd km, 410 m,
13.04.2017, M. Sağıroğlu 5787. **Medit.**

Ophrys mammosa Desf. subsp. *mammosa*

SAU campus, 150 m, 06.04.2019, M.
Sağıroğlu 6482. **Medit.**

Ophrys oestrifera M. Bieb subsp.
oestrifera

SAU campus, Engineering M7, 90 m,
31.05.2012, M. Sağıroğlu 3319. **Medit.**

Ophrys apifera Huds.

Around SAU campus cafeteria, 100 m,
14.05.2010, M. Sağıroğlu 2874. **Medit.**

Orchis tridentata Scop.

SAU-Dereköy way, 90 m, 08.05.2011, M.
Sağıroğlu 3005. **Medit.**

Orchis lactea Poir.

Sakarya-Aşağıdereköy-Eşme way, 1.5 km,
55 m, 18.03.2012, M. Sağıroğlu 3213.
Medit.

Orchis purpurea Huds. subsp. *purpurea*

SAU campus, cafeteria, 18.05.2010,
M. Sağıroğlu 2896. **Euro.-Sib.**

Orchis simia Lam.

Pamukova, Şahmelek village, 650 m,
01.05.2017, M. Sağıroğlu 5901. **Medit.**

Orchis italica Poir.

Geyve-Kulfalar village, 700 m,
28.02.2017, M. Sağıroğlu 5548. **Medit.**

Orchis morio subsp. *morio* L.

SAU campus, Engineering Faculty, 90 m,
21.04.2010, M. Sağıroğlu 2828. **Unk.**

Orchis morio L. subsp. *picta* (Loisel.)
K. Richt.

Pamukova-Kazımiye, Kırca upland, 950 m,
01.05.2017, M. Sağıroğlu 5918. **Widesp.**

Orchis anatolica Boiss.

Geyve, Kulfalar – Kamışlı way,
12.03.2003, OUFE 12821 [8], **Medit.**

Orchis mascula (L.) L. subsp. *pinetorum*
(Boiss. & Kotschy) G. Camus

Geyve, Doğançıl village, 1300m,
18.05.2017, M. Sağıroğlu 6082-A.
Widespr.

Orchis pallens L.

Geyve, Doğançıl village, 1400 m,
18.05.2017, M. Sağıroğlu 6081. **Euro.-Sib.**

Orchis palustris Jacq. subsp. *palustris*

Geyve, north of Doğançıl village, 1400m,
18.05.2017, M. Sağıroğlu 6082-B.
Widesp.

Orchis laxiflora Lam. subsp. *laxiflora*

Around İkramiye village, clearings forest,
400 m, 13.05.2012, M. Sağıroğlu 3272,
Medit.

Orchis coriophora L. subsp. *coriophora*

SAÜ-Dereköy way, clearings forest, 50 m,
08.05.2011, M. Sağıroğlu 3004. **Medit.**

Serapias cordigera L. subsp. *cordigera*

Karasu-Acarlar longozu, 27.05.2012, D.
Karaduman 1371 [9]. **Medit.**

Serapias vomeracea (Burm.f.) Briq. subsp.
laxiflora (Soó) Gözl & H. R. Reinhard

Geyve, karaçam-İlimbey way, 12.03.2003,
OUFE 12809 [8]. **Medit.**

Serapias bergonii E.G. Camus

SAU campus, around cafeteria, 202 m,
31.05.2012, M. Sağıroğlu 3320. **Medit.**

OXALIDACEAE

*Oxalis acetosella*L.

Geyve, between Doğançay-Maksudiye, 200 m, 20.04.2017, M. Sağıroğlu 5805. **Unk.**

Oxalis articulata Savigny

Serdivan-Meşeli village, 110 m, 02.07.2011, M. Sağıroğlu 3144. **Unk.**

Oxalis corniculata L.

Sapanca-İkramiye valley, 70 m, 01.06.2011, M. Sağıroğlu 3066. **Unk.**

PAEONIACEAE

Paeonia peregrina Mill.

Geyve, Doğancıl village, 650 m, 18.05.2017, M. Sağıroğlu 6052. **Unk**

Paeonia arietina G. Anderson

Geyve-Tuzla, plateau path, 1450 m, 10.06.2020, M. Sağıroğlu 6697. **Ir.-Tur.**

PAPAVERACEAE

Corydalis caucasica DC. subsp. *abantensis* Lidén. **Endemic**

Geyve, Kamyşlı village, 1510 m, 30.03.2017, M. Sağıroğlu 5683. **Eux.**

Corydalis cava (L.) Schweigg. & Körtes subsp. *marschalliana* (Willd.) Hayek

Taraklı, Karagöl upland, 1100 m, 26.03.2017, M. Sağıroğlu 5663. **Euro.-Sib.**

Corydalis solida (L.) Clairv subsp. *solida*.

Pamukova, Kazımiye, Kırca upland, 950 m, 02.04.2017, M. Sağıroğlu 5690, **Euro.-Sib.**

POLYGONACEAE

Rumex tuberosus L. subsp. *creticus* (Boiss.) Rech.f.

Kaynarca-Oflak mountain, 150 m, 25.07.2013, M. Sağıroğlu 3956. **Medit.**

Rumex tuberosus L. subsp. *tuberosus*

SAU, Engineering M7, 180 m, 20.06.2012, M. Sağıroğlu 3543. **Medit.**

POACEAE

Hordeum bulbosum L.

Serdivan mountain, 220 m, 02.07.2011, M. Sağıroğlu 3431. **Widesp.**

Poa bulbosa L.

West of SAU campus, 110 m, 06.05.2011. M. Sağıroğlu 3256. **Widesp.**

Dactylis glomerata L. subsp. *glomerata*

SAU, Engineering M7, 80 m, 27.05.2012, M. Sağıroğlu 3306. **Euro.-Sib.**

PRIMULACEAE

Primula acaulis (L.) L. subsp. *acaulis*

Geyve, between Boğazköy-Koru, 600 m, 16.03.2017, M. Sağıroğlu 5637-A, **Euro.-Sib.**

Primula acaulis (L.) L. subsp. *rubra* (Sm.) Greuter & Burdet

Geyve, between Boğazköy-Koru villages, 600 m, 16.03.2017, M. Sağıroğlu 5637-B. **Eux.**

Cyclamen hederifolium Aiton

Geyve, Akıncı village, rocky fields, 210 m, 13.02.2013, M. Sağıroğlu 3810. **Medit.**

Cyclamen coum Mill. subsp. *coum*

Geyve, between Doğançay-Kışlaçay, 100 m, 14.11.2016, M. Sağıroğlu 5483. **Unk.**

Cyclamen coum Mill.subsp. *caucasicum*
(K. Koch) O. Schwarz

Karasu, Sinanoğlu village, 35 m, clearings
forest, 11.12.2016, M. Sağıroğlu 5510.
Unk.

Lysimachia vulgaris L.

Arifye- Kalaycı, 90 m, 25.05.2013, M.
Sağıroğlu 3931. **Widesp.**

Lysimachia punctata L.

Pamukova, Hüseyinli İnönü upland, 950
m, 26.07.2019, M. Sağıroğlu 6607. **Euro.-
Sib.**

Lysimachia verticillaris Spreng.

Hendek-Çamlıca village, 900 m,
04.08.2016, M. Sağıroğlu 5056. **Hyc.-
Eux.**

RANUNCULACEAE

Helleborus orientalis Lam.

SAU campus, Teras houses, 200 m,
14.04.2009, M. Sağıroğlu 2737. **Eux.**

Anemone coronaria L.

Pamukova-Şahmelek village way, 190 m,
28.02.2017, M.Sağıroğlu 5559. **Medit.**

Anemone hortensis L.

Pamukova, Mekece-Kemaliye road, 200 m,
22.03.2020, M. Sağıroğlu 6662. **Unk.**

Adonis aestivalis L. subsp. *aestivalis*

SAU campus, west entrance, 90 m,
08.05.2011, M. Sağıroğlu 3001. **Widesp.**

Adonis flammea Jacq.

Geyve, Akıncı village, 400 m, 04.05.2016,
M. Sağıroğlu 5001. **Widesp.**

Ranunculus brutius Ten.

Saparnca, around İkramiye village, 200 m,
30.09.2011, M. Sağıroğlu 3190. **Euro.-Sib.**

Ranunculus neapolitanus Ten.

SAU campus, Hillside, 90 m, 20.06.2012,
M. Sağıroğlu 3542. **Medit.**

Ranunculus velutinus Ten.

Geyve-Akıncı village, around church, 450
m, 25.04.2013, M. Sağıroğlu 3840. **Medit.**

Ranunculus repens L.

Sapanca Lake roadside, 30 m, 08.05.2011,
M. Sağıroğlu 3017. **Widesp.**

Ranunculus costantinopolitanus (DC.)
d'Urv.

Pamukova, Kırca upland, 950 m,
02.04.2017, M. Sağıroğlu 5690-A.
Widespr.

Ranunculus paludosus Poir.

Pamukova-Ahiler village, 250 m,
09.05.2014, M. Sağıroğlu 4979. **Unk.**

Ranunculus illyricus L. subsp. *illyricus*

Serdivan mountain, roadside, 150 m,
02.07.2011, M. Sağıroğlu 3153. **Widesp.**

Ranunculus gracilis E.D.Clarke.

Akyazı, between Şerefiye-Reşadiye, 1,5
km, 276 m, 08.05.2014, M. Sağıroğlu
4971. **Unk.**

Ranunculus ficaria L. subsp. *ficariformis*
Rouy & Foucaud

SAU campus-Eşme way, 240 m,
08.05.2011, M. Sağıroğlu 3003. **Unk.**

Ranunculus peltatus Schrank subsp.
fucoides (Freyn) Muñoz Garm.

Arifye-İkramiye village way, moist places,
150 m, 01.06.2011, M. Sağıroğlu 3053.
Unk.

ROSACEAE

Geum coccineum Sibth. & Sm.

Pamukova, İnönü upland way, 1000 m,
10.06.2019, M. Sağıroğlu 6533. **Euro.-Sib.**

Geum urbanum L.

Sapanca Lake, around Dereköy,
13.06.2012, M. Sağıroğlu 3473. **Widesp.**

SMILACACEAE

Smilax aspera L.

Sakarya, Serdivan mountain, 350 m,
31.05.2012, M. Sağıroğlu 3338. **Unk.**

Smilax excelsa L.

SAU campus, 140 m, 31.05.2012, M.
Sağıroğlu 3332. **Eux.**

TYPHACEAE

Sparganium erectum L. subsp. *neglectum*
(Beeby) K. Richt.

West of Sapanca Lake, 25 m, 10.06.2010,
M. Sağıroğlu 2956. **Euro.-Sib.**

XANTHORRHOEACEAE

Iris orientalis Mill.

Pamukova-Hayrettin village, 600 m,
05.06.2013, M. Sağıroğlu 3949. **Medit.**

Iris kerneriana Asch. & Sint. Ex Baker

Geyve, Taşoluk village, 2nd km, 600 m,
25.05.2017, M. Sağıroğlu 6236. **Euro.-Sib.**

Iris sintenisii Jankasubsp. *sintenisii*

Geyve, Akıncı village, 450 m, 26.05.2017,
M. Sağıroğlu 6200. **Euro.-Sib.**

Iris germanica L.

Akyazı-Sultanpınar upland, 3rd km, 450 m,
08.06.2017, M. Sağıroğlu 6241. **Widesp.**

Iris purpureabractea B. Mathew & T.
Baytop **Endemic**

Geyve-Doğançıl village, 1340 m,
18.05.2017, M. Sağıroğlu 6063. **Medit.**

Iris suaveolens Boiss. & Reut.

SAU campus, Hillside, 80 m, 27.05.2012,
M. Sağıroğlu 3305. **Medit.**

Iris pseudacorus L.

Acarlar Longoz, 6 m, 16.05.2010, M.
Sağıroğlu 2886. **Unk.**

Asphodeline lutea (L.) Rchb.

Geyve, Doğançıl village, 1350 m,
18.05.2017, M. Sağıroğlu 6064. **Medit.**

Asphodeline damascena (Boiss.) Baker
subsp. *damascena*

Geyve, Doğançay village, 100 m,
23.05.2017, M. Sağıroğlu 6172. **Medit.**

Aloe vera (L.) Burm.f.

SAU campus, Hillside, 40 m, 08.05.2011,
M. Sağıroğlu 3021. **Unk.**

Yucca filamentosa L.

Arifiye, Sapanca way, 40 m, 15.07.2010,
M. Sağıroğlu 2995. **Unk.**

CAPRIFOLIACEAE

Valeriana dioscoridis Sm.

Pamukova, Şahmelek köyü, 700 m, 02.04.
2017, M. Sağıroğlu 5698. **Medit.**

4. DISCUSSION and CONCLUSIONS

As a result of the diagnosis; taxa identified 80 genus, 220 in 29 families in research area. Of these, 29 were identified as endemic and rare species, 13.1% respectively. 29 taxa are endemic and non-endemic taxa (Table 1), risk categories of

CR, 2 EN, 15 VU, 2 NT and 8 LC. 5 families were the largest in terms of number of taxa included in the numerical distribution are as follows; Orchidaceae (43), Asparagaceae (37), Amaryllidaceae (21), Iridaceae (17), Ranunculaceae (15).

Siberian character, 41 multi phytogeographical region character, 34 unknown region character, 16 Euxine character, 7 Irano-Turanian character, 1 Hyrcano character, 1 Hyrcano-euxine character and North Americana character.

According to the taxa phytogeographic region distributions are as follows; 79 taxa Mediterranean character, 40 Euro-

Table 1
Endemic /rare taxon and their danger category for the current study

Familya	Taxon	Endemic / rare	Danger category
Asparagaceae	<i>Bellevalia clusiana</i>	Endemic	LC
Asparagaceae	<i>Hyacinthella lineata</i>	Endemic	LC
Asparagaceae	<i>Hyacinthella micrantha</i>	Endemic	VU
Asparagaceae	<i>Galanthus nivalis</i> subsp. <i>nivalis</i>	Rare	VU
Asparagaceae	<i>Muscari aucheri</i>	Endemic	LC
Asparagaceae	<i>Muscari bourgaei</i>	Endemic	LC
Iridaceae	<i>Crocus abantensis</i>	Endemic	EN
Iridaceae	<i>Crocus antalyensis</i> subsp. <i>antalyensis</i>	Endemic	NT
Iridaceae	<i>Crocus danfordiae</i> subsp. <i>danfordiae</i>	Endemic	LC
Iridaceae	<i>Crocus olivieris</i> subsp. <i>istanbulensis</i>	Endemic	CR
Iridaceae	<i>Crocus flavus</i> subsp. <i>dissectus</i>	Endemic	VU
Iridaceae	<i>Crocus pestalozzae</i> subsp. <i>pestalozzae</i>	Endemic	VU
Iridaceae	<i>Crocus speciosus</i> subsp. <i>sakariensis</i>	Endemic	CR
Iridaceae	<i>Iris purpureabractea</i>	Endemic	NT
Iridaceae	<i>Iris germanica</i>	Rare	VU
Iridaceae	<i>Iris suaveolens</i>	Rare	VU
Iridaceae	<i>Iris pseudacorus</i>	Rare	VU
Liliaceae	<i>Gagea bithynica</i>	Endemic	LC
Orchidaceae	<i>Dactylorhiza saccifera</i> subsp. <i>bithynica</i>	Endemic	VU
Orchidaceae	<i>Dactylorhiza nieschalkiorum</i>	Endemic	VU
Orchidaceae	<i>Orchis lactea</i>	Rare	VU
Orchidaceae	<i>Orchis anatolica</i>	Rare	VU
Orchidaceae	<i>Orchis coriophora</i> subsp. <i>coriophora</i>	Rare	VU
Paeoniaceae	<i>Paeonia peregrina</i>	Rare	VU
Papaveraceae	<i>Corydalis caucasica</i> subsp. <i>abantensis</i>	Endemic	EN
Araceae	<i>Arum higrrophyllum</i> subsp. <i>euxinum</i>	Endemic	LC
Araceae	<i>Dracunculus vulgaris</i>	Rare	LC
Amaryllidaceae	<i>Leucojum aestivum</i>	Rare	VU
Amaryllidaceae	<i>Panocratium maritimum</i>	Rare	VU

Five genus were the largest in terms of number of taxa included in the numerical distribution are as follows; *Allium* (15), *Crocus* (13), *Orchis* (12), *Ranunculus* (10), *Iris* (7).

220 plant taxa belonging to 29 families have been collected from the working area. Amongst them 18 are endemic. If we look at the geographical regions it seems that the endemic

taxa are focused on the south region of the city Sakarya. The towns Pamukova and Geyve display Mediterrenian like climate conditions. Therefore, the great amount of endemic taxa have been found in those regions.

studies on the geophyte plants are very limited in Turkey. In that current work we have investigated only the geophyte plants in the region of research area. In the works by Değerli (2018) and Öz (2019) the geophytes of the Muğla city have been investigated (Table 2). In these works Değerli (2018) has found 77 geophyte taxa, whereas Öz (2019) has observed 84 of them [10,11]. From that point of view this work is a comprehensive study carried out on a specific region.

Table 2
Comparison with other studies

Area worked	Taxa
Sakarya city	220 geophytes
Muğla, [11]	77 geophytes
Muğla (Dalaman) [12]	84 geophytes

People of Sakarya use plants intensively for ethnobotanical purposes [12,13, 14]. Some plants are used extensively by the public in the study area. The most important of these is the *Leucojum aestivum* (Göl Soğanı) plant [15]. As a result of scientific studies, this plant; The emergence of its usability in the treatment of Alzheimer's disease has further increased the public's demand for this plant. In addition to the use of the people, the plant is completely dismantled and sold. Unfortunately, this is not in a plan. Wherever the people find the plant, it disassembles and sells it. Similar or close conditions are valid for species belonging to *Asparagus*, *Aristolochia*, *Crocus*, *Orchis*, *Ophrys*, *Arum*, *Dracunculus* genus. This situation causes the natural populations of plants to decrease rapidly.

Our natural onions are at risk due to unconscious picking, grazing pressure, unconscious export, tourism activities and many other reasons. Our people should be properly trained in the use of these plants, both in terms of conservation of our biodiversity and our country's economy.

Acknowledgements

The author thank the Curators GAZI, ANK, HUB, who allowed me to study their Plant species, for their assistance in herbarium studies Didem KARADUMAN and Ali Can Bahadır SEMERCİ, Melike TURNA, and Sakarya University Project no: 2010-02-20-010, Dr. Kenan TUNÇ Sakarya University, from Akıncı village Kamuran TAN, Ministry of Agriculture and Forestry Project no: 2016/192135 (Sakarya İli Biyoçeşitliliği) for financial support.

Declaration of Conflict of Interest/Common Interest

No conflict of interest or common interest has been declared by the author.

The Declaration of Ethics Committee Approval

The author declares that this document does not require an ethics committee approval or any special permission.

The Declaration of Research and Publication Ethics

The author of the paper declares that he complies with the scientific, ethical and quotation rules of SAUJS in all processes of the paper and that he does not make any falsification on the data collected. In addition, he declares that Sakarya University Journal of Science and its editorial board have no responsibility for any ethical violations that may be encountered, and that this study has not been evaluated in any academic publication environment other than Sakarya University Journal of Science.

REFERENCES

- [1] S.C. Demir, İ. Eker. Petaloid Monocotyledonous Flora Of Bolu Province, Including Annotations On Critical Petaloid Geophytes Of Turkey. Pegem Akademi, Ankara, 2015.
- [2] P.H. Davis, 'Flora Of Turkey And The East Aegean Islands', Edinburgh, A.Univ. Press., Edinburgh, vol.1-9, 1965-1985.
- [3] P.H. Davis, R.R. Mill, K. Tan, 'Flora of Turkey and the East Aegean Islands', Edinburgh Univ. Press., Edinburgh, vol. 10, 1988.
- [4] A. Güner, N. Özhatay, T. Ekim, K.H.C. Başer, 'Flora of Turkey and the East Aegean Islands', (supple. 2), Edinburgh Univ. Press., Edinburgh, vol. 11, 2000.
- [5] A. Güner, B. Akyıldırım, M.F. Alkayış, B. Çingay, S.S. Kanoğlu, A.M. Özkan, M. Öztekin, G.N. Tuğ, Türkiye Bitkileri Listesi (Damarlı Bitkiler). Nezahat Gökyiğit Botanik Bahçesi ve Flora Araştırmaları Derneği Yayını. İstanbul, 2012.
- [6] T. Ekim, M. Koyuncu, M. Vural, H. Duman, Z. Aytaç, N. Adıgüzel, Türkiye Bitkileri Kırmızı Kitabı. Türkiye Tabiatını Koruma Derneği, Van 100. Yıl Üniv., Ankara, 2000.
- [7] IUCN Standards and Petitions Subcommittee, Guidelines for Using the IUCN Red List Categories and Criteria. Version 13. Prepared by the Standards and Petitions Subcommittee. <<http://www.iucnredlist.org/documents/RedListGuidelines.pdf>>, 2017.
- [8] O. Koyuncu, Ö.K. Yaylacı, Ö Derviş, S. Tokur, Vascular Plant Diversity in Geyve Gorge (Sakarya/Turkey) and its Environs. Biological Diversity and Conservation, vol. 5, no. 3, pp. 98-122, 2012.
- [9] D. Karaduman, Acarlar Longozu (Sakarya) Florası. Sakarya Üniversitesi Fen Bilimleri Enstitüsü Yüksek Lisans Tezi, Haziran, Sakarya.2019.
- [10] Y. Değerli, Ö. Varol, Geophytes of Kızıldağ, Masa Mountain and Yılanlı Mountain (Muğla/Turkey). Biological Diversity and Conservation, vol. 11, no. 3, pp. 71-75, 2018.
- [11] A. Öz, H. Akan, The geophyte flora of Dalaman and Ortaca districts of Muğla/Turkey province. Biological Diversity and Conservation, vol. 12, no.1, pp. 39-49, 2019.
- [12] M. Sağiroğlu, E. Olgaç B. Ertürk, M. Turna, An Ethnobotanical Survey from Şile (İstanbul) and Karasu (Sakarya). Ot Sistemik Dergisi, vol. 19, no. 2, pp. 93-104, 2012.
- [13] M. Sağiroğlu, S.T. Köseoğlu, M. Turna, Medicinal Plants in Flora of İkraniye Sapanca-Sakarya-Türkiye).Sakarya University Journal of Science, vol. 2, no. 3, pp. 527-539,2017.
- [14] J. Rukšāns, Seven new Corcuses from the Balkans and Turkey, Alpine Garden Society, pp. 13-21, June, 2013.
- [15] A. Demir, Medical Resource Value Appraisal for *Leucojum aestivum* in Turkey. American Journal of Alzheimer's Disease & Other Dementias, vol. 29, no. 5, pp. 448-451, 2014

JOURNAL OF SCIENCE



SAKARYA UNIVERSITY

Sakarya University Journal of Science

ISSN 1301-4048 | e-ISSN 2147-835X | Period Bimonthly | Founded: 1997 | Publisher Sakarya University |
<http://www.saujs.sakarya.edu.tr/en/>

Title: Groundwater Pollution Connected to Multiple Effect: A Case Study Kaman
(Kırşehir, Turkey)

Authors: Tülay EKEMEN KESKİN, Bahadır SUBAŞI, Feyza GİRİŞEN, Zeynel BAŞIBÜYÜK
Received: 2019-04-15 19:37:20

Accepted: 2020-07-27 22:28:21

Article Type: Research Article

Volume: 24

Issue: 5

Month: October

Year: 2020

Pages: 1008-1022

How to cite

Tülay EKEMEN KESKİN, Bahadır SUBAŞI, Feyza GİRİŞEN, Zeynel BAŞIBÜYÜK; (2020),
Groundwater Pollution Connected to Multiple Effect: A Case Study Kaman

(Kırşehir, Turkey). Sakarya University Journal of Science, 24(5), 1008-1022,

DOI: <https://doi.org/10.16984/saufenbilder.554148>

Access link

<http://www.saujs.sakarya.edu.tr/en/pub/issue/56422/554148>

New submission to SAUJS

<http://dergipark.org.tr/en/journal/1115/submission/step/manuscript/new>



Groundwater Pollution Connected to Multiple Effect: A Case Study Kaman (Kırşehir, Turkey)

Tülay EKEMEN KESKİN^{*1}, Bahadır SUBAŞI¹, Feyza GİRİŞEN¹, Zeynel BAŞIBÜYÜK²

Abstract

This study aim to detect the groundwater pollution connected to multiple effect such as the interaction of mineral/ore-water, mining destruction and agricultural activities in Kaman (Kırşehir). The study area has recently abandoned iron, antimony, gold and floride mine areas and so, there are a lot of mine piles. Mine waste is a rich source of hazardous trace elements to the environment. In many areas especially abandoned sulphidic mine wastes may cause to produce acid mine drainage. Although no acid mine drainage is observed in the study area, the region needs to be reworked for this purpose in the following years. The electrical conductivity, pH and Eh values of the waters range between 126-1994 $\mu\text{S}/\text{cm}$; 7.28-8.58; 222-649 mV respectively. In the rainy season, the pH values of the waters decreased due to the effect of slight acidic precipitation and in parallel with this decrease, EC, TDS, Ca, Na, SO_4 , HCO_3 , As, Sb, U concentrations of some waters increase due to the increase of solubility of elements. As, Sb, F, U, NO_3 , NH_4 concentrations some of water exceed the maximum limit values given in the Turkish and World Health Organization Standards. Especially As contamination is a big problem for the region, because of tens of times exceed drinking water regulations.

Keywords: Groundwater pollution, mineral-water interaction, mining destruction, agricultural activities, Kaman (Kırşehir)

*Corresponding author: tulayekemen@karabuk.edu.tr

¹Karabuk University, Faculty of Engineering, Civil Engineering Department, 78050, Karabük.
E-Mail: tulayekemen@karabuk.edu.tr; bahadir-subasi@hotmail.com; feyzagirisen@hotmail.com
ORCID: <https://orcid.org/0000-0002-1415-7098>; <https://orcid.org/0000-0003-2151-4206>;
<https://orcid.org/0000-0002-0880-3567>

²Ahi Evran University, E-Mail: zeynelbasibuyuk@gmail.com.
ORCID: <https://orcid.org/0000-0003-1853-8848>

1. INTRODUCTION

The diminished water resources due to the overuse, the contamination of surface and groundwater, and decline of the rainfall etc. is very big problem for the many region of the World. Especially in recent years, the water and soil are exposed the contamination due to the agricultural, mining and industrial activities and their wastes, geothermal water wastes, and rapid population growth. Therefore, many researchers focused on water and soil pollution studies to protect the environment. There are numerous groundwater pollution problems in Turkey associated with geogenic and/or anthropogenic pollution sources [1-5]. Geogenic factors occur as important as anthropogenic pollution sources affecting the quality of groundwater. Anthropogenic pollution sources such as mining and agricultural activities increases the negative effects of lithology on groundwater quality [1, 3, 6]. Turkey hosts numerous active and abandoned mine areas that are characterized by metal-rich water [2, 4]. Figure 1 show the study region that is located north of Kırşehir (Central Anatolia Region of Turkey). This study purposes at elucidating the groundwater pollution resulting from water-rock interaction, mining and agricultural activities and mine tailings at the study area and especially, it is aimed to assign the origin of trace element impurities in water. For this aim, insitu physical measurements were made, and for chemical and isotopical analysis groundwater samples were taken, and As, Sb, F, U, NO₃, NH₄ element pollution was observed in groundwater. Pollutant levels were especially higher in groundwaters from discharging Kızılırmak and Meşeköy formations consisting of clastic rocks and magmatic rocks consisting of Fe, Sb, Au and F ores.

Many toxic contaminants and heavy metals can originate from many natural and anthropogenic pollutant sources. While agricultural, mining and industrial activities are anthropogenic, rock weathering and thermal environment compose natural or geological sources [8]. Many of trace elements such as As, Sb, Pb etc. are one of the most serious nature contaminants due to high toxicity [7]. Arsenic cause discomfort of many

organ systems. Furthermore, it is determined that, chronic arsenic exposure is related to bladder, kidney, skin, and liver cancers. Also it is know that inorganic arsenic is more harmful than organic arsenic [9-11].

2. MATERIAL AND METHODS

The study was performed between June 2016 and May 2017. The EC (Electrical conductivity), TDS (Total Dissolved Solids), T (Temperature), pH, ORP, and Q (Discharge) were measured on site with multiparameter (YSI-256 Instrument) of the 42 water samples (28 springs, 13 wells and 1 surfacewater) in the study region. Polyethylene bottles were preferred for the chemical and isotopic analysis of water. The pH meter was calibrated against to pH 4, 7, and 10 buffer solutions. The Oxidation Reduction Potential (ORP) measurements were conducted using a platinum electrode calibrated with a zobell reference. The ORP values were converted to the Eh by adding approximately 200 mV as specified by the YSI-256 instrument catalog. Acidification to pH < 2.0 for trace element analysis was made using pure nitric acid. The high-performance ion chromatography system (HPIC) and inductively coupled plasma-mass spectroscopy (ICP-MS) at Hacettepe University were used for major ion and trace element analyses, respectively. Tritium and oxygen-18-deuterium isotopes analyses were carried out at the Environmental Tritium Laboratory and International Karst Water Resources Application and Research Center of the Geological Engineering Department Hacettepe University, respectively.

3. GEOLOGICAL BACKGROUND and HYDROGEOLOGY

The base rocks of the study area are Paleozoic aged Kırşehir massive (Kalkanlıdağ, Kervansaraydağ, Bozcaldag and Hacıselimli Formation) consisting of massive, gnays, green schist, marble, amfibolite and metagabbro with magmatic origin. Massif in metamorphic rocks tectonically covered by the Çiçekdağ Formation which consists of volcanic rocks intercalated Cenomanian-Santonian aged pelagic sediments. These units are overlain by Campanian-Maestrichian aged intrusions named Baranadağ

Granitoid and Buzlukdağ Siyenitoid which show large expansions in the region. Another unit occupying a large area in the study area is defined as Kızılırmak Formation, which contains layerless, blocky, conglomerate, sandstone, limestone, tuff, gypsum and mudstones and defined as Meşeköy Formations, which contains conglomerate, sandstone, mudstone with limestone [12-14] (Figure 2). The floride mineralization in the Bayındır region has developed as vein type ores and is located within the fractures/cracks of Buzlukdağ Siyenitoid [15]. The reason for magnetite mineralization in Durmuşlu and Büğüz regions are the rise during orogenic activity of Paleozoic aged marbles and the mix of this marble when after a long period of wear with basic magma blocks in the Upper Cretaceous. Briefly, ores have generally developed due to orogenic activity and subsequent acid intrusions [16].

The main aquifers in the study area are conglomeratic and sandy levels of Kızılırmak Formation and Meşeköy Formations; the Baranadağ Granitoid consisting of granites and the Buzlukdağ Siyenitoid consisting of syenites. While the conglomerate and sandstone show grained aquifer properties, granites and syenites show fractured-cracked aquifer properties. Kervansaraydağ Formation with quartzite, schist, marble strips and Bozçaldağ Formation consisting of marble show aquiferous features in fracture-cracked levels in some places. All of these springs and wells measured in the study region are used as drinking, domestic and/or irrigation aims. The geological-hydrogeological map which included water sampling points are given in the Figure 2.

Table 1 show physical and chemical properties of waters. 10 springs discharges from the Kızılırmak Formation with flow rates between 0.15 and 3.32 L/s. There are also 6 wells drilled in the formation. There are 3 springs and 6 wells discharging from the Meşeköy Formation. 4 springs discharges from Baranadağ Granitoid with flow rates between 0.23 and 2.97 L/s. There are 4 springs with flow rates between 0.035 and 0.4 L/s discharging from the Buzlukdağ Siyenitoid. 1 spring was observed in the

Kervansaraydağ Formation and there are 5 springs discharging from the contact of Baranadağ Granitoid and Kervansaraydağ Formations.

4. WATER CHEMISTRY AND POLLUTION

There are different geological units, generally abandoned iron, gold, antimony and floride mine area and mining and agricultural activity in the study region. Therefore groundwater show large differences due to physical and chemical properties and the groundwaters are contaminated with depending As, Sb, F, U, NO₃ and NH₄.

Electrical conductivity (EC) and pH values of waters (KM-K1, KM-K3, KM-K4, KM-K5, KM-K6, KM-K7, KM-K8, KM-K9, KM-K10, KM-K13, KM-G9, KM-G10, KM-G12, KM-G13, KM-G14, KM-G16, KM-G18) discharging from Kızılırmak Formation consisting of clastic levels with block are between 352 and 963 $\mu\text{S}/\text{cm}$; and 7.28 and 8.15, respectively. EC and pH values of waters (KM-G1, KM-G2, KM-G3, KM-G4, KM-G5, KM-G6, KM-G7, KM-G8, KM-G19) discharging from Meşeköy Formation formed of clastics are between 430 and 781 $\mu\text{S}/\text{cm}$; and 7.29 and 8.70, respectively. It is thought that the variation in EC values of spring discharging from these formation is due to different groundwater residence times. Furthermore, the various rock types, such as conglomerate, sandstone, mudstone have different dissolution and permeability value. EC and pH values of waters (KM-K12, KM-K18, KM-G15) discharging from Baranadağ Granitoid are between 126 and 314 $\mu\text{S}/\text{cm}$; and 7.92 and 8.53, respectively. EC and pH values of waters (KM-K14, KM-K15, KM-K17) discharging from Buzlukdağ Syenitoid are between 268 and 516 $\mu\text{S}/\text{cm}$; and 7.36 and 8.05, respectively. It is thought that the EC values of waters discharging from magmatic rocks such as granite and syenite, especially around ore deposits, may have been affected by the mineralizations found in these rocks and the destruction during the mining activities.

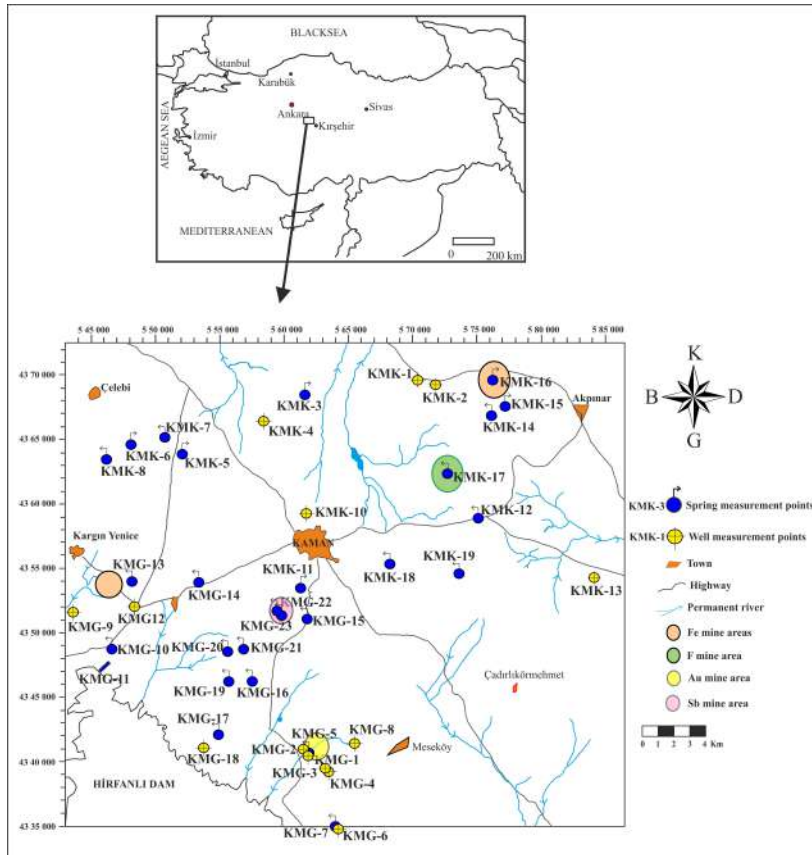


Figure 1 Location of the study area and its vicinity

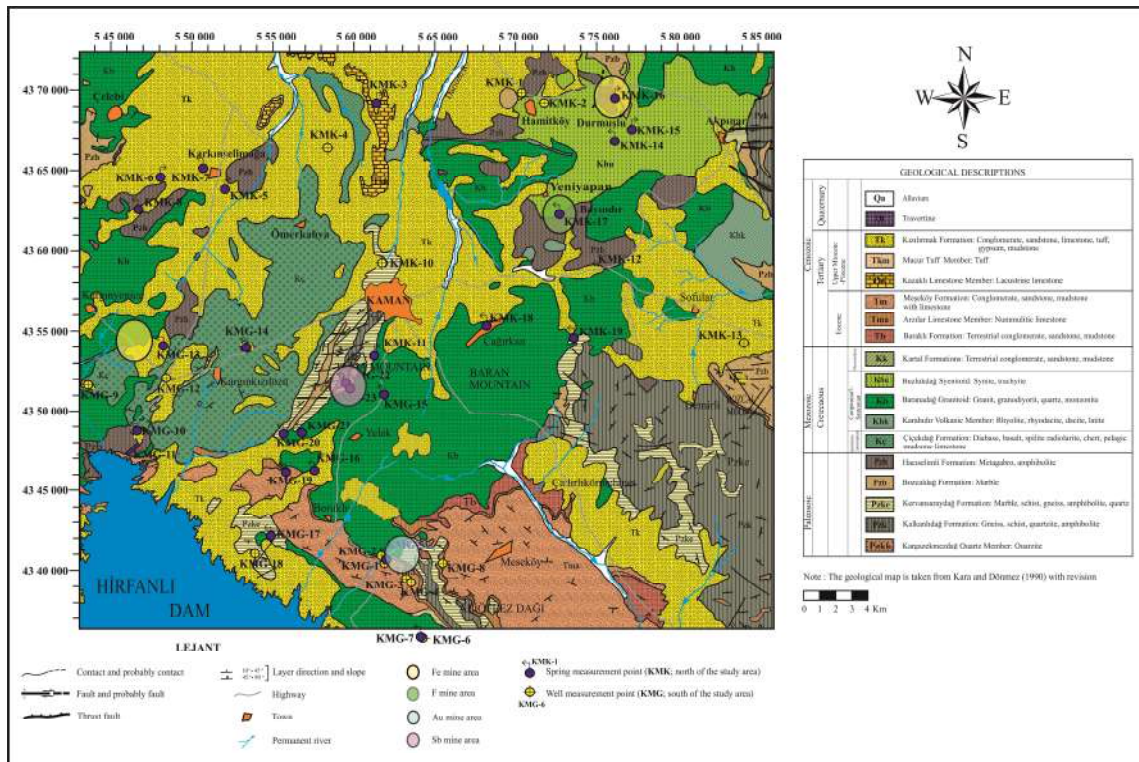


Figure 2 Geological-hydrogeology map of the study area and its vicinity (The geological maps are taken from Kara and Dönmez (1990) [10] with revision)

Table 1
Field measurement datas and chemical analysis results (meq/l) of the groundwaters in the study area and Turkish Standards for Water Intended for Human Consumption (EC ($\mu\text{S}/\text{cm}$), TDS (mg/L), Eh (mV), Temperature ($^{\circ}\text{C}$))

No	Date	EC	TDS	pH	Eh	Temp.	Na ⁺	K ⁺	Mg ⁺⁺	Ca ⁺⁺	CO ₃ ⁻	HCO ₃ ⁻	Cl ⁻	SO ₄ ⁻	NH ₄ ⁺	NO ₂ ⁻	NO ₃ ⁻	F ⁻	As	Sb	U
KM-K1	28.06.2016	499	325	8.15	275	18.58	0.94	0.05	1.75	3.14	0.00	4.71	0.25	0.46	0.11	0.00	0.38	0.05	5.5	0.33	9.6
KM-K2	28.06.2016	461	299	8.11	283	19.71	0.72	0.02	1.87	3.08	0.00	4.41	0.18	0.41	0.05	0.00	0.24	0.08	2.4	0.08	17.5
“	03.05.2017	494	321	7.64	326	12.65	0.39	0.01	0.86	3.17	0.00	4.37	0.07	0.23	0.00	0.00	0.15	0.03	1.90	0.07	16.48
KM-K3	28.06.2016	731	475	8.04	292	20.78	3.30	0.03	2.12	3.36	0.59	5.10	0.98	0.27	0.04	0.00	1.17	0.06	11.7	0.04	8.0
“	03.05.2017	786	511	7.28	354	13.65	1.80	0.01	1.00	3.56	0.00	5.73	0.46	0.15	0.00	0.00	0.57	0.02	10.36	0.08	7.32
KM-K4	28.06.2016	481	313	8.15	302	19.98	0.52	0.01	1.84	3.35	0.00	4.12	0.12	0.23	0.02	0.00	0.91	0.03	0.4	0.03	2.4
“	03.05.2017	515	335	7.62	347	13.52	0.46	0.01	1.24	3.91	0.00	3.88	0.09	0.27	0.00	0.00	0.88	0.03	0.33	0.02	2.30
KM-K5	28.06.2016	613	399	8.02	649	17.55	1.24	0.02	2.75	3.51	0.00	5.88	0.30	0.40	0.04	0.00	0.48	0.03	24.6	0.17	5.4
“	03.05.2017	637	414	7.75	344	12.20	1.30	0.00	1.78	4.32	0.00	5.73	0.28	0.49	0.00	0.00	0.40	0.02	21.53	0.15	4.78
KM-K6	28.06.2016	488	317	8.14	367	17.34	0.63	0.02	1.86	3.42	0.00	4.71	0.12	0.28	0.04	0.00	0.46	0.02	23.4	0.34	2.9
“	03.05.2017	512	333	7.62	347	11.58	0.57	0.01	1.07	4.11	0.00	4.37	0.13	0.31	0.00	0.00	0.42	0.03	20.32	0.31	2.67
KM-K7	28.06.2016	469	305	8.04	352	14.14	0.82	0.02	2.09	3.05	0.59	4.12	0.13	0.21	0.03	0.00	0.43	0.02	19.4	0.20	2.5
“	03.05.2017	503	327	7.56	356	11.65	0.86	0.00	1.46	3.74	0.00	4.76	0.09	0.23	0.00	0.00	0.43	0.04	18.13	0.28	2.47
KM-K8	28.06.2016	529	344	7.94	334	14.13	0.87	0.04	2.43	3.35	0.00	5.20	0.27	0.30	0.07	0.00	0.37	0.04	12.7	0.17	4.7
“	03.05.2017	568	369	7.53	361	12.91	0.91	0.03	1.50	4.04	0.00	4.95	0.21	0.35	0.00	0.00	0.40	0.02	16.22	0.17	4.99
KM-K10	29.06.2016	624	406	7.65	313	16.01	0.66	0.07	1.34	5.52	0.00	4.90	0.69	0.86	0.07	0.00	0.63	0.00	7.9	0.25	0.7
“	04.05.2017	711	462	7.30	348	16.19	0.63	0.09	1.06	6.28	0.00	5.24	0.76	1.05	0.00	0.00	0.68	0.00	9.03	0.24	1.50
KM-K11	29.06.2016	390	253	8.07	295	14.39	0.14	0.01	0.44	3.32	0.00	3.31	0.08	0.20	0.01	0.00	0.11	0.00	1.1	0.18	2.6
KM-K12	29.06.2016	314	204	7.92	301	13.85	0.42	0.02	1.08	2.42	0.00	2.94	0.07	0.29	0.01	0.00	0.43	0.02	1.3	0.04	3.3
KM-K13	29.06.2016	352	229	7.91	300	22.03	0.10	0.01	1.02	3.08	0.00	3.82	0.05	0.07	0.01	0.00	0.25	0.00	0.7	0.03	0.6
KM-K14	29.06.2016	457	297	8.05	257	14.15	0.93	0.02	1.59	3.36	0.00	5.10	0.11	0.31	0.01	0.00	0.01	0.07	6.8	0.20	14.9
KM-K15	30.06.2016	268	174	7.87	282	16.23	0.81	0.02	0.69	2.03	0.00	2.94	0.07	0.18	0.01	0.00	0.01	0.10	2.3	0.14	13.1
“	03.05.2017	289	185	7.53	339	11.55	0.83	0.02	0.50	2.02	0.00	2.72	0.08	0.23	0.00	0.00	0.01	0.10	2.03	0.10	9.56
KM-K16	30.06.2016	459	298	7.8	279	16.51	0.83	0.02	2.03	3.03	0.00	4.80	0.10	0.47	0.03	0.00	0.19	0.05	2.0	0.18	20.7
“	03.05.2017	500	325	7.65	317	12.91	0.86	0.02	1.27	3.82	0.00	4.66	0.08	0.62	0.00	0.00	0.21	0.05	1.77	0.06	19.95
KM-K17	30.06.2016	491	319	7.86	272	14.76	0.82	0.02	1.88	3.49	0.00	4.61	0.28	0.52	0.02	0.00	0.17	0.18	10.5	0.28	36.9
“	03.05.2017	516	335	7.36	354	13.75	0.85	0.01	1.35	4.13	0.00	4.76	0.25	0.58	0.00	0.00	0.17	0.17	9.39	0.26	33.69
KM-K18	30.06.2016	199	131	8.03	275	15.42	0.37	0.01	0.59	1.74	0.00	2.16	0.06	0.29	0.01	0.00	0.01	0.01	27.4	0.06	2.3
“	03.05.2017	229	149	7.92	333	11.19	0.40	0.01	0.46	2.04	0.00	2.04	0.08	0.56	0.00	0.00	0.01	0.01	23.94	0.06	1.44
KM-K19	30.06.2016	299	135	7.87	277	15.95	0.27	0.03	0.77	2.90	0.00	3.33	0.06	0.18	0.01	0.00	0.07	0.01	23.9	0.06	1.2
“	03.05.2017	233	151	7.61	350	11.97	0.37	0.02	0.44	2.03	0.00	2.14	0.05	0.36	0.00	0.00	0.04	0.02	2.85	0.03	0.90
Sağ. Bak. (2013)															0.03		0.81	0.08	10	5	

Table 1 Continue

No	Date	EC	TDS	PH	Eh	Temp.	Na ⁺	K ⁺	Mg ⁺⁺	Ca ⁺⁺	CO ₃ ⁻	HCO ₃ ⁻	Cl ⁻	SO ₄ ⁻	NH ₄ ⁺	NO ₂ ⁻	NO ₃ ⁻	F ⁻	As	Sb	U
KM-G1	27.06.2016	549	357	8.58	221.7	16.39	0.78	0.08	1.67	4.17	0.00	4.80	0.38	0.89	0.00	0.03	0.14	0.02	69.3	0.97	1.6
“	04.05.2017	595	386	7.29	320.6	15.35	0.45	0.04	0.78	3.85	0.00	4.85	0.18	0.51	0.00	0.00	0.06	0.03	87.36	1.07	2.71
KM-G2	27.06.2015	439	285	8.32	238.6	19.23	0.49	0.05	1.21	3.66	0.00	4.31	0.25	0.42	0.00	0.03	0.14	0.01	398.4	0.32	3,0
KM-G3	27.06.2016	497	323	8.23	257.5	22.35	0.74	0.04	2.00	3.07	0.00	4.02	0.34	0.87	0.00	0.02	0.23	0.01	16.2	0.78	2.0
KM-G4	27.06.2016	502	326	8.15	255.9	15.24	0.58	0.04	1.82	3.80	0.00	4.22	0.29	0.87	0.00	0.02	0.32	0.01	23.1	0.95	1.2
KM-G5	27.06.2016	430	280	8.70	256.5	21.75	0.62	0.04	1.03	3.48	0.00	3.92	0.26	0.43	0.00	0.02	0.15	0.01	221.5	0.27	1.1
“	04.05.2017	506	331	7.43	283.9	16.49	0.33	0.02	0.67	3.54	0.00	4.37	0.16	0.35	0.00	0.00	0.11	0.00	256.69	0.42	2.62
KM-G6	27.06.2016	453	316	8.14	257.5	21.43	0.87	0.05	1.70	3.12	0.00	4.12	0.42	0.38	0.00	0.02	0.46	0.03	30.7	0.75	4.6
“	04.05.2017	504	328	7.46	334.4	15.74	0.45	0.02	0.83	3.25	0.00	4.27	0.20	0.22	0.00	0.00	0.18	0.04	37.69	0.74	4.39
KM-G7	27.06.2017	510	332	8.01	259.2	19.84	1.85	0.04	1.56	2.29	0.00	4.02	0.47	0.49	0.00	0.05	0.32	0.06	43.3	0.12	15.0
“	04.05.2017	550	358	7.35	335	13.64	1.06	0.02	0.91	2.83	0.00	4.47	0.26	0.31	0.00	0.00	0.17	0.06	38.53	0.13	14.05
KM-G8	27.06.2017	781	512	7.92	255.7	14.38	0.74	0.04	2.19	6.39	0.00	4.61	1.71	0.68	0.00	0.03	1.76	0.01	54.2	0.16	0.9
“	04.05.2017	511	332	7.38	308.2	14.45	0.29	0.02	0.64	3.70	0.00	4.27	0.17	0.21	0.00	0.00	0.21	0.00	68.10	0.20	2.18
KM-G9	28.06.2016	856	556	8.03	319.6	15.90	4.01	0.12	3.41	3.40	0.78	4.02	0.68	3.52	0.00	0.02	1.04	0.13	9.8	0.11	8.5
“	04.05.2017	963	626	7.76	318.5	13.45	1.86	0.07	1.81	3.40	0.00	4.56	0.40	2.27	0.00	0.00	0.49	0.05	8.48	0.13	7.98
KM-G10	28.06.2016	801	521	8.08	494.4	24.19	4.16	0.03	2.16	3.19	0.98	4.31	1.43	1.48	0.00	0.05	0.67	0.05	0.6	0.03	5.3
KM-G11	28.06.2016	1994	1296	8.05	372.2	16.22	6.62	0.16	4.27	8.57	0.00	2.95	7.47	7.39	0.01	0.04	0.01	0.01	11.2	0.31	2.0
KM-G12	28.06.2016	586	381	8.11	321.4	13.88	1.08	0.02	1.89	3.31	0.00	4.92	0.20	0.37	0.00	0.02	0.29	0.03	0.8	0.06	3.7
KM-G13	28.06.2016	516	335	8.01	322.4	14.67	0.99	0.08	1.97	3.17	0.59	4.02	0.15	0.41	0.00	0.02	0.50	0.03	14.4	0.10	4.1
“	04.05.2017	567	369	7.75	319.7	13.45	0.45	0.02	1.05	3.53	0.00	4.85	0.09	0.18	0.00	0.00	0.34	0.04	1.68	0.07	1.71
KM-G14	28.06.2016	502	326	8.09	323.8	18.32	0.68	0.01	2.18	3.35	0.39	4.31	0.10	0.27	0.00	0.01	0.64	0.02	0.6	0.04	1.6
KM-G15	29.06.2016	126	82	8.53	289.3	14.18	0.30	0.01	0.57	1.42	0.00	1.26	0.27	0.15	0.00	0.01	0.41	0.01	0.3	0.03	0.1
KM-G16	29.06.2016	508	330	8,07	307.2	18.63	0.53	0.02	1.50	4.14	0.00	4.90	0.13	0.34	0.00	0.03	0.46	0.03	2.8	0.11	5.3
KM-G17	29.06.2016	339	221	8.15	313.2	16.09	0.27	0.02	0.90	2.74	0.00	2.94	0.20	0.30	0.00	0.01	0.19	0.01	6.2	0.03	0.7
KM-G18	29.06.2016	826	537	7.99	311.7	19.48	2.17	0.04	2.60	5.06	0.00	4.22	1.77	1.31	0.00	0.03	1.78	0.03	14.0	0.04	10.3
“	04.05.2017	875	569	7.46	329.9	15.88	1.07	0.02	1.16	4.48	0.00	4.27	0.85	0.74	0.00	0.00	0.77	0.01	15.37	0.06	11.06
KM-G19	29.06.2016	465	302	8.17	314.4	23.56	0.36	0.02	1.48	3.84	0.00	4.31	0.17	0.38	0.00	0.01	0.47	0.01	2.5	0.09	3.1
KM-G20	29.06.2016	335	218	8.05	308.2	15.42	0.17	0.01	1.12	3.01	0.00	3.53	0.08	0.23	0.00	0.01	0.12	0.00	2.7	0.03	0.3
KM-G21	29.06.2016	318	207	8.17	305.7	18.57	0.09	0.01	0.36	3.53	0.00	3.53	0.06	0.16	0.00	0.01	0.06	0.00	20.5	0.04	0.5
KM-G22	29.06.2016	361	234	7.94	309.1	13.15	0.21	0.03	0.72	3.45	0.00	3.73	0.08	0.22	0.00	0.01	0.17	0.01	119.6	11.03	1.2
“	04.05.2017	389	253	7.59	346.4	11.37	0.15	0.01	0.37	3.45	0.00	3.88	0.04	0.15	0.00	0.00	0.09	0.01	148.61	12.66	2.74
KM-G23	29.06.2016	286	186	7.86	310.5	15.5	0.14	0.04	0.39	3.08	0.00	3.24	0.06	0.14	0.00	0.01	0.05	0.00	11.7	1.27	4.1

Electrical conductivity (EC) and pH values of waters (KM-G17, KM-G20, KM-G21, KM-G22, KM-G23) discharging from contact of Baranadağ Granitoid and Kervansaraydağ Formations consisting of quartzite, schist, marble are between 286 and 389 $\mu\text{S}/\text{cm}$; and 7.59 and 8.17, respectively.

In the rainy season (April-May), the discharge of waters have increased slightly. In parallel with this situation, the pH values have fallen due to the effect of the slightly acidic rain water. This decline led to an increase in the EC, TDS, Ca, Na, SO_4 and HCO_3 values of many waters. It is believed that the reason for these increases is the increase in the solubility of ore deposits and associated rocks in the study area due to this precipitation water.

During the dissolution of the altered rocks, ores and mine piles, some elements were free by hydrolysis along various flowways. Furthermore, it is thought that mining activities and abandoned mine areas accelerated dissolution. In addition that in most region in the world waters were polluted due to chemicals used in agricultural activities. Because the use of fertilizers and pesticides increase for enhance productivity. According to many studies, some major ions, nitrogen pollutants, and trace elements were found in fertilizers and pesticides [17-19, 1].

The NH_4 values of waters range between 0.09 and 1.99 mg/L, and the NH_4 values of the water (KM-K1, KM-K2, KM-K3, KM-K5, KM-K6, KM-K7, KM-K8, KM-K10, KM-G1, KM-G2, KM-G7, KM-G8, KM-G10, KM-G11, KM-G18) discharging from the Kızılırmak and Meşeköy formations (excluding KM-G11), which consists of clastic units, are several times higher than the 0.5 mg/L value given in Turkish Drinking Water Standards [20]. KM-G11 is a water that represents the dam water and is used for domestic purposes after passing through rough grate. Agricultural activities are performed in these regions, and the waters discharging from these lithologies are generally used as drinking, domestic and irrigation water purposes. It is thought that the KM-K10 well is particularly

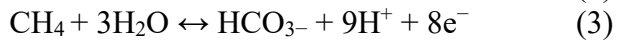
important, because of providing the drinking water of the Kaman District. Similarly, the NO_3 values of waters range between 0.68 and 109.04 mg/L, and the NO_3 values of the water (KM-K3, KM-K4, KM-K10, KM-G8, KM-G9, KM-G18) discharging from the Kızılırmak and Meşeköy formation are several times higher than the 50 mg/L value given in Turkish Drinking Water Standards and World Health Organization standards [21]. Nitrate generally finds in waters organically and anthropogenically. The high nitrate concentrations in the drinking water can cause the "blue disease" in babies because of decreases the oxygen carrying capacity of the blood [22]. In addition WHO (1984) [22] and Uslu and Türkman (1987) [23] said that, nitrate may readily converted to nitrite at body part where acidity is relatively low, and nitrite may have strong carcinogenic effects.

The trace elements concentration in water samples are given in Table 1. The As, Sb, F and U amount of waters range between 0.3 and 398.4 ppb ($\mu\text{g}/\text{L}$); 0.03 and 11.66 ppb ($\mu\text{g}/\text{L}$); < 0.01 and 3.35 mg/L; 0.01 and 36.9 $\mu\text{g}/\text{L}$, respectively. Trace element pollutants (As, Sb, F, U) are observed in water (spring and well; KM-K2, KM-K3, KM-K5, KM-K6, KM-K7, KM-K8, KM-K9, KM-K10, KM-K15, KM-K16, KM-K17, KM-K18, KM-K19, KM-G1, KM-G2, KM-G3, KM-G4, KM-G5, KM-G6, KM-G7, KM-G8, KM-G9, KM-G11, KM-G13, KM-G18, KM-G21, KM-G22, KM-G23) discharging from the Kızılırmak and Meşeköy formations consisting of clastics and magmatic (Baranadağ Granitoide and Buzlukdağ Siyenenitoide) rocks, and contact with metamorphic of magmatic rocks (Kervansaraydağ/Hacıselimli formations) consisting of Fe, Sb, Au and F mine veins.

Arsenic pollution can be seen in two forms as natural and anthropological. For example, high arsenic contents can also be seen in Pliocene sediments, mining sites, volcanic/magmatic rocks, lakes, and black shales [24-25]. Geological structure is very important in the amount of arsenic originating from natural sources in soils and water. The average arsenic value detectable on the continental crust varies from 1.5 to 2 ppm [26]. Arsenic can be

determined in quartz, feldspar, aluminosilicates and iron ore minerals and the feldspar found in magmatic rocks probably accounts for more than half of total arsenic [27]. Due to this information, it is thought that the sources of pollution in the KM-K17, KM-G1, KM-G2, KM-G5, KM-G22 waters discharging from magmatic and metamorphic rocks near the abandoned iron, antimony, gold and fluoride mine and the KM-K18 Spring discharging from Baranadağ Granitoides are the natural washings from the magmatic rocks and mineralizations. However, it is believed that the mining process accelerates the dissolution of trace elements from the rocks and may cause a higher amount of trace elements in the water.

Arsenic amount is correlated with the ammonium concentrations, which is formed by the decay of organic matter. The equations given below prove that there may be a relationship between the input of As into the groundwater and the decay of organic product (Eq. 1, 2, 3) [28-30, 11].



In addition that, it is also thought that there are two causes of As pollution in other waters which are discharging from Kızılırmak and Meşeköy formation consisting of clastic levels that have carried out agricultural activities. The source rocks of the clastic levels are magmatic and metamorphic rocks in the upper elevations. The first of these reasons is the water-rock interaction, i.e. naturally washing of the rocks, and the second one is the anthropological pollution due to agricultural activities. Pesticides, drying agents and feed additives that are used for agricultural productivity are among the wide use areas of arsenic [26, 27, 31]. This idea is reinforced by a positive association between concentrations of As and NH_4 in the waters. Long-term consumption of arsenic can cause various discomforts in the body. Arsenic accumulated in skin, hair and nails causes color changes in the hands and feet, and can lead to a disease called skin cancer and black foot

(blackfoot) in the progressive stages [32-36]. In addition, many studies have indicated that it can cause problems such as respiration, kidney, stomach, heart disorders, blood disorders, diabetes, growth problems in children and intelligence [37-38].

It is believed that the Sb (KM-G22), F (KM-K9, KM-K15, KM-K17, KM-G9), and U (KM-K2, KM-K9, KM-K14, KM-K16, KM-K17, KM-G7) pollutions observed in this waters is due to the water-rock interaction and mining activities. Antimony negatively affects the nerve, respiratory and digestive systems and causes collapse in the immune system [39-40]. Fluoride consumption can often cause discomfort in the teeth and disrupt bone structure in the skeletal system [41]. In addition to long term and high amount of uranium consumption causes kidney disorders and, because it is a radioactive element, it can carry cancer risk [42].

The Piper diagrams [43] that show major anion and cation percentages of the waters in the study region are given in Figure 3. Generally, while groundwater has Ca-HCO_3 facies, KM-K3, KM-K5, KM-G7, KM-G9, KM-G10, KM-G11 discharging from Kızılırmak and Meşeköy formation have mixed type (Na-Ca-Mg facies). In addition that, KM-G9 and KM-G11 has HCO_3SO_4 and $\text{SO}_4\text{ClHCO}_3$ type according to anion respectively. KM-G11 is dam water. No changes were made during the rainy (April-May) season. It is thought that the Na-Ca-Mg- HCO_3 type were mostly according to different clastic levels with different original levels such as conglomerate, sandstone, mudstone and locally clayey limestone, tuff, gypsum, anhydrite and ion exchange reactions between water and clastic rocks.

5. ISOTOPE CHEMISTRY

The ^{18}O , ^2H , and tritium (^3H) isotopes were analysed because to determine the origins and underground residence time of groundwater. The ^{18}O , ^2H , are stable isotopes; and tritium (^3H) is a radioactive isotope. The results of waters with the large discharge and around the ore deposits according to study aim are given in Table 2.

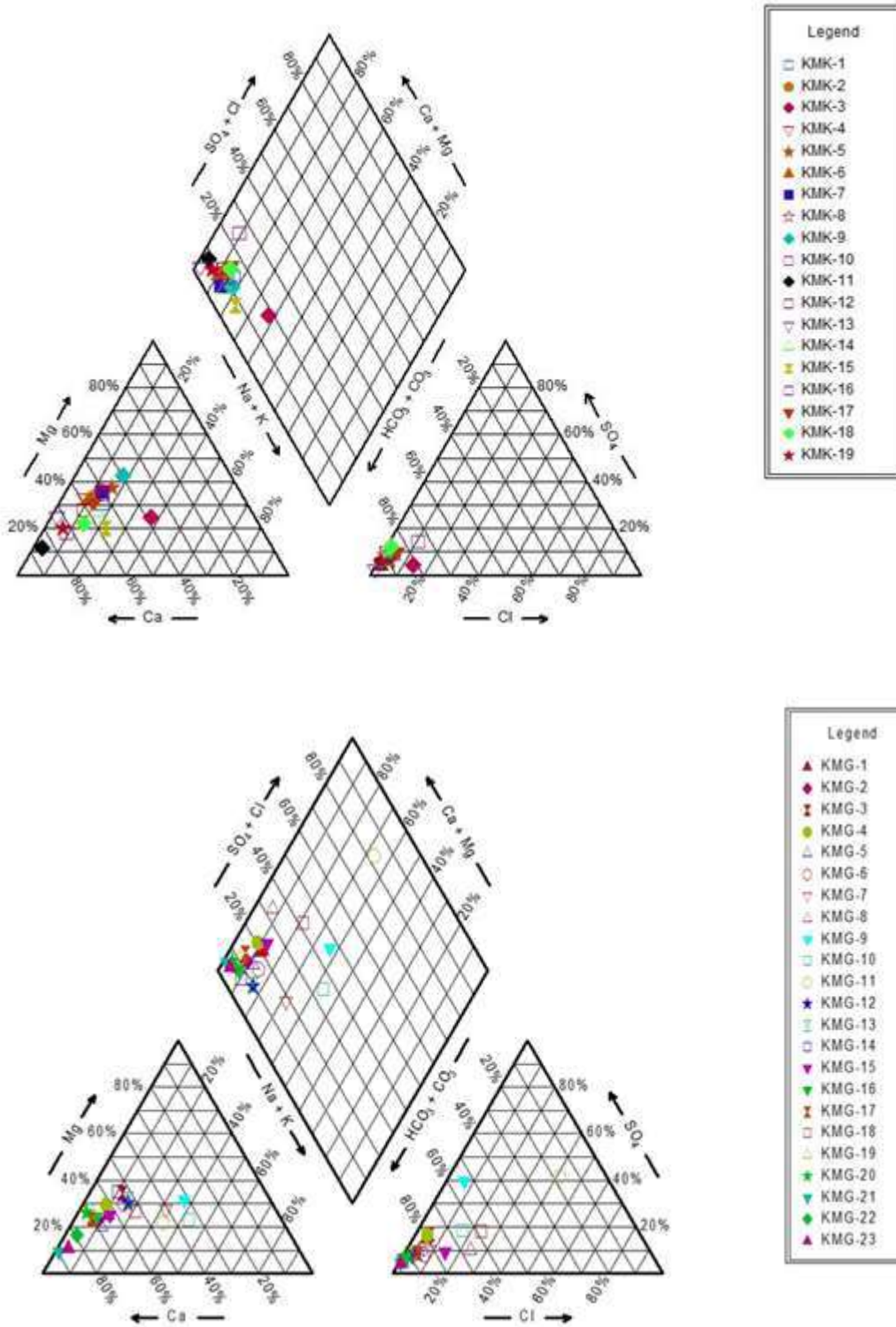


Figure 3 Piper diagram of the groundwaters in the study area (dry period)

Table 2
Isotope analysis results some groundwater in the study area

No	Date	Tritium (TU)	Oxygen-18 (VSMOW ‰) (± 0.15)	Deuterium (VSMOW ‰) (± 2)
KM-K8	28.06.2016	3.02 \pm 0.28	-8.49 \pm 0.20	-63.41 \pm 1.49
KM-K10	29.06.2016	3.09 \pm 0.28	-10.31 \pm 0.05	-71.10 \pm 0.57
KM-K13	29.06.2016	2.11 \pm 0.26	-10.12 \pm 0.15	-70.16 \pm 1.23
KM-K15	30.06.2016	3.92 \pm 0.29	-10.74 \pm 0.21	-72.92 \pm 1.04
“	03.05.2017	3.39 \pm 0.30	(-)	(-)
KM-K16	30.06.2016	4.45 \pm 0.30	-9.81 \pm 0.05	-69.31 \pm 0.61
KM-K17	30.06.2016	2.99 \pm 0.29	-10.33 \pm 0.30	-74.28 \pm 1.90
“	03.05.2017	3.87 \pm 0.32	(-)	(-)
KM-K18	30.06.2016	3.69 \pm 0.30	-10.13 \pm 0.04	-71.02 \pm 0.55
KM-G1	27.06.2016	3.25 \pm 0.31	-9.80 \pm 0.08	-70.79 \pm 0.30
KM-G4	27.06.2016	3.34 \pm 0.32	-10.30 \pm 0.10	-72.73 \pm 0.71
KM-G5	27.06.2016	3.14 \pm 0.30	-10.09 \pm 0.06	-69.69 \pm 0.69
“	04.05.2017	3.04 \pm 0.29	(-)	(-)
KM-G8	27.06.2016	3.20 \pm 0.30	-9.99 \pm 0.25	-68.20 \pm 1.52
KM-G11	29.06.2016	3.68 \pm 0.30	-6.89 \pm 0.14	-51.65 \pm 1.82
KM-G13	29.06.2016	3.71 \pm 0.30	-9.47 \pm 0.08	-66.55 \pm 0.76
KM-G15	29.06.2016	3.34 \pm 0.30	-10.81 \pm 0.27	-68.27 \pm 0.82
KM-G20	29.06.2016	3.92 \pm 0.30	-10.66 \pm 0.03	-71.59 \pm 0.56
KM-G22	29.06.2016	3.33 \pm 0.31	-10.88 \pm 0.10	-73.00 \pm 1.17
“	04.05.2017	3.31 \pm 0.29	(-)	(-)

The $\delta^{18}\text{O}$, $\delta^2\text{H}$ and tritium isotope values of the springs range between -10.88 and -8.49 ‰, -74.28 and -63.41 ‰, 2.11 and 4.45 TU, respectively.

Figure 4 shows the ^{18}O - ^2H graph for determine the origin of water [44-46]. The waters are generally located on the Ankara Meteoric Line (MWL) [44], so waters are meteoric origin. Otherwise, KM-K8 water has remained under some amount of Ankara Meteoric Water Line due to the enrichment with $\delta^{18}\text{O}$ and $\delta^2\text{H}$ because of evaporation an/or feeding from lower elevations compared to other waters.

When the tritium results of waters in the study area are appreciated using the assignation given in Table 3 [47], it can be determined that waters may have “mixture of half-modern and present recharge”. This is evidenced by the fact that the discharge of the waters have not increased much during the rainy season.

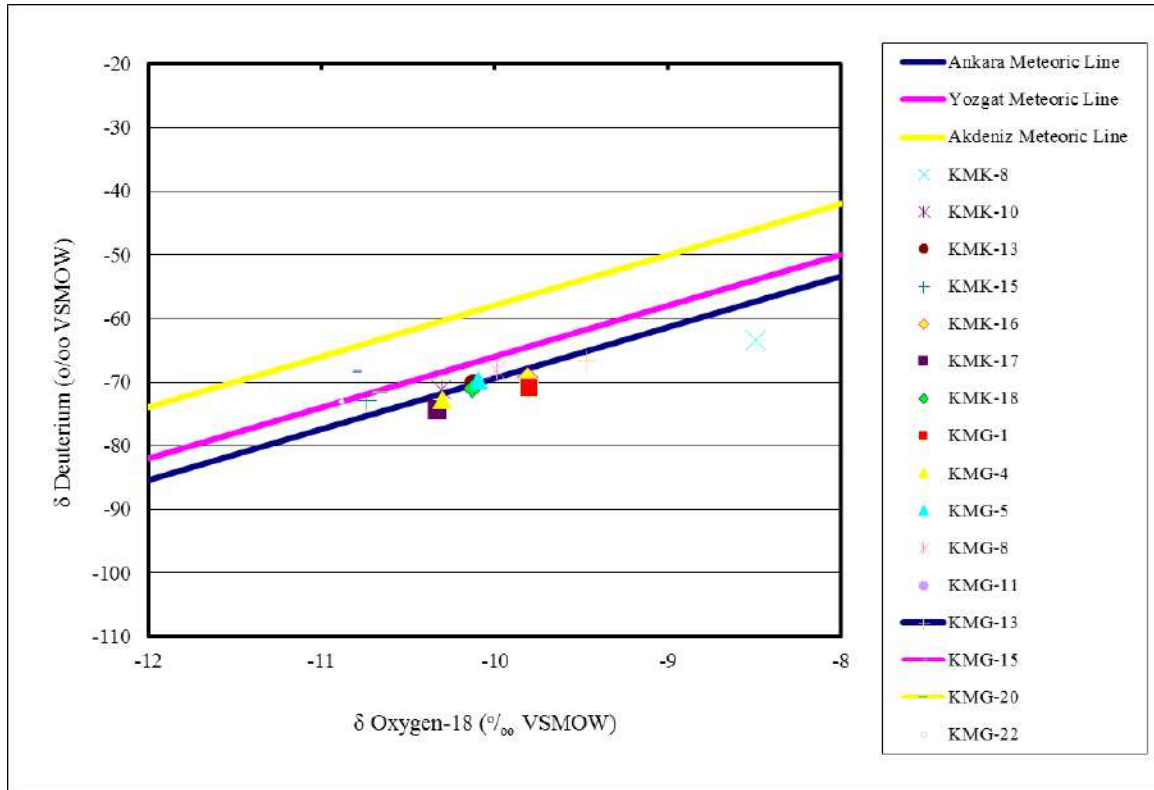


Figure 4 $\delta^{18}\text{O} - \delta^2\text{H}$ graphs of groundwater large and/or discharging from Yemişliçay Formation in the study area (Ankara meteoric water line (MWL) from Sayın and Eyüpoğlu 2005 [44]; Yozgat MWL from Şimşek, 1993[45]; Mediterranean MWL from Payne and Dinçer 1965 [46])

Table 3

Qualitative dating of groundwaters in continental regions (from Clark and Fritz 1997) [47]

Tritium Value (TU)	Dating
<0.8 TU	Submodern-recharged prior to 1952
0.8 ~4 TU	Mixture between submodern and recent recharge
5 -15 TU	Modern (<5 to10 yr)
15 – 30 TU	Some “bomb” ^3H present
>30 TU	Considerable component of recharge from 1960s or 1970s
>50 TU	Dominantly the 1960s recharge

6. CONCLUSION

This study aims to determine water pollution and hydrogeological properties of Kaman (Kırşehir). While the conglomeratic and sandy levels are the grained aquifer, granites and syenites are fractured-cracked aquifers of the study area. The isotope analysis showed that the waters have generally meteoric origin and mixture of half-modern and present recharge.

In the study area, a lot of pollutants sources accompany each other and threaten public health. Many cancer cases are reported in the region. As revealed by the analysis, the study area has dual pollution sources natural pollution caused by water-rock interactions, and anthropogenic pollution originating from agricultural and mining activities, and these

sources are effective processes resulting in water pollution. The concentrations of As, Sb, F, U, elements and NO₃, NH₄ ions in water samples exceed the Turkish and WHO drinking water standards. Pollutant levels of these elements were especially higher in groundwaters from discharging Kızılırmak and Meşeköy formations consisting of clastic rocks where were performed the agricultural activities. and magmatic rocks consisting of Fe, Sb, Au and F ores.

The As, Sb, F and U amount of waters vary between 0.3–398.4 ppb, 0.03–11.66 ppb, < 0.01–3.35 mg/L, 0.01–36.9 ppb, respectively. Especially it is thought that As contamination is a big problem for the region, because of tens of times exceed drinking water regulations. The sources of trace elements contamination in water discharging from magmatic and methamorphic rocks are the natural washings from ores/rocks. Furthermore, the mining process accelerates the dissolution of trace elements from the rocks. Also, there are two causes of As contamination waters which are discharging from clastic levels that have achieved agricultural activities. The first of these reasons is the water-rock interaction. The source rocks of the clastic levels are magmatic and metamorphic rocks in the upper elevations. The second is the anthropological pollution due to agricultural activities. The NH₄ values of waters vary between 0.09–1.99 mg/L, and the values are several times higher than value given in standarts in water discharging from the Kızılırmak and Meşeköy formations. Furthermore, generally, the NO₃ values of these are several times higher than the 50 mg/L value given in standards.

These contaminant resulting from mining and agricultural activities accumulate in the soil, percolate to the groundwater, and may increase over time. Furthermore it may cause the very important pollution risk in terms of water and soil in the future. So, it is recommended that long-term environmental monitoring studies should be conducted in the area in terms of especially the As, Sb, F, U, NO₃ and NH₄ element/ion.

Acknowledgements

The authors would like to thank the Karabük University Scientific Research Projects Commission (BAP) for contributing to the financial portion of the project.

Funding

This project studies were supported by Karabük University Scientific Research Projects Commission. Project numbers were KBÜ-BAP-16/1-YL-091 and KBÜ-BAP-16/1-YL-092

The Declaration of Conflict of Interest/ Common Interest

No conflict of interest or common interest has been declared by the authors.

Authors' Contribution

This study is the master's thesis of Bahadır SUBAŞI and Feyza GİRİŞEN, and the idea of the studies belongs to supervisor that is Tülay EKEMEN KESKİN. Tülay EKEMEN KESKİN had a great contribution in providing support for the study, field studies, analyzing the waters, interpreting the findings and writing the thesis. Zeynel BAŞIBÜYÜK contributed during the fieldwork

The Declaration of Ethics Committee Approval

The authors declare that this document does not require an ethics committee approval or any special permission.

The Declaration of Research and Publication Ethics

The authors of the paper declare that they comply with the scientific, ethical and quotation rules of SAUJS in all processes of the article and that they do not make any falsification on the data collected. In addition, they declare that Sakarya University Journal of Science and its editorial board have no responsibility for any ethical violations that may be encountered, and

that this study has not been evaluated in any academic publication environment other than Sakarya University Journal of Science.

REFERENCES

- [1] T. E. Keskin, "Nitrate and heavy metal pollution resulting from agricultural activity: a case study from Eskipazar (Karabük, Turkey)," *Environmental Earth Sciences*, vol. 61, pp. 703–721, 2010.
- [2] T. E. Keskin and S. Toptaş, "Heavy metal pollution in the surrounding ore deposits and mining activity: a case study from Koyulhisar (Sivas–Turkey)," *Environmental Earth Sciences*, vol. 67, pp. 859–866, 2012.
- [3] A. Baba and O. Gündüz, "Effect of geogenic factors on water quality and its relation to human health around Mount Ida, Turkey," *Water*, vol. 9, no. 1, pp. 66, 2017.
- [4] D. S. Yücel and A. Baba, "Determining water and sediment quality related to lead-zinc mining activity," *Archives of Environmental Protection*, vol. 44, pp. 19–30, 2018.
- [5] N. Balcı and C. F. Demirel, "Prediction of acid mine drainage (AMD) and metal release sources at the Küre Copper Mine Site, Kastamonu, NW Turkey," *Mine Water and the Environment*, vol. 37, pp. 56–74, 2018.
- [6] N. Balcı, B. Brunner, and A.V. Turchyn, "Tetrathionate and elemental sulfur shape the isotope composition of sulfate in acid mine drainage". *Frontiers in Microbiology*, vol. 8, article 1564, 2017.
- [7] F. N. Assubaie, "Assessment of the levels of some heavy metals in water in Alahsa Oasis farms, Saudi Arabia, with analysis by atomic absorption spectrophotometry," *Arabian Journal of Chemistry* vol. 8, pp. 240–245, 2015.
- [8] C. Zhang, O. Selinus, and G. Kjellstrom, "Discrimination between natural background and anthropogenic pollution in environmental geochemistry-exemplified in an area of southeastern Sweden," *Science of the Total Environment*, vol. 243–244, pp. 129–140, 1999.
- [9] D. Postma, S. Jessen, N. Hue, M. Duc, C. Koch, P. Viet, P. Nhan, and F. Larsen, "Mobilization of arsenic and iron from Red River floodplain sediments, Vietnam," *Geochim Cosmochim Acta* vol. 74, pp. 3367–3381, 2010.
- [10] T. Agusa, T. Kunito, T. Minh, P. Trang, H. Iwata, P. Viet, and S. Tanabe, "Relationship of urinary arsenic metabolites to intake estimates in residents of the Red River Delta, Vietnam," *Environ. Pollut.* vol. 157, pp. 396–403, 2009.
- [11] T. L. Luu, "Remarks on the current quality of groundwater in Vietnam," *Water. Industry: water-energy-health nexus, environ sci pollut res*, doi 10.1007/s11356-017-9631-z, 2017.
- [12] İ. Seymen, "Kaman (Kırşehir) dolayısında Kırşehir Masifi'nin stratigrafisi ve metamorfizması," *Türkiye Jeoloji Kurumu Bülteni*, vol. 24, pp. 7–4, 1981.
- [13] H. Kara and M. Dönmez, "1/100.000 Ölçekli Açın Sana Nitelikli Türkiye Jeoloji Haritaları-Kırşehir G17 Paftası," MTA Genel Müdürlüğü, Jeoloji Etütleri Dairesi, No, 34, Ankara, 1990.
- [14] A. E. Akçay, M. Dönmez, H. Kara, A. F. Yergök, and K. Esentürk, "1/100.000 Ölçekli Açın Sana Nitelikli Türkiye Jeoloji Haritaları-Kırşehir J30 Paftası," MTA Genel Müdürlüğü, Jeoloji Etütleri Dairesi, No, 91, Ankara, 2008.
- [15] Ş. Koç and Ö. Özmen, "Bayındır, İsağocalı, Yeniyan ve Alişar (Kaman-Kırşehir) Fluoritlerinin sıvı kanyon incelemleri," *Gazi Üniversitesi Fen Bilimleri Enstitüsü Dergisi*, vol. 13, no. 2, pp. 501–508, 2000.
- [16] M. Öztürk, "Kırşehir-Kaman-Durmuşlu Demir Madeni Ruhsat Sahasının Jeolojik Etüt Raporu," MTA Raporları No: 6199, Ankara, 1978.
- [17] L. M. Chu and M. H. Wong, "Application of refuse compost: yield and metal uptake

- of three different food crops,” *Conserv Recycl*, vol. 7, pp. 221–234, 1984.
- [18] A. R. Mermut, J. C. Jain, L. Song, R. Kerrich, L. Kozak, and S. Jana, “Trace element concentrations of selected soils and fertilizers in Saskatchewan Canada,” *J Environ Qual*, vol. 25, pp. 845–853, 1996.
- [19] F. D. Mikayilov and B. Acar, “Toprak ekosistemlerinde kirleticilerin taşınım mekanizmasının incelenmesi ve modellenmesi (Investigation and modelling of contaminant’s movement processes within the soil ecosystems),” *Ekoloji*, vol. 7, no. 28, pp. 20–23, 1998.
- [20] Sağlık Bakanlığı, “İnsani Tüketim Amaçlı Sular Hakkında Yönetmelik (Turkish Standards for Water Intended for Human Consumption),” Sağlık Bakanlığı, Ankara, Turkey, 2013.
- [21] WHO, “Guidelines for Drinking-Water Quality,” First Addendum to Third Edition, 1, Recommendation. Geneva Switzerland, 2013.
- [22] WHO (World Health Organization), “Guidelines for drinkingwater quality,” Vol 2, Health criteria and other supporting information, WHO Publ, Geneva, 335, 1984.
- [23] O. Uslu and A. Türkman, “Su kirliliği ve kontrolü (Water pollution and control),” Publication series of Environment General Directorate of Prime Ministry of Turkish Republic, vol. 1, pp. 251–265, 1987.
- [24] H. A. L. Rowland, E. O. Omeregic, R. Millot, J. Cristina, J. Mertens, B. Valin, S. J. Hug, and M. Berg, “Geochemistry and arsenic behaviour in groundwater resources of the Pannonian Basin (Hungary and Romania),” *Appl. Geochem.*, vol. 26, pp. 1–17, 2011.
- [25] C. Şimşek, “Assessment of naturally occurring arsenic contamination in the groundwater of Şarkısla Plain (Sivas/Turkey),” *Environmental Earth Sciences*, vol. 68, pp. 691–702, 2013.
- [26] NAS, “Medical and Biologic Effects of Environmental Pollutants: Arsenic,” National Academy of Science, Washington D.C., 1977.
- [27] H. Onishi and E. B. Sandell, “Geochemistry of Arsenic,” *Geochimica et Cosmochimica Acta*, vol. 7, pp. 1–33, 1955.
- [28] W. Lawati, A. Rizoulis, E. Eiche, C. Boothman, D. Polya, J. Lloyd, M. Berg, P. Aguilar, and B. Dongen, “Characterisation of organic matter and microbial communities in contrasting arsenic-rich Holocene and arsenic-poor Pleistocene aquifers, Red River Delta, Vietnam,” *Appl. Geochem.* vol. 27, pp. 315–325, 2012.
- [29] L. Minh, G. Josette, B. Gilles, O. Didier, N. Julien, L. Quynh, T. Thai, and L. Anh, “Hydrological regime and water budget of the Red River Delta (Northern Vietnam),” *J. Asian. Earth. Sci.* vol. 37, pp. 219–228, 2010.
- [30] S. Guillot, S. Chakraborty, A. Gajurel, and B. Upreti, “Comparison of arsenic concentrations in simultaneously-collected groundwater and aquifer particles from Bangladesh, India,” Vietnam, and Nepal. *Appl. Geochem.* vol. 23, pp. 3244–3251, 2008.
- [31] J. T. Hindmarsh, R. F. McCurdy, and G. R. Peters, “Clinical and environmental aspects of arsenic toxicity,” *CRC Critical Reviews in Clinical Laboratory Sciences*, vol. 23, pp. 315–347, 1986.
- [32] WHO, “Arsenic in Drinking Water,” Background document for development of WHO Guidelines for Drinking-water Quality, 2011.
- [33] W. P. Tseng, “Effect of dose-response relationship of skin cancer and blackfoot disease with arsenic,” *Environmental Health Perspectives*, vol. 19, pp. 109–119, 1997.
- [34] R. Zaldivar and G. L. Ghai, “Clinical epidemiological studies on endemic chronic arsenic poisoning in children and adults, including observations on children with high- and low-intake of dietary

- arsenic,” *Zentralblatt für Bakteriologie und Hygiene, Abteilung I: Originale B*, vol. 170, pp. 409–421, 1980.
- [35] J. L. Valentine, D. S. Champion, and M. D. Schluchter, “Arsenic effects on human nerve conduction,” In: Howell JC, Gawthorne JM, White L, eds, *Proceedings of the 4th International Symposium on Trace Element Metabolism in Man and Animals*, Berlin, 409, 1981.
- [36] M. E. Cebrian, A. Albores, and M. Aguilar, “Chronic arsenic poisoning in the north of Mexico,” *Human Toxicology*, vol. 2, pp. 121–133, 1983.
- [37] P. B. Tchounwou, A. K. Patlolla, and J. A. Centeno, “Carcinogenic and systemic health effects associated with arsenic exposure-A Critical Review,” *Toxicologic Pathology*, vol. 31, pp. 575–588, 2003.
- [38] S. X. Wang, Z. H. Wang, X. T. Cheng, J. Li, Z. P. Sang, X. D. Zhang, L. L. Han, X. Y. Qiao, Z. H. Wu, and Z. Q. Wang, “Arsenic and Fluoride exposure in drinking water: Children’s IQ and growth in Shanyin County, Shanxi Province, China,” *Environmental Health Perspectives*, vol. 115, no. 4, pp. 643–647, 2003.
- [39] F. Habashi, “*Handbook of Extractive Metallurgy*,” Volume II, WILEY-VCH, Germany, 1997.
- [40] ATSDR, “Toxicological profile for antimony and Compounds,” 1992.
- [41] J. Fawell, K. Bailey, J. Chilton, E. Dahi, L. Fewtrell, and Y. Magara, “Flouride in Drinking Water,” World Health Organization, Iwa Publishing Inc, 134, 2006.
- [42] HHS, “Agency for Toxic Substances and Disease Registry Division of Toxicology Information Branch,” U.S. Department of Health and Human Services (Public Health Service), Atlanta Georgia, 462, 1999.
- [43] A. M. Piper, “A graphical procedure in the geochemical interpretation of water analyses,” *American Geophysical Union Trans.*, vol. 25, pp. 914–923, 1944.
- [44] M. Sayın, and S. Ö. Eyüpoğlu, “Türkiyedeki yağışların kararlı izotop içeriklerini kullanarak yerel meteorik doğruların belirlenmesi (Determination of the local meteoric water lines using stable isotope contents of precipitation in Turkey),” II. Ulusal Hidrolojide İzotop Teknikleri Sempozyumu (Second National Symposium on Isotope Technics in Hydrology). Izmir, Turkey, September, 2005.
- [45] B. Payne, and T. Dinçer, “Isotope survey of karst region of southern Turkey,” *Proceedings of 6th International Conference of radiocarbon and Tritium Dating*, no. 620652, IAEA, Vienna, 1965.
- [46] Ş. Şimşek, “Isotope and geochemical techniques applied to geothermal investigations”, *International Atomic Energy Agency, TECDOC No. 788*, pp. 232-248, 1993.
- [47] I.C. Clark, and P. Fritz, “*Environmental Isotopes in Hydrogeology*.” Lewis Publishers, New York, 1997.

JOURNAL OF SCIENCE



SAKARYA UNIVERSITY

Sakarya University Journal of Science

ISSN 1301-4048 | e-ISSN 2147-835X | Period Bimonthly | Founded: 1997 | Publisher Sakarya University |
<http://www.saujs.sakarya.edu.tr/en/>

Title: Synthesis And Characterization Of Maleic Anhydride Modified Poly (Ethylene Glycol) As Polymeric Solid-Solid Phase Change Materials

Authors: Tuğba GÜNGÖR ERTUĞRAL, Cemil ALKAN

Received: 2020-01-22 11:34:49

Accepted: 2020-08-04 18:43:55

Article Type: Research Article

Volume: 24

Issue: 5

Month: October

Year: 2020

Pages: 1023-1028

How to cite

Tuğba GÜNGÖR ERTUĞRAL, Cemil ALKAN; (2020), Synthesis And Characterization Of Maleic Anhydride Modified Poly (Ethylene Glycol) As Polymeric Solid-Solid Phase Change Materials. Sakarya University Journal of Science, 24(5), 1023-1028, DOI:

<https://doi.org/10.16984/saufenbilder.678545>

Access link

<http://www.saujs.sakarya.edu.tr/en/pub/issue/56422/678545>

New submission to SAUJS

<http://dergipark.org.tr/en/journal/1115/submission/step/manuscript/new>



Synthesis and Characterization of Maleic Anhydride Modified Poly (Ethylene Glycol) as Polymeric Solid-Solid Phase Change Materials

Tuğba GÜNGÖR ERTUĞRAL^{*1}, Cemil ALKAN²

Abstract

In this study, a novel type of polymeric solid-solid phase change materials (SSPCMs) and Maleic anhydride (MA) modified poly (ethylene glycol) PEG. MAM-PEG polymers were synthesized from different molecular weight PEG (Mw: 4000, 6000) .On the other hand two different catalyst system was used; para toluene sulfonic acid (PTSA) and 1,8-Diazabicyclo [5.4.0] undec-7-ene (DBU).The PEG bound to the backbone of the polymers formed crystalline regions responsible from latent heat storage with reversible crystalline to amorphous phase transition as linked unit prevented total melting of the structure. Also MAM-PEG polyester polymers acid and hydroxyl values were determined for number of average molecular weight (Mn) and calculated as 36232 and 49020. Characterization and thermal properties of SSPCMs were performed by using fourier transform infrared (FT-IR) spectroscopy and differential scanning calorimetry (DSC) techniques mainly. DSC results showed that solid-solid transitions 36-54 °C temperature range and 163-153 Jg⁻¹ enthalpy. As a result, MAM-PEG polymers were found potential for thermal energy storage (TES) applications.

Key words: Thermal energy storage, maleic anhydride, PEG, PCM

1. INTRODUCTION

There are some important environmental problems that global warming, climate change and environmental pollution are emerging as a result of using coal, oil and natural gas, as an energy source of fossil fuels. Recently, the number of studies on cleaner and environmentally friendly renewable energy resources has

increased significantly as a solution to these problems. Presence of different monomers in a polymer molecule can lead to production materials of commercial importance. One of the thermal energy storage methods is the latent heat storage method. Phase change materials (PCMs) are capable of storing and releasing latent heat energy reversibly during phase change. The latent heat is the amount of heat which changes the physical structure of the material (solid, liquid and

* Corresponding Author: tugbagungor@comu.edu.tr

¹ Çanakkale Onsekiz Mart University, Çanakkale School of Applied Sciences.

ORCID: <https://orcid.org/0000-0002-1306-3399>

² Gaziosmanpasa University, Department of Chemistry. E-mail: cemil.alkan@gop.edu.tr

ORCID: <https://orcid.org/0000-0002-1509-4789>

gaseous) [1], [2]. Solid-solid phase changes are preferred mostly small volume according to solid-liquid PCMs. PCMs and their eutectic mixtures have different uses in textiles, electronics, biomedical and biology and so on [3],[4],[5].

PEGs are non-toxic materials that have excellent thermal storage properties and they can maintain chemical stability during long-term use [6] and they have high fission energy [7] and MA is used in some applications such as artificial sweeteners, food enhancers, paper processing, water treatment chemicals.

SSPCMs can store highly latent heat at the time of conversion from crystal phase to amorphous phase. SSPCMs don't produce toxic substances, pollute the environment and don't need a different energy source as they perform latent heat storage through phase transition. Therefore, it was an environmentally friendly application [8] and so on SSPCM investigations with high TES characteristics include several PEG-based polymeric SSPCMs such as polyurethane-graft-PEG [9], cellulose diacetate-graft-PEG [10], polypropylene-graft-PEG [11], cellulose-graft-PEG [12], [13], poly(vinyl alcohol)-graft-PEG [14] and Poly(styrene-co-maleic anhydride)-graft-PEG [15] as SSPCMs have been prepared or modified by various methods [16], MAM-PEG was synthesized new SSPCM. MAM-PEG stores latent heat through the change from the crystalline to the amorphous phase of PEG bound. MA modified to PEG by ring opening reaction. MAM-PEG polyester polymers were synthesized by PTSA catalyst system and DBU and latent heat energy storage capacities compared PEG 4000 and PEG 6000. Fisher esterification method applied to synthesis. In this study, acid and hydroxyl values of polyester polymers were determined and the number of average molecular weight (Mn) was calculated. The effect of catalysts and molecular weight change in PEG on latent heat storage capacity was determined using DSC technique. As a result MAM-PEG polymer can be used as energy storage material for food packaging industry and especially for foods that need to be transported or stored in heat food as catering and process of factory fermentation units or incubation rooms.

2. MATERIAL AND METHODS

2.1. Materials

Maleic anhydride (MA), poly (ethylene glycol) PEG (Mw: 4000, 6000), p-toluenesulfonic acid (PTSA) and 1,8-Diazabicyclo [5.4.0] undec-7-ene (DBU) catalysts were purchased from Aldrich Company. Toluene solution, Potassium hydroxide (KOH), Phenolphthalein and Ethanol were purchased from Merck Company. All were used without further purifications.

2.2. Methods

2.2.1. Synthesis of MAM-PEG Polymers

MAM-PEG polymers have been synthesized by ring opening reaction of MA to connect PEG units each other as shown in Figure 1. The reaction was established in a nitrogen atmosphere containing a 500 ml dispenser apparatus system with reflux condenser and mechanical stirrer. First in reaction MA and PEG calculated 20:19 molar ratio and added at 300 ml toluene solution. Reaction system was catalyzed with 2–3 drops PTSA 160 °C temperature in 2 hours and 800 rpm. Furthermore, the same procedure was performed with DBU catalyst system at a 20:19 molar ratio.

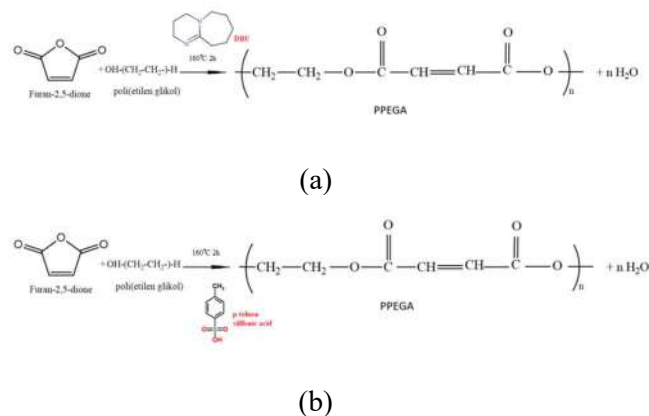


Figure 1 Synthesis of MAM-PEG Polymers Using (a) DBU catalyst and (b) PTSA catalyst

2.2.2. Number Average Molecular Weight (M_n) of MAM-PEG polymers

The acid and hydroxyl values were determined by standard methods described elsewhere and from these values the molecular weight of polyesters was estimated [17]. The acid value of the carboxyl-terminated ester was calculated by titration of product with ethanolic potassium hydroxide (KOH) solution. As known typical method, 1.3 g of sample was taken in a flask and 5 ml of water and 25 ml ethanol were added to flask. The mixture was stirred for 10–15 min until dissolved all of them. 2–3 drops of phenolphthalein indicator were added, followed by titration with 0.1 N ethanolic KOH. The turning point was determined as a change from colorless to pink and acid value was estimated [18]. MAM-PEG 4000 and MAM-PEG 6000 were number average molecular weight 36232 and 49020 as depicted in Table 1.

The number-average molecular weight (M_n) of polymers was calculated the following formula (1)[19].

$$M_n = 1 / (\text{Acid value} + \text{Hydroxyl value}) / (2 \times 56.1 \times 1000) \quad (1)$$

Table 1
M_n Analysis of MAM-PEG polymers

Compound	Acid value	OH value	M _n
MAM-PEG 4000	1.6	1.5	36232
MAM-PEG 6000	1.2	1.1	49020

2.3. Characterization

FT-IR spectra of SSPCMs were recorded with FT-IR spectrophotometer (JASCO 430 model) in 4000-400 cm⁻¹ wavelength range and on KBr disks. Thermal energy storage characteristics were determined by using a Perkin Elmer Jade model DSC instrument in the range of -15 °C - 90 °C and at a heating-cooling ramp of 10 °C min⁻¹.

3. RESULTS AND DISCUSSION

3.1. FT-IR Spectroscopy Analysis of MAM-PEG Polymers

Ester and carboxylic acid groups of MAM-PEG 4000 polymer produced tensile vibration at 1710 cm⁻¹ at FTIR spectra. It can be considered that decrease in O-H functional group with change in peak at approximately 3500 cm⁻¹. MA has characteristic peaks of 2923 and 2850 cm⁻¹, 1463 cm⁻¹, 1066 cm⁻¹, and 722 cm⁻¹. MAM-PEG 4000 polymer reduces O-H tensile vibration of MA in range of about 2500-3000 cm⁻¹ and decrease in characteristic peaks of 1066 cm⁻¹. MA copolymerization FT-IR spectrums shown in Figure 2.

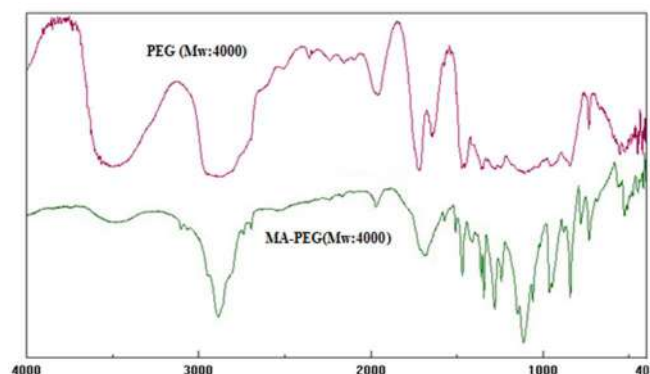


Figure 2 FT-IR spectra of PEG 4000 and MAM-PEG 4000 polymer (produced using DBU catalyst)

3.2. Thermal Reliability of MAM-PEG Polymers

When the DSC curve of MAM-PEG 4000 polymer produced using PTSA catalyst was examined, melting and solidification temperature difference was measured as 18.6 °C and melting and solidification enthalpy difference as 7.6 Jg⁻¹ and overcooling observed at 33.4 °C (Figure 3), DSC curve of DBU catalyst, melting and solidification temperature difference was 14.8 °C and enthalpy difference of melting and solidification was 10.2 Jg⁻¹ (Figure 4). It was close to the phase change temperature of PEG 4000 with a melting point of 55.6 °C. MAM-PEG 6000 polymer produced using PTSA as a catalyst, melting and solidification temperature difference was 13 °C and the enthalpy difference of melting

and solidification was 16 Jg^{-1} with the effect of the catalyst, energy storage capacity increased and the melting point decreased and overcooling observed at $33.6 \text{ }^\circ\text{C}$ (Figure 5). DSC curve of DBU as a catalyst was examined melting and solidification temperature difference was $13.6 \text{ }^\circ\text{C}$ and the enthalpy difference of melting and solidification was 0.4 Jg^{-1} (Figure 6). DSC analysis results of SSPCMs was showed in Figure 3, 4, 5, 6 and Table 2 respectively.

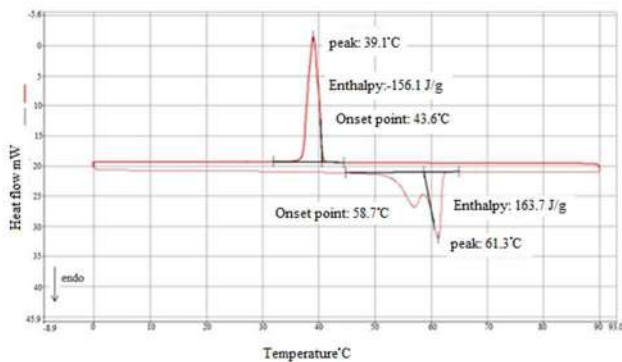


Figure 3 DSC curve of MAM-PEG 4000 polymer produced using PTSA catalyst

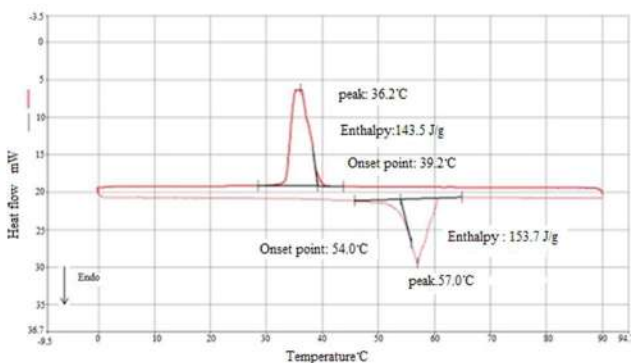


Figure 4 DSC curve of MAM-PEG 4000 polymer produced using DBU catalyst

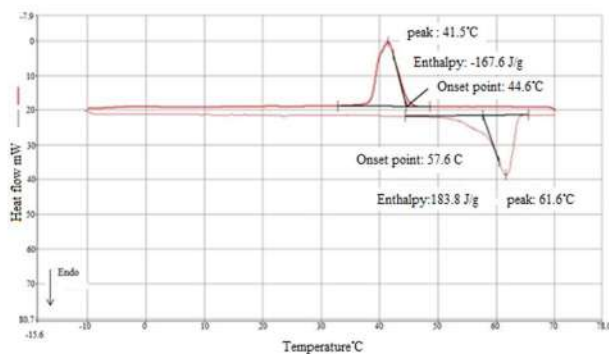


Figure 5 DSC curve of MAM-PEG 6000 polymer produced using PTSA as a catalyst

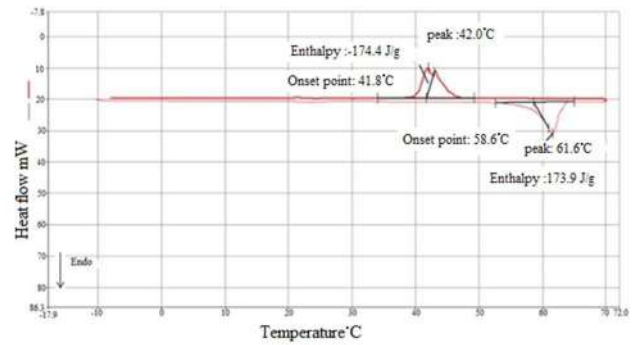


Figure 6 DSC curve of MAM-PEG 6000 polymer produced using DBU as a catalyst

Table 2

The latent heat thermal energy storage specifications of pure PEGs and SSPCMs

	Heating period		Cooling period		
	T_{s-s} ($^\circ\text{C}$)	ΔH_{s-s} (J g^{-1})	T_{s-s} ($^\circ\text{C}$)	ΔH_{s-s} (J g^{-1})	
PEG 4000	40.5	171.5	53.9	174.2	[15]
MAM-PEG 4000 (DBU)	54	153.7	39.2	143.5	
MAM-PEG 4000 (PTSA)	58.7	163.7	43.6	156.1	
PEG 6000	42.3	190	59.9	196.3	[15]
MAM-PEG 6000 (DBU)	58.6	173.9	41.8	174.4	
MAM-PEG 6000 (PTSA)	57.6	183.8	44.6	167.6	

Ts-s: Solid-solid heating and cooling temperature

4. CONCLUSIONS

MAM-PEG polymers were synthesized as thermally protecting food packaging materials. MAM-PEG polymers gained latent heat storage feature from the crystalline phase to semi crystalline phase. MAM-PEG 4000 polymer reduced tensile vibration at 3453 cm^{-1} –O-H absorption peaks and 2867 cm^{-1} for –C-H stretching, decreased in the characteristic peak 1066 cm^{-1} of MA by modification. Ester and carboxylic acid group of MAM-PEG produced tensile vibration at 1710 cm^{-1} . DSC curve of MAM-PEG 4000 polymer was examined, melting and solidification temperature difference was measured as $18 \text{ }^\circ\text{C}$ and melting and solidification enthalpy difference was measured as 8 Jg^{-1}

(Figure 3), DSC curve of the MAM-PEG 4000 polymer synthesized using DBU as a catalyst, melting and solidification temperature difference was 14.8 °C and enthalpy difference of melting and solidification was 10.2 Jg⁻¹ (Figure 4) and it was close to the phase change temperature of PEG 4000 with a melting point of 55.6 °C. Melting and solidification temperature difference 13 °C and enthalpy difference 16 Jg⁻¹ with effect of catalyst so that energy storage capacity increased and melting point decreased. DSC measurements shows that PEG chains attached to main chain so copolymers have phase transition temperatures of 40-58 °C and high latent heat storage capacity in the range of 153-183 Jg⁻¹. The synthesized MAM-PEG polymer usable TES material for food packaging and storage industry (ready food industry, fast food etc.).

Acknowledgements

The authors thank the anonymous reviewers for constructive suggestions, which improve the quality of the paper.

Funding

The author received no financial support for the research, authorship, and/or publication of this paper.

The Declaration of Conflict of Interest/ Common Interest

No conflict of interest or common interest has been declared by the authors.

Authors' Contribution

T.G.E synthesized Maleic Anhydride Modified Poly (Ethylene Glycol), calculate average molecular weight and C.A made polymer characterization. This study was produced from the corresponding author's PhD thesis.

The Declaration of Ethics Committee Approval

The authors declare that this document does not require an ethics committee approval or any special permission.

The Declaration of Research and Publication Ethics

The authors of the paper declare that they comply with the scientific, ethical and quotation rules of SAUJS in all processes of the paper and that they do not make any falsification on the data collected. In addition, they declare that Sakarya University Journal of Science and its editorial board have no responsibility for any ethical violations that may be encountered, and that this study has not been evaluated in any academic publication environment other than Sakarya University Journal of Science.

REFERENCES

- [1] B. Zalba, J.M. Marin, L.F. Cabeza, and H. Mehling, "Review on thermal energy storage with phase change: materials, heat transfer analysis, and applications," *Appl. Therm. Eng.*, vol. 23, no. 3, pp. 251–283, 2003.
- [2] M. Kenisarin and K. Mahkamov, "Solar energy storage using phase change materials," *Renew. Sust. Energy Rev.*, vol. 11, no. 9, pp. 1913–1965, 2007.
- [3] C. Chen, L. Wang, and Y. Huang, "Crosslinking of the electrospun polyethylene glycol/ cellulose acetate composite fibers as shape-stabilized phase change materials," *Mater. Lett.*, vol. 63, no. 5, pp. 569-571, 2009.
- [4] C. Chen, L. Wang, and Y. Huang, "Morphology and thermal properties of electrospun fatty acids/polyethylene terephthalate composite fibers as novel form-stable phase change materials," *Sol. Energ. Mater. Sol. Cells*, vol. 92, no. 11, pp. 1382-1387, 2008.
- [5] M. Li, Z. Wu, and H. Kao, "Study on preparation and thermal properties of binary fatty acid/diatomite shape-stabilized phase change

- materials,” *Sol. Energy Mater. Sol. Cells*, vol. 95, no. 8, pp. 2412–2416, 2011.
- [6] Y. Wang, A. Yuan, Y. Zhao, Q. Liu., and J. Lei, “Phase change material with flexible crosslinking for thermal energy storage,” *J. Appl. Polym. Sci.*, vol. 137, no. 13, pp. 48497, 2020.
- [7] S. Sundararajan, A.B. Samui, and P.S. Kulkarni “Versatility of polyethylene glycol (PEG) in designing solid-solid phase change materials (PCMs) for thermal management and their application to innovative technologies,” *J. Mater. Chem.A*, vol. 5, no. 35, pp. 18379-18396, 2017.
- [8] L. Liu, L. Kong, H. Wang, R. Niu, and H. Shi, “Effect of graphene oxide nanoplatelets on the thermal characteristics and shape-stabilized performance of poly(styrene-co-maleic anhydride)-g-octadecanol comb-like polymeric phase change materials,” *Sol. Energ. Mater. Sol. Cells*, vol. 149, pp. 40-48, 2016.
- [9] X. Fu, W. Kong, Y. Zhang, L. Jiang, J Wang., and J. Lei, “Novel solid–solid phase change materials with biodegradable trihydroxy surfactants for thermal energy storage,” *RSC Adv.*, vol. 5, no. 84, pp. 68881–68889, 2015.
- [10] Y. Jiang, E. Ding, and G. Li, “Study on transition characteristics of PEG/CDA solid–solid phase change materials,” *Polymer*, vol. 43, no. 1, pp. 117–122, 2002.
- [11] Y.N. Zang and E.Y. Ding, “Energy storage properties of phase change materials prepared from PEG/PPP,” *Chin. Chem. Lett.*, vol. 16, no. 10, pp. 1375–1378, 2005.
- [12] X.H. Liang, Y.Q. Guo, L.Z. Gu, and E.Y. Ding, “Crystalline–amorphous phase- transition of a poly(ethylene glycol) cellulose blend,” *Macromolecules*, vol. 28, no. 19, pp. 6551–6555, 1995.
- [13] X.P. Yua and E.Y. Ding, “Synthesis and characterization of storage energy materials prepared from nano-crystalline cellulose/polyethylene glycol,” *Chin. Chem. Lett.*, vol. 17, no. 8, pp. 1129–1132, 2006.
- [14] M. Zhang, Y. Na, and Z.H. Jiang, “Preparation and properties of polymeric solid–solid phase change materials of polyethylene glycol (PEG)/poly(vinyl alcohol) (PVA) copolymers by graft copolymerization,” *Chem. J. Chin. Univ.*, vol. 26, no.1, pp. 170–174, 2005.
- [15] A. Sari, A. Biçer, and C. Alkan, “Thermal energy storage characteristics of poly(styrene-co-maleic anhydride)-graft-PEG as polymeric solid–solid phase change materials,” *Sol. Energ. Mater. Sol. Cells*, vol. 161, pp. 219–225, 2017.
- [16] X. Huang, J. Guo, Q. An, X. Gong, Y. Gong, and S. Zhang, “Preparation and characterization of di-hexadecanol maleic/triallyl isocyanurate cross-linked copolymer as solid–solid phase change materials,” *J. Appl. Polym. Sci.*, vol. 133, no. 40, pp. 44065, 2016.
- [17] W.R. Sorenson and T.W. Campbell, “Preparative Methods of Polymer Chemistry, Interscience Publishers,” New York, pp. 130-154, 1968.
- [18] S. Sundararajan, A. Kumar, B.C. Chakraborty, A.B.Samui, and P.S. Kulkarni, “Poly(ethylene glycol) (PEG)-modified epoxy phase-change polymer with dual properties of thermal storage and vibration damping,” *Sust. Energ. Fuels*, vol. 2, no. 3, pp. 688-697, 2018.
- [19] Liu H.J., L.H. Lin, and K.M. Chen, “Preparation and Properties of Water-Soluble Polyester Surfactants. III. Preparation and Wetting Properties of Polyethylene Glycol–Polydimethylsiloxane Polyester Surfactants,” *Appl. Polym. Sci.*, vol. 88, no. 5, pp. 1236–1241, 2003.

JOURNAL OF SCIENCE



SAKARYA UNIVERSITY

Sakarya University Journal of Science

ISSN 1301-4048 | e-ISSN 2147-835X | Period Bimonthly | Founded: 1997 | Publisher Sakarya University |
<http://www.saujs.sakarya.edu.tr/en/>

Title: Synthesis, Characterization and Photocatalytic Properties of Non-peripherally 3-(pyridin-4-yl) propane-1-oxy Groups Substituted Cu (II) Phthalocyanineand Water Soluble Derivative

Authors: Ece Tuğba SAKA

Recieved: 2019-10-07 13:52:27

Accepted: 2020-08-06 12:42:15

Article Type: Research Article

Volume: 24

Issue: 5

Month: October

Year: 2020

Pages: 1029-1039

How to cite

Ece Tuğba SAKA; (2020), Synthesis, Characterization and Photocatalytic Properties of Non-peripherally 3-(pyridin-4-yl) propane-1-oxy Groups Substituted Cu (II) Phthalocyanineand Water Soluble Derivative. Sakarya University Journal of Science, 24(5), 1029-1039, DOI:

<https://doi.org/10.16984/saufenbilder.630325>

Access link

<http://www.saujs.sakarya.edu.tr/en/pub/issue/56422/630325>

New submission to SAUJS

<http://dergipark.org.tr/en/journal/1115/submission/step/manuscript/new>



Synthesis, Characterization and Photocatalytic Properties of Non-peripherally 3-(pyridin-4-yl) propane-1-oxy Groups Substituted Cu (II) Phthalocyanine and Water Soluble Derivative

Ece Tuğba SAKA^{*1}

Abstract

Cu (II) phthalocyanine compound and its water-soluble derivative containing 3- (pyridin-4-yl) propane-1-oxy groups in non-peripheral positions were synthesized for the first time and their structures were elucidated. The photocatalytic properties of Cu (II) phthalocyanine compounds, which were synthesized and characterized, were investigated on the photocatalytic degradation reactions of 4-nitrophenol, one of the important environmental pollutants. In the photocatalysis reactions that took place in the photoreactor for 2 hours without using any oxidant, 4-nitrophenol compound was completed with 94.4% and 98.6% conversion to toxic and non-harmful species. The hydroquinone compound was identified as the main product and the benzoquinone compound as the by-product. The conversion number for the non-peripheral Cu (II) phthalocyanine compound and its water-soluble derivative was 471 and 488 and the conversion frequency was 235.5 and 244,0 respectively. Finally, recovery studies were carried out for water soluble Cu (II) phthalocyanine used as photocatalyst and the number of cycles was determined as 5.

Keywords: Non-peripheral, Phthalocyanine, Copper, Photocatalytic, 4-Nitrophenol

* Corresponding Author: ece_t_saka@hotmail.com

¹ Karadeniz Technical University, ORCID: <https://orcid.org/0000-0002-1074-7752>

1. INTRODUCTION

Phthalocyanines, which are macrocyclic compounds with characteristic blue-green color, are being studied with increasing interest by scientists due to their applicability in the fields of catalysis, solar cells, photodynamic therapy of cancer, non-linear optics, gas sensor and laser dye [1]. However, the most important properties that limit the applicability of phthalocyanine compounds in their application areas are their low solubility in common organic solvents and in water. As a solution to this problem; by peripheral or axial substitution of bulky or long alkyl chain groups, phthalocyanines are dissolved in apolar solvents, while the addition of sulfonyl, carboxyl or quaternary amino groups results in water-soluble phthalocyanines [2-4]. Phthalocyanines with increased solubility by these groups find very wide application areas. In recent years, the use of phthalocyanine compounds containing different metal ions as photocatalysts in the disintegration of dyes, chlorinated phenol compounds and other substituted phenol compounds, which are the main environmental pollutants, has attracted considerable attention [5-8].

In the last decade, due to the rapid urbanization and industrialization in the world, high amounts of organic pollutants are released into nature. Petroleum refining, plastic and resin production, papermaking process, carbon liquefaction processes and pharmaceutical industry are also sources of environmental pollutants. It has been determined that substituted phenol compounds and dyes can have carcinogenic and mutagenic effects on human health and other aquatic organisms due to their high solubility, stability, easy assimilation in water according to the USEPA reports. It is therefore urgent to develop an environmentally friendly and effective method for the removal of such environmental pollutants in aqueous systems. In the early 1990s, Paul Anastas, while serving at the United States Environmental Protection Agency (USEPA), introduced the term 'Green Chemistry', which means the design of new products and processes that reduce or eliminate the use and production of hazardous substances

[9]. The use of environmentally friendly solvents (water, supercritical carbon dioxide, ionic liquids, etc.), selective catalysts and renewable raw materials is essential under moderate conditions (such as low temperature, atmospheric pressure) to meet the principles of the definition of green chemistry. In recent years, many researchers aim to develop alternative environmentally friendly systems for the disposal of industrial wastes based on this definition [10-12].

Phthalocyanine compounds are used as photocatalysts in light applications due to their wide absorption in the near infrared region and substituted phenols are known to be used for the removal of different toxic dyes and ions [13-16]. Since global warming has become a serious issue in our lives, protecting the existing water resources and recycling wastewater is one of the most important elements. 4-Nitrophenol is a toxic, environmental and human health harmful, carcinogen, synthetic compound containing many nitrogen and hydroxide groups in the wastes in many branches of industry such as pharmaceuticals, petrochemicals, fungicides, rubber, wood protection processes, paints and leather industry. is a compound [17-18]. 4-Nitrophenol compound exposure to blood cell damage, damage to the nervous system and mutagenic effects on organisms, as well as all human and aquatic life-threatening cancer-causing chemicals have been proven as a result of studies [19-21]. Therefore, removal of 4-nitrophenol compound and conversion to non-toxic, biodegradable, harmless species have gained importance.

In this study, the solubility in organic solvents with 3- (pyridin-4-yl) propane-1-oxy groups and conversion of these groups to quaternary derivatives provided solubility in water and alcohol. It was aimed to design an ideal photocatalyst using a cheap and low cost metal having different oxidation steps as the central atom in the phthalocyanine compound. The photocatalytic activities of the obtained non-peripheral Cu (II) phthalocyanine and water-soluble derivatives were investigated in the disintegration reaction of 4-nitrophenol which is an important environmental pollutant and

recovery studies of photocatalysts were performed.

2. EXPERIMENTAL

2.1. Materials and Equipments

All materials and equipments are given as supplementary materials.

2.2. Synthesis

2.2.1. Synthesis of 3-(3-(pyridine-4-yl)propoxy)phthalonitrile (3)

Compound 3 is obtained as given in the literature [22]. Yield: 2.81 g (73%), m.p. : 80-82 °C. IR (KBr pellet), $\nu_{\max}/\text{cm}^{-1}$: 3071, 3019 (Ar-H), 2961, 2928, 2892 (Alip. C-H), 2230 (C≡N), 1582, 1498, 1475, 1416, 1392, 1344, 1295, 1268, 1243, 1178, 1093, 1058, 1021, 992, 884, 841, 733, 690. ¹H-NMR. (CDCl₃), (δ :ppm): 8.34-8.02 (m, 4H, Ar-H), 7.85-7.55 (m, 3H, Ar-H), 4.33 (t, 2H, CH₂-O), 2.82 (t, 2H, CH₂-Ar), 1.79 (m, 2H, CH₂-Alip.) ¹³C-NMR. (CDCl₃), (δ :ppm): 166.22 (ArC-O), 149.55 (ArC-N), 148.50 (ArC-N), 147.16 (ArC), 133.51 (ArC), 130.37 (ArC), 128.88 (ArC), 125.39 (ArC), 122.85 (ArC), 121.90 (ArC), 118.21 (C≡N), 116.20 (C≡N), 101.33 (ArC), 70.30 (CH₂-O), 36.26 (CH₂-Ar), 34.10 (CH₂-Alip.). MALDI-TOF-MS, (m/z): Calculated: 263.29; Found: 263.60 [M]⁺.

2.2.2. Synthesis of Cu(II) Phthalocyanine (4)

Compound 4 is obtained as given in the literature [22]. Yield: 700 mg (44%). Mp >300°C. FT-IR $\nu_{\max}/\text{cm}^{-1}$ (KBr pellet): 3093, 3063 (Ar-H), 2997, 2960, 2571 (Aliph. C-H), 1559, 1466, 1448, 1422, 1401, 1369, 1339, 1287, 1265, 1255, 1232, 1195, 1075, 1058, 1045, 1038, 996, 955, 878, 834, 790, 680. UV-Vis (CHCl₃): λ_{\max} , nm (log ϵ): 687 (4.75), 662 (4.56), 341 (4.64), 280 (4.58). MALDI-TOF-MS, (m/z): Calculated: 1116.72; Found: 1116.158 [M]⁺. Solubility: CHCl₃, CH₂Cl₂, DMF, DMSO.

2.2.3. Synthesis of Water soluble Cu(II) Phthalocyanine (5)

Compound 5 is obtained as given in the literature [22]. Yield: 456 mg (57%) Mp >300°C. FT-IR $\nu_{\max}/\text{cm}^{-1}$ (KBr pellet): 3085, 3059 (Ar-H), 2997, 2950, 2844 (Aliph. C-H), 1560, 1468, 1463, 1438, 1401, 1376, 1367, 1281, 1276, 1249, 1238, 1194, 1089, 1065, 1045, 990, 894, 780, 689. UV-Vis (CHCl₃): λ_{\max} , nm (log ϵ): 684 (4.68), 621 (4.64), 343 (4.38), 279 (4.59). MALDI-TOF-MS, (m/z): Calculated: 1684.47; Found: 293.35 [M-4H]⁺. Solubility: DMF, DMSO, water and ethanol.

2.3. Photocatalytic Studies

The photocatalytic activity of Cu (II) phthalocyanine containing non-peripheral 3-(pyridin-4-yl) propoxy groups and the quaternized water-soluble derivative of Cu (II) on photooxidation reactions of the 4-nitrophenol compound using a photoreactor during the catalysis processes will be examined. For the photooxidation study in which water is used as the solvent, firstly a specified amount of substrate, a calculated amount of catalyst and a total of 10 ml of solvent will be added to the Schlenk container. The reaction time was determined as 2 hours. This point will be taken as the starting time of the reaction by taking some samples from the reaction medium by pipetting into the glass tube. When the specified reaction time is completed, the samples taken from the reaction vessel will be analyzed on a gas chromatography device and the time dependent change profile of the product will be obtained.

3. RESULTS and DISCUSSION

3.1. Synthesis and Characterization

After dissolving 3-(pyridin-4-yl) propan-1-ol **1** and 3-nitrophthalonitrile in dry DMF, anhydrous K₂CO₃ was added equal amounts in 2 hours and at 50°C for 72 hours in nitrogen atmosphere with a yield of 73% (Şekil 1).

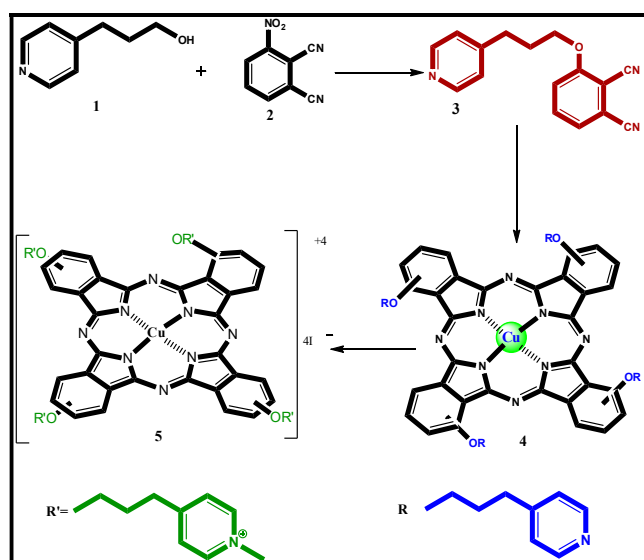


Figure 1 Synthetic ways of compounds 3, 4 and 5

In the IR spectrum of the synthesized compound 3, the disappearance of the OH and NO₂ group vibrations (3390, 3402 and 1538-1355 cm⁻¹) of the starting compounds and instead of the vibrations of the C≡N group at 2230 cm⁻¹, supports IR spectrum of the synthesized compounds. The disappearance of the peak of the OH group seen in the range of 4.64-2.40 ppm of the starting materials in the ¹H-NMR spectrum of the compound 3 and the order of the peaks of the aromatic protons in the structure are 8.34, 8.22, 8.18, 8.02, 7.85, 7.68, 7.55 ppm. It supports the structure of compound 3. The peaks of the C atoms of C≡N group at 118.21 and 116.20 ppm in the ¹³C-NMR spectra of the compound 3 support the structure. Finally, the molecular ion peak at 263.60 [M]⁺ in the mass spectrum obtained for using the MALDI / TOF technique supports the structure of the new compound 3 (Supplementary Files Figure 1). The non-peripheral copper phthalocyanine compound 4 was prepared by cyclotetramerization of the dinitrile-derived compound 3. Non-peripheral tetra-substituted copper phthalocyanine compound 4 was synthesized in 40% yield by mixing anhydrous CuCl₂ and DBU in a dinitrile derivative compound n-pentanol (3) under nitrogen atmosphere for 24 hours at 160 °C. Non-peripheral tetra-substituted copper phthalocyanine compound In the IR spectrum of 4, the loss of C≡N vibrations of the phthalonitrile compound 3 at 2230 cm⁻¹ indicates that the non-peripheral tetra substituted copper

phthalocyanine compound was formed as a result of the cyclotetramerization reaction. The ¹H-NMR and ¹³C-NMR spectra of the compound 4 cannot be obtained because the copper (II) ion causes a paramagnetic electron distribution [23]. The most important illumination technique for the characterization of phthalocyanine compounds is characterization by UV-Vis spectrum. The fact that the phthalocyanine compounds have sharp colors that vary from blue to green and have an 18-π electron system will result in a sharp Q band in the 650-700 nm range and a weak B band (Soret band) around 350 nm. Observation of the Q-band of metallic phthalocyanine compounds in D_{4h} symmetry as a sharp peak [24] results from four equivalent nitrogen atoms capable of bonding with the metal atom present in the phthalocyanine ring. In the UV-Vis spectrum of the non-peripheral copper phthalocyanine compound 4 taken in DMSO at a concentration of 1x10⁻⁵ M at room temperature, the Q band appeared as a sharp single band at 687 nm. In addition, low intensity peaks were observed at 662 nm in the low wavelength portion of the Q band (Figure 2).

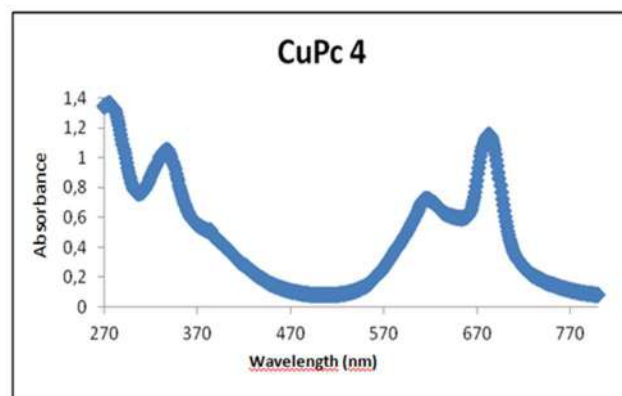


Figure 2 UV-vis spectrum of compound 4

Interpretation of the mass spectra of phthalocyanine compounds is not easy due to their high molecular weight and low solubility. However, the mass spectrum of the non-peripheral copper phthalocyanine compound 4 was taken using the MALDI-TOF technique and the molecular ion peak was observed at 1116.158 [M]⁺ (Supplementary Files Figure 2).

Water-soluble non-peripheral tetra-substituted copper phthalocyanine compound 5 was

obtained by dissolving compound 4 in chloroform and mixing with methyl iodide at room temperature for 1 day. There was not much difference between the IR spectrum of the water-soluble non-peripheral copper phthalocyanine compound and the IR spectrum of the water-insoluble non-peripheral copper phthalocyanine compound. A mass peak of 293.35 $[M-4I-H]^{+4}$ was observed in the mass spectrum of the compound 5 taken by the MALDI-TOF technique. In the UV-Vis spectrum of the water-soluble non-peripheral copper phthalocyanine compound 5 taken in DMF at a temperature of 1×10^{-5} M at room temperature, the Q band appeared as a sharp single band at 684 nm. In addition, low intensity peak was observed at 621 nm in the low wavelength portion of the Q band (Figure 3).

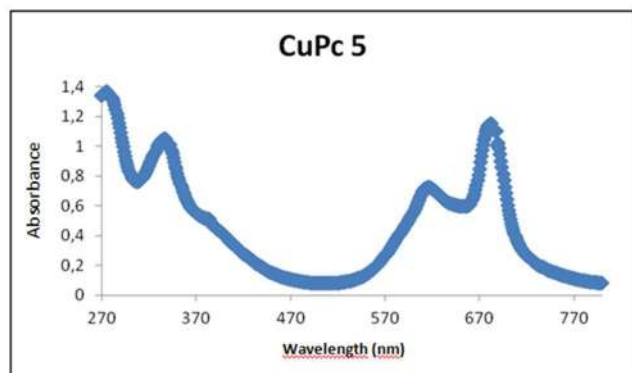


Figure 3 UV-vis spectrum of compound 5

3.2. Photocatalytical Studies

The photocatalytic activities of Cu(II) phthalocyanine 4 and its water soluble derivative 5 were investigated on 4-nitrophenol oxidation by photoreactor equipped with 8 pieces 16W lamps at room temperature. The single phase homogeneous solvent system was used for the compound 4 and the two phase heterogeneous solvent system was used for the compound 5 because of its water solubility and the reaction time was determined as 2 hours. The contents of the sample samples taken from the reaction medium for 30 minutes were examined by gas chromatography and product conversions were determined. According to these results, hydroquinone was determined as the main product and benzoquinone as the by-product.

When the same reactions were repeated at room temperature in the dark, it was determined that the 4-nitrophenol compound did not undergo any oxidation. The 4-nitrophenol photooxidation reaction wherein compound 4 was present as a photocatalyst was 94.4% after 2 hours; 4-nitrophenol photooxidation reaction with compound 5 as the photocatalyst 98.6% yield conversion was determined after 2 hours. When the product transformations were examined, 58.6% hydroquinone, 30.8% benzoquinone and 5% undetermined product were obtained with compound 4. Compound 5 yielded 62.3% hydroquinone, 33.3% benzoquinone and 3% undetermined product (Table 1).

Table 1
Experimental results with catalysts 4 and 5

Entry	Conversion (%)		Selectivity ^a		TON		TOF (h)	
	4	5	4	5	4	5	4	5
I	94.4	98.6	62.0	63.1	47	48	235	244
II (in dark)	-	-	-	-	-	-	-	-

Selectivity^a: Hydroquinone selectivity

At the end of the photooxidation studies, the amount of photodegradation of 4-nitrophenol was determined in the presence of both photocatalysts 4 and 5. For this, the equation given below is used.

$$X(t) = C_0 - C(t) / C_0$$

In the above equation, $X(t)$ is the molar fraction of 4-nitrophenol, C_0 , initial concentration and $C(t)$ is the concentration of 4-nitrophenol as a function of illumination time. This equation shows a similar profile to the photocatalytic degradation of other dyes [25-26]. For this purpose, 100 mL of a 0.025 M solution of 4-nitrophenol and 5 mg of solid catalyst were

reacted in a photo-reactor under visible light for 2 hours. During the photocatalytic reaction, all samples from the reaction medium were diluted with dichloromethane and injected into the GC apparatus. As a result, we observed that most of the 4-nitrophenol were degraded and the rate of degradation was fixed after 120 minutes. Data on photocatalytic degradation of 4-nitrophenol sensitized with both photocatalysts under visible light are presented in Figure 4.

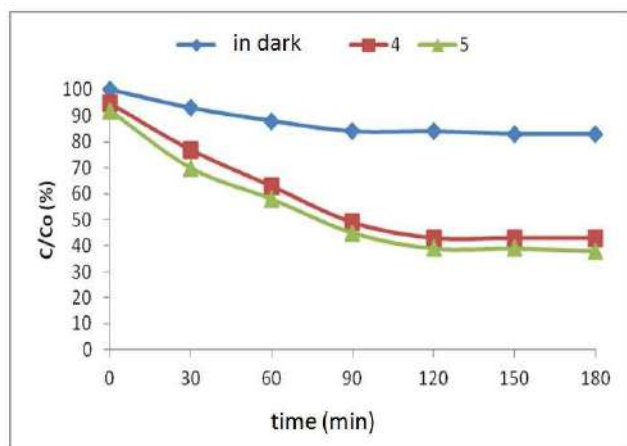


Figure 4 Effect of compound 4 and 5 on the degradation of 4-nitrophenol

Recycling studies have been carried out considering the importance of recyclability of photocatalysts for the environment. For this application, water-soluble non-peripheral copper (II) phthalocyanine compound 5 was used as photocatalyst. 100 ml of 0.015 M 4-nitrophenol solution, 5 mg of compound 5 were treated with UV irradiation in the photoreactor for 120 minutes. At the end of each reaction, the catalyst was removed by extraction with water 3 times and made ready for use in the new photooxidation reaction. It was determined that photocatalytic activity gradually decreased from 98.6% to 88.3% in reuse and 68% in 5th time use. This reduction can be explained by the fact that the phthalocyanine compound also degrades during photooxidation and forms different species. As a result, compound 5 gives 68% yield conversion even after 5 cycles (Figure 5).

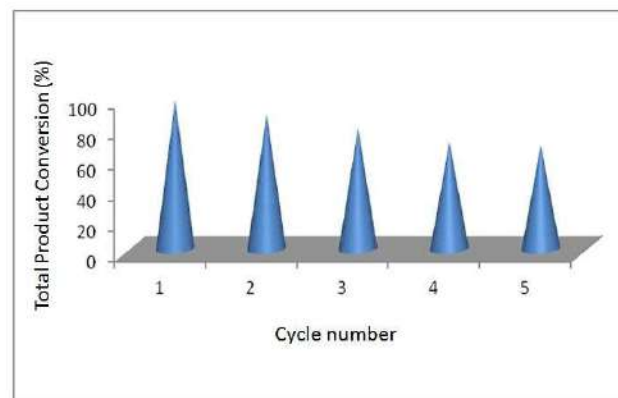


Figure 5 Recycling results with compound 5

Cobalt (II), iron (II), aluminum (III), copper (II) and metal-free phthalocyanines in which different groups have been substituted for the photooxidation of different pollutants have been studied [27-33]. Nyokong et al. Studied the photocatalytic activity of seven octane substituted thio and aryloxy palladium and platinum phthalocyanines in the breakdown of 4-nitrophenol [34]. According to the kinetic studies of this study, two reaction pathways have been identified for the degradation of 4-nitrophenol with phthalocyanine catalyst [34]. In another study by T. Nyokong, quantitative yields of singlet oxygen and photodissection of 4-nitrophenol in the presence of zinc tetrasulfatophthalocyanine ($ZnPcS_4$), zinc octacarboxyphthalocyanine ($ZnPcS_4(COOH)_8$) were investigated [35]. This study is important because it is the first study in this field to investigate the photooxidation of 4-nitrophenol using non-peripheral copper (II) phthalocyanine and its water-soluble derivative as photocatalyst without any oxygen source. The results of photocatalytic experiments can generate promising new research and micro-scale application.

In the literature, although many studies on the catalytic activities of phthalocyanine [36-41] are available, only a few have examined photooxidation reactions using UV radiation. Table 2 summarizes some of these literature.

Table 2
Phthalocyanines used as photocatalysts in photooxidation reactions of different organic pollutants

Catalyst	Substrate	Reaction Time (s)	Reaction Temperature (°C)	Oxidant	Conversion (%)	Reference
ZnPc ^a	Methyl orange- Orange G	10 min	Not reported	O ₂	Not reported	[27]
FePc ^b	Ethyl benzene	9	25	O ₂	>99	[28]
CoPc ^c	Malakhite green	30 dak	Not reported	-	99.2	[29]
CoPc ^d	2-mercaptoethanol	2	25	-	nr ^e	[30]
Metal freePc ^f	Sülfite ion	1	25	O ₂	70	[31]
CuPc ^g	4-nitrophenol	5	27	-	Not reported	[32]
CoPc ⁱ	4-chlorophenol	3	25	O ₂	99.99	[33]
ZnPc ⁱ					97.05	

ZnPc^a= 2-[5-(phenoxy)-izophthalic acid] 9(10), 16(17), 23(24)-tris (tertbutyl) phthalociyaninato Zn (II)

FePc^b= four branched tetra-amine FePc- organik framework

CoPc^c = Tetranitrocobalt phthalociyanin/ ternary chalcogenit

CoPc^d=Cobaltphthalocyanine/C₆₀

Metal free Pc^f= Metal free phthalocyanine /TiO₂

CuPc^g= Copper phthalocyanine / TiO₂CoPcⁱ= 2,9,16,23-tetrakis-(4- carboxyphenylsulphonyl) phthalociyaninato cobalt(II) / TiO₂

ZnPcⁱ= 2,9,16,23-tetrakis-(4- carboxyphenylsulphonyl) phthalociyaninato Zn (II) / TiO₂

nr^e=turnover number: 8.4

nr^h=quantum yield: 1.9

4. CONCLUSION

In the study, non-peripheral copper (II) phthalocyanine compound 4 and its water-soluble quaternized derivative 5 containing 3-(pyridin-4-yl)propane-1-oxo groups were synthesized for the first time and their structures were illuminated by spectroscopic data. Compounds 4 and 5 used as photocatalysts in the photooxidation reaction of 4-nitrophenol, an important environmental pollutant, yielded 94.4% and 98.6% yield conversion, respectively. Hydroquinone (main product) was obtained as benzoquinone (by-product) in the product distribution. The high conversion of 4-nitrophenol into non-toxic species by photooxidation makes the study important. The high product conversion and selectivity of the obtained photocatalysts in homogeneous and heterogeneous solvent systems make this study innovative in terms of shedding light on new studies on developing environmentally cleaner and more efficient systems.

Funding

This study is supported by Karadeniz Technical University Scientific Research Projects Coordination Unit. Project Number: 7687

The Declaration of Conflict of Interest/ Common Interest

No conflict of interest or common interest has been declared by the author.

The Declaration of Ethics Committee Approval

The author declares that this document does not require an ethics committee approval or any special permission.

The Declaration of Research and Publication Ethics

The author of the paper declares that she complies with the scientific, ethical and quotation rules of SAUJS in all processes of the article and that she does not make any falsification on the data collected. In addition,

she declares that Sakarya University Journal of Science and its editorial board have no responsibility for any ethical violations that may be encountered, and that this study has not been evaluated in any academic publication environment other than Sakarya University Journal of Science.

REFERENCES

- [1] C.C. Lezznof and A.B.P. Lever, "Phthalocyanines, Properties and Applications", 4, VCH Publisher, New York, 1996.
- [2] G. Guillaud, J. Simon, and J.P. Germain, "Metallophthalocyanines: gas sensors, resistors and field effect transistors", Coordination Chemistry Reviews, 178, pp. 1433–1484, 1998.
- [3] M. Durmus and T. Nyokong "The synthesis, fluorescence behaviour and singlet oxygen studies of new water-soluble cationic gallium(III)phthalocyanines", Inorganic Chemistry Communications, 10, pp 332–338, 2007.
- [4] H.A. Abdeldayem, D.O. Frazier, B.G. Penn, D.D. Smith, and C.E. Banks, "Non-linear op-tothermal properties of metal-freephthalocyanine", Thin Solid Films, 350, pp 245–248, 1999.
- [5] Q. Luo, H. Tian, B. Chen, and W. Huang, "Effective non-destructive read out of photo-chromic bithienyletheneepthalocyanine hybrid", Dyes and Pigments, 73, pp 118–120, 2007.
- [6] W.S.G. Medina N.A.G. dosSantos C. Curti A.C. Tedesco, and A.C. dosSantos, "Effects of zincphthalocyaninetetrasulfonate-based photodynamic therapy on rat brain isolated mitochondria", Chemico Biological Interactions, 79, pp. 402–406, 2009.

- [7] B.G.Fanchiotti, M.P. ZamprognoMachado, L.C. Paula, M. Durmus, T. Nyokong, A.S. Gonçalves, and A.R. Silva, "The photobleaching of the free and encapsulated metallic phthalocyanine and its effect on the photooxidation of simple molecules", *Journal of Photochemistry and Photobiology B: Biology*, 165, pp. 10-23, 2016.
- [8] Z. Biyiklioglu, V. Cakir, A. Koca, and H. Kantekin, "Synthesis, electrochemical, in-situ spectro electrochemical and in-situelectrocolorimetric characterization of non-peripheral tetra substituted metal-free and metallophthalocyanines", *Dyes and Pigments*, 89, pp. 49-55, 2011.
- [9] P.T. Anastas and J.C. Warner, "Green Chemistry Theory and Practice", 148, Oxford University Press, New York, 1998.
- [10] Y. Ding, F. Yang, L. Zhu, N. Wang, and H. Tang, "Synergistic photocatalytic properties and mechanism of g-C₃N₄ coupled with zinc phthalocyanine catalyst under visible light irradiation", *Applied Catalysis B: Environmental*, 164, pp. 151-158, 2015.
- [11] F. Goettmann, A. Fischer, M. Antonietti, and A. Thomas, "Chemical synthesis of mesoporous carbon nitrides using hard templates and their use as a metal-free catalyst for Friedel-Crafts reaction of benzene", *Angewandte Chemie International Edition*, 45, pp. 4467-4471, 2006.
- [12] S. Yan, S. Lv, Z. Li, and Z. Zou, "Organic-inorganic composite photocatalyst of g-C₃N₄ and TaON with improved visible light photocatalytic activities", *Dalton Transactions*, 39, pp. 1488-1491, 2010.
- [13] H. Li, J. Liu, W. Hou, N. Du, R. Zhang, and X. Tao, "Synthesis and characterization of g-C₃N₄/Bi₂MoO₆ heterojunctions with enhanced visible light photocatalytic activity", *Applied Catalysis B: Environmental*, 160-161, pp. 89-97, 2014.
- [14] S. Wang, D. Li, C. Sun, S. Yang, Y. Guan, and H. He, "Synthesis and characterization of g-C₃N₄/Ag₃VO₄ composites with significantly enhanced visible-light photocatalytic activity for triphenylmethane dye degradation", *Applied Catalysis B: Environmental*, 144, pp. 885-892, 2014.
- [15] W. Wang, J.C. Yu, D. Xia, P.K. Wong, and Y. Li, "Graphene and g-C₃N₄ Nanosheets Cowrapped Elemental α -Sulfur As a Novel Metal-Free Heterojunction Photocatalyst for Bacterial Inactivation under Visible-Light", *Environmental Science and Technology*, 47, pp. 8724-8732, 2013.
- [16] J. Xu, G. Wang, J. Fan, B. Liu, S. Cao, and J.J. Yu, "g-C₃N₄ modified TiO₂ nanosheets with enhanced photoelectric conversion efficiency in dye-sensitized solar cells", *Power Sources*, 274, pp. 77-84, 2015.
- [17] A. Hernández-Gordillo, A.G. Romero, F. Tzompantzi, and R. Gómez, "Kinetic study of the 4-Nitrophenol photooxidation and photo reduction reaction using CdS", *Applied Catalysis B: Environmental*, 144, pp. 507-513, 2014.
- [18] W. Muersa and G.S. Pozan Soylu, "Effects of metal oxide semiconductors on the photocatalytic degradation of 4-nitrophenol", *Journal of Molecular Structure*, 1174, pp. 96-102, 2018.
- [19] L. Coche-Guerente, P. Labbe, and V. Mengerand, "Theoretical and experimental study of the phenol-polyphenol oxidase system immobilized in Laponite hydrogels and layer-by-layer

- self-assembled structures”, *Analytical Chemistry*, 73, pp. 3206-3216, 2001.
- [20] A.E. Navarro, N.A. Cuizano, R.F. Portales, and B.P.Llanos, “Adsorptive removal of 2- nitrophenol and 2-chlorophenol by cross-linked algae from aqueous solutions”, *Separation Science and Technology*, 43, pp. 3183-3199, 2008.
- [21] S.Q. Yu, J. Hu, and J.L. Wang, “Gamma radiation-induced degradation of p-nitrophenol (PNP) in the presence of hydrogen peroxide (H₂O₂) in aqueous solution, *Journal of Hazardous Materials*, 177, 1061-1067, 2010.
- [22] E.T. Saka, “Preparation, characterization of new Co(II) and Cu(II) phthalocyanines and their catalytic performances in aerobic oxidation of substituted phenols”, *Journal of Inclusion Phenomena and Macrocyclic Chemistry*, 91, pp. 61-69, 2018.
- [23] Y. Unver, H. Bas, and Z. Biyiklioglu, “Non-peripherally 4-{(1E)-1-benzothien-2-ylmethylene}amino}phenol substituted zinc(II), manganese(III), cobalt(II) phthalocyanines: Synthesis and electrochemistry”, *Journal of Molecular Structure*, 1178, pp. 508-513, 2019.
- [24] E. Turker Acar, T. Akkızlar Tabakloglu, D. Atilla, F. Yüksel, and G. Atun, “Synthesis, electrochemistry and electrocatalytic activity of cobaltphthalocyanine complexes – Effects of substituents for oxygen reduction reaction”, *Polyhedron*, 152, pp. 114-124, 2019.
- [25] I. Altın, M. Sokmen and Z. Biyiklioglu, “Quaternized zinc(II) phthalocyanine-sensitized TiO₂: surfactant-modified sol-gel synthesis, characterization and photocatalytic applications” *Desalination and Water Treatment*, 57, pp. 16196-16207, 2016.
- [26] R. Bayrak, C. Albay, M. Koç, I. Altın, I. Degirmenci, and M. Sokmen, “Preparation of phthalocyanine/TiO₂ nanocomposites for photocatalytic removal of toxic Cr(VI) ions”, *Process Safety and Environmental Protection*, 102, pp. 294-302, 2016.
- [27] S. Mapukata N. Kobayashi, M. Kimura, and T. Nyokong, “Asymmetrical and symmetrical zinc phthalocyanine-cobalt ferrite conjugates embedded in electrospun fibers for dual photocatalytic degradation of azo dyes: Methyl Orange and Orange G” *Journal of Photochemistry and Photobiology A: Chemistry*, 379, pp. 112-122, 2019.
- [28] W.L.He and C.D.Wu, “Incorporation of Fe-phthalocyanines into a porous organic framework for highly efficient photocatalytic oxidation of arylalkane” *Applied Catalysis B:Environmental*, 234, pp. 290-295, 2018.
- [29] M. Lu, B. Li, Y. Zhang, Q. Liang, X. Li, S. Xu, and Z. Li, “Facile synthesis and characterization of a cobalt phthalocyanine sensitized SnIn₄S₈ composites toward enhanced photocatalytic activity, *Journal of Materials Science: Materials in electronics*” 29, pp. 16680–16690, 2018.
- [30] P. Arunachalam, S. Zhang, T. Abe, M. Komura, T. Iyoda, and K. Nagai, “Weak visible light (~mW/cm²) organophotocatalysis for mineralization of amine, thiol and aldehyde by biphasic cobalt phthalocyanine/fullerene nanocomposites prepared by wet process” *Applied Catalysis B:Environmental*, 193, pp. 240-247, 2016.
- [31] V. Iliev and D. Tomova, “Photocatalytic oxidation of sulfide ion catalyzed by phthalocyanine modified titania” *Catalysis Communications* 3, pp. 287–292, 2002.

- [32] G.Mele, R. Del Sole, G. Vasapollo, E. García-López, L. Palmisano, and M. Schiavello, "Photocatalytic degradation of 4-nitrophenol in aqueous suspension by using polycrystalline TiO₂ impregnated with functionalized Cu(II)–porphyrin or Cu(II)–phthalocyanine" *Journal of Catalysis*, 217, pp. 334–342, 2003.
- [33] Y. Mahmiani, A.M. Sevim, and A. Gül, "Photocatalytic degradation of 4-chlorophenol under visible light by using TiO₂ catalysts impregnated with Co(II) and Zn(II) phthalocyanine derivatives" *Journal of Photochemistry and Photobiology A: Chemistry*, 321, pp. 24–32, 2016.
- [34] T.B. Ogunbayo, E. Antunes, and T. Nyokong, "Investigation of homogeneous photosensitized oxidation activities of palladium and platinum octasubstituted phthalocyanines: Oxidation of 4-nitrophenol" *Journal of Molecular Catalysis A: Chemical*, 334, pp. 123–129, 2011.
- [35] E. Marais, R. Klein, E. Antunes, and T. Nyokong, "Photocatalysis of 4-nitrophenol using zinc phthalocyanine complexes" *Journal of Molecular Catalysis A: Chemical*, 261, pp. 36–42, 2007.
- [36] A.A. Kamiloglu, I. Acar, Z. Bıyıklıoğlu, and E.T. Saka, "Peripherally tetra-{2-(2,3,5,6-tetrafluorophenoxy)ethoxy} substituted cobalt(II), iron(II) metallophthalocyanines: Synthesis and their electrochemical, catalytic activity studies" *Journal of Organometallic Chemistry*, 828, pp. 59-67, 2017.
- [37] A.A. Kamiloglu, I. Acar, E.T. Saka, and Z. Bıyıklıoğlu, "Synthesis of polyfluoro substituted Co(II), Fe(II) phthalocyanines and their usage as catalysts for aerobic oxidation of benzyl alcohol" *Journal of Organometallic Chemistry*, 815-816, pp.1-7, 2016.
- [38] V. Cakır, E.T. Saka, Z. Bıyıklıoğlu, and H. Kantekin, "Highlyselective oxidation of benzyl alcohol catalyzed by new peripherally tetra-substituted Fe(II) and Co(II) phthalocyanines" *Synthetic Metals*, 197, pp. 233-239, 2014.
- [39] A.A. Kamiloglu, E.T. Saka, Z. Bıyıklıoğlu, I. Acar, and H. Kantekin, "Investigation of catalytic activity of new Co(II) phthalocyanine complexes in cyclohexene oxidation using different type of oxidants" *Journal of Organometallic Chemistry*, 745-746, pp. 18-24, 2013.
- [40] Z. Bıyıklıoğlu, E.T. Saka, S. Gökçe, and H. Kantekin, "Synthesis, characterization and investigation of homogeneous oxidation activities of peripherally tetra-substituted Co(II) and Fe(II) phthalocyanines: Oxidation of cyclohexene" *Journal of Molecular Catalysis A:Chemical*, 378, pp. 156-163, 2013.
- [41] E.T. Saka, G. Sarkı, H. Kantekin, and A. Koca, "Electrochemical, spectroelectrochemical and catalytic properties of new Cu(II) and Co(II) phthalocyanines" *Synthetic Metals*, 214, pp. 82-91, 2016.

JOURNAL OF SCIENCE



SAKARYA UNIVERSITY

Sakarya University Journal of Science

ISSN 1301-4048 | e-ISSN 2147-835X | Period Bimonthly | Founded: 1997 | Publisher Sakarya University |
<http://www.saujs.sakarya.edu.tr/en/>

Title: Investigation of the Frequency and Voltage Dependent Dielectric Properties of Au/n-SiC Metal Semiconductor (MS) and Au/Al₂O₃/n-SiC Metal-Insulator-Semiconductor (MIS) Structures

Authors: Gülçin ERSÖZ DEMİR, İbrahim YÜCEDAĞ

Received: 2020-05-28 14:54:52

Accepted: 2020-08-08 00:30:38

Article Type: Research Article

Volume: 24

Issue: 5

Month: October

Year: 2020

Pages: 1040-1052

How to cite

Gülçin ERSÖZ DEMİR, İbrahim YÜCEDAĞ; (2020), Investigation of the Frequency and Voltage Dependent Dielectric Properties of Au/n-SiC Metal Semiconductor (MS) and Au/Al₂O₃/n-SiC Metal-Insulator-Semiconductor (MIS) Structures. Sakarya

University Journal of Science, 24(5), 1040-1052, DOI:

<https://doi.org/10.16984/saufenbilder.744111>

Access link

<http://www.saujs.sakarya.edu.tr/en/pub/issue/56422/744111>

New submission to SAUJS

<http://dergipark.org.tr/en/journal/1115/submission/step/manuscript/new>

Investigation of the Frequency and Voltage Dependent Dielectric Properties of Au/n-SiC Metal Semiconductor (MS) and Au/Al₂O₃/n-SiC Metal-Insulator-Semiconductor (MIS) Structures

Gülçin ERSÖZ DEMİR^{*1}, İbrahim YÜCEDAĞ²

Abstract

In this study, we investigated the fabrication of Au/n-SiC (MS) and Au/Al₂O₃/n-SiC (MIS) type structures with atomic layer deposition (ALD) technique and their dielectric properties. The dielectric characteristics of structures were analyzed at frequency range of 1 kHz-500 kHz and by applying a (-3V)-(9V) bias voltage at 300 K. The significant dielectric parameters such as dielectric constant (ϵ') and dielectric loss (ϵ''), real and imaginary parts of electrical modulus (M' and M''), loss tangent ($\tan\delta$) were calculated by depending on frequency and voltage from capacitance-voltage ($C-V$) and conductance-voltage ($G/\omega-V$) data. Thereby, the effect of frequency on MS and MIS was searched in detail. The effect of the interface states occurred in the low frequency region can be attributed to the variation of the characteristic behavior of these parameters. It is clear that the dielectric parameters highly depend on the frequency and voltage at depletion and accumulation regions. Moreover, the peak position of M'' shifts to the left side of the graphic due to the effect of the insulating layer. It can be deduced from the obtained results that the interfacial polarization is easier at low frequencies. Also the interfacial polarization can contribute more to the variation of the dielectric properties.

Keywords: Au/Al₂O₃/n-SiC (MIS) type structures, AC electrical conductivity, Dielectric Properties, Impedance measurements.

1. INTRODUCTION

Metal-semiconductor (MS) structures which are used to determine the characteristic behavior of the semiconductor materials are significant investigation topics [1-4]. MS structures can be transformed into metal-insulator-semiconductor (MIS) structures through the insulator layer coated between metal and semiconductor. Interface

diffusion and reaction formed between the metal and semiconductor interface can be dramatically reduced because of the presence of an insulator layer. The structural properties of the insulator layer at the M/S interface, series resistance (R_s) and particular distribution of interface states between metal and semiconductor affect the electrical characteristics of the devices [5-7]. Degenerate bond structures in the semiconductor surface are

* Corresponding Author: glcnersoz@gmail.com

¹Department of Management Information Systems, Faculty of Management, Selçuk University, Konya 42700, Turkey. ORCID: <http://orcid.org/0000-0002-4813-4003>

²Department of Computer Engineering, Faculty of Technology, Düzce University, Düzce 81620, Turkey. E-Mail: yucedagi@gmail.com, ORCID: <http://orcid.org/0000-0003-2975-7392>

destroyed by the interfacial dielectric film. This dielectric film, which is between metal and semiconductor, decreases surface charge traps that are generally located at the Fermi level [8]. The alteration of barrier height by means of the presence of insulator layer on the M/S interface was ascribed to the interface dipole [9]. The performance, reliability and stability of the device are influenced predominantly because of the interfacial layer [10].

Among the different insulating materials, Aluminum oxide (Al_2O_3) nanomaterial has been regarded as one of the most promising materials due to its fabricate potential that has low-cost, stable and flexible electronic devices [11, 12]. Al_2O_3 has some interesting properties such as dielectric permeability (~ 9), wide band gap (9 eV) [13], and its formation of uniform interface with semiconductors. These provide the reduction of leakage of currents in devices, kinetics and thermodynamic stabilities of the semiconductor at high-temperatures. They also give rise to low interface defects as well as amorphous materials [14].

Techniques such as Sputtering, Spray pyrolysis, RF magnetron, electron beam evaporation, atomic layer deposition (ALD) were used to form Al_2O_3 thin films. The ALD technique is one of the most preferred methods for creating an interface layer with a high dielectric property on the substrate, since it has unique deposition characteristics such as precise thickness control, low impurity ratio, low processing temperature and excellent thickness uniformity on substrate areas [15-18]. Al_2O_3 thin film created by using the ALD showed excellent electrical properties. [18] The thin layers of Aluminum oxide obtained by the ALD technique have caught attention recently because of their excellent potential for highly effective and homogeneous surface passivation of semiconductor substrates [19-21]. Today, these kinds of devices generated by means of the silicon (Si) have been made convenient to daily usage as a result of long term studies. In spite of the great progress in material processing technology, device performance is confined due to the inadequacy of natural features in Si. To overcome this problem, there has been increasing necessity for studies into alternative materials to silicon (Si) to use in the power electronics. GaN, GaAs, and SiC are

materials that have emerged as alternatives to Si [22]. Among these materials, silicon carbide (SiC) semiconductor is mostly preferred because of its important properties in power electronic applications especially at the work with high voltage/temperature. Si and GaAs, based on appliances in power switching devices, have 8-10 times weaker performance than SiC based devices. This entails SiC to become a perfect candidate for these applications [23]. In general, MIS structure obtained from SiC is attractive due to low initial voltage (compared to SiC p-n diodes) and irreversibility.

According to literature, Al_2O_3 was used as interfacial layer on semiconductor substrates such as p-Si [24], n-Si [25], InP [26], n-GaAs [27], and SiC [28-30]. In this study, both Au/n-SiC metal/semiconductor (MS) and Au/ Al_2O_3 /n-SiC metal/insulator/semiconductor (MIS) type structures were produced by forming Al_2O_3 on n-SiC using the atomic layer deposition (ALD) technique. Therefore, we aimed to investigate dielectric and electrical behaviors of the Au/ Al_2O_3 /n-SiC type structures. Thereby, basic parameters such as the dielectric properties, electric modulus and conductivity of structures with and without Al_2O_3 interfacial layer were deeply investigated. For both structures, the permittivity (ϵ' and ϵ''), loss tangent ($\tan\delta$), electrical modulus (M' and M''), and ac electrical conductivity (σ_{ac}) parameters which depend on the frequency and voltage were researched on the frequency and voltage range of 1 kHz- 500 kHz and (-3V) - (9V), respectively, by measuring capacitance-voltage ($C-V$) and conductance-voltage ($G/\omega-V$) measurements at 300 K. Experimental results indicate that all these parameters are strong functions of frequency, voltage and Al_2O_3 interfacial layer.

2. MATERIALS AND METHODS

In this experimental work, n-Type, 8° off (0001) oriented, 4H-SiC wafers were used to produce the MS and the MIS type structures. Before the production of MS and MIS structures, wafers were sonicated for five minutes in acetone and five minutes in isopropanol and then rinsed in deionize (DI) water with resistivity of 18 $\text{M}\Omega\cdot\text{cm}$ for a prolonged time and wafers were dried under N_2 flow. After surface cleaning of n-4H-SiC high

purity Au (99.999%) was evaporated on the whole back of wafer by thermal evaporation method with 2000 Å at 1×10^{-6} Torr. In order to get low resistivity ohmic back contact, Au coated wafers were annealed at 500°C in the nitrogen ambient. Then, they were prepared with atomic layer deposition (ALD) system for Al₂O₃ coating on MS type structure. Under UV radiation, deposition process was carried out and it was heated at 370°C using trimethylaluminum and water. The deposited Al₂O₃ thickness was 70 Å. Finally, high purity Au was deposited on the Al₂O₃ at 1×10^{-6} Torr in the same thermal evaporation system. In order to perform electrical measurements of these MS and MIS type structures, the fabricated samples were mounted on a copper holder with the help of silver dag. The electrical contacts were made to the upper electrodes by use of tiny silver coated wires with silver paste. The forward and reverse bias $C-V$ and $G/\omega-V$ measurements were obtained by using an HP4192A LF impedance meter in the frequency range of 1 kHz-500 kHz. All measurements were realized with the help of a microcomputer through an IEEE-488 AC/DC converter card.

3. RESULT AND DISCUSSION

The forward (9V) and reverse (-3V) bias voltage $C-V$ measurements of Au/n-SiC (MS) and Au/Al₂O₃/n-SiC (MIS) structures were obtained by using an HP4192A LF impedance meter in the frequency range of 1 kHz-500 kHz at 300 K. The obtained results were presented in Fig.1 (a) and (b), respectively. When the Figs. 1 (a) and (b) are carefully examined, it can be seen that the obtained C values are strongly dependent on frequency in depletion and accumulation regions. The C values of the MS and MIS structures decrease with increasing frequency. These behaviors were ascribed to traps in the interface between metal and semiconductor.

Although the capacitance of the MS structure reaches a maximum value, it does not have a peak in depletion region. Fig. 1 (b) shows that a dielectric interface layer between the metal and the semiconductor corrects the capacitance behavior of the MS structure [31].

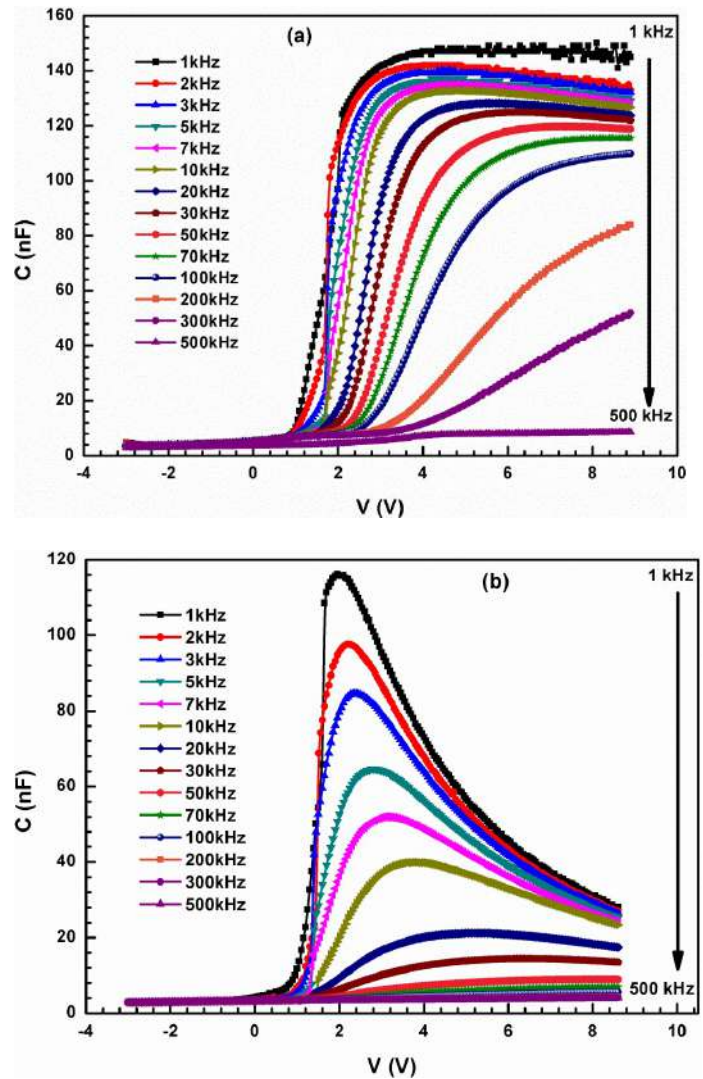


Figure 1 Frequency dependent plot of the $C-V$ characteristics of (a) Au/n-SiC and (b) Au/Al₂O₃/n-SiC structures

As it can be seen in Fig 1 (b); inversion takes place in the voltage range of (-3 V) - (1 V), depletion is in (1 V) - (5 V), and finally accumulation region is in the range of (5 V) - (9 V) capacitance-voltage curves. These regions can be clearly seen in Fig. 1 (b). However, inversion and depletion regions are dominant in Fig. 1 (a). Fig. 1 (b) shows that capacitance behavior at particularly low frequencies (1 kHz-10 kHz) gives a strong peak in the depletion region for MIS structure. This peak can be attributed to the interfacial distribution of metal-insulator-semiconductor interfaces, the series resistance, and the density of the interface insulation layer [32]. For both structures, the increase in $C-V$ values, in the depletion region can be attributed to the presence of interfacial states at low frequencies. Moreover, the separation of $C-V$ curves in the accumulation region,

can also be attributed to the value and magnitude of series resistance at high frequencies [33].

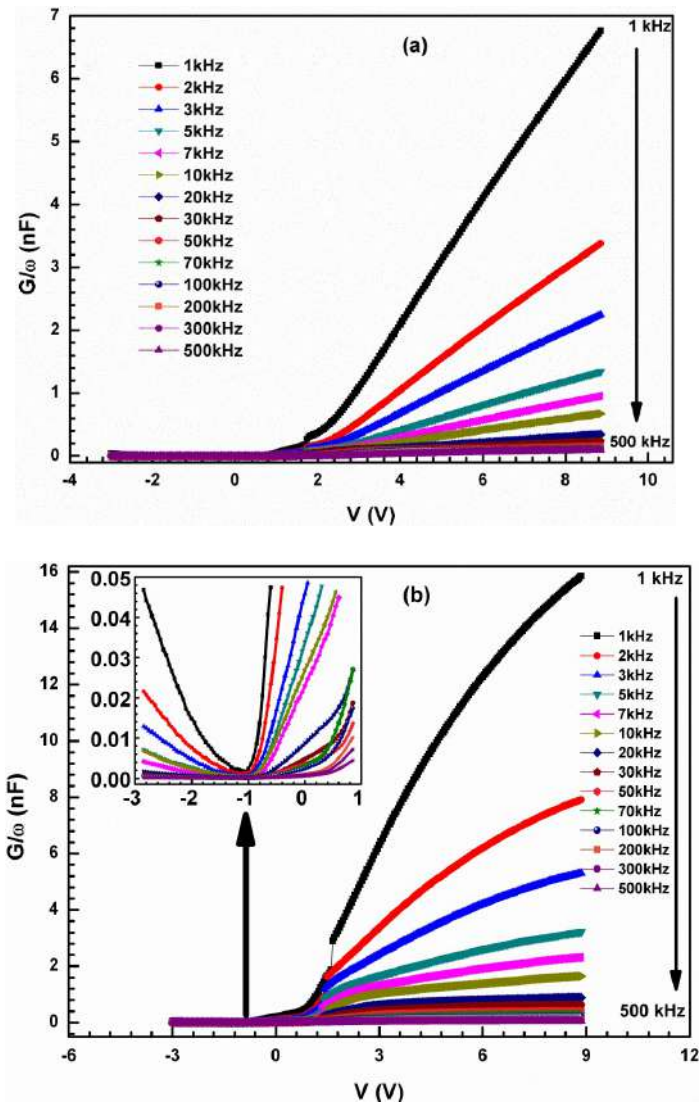


Figure 2 Frequency dependent plot of the G/ω - V characteristics of (a) Au/n-SiC and (b) Au/Al₂O₃/n-SiC structures

Figs. 2 (a) and (b) illustrate that the variation in conductivity (G/ω - V) the forward (9 V) and the reverse (-3V) bias voltage for the same frequency ranges show similar behaviors to the C - V variations in Figs. 1 (a) and (b). The separation occurring in the C - V and G/ω - V characteristics, can be ascribed to the presence of interface state densities (N_{ss}) and their different carrier lifetimes (τ) at low frequencies in the depletion region. While the interface charges can follow the AC signal at low frequencies, these charges cannot follow the AC signal on high frequencies (the carrier life time τ is much larger than $1/2\pi f$ are reached) [11, 33]. Both

C and G/ω values decrease with increasing frequency, the changing C and G/ω values are considerably higher at low frequencies than at higher frequencies. The inset in Fig. 2 (b) exhibits G/ω - V characteristics of Au/Al₂O₃/n-SiC structure in inversion region. As can be seen from this inset, G/ω - V characteristics of Au/Al₂O₃/n-SiC structure in inversion region shows U-shaped behavior. This proves that Au/Al₂O₃/n-SiC structures do not have conductive properties at -1 V due to the fact that all free charges are caught in traps.

The carrier lifetime is much larger than the inverse of the angular frequencies and the charges in the interface cannot follow the AC signal. In such cases, the capacitance and conductance decrease as the frequency increases [34].

The electrical performance of devices such as MS, and MIS depends on crucially the properties of dielectric parameters. Therefore, all properties belong to the dielectric parameters such as electrical modulus, real and imaginary parts of (ϵ' , ϵ'') of complex permittivity (ϵ^*), and $\tan\delta$ for Au/n-SiC (MS) and Au/Al₂O₃/n-SiC MIS structures have been examined with all details by using C and G/ω results in the frequency steps from 1 kHz to 500 kHz and applying voltage sweep from forward (9V) to reverse (-3V) at 300 K.

The dielectric spectroscopy method has been commonly used to determine the dielectric properties of MS and MIS structures in the literature [35, 36]. The ϵ^* is the most basic point in this method and it is defined with the formula below [33, 34]:

$$\epsilon^* = \epsilon' - i\epsilon'' \quad (1)$$

The real part ϵ' and imaginary part ϵ'' parameters were acquired from voltage and frequency dependent C and G/ω analyses by using the formulas below [36]:

$$\epsilon' = \frac{C}{C_0} \quad (2)$$

$$\epsilon'' = \frac{G/\omega}{C_0} \quad (3)$$

In Eqs. 2 and 3, $C_0 (= \epsilon_0 A/d_i)$ is the empty capacitor, ϵ_0 is the permittivity of free-space or vacuum, d_i is the thickness of insulator layer and A is the rectifier contact area of device.

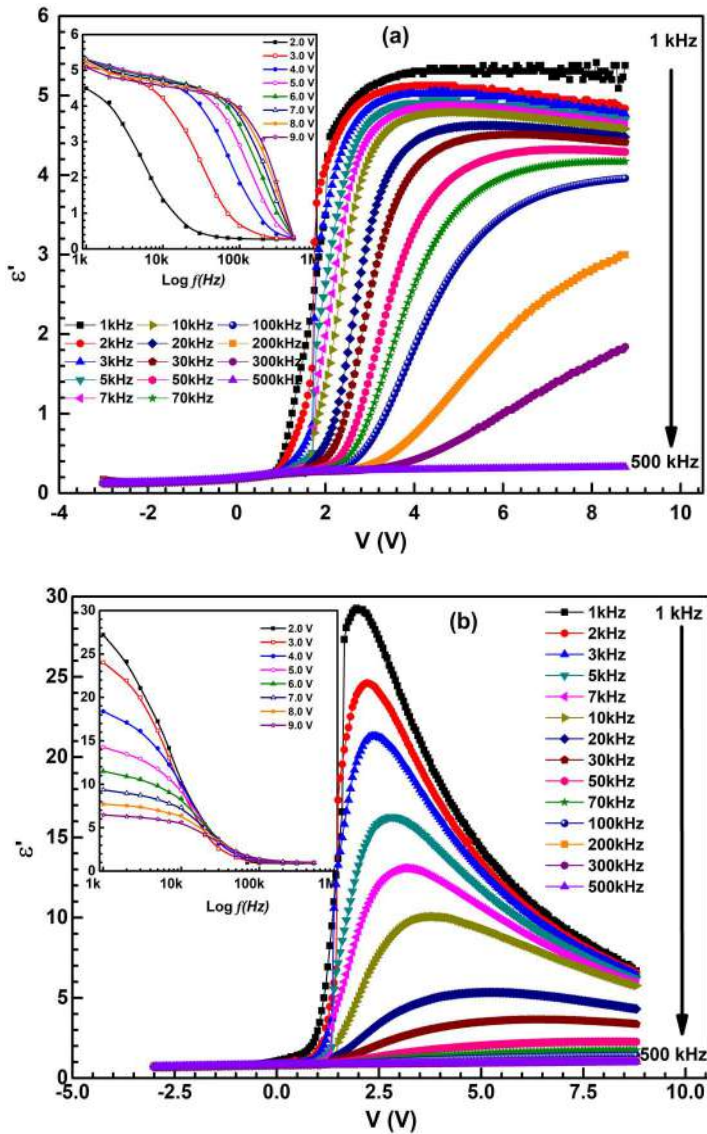


Figure 3 The frequency and voltage dependent comparative plots of the dielectric constant (ϵ') in the depletion region of (a) Au/n-SiC and (b) Au/Al₂O₃/n-SiC structures

Fig. 3 exhibits the ϵ' -V and ϵ' -logf (inset figure) graphs for MS and MIS structures. According to inset figure of Fig. 3, ϵ' sharply decreases between 1 kHz and 100 kHz at low voltages, while ϵ' decreases between 100 kHz and 500 kHz at high voltages for Au/n-SiC structures. Moreover, ϵ' sharply decreases between 1 kHz and 100 kHz at all voltages, while its value is almost the same constant value from 100 kHz to 500 kHz for Au/Al₂O₃/n-SiC

structures. There is an exponential decrease for both the Au/n-SiC and the Au/Al₂O₃/n-SiC structures. Fig. 3 also exhibits that the value of the ϵ' is as low as about four times by means of the interfacial insulating layer at the low frequency region. The graph of ϵ' -logf shows that ϵ' values decrease with increasing frequency. As can be understood from the inset graph of Fig. 3 (a), ϵ' values in MS structure increase with increasing voltage, while the ϵ' values in MIS decrease with increasing voltage in the inset graph of Fig. 3 (b).

Comparing the Fig. 3 (a) and (b), it should also be noted that the MIS structure provides a dielectric increase due to the insulating interface. Dielectric interfaces are expected to increase dielectric constant. In the MS and MIS structures, ϵ' commonly decreases as frequency increases. This decrease in ϵ' due to the increase in frequency stems from the factors such as the orientation of molecules, interface polarization and ionic polarization [34]. The value of the dielectric constant decreases as the alignment of the dipoles at higher frequencies is faster [37].

Fig. 4 exhibits the ϵ'' -V and ϵ'' -logf (inset figure) graphs for MS and MIS structures. According to inset figure of Fig. 4, ϵ'' sharply decreases between 1 kHz and 10 kHz at all voltages for Au/n-SiC and Au/Al₂O₃/n-SiC structures. The ϵ'' is almost the same constant value from 100 kHz to 500 kHz in the accumulation region for Au/n-SiC and Au/Al₂O₃/n-SiC structures. There is an exponential decrease for both the Au/n-SiC and the Au/Al₂O₃/n-SiC structures. Just as the Fig. 3, the Fig. 4 shows that there is a decrease in the imaginary dielectric constant with frequency, while it exhibits an increase with voltage especially in the depletion region. The characteristic behavior in Fig. 4 demonstrates that the energy distribution of the MS and MIS constructions decrease as the frequency increases [38].

Fig. 4 also demonstrates that the value of the ϵ'' is as low as about four times by means of the interfacial insulating layer at the low frequency region. The dipoles in the insulator material can be polarized under an external applied bias voltage or an electric field that displaces the charges from their equilibrium position or traps at low and medium

frequencies. This explains the evolution of dielectric performance as a consequence of relaxation time [37, 38]. On the other hand, the change of dielectric loss starts in the depletion and accumulation regions. Namely there is no change in dielectric loss due to no energy loss in inversion region. ε' and ε'' values are compatible with the results obtained in similar studies in the literature [38].

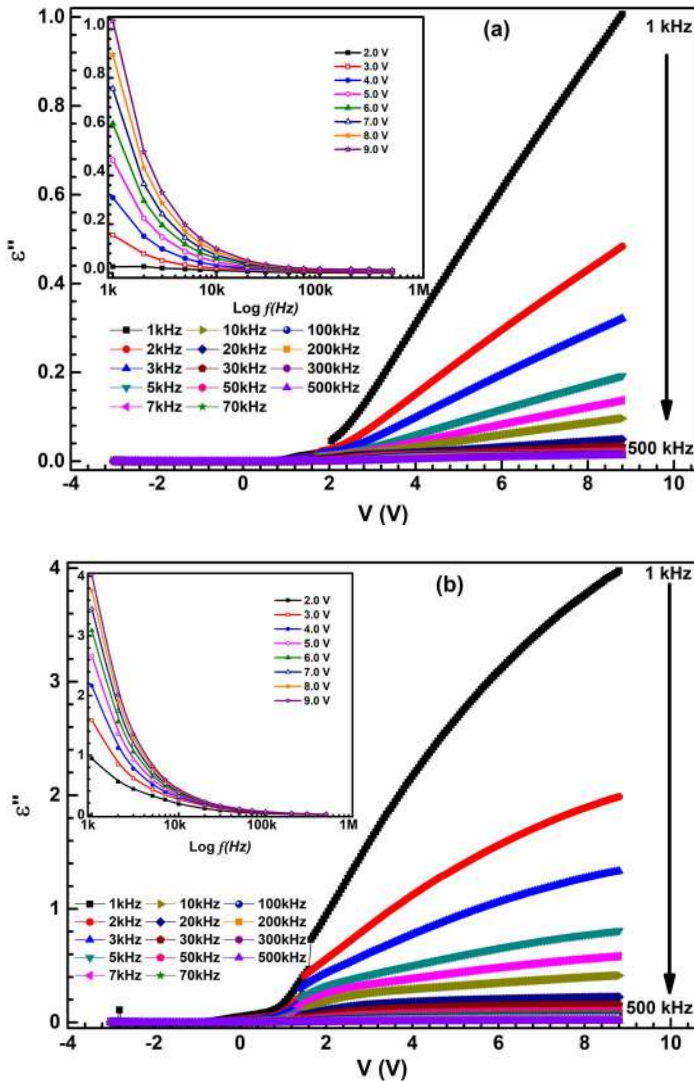


Figure 4 The frequency and voltage dependent comparative plots of the dielectric loss (ε'') in the depletion region of (a) Au/n-SiC and (b) Au/Al₂O₃/n-SiC structures

The experimental results in this research demonstrate that both dipole and interface polarizations can easily occur at low frequencies and trapped charges can follow the AC signal. In such a case, the dielectric loss in the inversion region does not change even if the frequency

increases. Therefore, the dielectric loss in the inversion remains almost constant.

The $\tan\delta$ is expressed in the formula below [36]:

$$\tan\delta = \frac{\varepsilon''}{\varepsilon'} \quad (4)$$

Fig. 5 exhibits the $\tan\delta$ -V and $\tan\delta$ -logf (inset figure) graphs for MS and MIS structures. According to inset figure of Fig. 5, $\tan\delta$ rapidly decreases between 1 kHz and 10 kHz at all voltages for Au/n-SiC and Au/Al₂O₃/n-SiC structures.

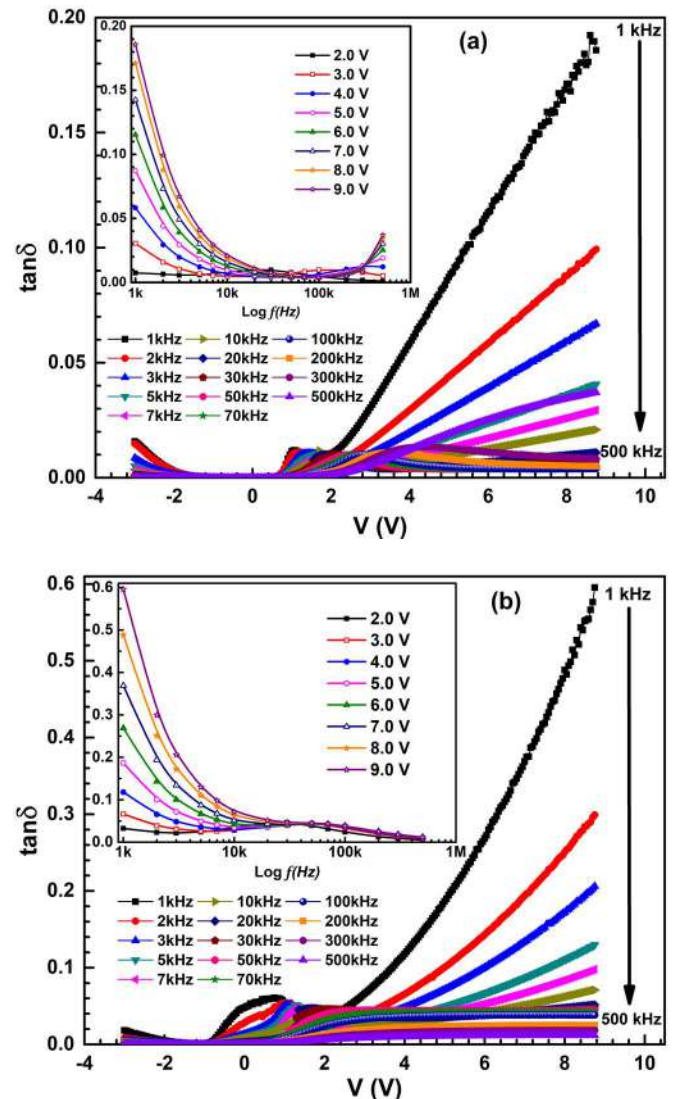


Figure 5 The frequency and voltage dependent comparative plots of the loss tangent ($\tan\delta$) in the depletion region of (a) Au/n-SiC and (b) Au/Al₂O₃/n-SiC structures

The $\tan\delta$ has almost the same constant value from 10 kHz to 500 kHz for Au/n-SiC and Au/Al₂O₃/n-

SiC structures. There is an exponential decrease for both the Au/n-SiC and the Au/Al₂O₃/n-SiC structures. The $\tan\delta$ -V (Fig. 5) and $\tan\delta$ -logf diagrams (Fig. 5 inset), which are determined based on both ε' and ε'' values, exhibit peak behavior in the medium frequency domain (10 kHz-100 kHz) and in the depletion region for the MIS structure, while MS structure exhibits peak behavior in the high frequency domain and in the depletion region (between 1 V and 5V) [39].

While frequency increases, $\tan\delta$ -logf (inset figure) values decrease. The peak position for the MS and MIS structures has shifted towards the middle frequency region due to the restructuring and rearrangement of the surface state. The Fig. 5 also shows that there is a decrease in the loss tangent with frequency, while it exhibits an increase with voltage, especially in the depletion region. This increase begins after 5 V for MS structure, while it begins after 3 V. On the other hand, it is well known that the interfacial properties of C and G/ω are extremely sensitive to the properties and are the effect of R_s [39]. It is seen that surface state density and interface polarization values affect the $\tan\delta$ -V and the $\tan\delta$ -logf characteristic values when a bias voltage is applied to MS and MIS structure according to the literature [40]. This peak behavior in the $\tan\delta$ -V and the $\tan\delta$ -logf plots can only be attributed to the interface states. Bulk phenomenon in complex systems can easily be interpreted by means of electrical modulus formalism. The evaluation of the electrical modulus as a function of the frequency gives rise to understand the relaxation processes in the studied materials. The Complex dielectric data are converted to the M^* equation using the following formula [41]:

$$M^* = \frac{1}{\varepsilon^*} = M' + jM'' = \frac{\varepsilon'}{\varepsilon'^2 + \varepsilon''^2} + \frac{\varepsilon''}{\varepsilon'^2 + \varepsilon''^2} \quad (5)$$

Here, j is the imaginary root (-1), M' and M'' are respectively the real and the imaginary parts of complex modulus. Fig. 6 (a) and (b) indicate the M' -V graph while Fig. 6 (c) and (d) indicate M'' -V plots for MS and MIS structures. The value of M' for MS structure changes between 6.0 and 8.0 in inversion region, while it changes between 0.3 and 4.5 as rising from low frequency to high frequency in depletion and accumulation regions. The value of

M' for MIS structure changes between 1.2 and 1.4 in inversion region, while it changes between 0.1 and 1.2 as rising from low frequency to high frequency in depletion and accumulation regions. When Fig. 6 (a) and (b) are examined, the rise of M' values of MS and MIS structures with increasing frequency in depletion region is observed. The values of M' in the reverse bias exhibit independent behavior from frequency. So the characteristics of the real electrical modulus versus frequency only in the depletion region have been investigated. It is also indicated that there is an increase with the frequency and a decrease with the voltage in the internal graphics of Fig. 6 (a) and (b). The polarization effect may cause these characteristic behaviors to occur in MS and MIS.

In addition, the electrical modulus values reach their maximum level at high frequencies due to the relaxation processes [42]. This can be explained as the almost zero approximation of M' values at low frequencies. In the Fig. 6 (a) and (b), especially about 100 kHz for MS structure and 10 kHz for MIS structure, M' increases rapidly as frequency increases. From 100 kHz to 500 kHz for MS structure and from 10 kHz to 500 kHz for MIS structure, the conduction mechanism can be positively affected by the short-range mobility of the charge carriers in the interfaces of structures. This indicates that there is no restoring force under the influence of a constant electric field. That means, the charge flow may not occur. [43]. The value of M'' for MS structure changes between 0.01 and 0.095 in inversion region, while it changes between 0 and 0.035 in depletion region and between 0 and 0.040 accumulation regions. The value of M'' for MIS structure changes between 0 and 0.035 in inversion region, while it changes between 0 and 0.05 in depletion region and between 0.01 and 0.065 accumulation regions. In the Fig. 6 (c) and (d), the M'' -V plot has a peak point for both samples in a given voltage range. The voltage ranges from bottom to the peak positions of the M'' -V characteristics with increasing frequency to determine the distance that the load carriers are mobile at long distances.

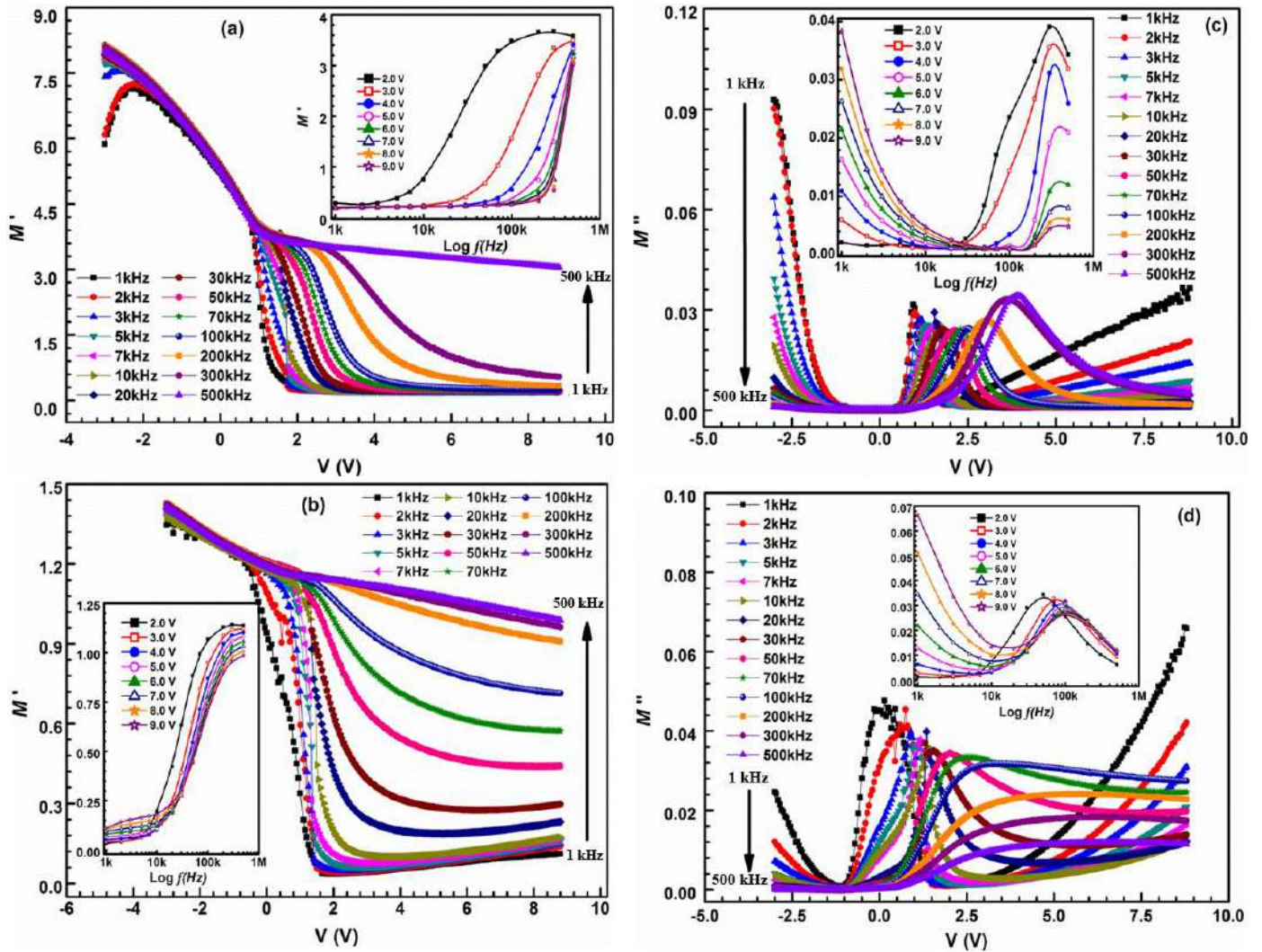


Figure 6 (a) and (b) characteristics of the real electrical modulus for Au/n-SiC and Au/Al₂O₃/n-SiC structures, respectively. (c) and (d) characteristics of the imaginary electrical modulus for Au/n-SiC and Au/Al₂O₃/n-SiC structures, respectively

The values in both the reverse and forward bias exhibit frequency dependent behavior. There is also a decrease with increasing frequency in the reverse bias region.

However, peak distribution in the imaginary electrical modulus of both samples exhibit only in the depletion region. So the characteristics of the imaginary electrical modulus versus frequency only in the depletion region have been investigated. In this study the Fig. 6 (c) and (d) shows that there is a decrease with the frequency. Moreover, there is an increase with the voltage at low frequency region, while there is a decrease with voltage at high frequency region in the internal graphics.

On the other hand, a very distinct peak is seen in the internal graph of Fig.6 (d) and increasing voltage

shifts the peak position towards the high frequency region. This characteristic change in the imaginary electrical modulus of the insulator interfacial material can be attributed to surface polarization effects and the relaxation mechanism of dipoles formed between semiconductor and insulator [41]. Otherwise, the peak position of M'' shifts to the left due to the effect of the insulating layer since, the insulating layer reduces the contribution to the values of ϵ' and ϵ'' by regulating the interface states. By means of the insulation layer, the shifting modulus peak also contributes significantly to the correlation between the mobility of the moving load carriers [43]. M' and M'' values are compatible with the results obtained in similar studies in the literature [24, 38].

The frequency and voltage dependent AC electrical conductivity of both MS and MIS structures are given by the following formula [33] and the characteristic in the depletion region is exhibited in Fig. 7.

$$\sigma_{ac} = \omega C \tan \delta (d/A) = \varepsilon'' \omega \varepsilon_0 \quad (6)$$

It is also seen in the Fig. 7 (b), σ_{ac} reaches to higher values by means of interfacial layer. Compared the Fig. 7 (a) and (b), it is also clear that the MIS structure has higher conductivities than MS. The increase in AC conductivity can be ascribed to the characterization of the loss tangent as well as to the reduction of defects at interfaces with increasing frequency [44].

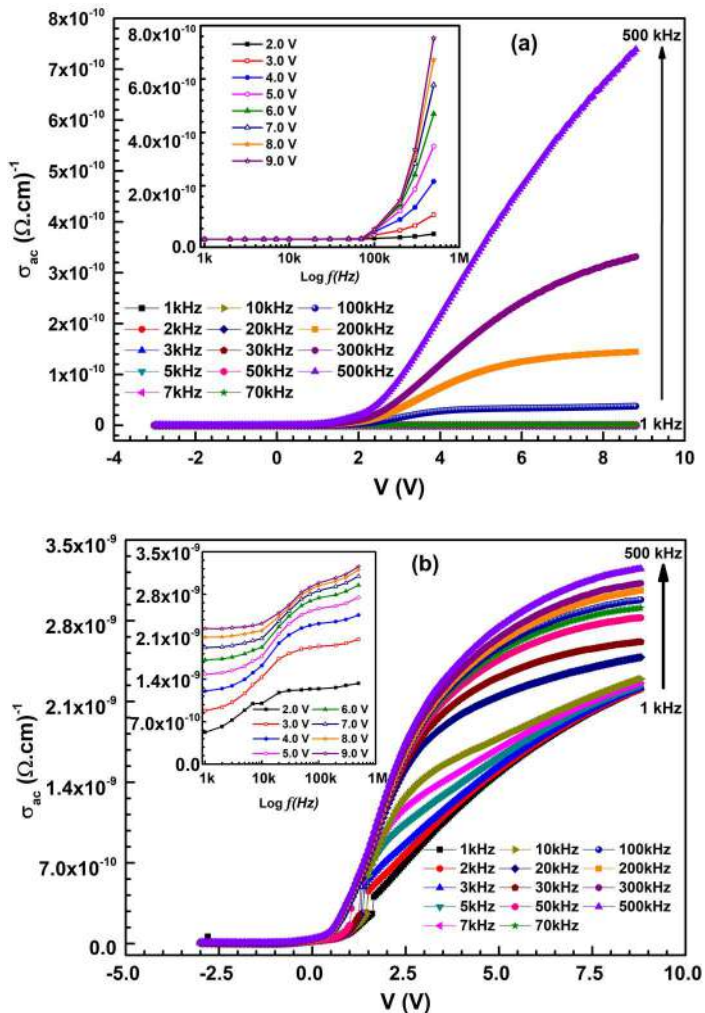


Figure 7 The frequency and voltage dependent comparative plots of the ac electrical conductivity (σ_{ac}) in the depletion region of (a) Au/n-SiC and (b) Au/Al₂O₃/n-SiC structures

It is obviously seen from Fig. 7 (a) and (b) that AC electrical conductivity has higher values in the

depletion and accumulation regions. Then, it is saturated in the accumulation region (high forward bias) due to series resistance of samples. Moreover, σ_{ac} increases as the frequency increases. This characteristic change in the σ_{ac} can be ascribed to the increase of surface polarization effects with increasing frequency and the occurrence of series resistance in the high voltage region [45]. As a result, these characteristic behaviors that the dielectric properties were developed by means of the Al₂O₃ layer effect.

4. CONCLUSION

In this study, Au/n-SiC Metal-semiconductor (MS) and Au/Al₂O₃/n-SiC Metal-Insulator-Semiconductor (MIS) structures were produced to investigate the electric and dielectric properties at room temperature. For this research, the dielectric characteristics of the structures were carried out by applying a (-3V) - (9V) bias voltage at a frequency range of 1 kHz-500 kHz and at room temperature. Al₂O₃ (70 Å thick) was used as a high dielectric interfacial insulating layer between the metal and the semiconductor to enhance the performance of the MIS structure compared with the MS structure. It is evident that the dielectric parameters strongly depend on the frequency and voltage in the depletion and accumulation regions mainly due to the interface polarization and interface traps. The obtained results show that each of the parameters ε' , ε'' and $\tan \delta$ exhibits a sharp decrease with increasing frequency due to the applied bias voltage, whereas real part of electrical modulus characteristics increase with increasing frequency at high forward bias region. However, imaginary part of electrical modulus characteristics decreases with increasing frequency at low reverse bias region. The high frequency variation in ε' and ε'' can be ascribed to Maxwell-Wagner and field charge polarization. The larger values of ε' may depend on the dielectric properties of the insulator Al₂O₃ and the trapped electron density at the interfaces between MS and MIS structures. The M'' has a peak point for both structures in a given frequency range. The frequency ranges from the bottom to peak position of the M'' characteristics determine the mobile distances of the charge carriers at long distances. Otherwise, the peak position of M'' shifts to the left due to the effect of the insulating layer.

We believe this study will clarify the characteristics of MIS capacitors and help in finding solutions to some problems in interface states due to the fact that minimizing the interface states between metal-semiconductor on MIS structure with high dielectric material Al_2O_3 . Hence, our method in this study will considerably contribute to the production of electronic devices with metal-insulator-semiconductor. In addition, it is thought that such materials will increase the current level of MIS electronic devices in the future due to the minimum interface conditions. In conclusion, the Al_2O_3 interface insulating layer leads to a significant improvement in capacitance and dielectric constant compared to SiO_2 so that more charge or energy can be stored.

Funding

This work was supported by the Düzce University Scientific Research Projects [Project number: 2013.07.02.204]

The Declaration of Conflict of Interest / Common Interest

No conflict of interest or common interest has been declared by the authors.

Authors' Contribution

In this study, the contributions of the authors in the research, writing and Review & Editing stages are equal.

The Declaration of Ethics Committee Approval

The authors declare that this document does not require an ethics committee approval or any special permission.

The Declaration of Research and Publication Ethics

The authors of the paper declare that they comply with the scientific, ethical and quotation rules of SAUJS in all processes of the paper and that they do not make any falsification on the data collected. In addition, they declare that Sakarya University Journal of Science and its editorial board have no

responsibility for any ethical violations that may be encountered, and that this study has not been evaluated in any academic publication environment other than Sakarya University Journal of Science.

REFERENCES

- [1] J. Zhang, G. Zhao, Y. Li, Y. Li, and W. Liu, "Effect of Al-Zr co-doping on the electrical properties of graphene/ZnO Schottky contact," *Materials Research Express*, vol. 6, no. 12, pp. 125911, 2020.
- [2] A. Demir, İ. Yücedağ, G. Ersöz, Ş. Altındal, N. Baraz, and M. Kandaz, "A Comparative Study on the Main Electrical Parameters of Au/n-Si, Au/Biphenyl-CuPc/n-Si and Au/Biphenylsub-CoPc/n-Si Type Schottky Barrier Diodes," *Journal of Nanoelectronics and Optoelectronics*, vol. 11, no. 5, pp. 620-625, 2016.
- [3] Ç. S. Güçlü, A. F. Özdemir, A. Kökce, and Ş. Altındal, "Frequency and Voltage-Dependent Dielectric Properties and AC Electrical Conductivity of (Au/Ti)/ Al_2O_3 /n-GaAs with Thin Al_2O_3 Interfacial Layer at Room Temperature," *Acta Physica Polonica A*, vol. 130, no. 1, pp. 325-330, 2016.
- [4] N. Kumar and S. Chand, "Effects of temperature, bias and frequency on the dielectric properties and electrical conductivity of Ni/ SiO_2 /p-Si/Al MIS Schottky diodes," *Journal of Alloys and Compounds*, vol. 817, pp. 153294, 2020.
- [5] S. M. Sze and K. K. Ng "Physics of semiconductor devices," New York: John Wiley & Sons, 2006.
- [6] E. H. Rhoderick and R. H. Williams, "Metal Semiconductor Contacts," Oxford: Oxford University Press, 1988.

- [7] E. H. Nicollian and J. R. Brews, "MOS (metal oxide semiconductor) physics and technology," New York: John Wiley & Sons, 1982.
- [8] Y. Zhou, M. Ogawa, X. Han, and K. Wang, "Alleviation of Fermi-level pinning effect on metal/germanium interface by insertion of an ultrathin aluminum oxide," *Applied Physics Letters*, vol. 93, no. 20, pp. 202105(1-3), 2008.
- [9] S. Zheng, W. Yang, Q. Sun, L. Chen, P. Zhou, P. Wang, D. Zhang, and F. Xiao, "Schottky barrier height reduction for metal/n-InP by inserting ultra-thin atomic layer deposited high-k dielectrics," *Applied Physics Letters*, vol. 103, no. 26, pp. 261602(1-4), 2013.
- [10] Ç. G. Türk, S. O. Tan, Ş. Altındal, and B. İnem, "Frequency and voltage dependence of barrier height, surface states, and series resistance in Al/Al₂O₃/p-Si structures in wide range frequency and voltage," *Physica B: Condensed Matter*, vol. 582, pp. 411979(1-8), 2020.
- [11] A. Baradeswaran and A. E. Perumal, "Study on mechanical and wear properties of Al 7075/Al₂O₃/graphite hybrid composites," *Composites Part B: Engineering*, vol. 56, pp. 464-471, 2014.
- [12] M. W. Akhtar, Y. S. Lee, D. J. Yoo, and J. S. Kim, "Alumina-graphene hybrid filled epoxy composite: Quantitative validation and enhanced thermal conductivity," *Composites Part B: Engineering*, vol. 131, pp. 184-195, 2017.
- [13] S. Hlali, N. Hizem, and A. Kalboussi, "High-k dielectric materials for the gate oxide of a MIS capacitor: effect of interface states on the C-V characteristics," *Journal of Computational Electronics*, vol. 15, no. 4, pp. 1340-1350, 2016.
- [14] G. D. Wilk, R. M. Wallace, and J. M. Anthony, "High-κ gate dielectrics: Current status and materials properties considerations," *Journal of Applied Physics*, vol. 89, no. 10, pp. 5243-5275, 2001.
- [15] D. Shahrjerdi, E. Tutuc, and S. K. Banerjee, "Impact of surface chemical treatment on capacitance-voltage characteristics of GaAs metal-oxide-semiconductor capacitors with Al₂O₃ gate dielectric," *Applied Physics Letters*, vol. 91, no. 6, pp. 063501(1-4), 2007.
- [16] D. Hoogeland, K. B. Jinesh, F. Roozeboom, W. F. Besling, M. C. M. Van De Sanden, and W. M. M. Kessels, "Plasma-assisted atomic layer deposition of TiN/Al₂O₃ stacks for metal-oxide-semiconductor capacitor applications," *Journal of Applied Physics*, vol. 106, no. 11, pp. 114107(1-7), 2009.
- [17] Y. Xuan, P. D. Ye, and H. C. Lin, "Minority-carrier characteristics of InGaAs metal-oxide-semiconductor structures using atomic-layer-deposited Al₂O₃ gate dielectric," *Applied Physics Letters*, vol. 89, no. 13, pp. 132103(1-3), 2006.
- [18] G. Dingemans and W. M. M. Kessels, "Aluminum oxide and other ALD materials for Si surface passivation," *ECS Transactions*, vol. 41, no. 2, pp. 293-301, 2011.
- [19] J. Benick, A. Richter, M. Hermle, and S. W. Glunz, "Thermal stability of the Al₂O₃ passivation on p-type silicon surfaces for solar cell applications," *Physica Status Solidi-Rapid Research Letters*, vol. 3, no. 7-8, pp. 233-235, 2009.
- [20] G. Agostinelli, A. Delabie, P. Vitanov, Z. Alexieva, H. F. W. Dekkers, S. De Wolf, and G. Beaucarne, "Very low surface recombination velocities on p-type silicon wafers passivated with a dielectric with fixed negative charge,"

- Solar Energy Materials & Solar Cells, vol. 90, no. 18-19, pp. 3438-3443, 2006.
- [21] J. Schmidt, A. Merkle, R. Brendel, B. Hoex, M. C. M. Van De Sanden, and W. M. M. Kessels, "Surface passivation of high-efficiency silicon solar cells by atomic-layer-deposited Al_2O_3 ," *Progress in Photovoltaics: Research and Applications*, vol. 16, no. 6, pp. 461-466, 2008.
- [22] J. A. Cooper and A. Agarwal, "SiC power-switching devices-the second electronics revolution?," *Proceedings of the Institution of Electrical Engineers*, vol. 90, no. 6, pp. 956-968, 2002.
- [23] R. J. Trew, J. Yan, and P. M. Mock, "The potential of diamond and SiC electronic devices for microwave and millimeter-wave power applications," *Proceedings of the Institution of Electrical Engineers*, vol. 79, no. 5, pp. 598-620, 1991.
- [24] S. Hlali, A. Farji, N. Hizem, L. Militaru, A. Kalboussi, and A. Souifi, "High temperature and voltage dependent electrical and dielectric properties of $\text{TiN}/\text{Al}_2\text{O}_3/\text{p-Si}$ MIS structure," *Journal of Alloys and Compounds*, vol. 713, pp. 194-203, 2017.
- [25] S. Parui, A. Atxabal, M. Ribeiro, A. Bedoya-Pinto, X. Sun, R. Llopis, F. Casanova, and L. E. Hueso, "Reliable determination of the Cu/n-Si Schottky barrier height by using in-device hot-electron spectroscopy," *Applied Physics Letters*, vol. 107, no. 18, pp. 183502(1-5), 2015.
- [26] H. Kim, Y. Kim, and B. J. Choi, "Interfacial characteristics of $\text{Au}/\text{Al}_2\text{O}_3/\text{InP}$ metal-insulator-semiconductor diodes," *American Institute of Physics Advances*, vol. 8, no. 9, pp. 095022(1-8), 2018.
- [27] Ç. Ş. Güçlü, A. F. Özdemir, A. Karabulut, A. Kökçe, and Ş. Altındal, "Investigation of temperature dependent negative capacitance in the forward bias C-V characteristics of $(\text{Au}/\text{Ti})/\text{Al}_2\text{O}_3/\text{n-GaAs}$ Schottky barrier diodes (SBDs)," *Materials Science in Semiconductor Processing*, vol. 89, pp. 26-31, 2019.
- [28] F. Zhang, G. Sun, L. Zheng, S. Liu, B. Liu, L. Dong, L. Wang, W. Zhao, X. Liu, G. Yan, L. Tian, and Y. Zeng, "Interfacial study and energy-band alignment of annealed Al_2O_3 films prepared by atomic layer deposition on 4H-SiC," *Journal of Applied Physics*, vol. 113, no. 4, pp. 044112, 2013.
- [29] E. Schilirò, R. L. Nigro, P. Fiorenza, and F. Roccaforte, "Negative charge trapping effects in Al_2O_3 films grown by atomic layer deposition onto thermally oxidized 4H-SiC," *AIP Advances*, vol. 6, no. 7, pp. 075021, 2016.
- [30] C. M. Tanner, Y.-C. Perng, C. Frewin, S. E. Saddow, and J. P. Chang, "Electrical performance of Al_2O_3 gate dielectric films deposited by atomic layer deposition on 4 H-Si C," *Applied Physics Letters*, vol. 91, no. 20, pp. 203510, 2007.
- [31] G. Ersöz, İ. Yücedağ, Y. Azizian-Kalandaragh, I. Orak, and Ş. Altındal, "Investigation of electrical characteristics in $\text{Al}/\text{CdS-PVA}/\text{p-Si}$ (MPS) structures using impedance spectroscopy method," *Ieee Transactions on Electron Devices*, vol. 63, no. 7, pp. 2948-2955, 2016.
- [32] İ. Yücedağ, "On the anomalous peak at low and moderate frequency C-V curves of $\text{Al}/\text{SiO}_2/\text{p-Si}$ structure at the forward bias region," *Optoelectronics and Advanced Materials-Rapid Communications*, vol. 3, no. 6, pp. 612-615, 2009.
- [33] A. Gümüş, G. Ersöz, İ. Yücedağ, S. Bayrakdar, and Ş. Altındal, "Comparative study of the temperature-dependent dielectric properties of

- Au/PPy/n-Si (MPS)-type Schottky barrier diodes,” *Journal of the Korean Physical Society*, vol. 67, no. 5, pp. 889-895, 2015.
- [34] N. Baraz, İ. Yücedağ, Y. Azizian-Kalandaragh, G. Ersöz, İ. Orak, Ş. Altındal, B. Akbari, and H. Akbari, “Electric and dielectric properties of Au/ZnS-PVA/n-Si (MPS) structures in the frequency range of 10-200 kHz,” *Journal of Electronic Materials*, vol. 46, no. 7, pp. 4276-4286, 2017.
- [35] F. I. H. Rhouma, A. Dhahri, J. Dhahri, and M. A. Valente, “Dielectric, modulus and impedance analysis of lead-free ceramics $Ba_{0.8}La_{0.133}Ti_{1-x}Sn_xO_3$ ($x=0.15$ and 0.2),” *Applied Physics A Materials Science & Processing*, vol. 108, no. 3, pp. 593-600, 2012.
- [36] N. Shiwakoti, A. Bobby, K. Asokan, and B. Antonya, “Temperature dependent dielectric studies of Ni/n-GaP Schottky diodes by capacitance and conductance measurements,” *Materials Science in Semiconductor Processing*, vol. 42, pp. 378-382, 2016.
- [37] H. N. Chandrakala, B. R. Shivakumaraiah, and G. M. M. Siddaramaiah, “The influence of zinc oxide-cerium oxide nanoparticles on the structural characteristics and electrical properties of polyvinyl alcohol films,” *Journal of Materials Science*, vol. 47, no. 23, pp. 8076-8084, 2012.
- [38] D. E. Yıldız, M. Yıldırım, and M. Gökçen, “Investigation on dielectric properties of atomic layer deposited Al_2O_3 dielectric films,” *Journal of Vacuum Science & Technology A*, vol. 32, no. 3, pp. 031509(1-5), 2014.
- [39] İ. Yücedağ, A. Kaya, and Ş. Altındal, “On the frequency dependent negative dielectric constant behavior in Al/Co-doped (PVC+TCNQ)/p-Si structures,” *International Journal of Modern Physics B*, vol. 28, no. 23, pp. 1450153(1-15), 2014.
- [40] İ. Yücedağ, A. Kaya, H. Tecimer, and Ş. Altındal, “Temperature and voltage dependences of dielectric properties and ac electrical conductivity in Au/PVC+TCNQ/p-Si structures,” *Materials Science in Semiconductor Processing*, vol. 28, pp. 37-42, 2014.
- [41] A. Kaya, İ. Yücedağ, H. Tecimer, and Ş. Altındal, “A comparative electric and dielectric properties of Al/p-Si structures with undoped and Co-doped interfacial PVA layer,” *Materials Science in Semiconductor Processing*, vol. 28, pp. 26-30, 2014.
- [42] Y. Şafak Asar, T. Asar, Ş. Altındal, and S. Özçelik, “Investigation of dielectric relaxation and ac electrical conductivity using impedance spectroscopy method in (AuZn)/TiO₂/p-GaAs(110) schottky barrier diodes,” *Journal of Alloys and Compounds*, vol. 628, no. 442-449, 2015.
- [43] T. Badapanda, S. Sarangi, S. Parida, B. Behera, B. Ojha, and S. Anwar, “Frequency and temperature dependence dielectric study of strontium modified Barium Zirconium Titanate ceramics obtained by mechanochemical synthesis,” *Journal of Materials Science: Materials in Electronics*, vol. 26, no. 5, pp. 3069-3082, 2015.
- [44] M. N. Siddique, A. Ahmed, and P. Tripathi, “Dielectric relaxation and Hopping conduction mechanism in $Ni_{1-x}Sr_xO$ nanostructures,” *Materials Chemistry and Physics*, vol. 239, pp. 121959, 2020.
- [45] S. Kraiem, K. Khirouni, and S. Alaya, “AC electrical properties of Schottky diode based on nanocrystalline silicon thin films,” *Physica B: Condensed Matter*, vol. 584, pp. 412108, 2020.

JOURNAL OF SCIENCE



SAKARYA UNIVERSITY

Sakarya University Journal of Science

ISSN 1301-4048 | e-ISSN 2147-835X | Period Bimonthly | Founded: 1997 | Publisher Sakarya University |
<http://www.saujs.sakarya.edu.tr/en/>

Title: Phytochemical Screening of Bioactive Components of Medicinal Plant *Ajuga chamaepitys* subsp. *laevigata* (Banks & Sol.) P.H.Davis and *Ajuga bombycina* Boiss. by GC-MS Analysis

Authors: Alevcan KAPLAN

Received: 2020-05-26 03:45:08

Accepted: 2020-08-08 22:15:51

Article Type: Research Article

Volume: 24

Issue: 5

Month: October

Year: 2020

Pages: 1053-1064

How to cite

Alevcan KAPLAN; (2020), Phytochemical Screening of Bioactive Components of Medicinal Plant *Ajuga chamaepitys* subsp. *laevigata* (Banks & Sol.) P.H.Davis and *Ajuga bombycina* Boiss. by GC-MS Analysis. *Sakarya University Journal of Science*, 24(5), 1053-1064, DOI: <https://doi.org/10.16984/saufenbilder.742691>

Access link

<http://www.saujs.sakarya.edu.tr/en/pub/issue/56422/742691>

New submission to SAUJS

<http://dergipark.org.tr/en/journal/1115/submission/step/manuscript/new>



Phytochemical Screening of Bioactive Components of Medicinal Plant *Ajuga chamaepitys* subsp. *laevigata* (Banks & Sol.) P.H.Davis and *Ajuga bombycina* Boiss. by GC-MS Analysis

Alevcan KAPLAN*¹

Abstract

Herbal plants have been a source of food for human beings for many years; they have also frequently been used as an alternative to modern medicine. Because synthetic drugs have possible side effects and are often considerably expensive, understanding how various plants are used for the treatment of specific ailments has become increasingly important. Plant extracts contain multiple active constituents and this has led to the production of new drugs and chemicals derived from the various parts of plants. In Anatolian folk medicine, *Ajuga* L. (Lamiaceae) species are used by people in many villages and towns for the therapeutic value of their bioactive components. This study was thus designed to examine the possible bioactive components of *Ajuga bombycina* Boiss. (an endemic species) and *Ajuga chamaepitys* subsp. *laevigata* (Banks & Sol.) P.H.Davis. In the study the bioactive components of the GC-MS analysis of dried leaves and flower samples were screened using an Agilent 7890B GC-5977MSD model with hexane as solvent. Phytochemicals which have a wide range of biological applications and high therapeutic value were found in the samples.

Keywords: Medicinal plants, bioactive components, GC-MS analysis, *Ajuga* L.

*Corresponding Author: kaplanalevcan@gmail.com

¹ Batman University, ORCID: <https://orcid.org/0000-0001-6738-7527>

1. INTRODUCTION

For centuries, herbal medicine has been one of the bases of medical treatment, and such traditional medicine is still widely practiced today. The World Health Organization (WHO) has estimated that up to 80 % of people worldwide still rely on traditional medical remedies such as the use of plants [1-2]. Modern medicine recognizes herbal medicine as a form of alternative medicine because its practice is not strictly based on evidence gathered using the scientific method. On the other hand, modern medicine does use many plant-derived compounds as the basis for evidence-tested pharmaceutical drugs. Phytotherapy works to apply modern standards of testing to medicines that are derived from natural sources. Analyzing the bioactive compounds in plants has led to the discovery of new drugs which provide effective protection and treatment against various diseases [3-4].

The genus *Ajuga* L. consists of about 90 species, mostly scattered across the northern temperate zone. The genus is also seen in South Africa and Australia. Members of the genus *Ajuga* L., which belongs to the family Lamiaceae, grow naturally or are cultivated in Europe, Asia, Africa, Australia and North America [6]. The *Ajuga* genus is represented in Anatolia by 23 taxa, 13 species and 10 subspecies [7]. Most of the plants belonging to this genus are used as an anthelmintic, diuretic, anti-fungal, anti-inflammatory and antimycobacterial agents, and, in traditional medicine, for fever, toothache, dysentery, high blood pressure and gastrointestinal disorders. In addition, they are used to prevent pest growth. Phytoecdysteroids, neo-clerodane-diterpenes, diterpenes, triterpenes, sterols, anthocyanidin-glycosides, iridoid glycosides, withanolides, flavonoids, triglycerides and essential oils have been isolated from one of the members of the *Ajuga* genus. The biological, pharmacological and therapeutic properties of these compounds include anabolic, analgesic, antibacterial, antiestrogenic, anti-hypertensive, antitumor, antimalarial/antiplasmodial, antimycobacterial, antioxidant, antipyretic, larvae and insect

antifeedant, cardiotoxic, cytotoxic, hypoglycemic, vascular-relieving and insect growth effects. The *Ajuga* genus thus has both medical and economic significance. [6]

In the present study, phytochemical analysis of *A. bombycina* and *Ajuga chamaepitys* subsp. *laevigata* was carried out to identify their therapeutic value. Prior to this study, it was found that there was only a limited number studies of the bioactive composition of *A. bombycina* and *Ajuga chamaepitys* subsp. *laevigata* in the scientific literature. This research was thus conducted to define the qualitative bioactive compositions of these traditionally used medicinal plants, to identify possible drug precursors and to point the way towards further studies.

2. MATERIAL AND METHOD

2.1. Collection and Identification of Plant Material

Fully matured leaves and flowers were collected from Konya Kent Ormanı, Konya, Turkey (*Ajuga bombycina*), and Batı Raman Campus, Batman, Turkey (*Ajuga chamaepitys* subsp. *laevigata*) (Figure 1). The botanical identity of the plant was confirmed by Dr. Alevcan Kaplan. This identification was made using Volume 7 of the Flora of Turkey [8]. The collected, disease-free leaves and flowers were washed to remove dust and other plant materials, and were shade-dried at room temperature. The dried leaves and flowers were then ground to a powder using an electric grinder and kept separately for future research in lidded containers.

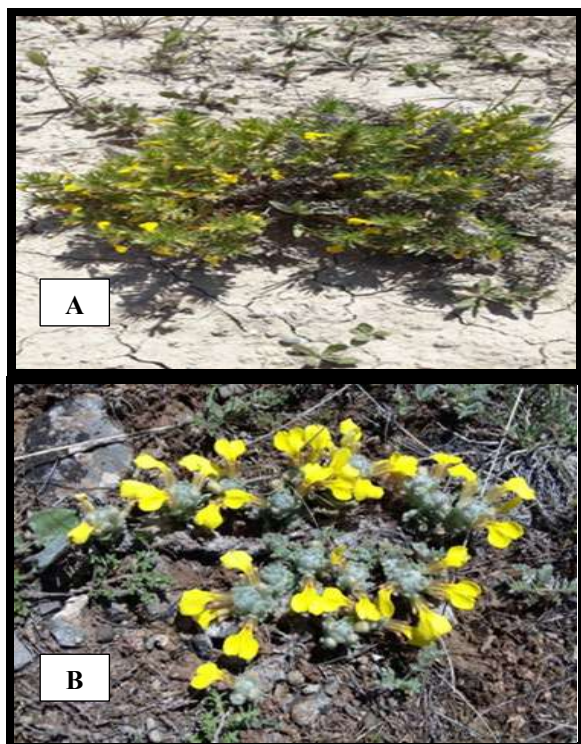


Figure 1 General view of plants (A: *Ajuga chamaepitys* subsp. *laevigata* B: *Ajuga bombycina*)
Photo: A. Kaplan

2.2. Plant Sample Extraction for GC-MS Analysis

The n-hexane extract of the plants was obtained using the Soxhlet extractor. 10 g of powdered plant samples were put into the Soxhlet extractor and the required amount was obtained by repeatedly using 100 ml of n-hexane (boiling point about 40 - 60 ° C) as solvent extract for four (4) hours. The oil was kept in a refrigerator without further processing until required for analysis.

2.3. Gas Chromatography-Mass Spectrometry Analysis

Gas chromatography-Mass spectrometry (GC-MS) analysis of n-hexane extracts of plants were performed using Agilent 7890B GC- 5977MSD model with the column length (30 m), diameter (250 μ m) and film thickness (0.25 μ m) was used with Helium (99.9995 % purity) as the carrier gas, operating in electron impact mode at 70 eV. and the GS-MS condition during the research is

following conditions. Injector temperature was 250 °C, ion-source temperature 200 °C split flow was 2.4 ml / min. The oven temperature was programmed 120 °C (5 °C / min, 7 min), 150 °C (5 °C / min, 7 min), 200 °C (5 °C / min, 7 min), 220 °C (5 °C / min, 7 min), 240 °C (5 °C / min, 7 min), 250 °C (5 °C / min, 7 min). Split flow was 2.4 ml / min and an injection volume of 1 μ l was employed (split ratio of 2:1). The hexane extract of plants were injected with syringe manually for total bioactive components of leaf and flower samples. Total GC running time is 68 min.

2.4. Identification of Compounds

Interpretation of bioactive components on mass spectrum of GC-MS was carried out using spectrometric electronic libraries (W9N11.L, MPW2011.L and RTLPEST3.L). The mass spectrum of the unknown component was compared to the spectrum of the known components stored in these libraries. The name, the nature of the compound, molecular weight, molecular formula and structure of the components of the test materials have been confirmed.

3. RESULTS AND DISCUSSIONS

Medicinal plants a revaluable sources of treatments for the prevention of diseases and protection of human health [9]. Turkey has a long tradition and knowledge of folkloric medicine and an abundance of flora, and thus provides a rich source of research on this topic. Most Turkish people living in the countryside have traditionally used plants for therapeutic purposes, generally using herbs both for nutrition and as forms of medicine. In recent years, this traditional use of plants to combat disease in Turkey has attracted the attention of a number of researchers [10]. To study this usage, plant metabolites are extracted using various methods, including maceration, boiling, Soxhlet extraction, microwave-assisted extraction, supercritical fluid extraction and the ultrasound assisted extraction method [11]. As the Soxhlet extraction technique is the easiest method, one that uses simple and inexpensive equipment and

that requires little effort, it is still routinely used in laboratories today [12]. The efficiency of extraction depends on various factors, such as the nature of the phytochemical components, the extraction method, the particle size, extraction time, temperature, pH, solute/solvent ratio, and solvent polarity [13]. Proper use of the solvent system is essential in order to achieve higher extract yields, polyphenols and bioactive compounds [14]. Hexane is used because it is a solvent that can be easily removed without leaving any residue, has a low moisture absorption and a relatively low boiling point (nonpolar solvent; dipole moment <0.1), and can easily penetrate into particles without toxicity in both liquid and vapor [15]. In this context, the bioactive composition and the main ingredients present in the *Ajuga chamaepitys* subsp. *laevigata* and *Ajuga bombycina* are shown in Tables 1 and 2, and chromatograms are presented in Figures 2 and 3, respectively.

The leaf and flower sample of *Ajuga chamaepitys* subsp. *laevigata* was air-dried and powdered and subjected to qualitative phytochemical analysis with hexane. Approximately seven bioactive compounds were identified from the sample (leaves and flowers together). The retention time of the bioactive compounds of sample varied from 11.650 to 65.225, and the area percentage varied from 1.26 to 47.57. A list of the bioactive components of the sample is given in the Table 1, with the name of the compound, molecular formula, molecular weight, retention time, peak area percentage, and the nature of the compound. The chromatogram information for the sample is given in Figure 2. It was found that main constituents of sample were 2-ethyl-1,3-hexanediol (6.27 %), neophytadiene (4.02 %), tricosane (1.26 %), pentacosane (1.86 %), heptacosane (47.57 %), eicosane (1.50 %), celidoniol (35.46 %). The compound 2-ethyl-1,3-hexanediol is known for its antiparasitic qualities and is used in ectoparasiticides, incl. scabicides, insecticides and repellents [16-17]. Neophytadiene has been reported to have antimicrobial, antioxidant, antiviral, antifungal activities, to be effective against lung cancer cells and to have good analgesic, antipyretic and anti-inflammatory






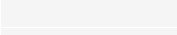

effects [18-23]. Tricosane is known for to be effective against the foraging behavior of *Trichogrammatids*, cruciferous host plants and host larval bodies of *Plutella xylostella* and for behavioural manipulation of *Cotesia plutellae* [24-25-26]. Pentacosane is a volatile pheromone and induces avoidance responses in aphid parasitoids with varying host ranges [27-28]. Heptacosane has antioxidant, antibacterial, antimalarial, antitumor and antidermatophytic effects [29-30-31]. Eicosane is known for its antioxidant and antitumor activity [32]. Celidoniol is antibacterial and anti-inflammatory, and is involved in chemical communication especially in the *Anopheles stephensi* mosquito and is a pheromone of *Orgyia leucostigma* [33-34-35-36]. Based on GC-MS studies, most of the chemical components appear to be biologically active compounds and have been found to have pharmacological activities that have therapeutic effects. The presence of different bioactive compounds justifies the use of the leaf for various ailments by traditional practitioners. In particular, the high percentage of celidoniol and heptacosane, which are major components with very different biological activities, is advantageous in using the plant. In addition, the results of the GC-MS profile can be used as a pharmacognostical tool for plant identification. [37] isolated a new clerodane diterpene and some other compounds from the *Ajuga chamaepitys* subsp. *laevigata* plant. Among the compounds they isolated were ajugalaevigatic acid, a diterpene, (13S)-15-hydroxyabd-8 (17)-en-19-oic acid, a steroidal glucoside, 3-O- β -D-glucopyranosyl-stigmasta-5,25-diene, and triterpenes, α - and β -amyrin and ursolic acid. They performed a structural elucidation of the compounds by NMR and MS spectroscopic analysis. [38] detected 19 bioactive components in leaf extracts and 13 in flower extracts of *Tagetes erecta* L. This is similar to present study, in which celidoniol was found to be among the dominant components. In addition, [39] determined the bioactive components of *Barleria courtallica* in which heptacosane was among the dominant compounds in their studies. This result is similar to that of the present study. Most of these phytochemicals were also identified from

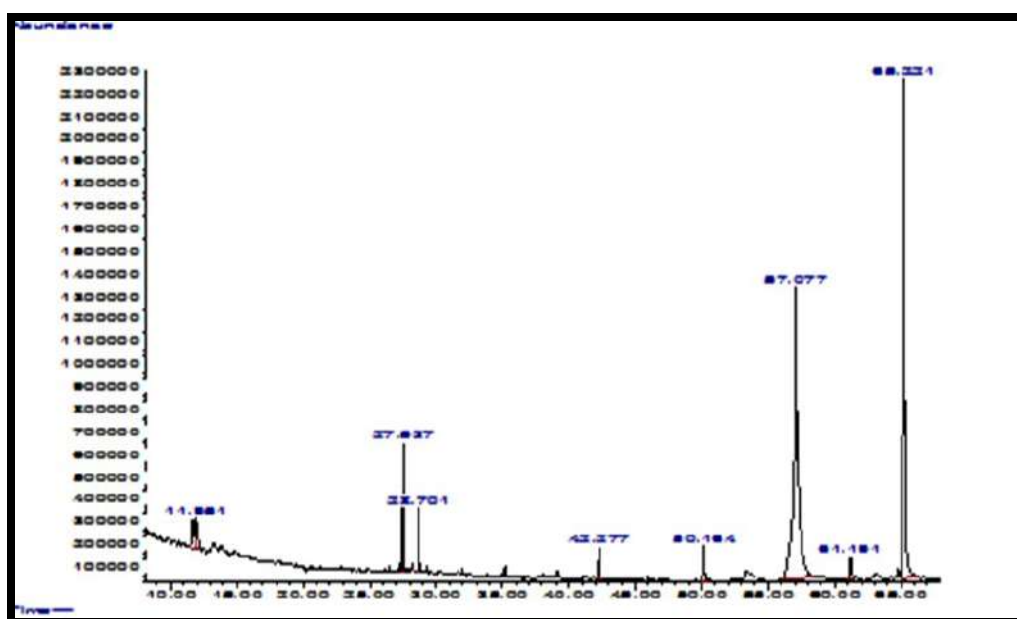
various plant extracts by [40] from *Hugonia mystax* L.; [41] from *Lawsonia inermis* Linn.;

[42] from *Aplotaxis auriculata*.

Table 1

GC-MS analysis of bioactive components in hexane extract of *Ajuga chamaepitys* subsp. *laevigata*

No	Name of the compound	Molecular formula	Molecular weight	RT	Peak area(%)	Nature of the compound	Chemical structure
1	2-Ethyl-1,3hexanediol	C ₈ H ₁₈ O ₂	146.23 g mol ⁻¹	11.650	6.27	Aliphatic alcohol	
2	Neophytadiene	C ₂₀ H ₃₈	278.5 g mol ⁻¹	27.534	4.02	Aliphatic acyclic compound	
3	Tricosane	C ₂₃ H ₄₈	324.6 g mol ⁻¹	42.273	1.26	N-Alkane	
4	Pentacosane	C ₂₅ H ₅₂	352.7 g mol ⁻¹	50.157	1.86	N-Alkane	
5	Heptacosane	C ₂₇ H ₅₆	380.7 g mol ⁻¹	57.083	47.57	N-Alkane	
6	Eicosane	C ₂₀ H ₄₂	282.5 g mol ⁻¹	61.190	1.50	N-Alkane	
7	Celidoniol	C ₂₉ H ₆₀ O	424.8 g mol ⁻¹	65.225	35.46	N-Alkane	

Figure 2 Chromatogram of *Ajuga chamaepitys* subsp. *laevigata*





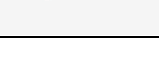
The leaf and flower sample of *Ajuga bombycina* was also air-dried and powdered and subjected to qualitative phytochemical analysis with hexane. Approximately five bioactive compounds were identified from the sample (leaves and flowers together) extracts. The retention time of the

bioactive compounds of sample varied from 11.621 to 65.225 and the area percentage varied from 2.46 to 44.52. A list of bioactive components from the sample is given in the Table 2 with the name of the compound, molecular formula, molecular weight, retention

time, peak area percentage, and the nature of the compound. The chromatogram information for the sample is given in Figure 3. It was found that main constituents of the sample were 2-ethyl-1,3hexanediol (2.46 %), trans-caryophyllene (5.80 %), docosane (45.34 %), eicosane (1.45 %), celidoniol (44.52 %). From these bioactive ingredients, docosane is report to aid in host egg parasitization, and can be used as a biocontrol agent and for antimicrobial, antioxidant and functional food nutraceutical applications [43-44-45]. Trans-caryophyllene is known for its anti-inflammatory, analgesic, antipyretic, and platelet-inhibitory activities. It acts by blocking the synthesis of prostaglandins by inhibiting cyclooxygenase, which converts arachidonic acid to cyclic endoperoxides, the precursors of prostaglandins [46-47-48]. In particular, the high percentage of celidoniol and docosane, which are major components with very different biological activities, is advantageous in using the plant in the same way. [49] screened water-distilled essential oil from *Ajuga bombycina* analyzed by GC-MS. GC-MS analysis of extract of *Ajuga bombycina* aerial parts revealed the presence of various chemical component and the prevailing

components in water extract were β -pinene (28.2 %), α -pinene (18.5 %), germacrene D (8.5 %), and β -phellandrene + limonene (6.9 %). [50] screened the bioactive components of *Plectranthus amboinicus* leaves using GC-MS. GC-MS analysis of extract of *Plectranthus amboinicus* leaves found that they also contained celidoniol (nonacosane) as the dominant component. While [41] and [51] found that the plant extracts used in their studies contain less docosane (0.17 % and 0.29 %, respectively), a high amount of docosane was obtained in the present study (45.34 %). This suggests that using the plant in areas where the docosane molecule is frequently used will be advantageous. Similarly, a GC-MS analysis of the bioactive components of *Evolvulus alsinoides* (L.) was performed by [52]. They identified 16 bioactive compounds from whole plant ethanolic extracts and reported that the bioactive compounds contained in *Evolvulus alsinoides* had a wide range of benefits. The study thus supported their traditional use for various disorders.

Table 2
GC-MS analysis of bioactive components in hexane extract of *Ajuga bombycina*

No	Name of the compound	Molecular formula	Molecular weight	RT	Peak area (%)	Nature of the compound	Chemical structure
1	2-Ethyl-1,3hexanediol	C ₈ H ₁₈ O ₂	146.23 g mol ⁻¹	11.621	2.46	Aliphatic alcohol	
2	trans-Caryophyllene	C ₁₅ H ₂₄	204.35 g mol ⁻¹	11.936	5.80	Aliphatic heteropolycyclic compound	
3	Docosane	C ₂₂ H ₄₆	310.6 g mol ⁻¹	57.083	45.34	N-Alkane	
4	Eicosane	C ₂₀ H ₄₂	282.5 g mol ⁻¹	61.190	1.56	N-Alkane	
5	Celidoniol	C ₂₉ H ₆₀ O	424.8 g mol ⁻¹	65.225	44.52	N-Alkane	

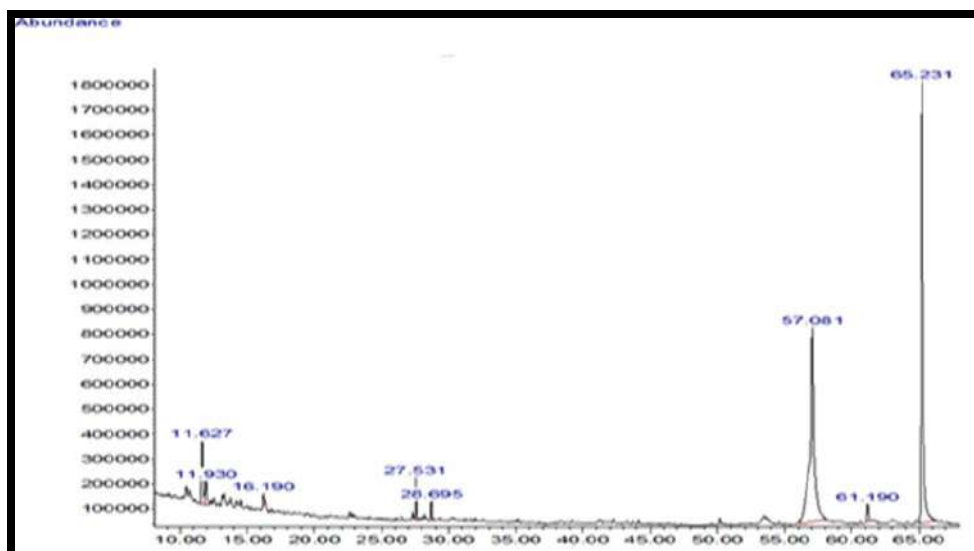


Figure 3 Chromatogram of *Ajuga bombycina*

This study subjected the hexane extracts of *Ajuga bombycina* and *Ajuga chamaepitys* subsp. *laevigata* to GC-MS analysis and various major phytochemicals were identified. Both species contain significant amounts of compounds with biologically significant activity. The physical and chemical properties of vegetable oils largely depend on the percentages and types of fatty acids they contain, and the fatty acid composition of plants is not constant. The synthesis and content of fatty acids can vary depending on genetic, ecological, morphological, physiological and cultural practices, as well as on other factors [53]. The presence of various bioactive chemical compounds supports the use of this plant by traditional medicine practitioners for various ailments [9]. Studies have been carried out in this field for a considerable period of time and this research continues today [54-61]. The present study investigated the potential for using specific plants rich in bioactive chemical components for their therapeutic effects.

4. CONCLUSION

This current investigation of *Ajuga bombycina* and *Ajuga chamaepitys* subsp. *laevigata* samples (leaf and flower) revealed that they contain a wide range of bioactive phytochemicals with high therapeutic values. In particular, celidoniol, heptacosane and docosane molecules were found in large amounts, showing that these plants are a

candidate drug plant that can be used for antibacterial, anti-inflammatory, antitumor, pheromone, antimalarial, antioxidant, antidermatophytic purposes and as nutraceutical and functional food nutraceutical ingredients. On the other hand, the remaining phytochemicals can be used for their antiparasitic and platelet-inhibitory activities, as insecticides, and are analgesics and antipyretics etc. More research on these phytochemicals will lead to lower-cost drug interventions with fewer side effects. At the same time, it will be necessary to further purify and analyze these major chemical components that play biologically active roles and to investigate them in greater details. Further research will also be necessary in order to develop these plants for use in treating specific illnesses.

Acknowledgements

The author thanks David Duffy for linguistically reviewing the paper.

Funding

The author received no financial support for the research, authorship, and/or publication of this paper.

The Declaration of Conflict of Interest/ Common Interest

No conflict of interest or common interest has been declared by the author.

The Declaration of Ethics Committee Approval

The author declares that this document does not require an ethics committee approval or any special permission.

The Declaration of Research and Publication Ethics

The author of the paper declares that she complies with the scientific, ethical and quotation rules of SAUJS in all processes of the article and that she does not make any falsification on the data collected. In addition, she declares that Sakarya University Journal of Science and its editorial board have no responsibility for any ethical violations that may be encountered, and that this study has not been evaluated in any academic publication environment other than Sakarya University Journal of Science.

REFERENCES

- [1] L. Tripathi and JN. Tripathi, "Role of Biotechnology in Medicinal Plants", *Tropical Journal of Pharmaceutical Research*, vol. 2, no. 2, pp.243-253, 2003.
- [2] SO. Odesanmi, RA. Lawal, SA. Ojokuku, "Effects of ethanolic extract of *Tetrapleura tetraptera* on Liver Function Profile and Histopathology in Male Dutch White Rabbits", *International Journal of Tropical Medicine*, vol. 4, no. 4, pp.136-139, 2009.
- [3] K. Sheeja, C. Karthar, "Activation of cytotoxic Tlymphocyte responses and attenuation of tumor growth in vitro by *Andrographis paniculata* extract and andrographolide", *Immunopharmacology and Immunotoxicology*, vol. 29, pp.81-93, 2007.
- [4] PK. Mukherjee, V. Kumar, PJ. Houjhtor, "Serenity of Indian medicinal Plants for acetyl cholinesterase inhibitory activity", *Phytotherapy Research*, vol.21 no. 12, pp. 1142-5, 2007.
- [5] YB. Köse, S. Alan, MB. Mutlu, T. Güner, *Batı Anadolu Bölgesinde Yayılış Gösteren Ajuga L. Cinsine Ait Taksonların Taksonomik ve Ekolojik Özellikleri*", Bilimsel Araştırma Projesi, Anadolu Üniversitesi, Eskişehir, 2011.
- [6] ZH. Israili, B. Lyoussi, "Ethnopharmacology of the Plants of Genus *Ajuga*", *Pakistan Journal of Pharmaceutical Sciences*, vol.22, no.4, pp. 425-462, 2009.
- [7] A. Güner, S. Aslan, T. Ekim, M. Vural, M. Babaç, "Türkiye Bitkileri Listesi Damarlı Bitkiler", *Nezahat Gökyiğit Botanik Bahçesi ve Flora Araştırmaları Derneği Yayını*, İstanbul, 2012.
- [8] PH. Davis, "Flora of Turkey and the East Aegean Islands, Edinburgh", *Edinburgh University Press*, vol.7, pp. 42- 52, 1982.
- [9] S. Padmavathy, DN. Nair, and T. Shanthi, "GC-MS Analyses of Bioactive Components in *Gaultheria fragratissima* Wall", *Asian Journal of Pharmaceutical and Clinical Research*, vol. 7, no. 1, pp. 83-85, 2014.
- [10] M. Nadiroğlu, L. Behçet, and Çakılcıoğlu U, "An ethnobotanical survey of medicinal plants in Karlıova (Bingöl-Turkey)", *Indian Journal of Traditional Knowledge*, vol.18, no. 1, pp. 76-87, 2019.
- [11] NN. Azwanida, "A review on the extraction methods use in medicinal plants, principle, strength and limitation", *Medicinal & Aromatic Plants*, vol. 4, no.3, pp. 196, 2015.
- [12] SE. Büyüktuncel, "Gelişmiş Ekstraksiyon Teknikleri I", *Hacettepe Üniversitesi*

- Eczacılık Fakültesi Dergisi, vol. 32, no. 2, pp. 209-242, 2012.
- [13] QD. Do, AE. Angkawijaya, PL. Tran-Nguyen, LH. Huynh, FE. Soetaredjo, S. Ismadji, YH. Ju, "Effect of extraction solvent on total phenol content, total flavonoid content, and antioxidant activity of *Limnophila aromatic*", Journal of Food and Drug Analysis, vol. 22, no. 3, pp. 296-302, 2014.
- [14] SB. Iloki-Assanga, LM. Lewis-Lujan, CL. Lara-Espinoza, AA. Gil-Salido, D. Fernandez-Angulo, JL. Rubio-Pino, DD. Haines, "Solvent effects on phytochemical constituent profiles and antioxidant activities, using four different extraction formulations for analysis of *Bucida buceras* L. and *Phoradendron californicum*", Complementary and Alternative Medicine BMC Research Notes, vol. 8, no. 1, pp. 396, 2015.
- [15] O. Sevindik, S. Selli, "Üzüm çekirdek yağı eldesinde kullanılan ekstraksiyon yöntemleri", Gıda, vol. 42, no. 1, pp. 95-103, 2017.
- [16] J. Drapeau, M. Verdier, D. Touraud, U. Kröckel, M. Geier, A. Rose, W. Kunz, "Effective insect repellent formulation in both surfactantless and classical microemulsions with a long-lasting protection for human beings", Chemistry & Biodiversity, vol. 6, no.6, pp. 934-47, 2009.
- [17] P. Fowler, K. Smith, J. Young, L. Jeffrey, D. Kirkland, S. Pfuhler, P. Carmichael, "Reduction of misleading ("false") positive results in mammalian cell genotoxicity assays. I. Choice of cell type", Mutation Research, vol. 742, no. 1-2, pp.11-25, 2012.
- [18] R. Jeyadevi, T. Sivasudha, A. Ilavarasi, and N. Thajuddin, "Chemical Constituents and Antimicrobial Activity of Indian Green Leafy Vegetable *Cardiospermum halicacabum*", Indian Journal of Microbiology, vol. 53, pp. 208-213, 2012.
- [19] S. Santoyo, L. Jaime, M. Plaza, M. Herrero, I. Rodriguez-Meizoso, E. Ibañez, and G. Reglero, "Antiviral compounds obtained from microalgae commonly used as carotenoid sources", Journal of Applied Phycology, vol. 24, pp. 731-741, 2012.
- [20] A. Maxia, D. Falconieri, A. Piras, S. Porcedda, B. Marongiu, M. Assunta Frau, MJ. Gonçalves, C. Cabral, C. Cavaleiro and L. Salgueiro, "Chemical Composition and Antifungal Activity of Essential Oils and Supercritical CO₂ Extracts of *Apium nodiflorum* (L.) Lag.", Mycopathologia, vol. 174, no. 1, pp. 61-67, 2012.
- [21] RB. Venkata, LA. Samuel, M. Pardha Saradhi, B. Narashimha Rao, A. Naga Vamsi Krishna, M. Sudhakar, TM. Radha Krishnan, "Antibacterial, antioxidant activity and GC- MS analysis of *Eupatorium odoratum*", Asian Journal of Pharmaceutical and Clinical Research, vol. 5, no.2, pp. 104-105, 2012.
- [22] JSM. Richardson, G. Sethi, G. Serm Lee, and SN. Abdul Malek, "Chalepin: isolated from *Ruta angustifolia* L. Pers induces mitochondrial mediated apoptosis in lung carcinoma cells", BMC Complementary and Alternative Medicine, vol. 16, pp. 389, 2016.
- [23] N. Balpınar and G. Okmen, "Biological Activities and Chemical Composition of *Senecio vernalis* Growing in the Lakes Region of Turkey", International Journal of Environmental Science and Technology, vol. 16, pp. 5205-5212, 2018.
- [24] T. Seenivasagan, AV. Paul, "Gas-chromatography and electroantennogram analysis of saturated hydrocarbons of cruciferous host plants and host larval body extracts of *Plutella xylostella* for behavioural manipulation of *Cotesia plutellae*", Indian Journal of Experimental Biology, vol. 49, no. 5, pp. 375-86. 2011.

- [25] S. Mathur, A. Zayeem, S. Kanameni, M. Tibrewal, N. Wadhwa, P. Arora, and A. Kumar, "Effect of Various Concentration of Octacosane, Pentacosane and Tricosane on Foraging Behavior of Trichogrammatids", *International Journal of Scientific and Research Publications*, vol. 2, Issue 6, 2012.
- [26] N. Samadi, A. Manayi, M. Vazirian, M. Samadi, Z. Zeinalzadeh, Z. Saghari, N. Abadian, VO. Mozaffarian, M. Khanavi, "Chemical composition and antimicrobial activity of the essential oil of *Anthemis altissima* L. var. *altissima*", *Natural Product Research*, vol. 26, no. 20, pp.1931-4, 2012.
- [27] Y. Nakashima, MA. Birkett, BJ. Pye, and W. Powell, "Chemically Mediated Intraguild Predator Avoidance by Aphid Parasitoids: Interspecific Variability in Sensitivity to Semiochemical Trails of Ladybird Predators", *Journal of Chemical Ecology*, vol. 32, pp. 1989-1998, 2006.
- [28] X. Sun, X. Zhang, G. Wu, X. Li, F. Liu, Z. Xin, and J. Zhang, "n-Pentacosane Acts as both Contact and Volatile Pheromone in the tea Weevil, *Mylocerinus aurolineatus*", *Journal of Chemical Ecology*, vol. 43, pp. 557- 562, 2017.
- [29] JR. Kuate, JM. Bessière, PH. Zollo, SP. Kuate, "Chemical composition and antidermatophytic properties of volatile fractions of hexanic extract from leaves of *Cupressus lusitanica* Mill. from Cameroon", *Journal of Ethnopharmacology*, vol. 16, no.103(2), pp. 160-5, 2006.
- [30] S. Kumar, R. Malhotra, D. Kumar, "*Euphorbia hirta*: Its chemistry, traditional and medicinal uses, and pharmacological activities", *Pharmacognosy Reviews*, vol. 4, no. 7, pp.58-61, 2010^a.
- [31] MB. Jemia, C. Formisano, S. Bancheva, M. Bruno, F. Senatore, "Chemical composition of the essential oils of *Centaurea formanekii* and *C. orphanidea* ssp. *thessala*, growing wild in Greece", *Natural product communications*, vol. 7, no.8, pp. 1083-6, 2012.
- [32] R. Sivasubramanian and P. Brindha, "*In-vitro* cytotoxic, antioxidant and GC-MS studies on *Centratherum punctatum* cass.", *International Journal of Pharmaceutical Sciences*, vol. 5, no. 3, pp. 364-367, 2013.
- [33] GG. Grant, D. Frech, L. MacDonald, KN. Slessor, and King GGS. "Copulation releaser pheromone in body scales of female whitemarked tussock moth, *Orgyia leucostigma* (Lepidoptera: Lymantriidae): identification and behavioral role", *Journal of Chemical Ecology*, vol. 13, pp. 345-356, 1987.
- [34] B. Brei, JD. Edman, B. Gerade, and JM. Clark, "Relative Abundance of Two Cuticular Hydrocarbons Indicates Whether a Mosquito Is Old Enough to Transmit Malaria Parasites", *Journal of Medicinal Entomology*, vol. 41, no. 4, pp. 807-809, 2004.
- [35] MB. Zakariaa, Z. Vijayasekarana Ilhama, and NA. Muhamad, "Anti-Inflammatory Activity of *Calophyllum inophyllum* Fruits Extracts", *Procedia Chemistry*, vol. 13, pp. 218-22, 2014.
- [36] YB. Köse, G. Iscan, and B. Demirci, "Antimicrobial Activity of the Essential Oils Obtained from Flowering Aerial Parts of *Centaurea lycopifolia* Boiss. et Kotschy and *Centaurea cheirolopha* (Fenzl) Wagenitz from Turkey", *Journal of Essent Oil Bear Plants*, vol. 19, no. 3, pp. 762-768, 2016.
- [37] G. Topçu, G. Kökdil, Z. Türkmen, W. Voelter, E. Adou, and G. David, "A new Clerrodane Diterpene and Other Constituents from *Ajuga chamaepitys* ssp. *laevigata*", *Zeitschrift für Naturforschung B*, vol.59, pp.1, 2014.
- [38] R. Devika and Justin K, "Screening and Evaluation of Bioactive Components of *Tagetes erecta* L. By GC-MS Analysis", *Asian Journal of Pharmaceutical and*

- Clinical Research, vol. 7, no.2, pp. 58-60, 2014.
- [39] A. Ponmathi Sujatha, R. Michael Evanjaline, S. Muthukumarasamy, V. Mohan, "Determination of Bioactive Components of *Barleria Courtallica* Nees (Acanthaceae) By Gas Chromatography-Mass Spectrometry Analysis", *Asian Journal of Pharmaceutical and Clinical Research*, vol. 10, no. 6, pp. 273-283, 2017.
- [40] G. Rajeswari, M. Murugan, VR. Mohan, "GC-MS analysis of bioactive components of *Hugonia mystax* L. (Linaceae)", *Research Journal of Pharmaceutical, Biological and Chemical Sciences*, vol. 3, no. 4, pp. 301-308, 2012.
- [41] SN. Chandra Dev, De and D. Kantishree, MW. Khan, "GC-MS Analysis of Phytochemicals of Methanolic Extract of Leaves of *Lawsonia inermis* Linn.", *Indian Journal of Medical and Pharmaceutical Sciences*, vol. 3, no. 6, pp. 77-82, 2016.
- [42] C. Arunmathi and T. Malarvili, "Analysis of bioactive compounds in methanol extract of *Aplotaxis auriculata* rhizome using GC-MS", *Journal of Pharmacognosy and Phytochemistry*, vol.6, no. 3, pp. 243-247, 2017.
- [43] AVN. Paul, S. Singh, and AK. Singh, "Kairomonal effect of some saturated hydrocarbons on the egg parasitoids, *Trichogramma brasiliensis* (Ashmead) and *Trichogramma exiguum* (Hymenoptera: Trichogrammatidae)", *Journal of Applied Entomology*, vol.126, pp. 409-416, 2002.
- [44] NM. Gungumjee and SA. Hajar, "Antibacterial activities and GC-MS analysis of phytocomponents of *Ehretia abyssinica* R.Br. ex *fresen*", *International Journal of Applied Biology Pharmaceutical Technology*, vol. 6, no.2, pp. 236-241, 2015.
- [45] D. Saïdana, MA. Mahjoub, O. Boussaada, J. Chriaa, I. Chéraif, Daami M, Z. Mighri, AN. Helal, "Chemical composition and antimicrobial activity of volatile compounds of *Tamarix boveana* (Tamaricaceae)", *Microbiological Research*, vol. 163, no. 4, pp. 445-55, 2008.
- [46] B. Bakır, A. Him, H. Özbek, E. Düz, M. Tütüncü, "Investigation of the Anti-inflammatory and Analgesic Activities of β -caryophyllene", *International Journal of Essential Oil Therapeutics*, vol. 2, pp. 41-44, 2008.
- [47] JP. Pinho, AS. Silva, BG. Pinheiro, I. Sombra, C. Bayma Jde, S. Lahlou, PJ. Sousa, PJ. Magalhães, "Antinociceptive and antispasmodic effects of the essential oil of *Ocimum micranthum*: potential anti-inflammatory properties", *Planta Medica*, vol. 78, no. 7, pp.681-5, 2012.
- [48] Anonymous.[internet]. Available from <https://pubchem.ncbi.nlm.nih.gov/compound/trans-Caryophyllene>, [cited 2020 April 09], 2020.
- [49] KHC. Baser, M. Kürkcüoğlu, and FZ. Erdemgil, "The Essential Oil of *Ajuga bombycina* from Turkey", *Chemistry of Natural Compounds*, vol.37, pp. 3, 2001.
- [50] MK. Swamy, G. Arumugam, R. Kaur, A. Ghasemzadeh, MM. Yusoff, and UR. Sinniah,"GC-MS. Based Metabolite Profiling, Antioxidant and Antimicrobial Properties of Different Solvent Extracts of Malaysian *Plectranthus amboinicus* Leaves", *Evidence-Based Complementary and Alternative Medicine*, 2017.<https://doi.org/10.1155/2017/1517683>.
- [51] A. Yaşar, O. Üçüncü, C. Güleç, H. İnceer, S. Ayaz, and N. Yaylı, "GC-MS Analysis of Chloroform Extracts in Flowers, Stems, and Roots of *Tripleurospermum callosum*", *Pharmaceutical Biology*, vol. 43, no. 2, pp. 108-112, 2005.

- [52] D. Gomathi, M. Kalaiselvi, G. Ravikumar, K. Devaki, C. Uma, "GC-MS analysis of bioactive compounds from the whole plant ethanolic extract of *Evolvulus alsinoides* (L.) L.", *Journal of Food Science and Technology*, vol. 52, no. 2, pp.1212- 1217, 2015.
- [53] Ö. Kılıç, "*Marrubium parviflorum* subsp. *parviflorum* Bitkisinin Yağ Asidi ve Uçucu Yağ Kompozisyonu", *Mus Alparslan University Journal of Science*, vol. 6, no. 1, pp. 487-491, 2018.
- [54] P. Kumar, PS. Kumaravel, and C. Lilitha, "Screening of Antioxidant, Total Phenolic and GC-MS study of *Vitex negundo*", *Africa Journal of Biochemistry and Research*, vol. 4, no.7, pp.191-195, 2010^b.
- [55] P. Kalaisezhiyen, V. Sasikumar, "GC-MS evaluation of Chemical constituents from methanolic leaf extract of *Kedrostis foetidissima* (Jacq.) Cogn.", *Asian Journal of Pharmaceutical and Clinical Research*, vol. 5, no. 4, pp. 77-81, 2012.
- [56] M. Sermakkani and V. Thangapandian, "GC-MS analysis of *Cassia italica* leaf methanol extract", *Asian Journal of Pharmaceutical Clinic Research*, vol. 5, no. 2, pp. 90-94, 2012.
- [57] MI. Bello, SB. Ishidi, and IY. Sudi, "Phytochemical Screening and Antimicrobial Activity of Ethanolic and Aqueous Stembark Extracts of *Boswellia dalzielii* (Hutch)", *Asian Journal of Biochemical and Pharmaceutical*, vol. 1, no. 3, pp. 194- 198, 2013.
- [58] K.Shibula, S. Velavan, "Determination of Phytocomponents in Methanolic Extract of *Annona muricata* Leaf Using GC-MS Technique", *International Journal of Pharmacognosy and Phytochemical Research*, vol. 7, no.6, pp. 1251-1255, 2015.
- [59] P. Powar and D. Gaikwad, "GC-MS Analysis of Bioactive Compounds of *Aegiceras corniculatum* Bark.", *Indian Journal of Plant Sciences*, vol. 5, no. 3, pp. 13-17, 2016.
- [60] A. Omoregbee, M. Idu, "GC-MS analysis of ethanolic extract of *Boswellia dalzielii* Hutch (Burseraceae) root from Nigeria", *Chemistry Research Journal*, vol. 2, no. 2, pp. 33-38. 2017.
- [61] P. Yamuna, P.Abirami, P. Vijayashalini, and M. Sharmila, "GC-MS analysis of bioactive compounds in the entire plant parts of ethanolic extract of *Gomphrena decumbens* Jacq.", *Journal of Medicinal Plants Studies*, vol. 5, no.3, pp. 31-37, 2017.

JOURNAL OF SCIENCE



SAKARYA UNIVERSITY

Sakarya University Journal of Science

ISSN 1301-4048 | e-ISSN 2147-835X | Period Bimonthly | Founded: 1997 | Publisher Sakarya University |
<http://www.saujs.sakarya.edu.tr/en/>

Title: Neuro Sliding Mode Control for Exoskeletons with 7 DoF

Authors: Haci Mehmet GUZEY

Received: 2020-03-29 18:33:24

Accepted: 2020-08-09 11:33:09

Article Type: Research Article

Volume: 24

Issue: 5

Month: October

Year: 2020

Pages: 1065-1073

How to cite

Haci Mehmet GUZEY; (2020), Neuro Sliding Mode Control for Exoskeletons with 7 DoF. Sakarya University Journal of Science, 24(5), 1065-1073, DOI:

<https://doi.org/10.16984/saufenbilder.710959>

Access link

<http://www.saujs.sakarya.edu.tr/en/pub/issue/56422/710959>

New submission to SAUJS

<http://dergipark.org.tr/en/journal/1115/submission/step/manuscript/new>

Neuro Sliding Mode Control for Exoskeletons with 7 DoF

Haci Mehmet GUZEY*¹

Abstract.

In this work, a novel neuro-sliding mode controller (NSMC) is developed for a 7 degree of freedom (DoF) upper limb exoskeleton. Even though the regular sliding mode controller (SMC) is very sufficient tool when the unknown dynamics of the system is time invariant, variation in the unknown dynamics cannot be handled by regular SMC. Therefore, two-layer neural network (NN) is used to approximate the exoskeleton dynamics in the structure of the SMC. Stability of the NSMC is developed by using Lyapunov stability criteria. To validate our theoretical claims and to compare NSMC with regular SMC, simulation results are provided at the end of the paper. In the simulation section, advantage of the NSMC over regular SMC is presented in the presence of time-varying unknown exoskeleton dynamics.

Keywords: Exoskeleton, sliding mode control, neural networks.

1. INTRODUCTION

Stroke or cerebrovascular accidents are one of the main chronic diseases that seriously affect patient's daily life [1]. Stroke cases are expected to increase rapidly in the future in the world. One of the biggest reasons for this can be given as the aging of the population. In this process, motor function or upper limb injuries are expected to continue increasingly. Current researches show that therapeutic treatments consisting of intensive repeated movements of the defective limbs are some of known adequate approaches to partially rehabilitate the motor ability [2]. Nonetheless, therapeutic treatments are labor-intensive and expensive, posing a potentially undesirable difficulty to patient's families' and national healthcare services while consuming a lot of time and energy. Therefore, it is obvious that there is a

significant demand for rehabilitation tools, such as exoskeletons, can be used to enhance the motor ability of upper/lower limbs and streamline the rehabilitation process [7].

In [3], the proposed control method comprises three major layers: an operating impedance control that estimates the users' arm's motion aims and guarantees an spontaneous response of the dress to the wearers' motions; a mid-level controller that compensates the transmission backlash and calculates desired position of the actuator from the reference arm motion ; a nonlinear low-level controller which drives the actuators by compensating the nonlinear dynamics to produce the desired assistive torques at the joints.

In [4], human-machine interaction is dealt. Intentional reaching direction (IRD) is estimated.

* Corresponding Author: mehmet.guzey@erzurum.edu.tr

¹ Erzurum Technical University, ORCID: <https://orcid.org/0000-0002-2215-9536>

Motion intentions of the wearers' upper limb is estimated by designing a human-robot interface which contains force-sensing resistors in real time.

The exoskeletons developed in [3], [4] controls only arm, excludes the hand and fingers. However, in [5], authors focused on the design and control of (CAREX-7), a 7-degree-of-freedom cable-driven arm exoskeleton used for active motion (inclusive of Rotation and translation) assistance or training of the whole-arm, including hand and fingers.

In all aforementioned works [3]-[5], nonlinear system Dynamics are assumed to be known. However, the dynamics model of the exoskeletons may not be accurate and changes for each patient. Therefore, uncertain exoskeleton dynamics should be approximated through neural network algorithms. Recently, an adaptive control algorithm was developed for the upper-limb exoskeleton in [6] by using NN.

In the meanwhile, one of nonlinear control schemes which does not require system's dynamic model is the SMC scheme. SMC can be considered as a simple and capable controller since it has been utilized in variety of motion control operations. One of the power of SMC is that closed loop stability of the controlled system is guaranteed through Lyapunov's stability theorem for either non model based or model based designs [6]-[12]. The performance of non-model based SMC lean on the properly selection of nonlinear gains, that is time consuming. Nonlinear gains have to handle the entire exoskeleton dynamics that is usually uncertain and time-varying/ patient-varying. To deal with the uncertainty problem, neural network is used [11]-[13], and fuzzy logic based controller is utilized in the structure of the SMC [14].

In this work, a two-layer neural network control is utilized to estimate the exoskeleton dynamics in the structure of the SMC. Combination of the SMC and NN forms the NSMC structure. Stability of the NSMC is developed by using Lyapunov stability theorem.



Figure 1 Myomo mPower100

Next, the dynamics of the exoskeleton shown in Figure 1 and saturated controller scheme is provided.

2. EXOSKELETON DYNAMICS AND SATURATED CONTROLLER DESIGN

The general exoskeleton dynamics with saturated control is considered similar as [6]

$$M(q)\ddot{q} + C(q, \dot{q})\dot{q} + G(q) = S(\tau) - f_{dis} \quad (1)$$

with $q \in \mathcal{R}^n$ being the joint variables vector, $S(\tau)$ is the function of saturation on control torque τ . $C(q, \dot{q}) \in \mathcal{R}^{n \times n}$, $M(q) \in \mathcal{R}^{n \times n}$ and $G(q) \in \mathcal{R}^n$ are the dynamics functions of q, \dot{q} . The matrix $C(q, \dot{q})$ which is defined as $\dot{M}(q) - 2C(q, \dot{q})$ is skew-symmetric. $f_{dis} \in \mathcal{R}^n$ represents the time varying disturbance, and there exists a nonnegative constant f_M^* such that $\|f_{dis}\| \leq f_M^*$.

According to (1), define the state variables as $x_1 = q, x_2 = \dot{q}$, then the exoskeleton Dynamics can be re-written as

$$\dot{x}_1 = x_2 \quad (2)$$

$$\dot{x}_2 = M(q)^{-1}(S(\tau) - f_{dis} - C(x_1, x_2)x_2 + G(x_1)) \quad (3)$$

Define the error signals as

$$\begin{aligned} z_1 &= x_1 - x_d \\ z_2 &= x_2 - \alpha_1 \end{aligned} \tag{4}$$

with x_d is the reference angles of each joints of exoskeleton, α_1 is the virtual controller being $\alpha_1 = \dot{x}_d - K_1 z_1$, $K_1 = K_1^T > 0$. In order to cancel the saturation nonlinearity effect, the auxiliary design system is provided similar to [6] as

$$\dot{\beta} = \begin{cases} -K_\beta \beta - \frac{|z_2^T \Delta \tau| + 0.5 \Delta \tau^T \Delta \tau}{\|\beta\|^2} \beta + \Delta \tau, & \|\beta\| \geq \chi \\ 0, & \|\beta\| < \chi \end{cases} \tag{5}$$

where; $\Delta \tau = S(\tau) - \tau$, $K_\beta = K_\beta^T > 0$, $\chi > 0$ is a small positive real number, and $\beta \in \mathbb{R}^n$ is the state of the auxiliary design system. Later, the controller signal is provided in [6] as

$$\begin{aligned} \tau &= -z_1 - K_2(z_2 + \beta) + f_{dis} \\ &+ C(x_1, x_2)\alpha_1 + G(x_1) + M(x_1)\dot{\alpha}_1 \end{aligned} \tag{6}$$

with $K_2 = K_2^T > 0$.

Realize that the control torque in (6) requires all the exoskeleton dynamics, accurately. In this work, NSMC in the presence of unknown exoskeleton dynamics is investigated.

Assumption 1: In this work, the saturation function $S(\tau)$ is assumed to be zero and the control torque in the dynamics (1) is denoted as τ

3. NEURO SLIDING MODE CONTROLLER DESIGN

In this part, the NSMC of an exoskeleton (1) with 7 DoF is proposed. The main contribution of this paper is taking second order SMC structure and upgrade it by using two-layer NN to approximate uncertain exoskeleton dynamics and develop a robust controller against time-varying uncertain exoskeleton dynamics.

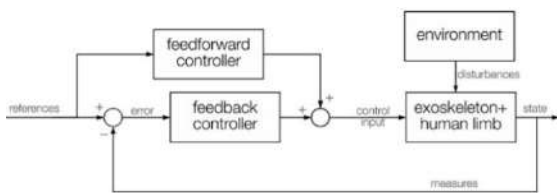


Figure 2 Exoskeleton controller scheme [15]

First, define the sliding surface as

$$s = k_1 z_1 + k_2 \dot{z}_1 \tag{7}$$

where $k_1 > 0, k_2 > 0$ are positive design parameters.

Define the Lyapunov function based on the sliding surface (7) as

$$L = \frac{1}{2} s^T s. \tag{8}$$

Take derivative of (8) and get

$$\begin{aligned} L &= s^T \dot{s} \\ &= s^T (k_1 \dot{z}_1 + k_2 \ddot{z}_1) \\ &= s^T (k_1 (x_2 - \dot{x}_d) + k_2 (\dot{x}_2 - \ddot{x}_d)) \\ &= s^T \begin{pmatrix} k_1 (x_2 - \dot{x}_d) \\ +k_2 \begin{pmatrix} M(q)^{-1} (\tau - f_{dis} - C(x_1, x_2)x_2) \\ +G(x_1) \\ -\ddot{x}_d \end{pmatrix} \end{pmatrix}. \end{aligned} \tag{9}$$

Define the control torque in (9) as

$$\tau = \frac{1}{k_2} \begin{pmatrix} M(q)(f_{dis} + C(x_1, x_2)x_2 - G(x_1)) \\ +\ddot{x}_d - k_1(x_2 - \dot{x}_d) - k_s s \end{pmatrix} \tag{10}$$

with $k_s > 0$ is a design parameter, then (9) becomes

$$L = -k_s \|s\|^2. \tag{11}$$

From (11), it can be concluded that the system exoskeleton (1) tracks its desired trajectory, x_d asymptotically.

However, when the dynamics equation used in controller (11) has uncertainties, the controller (10) is not feasible. To compensate the uncertain dynamics, SMC is provided in the literature by using sign function as

$$\tau = \frac{1}{k_2} (\ddot{x}_d - k_1(x_2 - \dot{x}_d) - k_s \text{sgn}(s)). \tag{12}$$

Realize that the controller in (12) does not require system dynamics and stability of the SMC (12) is proven in the literature [7],[10]. However, the chattering effect of the SMC and more importantly, time varying nature of the uncertain dynamics motivated the scientists to develop NN

based adaptive SMC. In order to develop the NSMC, combine the dynamics equations and define

$$f_{unc} = (f_{dis} + C(x_1, x_2)x_2 - G(x_1)). \quad (13)$$

The uncertain nonlinear dynamics (13) are given as

$$f_{unc}(\bar{z}) = \Theta^T \psi(H^T \bar{z}) + \varepsilon \quad (14)$$

where $\Theta \in \mathbb{R}^{2 \times h}$ is the ideal NN weights with h is the number of hidden layer neurons, $\psi(H^T \bar{z})$ is the basis function with $H^T \in \mathbb{R}^{h \times n}$ is the mapping from the inputs to the hidden-layer neurons, n is the number of NN inputs, ε is the NN reconstruction error that is bounded and satisfying $\|\varepsilon\| \leq \varepsilon_M$, with a positive constant ε_M , \bar{z} is the NN inputs to estimate the exoskeleton dynamics. The unknown NN weights are estimated as $\hat{\Theta}$ and estimated uncertain dynamics can be given by

$$\hat{f}_{unc}(\bar{z}) = \hat{\Theta}^T \psi(\bar{z}). \quad (15)$$

Now, the NN weight estimation errors are described as $\tilde{\Theta} = \Theta - \hat{\Theta}$ and the estimation error dynamics are reached as $\dot{\tilde{\Theta}} = -\dot{\hat{\Theta}}$. The control torque, using (15), is obtained as

$$\tau = \frac{1}{k_2} (\hat{f}_{unc} + \ddot{x}_d - k_1(x_2 - \dot{x}_d) - k_s s). \quad (16)$$

Assumption 2. The ideal NN weights are bounded such that $\|\Theta\| \leq \Theta_M$ with Θ_M being a positive bounded real number.

Theorem. Consider the exoskeleton system (1) along with the control torque (16) using the NN estimate (15) of the uncertain dynamics by using the following NN weight update rule

$$\dot{\hat{\Theta}} = \psi(z)s - k_\Theta \hat{\Theta} \quad (17)$$

where $k_\Theta > 0$ is the small positive learning rate. Consider Assumption 1 and assumption 2 holds. Then, the tracking errors and the NN weight estimation errors are semi globally uniformly ultimately bounded (SGUUB).

Proof. Define the NN estimation error on the uncertain dynamics as

$$\tilde{f}_{unc}(\bar{z}) = \tilde{\Theta}^T \psi(z) + \varepsilon \quad (18)$$

and the Lyapunov function based on the sliding surface as well as the NN estimation error as

$$L_u = \frac{1}{2} s^T s + \frac{1}{2} tr \{ \tilde{\Theta}^T \tilde{\Theta} \}. \quad (19)$$

Take derivative of (19) and get

$$\begin{aligned} \dot{L}_u &= s^T \dot{s} + tr \{ \tilde{\Theta}^T \dot{\tilde{\Theta}} \} \\ &= s^T (k_1 \dot{z}_1 + k_2 \dot{z}_2) + tr \{ \tilde{\Theta}^T \dot{\tilde{\Theta}} \} \\ &= s^T (k_1 (x_2 - \dot{x}_d) + k_2 (\dot{x}_2 - \ddot{x}_d)) + tr \{ \tilde{\Theta}^T \dot{\tilde{\Theta}} \} \\ &= s^T (k_1 (x_2 - \dot{x}_d) + k_2 (M(q)^{-1} (\tau - f_{unc}) - \ddot{x}_d)) \\ &\quad + tr \{ \tilde{\Theta}^T \dot{\tilde{\Theta}} \}. \end{aligned} \quad (20)$$

Use the controller (16) in (20) and obtain

$$\begin{aligned} \dot{L}_u &= s^T (\tilde{f}_{unc} - k_s s) + tr \{ \tilde{\Theta}^T \dot{\tilde{\Theta}} \} \\ &= -k_s \|s\|^2 + s^T \tilde{\Theta}^T \psi(z) + s^T \varepsilon - tr \{ \tilde{\Theta}^T \dot{\tilde{\Theta}} \} \end{aligned} \quad (21)$$

By using adaptation law (17) in (21) yields

$$\begin{aligned} \dot{L}_u &= -k_s \|s\|^2 + s^T \varepsilon + k_\Theta tr \{ \tilde{\Theta}^T \dot{\tilde{\Theta}} \} \\ &= -k_s \|s\|^2 + s^T \varepsilon + k_\Theta tr \{ \tilde{\Theta}^T (\Theta - \tilde{\Theta}) \} \\ &= -k_s \|s\|^2 + s^T \varepsilon - k_\Theta \|\tilde{\Theta}\|^2 + k_\Theta tr \{ \tilde{\Theta}^T \Theta \}. \end{aligned} \quad (22)$$

Using upper bounds on NN approximation error and NN weight estimation error, ε_M, Θ_M respectively in (22) yields

$$\dot{L}_u \leq -k_s \|s\|^2 + s^T \varepsilon_M - k_\Theta \|\tilde{\Theta}\|^2 + k_\Theta \|\tilde{\Theta}\| \Theta_M.$$

Now, use the Young's inequality to get

$$\begin{aligned} \dot{L}_u &\leq -k_s \|s\|^2 + \frac{1}{2} \|s\|^2 + \frac{1}{2} \varepsilon_M^2 - k_\Theta \|\tilde{\Theta}\|^2 \\ &\quad + \frac{k_\Theta}{2} \|\tilde{\Theta}\|^2 + \frac{k_\Theta}{2} \Theta_M^2. \end{aligned} \quad (23)$$

Combine the similar terms in (23) and obtain

$$\dot{L}_u \leq -\left(k_s - \frac{1}{2}\right)\|s\|^2 - \frac{k_\Theta}{2}\|\tilde{\Theta}\|^2 + \frac{1}{2}\varepsilon_M^2 + \frac{k_\Theta}{2}\Theta_M^2. \quad (24)$$

Assume that we choose $k_s > \frac{1}{2}$ and define sum of the positive terms in (24) as $Pt = \frac{1}{2}\varepsilon_M^2 + \frac{k_\Theta}{2}\Theta_M^2$, the bounds on NN estimation error and sliding surface can be calculated as

$$0 \geq -\left(k_s - \frac{1}{2}\right)\|s\|^2 + Pt$$

$$\left(k_s - \frac{1}{2}\right)\|s\|^2 \geq Pt$$

$$\|s\| \geq \sqrt{\frac{Pt}{\left(k_s - \frac{1}{2}\right)}} \quad (25)$$

The exoskeleton system becomes asymptotically stable when it moves away from the sliding surface with the altitude of (25). The bound can be reduced by choosing k_s as large as possible. Or, second bound can be found as

$$0 \geq -\frac{k_\Theta}{2}\|\tilde{\Theta}\|^2 + Pt$$

$$\frac{k_\Theta}{2}\|\tilde{\Theta}\|^2 \geq Pt$$

$$\|\tilde{\Theta}\| \geq \sqrt{\frac{2Pt}{k_\Theta}} \quad (26)$$

Finally, if one of the bounds (25) or (26) satisfies, the system becomes asymptotically stable. Therefore, the system is SGUUB.

Next, simulation results are provided to validate our theoretical claims.

4. SIMULATION RESULTS

In this part, an exoskeleton system with seven degree of freedom is controlled through NSMC. Each link is forced to track a sinusoidal trajectory given as

$$x_d = \begin{bmatrix} \sin(t) + 1, \cos(t), 2\sin(t) + 1, 2\cos(t) + 2, \\ \cos(t) + 3, \sin(t) + 3, 3\cos(t) \end{bmatrix}.$$

The controller gains are selected as

$k_1 = 10.2, k_2 = 10.1, K_1 = 1.3, k_s = 120.3$ while the initial conditions are chosen as

$$q(0) = [15 \ 14 \ 13 \ 12 \ 11 \ 10 \ 9]$$

$$\dot{q}(0) = [-1 \ -1 \ -1 \ -1 \ -1 \ -1 \ -1]$$

Case1: Time invariant Uncertain Dynamics.

In the first case, the uncertain dynamics of the exoskeleton system are assumed to be time invariant. For this scenario, two different controllers are applied: Regular SMC (12) and the NSMC (16).

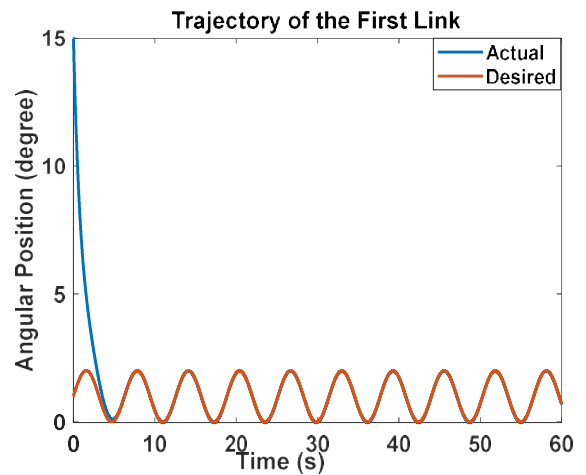


Figure 3 Desired vs actual trajectories of the first link of the Exoskeleton with NSMC

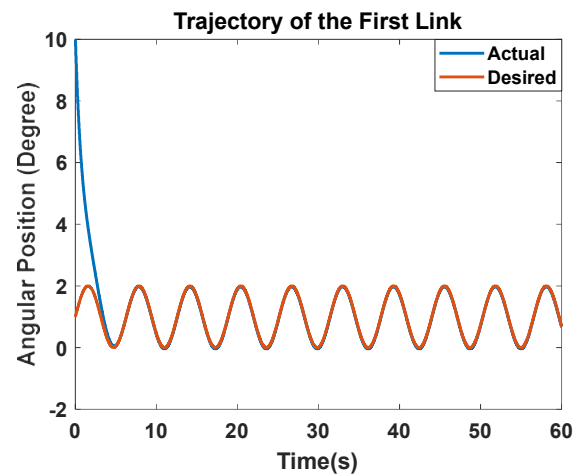


Figure 4 Desired vs actual trajectories of the first link of the Exoskeleton with SMC

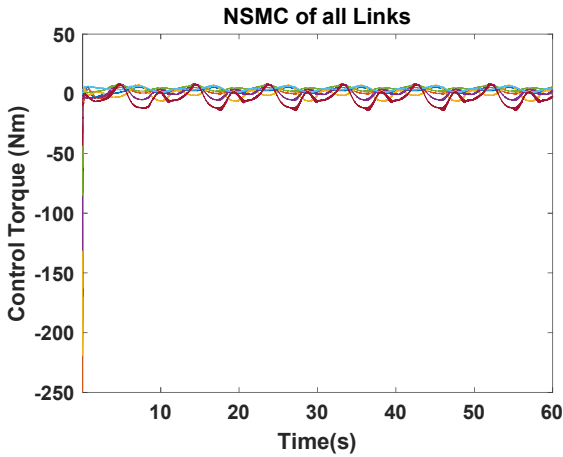


Figure 5 NSMC signal of the first Link

As shown in Fig.3 and Fig. 4, both SMC (12) and the NSMC (16) is able to stabilize the exoskeleton system in the presence of time invariant uncertain system dynamics.

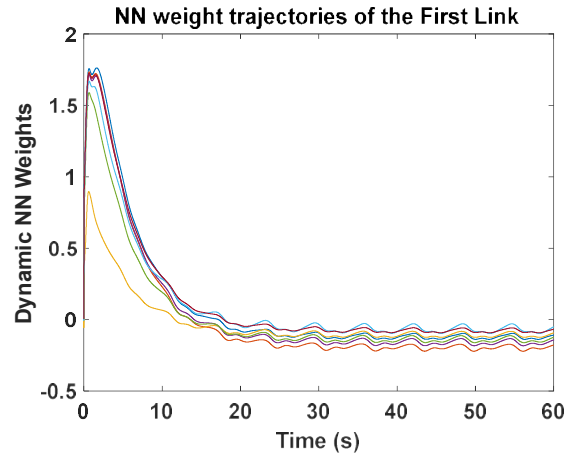


Figure 7 Trajectories of the dynamic NN weights of the first link of Exoskeleton

Fig. 7 depicts the NN weights trajectories of the first link. It is obvious that the NN weights converge after some time which means the dynamics of the exoskeleton estimated through our two layer NN design.

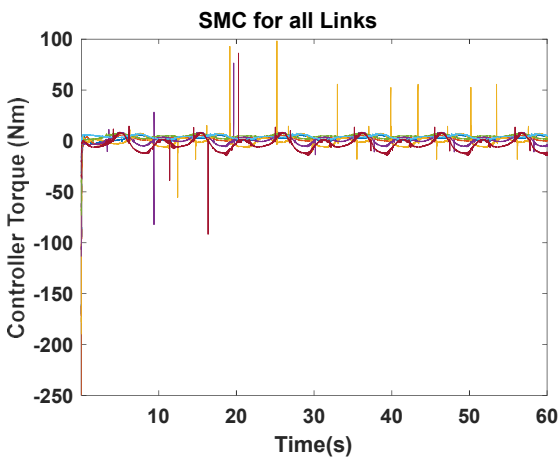


Figure 6 SMC signal of the first Link

Fig. 5 and Fig.6 illustrates the control signal of the NSMC and the regular SMC control of the first link of the exoskeleton. When compare two controller signals, it can be seen that the NSMC is smoother than the SMC. There are spikes, which is not desirable, on SMC as can be realized on Fig.6.

Fig.8 illustrates the trajectories of the other links of the exoskeleton. As can be seen, all of them converge to the desired trajectories in 4-5 seconds. The actual trajectories remain same with the desired trajectories as time evolves.

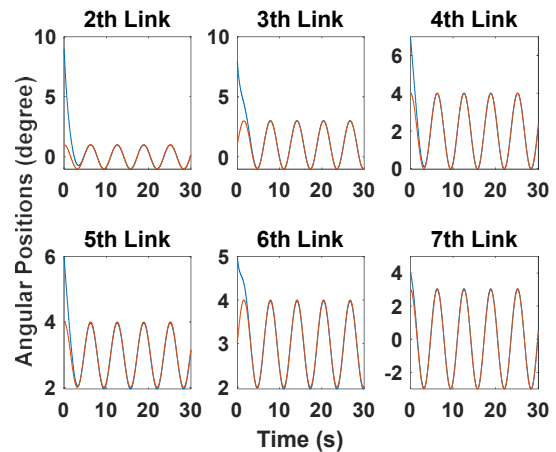


Figure 8 Desired vs actual trajectories of the other links of the Exoskeleton with NSMC

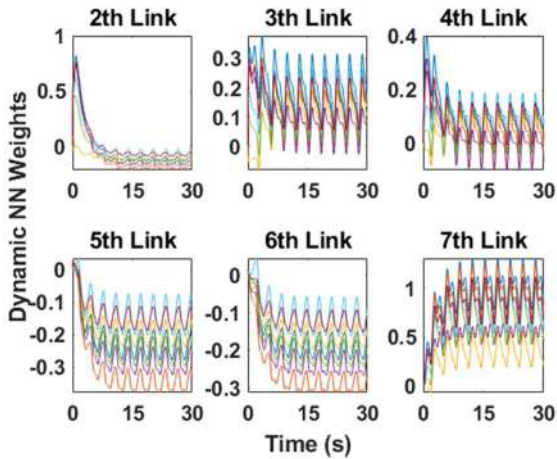


Figure 9 Trajectories of the dynamic NN weights of the other links of Exoskeleton

Dynamics weights of the NN of each link is depicted in Fig.9. Similar to the first link dynamical NN weights on Fig. 7, other links' NN weights converge after some time.

Remark: In this case, performance of the NSMC is shown and it is compared with regular SMC. Even though chattering affect is compensated for the SMC in the literature, time varying uncertain dynamics' effect cannot be compensated by using regular SMC. In the next case, performances of both SMC and NSMC compared in the presence of time varying uncertain dynamics.

Case2: Time Varying Uncertain Dynamics.

In the previous case (case 1), the dynamics of the exoskeleton is assumed to be uncertain and time invariant. In this case, the uncertain dynamics are changed on 20th second. This scenario can be applicable for most of the electro-mechanical systems.

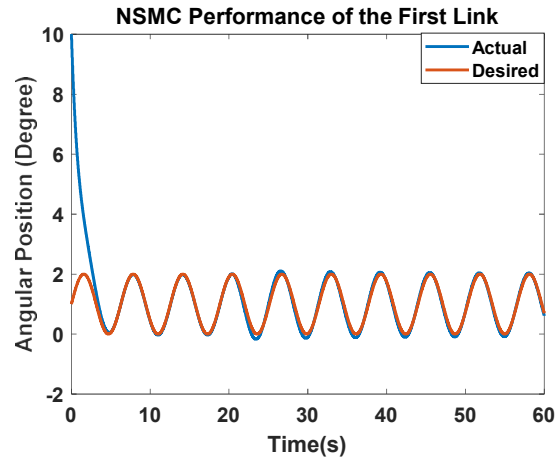


Figure 10 Desired and actual trajectory of the first link of the Exoskeleton with NSMC in the presence of time-varying uncertain dynamics

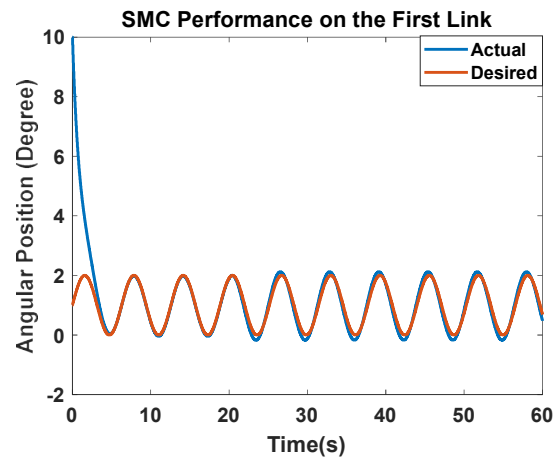


Figure 11 Desired and actual trajectory of the first link of the Exoskeleton with SMC in the presence of time-varying uncertain dynamics

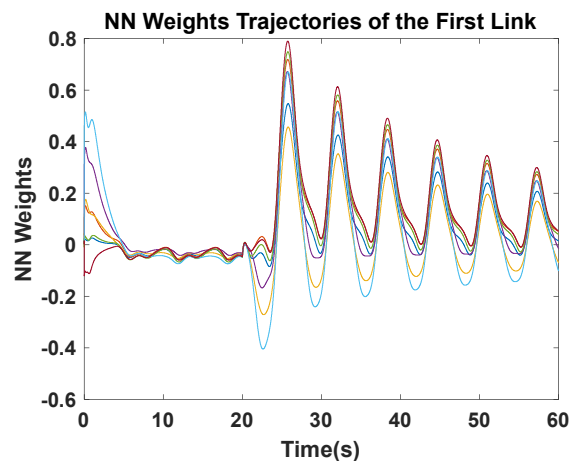


Figure 12 Trajectories of the dynamic NN weights of the first link of Exoskeleton in the presence of time-varying uncertain dynamics

Fig. 10 and Fig.11 illustrates the tracking performance of NSMC and SMC of exoskeleton in the presence of time varying uncertain dynamics. In both controllers, the dynamics are changed significantly after 20th second. Tracking performance of NSMC is effected due to significant change on system dynamics initially but it fixes the tracking error eventually as shown in Fig.10. However, the same performance cannot be seen from regular SMC on Fig. 11. The tracking error remains same after 20th second.

Dynamic NN weights trajectories of the first link can be viewed on Fig. 12. The weights converge before the dynamics change which means learns the dynamics. After the 20th second, the weights start searching again to adapt the new dynamics. It takes longer to learn the dynamics after 20th second when compare to the initial learning time. This is probably because the system angular velocities were zero at the beginning while it is nonzero on 20th second.

In the next section, some concluding remarks are given.

5. CONCLUSIONS AND FUTURE WORK

In this work, a NSMC was designed for an exoskeleton with 7 DoF in the presence of time-varying uncertain system dynamics through Lyapunov stability theorem. Both sliding surface errors and NN weight estimation errors were shown to be SGUUB with controllable bounds those are controlled through control gains and the NN weights' learning rate. Simulation results were utilized to validate that our proposed NSMC provides significantly adequate outcomes when compared to regular SMC in the presence of time-varying uncertain dynamics. For the future work, the authors can consider saturation on the control torque.

Funding

The work described in this paper is supported by (The Scientific and Technological Research Council of Turkey) TUBITAK with project number: 217E138.

The Declaration of Conflict of Interest/ Common Interest

No conflict of interest or common interest has been declared by the author.

The Declaration of Ethics Committee Approval

The author declares that this document does not require an ethics committee approval or any special permission.

The Declaration of Research and Publication Ethics

The author of the paper declares that he complies with the scientific, ethical and quotation rules of SAUJS in all processes of the article and that he does not make any falsification on the data collected. In addition, he declares that Sakarya University Journal of Science and its editorial board have no responsibility for any ethical violations that may be encountered, and that this study has not been evaluated in any academic publication environment other than Sakarya University Journal of Science.

REFERENCES

- [1] TheWorldHealthReport,2008.[Online].Available:<http://www.who.int/whr/2008/en>
- [2] S.Barreca,L.Wolf,S.Fasoli,andR.Bohannon,“Treatmentinterventionsfortheperipareticupperlimbofstrokesurvivors:Acriticalreview,” *Neurorehabilitation and Neural Repair*, vol. 17, no. 4, pp. 220–226, 2003.
- [3] B. K. Dinh, M. Xiloyannis, C. W. Antuvan, L. Cappello and L. Masia, "Hierarchical Cascade Controller for Assistance Modulation in a Soft

- Wearable Arm Exoskeleton," in *IEEE Robotics and Automation Letters*, vol. 2, no. 3, pp. 1786-1793, July 2017.
- [4] J. Huang, W. Huo, W. Xu, S. Mohammed and Y. Amirat, "Control of Upper-Limb Power-Assist Exoskeleton Using a Human-Robot Interface Based on Motion Intention Recognition," in *IEEE Transactions on Automation Science and Engineering*, vol. 12, no. 4, pp. 1257-1270, Oct. 2015.
- [5] X. Cui, W. Chen, X. Jin and S. K. Agrawal, "Design of a 7-DOF Cable-Driven Arm Exoskeleton (CAREX-7) and a Controller for Dexterous Motion Training or Assistance," in *IEEE/ASME Transactions on Mechatronics*, vol. 22, no. 1, pp. 161-172, Feb. 2017.
- [6] W. He, Z. Li, Y. Dong and T. Zhao, "Design and Adaptive Control for an Upper Limb Robotic Exoskeleton in Presence of Input Saturation," in *IEEE Transactions on Neural Networks and Learning Systems*, vol. 30, no. 1, pp. 97-108, Jan. 2019.
- [7] H. Hashimoto, "A microprocessor-based robot manipulator control with sliding mode", *IEEE Trans. on Industrial Electronics*, vol. 34, no. 1, pp. 11-18, 1987.
- [8] İ. Yazıcı, and E. K. Yaylacı "Improving Efficiency of the Tip Speed Ratio-MPPT Method for Wind Energy Systems by Using an Integral Sliding Mode Voltage Regulator", *ASME. J. Energy Resour. Technol.* May 2018; 140(5):051203. <https://doi.org/10.1115/1.4038485>.
- [9] İ. Yazıcı and E. K. Yaylacı "Fast and robust voltage control of DC–DC boost converter by using fast terminal sliding mode controller", *IET Power Electronics*, 2016, 9, (1), p. 120-125, doi: 10.1049/iet-pel.2015.0008
- [10] Y. I Stefanopoulos, E. M. Jafarov, and M. N. A. Parlakci, "A new robust continuous sliding mode control for robot manipulators with parameter perturbation", *American Control Conference*, pp. 3202-3205, 2002.
- [11] M. Soltanpour, P. Otadolajam, M. H. Khoban, "Robust control strategy for electrically driven robot manipulators: adaptive fuzzy sliding mode", *IET Science, Measurement, & Technology*, pp. 322-334, 2015.
- [12] D. E. Chaouch, Z. Ahmed-Foith, and M. F. Khelifi, "A sliding mode based control of 2dof robot manipulator using neural network", *International conference on Sciences of Electronics Technologies of Information and Telecommunications*, pp. 906-911, 2012.
- [13] Z. Chen, J. Zhang, Z. Wang, J. Zeng, "Sliding mode control of robot manipulators based on neural network reaching law", *IEEE Conference on Control and Automation*, pp. 370-373, 2007.
- [14] M. Salen and M. F. Khelifi, "Online RBF and fuzzy based sliding mode control of robot manipulator", *International conference on Sciences of Electronics Technologies of Information and Telecommunications*, pp. 896-901, 2012.
- [15] Jarrasse, Nathanael & Proietti, Tommaso & Crocher, Vincent & Robertson, Johanna & Sahbani, Anis & Morel, Guillaume & Roby-Brami, Agnes. (2014). *Robotic Exoskeletons: A Perspective for the Rehabilitation of Arm Coordination in Stroke Patients*. *Frontiers in Human Neuroscience*. 8. 10.3389/fnhum.2014.00947.

JOURNAL OF SCIENCE



SAKARYA UNIVERSITY

Sakarya University Journal of Science

ISSN 1301-4048 | e-ISSN 2147-835X | Period Bimonthly | Founded: 1997 | Publisher Sakarya University |
<http://www.saujs.sakarya.edu.tr/en/>

Title: The Role of Sodium Lauryl Sulfate on the Film Properties of Styrene-Butyl Acrylate-Acrylic Acid Copolymer Latex

Authors: Bilge EREN, Yasemin SOLMAZ

Received: 2020-07-01 12:30:06

Accepted: 2020-08-11 14:49:18

Article Type: Research Article

Volume: 24

Issue: 5

Month: October

Year: 2020

Pages: 1074-1080

How to cite

Bilge EREN, Yasemin SOLMAZ; (2020), The Role of Sodium Lauryl Sulfate on the Film Properties of Styrene-Butyl Acrylate-Acrylic Acid Copolymer Latex. Sakarya University Journal of Science, 24(5), 1074-1080, DOI:

<https://doi.org/10.16984/saufenbilder.761756>

Access link

<http://www.saujs.sakarya.edu.tr/en/pub/issue/56422/761756>

New submission to SAUJS

<http://dergipark.org.tr/en/journal/1115/submission/step/manuscript/new>



The Role of Sodium Lauryl Sulfate on the Film Properties of Styrene-Butyl Acrylate-Acrylic Acid Copolymer Latex

Bilge EREN^{*1}, Yasemin SOLMAZ²

Abstract

In this study, the concentration effect of sodium lauryl sulfate (SLS) as a surfactant in the synthesis of styrene/acrylic acid/butyl acrylate copolymer (SAC) latex particles via seeded emulsion polymerization technique was investigated. Scanning electron microscopy (SEM), minimum film-forming temperature (MFFT), differential scanning calorimetry (DSC), dynamic light scattering (DLS), and thermal gravimetric analysis (TGA) techniques were used to explain the change on physicochemical properties and morphology. The main goal is to determine an optimal surfactant concentration to obtain latexes with low MFFT. DLS studies showed that the particle size decreases 118.30 to 75.18 nm with the increase of SLS concentration. MFFT of latexes decreased with increasing SLS concentration. From the TGA curves, it was found that all the SAC latex particles exhibit a three-step decomposition process. The observed single T_g values for SAC particles showed that the latexes were prepared successfully.

Keywords: Latex, Emulsion polymer, Acrylate, Styrene.

1. INTRODUCTION

In the last decade, there has been an increase in the number of studies aimed at the development of high performance, easy to apply, low cost, and environmentally friendly binders used in the coating industry. Styrene acrylate copolymer (SAC) latexes are one of the most preferred binders due to their properties such as good dispersion in water, strong bonding with

substrates, low film-forming temperature, mechanical and chemical stability. In addition to binder applications, SAC latexes have a wide range of work in industrial applications like paint, coating, ink and adhesive [1-5]. Due to the wide range of applications of SAC latexes, there has been an increase in the number of studies focused on improving the chemical properties of SAC latexes in recent years [6-12].

* Corresponding Author: bilge.eren@bilecik.edu.tr

¹ Bilecik Şeyh Edebali University, ORCID: <http://orcid.org/0000-0001-9775-9360>

² Bilecik Şeyh Edebali University, E-Mail: yaseminnsolmazz@gmail.com
ORCID: <http://orcid.org/0000-0001-9585-9587>

SAC latexes having a minimum film-forming temperature above the application temperature show surface defects after coating [13,14]. Therefore, in practical applications, the MFFT value of the SAC latex is reduced by adding volatile aliphatic or aromatic compounds. However, many countries have regulations regarding the amount of volatile organic compounds (VOCs) that can be found in a product. For this purpose, it is necessary to develop SAC latexes containing low VOC with appropriate MFFT [15-19].

Anionic surfactants contain an anionic group attached to a long hydrophobic backbone. The negatively charged group of the surfactant used in the emulsion polymerization reaction affects the latex stability, while the hydrophobic group affects the critical micelle concentration (CMC) value, the interface tension between water and the monomer. Anionic surfactants are often used to adjust the particle size of SAC latexes and give them particle stability [20-23].

Amalvy [24] found that the particle size decreased with the increased amount of surfactant and particle stability reached a maximum value. Also, the author indicated that the water adsorption and the stability of films were changed considerably with increasing surfactant amount. Zhang et al. [25] investigated the effect of surfactant amount and surfactant types on the physical properties of latex particles. They indicated that when SLS and p-octyl polyethylene glycol phenyl ether (OP) mixed surfactants were added, at the amount of 3%, and a ratio of SLS/OP of 4/6, the latex showed lower coagulum. Chanra et al. [26] showed that monomer conversion rate (> 99%) increased with the increasing amount of water-soluble surfactant SDS from 2.0 to 4.0 wt%, but particle size increased from 80 to 102 nm [26].

Surfactants behave as "solubilizing" non-polar substances like organic monomers above their CMC. The stability of latex during and after production is important issue in latex production. The amount of surfactant has an effect on overall latex stability. Thus, the concentration of surfactant is an important consideration when designing a latex formulation. Also, the amount of surfactant used in emulsion polymerization has

a strong effect on particle size and distribution, thermal characteristics, and film formation. The goal of present study is to examine the role of anionic surfactant on the styrene-acrylic emulsion polymerization. For this purpose, the concentration effect of SLS on the physicochemical characteristics of SAC particle properties have been studied in detail. The physical and chemical properties of SAC particles were elucidated by SEM, MFFT, DSC, TGA and DLS techniques.

2. MATERIALS AND METHODS

Styrene (Sty), butyl acrylate (BA), acrylic acid (AAc) and SLS, ammonium persulfate (APS, initiator), NaHCO₃ and ammonia were all obtained from Merck. All reagents were all of analytical grades and used without further purification.

The thermal gravimetric analysis (TGA) studies were made using EXSTAR SII TGA/DTA 7200 TG/DTG apparatus. Perkin Elmer DSC 6000 apparatus were used to obtain T_g values of the latex films under N₂ atmosphere (10°C/min heating rate). Morphology of SAC particles were studied using a ZEISS Supra 40 VP model field emission scanning electron microscopy (SEM). Particle size of latexes was determined using MALVERN Nano-ZS Zeta Potentiometer. MFFT of the latex particles were determined by Rhopoint MFFT 90 device.

Sty, BA, and AAc ratios were 44/54/2 wt%, respectively. Polymerization was conducted according to our previous study about seeded emulsion polymerization [27]. Latex particle compositions are given in Table 1. The feeding and agitation speed rate were 0.1 ml/min and 200 rpm, respectively. After 10 min of seed latex particles formation, the emulsion feed was started. The SLS concentration was changed from 0.5 to 3 % of total monomers. Samples containing surfactant as 0.5, 0.9, 1.5, and 3 % of total monomer mass were designated as SAC-1, SAC-2, SAC-3, and SAC-4, respectively.

Table 1
Copolymer formulation

Components	Reactor Charge (g)	Feeding (g)
Sty	-	39.60
BA	-	48.60
AAc	0.90	0.90
APS	0.36	
Water	88.30	14.80
SLS	0.45-2.70	0.45-2.70
NaHCO ₃	0.72	0.27

3. RESULTS AND DISCUSSION

The effects of the change in surfactant concentration on the thermal behavior of latex films are shown in Figure 1. TGA measurements indicated a shift in maximum decomposition temperature (T_{max}) with increasing of surfactant concentration due to partial penetration of the polymer surface by SLS. As given in Table 1, it was found that all the SAC latex particles exhibit a three-step decomposition process. The first step about 100 °C is related to the loss of the absorbed water. The second step, between 330 °C and 420 °C, can be assigned to the decomposition of the copolymer main chain, the breakage of the ester bonds. [27,28]. The third step, between 600-800 °C, the copolymer decomposes collectively and carbonization (charcoal formation) followed by oxidation takes place [29]. The second maximum decomposition temperature (T_{max2}) for SAC samples was observed the temperature range of 383-405 °C. This means that the latex thermal stability changed with the increased SLS concentration. Also, the decomposition rate at second step increased from 15.37 to 19.85 %/min with increasing SLS concentration (Table 2). This result means that the decomposition of latex catalyzed by sulfonic acid moiety on SLS as a weak acid.

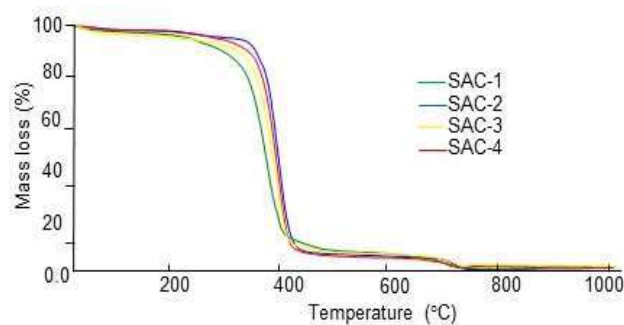


Figure 1 TG curves of the latex films recorded in nitrogen atmosphere depending on the amount of surfactant

Table 2

The effect of the amount of surfactant on the decomposition temperatures and thermal stability of latex films

Latex	T_{max} (°C)	Decomposition Rate (%/min)	$T_{%10}$ (°C)	$T_{%50}$ (°C)
SAC-1	48	0.67		
	383	15.37	277	377
	705	1.08		
SAC-2	71	0.32		
	405	18.66	332	384
	716	0.72		
SAC-3	54	0.85		
	392	16.31	306	384
	718	1.1		
SAC-4	80	0.34		
	403	19.85	327	383
	719	1.4		

The DSC curves of the prepared SAC latex films depending on the amount of SLS are given comparatively in Figure 2. The latex particles showed only a single T_g , indicating that the latex is a kind of random copolymer. The T_g values of SAC latexes decreased with increasing amount of SLS (Table 3). When the SLS amount was adjusted to be 0.5, 0.9, 1.5 and 3% of the total monomer mass, the T_g values of SAC latexes were determined to be 8.6, 7.5, -0.8 and -9.7°C, respectively. This indicates that SLS emulsifies monomers into small droplets and forms more micelles that provide the polymerization zone

[30]. When the amount of SLS is low, a sufficient amount of micelle cannot be formed, causing the monomers to not be fully emulsified. Low T_g values obtained as the amount of SLS increases means that it is difficult for Sty monomers to enter SLS micelles, and more reactive centers are encouraged for BA monomers.

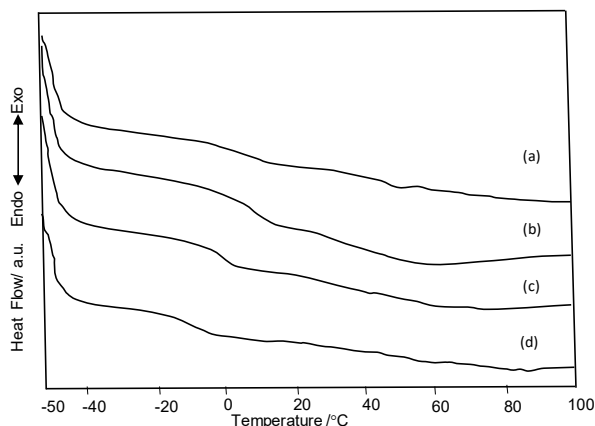


Figure 2 DSC figures of the SAC particles; SAC-1 (a), SAC-2 (b), SAC-3 (c) and SAC-4 (d)

MFFT values fluctuated with the increased amount of SLS (Table 3). This could be due to the plasticizing influence of water and SLS present in the latex during particle coalescence. However, it can be said that MFFT of latexes decreased with the decrease in T_g value as expected.

Table 3

The effect of surfactant amount on the T_g and MFFT values of the SAC latexes

Latex	T_g (°C)	MFFT (°C)
SAC-1	8.6	1
SAC-2	7.5	5.0
SAC-3	-0.8	0.3
SAC-4	-9.7	0.7

Morphological structures, average particle size and size distributions of prepared latexes were determined by SEM and DLS techniques. As seen in Figure 3, SEM images obtained can be observed quite stably, even approximately 6 months after their preparation. Figure 3 shows the role of surfactant amount on the average particle size of SAC latexes obtained using DLS technique. Average particle size obtained by both techniques are compatible with each other. As

seen in Table 3, the average particle size of prepared latexes are between 75-118 nm according to DLS data and are compatible with SEM data. According to DLS measurements, the particle size increased from 75.25 to 118.30 nm with 0.9 % SLS addition, and decreased to 75.18 nm with further increase of SLS concentration to 3.0%. It is known that the latex particles are formed by homogeneous nucleation mechanism at SLS concentration below critic micelle concentration [31]. According to this mechanism, SLS retained on monomer droplets can leave the droplet surface and then adsorb on the growing particle surface. The amount of the SLS molecules increases gradually on the surface with increasing SLS concentration in the reaction medium. It results in more suppression of growing the particles in the expanding step. Thus, the particle size becomes smaller due to higher surface charges in case of higher concentration of SLS used. The experimental particle size data of the present investigation are comparable with reported values. Amalvy [24] reported that the particle size in acrylate emulsion was decreased from 110 to 80 nm after increasing the amount of SLS from 1% to 4%. Zhang et al. [25] have found that the particle size of BA/MMA/AA copolymer was decreased from 145 to 122 nm when the surfactant concentration increased from 1.5% to 4%. Chanra et al. [26] calculated that the particle size for poly-(St-co-BA-co-MMA) decreased from 156 to 80 nm as the SDS concentration increased from 0.50 to 4.00 %.

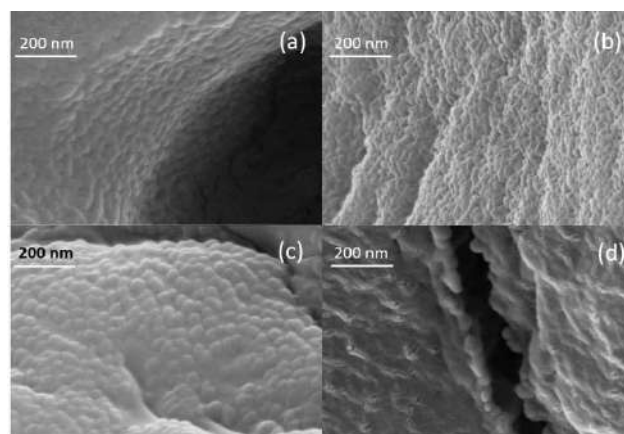


Figure 3 SEM images of the SAC particles; SAC-1 (a), SAC-2 (b), SAC-3 (c) and SAC-4 (d)

Table 4
The effect of surfactant amount on the average particle size values of the SAC latexes

Latex	Average Particle Size (nm)		PDI
	SEM	DLS	
SAC-1	87	78.25	0.014
SAC-2	110	118.30	0.150
SAC-3	83	85.16	0.073
SAC-4	72	75.18	0.236

4. CONCLUSION

In this study, optimization of process parameters was studied in detail in the preparation of SAC latexes. All prepared SAC latex particles have a single T_g value. This showed that all monomers were involved in the polymerization to form latex and copolymer formed during polymerization. It has been determined that all particles are homogeneous and the particle size and size distributions are sufficient for practical applications. The thermal stability of SAC latexes changed with the increasing amount of SLS. When the SLS amount is 0.9 %, latex is the highest of thermal stability. It was observed that T_g values of SAC latexes increased in parallel with the hard monomer ratio. MFFT values were also found to be suitable for practical coating applications. Optimization studies have shown that the thermal stability, T_g , MFFT and particle size values expected from binding acrylic latexes in industry applications are best provided by SAC-2 latex. The amount of SLS in the pre-emulsion and reactor loading stages is 0.9 % of the total monomer mass.

Acknowledgments

The authors would thank DYO Boya Fabrikaları Sanayi ve Ticaret A.Ş., İzmir for MFFT and DSC analysis of the polymers.

Funding

This study was supported by Bilecik Şeyh Edebali University with the project number of 2018-01.BŞEÜ.04-07.

The Declaration of Conflict of Interest/ Common Interest

No conflict of interest or common interest has been declared by the authors.

Authors' Contribution

B.E. planned and supervised the project. Y.S. carried out the experiments and performed the thermal analysis of samples. B.E. analyzed the results and wrote the manuscript.

The Declaration of Ethics Committee Approval

The authors declare that this document does not require an ethics committee approval or any special permission.

The Declaration of Research and Publication Ethics

The authors of the paper declare that they comply with the scientific, ethical and quotation rules of SAUJS in all processes of the paper and that they do not make any falsification on the data collected. In addition, they declare that Sakarya University Journal of Science and its editorial board have no responsibility for any ethical violations that may be encountered, and that this study has not been evaluated in any academic publication environment other than Sakarya University Journal of Science.

REFERENCES

- [1] N. K. Ray and V. Gundabala, "Synthesis and characterization of titanium dioxide encapsulated poly (styrene-co-butyl acrylate-co-acrylic acid) nanocomposite latex," *Progress in Organic Coatings*, vol. 111, pp. 93-98, 2017.
- [2] T. Ramde, L.G. Ecco and S. Rossi, "Visual appearance durability as function of natural and accelerated ageing of electrophoretic styrene-acrylic coatings: Influence of yellow

- pigment concentration,” *Progress in Organic Coatings*, vol. 103, pp. 23-32, 2017.
- [3] W. J. Grigsby. “Photooxidative stability provided by condensed tannin additives in acrylic-based surface coatings on exterior exposure,” *Journal of Coatings Technology and Research*, vol. 15, pp. 1273-1282, 2018.
- [4] M. Ataefard, “Preparing nanosilver/styrene-butyl acrylate core-shell composite via eco-friendly emulsion aggregation method as a printing ink,” *Colloid and Polymer Science*, vol. 296, pp. 819-827, 2018.
- [5] A. Rajaei and G. Farzi, “Encapsulation of paclitaxel in ultra-fine nanoparticles of acrylic/styrene terpolymer for controlled release,” *Colloid and Polymer Science*, vol. 294, pp. 95-105, 2016.
- [6] E. Limousi, N. Ballard and J. M. Asua, “The influence of particle morphology on the structure and mechanical properties of films cast from hybrid latexes,” *Progress in Organic Coatings*, vol. 129, pp. 69-76, 2019.
- [7] H. A. Abdel-Rahman, M.M. Younes and M.M. Khatta, “Effect of waste glass content on the physico-chemical and mechanical properties of styrene acrylic ester blended cement mortar composites,” *Polymers and Polymer Composites*, vol. 39, pp. 985-996, 2018.
- [8] I. Barata, A. C. Fonseca, C. S. M. F. Costa, L. Ferreira, E. Julio and J. F. J. Coelho, “Insights into the thermo-mechanical properties of films cast from emulsion terpolymers,” *Progress in Organic Coatings*, vol. 77, pp. 790-797, 2014.
- [9] O. F. Pacheco-Salazar, S. Wakayama, T. Sakai, C. R. Rios-Soberanis, J. V. Cauich-Rodriguez and J.M. Cervantes-Uc, “Damage accumulation studied by acoustic emission in bone cement prepared with core-shell nanoparticles under fatigue,” *Journal of Materials Science*, vol. 51, pp. 5635-5645, 2016.
- [10] L. Shao-Jie, H. Qian-Qian, Z. Feng-Qing and C. Xiao-Menga, “Utilization of steel slag, iron tailings and fly ash as aggregates to prepare a polymer-modified waterproof mortar with a core shell styrene-acrylic copolymer as the modifier,” *Construction and Building Materials*, vol. 72, pp. 15-22, 2014.
- [11] F. Z. Wang, Y. W. Luo, B. G. Li and S. P. Zhu, “Synthesis and Redispersibility of Poly(styrene-block n-butyl acrylate) Core-Shell Latexes by Emulsion Polymerization with RAFT Agent-Surfactant Design,” *Macromolecules*. vol. 48, pp. 1313-1319, 2015.
- [12] K. K. Jaiswal, D. Manikandan, R. Murugan and A. P. Ramaswamy, “Microwave-assisted rapid synthesis of Fe₃O₄/poly(styrene-divinylbenzene-acrylic acid) polymeric magnetic composites and investigation of their structural and magnetic properties,” *European Polymer Journal*, vol. 98, pp. 177-190, 2018.
- [13] P. A. Stewarda, J. U. Hearn and M. C. Wilkinson, “An overview of polymer latex film formation and properties,” *Advances in Colloid and Interface Science*, vol. 86, pp. 195-267, 2000.
- [14] V. Kumthekar and S. Kolekar, “Attributes of the latex emulsion processing and its role in morphology and performance in paints,” *Progress in Organic Coatings*, vol. 72, pp. 380-386, 2011.
- [15] H. Mori and A. H. E. Muller, “New polymeric architectures with (meth)acrylic acid segments,” *Progress in Polymer Science*, vol. 28, pp. 1403-1439, 2003.
- [16] M. A. Trojer, L. Nordstierna, J. Bergek, H. Blanck, K. Holmberg and M. Nydén, “Use of microcapsules as controlled release devices for coatings,” *Journal of Colloid and Interface Science*, vol. 222, pp. 18-43, 2015.
- [17] S. Srivastava, “Co-polymerization of Acrylates,” *Designed Monomers and Polymers*, vol. 12, pp. 1-18, 2009.

- [18] Z. W. Wicks, D.A. Wicks and J. W. Rosthauser, "Two package waterborne urethane systems," *Progress in Organic Coatings*, vol. 44, pp. 161-183, 2002.
- [19] J. Huybrechts, P. Bruylants, A. Vaes and A. D. Marre, "Surfactant-free emulsions for waterborne, two-component polyurethane coatings," *Progress in Organic Coatings*, vol. 38, pp. 67-77, 2000.
- [20] C. H. Lee and R. G. Mallinson, "Surfactant effects in the emulsion polymerization of vinyl acetate," *Journal of Applied Polymer Science*, vol. 39, pp. 2205-2218, 1990.
- [21] L. M. Gan, K. C. Lee, C. H. Chew and S. C. Ng, "Effects of Surfactant Concentration on Polymerization of Methyl Methacrylate and Styrene in Emulsions and Microemulsions," *Langmuir*, vol. 11, pp. 449-454, 1995.
- [22] S. Feiz and A. H. Navarchian, "Emulsion polymerization of styrene: Simulation the effects of mixed ionic and non-ionic surfactant system in the presence of coagulation," *Chemical Engineering Science*, vol. 69, pp. 431-439, 2012.
- [23] F. A. Hassaroeieh, F. F. Tabrizi and H. Abedini, "Effect of Surfactant Concentration on the Dispersion Coefficient for the Comparison of Model and Experimental Results in Emulsion Polymerization of Butadiene," *Chemical Engineering Communications*, vol. 203(5), pp. 609-618, 2016.
- [24] J. I. Amalvy, "Colloidal and film properties of carboxylated acrylic latices - effect of surfactant concentration," *Pigment & Resin Technology*, vol. 27, pp. 20-27, 1998.
- [25] Z. Faai, Y. Wang, L. Yuan and C. Chai, "Synthesis of Acrylic Emulsion Containing High Hydroxyl Content," *Journal of Macromolecular Science, Part A*, vol. A41, pp. 15-27, 2004.
- [26] J. Chanra, E. Budianto and B. Soegijono, "The Role of SDS Surfactant in The Synthesis of Polymer Hybrid Latex Poly-(St-co-BA-co-MMA) with OMMT as Filler via Mini-Emulsion Polymerization," *IOP Conference Series: Materials Science and Engineering*, vol. 515(1), 012059, 2019.
- [27] B. Eren and Y. Solmaz, "Preparation and properties of negatively charged styrene acrylic latex particles cross-linked with divinylbenzene," *Journal of Thermal Analysis and Calorimetry*, vol. 41, pp. 1331-1339, 2020.
- [28] B. Podkościelna, M. Sobiesiak, Y. Zhao, B. Gawdzik and O. Sevastyanova, "Preparation of Lignin-containing Porous Microspheres through the Copolymerization of Lignin Acrylate Derivatives with Styrene and Divinylbenzene," *Holzforschung*, vol. 69, pp. 769-776, 2015.
- [29] H. J. Naghash, A. Karimzadeh, A. R. Momeni, A. R. Massah and H. Alian, "Preparation and Properties of Triethoxyvinylsilane-Modified Styrene- Butyl Acrylate Emulsion Copolymers," *Turkish Journal of Chemistry*, vol. 31, pp. 267-269, 2007.
- [30] W. Yang, Y. Chen, D. Han and L. Zhu, "Synthesis and characterization of the fluorinated acrylic latex: Effect of fluorine-containing surfactant on properties of the latex film," *Journal of Fluorine Chemistry*, vol. 149, pp. 8-12, 2013.
- [31] N. Visaveliya, C. Hoffmann, A. Groß, E. Täuscher, U. Ritter and J. M. Koehler, "Micro-flow assisted synthesis of fluorescent polymer nanoparticles with tuned size and surface properties," *Nanotechnology Reviews*, vol. 5(2), pp. 259-272, 2016.

JOURNAL OF SCIENCE



SAKARYA UNIVERSITY

Sakarya University Journal of Science

ISSN 1301-4048 | e-ISSN 2147-835X | Period Bimonthly | Founded: 1997 | Publisher Sakarya University |
<http://www.saujs.sakarya.edu.tr/en/>

Title: Removal of Maxilon Golden Yellow GL EC 400% from the Wastewater by Adsorption Method Using Different Clays

Authors: Sevgi GÜNEŞ DURAK

Received: 2019-02-14 11:18:36

Accepted: 2020-08-11 16:03:09

Article Type: Research Article

Volume: 24

Issue: 5

Month: October

Year: 2020

Pages: 1081-1093

How to cite

Sevgi GÜNEŞ DURAK; (2020), Removal of Maxilon Golden Yellow GL EC 400% from the Wastewater by Adsorption Method Using Different Clays. Sakarya University

Journal of Science, 24(5), 1081-1093, DOI:

<https://doi.org/10.16984/saufenbilder.526957>

Access link

<http://www.saujs.sakarya.edu.tr/en/pub/issue/56422/526957>

New submission to SAUJS

<http://dergipark.org.tr/en/journal/1115/submission/step/manuscript/new>



Removal of Maxilon Golden Yellow GL EC 400% from the Wastewater by Adsorption Method Using Different Clays

Sevgi GÜNEŞ DURAK*¹

Abstract

This study was to evaluate the adsorption capability of clay minerals of halloysite, bentonite, kaolinite, and natural clay (obtained from the Avanos) to remove Maxilon Golden Yellow GL EC 400% (MGY400) from aqueous solution. Different amounts of adsorbents (0.5, 1.0, 1.5 and 2.0 g.) were taken from the samples and obtained the most dye-removal clay material and adsorbent amount were found according to the results. Adsorption was applied on all clays at 25 °C temperature, 200 rpm mixing speed and different contact times (2, 5, 10, 20, 30, 40, 50, 60 min) in the batch reactor. Bentonite provided the highest dyestuff removal. Therefore, the second phase adsorption was continued with bentonite. The adsorption with bentonite were performed at different temperature (13 °C, 25 °C, 50 °C) and pH values (2, 4, 6, 8, 10, 12). When the pH was 12 and the temperature was 25 °C, it was determined that the removal rate of the dyestuff of bentonite reached up to 99.7%. According to the results, adsorption kinetics and isotherms were investigated, and evaluation was made for working conditions.

Keywords: adsorption, bentonite, clay, dyestuff, halloysite

* Corresponding Author: ssevgigunes@gmail.com

¹ Nevşehir Hacı Bektaş Veli University, ORCID: <https://orcid.org/0000-0003-4273-7417>

1. INTRODUCTION

Significant environmental problems occur when the toxic hydrophobic organic components of industrial and agricultural activities increase uncontrollably in the soil and water [1]. The receiving environment in which the wastewater is discharged without treatment can be contaminated with several contaminants including acidic and basic substances, toxic organics, inorganics and heavy metals. Particularly, the solids and dyes resulting from the textile industry are among the important pollutant industries because they disrupt the ecological balance and cause problems in aesthetic terms [2]. In general, wastewater with dyestuff has a strong color, high pH, high chemical oxygen demand and low biodegradability [3]. Therefore, color removal from wastewater must be done before the discharge of wastewater. Many physical, chemical, and biological decolorization methods such as aerobic and anaerobic microbial degradation, coagulation, chemical oxidation, membrane separation processes, adsorption, electrochemical separation, dilution, filtration, flotation and reverse osmosis are applied for color removal. Among these methods, the most economical method is the adsorption method [2].

Adsorption is the collection of the substances dissolved in the solution on a suitable interface. As inorganic and organic substances, silica-based porous inorganic/organic hybrid substances can be used as adsorbents [4]. Adsorption processes are effective and attractive for the removal of dyestuff from the wastewater. The most commonly used of these substances is activated carbon. Activated carbon is expensive as well as it is costly to renew by thermal and chemical procedures when exhausted and leads to sorbent loss [5]. However, the use of low-cost adsorbents makes the treatment more economical. For this, as the adsorbent, the clay material often found in nature is utilized. To achieve a high efficiency of adsorption, the ion exchange capacity of the clay should be high. The substances that are to be removed from the wastewater are called adsorbate. Clay materials are of great interest due to their low costs,

abundant availability, easy accessibility, environmental friendliness and surface reactivity. The structural variability of clays, chemical stability and high specific surfaces were important in clay minerals. Clays are natural and cost-effective adsorbents which are used as catalysts in wastewater treatment [3]. Also, the clays have a high specific surface and are suitable for adsorption and removal of organic contaminants. In the production of nanocomposite polymers, as heavy metal ion adsorbents, in the production of ceramics, paper fillings and coatings, sensors and biosensors are frequently used due to their structural properties such as chemical and mechanical stability and surface diversity [6]. Many color removal studies have been carried out with the adsorption method using clays that are cheap and easy to find in nature [2], [7–11].

Adsorption is divided into three as physical, chemical and ionic. In physical adsorption, Van Der Waals forces are effective and low temperatures are sufficient for adsorption. Here, the adsorption is reversible. Chemical adsorption is irreversible. It usually occurs at high temperatures. In ionic adsorption, it is based on the principle of attracting adsorbents with electrostatic forces on the surface loaded areas. Although there is no distinction for three types, they can occur together and sequentially in an adsorption process.

The factors affecting adsorption are film diffusion, pore diffusion, mixing speed, pH, temperature, type and amount of adsorbent and properties of the solvent. In some studies, it is stated that there is a correlation between the organic matter content of the soil and the adsorption, and in some of them, there is a correlation between the adsorption and the clay content of the soil. However, in other studies, it has been stated that the behavior of the components in the soil is related to the adsorption capacity of different clay minerals and the diversity of the mineralogical structure of the soil [1]. Furthermore, the cationic dye molecules have a very high affinity for clay surfaces and are easily adsorbed when added to the clay suspension [5].

Many isotherms are used to determine the efficiency of adsorption and the factors affecting the adsorption. The most commonly used isotherms are Freundlich and Langmuir Isotherms.

Although the Langmuir equation describes adsorption on very strong homogeneous surfaces, this is not true for natural adsorbents. Because; natural adsorbents show chemical heterogeneity, indicated by different functional groups. The Langmuir equation was developed by the American scientist Irwing Langmuir, known for his work in surface chemistry. The Langmuir isotherm model, which is widely used in the explanation of chemical adsorption processes, can also be used to describe single-layer physical adsorption and adsorption processes from solution. Langmuir has developed an isotherm model for the monomolecular adsorption process by emphasizing that the active centers of the adsorbent micropore size are too small to adsorb in multiple layers [12].

The equation developed by the German physiologist Freundlich describes the physical adsorption phenomena occurring on the surface of the adsorbent in a heterogeneous structure. The surface energy distribution of the adsorbent is heterogeneous in the adsorption systems which are compatible with this equation. In other words, each of the adsorbent surface adsorption sites has different adsorption potential and each area is considered to be homogeneous in itself. Freundlich equation is derived based on the acceptance of adsorption of adsorbed molecules after adsorption on the adsorbent surface.

In this study, halloysite, bentonite, kaolinite and raw clay were used as adsorbents. MGY400 was chosen as a dyestuff. Different amounts of adsorbent (0.5, 1.0, 1.5 and 2.0 g) were taken from the samples and the most color-removing clay material and adsorbent amount was found according to the results. The highest adsorption was obtained from bentonite. Therefore, the experiments in the second stage were continued with bentonite. According to the results, adsorption capacity and isotherms were

examined and the different working conditions (pH, temperature) were evaluated.

2. MATERIALS and METHODS

2.1. Materials

Halloysite, kaolinite and bentonite were obtained from Oltu district of Erzurum. The clay which is defined as raw clay is obtained from Avanos District of Nevşehir. These four clays were first washed with 1 N H₂SO₄ and then with pure water until neutral pH. As the natural clay from the dried clay samples had a larger particle diameter, it was brought to the size range of 150-200 µm with the sieve after being beaten in the muller. Then, four samples were kept in a desiccator for use in batch adsorption test. MGY 400 was used as a dyestuff in the study. The reason for the use of this dyestuff is that it is not widely studied in the literature and is frequently used in the dyeing of fabrics in the textile industry. The chemical structure of MGY 400 is given in Figure 1 [13].

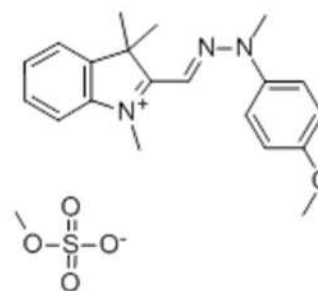


Figure 1 Chemical structure of MGY 400

Halloysite is an alumino-silicate clay mineral and its empirical formula is Al₂Si₂O₅(OH)₄. Halloysite was formed by the hydrothermal change of alumino-silicate minerals [14]. Kaolinite is clay from the industrial mineral group. Its chemical formula is Al₂Si₂O₅(OH)₄. Single-Atom alumina (AlO₆) consists of a layered silicate mineral with tetrahedral silica (SiO₄) layer attached to the octahedral layer by oxygen atoms [15]. The main component of bentonite montmorillonite and it is abundant. It consists of twin layers of tetrahedral silica sandwiching a single octahedral alumina sheet. [3]. The raw clay is brown-red. Red is due to the presence of iron oxide content. The kaolinite

used in the study is white. Research and cation exchange capacity, the pH of the initial solution, and the adsorption curves of the raw clay is a type of kaolinite is possible to say that the red form. The cation exchange capacity of halloysite, kaolinite, bentonite and raw clay was determined as 8, 4, 53 and 6 meq/100 g at pH 7 by applying the ammonium acetate method [16].

2.2. Adsorption Experiments

Adsorption experiments were performed using a mechanical shaker. Ultrapure water was used for all solutions. In the first stage, the temperature in the agitator was carried out separately for each clay at 25 °C and 200 rpm at the natural pH of each solution and 2, 5, 10, 20, 30, 40, 50 and 60 minutes. To determine the amount of active adsorbent, 0.5 g, 1.0 g, 1.5 g and 2.0 g of each clay were taken and adsorbed with 100 mL solution of dyestuff solution. The initial pH values of the clay-added dyestuff solutions are given in Table 1. There was no significant relationship between natural pH values and different concentrations of four different clays.

Table 1
Initial pHs of clay-added dyestuff solutions (In 100 mL solution)

Clay type/amount	0.5 g	1.0 g	1.5 g	2.0 g
Holloysite	7.56	7.93	8.14	8.22
Bentonite	7.00	7.06	7.01	6.86
Kaolinite	7.16	7.19	7.17	7.15
Raw Clay	7.06	7.18	7.17	7.13

The concentration of dyestuff was prepared as 100 mg/L. Adsorption time ended samples were taken to NÜFE, NF 200 device, and centrifuged for 5 min at a mixing speed of 2400 rpm and then color analyzes of solutions were performed on a spectrophotometer at 438 nm wavelength. By these measurements, the effect of adsorption time, adsorbent material and adsorbent amount on adsorption were investigated. According to the results obtained as the most color removal bentonite provides, so the second stage of the adsorption study was continued with bentonite. For this, using the amount of bentonite (0.5 g) providing the most color removal, at mixing speed of 300 rpm, different contact times (5, 10,

20, 30, 60, 120, 150, 200, 240 and 270 min), different temperatures (13 °C, 25 °C, and 50 °C) and at different pH levels (2, 4, 6, 8, 10 and 12) were studied. The reason for working in wide pH ranges and the wide temperature is that solutions consisting of clay and dyestuff give high pH [17–19] or low pH [20–22] value. The reason for working in wide temperature ranges is the thermal stability in the solution and the changes that may occur in the structural hydroxyl groups [23].

2.3. Data Analysis: Adsorption Capacity

Equation 1 is used to calculate the amount of adsorbed dye at any time in kinetic experiments.

$$q_t(\text{mg/g}) = (C_0 - C_t) \cdot \frac{V}{m} \quad (1)$$

Here C_0 , the initial liquid phase concentration (mg/L); C_t , liquid phase concentration at any one time (mg/L), q_t ; the concentration of dye in any adsorbent (mg/g); V , the volume of dye solution (L); m , mass (g) of clay used.

2.4. Data Analysis: Langmuir and Freundlich Isotherms

The most commonly used isotherms for the determination of adsorption capacity are Freundlich and Langmuir Isotherms. Although the Langmuir equation describes adsorption on very strong homogeneous surfaces, this is not true for natural adsorbents. Because; natural adsorbents, indicated by different functional groups, show chemical heterogeneity [24]. Freundlich equation is an experimentally developed isotherm used for adsorption on heterogeneous surfaces [25]. Freundlich and Langmuir Isotherms are expressed as Equation 2 and Equation 3 [26]:

$$\text{Freundlich isotherm: } \log q_e = \log K_f + (1/n) \log C_e \quad (2)$$

$$\text{Langmuir isotherm: } C_e/q_e = (1/Q_0b) + (C_e/Q_0) \quad (3)$$

Here K_f (mg/g) is the Freundlich constant, n is the Freundlich coefficient. The n parameter

describes the active sites on the adsorbent surface with low energy heterogeneity of these natural adsorbents. This value is also the adsorption density and the value between 1 and 10 is a sign of good adsorption. If n is less than 1, the adsorption is chemical. On the contrary, it can be called physical [24].

Where q_e (mg/g) amount of MGY400 dyestuff adsorbed at equilibrium, C_e (mg/L) unadsorbed MGY400 dyestuff concentration at equilibrium, b is Langmuir constant obtained from plot of $\frac{C_e}{q_e}$ versus C_e . The b value and the initial concentration C_0 used to calculate the separation factor R_L , are expressed as in Equation 4 [27].

$$R_L = 1/(1 + bC_0) \quad (4)$$

It is not desirable to have R_L greater than 1. If R_L is equal to 1, the adsorption is linear, if it is between 0 and 1, the adsorption is suitable, that is, the adsorption can be realized without taking energy from outside [26].

3. RESULTS and DISCUSSION

3.1. Effect of Initial Adsorbent Amount, Adsorbent Type and Contact Time to Adsorption Rate

One of the two factors that are important for adsorption is film diffusion and the other is pore diffusion. The material to be removed in film diffusion passes through the liquid film surrounding the adsorbent. In pore diffusion, there is a transition to pores in the inner layer of the adsorbent material. Then, the adsorbent bonding process of the desired substance is realized. Adsorption capacity, mixing speed, mixing temperature, starting pH of the mixture solution, the type and amount of adsorbent vary according to the type and amount of the adsorbed material.

The contact time is very important in adsorption applications in wastewater treatment. The fact that the adsorption reaches equilibrium is an indication of the end of the adsorption capacity. Usually, rapid adsorption occurs in the first 5 minutes depending on the surface area of the

adsorbent. By gradually filling up the adsorption areas, the adsorption becomes less efficient. The adsorption at this initial stage reflects the maximum dyestuff adsorption capacity of the adsorbent [2].

When the amount of halloysite, bentonite, kaolinite and raw clay adsorbed at different concentrations were examined, it was determined that the maximum adsorption was obtained in the amount of 0.5 g adsorbent (Fig. 2-5). The adsorption value was decreased for the amounts of 1.0, 1.5 and 2.0 g adsorbents, respectively. One of the reasons is that concentration affects chemical equilibrium. Depending on the maximum amount of adsorbent adsorbed, there is a difference between adsorption capacity and adsorbed adsorbent [28]. Another explanation for this situation is that the unit adsorption q_t decreases as the amount of adsorbent increases. That is, when the adsorption dose increases, the amount of adsorbed increases, but the unit adsorption is less since the adsorbent is calculated per unit [29].

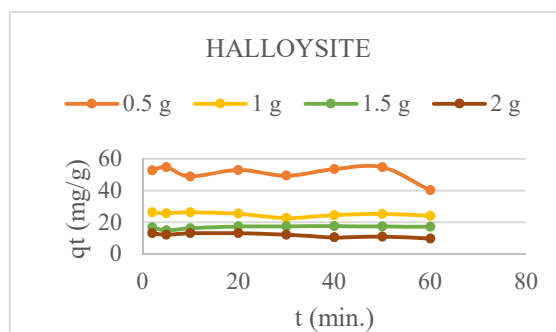


Figure 2 Changes according to the time of the amount of adsorption halloysite

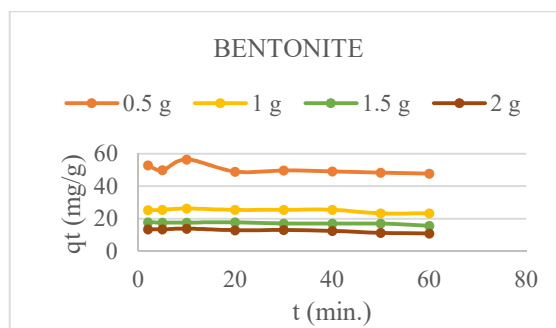


Figure 3 Changes according to the time of the amount of adsorption bentonite

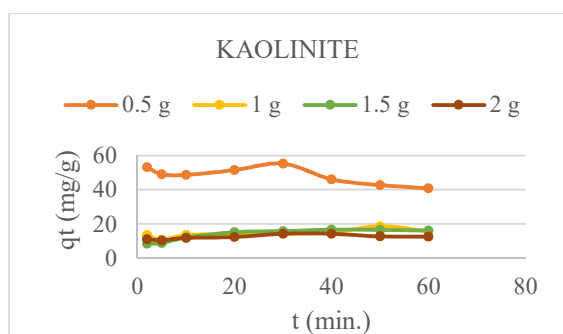


Figure 4 Changes according to the time of the amount of adsorption kaolinite

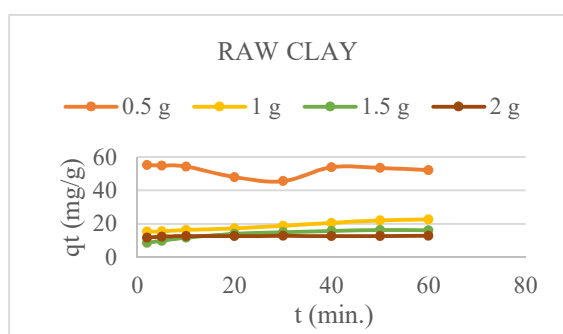


Figure 5 Changes according to the time of the amount of adsorption raw clay

When halloysite was used as the adsorbent, to reach maximum adsorption, the optimum contact times were determined as 5 minutes (54.65 mg/g) for 0.5 g adsorbent, 2 minutes (26.19 mg/g) for 1 g adsorbent, 20 minutes (17.3 mg/g) for 1.5 g adsorbent and 20 minutes (13.04 mg/g) for 2 g adsorbent (Fig. 2).

When bentonite was used as the adsorbent, to reach maximum adsorption, the optimum contact times were determined as 10 minutes (56.53 mg/g) for 0.5 g adsorbent, 10 minutes (26.27 mg/g) for 1 g adsorbent, 20 minutes (17.76 mg/g) for 1.5 g adsorbent and 10 minutes (13.86 mg/g) for 2 g adsorbent (Fig. 3).

When kaolinite was used as the adsorbent, to reach maximum adsorption, the optimum contact times were determined as 30 minutes (55.24 mg/g) for 0.5 g adsorbent, 50 minutes (18.63 mg/g) for 1 g adsorbent, 40 minutes (16.65 mg/g) for 1.5 g adsorbent and 30 minutes (14.21 mg/g) for 2 g adsorbent (Fig. 4).

When raw clay was used as the adsorbent, to reach maximum adsorption, the optimum contact

times were determined as 10 minutes (54.37 mg/g) for 0.5 g adsorbent, 60 minutes (22.69 mg/g) for 1 g adsorbent, 50 minutes (16.20 mg/g) for 1.5 g adsorbent and 60 minutes (12.80 mg/g) for 2 g adsorbent (Fig. 5).

When all results were examined, it was found that there were similar properties between halloysite and bentonite, and between kaolinite and raw clay.

The fact that halloysite has similar properties with bentonite can be explained by the fact that it has the same unstable structure with bentonite in terms of zeta potential. Therefore, it is possible to say that the zeta potential of halloysite is around -30 mV [30]. It is possible to say that the zeta potential value of bentonite, which gives similar values with halloysite in terms of contact time and amount of adsorption required for maximum adsorption, is around -30 mV. When the zeta potential value is below and above -30 mV and +30 mV, the material structure is stable. Therefore, the unstable structure of bentonite can be easily connected with MGY400, resulting in shorter and greater amounts of adsorption. Kaolinite can change from unstable to stable as the pH increases. In some studies, as the pH decreases, the zeta potential value of kaolinite approaches about -30 mV, so its stability decreases, and its binding capacity increases [31]. However, the ratio of adsorbent in the starting solution also affects zeta potential [32]. The time required for the raw clay to reach maximum adsorption is similar to that of kaolinite. Moreover, the increase of the adsorbent rate in the solution negatively affected both the adsorption time and the amount of adsorption.

However, as all of the clay types were examined, it was determined that bentonite provided the maximum dyestuff sorption (56.53 mg/g) and as soon as possible (5 min). According to this, the next step of experimental studies was continued with 0.5 g of bentonite, which provides the most effluent yield.

3.2. Effect of Initial pH, Adsorption Temperature and Contact Time to Adsorption Rate

In the second stage where the only bentonite was used, the temperature and pH were studied at six different pH values of 2, 4, 6, 8, 10 and 12 with three different temperatures as 13, 25 and 50 °C to determine the effect of the adsorption. The highest sorption in all temperature values was obtained at pH 12 (Fig. 6, Fig. 7 and Fig. 8). After pH 12 value, the optimum pH was determined as 10. The sorption amounts obtained at pH 2, 4, 6 and 8 values were similar. The optimum temperature for pH 2 was 25 °C (Fig. 7), the optimum temperature value for pH 4 was similar to 13 and 25 °C (Fig 6 and Fig. 7). The optimum temperature value for pH 6, pH 8 and pH 10 was 25 °C (Fig. 7) and for pH 12 the optimum temperature value was 50 °C. (Fig. 7 and Fig. 8). The reaction rate increases as the temperature increases. The adsorbent surface becomes active and adsorption capacity increases. That is the strength of the intermolecular forces between the adsorbent and the adsorbate increases [33]. When all the results are evaluated, it is possible to say that the most effective removal efficiency for adsorption is obtained at 25 °C and this is an advantage. Because there will be no energy requirement for heating or cooling to provide color removal in the regions with a temperate climate where the temperature is between 20-30 °C throughout the year. This will provide an economic advantage.

In the experiments performed for bentonite at 13 °C and different pHs, the amount of dyestuff initially adsorbed at all pHs was low while the adsorption at all pHs increased to 60 minutes. After 60 minutes, it continued in a balanced manner (Fig. 6). At a temperature of 25 °C, the sorption at all pH values increased to 60 minutes, which continued up to 240 minutes and the concentration of the dyestuff adsorbed to 270 minutes started to decrease (Fig. 7). At a temperature of 50 °C, the amount of adsorbed dyestuff at pH 10 and 12 reached the maximum level at 60 minutes. Until 270 minutes, it continued in a balanced manner. Similar values were obtained at pH 2, 4, 6 and 8, while the

amount of dyestuff initially induced showed a fluctuating increase, reaching the highest level at 240 minutes for each of the four pHs and decreased slightly at 270 minutes (Fig. 8).

Depending on the zeta potential, when the pH decreases, the negatively charged sites on the sorbent surface increase whereas the positively charged sites and the adsorption decreases [29], [34]. The number of hydroxyl groups increases with increasing pH, so the attraction area on the surface of MGY400 and adsorbent expands, increasing the number of negatively charged sites [35].

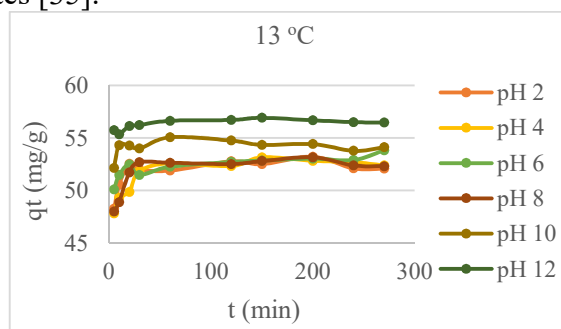


Figure 6 Amount of adsorbed substance at different pH values for 13 °C temperature

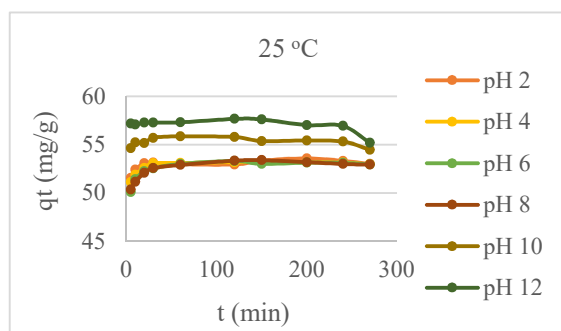


Figure 7 Amount of adsorbed substance at different pH values for 25 °C temperature

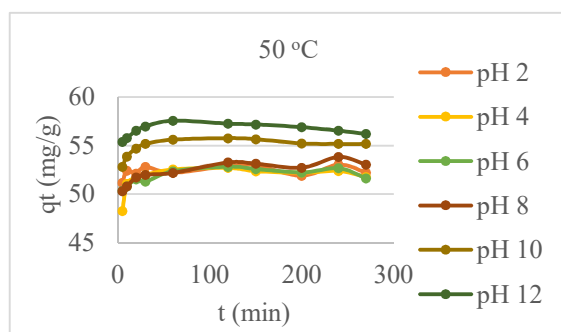


Figure 8 Amount of adsorbed substance at different pH values for 50 °C temperature

The pK_a value is a measure of the acid power in the dyestuff solution. According to all results, it is possible to say that the pK_a value of the adsorbate is less than 6.5 [36]. In the 7-12 pH range, the surface of bentonite is positively charged and dyestuff is negatively charged (PK_a of dyestuff <6.5) [37]. Because, when we examine the adsorption capacity of bentonite according to the pH values of the initial solution, there was a significant increase in capacity after pH 6.5, while the adsorption capacity at the values before pH 6.5 gave similar results. However, the fact that MGY400 is included in the cationic dyes class is also a reason why adsorption is more efficient at high pH [38].

3.3. Langmuir and Freundlich Isotherms

Table 2 and Table 3 show the Langmuir and Freundlich Isotherms for halloysite clay. According to the results, the adsorption was physical and the surface energy distribution of the adsorbent was heterogeneous and becomes more heterogeneous when the value approaches zero [29] as bentonite containing 0.5 g of adsorbent. Also, n values greater than 1 indicate that the adsorption was physical. It is also possible to say that maximum adsorption was obtained at a concentration of 0.5 g clay when K_f values were examined.

For bentonite clay, the Freundlich Isotherm was more suitable than the R^2 values. This indicates that the adsorption was physical. When n values were examined, 0.5 g. n value for bentonite was determined as 12.73. This is undesirable. When the K_f values are examined, it is possible to say that the maximum adsorption was obtained at a concentration of 0.5 g clay.

Kaolinite clay also conforms to the Freundlich Isotherm. This indicates that the adsorption was physical. When n values were examined, it is possible to say 11.01 for 2 g kaolinite and physical adsorption for other amounts. When all amounts and K_f values are examined, it is possible to say that 1.0 g of kaolinite was suitable for adsorption.

Table 2
Langmuir Isotherms and Isotherms Constants for Halloysite, Bentonite, Kaolinite, and Raw Clay

	Langmuir Isotherm	Langmuir Isotherms Constants		
	R^2	b (L/mg)	Q_{max} (mg/g)	R_L
Halloysite				
0.5 g	0.68	0.00022	103.09	0.97
1.0 g	0.90	0.0012	38.61	0.95
1.5 g	0.92	0.0030	23.47	0.93
2.0 g	0.87	0.0095	11.198	0.90
Bentonite				
0.5 g	0.80	0.000043	476.19	0.98
1.0 g	0.93	0.0012	37.31	0.95
1.5 g	0.89	0.0018	37.31	0.93
2.0 g	0.67	0.0021	40.65	0.92
Kaolinite				
0.5 g	0.65	0.00019	121.95	0.977
1.0 g	0.83	0.107	1.20	0.88
1.5 g	0.84	0.035	3.47	0.89
2.0 g	0.64	0.00074	116.28	0.92
Raw Clay				
0.5 g	0.81	0.00012	175.43	0.98
1.0 g	0.91	0.0195	4.127	0.92
1.5 g	0.82	0.036	3.303	0.89
2.0 g	0.97	0.0058	16.313	0.91

When the adsorption values for Raw Clay were examined, it was seen that the determination of ion exchange capacity and initial pH value at the beginning of the study were similar with the evidence of kaolinite (Table 1, Table 2 and Table 3).

Table 3
Freundlich Isotherms and Isotherms Constants for Halloysite, Bentonite, Kaolinite and Raw Clay

	Freundlich Isotherm	Freundlich Isotherms Constants	
	R^2	K_f (mg/g)	n
Halloysite			
0.5 g	0.91	60.64	5.98
1.0 g	0.97	31.21	5.94
1.5 g	0.98	20.96	5.66
2.0 g	0.96	16.75	4.38
Bentonite			
0.5 g	0.93	55.19	12.73
1.0 g	0.98	31.32	5.88
1.5 g	0.97	20.04	7.09
2.0 g	0.91	14.71	7.35

Kaolinite			
0.5 g	0.90	60.09	6.32
1.0 g	0.95	170.46	1.07
1.5 g	0.96	33.02	2.10
2.0 g	0.84	13.57	11.01
Raw Clay			
0.5 g	0.95	57.95	8.25
1.0 g	0.98	58.85	1.97
1.5 g	0.95	35.44	2.07
2.0 g	0.99	15.87	5.63

According to the adsorption isotherms, it was determined that color removal from bentonite clay was higher. Accordingly, different temperature ranges and different starting pH values were continued with bentonite clay. Tables 4 and 5 show the Langmuir and Freundlich Isotherm values at pH values of 2, 4, 6, 8, 10 and 12 for 13 °C, 25 °C and 50 °C. It is possible to say that adsorption for 13 °C is suitable for Langmuir Isotherm as a single layer of physical adsorption. The maximum adsorption was obtained at pH 12. When the b values were examined, the maximum adsorption energy was obtained at pH 8 and the best value was obtained at pH 12 according to R_L value and all of the adsorptions were carried out without the need for external energy. It was similar for the adsorption capacity of 25 °C and 50 °C. Although the R^2 values for pH 12 were low, it can be said that the Langmuir isotherm complied with the other parameters.

Table 4
Langmuir Isotherms and Isotherms Constants for Bentonite at 13 °C, 25 °C and 50 °C

	Langmuir Isotherm	Langmuir Isotherms Constants		
	R^2	b (L/mg)	Q_{max} (mg/g)	R_L
13 °C				
pH 2	0.73	0.00014	147.05	0.979
pH 4	0.96	0.00019	113.63	0.978
pH 6	0.94	0.00012	178.57	0.979
pH 8	0.50	0.0002	112.36	0.978
pH 10	0.67	0.000037	526.32	0.980
pH 12	0.90	0.0000054	3333.3	0.982
25 °C				
pH 2	0.98	0.0001	208.33	0.979
pH 4	0.99	0.00011	181.81	0.98
pH 6	0.94	0.00013	158.73	0.979

pH 8	0.97	0.00012	166.66	0.98
pH 10	0.96	0.00002	909.09	0.98
pH 12	0.37	7.08×10^{-8}	25000	0.98
50 °C	R^2	b (L/mg)	Q_{max} (mg/g)	R_L
pH 2	0.98	0.00011	178.57	0.98
pH 4	0.95	0.00021	105.26	0.978
pH 6	0.98	0.00014	147.05	0.975
pH 8	0.95	0.00011	181.81	0.98
pH 10	0.92	0.00003	625	0.98
pH 12	0.59	0.0000014	12500	0.98

Table 5
Freundlich Isotherms and Isotherms Constants for Bentonite at 13 °C, 25 °C and 50 °C

	Freundlich Isotherm	Freundlich Isotherms Constants	
	R^2	K_f (mg/g)	n
13 °C			
pH 2	0.80	58.75	8.88
pH 4	0.29	52.66	39.37
pH 6	0.98	58.32	9.15
pH 8	0.49	59.56	7.26
pH 10	0.68	55.91	19.45
pH 12	0.97	55.80	36.10
25 °C			
pH 2	0.99	57.81	10.06
pH 4	0.99	58.13	9.48
pH 6	0.99	58.60	8.75
pH 8	0.99	58.40	9.02
pH 10	0.99	55.86	21.36
pH 12	0.77	56.07	71.94
50 °C			
pH 2	0.99	58.24	9.37
pH 4	0.99	60.38	7.08
pH 6	0.99	58.90	8.49
pH 8	0.99	58.20	9.30
pH 10	0.99	56.02	16.66
pH 12	0.89	55.95	58.47

4. CONCLUSIONS

The adsorption isotherms were obtained under different adsorption conditions (temperature, pH, contact time) for MGY400 adsorption of halloysite, bentonite, kaolinite and raw clay.

MGY400 is a less commonly used dyestuff in the literature. Also, the clay materials used in the study are completely natural and it was tried to be shown that adsorbents with the potential to be used in color removal from wastewater can be obtained economically and can be effective in color removal. Therefore, it has been determined that a rare type of adsorbate is used in the current study, and an effective color removal can be achieved with easily available adsorbents that have no financial value. In addition, the adsorption study was carried out in wide pH and temperature ranges.

The obtained values are expressed by the adsorption isotherms, Freundlich ($r \geq 0.84$) and Langmuir ($r \geq 0.64$) adsorption equations. Q_{\max} values ranged from 1.20 to 476 mg/g. The b values expressing the adsorbent-adsorbate interaction energy ranged between 0.000043 and 0.107 L/mg.

It can be seen that the adsorption of dyestuff by clay minerals depends on the structure of raw clay minerals. When all adsorption data were examined, it was found that the maximum color removal efficiency was obtained from 0.5 g bentonite clay. It was determined that as the starting pH of the solution increased, the efficiency of adsorption increased, besides, adsorption occurred as physical adsorption and monolayer physical adsorption.

The results show that it is necessary to know in advance the fractions of clay minerals to be used in water and soil treatment technologies. The type of clay minerals will determine the effectiveness of this technology and contribute to the selection of the type of substance to be adsorbed.

Acknowledgements

The author wishes to thank Prof. Dr. Neşe Tüfekci for her suggestions on preparing the manuscript and providing adsorbents.

Funding

The author received no specific funding for this study.

The Declaration of Conflict of Interest/ Common Interest

No conflict of interest or common interest has been declared by the author.

The Declaration of Ethics Committee Approval

The author declares that this document does not require an ethics committee approval or any special permission.

The Declaration of Research and Publication Ethics

The author of the paper declares that she complies with the scientific, ethical and quotation rules of SAUJS in all processes of the paper and that she does not make any falsification on the data collected. In addition, she declares that Sakarya University Journal of Science and its editorial board have no responsibility for any ethical violations that may be encountered, and that this study has not been evaluated in any academic publication environment other than Sakarya University Journal of Science.

REFERENCES

- [1] M. J. Sánchez-Martín, M. C. Dorado, C. del Hoyo, and M. S. Rodríguez-Cruz, "Influence of clay mineral structure and surfactant nature on the adsorption capacity of surfactants by clays," *J. Hazard. Mater.*, vol. 150, no. 1, pp. 115–123, 2008.
- [2] M. Doğan, M. H. Karaoğlu, and M. Alkan, "Adsorption kinetics of maxilon yellow 4GL and maxilon red GRL dyes on kaolinite.," *J. Hazard. Mater.*, vol. 165, no. 1–3, pp. 1142–51, 2009.
- [3] G. Jing, Z. Sun, P. Ye, S. Wei, and Y. Liang, "Clays for heterogeneous photocatalytic decolorization of wastewaters contaminated with synthetic dyes: a review," *Water Pract. Technol.*, vol. 12, no. 2, pp. 432–443, 2017.

- [4] M. Tanyol, "Removal of Remazol Brilliant Blue R from aqueous solutions using raw and modified bentonite," *Kafkas Univ. J. Sci.*, vol. 9, no. 1, pp. 46–52, 2016.
- [5] A. Ghribi and M. Bagane, "Kinetic modeling for the adsorption of methylene blue from aqueous solutions using Tunisian clay," in *IREC2015 The Sixth International Renewable Energy Congress*, 2015.
- [6] P. Liu and L. Zhang, "Adsorption of dyes from aqueous solutions or suspensions with clay nano-adsorbents," *Sep. Purif. Technol.*, vol. 58, no. 1, pp. 32–39, 2007.
- [7] A. Gürses, Ç. Doğar, M. Yalçın, M. Açıkyıldız, R. Bayrak, and S. Karaca, "The adsorption kinetics of the cationic dye, methylene blue, onto clay," *J. Hazard. Mater.*, vol. 131, no. 1–3, pp. 217–228, 2006.
- [8] S. S. Tahir and N. Rauf, "Removal of a cationic dye from aqueous solutions by adsorption onto bentonite clay," *Chemosphere*, vol. 63, no. 11, pp. 1842–1848, 2006.
- [9] E. Errais, J. Duplay, F. Darragi, I. M'Rabet, A. Aubert, F. Huber, G. Morvan, "Efficient anionic dye adsorption on natural untreated clay: Kinetic study and thermodynamic parameters," *Desalination*, vol. 275, no. 1–3, pp. 74–81, 2011.
- [10] N. Abidi, E. Errais, J. Duplay, A. Berez, A. Jrad, G. Schäfer, M. Ghazi, K. Semhi, M. Trabelsi-Ayadi, "Treatment of dye-containing effluent by natural clay," *J. Clean. Prod.*, vol. 86, pp. 432–440, 2015.
- [11] Z. Hicham, Z. Bencheqroun, I. El Mrabet, M. Kachabi, M. Nawdali, and I. Neves, "Removal of Basic Dyes from Aqueous Solutions by Adsorption onto Moroccan Clay (Fez City)," *Mediterr. J. Chem.*, vol. 8, no. 3, pp. 158–167, 2019.
- [12] E. Kayman, "Adsorption of lead ions from aqueous solutions by activated carbon produced from chestnut shell and apricot stone," Istanbul Technical University, Institute of Science and Technology, MSc. Thesis, 2009.
- [13] "C.I. Basic yellow 28 | C₂₁H₂₇N₃O₅S - PubChem." https://pubchem.ncbi.nlm.nih.gov/compound/Basic_Yellow_28#section=2D-Structure (accessed Feb. 13, 2019).
- [14] P. F. Kerr, "Formation and occurrence of clay minerals," *Clays Clay Miner.*, vol. 1, pp. 19–32, 1952.
- [15] W. A. Deer, R. A. Howie, and J. Zussman, *An introduction to the Rock-forming Minerals*. 1992.
- [16] M. L. Jackson, "Soil chemical analysis. Verlag: Prentice Hall, Inc., Englewood Cliffs, NJ. 1958, 498 S. DM 39.40," *Zeitschrift für Pflanzenernährung, Düngung, Bodenkd.*, vol. 85, no. 3, pp. 251–252, 1959.
- [17] Ö. Şahin, M. Kaya, and C. Saka, "Plasma-surface modification on bentonite clay to improve the performance of adsorption of methylene blue," *Appl. Clay Sci.*, vol. 116–117, pp. 46–53, 2015.
- [18] O. Sözüdoğru, B. A. Fil, R. Boncukcuoglu, E. Aladag, and S. Kul, "Adsorptive removal of cationic (BY2) dye from aqueous solutions onto Turkish clay: Isotherm, kinetic, and thermodynamic analysis," *Part. Sci. Technol.*, vol. 34, no. 1, pp. 103–111, 2016.
- [19] Q. Zhou, Q. Gao, W. Luo, C. Yan, Z. Ji, and P. Duan, "One-step synthesis of amino-functionalized attapulgite clay nanoparticles adsorbent by hydrothermal carbonization of chitosan for removal of methylene blue from wastewater," *Colloids Surfaces A Physicochem. Eng. Asp.*, vol. 470, pp. 248–257, 2015.

- [20] B. A. Fil, K. Z. Karakas, R. Boncukcuoglu, and A. E. Yilmaz, "Removal of Cationic Dye(Basic Red 18) from Aqueous Solution Using Natural Turkish Clay," *Glob. NEST J.*, vol. 15, no. 4, pp. 529–541, 2013.
- [21] B. Makhoukhi, M. A. Didi, H. Moulessehoul, A. Azzouz, and D. Villemin, "Diphosphonium ion-exchanged montmorillonite for Telon dye removal from aqueous media," *Appl. Clay Sci.*, vol. 50, no. 3, pp. 354–361, 2010.
- [22] S. T. Akar and R. Uysal, "Untreated clay with high adsorption capacity for effective removal of C.I. Acid Red 88 from aqueous solutions: Batch and dynamic flow mode studies," *Chem. Eng. J.*, vol. 162, no. 2, pp. 591–598, 2010.
- [23] B. B. Johnson, "Effect of pH, temperature, and concentration on the adsorption of cadmium on goethite," *Environ. Sci. Technol.*, vol. 24, no. 1, pp. 112–118, 1990.
- [24] S. Kayacan, "Removal of dye materials from aqueous solutions by adsorption on coals and cokes," Ankara University, Institute of Science and Technology, MSc Thesis, 2007.
- [25] R. Gürellier, "Adsorption kinetic investigations of low concentrated uranium in aqua media by polymeric adsorban," Ankara University, Institute of Science and Technology, MSc Thesis, 2004.
- [26] J. Wang, G. Liu, T. Li, and C. Zhou, "Physicochemical studies toward the removal of Zn(II) and Pb(II) ions through 1 adsorption on montmorillonite-supported zero-valent iron nanoparticles," *RSC Adv.*, no. 38, pp. 29609–30408, 2015.
- [27] K. A. Kareem, "Removal and Recovery of Methylene Blue Dye from Aqueous Solution using Avena Fatua Seed Husk," *Ibn Al-Haitham J. Pure Appl. Sci.*, vol. 29, no. 3, pp. 179–194, 2016.
- [28] G. Labuto, D. S. Cardona, K. B. Debs, A. R. Imamura, K. C. H. Bezerra, E. N. V. M. Carrilho, P. S. Haddad, "Low-cost agroindustrial biomasses and ferromagnetic bionanocomposites to cleanup textile effluents," *Desalin. Water Treat.*, vol. 112, pp. 80–89, 2018.
- [29] M. Kılıç and A. S. K. Janabi, "Investigation of Dyes Adsorption with Activated Carbon Obtained from *Cordia myxa*," *Bilge Int. J. Sci. Technol. Res.*, vol. 1, no. 2, pp. 87–104, 2017.
- [30] Y. M. Lvov, D. G. Shchukin, E. Abdullayev, D. Shchukin, and Y. Lvov, "PMSE 193-Halloysite clay nanotubes as a reservoir for corrosion inhibitors and template for layer-by-layer encapsulation" *Polym. Mater. Sci. Eng.*, vol. 99, pp. 331–332, 2008.
- [31] P. I. Au and Y. K. Leong, "Rheological and zeta potential behaviour of kaolin and bentonite composite slurries," *Colloids Surfaces A Physicochem. Eng. Asp.*, vol. 436, pp. 530–541, 2013.
- [32] G. Nechifor, D. E. Pascu, M. Pascu (neagu, G. A. Traistaru, A. A. Bunaciu, and H. Y. Aboul-Enein, "Study of Adsorption Kinetics and Zeta Potential of Phosphate and Nitrate Ions on a Cellulosic Membrane," *Rev. Roum. Chim.*, vol. 58, no. 8, pp. 591–597, 2013.
- [33] V. K. Gupta, S. Agarwal, H. Sadegh, G. A. M. Ali, A. K. Bharti, and A. S. Hamdy Makhlof, "Facile route synthesis of novel graphene oxide- β -cyclodextrin nanocomposite and its application as adsorbent for removal of toxic bisphenol A from the aqueous phase," *J. Mol. Liq.*, vol. 237, pp. 466–472, 2017.
- [34] A. Olgun and N. Atar, "Equilibrium and kinetic adsorption study of Basic Yellow 28 and Basic Red 46 by a boron industry

waste,” *J. Hazard. Mater.*, vol. 161, no. 1, pp. 148–156, 2009.

- [35] I. Twardowska, H. E. Allen, A. F. Kettrup, and W. J. Lacy, *Solid Waste: Assessment, Monitoring and Remediation*, 1st ed., vol. 4. Pergamon, 2004.
- [36] H. I. Albroomi, M. Abouelfotoh Elsayed, A. Baraka, and M. K. Abdelmaged, “Factors Affecting the Removal of a Basic and an Azo Dye from Artificial Solutions by Adsorption Using Activated Carbon,” *J. Turkish Chem. Soc. Sect. A Chem.*, vol. 2, no. 1, pp. 17–33, 2015.
- [37] Y. S. Al-Degs, M. I. El-Barghouthi, A. H. El-Sheikh, and G. M. Walker, “Effect of solution pH, ionic strength, and temperature on adsorption behavior of reactive dyes on activated carbon,” *Dye. Pigment.*, 2008.
- [38] G. Annadurai, R.-S. Juang, and D.-J. Lee, “Use of cellulose-based wastes for adsorption of dyes from aqueous solutions,” *J. Hazard. Mater.*, vol. 92, no. 3, pp. 263–274, 2002.

JOURNAL OF SCIENCE



SAKARYA UNIVERSITY

Sakarya University Journal of Science

ISSN 1301-4048 | e-ISSN 2147-835X | Period Bimonthly | Founded: 1997 | Publisher Sakarya University |
<http://www.saujs.sakarya.edu.tr/en/>

Title: Determining the Factors that Influence the Effectiveness of the Health Sector in the OECD Countries

Authors: Selin Ceren TURAN, Mehmet Ali CENGİZ

Received: 2020-04-05 18:51:24

Accepted: 2020-08-23 20:20:14

Article Type: Research Article

Volume: 24

Issue: 5

Month: October

Year: 2020

Pages: 1094-1104

How to cite

Selin Ceren TURAN, Mehmet Ali CENGİZ; (2020), Determining the Factors that Influence the Effectiveness of the Health Sector in the OECD Countries. Sakarya University Journal of Science, 24(5), 1094-1104, DOI:

<https://doi.org/10.16984/saufenbilder.714736>

Access link

<http://www.saujs.sakarya.edu.tr/en/pub/issue/56422/714736>

New submission to SAUJS

<http://dergipark.org.tr/en/journal/1115/submission/step/manuscript/new>

Determining the Factors that Influence the Effectiveness of the Health Sector in the OECD Countries

Selin Ceren TURAN^{*1}, Mehmet Ali CENGİZ²

Abstract

The purpose of this study is to determine the factors that influence the effectiveness of the health sector by combining Stochastic Frontier Analysis (SFA), Generalized Linear Models (GLM) and Heuristic Algorithms methods. In accordance with this purpose, firstly, the health system efficiencies of 29 OECD countries are estimated by the SFA method. Within the scope of this study, it is also aimed to select the factors influencing the efficiency of the health systems in OECD countries by employing Heuristic Algorithm methods such as Artificial Bee Colony Algorithm, Genetic Algorithm, and Differential Evolution Algorithm. Furthermore, GLM's such as Truncated, Normal, Gamma and Tweedie distributions are employed for comparisons.

Keywords: Efficiency, Generalized linear models, Heuristic algorithms, SFA

1. INTRODUCTION

The budget that countries earmark for health expenditures is an important factor for the improvement of quality in healthcare. These expenditures have recently accelerated in order to improve the health systems of the countries. Health policymakers have initiated reforms to provide information for the countries so as to enhance the quality and performance of their health systems.

Nonparametric methods, such as Data Envelopment Analysis (DEA), and parametric

methods, such as Stochastic Frontier Analysis (SFA), can be used to compare the efficiencies of performances of health systems. DEA methods have been widely employed in measuring the efficiency of health systems of the countries in the Organization for Economic Co-operation and Development (OECD). Afonso and Aubyn [1] investigated the efficiency of the health system by using DEA. They used the life expectancy at birth, infant survival rate, and maternal mortality as output variables; while the number of hospital beds per thousand, and physician and nurse numbers were used as input variables. Spinks and Hollingsworth [2] conducted some analyses after

*Corresponding Author: scturan1@gmail.com

¹Ondokuz Mayıs University, ORCID: <https://orcid.org/0000-0002-0290-5298>

²Ondokuz Mayıs University, E-Mail: macengiz@omu.edu.tr
ORCID: <https://orcid.org/0000-0002-1271-2588>

determining education, income, per capita health expenditure as input variables, and life expectancy at birth as an output variable. Afonso and Aubyn [3] conducted another study using by DEA approach with non-discretionary inputs. Kujawska [4] applied DEA with additive and super efficiency models to estimate the efficiency of the health sector of OECD countries. Çetin and Bahçe [5] estimated the efficiency of the health systems of OECD countries by using input-oriented DEA. Özcan and Khushalani [6] calculated the health system efficiency of OECD countries by using Dynamic Data Envelopment Analysis.

SFA, which is a parametric method, has been used only a few times in the literature to compare health system efficiency in OECD countries since the World Health Organization (WHO) reports in 2000. Wranik [7] evaluated the policy-based characteristics of a healthcare system in terms of their contribution to the efficiency of health systems measured through the SFA method. The study of De Cos and Moral-Benito [8] focuses on the significant factors influencing the effectiveness of the health systems in OECD countries. They firstly examined and classified the health system efficiencies in OECD countries by benefiting from parametric and nonparametric methods. They also listed the efficiency values and determined the effective countries in accordance with the scores obtained via their estimations. Then, they regressed the efficiency scores on 20 different indicators obtained from the survey conducted in 2010 on the health sector determinants of OECD countries.

Şenel and Cengiz [9] use a similar dataset as in De Cos and Moral-Benito [8]. Firstly, they investigated the efficiency of health care system in 29 OECD countries using Bayesian Stochastic Frontier Analysis (BSFA). For this step, the variables used are obtained from the OECD Health Database for the time period between 1997 and 2009. Furthermore, the variables on the characteristics of the health system are chosen from the study carried out by Paris et al. [10] and cover the year 2009. Later, Bayesian beta regression has been performed to bring out the

relationship between the health system efficiency and the features of healthcare models in the relevant countries. In their study, they suffered overfitting problems. In regression analysis, overfitting a model is a real problem. An overfit model can cause the regression coefficients, p-values, and R-squared to be misleading. A modelling error which occurs when a function is too closely fit a limited set of data points. Overfitting the model generally takes the form of making an overly complex model to explain idiosyncrasies in the data under study. In reality, the data being studied often has some degree of error or random noise within it. Thus, making the model conform too closely to slightly inaccurate data can infect the model with substantial errors and reduce its predictive power. We suggest heuristics algorithm methods to avoid this problem.

At the first step of this study, the health system efficiency of OECD countries are estimated by Stochastics Frontier Analysis and then the factors affecting the health system efficiency across OECD countries are selected using truncated, normal, gamma and tweedie distributions in the context of Generalized Linear Models (GLM) and Heuristic algorithm methods such as Artificial Bee Colony Algorithm, Genetic Algorithm and Differential Evolution Algorithm.

2. MATERIAL AND METHODS

2.1. Stochastic Frontier Analysis

Stochastic Frontier Analysis assumes that a parametric function exists between production inputs and outputs. SFA is a parametric method that uses econometric methods. SFA establishes a functional relationship between the explained variables like cost, profit and production, and the explanatory variables like input, output, and other possible factors. In order to establish this relationship, the SFA model includes an error term. It is assumed that the error term in the model consists of two components. One of these components is the technical efficiency which is defined as achieving maximum output with the

existing inputs. The other component is the allocative efficiency which indicates the ability of these inputs to be used at the optimal rate when optimum prices for the inputs are available.

SFA approach proposed by Aigner et al. [11] can be specified as follows:

$$y_i = x_i \beta_i + \varepsilon_i$$

$$\varepsilon_i = v_i - u_i, i = 1, 2, \dots, N \quad (1)$$

where y_i is the log output, x_i is a vector of input measures, β_i is an unknown parameter vector, ε_i is the combined error term, v_i is the independent and identically distributed error term, and u_i is technically ineffective (non-negative random variable). Error term $\varepsilon_i = v_i - u_i$ has asymmetric distribution.

2.2. Generalized Linear Models

In simple linear regression models, the dependent variable and errors are assumed to have a normal distribution. Normality assumption may not be provided in cases where the dependent variables are discrete variables or binary. In such cases, classical linear models cannot be used. In addition, there may be situations where the dependent variable is continuous and does not show normal distribution. Generalized Linear Models (GLMs) are used in the analysis of data consisting of such variables.

GLMs, which are the generalized version of classical linear models, are tasked with modelling the transformed average as a linear function of explanatory variables. GLMs allow to fit regression models, if the dependent variable is from the exponential distribution family. If the probability density function of the dependent variable belongs to the exponential distribution family, the probability density function is as follows:

$$f(y) = \exp \left\{ \frac{y\theta - b(\theta)}{a(\phi)} + c(y, \phi) \right\} \quad (2)$$

Here, θ is the natural parameter and depends on the observations y_1, y_2, \dots, y_n . ϕ is the scale parameter related to the variance of the dependent variable (y) and is constant for each observation. $c(y, \phi)$ is a function of observations and dispersion parameter [12].

2.3. Heuristic Optimization Methods

Problems that arise in many areas can be modelled as linear or nonlinear optimization problems. When we look at the structure of the problems, we notice that most of the problems have nonlinear structures. Many methods have been developed for solving non-linear problems. Apart from that, it can be difficult to solve problems according to types of data and variable numbers. Therefore, sometimes the results cannot be reached or can be reached within the unacceptable time frame. To eliminate these problems, heuristic optimization methods have been developed.

Nowadays, there are many optimization algorithm methods available to solve optimization problems that use mathematical and heuristic methods. Classical algorithms are usually designed for a problem or trying to solve the problem by scanning the entire solution space of the problem. Usage of these algorithms is very costly and time-consuming in large problems. However, the heuristic algorithms are algorithms that can reach the closest solution in a very short period of time without scanning the whole solution space.

Artificial Bee Colony Algorithm (ABC), developed by Karaboğa [13], is an algorithm based on swarm intelligence which is the result of examining the nutritional search processes of honey bees. In the process, the nutritional search behaviours of the bees are modelled. The model consists of 3 components. These components are employed bees, unemployed bees, and food sources. A bee waiting on the dance area for making the decision to choose a food source is called onlooker and a bee going to the food source visited previously by itself is named employed bee. A bee carrying out a random search is called scout.

Like all living things, bees also need food to sustain themselves and survive. That is why they have to look for food. Therefore, these processes are carried out by organizing themselves and making a division of labour among them. There is a responsible bee for each food source. The number of bees in the algorithm equals the number of total food sources. In the ABC algorithm, the first half of the colony consists of employed artificial bees and the second half constitutes the onlookers. Employed bees are researching randomly while conducting a nutritional search in nature. The locations of the nutrient sources of the bee colonies correspond to the possible solutions to the present problem. In addition, the quantity of nutrients indicates the quality of the solution. Therefore, the artificial bee colony algorithm aims to determine the location of the source where the most nutrients are found and try to find the solution that gives the minimum or maximum of the problem from the search space solutions [14].

Genetic Algorithm (GA), developed by Holland [15], provides modelling of natural selection and genetic populations by taking the process of living creatures in nature as an example. It is a kind of heuristic algorithm that can be used in problems where mathematical modelling cannot be done and the final solution cannot be achieved. This algorithm is based on sustaining their lives if new individuals from the previous generation meet the necessary criteria. It is based on the principle that the good generations protect their own lives while the bad generations disappear. GA is different from other heuristic algorithm methods. The reason of this difference is the method of searching solution space. While GA seeks for the the solution in the population of points, other heuristic algorithms looks from point to point. [16].

In the solution of a problem with the GA method, the variables representing the chromosomes are firstly coded into arrays. In this coding process, (0, 1) binary system is widely used. The initial population is formed by the chromosomes which are obtained after coding. At this stage, chromosomes are subject to an evaluation

criterion in order to decide which chromosome will participate in the population. Fitness values are calculated to determine the success rates of chromosomes. In the selection phase, chromosomes with high fitness values are added to the population. Then, it is aimed to obtain new chromosomes with crossed and mutated chromosomes. Thus, the newly produced chromosomes participate in the new population. In this population where new chromosomes exist, the optimal solution is sought for the problem. These operations continue until a specified stop criterion is met. When the specified criterion is met, the algorithm stops.

The Differential Evolution Algorithm (DE) was developed by Storn and Price [17]. DE, which is a population-based and development-based heuristic algorithm method, has been developed for the minimization of functions with real-valued parameters. The DE and GA methods are similar algorithms. However, the most important distinction of the DE and GA is that the DE contains real-valued parameters. Unlike the GA method, each operator is subjected to the entire population in turn. With the DE method, it is possible to optimize a wide range of problems that are encountered in science, engineering and business environments.

DE is also based on mutation, crossover and selection operators. However, none of the previously defined probability-based mutations is used as in GA. Unlike the GA method, each operator is sequentially subjected to the entire population. Chromosomes are handled one by one and then it is aimed to obtain a new individual by using chromosomes along with other randomly chosen chromosomes. In this process, mutation and crossover operators are used. The fitness values of the new chromosomes obtained with the existing chromosomes are compared and checked again to determine the quality of the resulting solutions. The chromosome with a better fitness value is sent to the next population as a new individual. Thus, the algorithm is completed using the selection operator [18].

The simple mutation operation used in the DE increases the performance of the algorithm. Thus, it allows for the creation of new research areas, which makes it a more stable algorithm. This algorithm is structurally simple and fast. It is also very effective in solving complex problems. DE has advantages over other algorithms. They are easy to code, have effective global optimization capability, do not need a derivation of the objective function or constraint functions, and low cost of calculation since they do not have matrix multiplication and sorting operations.

2.4. Model Selection Criteria

Criteria are important in choosing a model or deciding which model is better. Information criteria can be used to interpret the results of the obtained models and reach the best estimation model. The Akaike Information Criterion (AIC) proposed by Akaike [19] was designed to be an approximately unbiased estimator of the Kullback-Leibler index of the fitted model relative to the true model. With this suggestion, which has led to improvements in statistical modelling and evaluation of models, AIC has become an asymptotic criterion frequently used in model selection. Hurvich and Tsai [20] presented a corrected version of AIC, denoted Modified Akaike Information Criterion (AICC), which is less biased in the finite sample case. The criterion proposed by Schwartz [21] and called the Bayesian Information Criteria (BIC) is a similarly consistent criterion based on Bayesian reasoning. Another important and widely used criterion is the Consistent Akaike Information Criterion (CAIC) proposed by Bozdogan [22].

Table 1
Information criteria

Criteria	Formula
AIC	$-2L + 2p$
BIC	$-2L + p \log(n)$
AICC	$-2L + 2p^n / (n - p - 1) - 2L$
CAIC	$-2L + p(\log n + 1)$

Table 1 contains the formulas for commonly used information criteria in the model selection stage

³ <https://data.oecd.org/health.htm>

of GLM and Heuristic Algorithms. Here, L denotes the maximum value of log likelihood, log pseudo-likelihood or log semi-likelihood. p indicates the size of the model. n indicates the size of the data. These measures are model dependent sizes. In model selection, the model with the minimum value of these criteria is preferred.

3. RESULTS and DISCUSSION

In this section, first, we measured the health system efficiencies of 29 OECD countries by SFA using the data from the OECD Health Database³. Determining the decision-making units (DMUs) is a crucial step of SFA. In this stage of the investigation it was primarily required to address the countries included in the OECD countries health sector determinants survey conducted by Paris et al. [10]. This dataset presents the information provided by 29 of OECD countries in 2009. The dataset was created according to this condition. Although they fulfilled this requirement and could be applied at this stage, the data of variables belonging to some countries to be used in the second stage could not be reached. This led us to exclude some countries from the study. In addition, countries with values that would disrupt the homogeneity of DMUs on the basis of variables were determined and were not included in the analysis.

The input and output variables used in the study were selected from the variables used in the health system efficacy analysis in the literature. Total health expenditure, public expenditure on health, practicing nurses, hospital beds, tobacco consumption, alcohol consumption, GDP per capita, education are used as input variables, while life expectancy at birth is used as an output variable for the SFA approach in the study. Statistical analyses in this study were carried out using MaxDEA, RStudio and IBM SPSS 20 programs.

The results of the SFA method, which is the first step of our study, are summarized in Table 2 by taking the averages of the technical efficiency

values obtained and the efficiency scores of all countries as well as their ranking according to their efficiency status.

Table 2
Efficiency scores derived from SFA

No	Countries (DMU)	Efficiency Scores	Ranks
1	Australia	0.844	19
2	Austria	0.914	7
3	Belgium	0.878	14
4	Canada	0.849	18
5	Czech Republic	0.765	25
6	Denmark	0.785	23
7	Finland	0.829	21
8	France	0.974	2
9	Germany	0.836	20
10	Greece	0.936	5
11	Hungary	0.698	28
12	Iceland	0.879	12-13
13	Ireland	0.859	16
14	Italy	0.976	1
15	Japan	0.945	4
16	Korea	0.694	29
17	Luxembourg	0.864	15
18	Mexico	0.789	22
19	Netherlands	0.893	9
20	New Zealand	0.766	24
21	Norway	0.897	8
22	Poland	0.742	26-27
23	Portugal	0.929	6
24	Slovakia	0.742	26-27
25	Spain	0.968	3
26	Sweden	0.890	10
27	Switzerland	0.879	12-13
28	Turkey	0.858	17
29	United Kingdom	0.883	11

In the second stage, the efficiency values obtained at the first stage are taken as a dependent variable, and other potential variables affecting this efficiency are considered as explanatory variables and different regression models such as are truncated, normal, gamma, gamma-power(2), tweedie and tweedie-power(2) were examined. These regression models also identify which factors may affect countries' health system efficiencies and which factors should be given priority to raising countries' health system effectiveness. For these models, 20 different variables from OECD countries' health sector determinants survey conducted in 2010 were used as explanatory variables in analyses. Those variables choice of insurer (x_1), insurer level for

competition (x_2), over the basic coverage (x_3), degree of private provision (x_4), volume incentives (x_5), regulation of prices billed by providers (x_6), user information on quality and prices (x_7), regulation of the workforce and equipment (x_8), the patient choice among providers (x_9), gatekeeping (x_{10}), price signals on users (x_{11}), priority setting (x_{12}), the stringency of the budget constraint (x_{13}), regulation of prices paid by third-party payers (x_{14}), degree of decentralization (x_{15}), degree of delegation to insurers (x_{16}), consistency in responsibility (x_{17}), breadth (x_{18}), the scope of basic coverage (x_{19}), and depth of coverage (x_{20}).

As seen in Table 3, estimated models with various distributions are calculated. Here, the model distributions and link functions are expressed. As a result of the analysis, it was concluded that gamma - power (2) and tweedie - power (2) models are the models with the most explanatory variables affecting the efficiency scores of countries ($p < 0.05$).

Table 3
Comparison of models

Distribution Link Function	Truncated		Normal identity		Gamma identity		Gamma power (2)		Tweedie identity		Tweedie power (2)	
	Coef.	P	Coef.	P	Coef.	P	Coef.	P	Coef.	P	Coef.	P
Intercept	-0.33	0.47	-0.26	0.53	-0.18	0.66	-0.91	0.18	-0.20	0.63	-0.95	0.17
x ₁	0.02	0.23	0.02	0.21	0.02	0.18	0.03	0.14	0.02	0.19	0.03	0.15
x ₂	-0.03	0.10	-0.03	0.08	-0.03	0.07	-0.05	0.05	-0.03	0.07	-0.05	0.06
x ₃	0.01	0.18	0.01	0.21	0.01	0.19	0.02	0.15	0.01	0.20	0.02	0.16
x ₄	0.00	0.89	0.00	0.87	0.00	0.86	0.00	0.86	0.00	0.87	0.00	0.87
x ₅	0.00	0.77	0.00	0.79	0.00	0.87	0.00	0.87	0.00	0.85	0.00	0.85
x ₆	-0.02	0.33	-0.01	0.34	-0.01	0.33	-0.03	0.29	-0.01	0.33	-0.03	0.30
x ₇	-0.03	0.12	-0.03	0.15	-0.03	0.15	-0.04	0.12	-0.03	0.15	-0.04	0.13
x ₈	-0.03	0.03	-0.02	0.04	-0.03	0.02	-0.05	0.01	-0.03	0.02	-0.05	0.01
x ₉	0.02	0.01	0.02	0.01	0.02	0.00	0.03	0.00	0.02	0.00	0.03	0.00
x ₁₀	0.02	0.01	0.02	0.02	0.02	0.01	0.04	0.01	0.02	0.01	0.04	0.01
x ₁₁	0.06	0.12	0.05	0.13	0.06	0.10	0.10	0.08	0.06	0.11	0.10	0.09
x ₁₂	0.02	0.20	0.02	0.21	0.02	0.29	0.02	0.34	0.02	0.27	0.02	0.32
x ₁₃	-0.02	0.02	-0.02	0.01	-0.02	0.01	-0.03	0.01	-0.02	0.01	-0.03	0.01
x ₁₄	0.03	0.17	0.02	0.22	0.02	0.25	0.04	0.20	0.02	0.25	0.04	0.20
x ₁₅	0.02	0.09	0.02	0.11	0.02	0.07	0.03	0.04	0.02	0.08	0.03	0.04
x ₁₆	0.03	0.11	0.02	0.16	0.03	0.13	0.05	0.09	0.03	0.13	0.05	0.10
x ₁₇	0.01	0.52	0.01	0.51	0.00	0.64	0.00	0.72	0.00	0.61	0.01	0.68
x ₁₈	-0.05	0.16	-0.04	0.24	-0.05	0.13	-0.09	0.06	-0.04	0.16	-0.09	0.07
x ₁₉	0.06	0.09	0.05	0.09	0.05	0.11	0.07	0.12	0.05	0.10	0.07	0.11
x ₂₀	0.17	0.01	0.16	0.01	0.16	0.01	0.28	0.00	0.16	0.01	0.27	0.00

The information criteria specified in Table 4 were used to determine the model quality for each distribution and to select the correct model. Table 4 shows the calculated test results to determine the quality of the models and to select the models.

Table 4
Information criteria of distributions

Criteria	Normal	Gamma	Gamma Power (2)	Tweedie	Tweedie Power (2)
AIC	-61.86	-61.94	-63.84	-61.86	-63.56
AICC	106.81	106.73	104.83	106.81	105.11
BIC	-31.78	-31.87	-33.76	-31.78	-33.47
CAIC	-9.78	-9.86	-11.76	-9.78	-11.47

When we compare the information criteria given in Table 4, the information criterion with the smallest value should be selected. When we consider each information criterion in Table 4, it can be said that the gamma - power (2) distribution is the most suitable distribution for modelling because it has the smallest value.

In this study, the heuristic optimization methods such as BC, DE and GA used to identify which factors may affect countries' health system

efficiencies. For this purpose, the parameters and values of these algorithms used are given in Table 5.

Table 5
Parameters used in heuristic algorithms

Parameters	Value
ABC algorithm:	
Number of individuals in the population	50
Number of elements in the row	40
Cross rate	0.8
Mutation rate	0.1
Number of iterations	1000
GA Algorithm:	
Number of individuals in the population	100
Cross rate	0.7
Scale parameter	1.2
Lower limit value	0
Upper limit value	1
Number of iterations	1000
DE algorithm:	
Quantity of food	20
Number of worker bees	20
Onlooker bee	20
Limit	100
Lower limit value	0
Upper limit value	1
Number of iterations	1000

Crossing rate, mutation rate and population size, which are control parameters, were determined as a result of preliminary tests. The combinations given in Table 5 converged to the better solution faster than the other tested combinations for the used parameter values. Thus, it has been seen that these decided combinations have optimal search capabilities in the solution spaces of the each algorithms. For the fixed number of iterations, as the population sizes increase, the solution time of the algorithms will increase, so the population sizes were taken as 50 for the ABC algorithm, 100 for the GA and 20 for the DE algorithm. Tests for 1000 iterations were carried out on the dataset. In addition, binary system was used in the coding process.

We had found that the model with the most explanatory variables affecting the efficiency scores of OECD countries is the gamma - power (2) model after applying SFA. Here, our main is to consider ABC, DE, and GA algorithms for gamma regression in variable selection process. These algorithms were used to achieve the selection task by minimizing a fitness function. The objective function value of the problem is computed as the fitness function value [17]. We selected AIC, AICC, BIC, and CAIC as the fitness function to compare the performance of the competitive models. All applications were made with packages in RStudio.

Table 6
Results of the information criteria of heuristic algorithms

Criteria	ABC	DE	GA
AIC	-75.27359	-75.27359	-75.27359
AICC	-88.48888	-88.48888	-88.48888
BIC	-61.36138	-61.36138	-61.36138
CAIC	-67.82476	-67.82476	-67.82476

Table 6 shows the results of the information criteria for the ABC, DE, and GA algorithms. In order to compare the models obtained by using ABC, DE and GA algorithms, which are part of the second stage of our study, AIC, AICC, BIC and CAIC information criteria were taken into consideration. When Table 6 is observed, we can conclude that the information criteria results of these three algorithms are converged to each

other. According to the criteria results, it can be said that it is appropriate to use these three algorithms in parameter selection. Also, it is seen that the AICC criterion has the lowest value for each heuristic algorithm and we stated that the AICC model, with which four of the four criteria agreed, would be chosen as the best model. Thus, in line with the data used in this study, the AICC model is can be said to be the best in identifying other indicators that affect the efficiencies of 29 OECD countries for which health system efficiency is calculated.

Table 7
AICC model of heuristic algorithms

AICC model	Coefficients	p value
constant	-1.09748	0.04587*
x_1	0.05102	0.06656
x_2	-0.08747	0.00794*
x_8	-0.03801	0.01554*
x_9	0.02650	0.02293*
x_{10}	0.01946	0.09319

*p<0.05

In Table 7, the variable coefficients and significance values of the model obtained according to AICC criteria for ABC, DE and GA are given. Considering Table 7, it can be said that the x_2 , x_8 and x_9 variables are important in determining the indicators affecting the health sector efficiencies of 29 OECD countries according to the AICC model, while the other variables are not.

All models obtained within the scope of this study are given in Table 8.

Table 8
Determination of significant variables

Models	Significant variables
Generalized Linear Models	
Truncated	$x_8, x_9, x_{10}, x_{13}, x_{20}$
Normal	$x_8, x_9, x_{10}, x_{13}, x_{20}$
Gamma	$x_8, x_9, x_{10}, x_{13}, x_{20}$
Gamma – Power (2)	$x_8, x_9, x_{10}, x_{13}, x_{15}, x_{20}$
Tweedie	$x_8, x_9, x_{10}, x_{13}, x_{20}$
Tweedie – Power (2)	$x_8, x_9, x_{10}, x_{13}, x_{15}, x_{20}$
Heuristic Algorithms (ABC, DE, GA)	
AIC	$x_2, x_9, x_{10}, x_{11}, x_{13}, x_{15}, x_{20}$
AICC	x_2, x_8, x_9
BIC	$x_2, x_8, x_9, x_{11}, x_{13}, x_{20}$
CAIC	$x_2, x_8, x_9, x_{11}, x_{13}, x_{20}$

The significant variables in the models with various distributions in the context of GLM are given in table 8, taking into account Table 3. Then, the significant variables included in the models obtained as a result of the applications performed using heuristic algorithms were summarized according to the information criteria. When the established GLMs with truncated, normal, gamma and tweedie distribution are examined, it is seen that x_8 , x_9 and x_{10} variables are common variables in each model. Similarly, when the models established as a result of the heuristic algorithms were compared, it is seen that the x_2 and x_9 variables are included in the model according to four information criteria. The point to note in Table 8 is that the models obtained by using each heuristic algorithm show similarity. That is, when the models obtained with ABC, DE and GA algorithms are compared, it is seen that the optimal solutions are the same.

4. CONCLUSION

In the first stage of this study, an efficiency analysis was carried out by the SFA approach to examine the health system efficiency status of OECD countries. The input variables used in this stage are total health expenditures per capita, public expenditures, number of nurses, number of beds, tobacco consumption, alcohol consumption, GDP per capita, and educational status. Life expectancy at birth is used as an output variable. The analysis was performed in software program R. Using the results obtained from the SFA approach, the efficiency scores of the countries are ranked and the most effective and least effective countries are determined. Among the 29 selected OECD countries, Italy was found to be the most effective country in terms of health system efficiency. This finding reveals that Italy is the country that completes the output transformation process of selected input variables for the study in the most efficient way. Additionally, according to the results of the SFA approach, it can be said that the country with the lowest health system efficiency is Korea.

In the second stage of this study, we aimed to identify the other indicators that could affect the health system efficiencies of 29 OECD countries and determine the factors that should be given priority for countries to increase their efficiencies in this sector. For this purpose, the effect of the 20 different indicators obtained from the 2010 health sector determinants surveys on OECD countries on the efficiency scores estimated by the SFA approach was analysed using different regression methods and heuristic algorithm methods in the context of generalized linear models. Parameter estimations made for GLM are based on IBM SPSS 20 package program. As a result of using heuristic algorithm methods, we decided that it is appropriate to use the three algorithms discussed in this study. Applications of the algorithms have been benefited from the R software program again.

While the insurer level for competition (x_2), the patient choice among providers (x_9) were related according to the heuristic algorithms, the regulation of the workforce and equipment (x_8), the patient choice among providers (x_9), gatekeeping (x_{10}) were related factors with the health system efficiency factors according to GLM.

In particular, the lowest effective countries should reconsider the health system policy and take precautions to improve the health system efficiency paying attention to important factors mentioned and highlighted above.

Acknowledgements

The authors would like to express our very great appreciation to Asst. Prof. Emre Dündar for his valuable and constructive suggestions during the development of this research study. Also, this study is a master's thesis written by SCT under MAC consultancy.

Funding

This study is supported by Ondokuz Mayıs University Scientific Research Projects

Coordination Unit. Project Number: PYO. SCIENCE. 1904.17.004.

The Declaration of Conflict of Interest/ Common Interest

No conflict of interest or common interest has been declared by the authors.

Authors' Contribution

MAC contributed to designing the study and providing data for the study. SCT conducted all statistical analyses and wrote the manuscript. All authors discussed the results and contributed to the final manuscript.

The Declaration of Ethics Committee Approval

The authors declare that this document does not require an ethics committee approval or any special permission.

The Declaration of Research and Publication Ethics

The authors of the paper declare that they comply with the scientific, ethical and quotation rules of SAUJS in all processes of the paper and that they do not make any falsification on the data collected. In addition, they declare that Sakarya University Journal of Science and its editorial board have no responsibility for any ethical violations that may be encountered, and that this study has not been evaluated in any academic publication environment other than Sakarya University Journal of Science.

REFERENCES

- [1] A. Afonso and M. St Aubyn, "Non-parametric approaches to education and health efficiency in OECD countries," *Journal of Applied Economics*, vol. 8, no. 2, pp. 227, 2005.
- [2] J. Spinks and B. Hollingsworth, "Health production and the socioeconomic determinants of health in OECD countries: the use of efficiency models," *Centre for Health Economics Working Paper 151*, pp. 3, 2005.
- [3] A. Afonso and M. St Aubyn, "Relative efficiency of health provision: A DEA approach with non-discretionary inputs," *ISEG-UTL Economics Working Paper*, no. 33, pp. 3, 2006.
- [4] J. Kujawska, "Measurement of healthcare system efficiency in OECD Countries," *Metody Ilościowe w Badaniach Ekonomicznych*, vol. 16, no. 2, pp. 23-32, 2015.
- [5] V. R. Çetin and S. Bahçe, "Measuring the efficiency of health systems of OECD countries by data envelopment analysis," *Applied Economics*, vol. 48, no. 37, pp. 3497-3507, 2016.
- [6] Y. A. Özcan and J. Khushalani, "Assessing the efficiency of public health and medical care provision in OECD countries after a decade of reform," *Central European Journal of Operations Research*, vol. 25, no. 2, pp. 325-343, 2017.
- [7] D. Wranik, "Healthcare policy tools as determinants of health system efficiency: evidence from the OECD," *Health Economics, Policy, and Law*, vol. 7, no. 2, pp. 197-226, 2012.
- [8] P. H. De Cos and E. Moral-Benito, "Determinants of health-system efficiency: evidence from OECD countries," *International Journal of Health Care Finance and Economics*, vol. 14, no. 1, pp. 69-93, 2014.
- [9] T. Şenel and M. A. Cengiz, "A Bayesian approach for evaluation of determinants of health system efficiency using stochastic frontier analysis and beta regression," *Computational and Mathematical Methods in Medicine*, vol. 2016, pp. 1-5, 2016.
- [10] V. Paris, M. Devaux, and L. Wei, "Health systems institutional characteristics: a

- survey of 29 OECD countries,” OECD Health Working Papers, no. 50, pp. 22-28, 2010.
- [11] D. Aigner, C. Lowell, and P. Schmidt, “Formulation and estimation of stochastic frontier production function models,” *Journal of Econometrics*, vol. 6, no. 1, pp. 21–37, 1977.
- [12] G. H. Dunteman, and M. H. R. Ho. “An introduction to generalized linear models”, vol. 145, Sage Publications, 2005.
- [13] D. Karaboğa, *Artificial Intelligence Optimization Algorithms*, Ankara: Nobel, 2011.
- [14] D. Karaboğa and B. Baştürk, “On the performance of artificial bee colony (ABC) algorithm,” *Applied Soft Computing*, vol. 8, no. 1, pp. 687-697, 2008.
- [15] J. H. Holland, *Adaptation in natural and artificial systems: an introductory analysis with applications to biology, control, and artificial intelligence*, USA: MIT Press, 1992.
- [16] Ç. Elmas, *Artificial Intelligence Applications*, Ankara: Seçkin, 2010.
- [17] R. Storn and K. Price, “Differential evolution a simple and efficient heuristic for global optimization over continuous spaces,” *Journal of Global Optimization*, vol. 11, no. 4, pp. 341-359, 1997.
- [18] T. Keskindürk, “Differential evolution Algorithm,” *Istanbul Commerce University Journal of Science*, vol. 9, pp. 85-99, 2006.
- [19] H. Akaike, “Information theory and extension of the maximum likelihood principle,” 2nd International Symposium on Information Theory, pp. 267-281, 1973.
- [20] Hurvich, C. M. and C. L. Tsai, “Regression and time series model selection in small samples,” *Biometrika*, vol. 76, no. 2, pp. 297-307, 1989.
- [21] G. Schwarz, “Estimating the dimension of model,” *Annals of Statistics*, vol. 6, pp. 461-464, 1978.
- [22] H. Bozdogan, “Model selection and Akaike’s Information Criterion (AIC): the general theory and its analytical extensions,” *Psychometrika*, vol. 52, no. 3, pp. 345-370, 1987.

JOURNAL OF SCIENCE



SAKARYA UNIVERSITY

Sakarya University Journal of Science

ISSN 1301-4048 | e-ISSN 2147-835X | Period Bimonthly | Founded: 1997 | Publisher Sakarya University |
<http://www.saujs.sakarya.edu.tr/en/>

Title: On a Generalized Difference Sequence Spaces of Fractional Order associated with Multiplier Sequence Defined by A Modulus Function

Authors: Taja YAYING

Received: 2020-05-29 12:39:03

Accepted: 2020-08-23 20:54:27

Article Type: Research Article

Volume: 24

Issue: 5

Month: October

Year: 2020

Pages: 1105-1114

How to cite

Taja YAYING; (2020), On a Generalized Difference Sequence Spaces of Fractional Order associated with Multiplier Sequence Defined by A Modulus Function. Sakarya University Journal of Science, 24(5), 1105-1114, DOI:

<https://doi.org/10.16984/saufenbilder.744881>

Access link

<http://www.saujs.sakarya.edu.tr/en/pub/issue/56422/744881>

New submission to SAUJS

<http://dergipark.org.tr/en/journal/1115/submission/step/manuscript/new>

On a Generalized Difference Sequence Spaces of Fractional Order associated with Multiplier Sequence Defined by a Modulus Function

Taja YAYING*¹

Abstract

Let $\Gamma(m)$ denotes the gamma function of a real number $m \notin \{0, -1, -2, \dots\}$. Then the difference matrix Δ^α of a fractional order α is defined as

$$(\Delta^\alpha v)_k = \sum_i (-1)^i \frac{\Gamma(\alpha+1)}{i! \Gamma(\alpha-i+1)} v_{k+i}.$$

Using the difference operator Δ^α , we introduce paranormed difference sequence spaces $N_\theta(\Delta^\alpha, f, \Lambda, p)$ and $S_\theta(\Delta^\alpha, f, \Lambda, p)$ of fractional orders involving lacunary sequence, θ ; modulus function, f and multiplier sequence, $\Lambda = (\lambda_k)$. We investigate topological structures of these spaces and examine various inclusion relations.

Keywords: Difference operator Δ^α , Paranormed sequence space, Lacunary sequence, Modulus function, Multiplier sequence.

1. INTRODUCTION

Let w denotes the space of all real valued sequences. Also ℓ_∞, c and c_0 will denote the spaces of bounded, convergent and null sequences, respectively. The spaces ℓ_∞, c and c_0 are Banach spaces normed by $\|v\|_\infty = \sup_k |v_k|$.

The notion of difference sequence spaces was first introduced by Kızmaz [1]. Later on, the notion was generalized by Et and Colak [2] as given below:

Let m be a non negative integer, then

$$\Delta^m(V) = \{v = (v_k) : \Delta^m v \in V\} \text{ for } V \in \{\ell_\infty, c, c_0\},$$

where $(\Delta^m v)_k = (\Delta^{m-1} v)_k - (\Delta^{m-1} v)_{k+1}$, $(\Delta^0 v)_k = v_k$ and

$$(\Delta^m v)_k = \sum_{i=0}^m (-1)^i \binom{m}{i} v_{k+i}.$$

These spaces are Banach spaces with the norm defined by

$$\|v\|_\Delta = \sum_{i=0}^m |v_i| + \sup_k |(\Delta^m v)_k|.$$

Furthermore, generalized difference sequence spaces were studied by Et and Esi [3], Et and

* Corresponding Author: tajayaying20@gmail.com

¹ Dera Natung Government College, Itanagar, ORCID: <https://orcid.org/0000-0003-3435-8417>

Başarır [4], Malkowsky and Parashar [5], Et and Tripathy [38], Çolak [6], and many others.

The notion of statistical convergence was independently introduced by Fast [31] and Schoenberg [32]. The concept lies on the asymptotic density of the subset E of natural numbers \mathbb{N} . A subset E of \mathbb{N} is said to have asymptotic density $\delta(E)$, if $\delta(E) = \lim_{n \rightarrow \infty} \frac{1}{n} \sum_{k=1}^n \chi_E(k)$ exists, where χ_E is the characteristic function of E .

A sequence $v = (v_i)$ is said to be statistically convergent to L if for every $\varepsilon > 0$,

$$\lim_{k \rightarrow \infty} \frac{1}{k} |\{k \in \mathbb{N}: |v_k - L| \geq \varepsilon\}| = 0,$$

where $|E|$ denotes the cardinality of the set E . In this case, we write $S - \lim v_k = L$ or $v_k \rightarrow L(S)$.

Let $\theta = (k_r)$ be the sequence of positive integers such that $k_0 = 0$, $0 < k_r < k_{r+1}$ and $h_r = k_r - k_{r-1} \rightarrow 0$ as $r \rightarrow \infty$. Then θ is called lacunary sequence. The intervals determined by θ will be denoted by $I_r = (k_{r-1}, k_r]$ and the ratio $\frac{k_r}{k_{r-1}}$ will be denoted by q_r . Freedman et. Al [44] introduced the sequence space N_θ given by

$$N_\theta = \left\{ v = (v_k) \in w: h_r^{-1} \sum_{k \in I_r} |v_k - L| \rightarrow 0, \text{ for some } L \right\};$$

and showed that the space N_θ is a BK space with the norm defined by

$$\|v\|_\theta = \sup_r \left(h_r^{-1} \sum_{k \in I_r} |v_k| \right).$$

The study on sequence spaces was extended by using the notion of associated multiplier sequences. Goes and Goes [40] defined the differentiated sequence space dE and the integrated sequence space $\int E$ for a given sequence space E , using the multiplier sequences

(k^{-1}) and (k) respectively. Different authors took different types of multiplier sequences for their study. In this article we shall consider a general multiplier sequence $\Lambda = (\lambda_k)$ of non-zero scalars.

Let $\Lambda = (\lambda_k)$ be a sequence of non-zero scalars. Then the multiplier sequence space $E(\Lambda)$, associated with the multiplier sequence Λ , of the sequence space E is defined as

$$E(\Lambda) = \{v = (v_k) \in w: (\lambda_k v_k) \in E\}.$$

The notion of a modulus function was introduced by Nakano [34]. A modulus is a function $f: [0, \infty) \rightarrow [0, \infty)$ such that

1. $f(v) = 0$ if and only if $v = 0$;
2. $f(v + u) \leq f(v) + f(u)$;
3. f is increasing;
4. f is continuous from right at 0.

Ruckle [36] and Maddox [35] used modulus function f to construct various sequence spaces. The following inequality (see [37]) will be used throughout in this article:

$$|a_k + b_k|^{p_k} \leq C(|a_k|^{p_k} + |b_k|^{p_k});$$

where $a_k, b_k \in \mathbb{C}$, $0 < p_k \leq \sup p_k = H$, $C = \max(1, 2^{H-1})$.

Proposition 1.1 [43] Let f be a modulus function and let $0 < \delta < 1$. Then for each $v \geq \delta$ we have $f(v) \leq 2f(1)\delta^{-1}v$.

2. FRACTIONAL DIFFERENCE OPERATOR AND GENERALIZED DIFFERENCE SEQUENCE SPACE OF FRACTIONAL ORDERS

Let $\Gamma(m)$ be the Gamma function of a real number m and $m \notin \{0, -1, -2, \dots\}$. Gamma function can be expressed as an improper integral

$$\Gamma(m) = \int_0^\infty e^{-t} t^{m-1} dx.$$

Recently, Baliarsingh and Dutta [10, 11] have introduced the generalized difference operator Δ^α , for a positive fraction α as follows:

$$(\Delta^\alpha v)_k = \sum_{i=0}^{\infty} (-1)^i \frac{\Gamma(\alpha+1)}{i! \Gamma(\alpha-i+1)} v_{k+i}.$$

In particular, we have

1. $(\Delta^{\frac{1}{2}} v)_k = v_k - \frac{1}{2} v_{k+1} - \frac{1}{8} v_{k+2} - \frac{1}{16} v_{k+3} - \frac{5}{128} v_{k+4} - \dots$
2. $(\Delta^{-\frac{1}{2}} v)_k = v_k + \frac{1}{2} v_{k+1} + \frac{3}{8} v_{k+2} + \frac{5}{16} v_{k+3} + \frac{35}{128} v_{k+4} + \dots$
3. $(\Delta^{\frac{2}{3}} v)_k = v_k - \frac{2}{3} v_{k+1} - \frac{1}{9} v_{k+2} - \frac{4}{81} v_{k+3} - \frac{7}{243} v_{k+4} - \dots$

Baliarsingh [12] defined the spaces $V(\Gamma, \Delta^\alpha, u)$ for $V \in \{\ell_\infty, c, c_0\}$ using the fractional difference operator Δ^α and studied their topological properties and obtained their α , β , and γ duals.

The studies on generalized difference sequence spaces of fractional orders were extended by Baliarsingh and Dutta [10, 11], Dutta and Baliarsingh [18], Kadak and Baliarsingh [19], Baliarsingh and Kadak [13], Meng and Mei [14], Yaying and Hazarika [16], Yaying et. al [15], Nayak et. al [26], Kadak [21, 22], Furkan [28], Özger [29, 30] etc. They studied different sequence spaces of fractional orders. Kadak in [23] determined a new classes of fractional difference sequence spaces $\Delta_v^\alpha(V)$ as follows:

$$\Delta_u^\alpha(V) = \{v = (v_k) \in w : (\Delta_u^\alpha v)_k \in V\},$$

where $(\Delta_u^\alpha v)_k = \sum_{i=0}^{\infty} (-1)^i \frac{\Gamma(\alpha+1)}{i! \Gamma(\alpha-i+1)} u_{k+i} v_{k+i}$ and $u = (u_k)$ is a sequence of positive real numbers. Using the fractional difference operator Δ_u^α , he defined strongly Cesàro summable and statistical difference sequence spaces of fractional orders involving lacunary sequence, θ and arbitrary sequence $p = (p_k)$ of positive real numbers.

Theorem 2.1. [12]

1. For a proper fraction α , $\Delta^\alpha: w \rightarrow w$ is a linear operator.

2. For proper fractions $\alpha, \beta > 0$, $\Delta^\alpha((\Delta^\beta v)_k) = (\Delta^{\alpha+\beta} v)_k$ and $\Delta^\alpha((\Delta^{-\alpha} v)_k) = v_k$.

The main objective of this article is to introduce generalized paranormed difference sequence spaces $N_\theta(\Delta^\alpha, f, \Lambda, p)$ and $S_\theta(\Delta^\alpha, f, \Lambda, p)$ of fractional orders involving lacunary sequence, θ ; modulus function, f and multiplier sequence, Λ and to investigate topological structures of these spaces and examine various inclusion relations.

3. MAIN RESULTS

Throughout the paper, $p = (p_k)$ is a sequence of positive scalars. By using the fractional difference operator Δ^α , we introduce some new generalized difference sequence spaces $N_\theta^0(\Delta^\alpha, f, \Lambda, p)$, $N_\theta(\Delta^\alpha, f, \Lambda, p)$ and $N_\theta^\infty(\Delta^\alpha, f, \Lambda, p)$ involving lacunary sequence, θ ; modulus function, f and multiplier sequence, Λ as follows:

$$\begin{aligned} N_\theta(\Delta^\alpha, f, \Lambda, p) &= \left\{ v = (v_k) \in w : \lim_{r \rightarrow \infty} h_r^{-1} \sum_{k \in I_r} f(|\lambda_k(\Delta^\alpha v)_k - L|)^{p_k} = 0, \text{ for some } L \right\}; \\ N_\theta^0(\Delta^\alpha, f, \Lambda, p) &= \left\{ v = (v_k) \in w : \lim_{r \rightarrow \infty} h_r^{-1} \sum_{k \in I_r} f(|\lambda_k(\Delta^\alpha v)_k|)^{p_k} = 0 \right\}; \\ N_\theta^\infty(\Delta^\alpha, f, \Lambda, p) &= \left\{ v = (v_k) \in w : \lim_{r \rightarrow \infty} h_r^{-1} \sum_{k \in I_r} f(|\lambda_k(\Delta^\alpha v)_k|)^{p_k} < \infty \right\}; \end{aligned}$$

Note that:

1. When $f(v) = v$, $\alpha = 0$, $\lambda_k = 1$, for all k and $p_k = 1$ for all k , then the above sequence spaces reduces to ordinary lacunary convergent sequence spaces as studied by Freedman et. Al [44].
2. When $\alpha = m \in \mathbb{N}$, $\lambda_k = 1$, for all k and $p_k = 1$ for all k , then the above sequence spaces reduces to $V(\Delta^m, f)$ where $V \in \{N_\theta^0, N_\theta, N_\theta^\infty\}$ as studied by Çolak [6].
3. When $\alpha = m \in \mathbb{N}$, and $\lambda_k = 1$, for all k , then the above sequence spaces reduces to the sequence spaces studied by Tripathy and Et [38].

4. When $\lambda_k = 1$ for all $k \in \mathbb{N}$, then the above class of sequence spaces reduce to $N_\theta^0(f, p)$, $N_\theta(f, p)$, $N_\theta^\infty(f, p)$ as studied by Yaying [27].

Theorem 3.1. The sequence spaces $N_\theta(\Delta^\alpha, f, \Lambda, p)$, $N_\theta^0(\Delta^\alpha, f, \Lambda, p)$ and $N_\theta^\infty(\Delta^\alpha, f, \Lambda, p)$ are linear spaces.

Proof. We shall prove for $N_\theta^0(\Delta^\alpha, f, \Lambda, p)$. Others can be proved in a similar fashion. Let $v, u \in N_\theta^0(\Delta^\alpha, f, \Lambda, p)$ and α' and β' be two scalars. Then there exist $M_{\alpha'} > 0$ and $K_{\beta'} > 0$ such that $|\alpha'| \leq M_{\alpha'}$ and $|\beta'| \leq K_{\beta'}$. Since f is subadditive and Δ^α is linear, we have

$$\begin{aligned} & h_r^{-1} \sum_{k \in I_r} f(|\lambda_k(\Delta^\alpha(\alpha'v + \beta'u))_k|)^{p_k} \\ & \leq h_r^{-1} \sum_{k \in I_r} [f(|\alpha'|\lambda_k|(\Delta^\alpha v)_k|) + \\ & \quad f(|\beta'|\lambda_k|(\Delta^\alpha u)_k|)]^{p_k} \\ & \leq C(M_{\alpha'})^H h_r^{-1} \sum_{k \in I_r} f(|\lambda_k(\Delta^\alpha v)_k|)^{p_k} + \\ & \quad C(K_{\beta'})^H h_r^{-1} \sum_{k \in I_r} f(|\lambda_k(\Delta^\alpha u)_k|)^{p_k} \rightarrow 0 \end{aligned}$$

as $r \rightarrow \infty$. This proves the linearity of $N_\theta^0(\Delta^\alpha, f, \Lambda, p)$.

Theorem 3.2. $N_\theta^0(\Delta^\alpha, f, \Lambda, p)$ is a paranormed sequence space paranormed by

$$g(v) = \sup_r \left(h_r^{-1} \sum_{k \in I_r} f(|\lambda_k(\Delta^\alpha v)_k|)^{p_k} \right)^{1/M};$$

where $M = \max(1, \sup_k p_k)$.

Proof. Clearly $g(\theta) = 0$ and $g(v) = g(-v)$ for all $v \in N_\theta^0(\Delta^\alpha, f, \Lambda, p)$. Using the linearity of Δ^α , definition of f and Minkowski's inequality, it is not difficult to show that $g(v + u) \leq g(v) + g(u)$, for any two sequences $v, u \in N_\theta^0(\Delta^\alpha, f, \Lambda, p)$.

It remains to show the continuity of the scalar multiplication. Let β be any scalar. By definition of modulus f , we have

$$\begin{aligned} g(\beta v) &= \sup_r \left(h_r^{-1} \sum_{k \in I_r} f(|\lambda_k(\Delta^\alpha \beta v)_k|)^{p_k} \right)^{1/M} \\ &\leq N_\beta^{H/M} g(v), \end{aligned}$$

where N_β is a positive number such that $|\beta| \leq N_\beta$ and $H = \sup p_k$.

Now, since f is modulus, we have $x \rightarrow 0$ implies $g(\beta v) \rightarrow 0$. Similarly, $v \rightarrow 0$ and $\beta \rightarrow 0$ implies $g(\beta v) \rightarrow 0$. Finally, keeping v fixed and letting $\beta \rightarrow 0$ implies $g(\beta v) \rightarrow 0$. This completes the proof.

Theorem 3.3. Let f be a modulus function, then $N_\theta^0(\Delta^\alpha, f, \Lambda, p) \subset N_\theta(\Delta^\alpha, f, \Lambda, p) \subset N_\theta^\infty(\Delta^\alpha, f, \Lambda, p)$.

Proof. The first inclusion is obvious. We provide the proof of the second inclusion.

Let $v \in N_\theta(\Delta^\alpha, f, \Lambda, p)$. By definition of f , we have,

$$\begin{aligned} & h_r^{-1} \sum_{k \in I_r} f(|\lambda_k(\Delta^\alpha v)_k|)^{p_k} \\ &= h_r^{-1} \sum_{k \in I_r} f(|\lambda_k(\Delta^\alpha v)_k - L + L|)^{p_k} \\ &\leq C h_r^{-1} \sum_{k \in I_r} f(|\lambda_k(\Delta^\alpha v)_k - L|)^{p_k} \\ & \quad + C h_r^{-1} \sum_{k \in I_r} f(|L|)^{p_k}. \end{aligned}$$

Now, there exist a positive integer K_L such that $|L| \leq K_L$. Hence, we have,

$$\begin{aligned} & h_r^{-1} \sum_{k \in I_r} f(|\lambda_k(\Delta^\alpha v)_k|)^{p_k} \\ &\leq C h_r^{-1} \sum_{k \in I_r} f(|\lambda_k(\Delta^\alpha v)_k - L|)^{p_k} \\ & \quad + C(K_L f(1))^H. \end{aligned}$$

This proves the result.

Theorem 3.4. If f, f_1, f_2 be modulus functions and $V \in \{N_\theta, N_\theta^0, N_\theta^\infty\}$, then

1. $V(\Delta^\alpha, f, \Lambda, p) \subset V(\Delta^\alpha, f \circ f_1, \Lambda, p)$.
2. $V(\Delta^\alpha, f_1, \Lambda, p) \cap V(\Delta^\alpha, f_2, \Lambda, p) \subset V(\Delta^\alpha, f_1 + f_2, \Lambda, p)$.

Proof. We shall prove for $N_\theta^0(\Delta^\alpha, f, \Lambda, p)$. Let $\varepsilon > 0$ and choose $0 < \delta < 1$ such that $f(t) < \varepsilon$ for $0 \leq t \leq \delta$. We write $u_k = f_1(|\lambda_k(\Delta^\alpha v)_k|)$ and consider

$$\sum_{k \in I_r} f(u_k)^{p_k} = \sum_1 f(u_k)^{p_k} + \sum_2 f(u_k)^{p_k}$$

where the first summation runs over $u_k \leq \delta$ and the second summation runs over $u_k > \delta$. Since f is continuous, we have

$$\sum_1 f(u_k)^{p_k} < h_r \varepsilon^H. \quad (3.1)$$

Also,

$$u_k < \frac{u_k}{\delta} \leq 1 + \frac{u_k}{\delta}.$$

Hence, by using Proposition 1.1, we can write

$$h_r^{-1} \sum_2 f(u_k)^{p_k} \leq \max\{1, (2f(1)\delta^{-1})^H\} h_r^{-1} \sum_{k \in I_r} u_k. \quad (3.2)$$

Using equations (3.1) and (3.2), we get $N_\theta^0(\Delta^\alpha, f, \Lambda, p) \subset N_\theta^0(\Delta^\alpha, f \circ f_1, \Lambda, p)$.

The proof of (ii) follows from the inequality

$$(f_1 + f_2)(|\lambda_k(\Delta^\alpha v)_k|)^{p_k}$$

$$\leq C f_1(|\lambda_k(\Delta^\alpha v)_k|)^{p_k} + C f_2(|\lambda_k(\Delta^\alpha v)_k|)^{p_k}.$$

The following result is an immediate consequence of Theorem 3.4 (i).

Corollary 3.5 Let f be a modulus function. Then $V(\Delta^\alpha, \Lambda, p) \subset V(\Delta^\alpha, f, \Lambda, p)$ where $V \in \{N_\theta, N_\theta^0, N_\theta^\infty\}$.

Theorem 3.6 Let $0 < p_k < q_k$ and $\left(\frac{q_k}{p_k}\right)$ be bounded then $V(\Delta^\alpha, f, \Lambda, q) \subset V(\Delta^\alpha, f, \Lambda, p)$.

Proof. The proof of the theorem is easy and hence omitted.

4. LACUNARY STATISTICAL CONVERGENCE OF FRACTIONAL ORDER DEFINED BY MODULUS FUNCTION

In this section we introduce the set of generalized lacunary statistical convergence of fractional orders associated with a multiplier sequence defined by a modulus function as follows:

$$S_\theta(\Delta^\alpha, f, \Lambda, p) = \left\{ v = (v_k) \in w: \lim_{r \rightarrow \infty} h_r^{-1} |\{k \in I_r: f(|\lambda_k(\Delta^\alpha v)_k - L|)^{p_k} \geq \varepsilon\}| = 0, \text{ for some } L \right\}.$$

When $p_k = 1$ for all $k \in \mathbb{N}$, we shall denote $S_\theta(\Delta^\alpha, f, \Lambda, p)$ by $S_\theta(\Delta^\alpha, f, \Lambda)$.

Note that:

1. When $f(v) = v$, $\alpha = 0$, $\lambda_k = 1$ for all $k \in \mathbb{N}$ and $p_k = 1$ for all $k \in \mathbb{N}$, then the above sequence spaces reduce to ordinary lacunary statistical convergent sequence spaces as studied by Fridy and Orhan [42].
2. When $\alpha = m \in \mathbb{N}$, $\lambda_k = 1$, for all $k \in \mathbb{N}$, then the above sequence spaces reduce to the sequence spaces as studied by Tripathy and Et [38].

Theorem 4.1. Let θ be a lacunary sequence. Then $S(\Delta^\alpha, f, \Lambda) \subset S_\theta(\Delta^\alpha, f, \Lambda)$, if $\liminf q_r > 1$.

Proof. Let $\liminf q_r > 1$, then there exist a $\delta > 0$ such that $1 + \delta \leq q_r$, for sufficiently large r . Since $h_r = k_r - k_{r-1}$, which implies that $\frac{h_r}{k_r} \geq \frac{\delta}{1+\delta}$.

Let $v \in S(\Delta^\alpha, f, \Lambda)$. Then for $\varepsilon > 0$

$$\begin{aligned} & \frac{1}{k_r} |\{k \leq k_r: f(|\lambda_k(\Delta^\alpha v)_k - L|) \geq \varepsilon\}| \\ & \geq \frac{1}{k_r} |\{k \in I_r: f(|\lambda_k(\Delta^\alpha v)_k - L|) \geq \varepsilon\}| \\ & \geq \frac{\delta}{1+\delta} h_r^{-1} |\{k \in I_r: f(|\lambda_k(\Delta^\alpha v)_k - L|) \geq \varepsilon\}|. \end{aligned}$$

This proves the result.

Theorem 4.2. Let θ be a lacunary sequence. Then $S_\theta(\Delta^\alpha, f, \Lambda) \subset S(\Delta^\alpha, f, \Lambda)$, if $\limsup q_r < \infty$.

Proof. Let $\limsup q_r < \infty$, then there is a $K > 0$ such that $q_r < K$, for all r . Let $v \in S_\theta(\Delta^\alpha, f, \Lambda)$ and let $\tau_r = |\{k \in I_r : f(|\lambda_k(\Delta^\alpha v)_k - L|) \geq \varepsilon\}|$.

Now by definition, for $\varepsilon > 0$ there is an integer r_0 such that

$$h_r^{-1} \tau_r < \varepsilon \text{ for all } r > r_0. \quad (4.1)$$

Now let $\gamma = \max\{\tau_r : 1 \leq r \leq r_0\}$ and let n be any integer satisfying $k_{r-1} < n \leq k_r$, then we can write

$$\begin{aligned} & \frac{1}{n} |\{k \leq n : f(|\lambda_k(\Delta^\alpha v)_k - L|) \geq \varepsilon\}| \\ & \leq \frac{1}{k_{r-1}} |\{k \leq k_r : f(|\lambda_k(\Delta^\alpha v)_k - L|) \geq \varepsilon\}| \\ & = \frac{1}{k_{r-1}} \{\tau_1 + \tau_2 + \dots + \tau_{r_0} + \tau_{r_0+1} + \dots + \tau_r\} \\ & \leq \frac{\gamma}{k_{r-1}} r_0 + \frac{1}{k_{r-1}} \left\{ h_{r_0+1} \frac{\tau_{r_0+1}}{h_{r_0+1}} + \dots + h_r \frac{\tau_r}{h_r} \right\} \\ & \leq \frac{\gamma}{k_{r-1}} r_0 + \frac{1}{k_{r-1}} \left(\sup_{r < r_0} \frac{\tau_r}{h_r} \right) (h_{r_0+1} + \dots + h_r) \\ & \leq \frac{\gamma}{k_{r-1}} r_0 + \varepsilon \frac{k_r - k_{r_0}}{k_{r-1}} \quad (\text{using equation (4.1)}) \\ & \leq \frac{\gamma}{k_{r-1}} r_0 + \varepsilon q_r \\ & \leq \frac{\gamma}{k_{r-1}} r_0 + \varepsilon K. \end{aligned}$$

This proves the result.

Following result is the direct consequence of theorems (4.1) and (4.2).

Corollary 4.3. Let θ be a lacunary sequence. Then $S(\Delta^\alpha, f, \Lambda) = S_\theta(\Delta^\alpha, f, \Lambda)$, if $1 < \liminf q_r \leq \limsup q_r < \infty$.

Theorem 4.4. Let f be a modulus function and $H = \sup p_k$. Then $N_\theta(\Delta^\alpha, f, \Lambda, p) \subset S_\theta(\Delta^\alpha, \Lambda)$.

Proof. Let $v \in N_\theta(\Delta^\alpha, f, \Lambda, p)$ and $\varepsilon > 0$ be given. Then,

$$\begin{aligned} & h_r^{-1} \sum_{k \in I_r} f(|\lambda_k(\Delta^\alpha v)_k - L|)^{p_k} \\ & = h_r^{-1} \sum_{k \in I_r} f(|\lambda_k(\Delta^\alpha v)_k - L|)^{p_k} \\ & \quad + h_r^{-1} \sum_{\substack{k \in I_r \\ |\lambda_k(\Delta^\alpha v)_k - L| < \varepsilon}} f(|\lambda_k(\Delta^\alpha v)_k - L|)^{p_k} \\ & \geq h_r^{-1} \sum_{\substack{k \in I_r \\ |\lambda_k(\Delta^\alpha v)_k - L| \geq \varepsilon}} f(|\lambda_k(\Delta^\alpha v)_k - L|)^{p_k} \\ & \geq h_r^{-1} \sum_{k \in I_r} f(\varepsilon)^{p_k} \\ & \geq h_r^{-1} \sum_{k \in I_r} \min(f(\varepsilon)^{\inf p_k}, f(\varepsilon)^H) \\ & \geq h_r^{-1} |\{k \in I_r : |\lambda_k(\Delta^\alpha v)_k - L| \geq \varepsilon\}| \min(f(\varepsilon)^{\inf p_k}, f(\varepsilon)^H). \end{aligned}$$

Taking the limit as $r \rightarrow \infty$,

$$\begin{aligned} & \lim_{r \rightarrow \infty} h_r^{-1} |\{k \in I_r : |\lambda_k(\Delta^\alpha v)_k - L| \geq \varepsilon\}| \\ & \leq \frac{1}{\min(f(\varepsilon)^{\inf p_k}, f(\varepsilon)^H)} \lim_{r \rightarrow \infty} h_r^{-1} \sum_{k \in I_r} f(|\lambda_k(\Delta^\alpha v)_k - L|)^{p_k} = 0. \end{aligned}$$

This proves the result.

Theorem 4.5. Let f be bounded and $0 < h = \inf p_k \leq p_k \leq \sup p_k = H < \infty$. Then $S_\theta(\Delta^\alpha, \Lambda) \subset N_\theta(\Delta^\alpha, f, \Lambda, p)$.

Proof. Since f is bounded, there exist some K such that $f(v) < K$ for all $v \geq 0$. Now,

$$h_r^{-1} \sum_{k \in I_r} f(|\lambda_k(\Delta^\alpha v)_k - L|)^{p_k}$$

$$\begin{aligned}
&= h_r^{-1} \sum_{\substack{k \in I_r \\ |\lambda_k(\Delta^\alpha v)_k - L| \geq \varepsilon}} f(|\lambda_k(\Delta^\alpha v)_k - L|)^{p_k} \\
&\quad + h_r^{-1} \sum_{\substack{k \in I_r \\ |\lambda_k(\Delta^\alpha v)_k - L| < \varepsilon}} f(|\lambda_k(\Delta^\alpha v)_k - L|)^{p_k} \\
&\leq h_r^{-1} \sum_{k \in I_r} \max(K_h, K_H) + h_r^{-1} \sum_{k \in I_r} f(\varepsilon)^{p_k} \\
&\leq \max(K_h, K_H) h_r^{-1} \{ |k \in I_r : |\lambda_k(\Delta^\alpha v)_k - L| \geq \varepsilon \} + \max(f(\varepsilon)^h, f(\varepsilon)^H)
\end{aligned}$$

Hence $v \in N_\theta(\Delta^\alpha, f, \Lambda, p)$.

The following result is an immediate consequence of the Theorem 4.4 and Theorem 4.5.

Corollary 4.6. *Let f be bounded and $0 < h = \inf p_k \leq p_k \leq \sup p_k = H < \infty$. Then $S_\theta(\Delta^\alpha, \Lambda) = N_\theta(\Delta^\alpha, f, \Lambda, p)$.*

5. CONCLUSION

Fractional order difference sequence space has been an active field of research during the recent times. Many authors have introduced different classes of difference sequence spaces of fractional orders, obtained their α , β and γ duals and matrix transformations. Recently, Kadak [24] introduced the notions of statistically Ω -convergence and Ω -statistically convergence by the weighted method with respect to the fractional difference operator $\Delta_h^{\alpha, \beta, \gamma}$. In his another work, Kadak [25] introduced the concepts of statistically weighted $\psi_\Delta^{p, q}$ -summability, weighted $\psi_\Delta^{p, q}$ -statistical convergence and weighted strongly $\psi_\Delta^{p, q}$ -summability with respect to a more generalized difference operator $\Delta_{h, p, q}^{\alpha, \beta, \gamma}$ including (p, q) -analogue of gamma function and obtained Korovkin type approximation theorems for function of two variables. In this article we tend to generalize the findings of the previous authors using modulus function and a multiplier sequence. We expect that the introduced notions and the results might be a reference for further studies in this field. For further studies one can

investigate and generalize this results using sequence of modulus functions, Orlicz function, etc. One can obtain similar results by employing more generalized fractional difference operator as defined by Kadak in [24, 25].

Acknowledgements

The author would like to thank the anonymous referees for necessary comments which have improved the presentation of the paper.

Funding

The author received no financial support for the research, authorship, and/or publication of this paper.

The Declaration of Conflict of Interest/ Common Interest

No conflict of interest or common interest has been declared by the author.

The Declaration of Ethics Committee Approval

The author declares that this document does not require an ethics committee approval or any special permission.

The Declaration of Research and Publication Ethics

The author of the paper declares that he complies with the scientific, ethical and quotation rules of SAUJS in all processes of the paper and that he does not make any falsification on the data collected. In addition, he declares that Sakarya University Journal of Science and its editorial board have no responsibility for any ethical violations that may be encountered, and that this study has not been evaluated in any academic publication environment other than Sakarya University Journal of Science.

REFERENCES

- [1] H. Kızmaz, On certain sequence spaces, Canadian Mathematical Bulletin, Vol. 24, no. 2, pp. 169-176, 1981.
- [2] M. Et, R. Çolak, On some generalized difference sequence spaces, Soochow Journal of Mathematics, Vol. 21, no. 4, pp. 377-386, 1995.
- [3] M. Et, A. Esi, On Köthe-Toeplitz duals of generalized difference sequence spaces, Bulletin of Malaysian Mathematical Science Society, Vol. 23, pp. 25-32, 2000.
- [4] M. Et, M. Başarır, On some new generalized difference sequence spaces, Periodica Mathematica Hungarica, Vol. 35, no. 3, pp. 169-175, 1997.
- [5] E. Malkowsky, S.D. Parashar, Matrix transformations in spaces of bounded and convergent difference sequences of order m , Analysis, Vol. 17, pp. 87-97, 1997.
- [6] R. Çolak, Lacunary strong convergence of difference sequences with respect to a modulus function, Filomat, Vol. 17, pp. 9-14, 2003.
- [7] C. Aydın, F. Başar, Some new difference sequence spaces, Applied Mathematics and Computation, Vol. 157, no. 3, pp. 677-693, 2004.
- [8] M. Mursaleen, Generalized spaces of difference sequences, Journal of Mathematical Analysis and Application, Vol. 203, no. 3, pp. 738-745, 1996.
- [9] Ç. A. Bektaş, M. Et, R. Çolak, Generalized difference sequence spaces and their dual spaces, Journal of Mathematical Analysis and Application, Vol. 292, pp. 423-432, 2004.
- [10] P. Baliarsingh, S. Dutta, A unifying approach to the difference operators and their applications, Boletim da Sociedade Paranaense de Matematica, Vol. 33, pp. 49-57, 2015.
- [11] P. Baliarsingh, S. Dutta, On the classes of fractional order difference sequence spaces and their matrix transformations, Applied Mathematics and Computation, Vol. 250, pp. 665-674, 2015.
- [12] P. Baliarsingh, Some new difference sequence spaces of fractional order and their dual spaces, Applied Mathematics and Computation, Vol. 219, pp. 9737-9742, 2013.
- [13] P. Baliarsingh, U. Kadak, On matrix transformations and Hausdorff measure of noncompactness of Euler difference sequence spaces of fractional order, Quaestiones Mathematica, DOI: 10.2989/16073606.2019.1648325.
- [14] J. Meng, L. Mei, Binomial difference sequence spaces of fractional order, Journal of Inequalities and Application, vol. 2018, 274, 2018.
- [15] T. Yaying, A. Das, B. Hazarika, P. Baliarsingh, Compactness of binomial difference sequence spaces of fractional order and sequence spaces, Rendiconti del Circolo Matematico di Palermo series II, vol. 68, 459-476, 2019.
- [16] T. Yaying, B. Hazarika, On sequence spaces generated by binomial difference operator of fractional order, Mathematica Slovaca, vol. 69, no. 4, pp. 901-918, 2019.
- [17] T. Yaying, Paranormed Riesz difference sequence spaces of fractional order, Kragujevac Journal of Mathematics, vol. 46, no. 2, pp. 175-191, 2022.
- [18] S. Dutta, P. Baliarsingh, A note on paranormed difference sequence spaces of fractional order and their matrix transformations, Journal of Egyptian Mathematical Society, vol. 22, pp. 249-253, 2014.

- [19] U. Kadak, P. Baliarsingh, On certain Euler difference sequence spaces of fractional order and related dual properties, *Journal of Nonlinear Science and Application*, vol. 8, pp. 997-1004, 2015.
- [20] P. Baliarsingh, U. Kadak, M. Mursaleen, On statistical convergence of difference sequences of fractional order and related Korovkin type approximation theorems, *Quaestiones Mathematica*, vol. 41, no. 8, pp. 1117-1133, 2018.
- [21] U. Kadak, Generalized statistical convergence based on fractional order difference operator and its applications to approximation theorems, *Iran Journal of Science and Technology Transactions A Science*, vol. 43, no. 1, 225-237, 2019.
- [22] U. Kadak, Generalized lacunary statistical difference sequence spaces of fractional order, *International Journal of Mathematics and Mathematical Science*, vol. 2015, Article ID 984283, 6 pages, 2015.
- [23] U. Kadak, Generalized Lacunary Statistical Difference Sequence Space of Fractional Order, *International Journal of Mathematics and Mathematical Sciences*, vol. 2015, Article ID 984283, 6 pages, 2015.
- [24] U. Kadak, Generalized weighted invariant mean based on fractional difference operator with applications to approximation theorems for functions of two variables, *Results Mathematics*, vol. 72, no. 3, pp. 1181-1202, 2017.
- [25] U. Kadak, Weighted statistical convergence based on generalized difference operator involving (p, q) -Gamma function and its application to approximation theorems, *Journal of Mathematical Analysis and Applications*, vol. 448, no. 2, pp. 1633-1650, 2017.
- [26] L. Nayak, M. Et, P. Baliarsingh, On certain generalized weighted mean fractional difference sequence spaces, *Proceedings of the National Academy of Sciences, India Section A: Physical Sciences*, vol. 89, pp. 163-170, 2019.
- [27] T. Yaying, On a new class of generalized difference sequence spaces of fractional order defined by modulus function, *Proyecciones*, vol. 38, no. 3, 485-497, 2018.
- [28] H. Furkan, On some λ -difference sequence spaces of fractional order, *Journal of Egyptian Mathematical Society*, vol. 25, no. 1, pp. 37-42, 2017.
- [29] F. Özger, Characterisations of compact operators on l_p -type fractional sets of sequences, *Demonstratio Mathematica*, vol. 52, pp. 105-115, 2019.
- [30] F. Özger, Some geometric characterisations of a fractional Banach set, *Communications Faculty of Sciences University of Ankara Series A1, Mathematics and Statistics*, vol. 68, no. 1, 546-558, 2019.
- [31] H. Fast, Sur la convergence statistique, *Colloquium Mathematicum*, vol. 2, pp. 241-244, 1951.
- [32] I.J. Schoenberg, The integrability of certain functions and related summability methods, *American Mathematical Monthly*, vol. 66, pp. 361-375, 1959.
- [33] I.J. Maddox, Paranormed sequence spaces generated by infinite matrices, *Proceedings of Cambridge Philosophical Society*, vol. 64, pp. 335-340, 1968.
- [34] H. Nakano, Concave Modulars, *Journal of Mathematical Society of Japan*, vol. 5, pp. 29-49, 1959.
- [35] I.J. Maddox, Spaces of strongly summable sequences, *The Quarterly Journal of Mathematics, Oxford*, vol. 18, no. 2, pp. 345-355, 1967.
- [36] W.H. Ruckle, FK spaces in which the sequence of coordinate vectors is bounded,

Canadian Journal of Mathematics, vol. 25,
pp. 973-978, 1973.

- [37] I.J. Maddox, Elements of Functional Analysis, Second edition., University Press, Cambridge, 1988.
- [38] B.C. Tripathy, M. Et, On Generalized Difference Lacunary Statistical Convergence, Studia Univ. "Babeş-Bolyai", Mathematica, L(1), 2015.
- [39] M. Et, Generalized Cesàro difference sequence spaces of non absolute type involving lacunary sequence, Applied Mathematics and Computation, vol. 219, pp. 9372-9376, 2013.
- [40] G. Goes, S. Goes, Sequences of bounded variation and sequences of Fourier coefficients, Mathematische Zeitschrift, vol. 118, pp. 93-102, 1917.
- [41] A. Esi, B.C. Tripathy, Strongly almost convergent generalized difference sequences associated with multiplier sequences, Mathematica Slovaca, vol. 57, no. 4, pp. 339-348, 2017.
- [42] J.A. Fridy, C. Orhan, Lacunary Statistical Convergence, Pacific Journal of Mathematics, vol. 160, no. 1, pp. 43-51, 1993.
- [43] S. Pehlivan, B. Fisher, On Some Sequence Spaces, Indian Journal of Pure and Applied Mathematics, vol. 25, no. 10, pp. 1067-1071, 1994.
- [44] A.R. Freedman, J.J. Sember, M. Raphael, Some Cesàro-type Summability Spaces, Proceedings of London Mathematical Society, vol. 37, no. 3, 508-520, 1978.

JOURNAL OF SCIENCE



SAKARYA UNIVERSITY

Sakarya University Journal of Science

ISSN 1301-4048 | e-ISSN 2147-835X | Period Bimonthly | Founded: 1997 | Publisher Sakarya University |
<http://www.saujs.sakarya.edu.tr/en/>

Title: Estimations of Cross-Sections for Photonuclear Reaction on Calcium Isotopes by Artificial Neural Networks

Authors: Serkan AKKOYUN, Hüseyin KAYA

Received: 2020-02-25 17:00:20

Accepted: 2020-08-24 17:20:01

Article Type: Research Article

Volume: 24

Issue: 5

Month: October

Year: 2020

Pages: 1115-1120

How to cite

Serkan AKKOYUN, Hüseyin KAYA; (2020), Estimations of Cross-Sections for Photonuclear Reaction on Calcium Isotopes by Artificial Neural Networks. Sakarya University Journal of Science, 24(5), 1115-1120, DOI:

<https://doi.org/10.16984/saufenbilder.694382>

Access link

<http://www.saujs.sakarya.edu.tr/en/pub/issue/56422/694382>

New submission to SAUJS

<http://dergipark.org.tr/en/journal/1115/submission/step/manuscript/new>



Estimations of Cross-Sections for Photonuclear Reaction on Calcium Isotopes by Artificial Neural Networks

Serkan AKKOYUN^{*1}, Hüseyin KAYA²

Abstract

The nuclear reaction induced by photon is one of the important tools in the investigation of atomic nuclei. In the reaction, a target material is bombarded by photons with high-energies in the range of gamma-ray energy range. In the bombarding process, the photons can statistically be absorbed by a nucleus in the target material. Then the excited nucleus can decay by emitting proton, neutron, alpha and light particles or photons. By performing photonuclear reaction on the target, it can be easily investigated low-lying excited states of the nuclei. In the present work, (γ , n) photonuclear reaction cross-sections on different calcium isotopes have been estimated by using artificial neural network method. The method is a mathematical model that mimics the brain functionality of the creatures. The correlation coefficient values of the method for both training and test phases being 0.99 indicate that the method is very suitable for this purpose.

Keywords: Photonuclear reaction, cross-section, calcium, artificial neural network

* Corresponding Author: sakkoyun@cumhuriyet.edu.tr

¹ Sivas Cumhuriyet University, Department of Physics, ORCID: <https://orcid.org/0000-0002-8996-3385>

² Sivas Cumhuriyet University, Department of Physics, E-Mail: hkaya@cumhuriyet.edu.tr
ORCID: <https://orcid.org/0000-0003-0093-8835>

1. INTRODUCTION

In the experimental nuclear physics studies, reactions induced by photons are one of the important tools. In these types of reactions, the target nuclei are bombarded by high-energy photons and the photons can be absorbed by a nucleus in the target material. Because of a nuclear process can be observed in the reaction, these are called as photonuclear reaction [1]. In order to release excess energy by the nucleus, one of the decay process is governed via emitting proton, neutron, alpha and light particles or photons. In the case of neutron emission, the reaction is called as photo-neutron reaction. By emitting particles from the target nucleus, a stable or unstable isotope can be formed. The unstable isotope goes to stable one by beta decays. The half-life of the radioisotopes can also be determined in these types of reactions.

The cross-section values for photo-neutron reactions for different isotopes and energies are determined either experimentally or theoretically [2, 3]. One of the most used theoretical codes for this purpose is TALYS computer code [4]. TENDL database [5] is based on this code and other sources such as ENDF [6]. The code is a system for the analysis and prediction of nuclear reactions. The basic objective behind its construction is the simulation of nuclear reactions that involve neutrons, photons, protons, deuterons, tritons, ^3He - and alpha-particles, in the 1 keV - 200 MeV energy range and for target nuclides of mass 12 and heavier. To achieve this, it is implemented a suite of nuclear reaction models into a single code system.

Calcium (Ca) is a metal with a silver color whose structure is cubic crystal [7]. It has 25 known isotopes and 5 of them are stable. The abundances of the isotopes in percentage are 96.941, 0.647, 0.135, 2.086 and 0.187 for ^{40}Ca , ^{42}Ca , ^{43}Ca , ^{44}Ca and ^{46}Ca , respectively. Ca has also long-lived unstable isotopes which are suitable for target material which are ^{41}Ca and ^{45}Ca isotopes with 99400 years and 162.6 days half-lives. Ca element is one of the fundamental target materials for experimental nuclear structure studies. It also plays a number of

biologically important roles that have been explored for a long time with various techniques available for medical science [8]. One of the most important of these techniques is investigation of calcium functions in the body with the assist of a radioactive isotope. Apart from the stable isotopes, the radioactive Ca isotopes have been artificially produced which are possible radioactive tracers.

The one of the way to produce the radioactive Ca isotopes is photo-neutron (γ, n) reaction. ^{41}Ca , ^{45}Ca and ^{47}Ca can be generated by using photo-neutron reactions performed on ^{42}Ca , ^{46}Ca and ^{48}Ca stable isotopes. Therefore, the information about the cross-sections on Ca according to different energy values for these reactions is important. In the present study, artificial neural network (ANN) method [9] has been used for the prediction of (γ, n) reaction cross sections in different energies from threshold energy values to 200 MeV on stable or long-lived Ca isotopes. The data are taken from TENDL2019 library [5]. ANN is a machine learning tool as a mathematical model that mimics brain functionality which is composed of layers including neurons in each. The method generates its own output as close as the desired values. One of the advantages of the method is it does not need any relationship between input and output data variables. Another advantage of the method is that in case of missing data, it can complete missing data thanks to its learning ability. Recently, ANN has been used in many fields in nuclear physics. Among them the studies performed by our group are developing nuclear mass systematic [10], obtaining fission barrier heights [11], obtaining nuclear charge radii [12], estimation of beta decay energies [13], approximation to the cross sections of Z boson [14, 15], determination of gamma-ray angular distributions [16] and estimations of radiation yields for electrons in absorbers [17].

2. MATERIAL and METHODS

ANN (artificial neural network) is a very powerful mathematical tool that is used when standard techniques fail [9]. The method mimics brain functionality and nervous system. It is composed of three different layers which are input, hidden and output layers. Each layer has its own neurons. The neurons are processing units. The neurons in a layer are connected to the neurons only in the next layer by adaptive synaptic weights. The input neurons receive the data which are independent variables of the problem. The data is transmitted to the hidden layer neurons by multiplying the weight values of the connections. The all data entering the neurons are summed and the summed net data are activated by appropriate functions. The hidden neuron activation function can be theoretically any well behaved nonlinear function. In this study, a sigmoid-like function (tangent hyperbolic) has been used for the activation. Finally, the data is transmitted to the output layer neurons and predictions have been done for the dependent variables. Because of the layered structure, a particular type of ANN is called layered ANN. In Fig.1, we have shown the 3-20-20-1 ANN structure which is used in this study for the prediction of the reaction cross sections.

The inputs were neutron number (N) of the target, mass number (A) of the target and photon energy (E) impinging upon the target. ^{40}Ca , ^{41}Ca , ^{42}Ca , ^{43}Ca , ^{44}Ca , ^{45}Ca , ^{46}Ca and ^{48}Ca isotopes are considered in the target. The desired output was photo-neutron reaction cross-section for these different Ca isotopes. There is no rule for the determination of the hidden layer and neuron numbers. It depends of problem nature and determined after several trials. In this work, two hidden layer with 20 neurons in each were chosen as 2 and 4 in each, respectively.

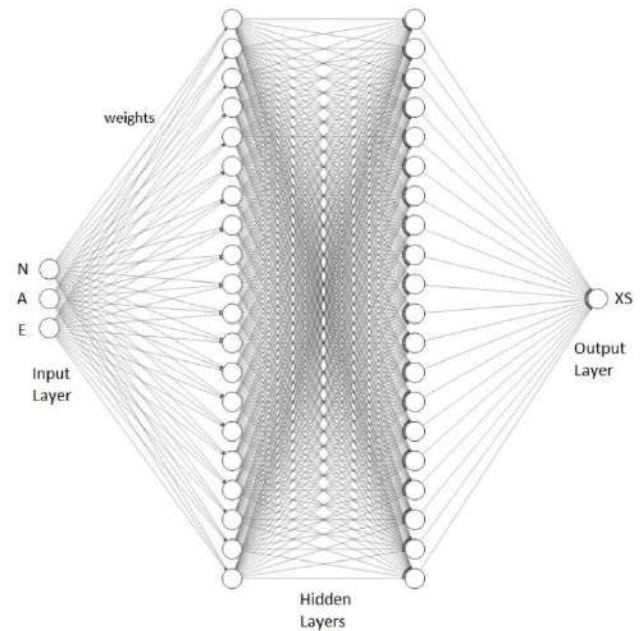


Figure 1 ANN with 3-20-20-1 structure for the prediction of photo-neutron cross sections performed on Ca isotopes

The main goal of the method is the determination of the final weight values between neurons by starting random values. The ANN with best weights can give the ANN outputs as close as to the desired values. ANN is two step processes. In the first, ANN is trained (training) for the determination of the final best weights by given input and output data values. By the appropriate modifications of the weights, ANN modifies its weights until an acceptable error level between ANN and desired outputs. The error function was mean square error (MSE) in this study. MSE gives the average of the squares of the difference between the desired and the neural network output values. Correlation coefficient (R) takes values between -1 and 1. It gives the correlation between values. Over-training and network memorization can be prevented by validation dataset which is not included in training. If validation is not made, it is not noticeable that the network is trained or memorized during the training stage.

In the second step (test), another dataset of the problem is given to ANN and the results are predicted by using the final weights. If the predictions of the test data are good, the ANN is

considered to have learned the relationship between input and output data.

In this work, neural network tool of MATLAB program [18] was used for the estimations. The data was divided into three separate sets for training (70%), validation (15%) and test (15%) stages. The whole data were obtained from TENDL database. In the training step, Levenberg–Marquardt [19, 20] backpropagation algorithm was used.

3. RESULTS and DISCUSSION

A total of 282 data were used for calculations, 198 of which are for training and 42 for the validation of ANN and 42 for the test of ANN. The data for (γ, n) reaction cross-sections in the literature are studied from threshold energy values to 200 MeV. After the determination of the final weights, the ANN is first used in the training and validation datasets. As can be seen in regression plots (Figure 2) that the R values are 0.99998 and 0.99827 for the training and validation data. All data concentrated on the $X = Y$ line indicates that the method is very suitable for this purpose.

For the test dataset R values is still high by getting values 0.9988. MSE, minimum and maximum errors for the all data are 0.202 mb, 10^{-5} mb and -3.27 mb, respectively. For the all data the R values is 0.99941. The R values obtained for each datasets which are close to 1 show the strength of the relationship. However, the R value in the test stage is lower than the training stage. This indicates that ANN does not memorize data, as can be seen also in the validation results. In the training stage, the MSE value gets its minimum value for the validation data in 43th epoch of total 1000. We have shown in Figure 3 that the plot for validation starts to increase after this epoch with the value of 0.66641. The final MSE value of the training is in the order of 10^{-5} .

In Figure 4, we have given the photo-neutron reaction cross section values for Ca isotopes from ANN method in comparison with the available literature data. As is clear in figure that the ANN estimations are in harmony with the

literature data. The eight peaks belong to ^{40}Ca , ^{41}Ca , ^{42}Ca , ^{43}Ca , ^{44}Ca , ^{45}Ca , ^{46}Ca and ^{48}Ca isotopes, respectively. For ^{40}Ca isotope, the reaction cross-section values are the lowest among the other isotopes for all energy values in the energy range. For ^{41}Ca isotope, the cross-sections are relatively lower than the other higher Ca isotopes. The larger cross-section values are for ^{44}Ca and ^{45}Ca isotopes.

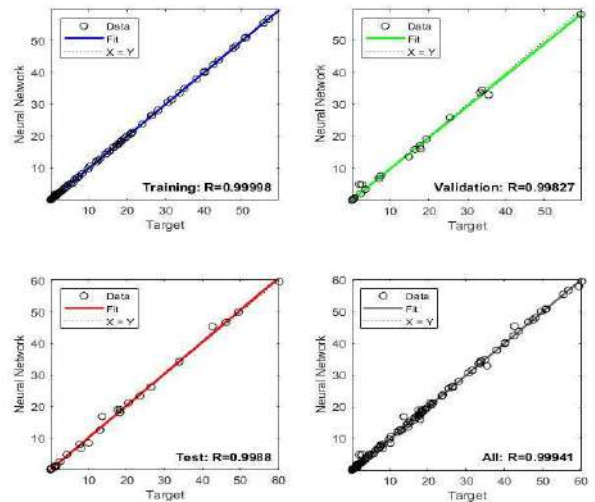


Figure 2 The comparisons of the ANN results by target values for training (upper-left), validation (upper right), test (lower-left) and all (lower-right) datasets.

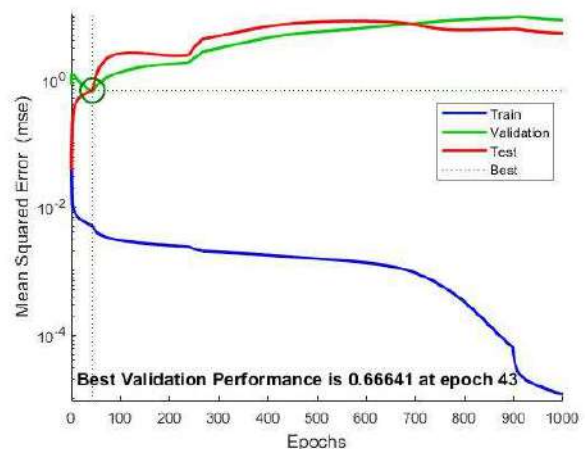


Figure 3 The performance plots of the ANN for training, validation and test datasets

Also, it can be seen in Figure 4 that the maximum cross-section values are 2.98 mb in 22 MeV for ^{40}Ca , 17.22 mb in 19 MeV for ^{41}Ca , 33.82 mb in 20 MeV for ^{42}Ca , 47.51 mb in 19 MeV for ^{43}Ca , 59.52 mb in 19 MeV for ^{44}Ca , 60.38 mb in 19 MeV for ^{45}Ca , 56.90 mb in 18 MeV for ^{46}Ca and 40.19 mb in 18 MeV for ^{48}Ca . The cross-sections get its maximums about 18-20 MeV in the investigated energy range of threshold to 200 MeV. The reaction thresholds are 16, 9, 12, 8, 12, 8, 11 and 10 MeV, respectively, for to ^{40}Ca , ^{41}Ca , ^{42}Ca , ^{43}Ca , ^{44}Ca , ^{45}Ca , ^{46}Ca and ^{48}Ca isotopes.

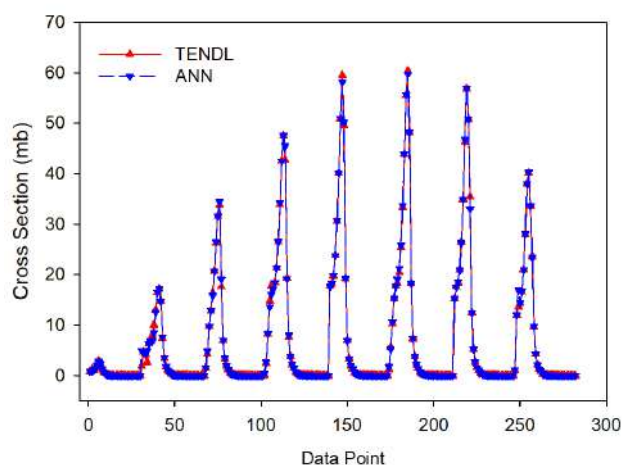


Figure 4 Photo-neutron reaction cross-sections performed on Ca isotopes from ANN estimation (ANN) and the literature data (TENDL).

4. CONCLUSIONS

In this work, (γ, n) photo-neutron reaction cross-sections of stable and long-lived Ca isotopes have been predicted by using artificial neural network (ANN) method in the threshold to 200 MeV energy range. The data for the applications of the ANN method have been borrowed from TENDL-2019 nuclear data library. According to the results, the ANN predictions for the cross-sections are very close to the available literature data. Therefore, one can use ANN method for the obtaining of photonuclear reaction cross-sections whose values are not available in the literature.

Funding

This study is supported by Sivas Cumhuriyet University Scientific Research Projects Coordination Unit. Project Number: F-616.

The Declaration of Conflict of Interest/ Common Interest

No conflict of interest or common interest has been declared by the authors.

Authors' Contribution

Problem is determined and methodology is constructed by S. Akkoyun. The ANN calculations have been performed by H. Kaya. Results have been discussed by S. Akkoyun. Paper is written by the both authors.

The Declaration of Ethics Committee Approval

The authors declares that this document does not require an ethics committee approval or any special permission.

The Declaration of Research and Publication Ethics

The authors of the paper declare that they comply with the scientific, ethical and quotation rules of SAUJS in all processes of the paper and that they do not make any falsification on the data collected. In addition, they declare that Sakarya University Journal of Science and its editorial board have no responsibility for any ethical violations that may be encountered, and that this study has not been evaluated in any academic publication environment other than Sakarya University Journal of Science.

REFERENCES

- [1] K. Strauch, "Recent Studies of Photonuclear Reactions", Ann. Rev. Nucl. Sci. vol. 2, pp. 105-128, 1953.

- [2] D. Brajnik, D. Jamnik, G. Kernel, U. Miklavzic and A. Stanovnik, "Photonuclear reactions in ^{40}Ca ", *Physical Review C*, vol. 9, no. 5, pp. 1901-1918, 1974.
- [3] Y. Utsuno, N. Shimizu, T. Otsuka, S. Ebata and M. Honma, "Photonuclear reactions of calcium isotopes calculated with the nuclear shell model", *Progress in Nuclear Energy*, vol. 82, pp. 102-106, 2015.
- [4] A. J. Koning, S. Hilaire, M. Duijvestijn, *Proceedings of the International Conference on Nuclear Data for Science and Technology (ND2004)*, Sep. 26 - Oct.1, 2004, Santa Fe, USA, edited by R.C. Haight, M.B. Chadwick, T. Kawano, P. Talou, *AIP Conf. Proc.* Vol. 769, pp. 1154, 2005.
- [5] TENDL 2019 Database, https://tendl.web.psi.ch/tendl_2019/gamma_html/Ca/GammaCa.html
- [6] ENDF Nuclear Data File, <https://www-nds.iaea.org/exfor/endl.htm>
- [7] K. A. Cockell, "CALCIUM | Properties and Determination", *Encyclopedia of Food Sciences and Nutrition (Second Edition)*, pp. 765-771, 2003.
- [8] L. W. Brady, M. N. Croll, L. Stanhon, D. Hyman and S. Rubins, "Evaluation of Calcium 47 in Normal Man and Its Use in the Evaluation of Bone Healing Following Radiation Therapy in Metastatic Disease", *Radiology*, vol. 78, no. 2, pp. 286-288, 1962.
- [9] S. Haykin, "Neural Networks: a Comprehensive Foundation", Englewood Cliffs, Prentice-Hall, New Jersey, 1999.
- [10] T. Bayram, S. Akkoyun, S. O. Kara, "A study on ground-state energies of nuclei by using neural networks", *Ann. Nucl. Energy* vol. 63, pp. 172-175, 2014.
- [11] S. Akkoyun and T. Bayram "Estimations of fission barrier heights for Ra, Ac, Rf and Db nuclei by neural networks", *Int. J. Mod. Phys. E* vol. 23, 1450064, 2014.
- [12] S. Akkoyun, T. Bayram, S. O. Kara and A. Sinan, "An artificial neural network application on nuclear charge radii", *J. Phys. G* vol. 40, 055106, 2013.
- [13] S. Akkoyun, T. Bayram and T. Turker, "Estimations of beta-decay energies through the nuclidic chart by using neural network", *radiation Physics and Chemistry*, vol. 96, pp. 186-189, 2014.
- [14] S. Akkoyun and S. O. Kara, "An approximation to the cross sections of Zl bosonproduction at CLIC by using neural networks", *Cent. Eur. J. Phys.* Vol. 11, no. 3, pp. 345-349, 2013.
- [15] S. Akkoyun, S. O. Kara and T. Bayram, "Probing for leptophilic gauge boson Zl ILC with $\sqrt{s}=1$ TeV by using ANN", *Int.J.Mod.Phys. A*, vol. 29, no.30, 1450171, 2014.
- [16] N. Yildiz, S. Akkoyun and H. Kaya, "Consistent Empirical Physical Formula Construction for Gamma Ray Angular Distribution Coefficients by Layered Feedforward Neural Network", *Cumhuriyet Sci. J.*, vol.39, no. 4, pp. 928-933, 2018.
- [17] S. Akkoyun, T. Bayram and N. Yildiz, "Estimations of Radiation Yields for Electrons in Various Absorbing Materials", *Cumhuriyet Sci. J.*, vol.37, Special Issue, pp. S59-s65, 2016.
- [18] Matlab, <https://www.mathworks.com/discovery/neural-network.html>
- [19] K. Levenberg, "A method for the solution of certain non-linear problems in least squares", *Quart. Appl. Math.*, vol. 2, pp. 164-168, 1944.
- [20] D. Marquardt, "An Algorithm for Least-Squares Estimation of Nonlinear Parameters", *SIAM J. Appl. Math.*, vol. 11, pp. 431-441, 1963.

JOURNAL OF SCIENCE



SAKARYA UNIVERSITY

Sakarya University Journal of Science

ISSN 1301-4048 | e-ISSN 2147-835X | Period Bimonthly | Founded: 1997 | Publisher Sakarya University |
<http://www.saujs.sakarya.edu.tr/en/>

Title: Low Power-High Gain Bulk-Driven 3 Stages CMOS Miller OTA in 130nm technology

Authors: Engin AFACAN

Received: 2020-04-24 17:01:01

Accepted: 2020-08-24 18:34:18

Article Type: Research Article

Volume: 24

Issue: 5

Month: October

Year: 2020

Pages: 1121-1134

How to cite

Engin AFACAN; (2020), Low Power-High Gain Bulk-Driven 3 Stages CMOS Miller OTA in 130nm technology. Sakarya University Journal of Science, 24(5), 1121-1134,

DOI: <https://doi.org/10.16984/saufenbilder.726396>

Access link

<http://www.saujs.sakarya.edu.tr/en/pub/issue/56422/726396>

New submission to SAUJS

<http://dergipark.org.tr/en/journal/1115/submission/step/manuscript/new>

Low Power-High Gain Bulk-Driven 3 Stages CMOS Miller OTA in 130nm Technology

Engin AFACAN*¹

Abstract

The requirement of low-power analog circuits has been raised in recent years due to the strict limitation of power consumption in modern applications. Therefore, the trend in analog circuit design has been changed such that they are able to meet the required specifications with lower power dissipation. Design of low power operational transconductance amplifiers, which are the main building blocks in many analog applications, has been more pronounced to keep the power dissipation below certain levels. In this concern, this study presents a low power, high-performing bulk-driven 3 stages CMOS OTA in a 130 nm standard CMOS technology. The proposed circuit leverages the bulk-driven architecture at the input stage; thus it can operate under sub 1-V. The design process of the proposed OTA is explained in detail and the results are validated via post-layout simulations. The proposed OTA is powered by ± 0.45 V symmetric voltage sources, where the power consumption is around $27 \mu\text{W}$. The area overhead is only $0.0017 \mu\text{m}^2$. The open-loop gain, unity gain frequency, and the phase margin are 73.24 dB, 5.167 MHz, and 78° , respectively. To demonstrate the performance of the proposed circuit, a comparison is made with other circuits published in the last five years considering the well-known figures of merit (FOMs). Comparison results indicate that the proposed solution outperforms the other circuits for small-signal operation while it is the runner-up for large-signal operation.

Keywords: Analog, CMOS, bulk-driven, low power, OTA, 130nm.

1 INTRODUCTION

Operational amplifiers are one of the most important building blocks in analog integrated circuit design, which has a wide range of applications (e.g., ADCs, DACs, and filters). Over the years, numerous different topologies (two stage, folded, telescopic, etc.) have been developed to design high performing operational amplifiers and the effort is still ongoing since the

requirements of the modern electronics have been changed.

Nowadays, a large portion of the consumer electronics consists of portable devices (e.g., PDAs and smart phones), so the power consumption has been strictly limited for those devices to increase working durations without charge plug-in. Therefore, low power design has become a major concern in recent years for IC industry [1-7].

* Corresponding Author: engin.afacan@lip6.fr

¹ Sorbonne University, Laboratoire d'Informatique Paris 6 (LIP6), Paris, FRANCE.

ORCID: <https://orcid.org/0000-0002-1581-3894>

Considering the analog design problem consisting of difficult trade-offs among specifications, designing low power circuits while keeping the performance of the circuits at certain levels is not trivial, even it is highly challenging. To demonstrate the analog circuit design essentials and trade-offs among several circuit specifications, an illustration is provided in Fig. 1.

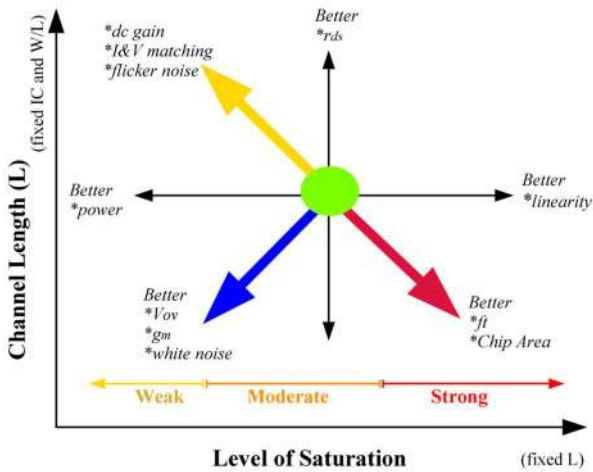


Figure 1 An illustration of saturation level vs. channel length guidance for analog circuit design [8,9]

As seen from the figure, both the channel length and the saturation level of the transistor are the major parameters to achieve the targeted design specifications for a given analog design problem (e.g., keeping the length minimum while pushing transistor into strong inversion provides higher bandwidth). Considering the low power analog circuit design, one possible solution is to design transistors such that they operate in weak inversion (sub-threshold) region. Since the bias current of transistors in the weak inversion is commonly a few nano-amperes, the power consumption can be reduced. However, the intrinsic unity-gain bandwidth of transistors decreases as the transistors come close to weak inversion region.

Therefore, weak-inversion based analog circuit design may not be a proper solution for low-power applications that also need high speed. Sub-threshold based designs addresses

ultrasonic, biomedical, and wireless sensor interface applications [5, 10-15]. The obstacle with design of low power analog circuits is relatively high threshold voltages, which is the result of scaling difference between the power supply and the threshold voltage (V_t). Intentionally, V_t has not been aggressively scaled to meet the noise performance of integrated circuits.

Employing low V_t transistors is another way to mitigate the power consumption; however, one should consider the noise problem and the increased cost bringing with the low V_t technology. Besides, the bulk-driven transistor approach is a quite efficient way to surpass the effect of threshold voltage, where the bulk terminal is used as the input of the circuit [16-23]. This modification enhances the low voltage operation capability of transistors and allows to low power high performing analog circuits. The idea behind the bulk-driven approach is to bias the gate properly and apply the signal to the bulk terminal in order to control the saturation current by $g_{mb}V_{bs}$. Therefore, there is no V_t barrier at the input, which enhances the dynamic input range and enables low-voltage operation [17]. A major problem of the bulk-driven transistors is that they have considerably lower transconductance (g_{mb}) compared to a typical connection (input applied to the gate terminal). In this paper, a low-power and high performing bulk-driven three-stage CMOS OTA is presented. To decrease the chip area and increase the DC gain, the circuit architecture presented in [5] has been adopted. The proposed circuit is explained in detail and validated through post-layout simulations.

The Remainder of the paper is as follows. The proposed solutions is described and analyzed in Sections 2 and 3, respectively. Experimental results are presented in Sections 4. Section 5 provides a comparison with other published solutions in the last five years is provided. Finally, the paper is concluded in Section 6.

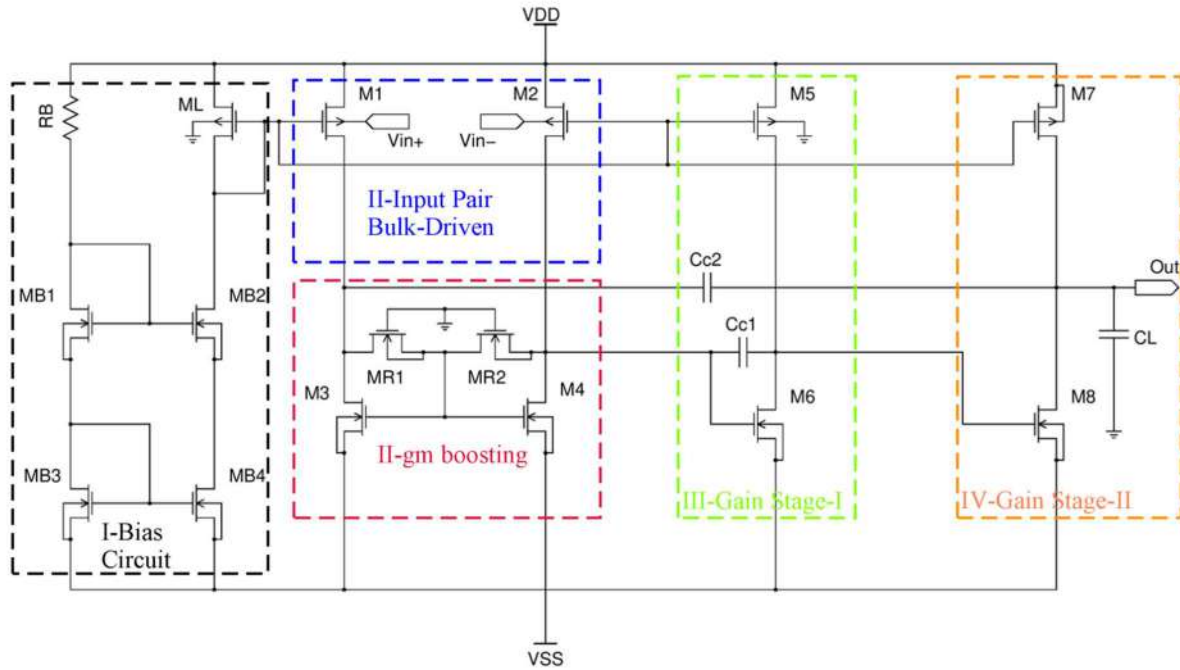


Figure 2 Schematic of the improved bulk-driven 3 stages operational transconductance amplifier

2. DESCRIPTION OF THE PROPOSED CIRCUIT

The circuit schematic of the proposed 3 stages Miller OTA circuit is given in Fig. 2. The proposed amplifier has been adopted from the circuit presented in [5], where a biasing circuit (cascode current mirror) has been replaced rather than a constant current source, the resistors in the gain boosting part have been replaced by MOSFETs acting as resistors, and two transistors at the output stage have been removed. The details for the applied modifications will be explained in the following section.

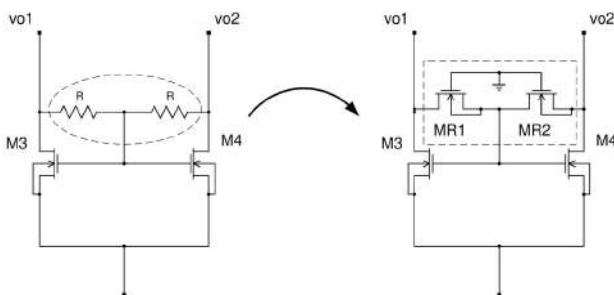


Figure 3 Modification of the effective g_m boosting stage. MR1 and MR2 operate in linear regime and act as resistors

As seen from the circuit schematic, the proposed circuit is comprised of four stages: Biasing, input differential pair, effective g_m boosting stage, the first gain stage, and the second gain stage (output stage). A cascode current mirror is employed to generate the bias current, where MB1-MB4 and RB are the components of the biasing circuit. The saturation currents of M1-M2 and M3-M4 transistors are determined via ML. As the input stage, M1-M2 transistors are used in the bulk-driven configuration, whose gate terminals connected to ML transistor's gate for biasing aim.

The circuit proposed in [5] includes a load part (g_m boosting) consisting of M3-M4 and two resistors. The resistor values are selected relatively large in order to boost the small bulk transconductance (g_{mb}). However, using large resistors may degrade the noise performance and increase the area overhead. To palliate those problems, the resistors have been replaced by the transistors MR1-MR2 operating in linear regime. Considering the requirement of large resistance at this part, the dimensions of those transistors are critical, where longer and narrower transistors should be preferred. Here, the DC

currents through MR1-MR2 are negligible. M3-M4 transistors can be assumed as diode connected and act as current mirror with M6. Similarly, the DC current of M8 is also determined through M3-M4 since they also act as current mirror. Therefore, the saturation currents of M6 and M8 can be determined by (1).

$$I_{d6} = \frac{I_{d3,4} \left(\frac{W}{L}\right)_6}{\left(\frac{W}{L}\right)_{3,4}}, I_{d8} = \frac{I_{d3,4} \left(\frac{W}{L}\right)_8}{\left(\frac{W}{L}\right)_{3,4}}. \quad (1)$$

As the first gain stage, M5-M6 transistors are employed in common-source configuration, where the size of M5 is determined considering the I_{d6} given in (1). The capacitor Cc1 is included for frequency compensation for this stage. At the last gain stage, again, an active loaded common-source configuration is used though M7-M8 transistors. The capacitor Cc2 is used in a feedback network for the purpose of pole splitting; thus, enhancing the frequency response. To determine the minimum supply voltage, the rail-rail voltage drop between VDD and VSS should be equal to at least,

$$VDD - VSS = V_{GS3} + V_{DS1}. \quad (2)$$

In [5], additional NMOS and PMOS transistors in cascade configuration are included to the end of the second stage for the purpose of properly biasing of M7; thus, canceling the systematic offset errors. However, careful sizing of transistors satisfies the same function; therefore, those transistors have been removed in the proposed circuit.

3. ANALYSIS FOR MAJOR DESIGN CONSIDERATIONS

Analog circuit design (sizing) is not a trivial problem such that it cannot be solved through blind sizing iterations. Therefore, the idea behind circuit sizing should be supported with theoretical calculations, which substantially reduce the search space and the duration to achieve targeted specifications. In this section, the circuit is explained in detail by giving fundamental equations.

3.1. Bias Current Determination

The first stage is an NMOS type cascade current mirror. Assuming all transistors are identical, for the sake of simplicity, the transistor sizing ratios can be selected as follows.

$$\frac{\left(\frac{W}{L}\right)_1}{\left(\frac{W}{L}\right)_2} = \frac{\left(\frac{W}{L}\right)_3}{\left(\frac{W}{L}\right)_4}. \quad (3)$$

The resulting output current can be calculated as;

$$I_o = \frac{I_{ref} \left(\frac{W}{L}\right)_2}{\left(\frac{W}{L}\right)_1}, \quad (4)$$

where I_o is the output current (bias current for differential pair) and I_{ref} is the current flow through the resistor RB. Once a reference current is constituted, the bias current is easily determined by using those simple equations.

3.2. Voltage Gain and Common-Mode Rejection Ratio (CMRR)

The proposed circuit includes 3 gain stages. In the first stage, a bulk driven circuit and a gain boosting circuit (Figure 3) are assigned. This type of active load stage enables also fully differential operation for pair M1-M2 [5]. Considering a gate-driven amplifier, the gain is typically expressed as $g_m r_o$, where r_o is the resistance seen from the output node and commonly equals to $r_{ds}/2$. However, the proposed circuit includes a bulk-driven pair at the input, which yields an output voltage as given in (5) when an input of v_i is applied.

$$v_{o1,2} = v_{gs3,4} \pm \frac{1}{2} v_i R g_{mb1,2}. \quad (5)$$

In (5), R denotes the equivalent resistance generated by the MOSFETs in linear regime and $v_{gs3,4} = v_{gs}$ denotes the gate to source voltages of M3-M4. Since the currents flow in the same branch will be equal to each other, it can be drawn that $g_{mb1}(v_i/2) = g_{m3}v_{gs}$ and $g_{mb2}(v_i/2) = g_{m4}v_{gs}$. By using these equalities, (5) can be rewritten as follows.

$$v_{o1,2} = \pm \frac{v_i}{2} \left(\frac{g_{mb1,2}}{g_{m3,4}} + R g_{mb1,2} \right). \quad (6)$$

Since $g_m \gg g_{mb}$, the output voltage of the first stage can be calculated as;

$$v_{o1,2} = \pm \frac{v_i}{2} (R g_{mb1,2}). \quad (7)$$

As seen from (7), the R value should be kept as large as possible to amplify even very small signals. Considering a MOSFET operating in linear regime, the resistance value can be calculated as follows.

$$R = L/W \mu_n c_{ox} (V_{GS} - V_t). \quad (8)$$

(8) shows that those transistors should be designed as narrower and longer as possible compared to the other transistors in order to achieve high resistance values. Moreover, one should also consider that the output resistance seen from the differential pair is actually $R // r_{ds3} // r_{ds4}$. After the first stage, the data signal is transmitted through two similar common-source amplifiers and the output voltage can be expressed as follows.

$$v_{out} = \frac{v_i}{2} (R g_{mb1,2}) g_{m6}(r_{out2}) g_{m8}(r_{out3}). \quad (9)$$

Once a bias current is determined (keeping small for low power), the transconductance values can be calculated; thus, a rough gain calculation can be performed.

CMRR exhibits performance of amplifier in terms of suppressing the common-mode voltage at the input. Considering the circuit schematic (g_m boosting part), resistors (MR1-MR2) sets the common mode gain through M3-M4. Namely, there is no current flow through MR1-MR2; thus, the gate and the drain voltages of M3-M4 are equal to each other. Let us apply a common voltage (v_{cm}) to the inputs of differential pair. A current of $g_{mb1,2} v_{cm}$ flows through transistors. This current is also equal to the current ($g_{m3,4} v_{gs}$) flows through M3-M4, where v_{gs} is equal to $v_{o1,2}$. The common-mode gain can be expressed as

$$A_{cm} = \left| \frac{v_o}{v_{cm}} \right| = \frac{g_{mb1}}{g_{m3}}. \quad (10)$$

As a result, the CMRR can be calculated as follows.

$$CMRR_{single_ended} = \left| \frac{A_o}{A_{cm}} \right| = \frac{1}{2} (R) g_{m3}. \quad (11)$$

According to (11), the resistor values (MR1-MR2) should be kept as large as possible to maximize the CMRR.

3.3. Frequency Response

The unity-gain bandwidth of a conventional Miller OTA circuit with compensation is simply approximated as

$$W_{GBW} \cong \frac{g_m}{C_c}, \quad (12)$$

where g_m is the transconductance of the input transistors and C_c is the compensation capacitor. Even though the frequency response is quite straightforward to be handled, the stability is highly problematic for multi-stage amplifiers, so further theoretical analysis is needed for pre-design phase.

A general form of transfer function of a system including multi-poles and zero can be expressed as

$$A_s \cong A_0 \frac{1 + \frac{s}{z}}{\left(1 + \frac{s}{p}\right) (as^2 + bs + 1)}. \quad (13)$$

Considering the compensation capacitors C_{c1} and C_{c2} and the current buffer through M3-M4 pair,

the dominant pole (p) and the zero (z) are calculated as

$$p = \frac{2}{g_{m6} g_{m8} R r_{out2} r_{out3} C_{c1}} \quad (14a)$$

$$z = \frac{g_{m3} g_{m6}}{2 C_{c1} g_{m6} - C_{c2} g_{m3}}. \quad (14b)$$

Considering (13), a and b denote the coefficients for non-dominant complex conjugate poles and given as

$$a = \frac{C_{c2}C_L(2g_{m6} + g_{m3})}{g_{m3}g_{m6}g_{m8}} \quad (16a)$$

$$b = \frac{C_L(C_{c1} + g_{m6}C_{c2}r_{out2})}{C_{c1}g_{m6}g_{m8}r_{out2}} \quad (16b)$$

To ensure the stability of the amplifier, the damping factor can be calculated similar to the expression given in [5] as follows;

$$\xi = \frac{b}{2\sqrt{a}} = \frac{C_{c1} + C_{c2}g_{m6}r_{out2}}{2C_{c1}r_{out2}} \quad (17)$$

$$x \sqrt{\frac{C_L g_{m3}}{g_{m6} g_{m8} C_{c2} (2g_{m6} + g_{m3})}}$$

The first design step is to determine the targeted bandwidth and calculation of required g_{mb} and C_{c1} from (12). Then, a suitable C_{c2} can be approximated from (17) to keep the damping ratio below certain level. Another suggestion is adjusting $g_{m6}/g_{m3} \gg C_{c2}/C_{c1}$ to avoid any negative zero [5].

4. EXPERIMENTAL RESULTS

The proposed circuit given in Fig. 2 was implemented in a 130nm standard CMOS technology. Mentor Graphics® and HSPICE® were used for design and simulation steps, respectively. Design parameters for the proposed circuit are listed in Table-1. The design parameters including transistors aspect ratios and other parameters were determined considering the design insight (major design equations) explained in Section 3. The power supply of the circuit was determined as ± 0.45 V, where the circuit drives a load of 25 pF. The targeted unity-gain frequency was 5 MHz. To achieve this bandwidth, the bias current for the transistors M1-M2 was calculated as 5 μ A. Then, the transistor widths were determined for the first level. Dimensions of the transistors MR1-MR2 were selected in order to achieve a considerable gain at the first stage. As previously mentioned, longer and narrower transistors were preferred in order to achieve high output resistance. The value of compensation capacitors were determined to obtain a sufficient phase margin. Some pre-layout measurements were summarized in Table 2. The total power consumption of the circuit is around 25.7 μ W. The layout is provided in Fig. 4. The total area occupation of the circuit is 1.1×10^{-3} mm².

Table 1

Design parameters for proposed circuit for ± 0.45 V power supply and 25 pF load capacitor

L	Rbias	WB1,2,3,4	WR,1,2	W3,4	W5	W6,8	W7	WR1,2	LR1,2	Cc1	Cc2
[μ m]	[Ω]	[μ m]	[μ m]	[μ m]	[μ m]	[μ m]	[μ m]	[μ m]	[μ m]	[fF]	[fF]
0.5	40k	12	12	2	30	5	20	0.18	10	250	10

Table 2

Pre-layout DC measurement results of some electrical parameters for the proposed circuit

I_{M1-M2}	$g_{mb1,2}$	$g_{m3,4}$	g_{m6}	g_{m8}	$r_{ds3,4}$	I_{DD}	I_{SS}
[μ A]	[μ A/V]	[μ A/V]	[μ A/V]	[μ A/V]	[Meg Ω]	[μ A]	[μ A]
5.18	12.3	100	255	58	0.45	25.7	25.7

The presented layout does not include the compensation capacitors since the values are comparable with the layout parasitic capacitances. Therefore, they are externally included to the post-layout netlist. Even they were included, the area occupation would be at worst $1.7 \times 10^{-3} \text{mm}^2$.

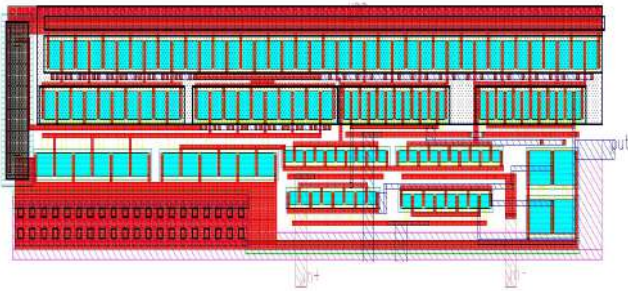


Figure 4 Layout of the proposed circuit

4.1. Frequency Domain Analysis Results

The post-layout bode plot of the proposed amplifier is provided in Fig. 5. According to the simulation results, the amplifier has 73.24 dB gain, where the gain margin is around 11dB. The unity-gain frequency was measured as 5.17 MHz. The phase margin of the amplifier is around 78° . CMRR and power supply rejection ratio (PSRR) were also measured for the circuit. The post-layout simulation result for CMRR is given in Fig. 6. According to the results, the amplifier has a CMRR of 97.7 dB. The reason of achieving such high value is using transistors in linear regime yielding high resistance values. The PSRR of the circuit was measured as 70 dB. These values are very competitive compared to the results reported in the literature.

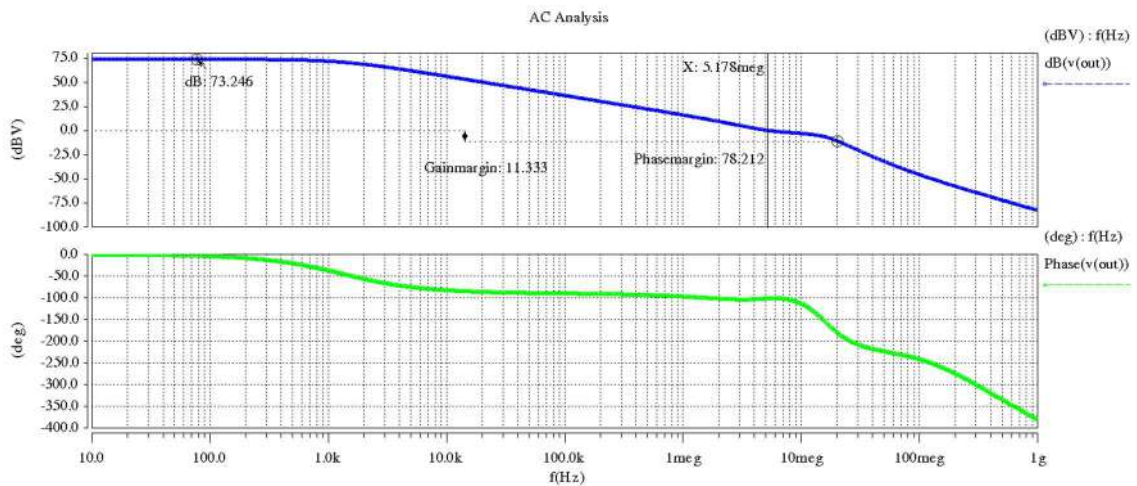


Figure 5 Post-layout bode-plot of the proposed amplifier

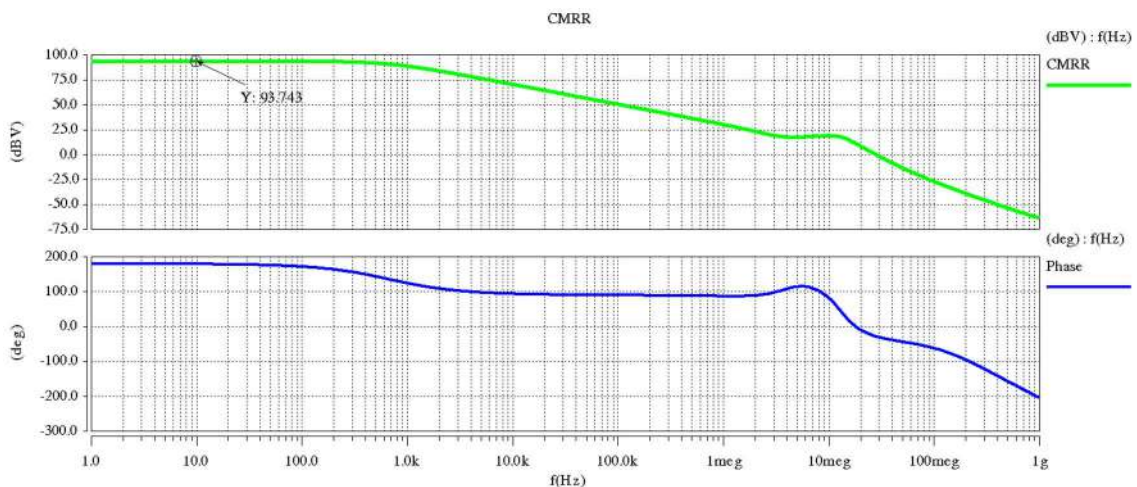


Figure 6 Post-layout simulation results for CMRR

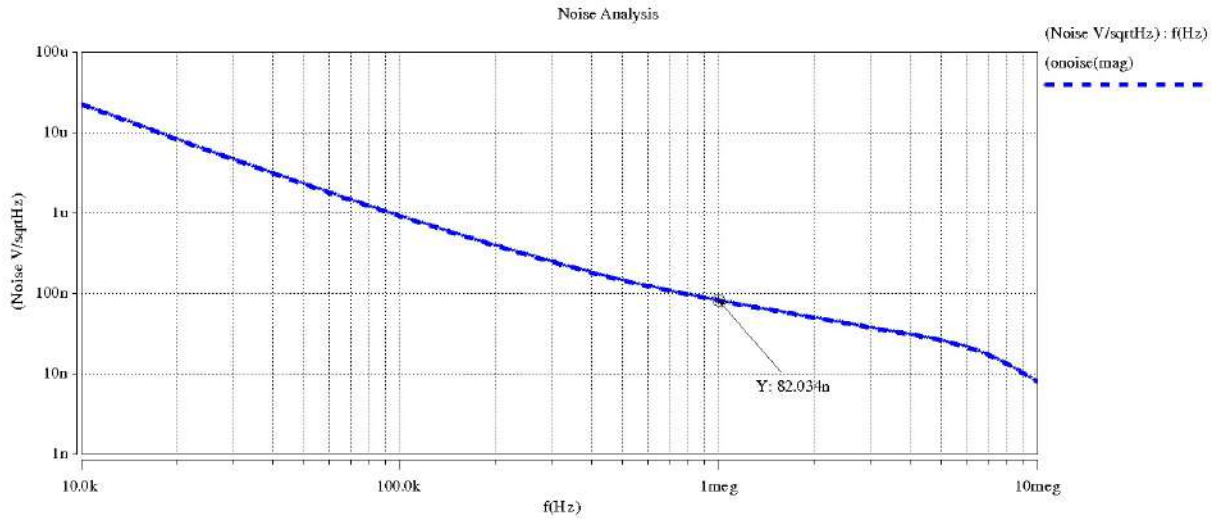


Figure 7 Post-layout simulation results for noise analysis of the proposed amplifier

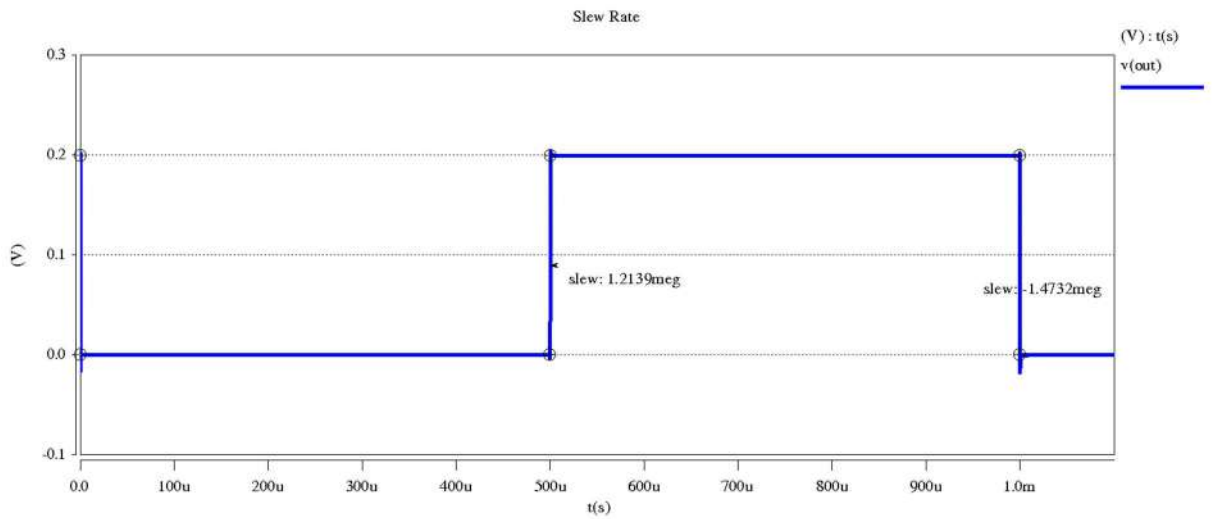


Figure 8 Slew-rate measurement result for 200 mVpp step input applied in unity-gain configuration

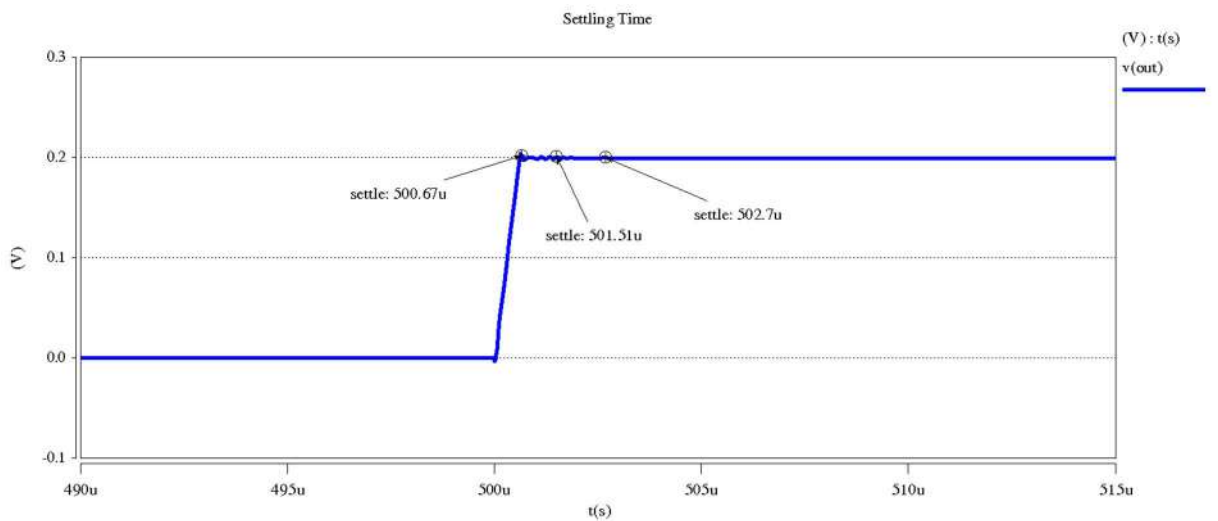


Figure 9 Settling-time measurement result for 200 mVpp step input applied in unity-gain configuration

Noise measurement result is shown in Fig. 7. The input referred noise density measured at 1 MHz is around $82 \text{ nV}/\sqrt{\text{Hz}}$.

4.2. Time Domain Analysis Results

To demonstrate the transient performance of the circuit, a $200 \text{ mV}_{\text{pp}}$ input step was applied in the unity gain configuration. The post-layout simulation result for the slew-rate is provided in Fig. 8. The positive and negative slew rate values were measured as $1.21 \text{ V}/\mu\text{s}$ and $1.47 \text{ V}/\mu\text{s}$, respectively. Moreover, the settling time was also measured using the same input configuration. According to the results provided in Fig. 9, the settling time for achieving 5%, 1%, and 0.1% maximum amplitude are $0.67 \mu\text{s}$, $1.51 \mu\text{s}$, and $2.7 \mu\text{s}$, respectively. The total current drawn from power supplies is $30 \mu\text{A}$. The total power consumption of the circuit was measured as $27 \mu\text{W}$. The output and input offset voltages were also measured, where the circuit has 68 mV output offset voltage whereas the input offset was measured as $32 \mu\text{V}$.

4.3. Variability Analysis: Process-Voltage-Temperature (PVT) Analysis

To verify the design against variation effects, PVT analysis was performed. To observe the process variations, Monte Carlo analysis was performed with 5000 samples. The histogram plots for the gain and the unity-gain bandwidth are provided in Fig. 10 and Fig. 11, respectively.

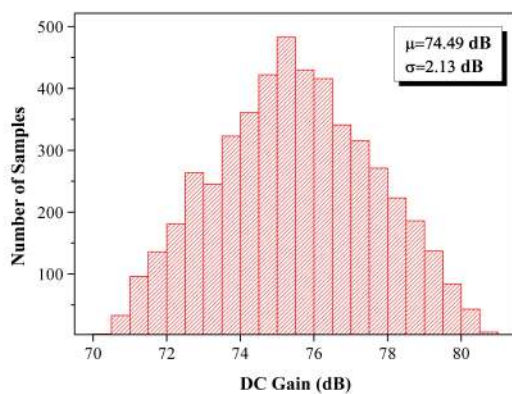


Figure 10 Monte Carlo analysis result for the gain

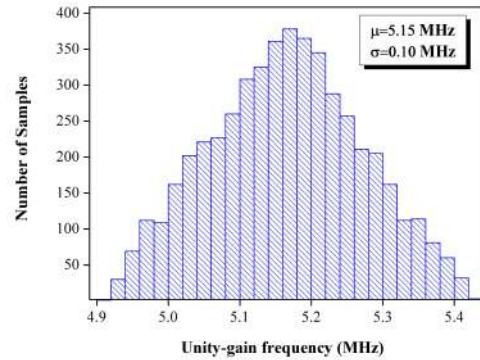


Figure 11 Monte Carlo analysis result for the unity gain-bandwidth

As seen from the results, the mean value of 5000 samples is around 5.15 MHz while the standard deviation is just 0.10 MHz. Similar results were obtained for the open loop gain, where the average gain value and the standard deviation are 74.5 dB and 2.13 dB, respectively. According to the results, the circuit can exhibit sufficient gain and bandwidth even the worst case occurs.

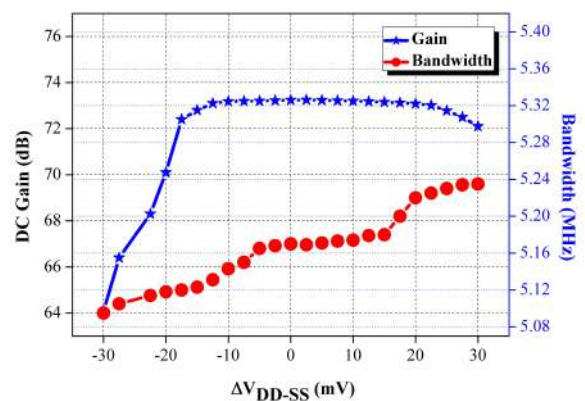


Figure 12 Monte Carlo analysis result for the gain. The sample size of the analysis is 5000

To consider the effect of variations in power supplies, the supply voltages were swept by up/down to $\pm 30 \text{ mV}$ and results are provided in Fig. 12. Simulation results indicate that the bandwidth of the circuit is not affected by the power supply variations. On the other hand, the open-loop-gain is quite different, where the gain decreases when a negative change in power supply occurs. For the positive variations, the gain is almost the same up to certain point, then, it also decreases.

At last, the temperature variation analysis was performed for the proposed circuit and the results are provided in Fig. 13. As seen from the results, the circuit performance degrades at low temperatures. The case for the high temperature is more dramatic, where a considerable performance loss occurs. Even though those degradations, the performance of the circuit is still sufficient to be used as an OTA.

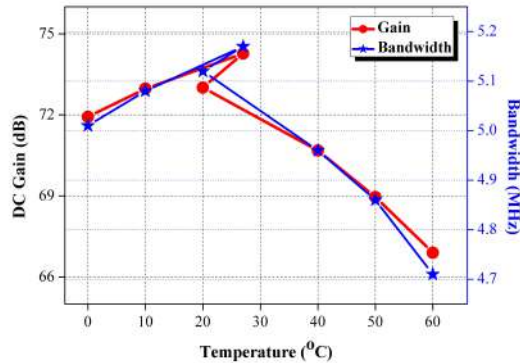


Figure 13 Effect of the temperature variations on the open-loop-gain and the unity gain frequency

4.4. Design Summary

A single-ended three stage OTA with low power consumption circuit was analyzed and designed in a 130 nm CMOS technology. Post-layout measurement results and the design details are summarized in Table 3.

Table 3
Summary of the design specifications of the proposed circuit

Specification	Value
Unity-gain frequency (MHz)	5.17
Open-loop-gain (dB)	73.24
Phase Margin (°)	78.21
Gain Margin (dB)	11.33
CMRR (dB)	93.74
PSRR (dB)	70
Input referred noise (nV/√Hz)	82
Slew Rate (V/μs) (Pos. - Neg.)	1,21-1.47
Settling Time (μs) (5% - 1% - 0.1%)	0.67 - 1.51 - 2.7
Input Offset Voltage (mV)	0.032
Output Offset Voltage (mV)	68
Power Consumption (μW)	27
Chip Area (mm ²)	6
Supply Voltage (V)	±0.45

Table 4
Benchmark comparison

Specification	This Work	2015 [24]	2016 [5]	2016 [19]	2017 [6]	2018 [25]	2019 [26]	2020 [27]	
Technology (nm)	130	65	180	180	350	180	180	40	
Supply Voltage (V)	±0.45	0.5	0.45	0.7	0.6	0.9	0.3	0.5	0.6
Load Capacitance (pF)	25	3	20	15	27	20	15	1	
Open-loop-gain (dB)	73.24	46	43	57.5	82	65	65.8	111.5	60
Unity-gain bandwidth (MHz)	5.17	38	3.6	3	0.019	1	0.0028	0.0095	45
Phase Margin (°)	78.21	57	56	60	60	60	61.2	66	86.5
Slew Rate (V/μs)	1.34	0.043	5.6	2.8	0.012	0.25	0.0072	0.0009	18.2
Settling Time (μs) (1%)	1.51	N.A.	1.15	75	1.8	166	N.A.	0.038	
Power Consumption (μW)	27	182	17	25.4	0.4	21.2	0.015	0.07	30
Chip Area (μm ²)	1700	5000	19800	40000	14000	8200	19700	1632	

5. DISCUSSION

To demonstrate the performance of the proposed circuit, a selection of sub-1V amplifiers published in the last five years has been explored and compared with the proposed circuit. The performance comparison table is provided in Table 4. According to the results, the proposed circuit has highly competitive specifications compared to the other circuits. Especially, the chip area, unity-gain bandwidth, phase margin, and capacitive loading capability of the proposed circuit are at the upper ranks. To generalize the comparison, the well-known two figures-of-merit given in (17) and (18) were considered. Typically, FOM_1 measures the AC performance of the circuit while FOM_2 measures the transient performance.

$$FOM_1 = \frac{UGF \cdot C_L}{Area \cdot Power} \quad (17)$$

$$FOM_2 = \frac{SR \cdot C_L}{Area \cdot Power} \quad (18)$$

UGF and SR denote unity-gain-frequency and slew rate, respectively.

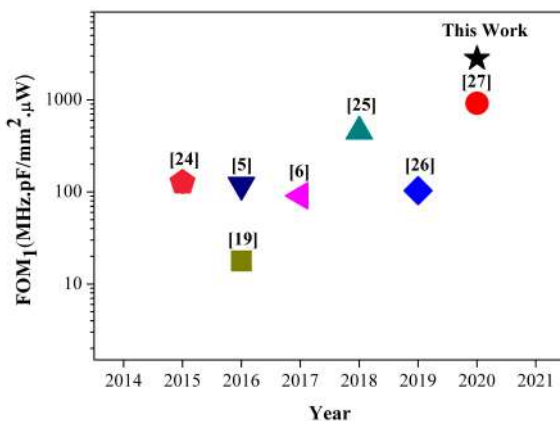


Figure 14 FOM_1 comparison results

FOM_1 and FOM_2 results of the all circuits are visually illustrated in Figures 14 and 15, respectively. Considering the FOM_1 results, it is apparently seen that the proposed circuit outperforms the all other circuits, where the

FOM_1 score of it is 2816 while the runner-up [27] has a FOM_1 of 920. Regarding the FOM_2 results, the proposed circuit exhibits quite good performance (the runner-up with 730 FOM_2 score) that is close to the best score (1170) achieved by [25].

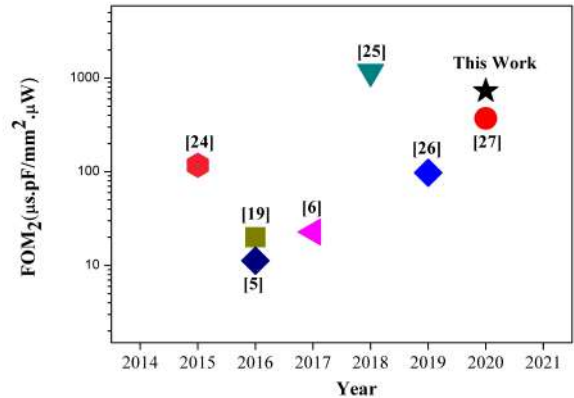


Figure 15 FOM_2 comparison results

6. CONCLUSION

In this paper, a modified bulk-driven 3 stages CMOS OTA in a 130 nm standard CMOS technology for low-power applications has been presented. Thanks to the bulk-driven configuration, the circuit can operate with sub 1-V power supply. The applied modification provides high gain and less area overhead. Post-layout simulation results indicate that the proposed circuit has 73.24 dB gain, 5.17 MHz bandwidth, and 78° phase margin, respectively. PVT analysis has been performed to verify the robustness of the circuit against process, voltage, and temperature variations. To compare the performance of the proposed circuit with the other circuits published in the last five years, the well-known figures of merit (FOMs) were calculated and demonstrated on a benchmark figure. Comparison results indicate that the proposed solution is highly competitive with the other circuits, whose ranks are 1st and 2nd for small-signal and large signal operations, respectively.

Acknowledgements

The author appreciates Abdulsamet Elik for his effort that initialize this study.

Funding

The author was financially supported by HADES Project through LIP6, Sorbonne University.

The Declaration of Conflict of Interest/ Common Interest

No conflict of interest or common interest has been declared by the author.

The Declaration of Ethics Committee Approval

The author declares that this document does not require an ethics committee approval or any special permission.

The Declaration of Research and Publication Ethics

The author of the paper declare that he complies with the scientific, ethical and quotation rules of SAUJS in all processes of the paper and that he does not make any falsification on the data collected. In addition, he declares that Sakarya University Journal of Science and its editorial board have no responsibility for any ethical violations that may be encountered, and that this study has not been evaluated in any academic publication environment other than Sakarya University Journal of Science.

REFERENCES

- [1] B. H. Calhoun, D. C. Daly, N. Verma, D. F. Finchelstein, D. D. Wentzloff, A. Wang, S. H. Cho, and A. P. Chandrakasan, "Design considerations for ultra-low energy wireless microsensor nodes", *IEEE Transactions on Computers*, vol. 54, no. 6, pp. 727-740, 2005.
- [2] A. Shikata, R. Sekimoto, T. Kuroda, and H. Ishikuro, "A 0.5 V 1.1 MS/sec 6.3 fJ/conversion-step SAR ADC with tri-level comparator in 40 nm CMOS", *IEEE Journal of Solid-State Circuits*, vol. 47, no.4, pp. 1022-1030, 2012.
- [3] Y. K. Ramadass and A. P. Chandrakasan, "Minimum energy tracking loop with embedded DC-DC converter enabling ultra-low-voltage operation down to 250 mV in 65 nm CMOS", *IEEE Journal of Solid-State Circuits*, vol. 43, no. 1, pp. 256-265, 2008.
- [4] B. G. Perumana, R. Mukhopadhyay, S. Chakraborty, C. H. Lee, and J. Laskar, "A low-power fully monolithic subthreshold CMOS receiver with integrated LO generation for 2.4 GHz wireless PAN applications", *IEEE Journal of Solid-State Circuits*, vol. 43, no. 10, pp. 2229-2238, 2008.
- [5] E. Cabrera-Bernal, S. Pennisi, A. D. Grasso, A. Torralba, and R. G. Carvajal, "0.7-V three-stage class-AB CMOS operational transconductance amplifier", *IEEE Transactions on Circuits and Systems I: Regular Papers*, vol. 63, no. 11, pp. 1807-1815, 2016.
- [6] A. D. Grasso, S. Pennisi, G. Scotti, and A. Trifeletti, "0.9-V class-AB Miller OTA in 0.35um CMOS with threshold-lowered non-tailed differential pair", *IEEE Transactions on Circuits and Systems I: Regular Papers*, vol. 64, no. 7, pp. 1740-1747, 2017.
- [7] A. Ballo, A. D. Grasso, and S. Pennisi, "CMOS Differential Stage with Improved DC Gain, CMRR and PSRR Performance", In *26th IEEE International Conference on Electronics, Circuits and Systems (ICECS)*, pp. 154-157, Nov 27 2019.
- [8] E. Afacan, "Inversion coefficient optimization based Analog/RF circuit

- design automation”, *Microelectronics Journal*, vol. 83, no. 1, pp. 86-93, 2019.
- [9] C. Enz, M. A. Chalkiadaki, and A. Mangla, “Low-power analog/RF circuit design based on the inversion coefficient”, In 41st European Solid-State Circuits Conference (ESSCIRC), pp. 202-208, Sep 14 2015.
- [10] C. Yadav and S. Prasad, “Low voltage low power sub-threshold operational amplifier in 180nm CMOS”, In 3rd International Conference on Sensing, Signal Processing and Security (ICSSS): 35-38, May 4, 2017.
- [11] A. N. Ragheb and H. Kim, “Ultra-low power OTA based on bias recycling and subthreshold operation with phase margin enhancement”, *Microelectronics Journal*, vol. 60, no. 1 pp. 94-101, 2017.
- [12] M. A. Eldeeb, Y. H. Ghallab, Y. Ismail, and H. Elghitani, “Low-voltage subthreshold CMOS current mode circuits: design and applications”, *AEU-International Journal of Electronics and Communications*, vol. 82, no.1, pp. 251-64, 2017.
- [13] A. J. Kumar, K. L. Krishna, K. A. Viswateja, K. Gopi, S. M. Rao, and B. Mamatha, “A high gain low power operational amplifier using class AB output Stage”. In 3rd International Conference on Computing Methodologies and Communication (ICCMC), pp. 409-413, Mar 27 2019.
- [14] R. Póvoa, R. Arya, A. Canelas, F. Passos, R. Martins, N. Lourenço, and N. Horta, “Sub- μ W Tow-Thomas based biquad filter with improved gain for biomedical applications”, *Microelectronics Journal*, vol. 95, no.1, p. 104675, 2020.
- [15] S.J. Choe, J. S. Lee, S. S. Park, and S. D. Yu, “Ultra-Low-Power Class-AB Bulk-Driven OTA with Enhanced Transconductance”, *IEICE Transactions on Electronics*, vol. 102, no. 5, pp. 420-430, 2019.
- [16] T. Kulej, “0.5-V bulk-driven CMOS operational amplifier”, *IET Circuits, Devices & Systems*, vol. 7, no. 6, pp. 352-360, 2013.
- [17] L. Zuo and S. K. Islam, “Low-voltage bulk-driven operational amplifier with improved transconductance”, *IEEE Transactions on Circuits and Systems I: Regular Papers*, vol. 60, no. 8, pp. 2084-2091, 2013.
- [18] S. M. Chaudhry, U. M. Minhas, and F. Abbas, “A high gain bulk driven OTA for Wireless Body Area Networks”, *National Academy Science Letters*, vol. 41, no. 1, pp. 41-55, 2018.
- [19] M. Akbari and O. Hashemipour, “A 0.6-V, 0.4- μ W bulk-driven operational amplifier with rail-to-rail input/output swing”, *Analog Integrated Circuits and Signal Processing*, vol. 86, no. 2, pp. 341-351, 2016.
- [20] M. Kumngern, F. Khateb, and T. Kulej, “0.5 V bulk-driven CMOS fully differential current feedbackoperational amplifier”, *IET Circuits, Devices & Systems*, vol. 13, no. 3, pp. 314-320, 2018.
- [21] T. Sharan and V. Bhadauria, “Fully differential, bulk-driven, class AB, sub-threshold OTA withenhanced slew rates and gain”, *Journal of Circuits, Systems and Computers*, vol. 26, no. 1, p. 1750001, 2017.
- [22] M. Kumngern, F. Khateb, and T. Kulej, “0.5 V bulk-driven CMOS fully differential current feedback operational amplifier”. *IET Circuits, Devices & Systems*, vol. 13, no. 3, pp. 314-320, 2018.
- [23] H. Veldandi and R. A. Shaik, “Low-voltage PVT-insensitive bulk-driven

OTA with enhanced DC gain in 65-nm CMOS process”, *AEU-International Journal of Electronics and Communications*, vol. 90, no. 1, pp. 88-96, 2018.

- [24] O. Abdelfattah, G. W. Roberts, I. Shih, and Y. C. Shih, “An ultra-low-voltage CMOS process-insensitive self-biased OTA with rail-to-rail input range”, *IEEE Transactions on Circuits and Systems I: Regular Papers*, vol. 62, no. 10, pp. 2380-2390, 2015.
- [25] T. Kulej and F. Khateb, “Design and implementation of sub 0.5-V OTAs in 0.18- μm CMOS”, *International Journal of Circuit Theory and Applications*, vol. 46, no. 6, pp. 1129-43, 2018.
- [26] B. Wen, Q. Zhang, and X. Zhao, “A two-stage CMOS OTA with enhanced transconductance and DC gain”, *Analog Integrated Circuits and Signal Processing*, vol. 15, no. 98, pp. 257-64, 2019.
- [27] D. Cellucci, F. Centurelli, V. Di Stefano, P. Monsurrò, S. Pennisi, et al, “A. 0.6-V CMOS cascode OTA with complementary gate-driven gain-boosting and forward body bias”, *International Journal of Circuit Theory and Applications*, vol. 48, no. 1, pp. 15–27, 2020.

JOURNAL OF SCIENCE



SAKARYA UNIVERSITY

Sakarya University Journal of Science

ISSN 1301-4048 | e-ISSN 2147-835X | Period Bimonthly | Founded: 1997 | Publisher Sakarya University |
<http://www.saujs.sakarya.edu.tr/en/>

Title: Modelling of Remazol Black-B Adsorption on Chemically Modified Waste Orange Peel: pH Shifting Effect of Acidic Treatment

Authors: Ceren KARAMAN, Zümriye AKSU

Received: 2020-06-11 15:51:04

Accepted: 2020-08-26 17:36:56

Article Type: Research Article

Volume: 24

Issue: 5

Month: October

Year: 2020

Pages: 1135-1150

How to cite

Ceren KARAMAN, Zümriye AKSU; (2020), Modelling of Remazol Black-B Adsorption on Chemically Modified Waste Orange Peel: pH Shifting Effect of Acidic Treatment.

Sakarya University Journal of Science, 24(5), 1135-1150, DOI:

<https://doi.org/10.16984/saufenbilder.751491>

Access link

<http://www.saujs.sakarya.edu.tr/en/pub/issue/56422/751491>

New submission to SAUJS

<http://dergipark.org.tr/en/journal/1115/submission/step/manuscript/new>

Modelling of Remazol Black-B Adsorption on Chemically Modified Waste Orange Peel: pH Shifting Effect of Acidic Treatment

Ceren KARAMAN^{*1}, Zümriye AKSU²

Abstract

The adsorption of Remazol Black-B (RBB) onto two different types of agricultural waste derived-adsorbents; dried-orange peel (DOP) and chemically modified orange peel (CMOP), was performed. The adsorption rate, capacity, and the dye removal efficiency were investigated in terms of initial pH ranged between 2.0 to 10.0 of the dispersion and the operating temperature of 25 °C, 35 °C, 45 °C . The Langmuir and Freundlich adsorption models were applied to the experimental data to model the adsorption equilibrium, and evaluated by regression analysis. The results indicated that the Langmuir model was more suitable to describe the adsorption equilibrium of RBB over CMOP. According to Langmuir model, while the highest RBB uptake capacity of DOP was determined as 62.4 mg.g⁻¹ at pH 2.0 and 25°C, this value was figured out for CMOP as 84.4 mg.g⁻¹ at pH 8.0 and 45°C. Furthermore, the adsorption kinetics followed both the pseudo-second order and the saturation type kinetic models for each adsorbent-dye system. The thermodynamic parameters of adsorption including the Gibbs free energy change (ΔG°), the enthalpy change (ΔH°), and the entropy change (ΔS°) were obtained by using thermodynamic equations. These parameters were calculated as -4.24 kJ.mol⁻¹, 43.77 kJ.mol⁻¹, 0.16 kJ mol⁻¹.K⁻¹ for CMOP respectively whereas for DOP -3.58 kJ.mol⁻¹, -19.79 kJ.mol⁻¹, -0.05 kJ mol⁻¹.K⁻¹ .

Keywords: Adsorption, Orange Peel, Remazol Black-B, Acidic Treatment, Chemical Modification, pH shifting, Agricultural Waste

1. INTRODUCTION

Since industrial wastewaters contain large amount and different types of pollutants such as dyes, surfactants, heavy metals and salts, they are one of the greatest threats to the environment. Among these pollutants, dyes, and pigments used in many industries (i.e., textile, pharmaceutical, paper,

plastic, petrochemical etc.) lead to severe harmful effects both to the ecosystem and to human health. Due to their synthetic origins and complex molecular structures, it is difficult to biodegrade dye effluents. These effluents not only significantly reduce sunlight penetration but also decrease the solubility of oxygen in the water. As a result, the photosynthetic activity of living

* Corresponding Author: cerenkaraman@akdeniz.edu.tr

¹ Akdeniz University, ORCID: <http://orcid.org/0000-0001-9148-7253>

² Hacettepe University, E-Mail: zakusu@hacettepe.edu.tr ORCID: <http://orcid.org/0000-0002-2812-5345>

organisms in the aquatic system is inhibited [1]. Therefore, removal of the dyes from wastewater before discharge into the environment is essential for the protection of the environment and human health. In order to contribute to the total solution of this problem, in addition to conventional technologies (like coagulation, flocculation, precipitation, ozonation, etc.), several treatment technologies have gained prominences, such as membrane processes, electrochemical techniques, photocatalytic oxidation/degradation, adsorption and combined methods [2]. Amongst them, adsorption processes generally have high removal efficiency and can be scaled-up [3]. Furthermore, adsorption attracts more attention because it allows the adsorbent regeneration, which is an important economic advantage [4].

In the last decades, plenty of research groups have been tried to develop alternative adsorbents, which are economic, environmentally friendly and reusable, to desalination the wastewater. To call an adsorbent as “alternative adsorbent”, it should be a waste or by-product of an industrial process. Besides, it should be plenty in nature or to be processed easily [5]. In light of this definition, agricultural wastes/by-products can be considered as the most important candidate of an alternative low-cost, non-toxic adsorbent for the removal of different kinds of contaminants such as dyes, heavy metals, and organics. They are lignocellulosic materials which mainly consist of cellulose, lignin, and hemicellulose. There are many studies which investigate the performance of agricultural waste/by-products to remove dyes or heavy metal ions from wastewater, peach stone [6], cherry stones [7], coconut shell [8-10], walnut shell, coffee bean husk, corn cob, rice husk, pecan shell and sugar cane bagasse [11,12].

In this study, the potential use of waste orange peel, one of the valued lignocellulosic agricultural wastes discharged from juice industry, and its derivative type, chemically modified orange peel, was investigated as an adsorbent for anionic reactive dye, RBB. Owing not only to its high content of different functional groups, such as carboxyl and hydroxyl groups but also to its lignocellulosic content such as of lignin, cellulose, hemicellulose, pectin and others, waste

orange peels can be used as a satisfactory adsorbent [13-15]. Although utilization of waste orange peels as adsorbents for removal of effluents in industrial wastewaters is one of the studies explored in literature, as far as the authors' knowledge, there seems to be no study which uses the chemically modified orange peel to remove textile dyes. This paper presents the outcomes about the application of DOP and CMOP as adsorbents for the removal of RBB from aqueous solution.

In this study, the effects of the temperature and the initial pH of the adsorption system on the RBB removal performance of orange peel derived adsorbents (DOP and CMOP) were investigated. Although some studies using the waste orange peel as an adsorbent have been published, especially the equilibrium, kinetic and thermodynamic modelling of RBB adsorption onto the chemically modified orange peel has not been studied comprehensively yet. Since the modelling of the adsorption process assists in optimizing the process' conditions, the Langmuir and Freundlich adsorption models were used to express adsorption of RBB in aqueous media and the effect of temperature on the model constants was evaluated. Moreover, because the thermodynamic parameters are also crucial in the design of the treatment processes, these fundamental data were calculated for further applications.

2. MATERIALS AND METHODS

2.1. Reagents and Preparation of Test Solutions

RBB supplied by Sigma-Aldrich was used without additional treatment (Figure A1.). The examples with the initial dye concentration range between 25 and 750 mg.L⁻¹ were prepared by diluting 1.0 g.L⁻¹ of RBB dye stock solution. The initial pH of each solution was set to the desired value by using 0.1 N HCl and 0.1 N NaOH solutions before introducing the adsorbent.

2.2. Adsorbent Preparation

The waste orange peels were obtained from the BELSO fruit juice production facility Ankara, Turkey, and they were washed with a large volume of tap water, followed by deionized (DI) water. Subsequently, they dried in a vacuum oven at 70 °C for 24 h. After ball milling, the adsorbents with 500-707 µm particle size range were stored in airtight containers ready for further use as the adsorbent named dried orange peel (DOP). During the acidic treatment of the DOP, an isothermal reactor unit consisting of a pyrex glass and a condenser was used. 1.0 g DOP was added to 250 mL of 1.0 M H₂SO₄ solution. The acidic treatment reaction was conducted for 6 hours at 25 °C. The hydrolysate fluid was then removed from the solid by centrifugation. The solid was washed DI water to reach a neutral pH and then dried at 75 °C in a vacuum oven for overnight. The acidic treated orange peels were stored in airtight containers ready to use as the adsorbent, named chemically modified orange peel (CMOP).

2.3. Characterization of The Adsorbents

The surface morphologies of the adsorbents were characterized by Hitachi S-4900 FE-SEM operating at 5.0 kV. The N₂ adsorption/desorption measurements (at 77 K) were performed by Quantachrome Nova 2200 automated surface area analyzer (Quantachrome Corporation, USA). The isotherm data supplied from N₂ adsorption/desorption experiments were applied to the Brunauer–Emmett–Teller (BET) theory for specific surface area. Pore size distributions (PSD) were measured based on the Barrett-Joyner-Halenda (BJH) method.

2.4. Evaluation of The Uptake Performance

Adsorption experiments were conducted by the batch technique in an Erlenmeyer (Pyrex glass) containing 100 mL of RBB solution. The experimental samples were placed in an incubator at a shaking rate of 100 rpm and set to the temperature of 25 °C, 35 °C, 45 °C, respectively. All of the adsorption studies were carried out for 24 h to reach the equilibrium conditions. For the

adsorption studies, 0.1 g of DOP or CMOP was added to 100 mL of the dye solution, and this moment was defined as t_0 . Subsequently, at pre-determined time intervals, periodically 5 mL of samples were taken from the system and centrifuged at 4000 rpm for 10 min. Then, the amount of dye uptake, percentage of dye removal, and adsorption rate values of the adsorbent were calculated with the help of Equations (1-3).

$$q = \frac{(C_0 - C)}{X} \quad (1)$$

$$\% \text{ removal efficiency} = \frac{(C_0 - C)}{C_0} \times 100 \quad (2)$$

$$r_{ad} = \frac{\Delta q}{\Delta t} \quad (3)$$

Where q (mg.g⁻¹) is the adsorption capacity; C_0 (mg.L⁻¹) is the initial RBB concentration; C (mg.L⁻¹) is the residual dye concentration at any time of the adsorption procedure; X is the adsorbent concentration (g.L⁻¹); r_{ad} the adsorption rate of the adsorbent (mg.g⁻¹ min⁻¹); t is the time (min).

The concentrations of RBB remaining in the aqueous phase were analyzed by UV-Vis spectrophotometer at the maximum adsorption peak (λ_{opt}) of 598.0 nm obtained experimentally for RBB. In order to determine the remaining RBB concentration in the aqueous phase, the calibration curve obtained experimentally for different RBB concentrations was used. All the experiments were repeated twice to verify the repeatability and accuracy, and the average of them were used for further calculations.

2.4.1. Effects of initial pH

Since the initial pH of the adsorption media affects the surface charge of the adsorbent, the ionization of the dye molecules or dissociation of the dye ions in the bulk solution, and also the interactions between the functional groups and unsaturated bonds, it is crucial to optimize the initial pH [1,16]. The effect of pH on the adsorption capacity of the adsorbent was investigated at the pH values of 2.0, 3.0, 4.0, 5.0, 6.0, 8.0, 10.0 at 25 °C, and at initial RBB concentration of 25 mg.L⁻¹.

2.4.2. Effects of initial RBB concentration and operation temperature

The effects of initial RBB concentration and operation temperature on the adsorption were investigated at initial dye concentrations of 25 mg.L⁻¹, 50 mg.L⁻¹, 100 mg.L⁻¹, 250 mg.L⁻¹, 500 mg.L⁻¹, and 750 mg.L⁻¹ and at operating temperatures of 25 °C, 35 °C, 45 °C. Each experiment was conducted at the optimum pH values for each adsorbent determined according to Section 2.4.1.

2.5. Modelling of The Adsorption

2.5.1. Modelling of adsorption kinetics: Application of simplified kinetic models

Since the adsorption is a time-dependent equilibrium process, it is important to well define the adsorption rate to control and to evaluate the process. To express the adsorption rate, simplified kinetic models including pseudo-first order, pseudo-second order and saturation type kinetic models were applied to the experimental data. The linearized equations of these models were depicted in Table A1. According to these linearized equations, to validate the applicability of pseudo-first order kinetics, the plot of t/q vs. t should give a linear relationship, with the help of this graph q_{eq} and $k_{2.ad}$ can be calculated from the slope and the intercept of the plot (Table A1).

2.5.2. Modelling of adsorption equilibrium: Application of adsorption equilibrium models

At equilibrium conditions of the adsorption process, the amount of effluent at the solid-liquid interface (q_{eq}) increases non-linearly with the concentration. To determine the maximum adsorption capacity of the adsorbent and to identify the type of adsorption equilibrium, the Langmuir and the Freundlich adsorption isotherms (two-parameter models) were applied to experimental data at different temperatures for each adsorbent-dye system. The non-linear equations of these models were presented in Table A2.

The Langmuir equation is valid for monolayer adsorption and has some assumptions as

following: (i) the adsorbent surface has a finite number active sites and all of these sites have the same adsorption energy (a homogenous surface); (ii) the adsorption process is reversible; (iii) there is no interaction between the adsorbed species; (iv) if an active site on the adsorbent absorbs an adsorbate, there is no way to occur another adsorption on that site [17]. According to this model, as the saturation of the adsorption is reached, no further binding sites are available on the adsorbent surface and the maximum adsorption capacity (Q^0) corresponding to complete monolayer coverage on the sorbent surface is obtained. The Langmuir model constants are significantly dependent on the adsorbent type and temperature. The linearized Langmuir model can be expressed in the form of Equation (4),

$$\frac{C_{eq}}{q_{eq}} = \frac{C_{eq}}{Q^0} + \frac{1}{Q^0 b} \quad (4)$$

where Q^0 (mg.g⁻¹), represents the maximum saturated monolayer adsorption capacity (maximum amount of adsorbate adsorbed per gram of adsorbent) under the given conditions. According to Equation (4), a plot of $1/q_{eq}$ vs. $1/C_{eq}$ should give a straight line with a slope of Q^0 , and an intercept of b . The Langmuir model constant b is related to the free energy of adsorbent and shows the affinity of the adsorbent for the binding of effluent.

Unlike the Langmuir model, the Freundlich empirical equation is based on the adsorption onto a heterogeneous adsorbent surface affected by temperature. This model suggests neither linearity at low effluent concentration nor a fixed adsorption capacity as any saturation is reached. According to this model, the multilayer adsorption on the heterogeneous adsorbent surface is occurred [18]. As a result, an exponential shaped theoretical equilibrium curve is obtained. The linearized form of the Freundlich model equation is given as in Equation (5),

$$\ln q_{eq} = \ln K_F + \frac{1}{n} \ln C_{eq} \quad (5)$$

A linear plot of $\log q_{eq}$ vs. $\log C_{eq}$ was plotted to determine the n (adsorption intensity) and K_F (adsorption capacity) model constants with the

help of the slope and the intercept of the graph, respectively. The higher n value means the stronger adsorption intensity, and generally, $n > 1$ indicates that adsorbate is favorably adsorbed on the adsorbent [19]. K_F , is one of the Freundlich model constants related to the adsorption capacity of the adsorbent.

2.5.3. Modelling of adsorption thermodynamics

In the adsorption process, it is important to establish the adsorption mechanism such as chemical or physical adsorption. While during physical adsorption, the relatively weak interaction is taken into account, in chemisorption stronger chemical interactions take place [17]. To distinguish the physical and chemical adsorption, it is essential to determine the thermodynamic parameters, including the Gibbs free energy change (ΔG^0 ; kJ mol^{-1}), the enthalpy change (ΔH^0 ; kJ mol^{-1}), and the entropy change (ΔS^0 ; $\text{kJ mol}^{-1}\text{K}^{-1}$) in the system.

The Gibbs free energy of the system can be obtained using the following relationship;

$$\Delta G^0 = -RT \ln K_c^0 \quad (6)$$

where K_c^0 is the thermodynamic equilibrium constant, R is the universal gas constant ($8.314 \text{ J.mol}^{-1}\text{K}^{-1}$) and T is the temperature (K). Since the adsorption process is a heterogeneous equilibrium process, it can be summarized by the reversible process between the effluent in solution and the effluent-adsorbent. The apparent equilibrium constant (K_c') of this system can be defined as;

$$K_c' = \frac{C_{ad,eq}}{C_{eq}} \quad (7)$$

where $C_{ad,eq}$ is the concentration of the effluent on the adsorbent at the equilibrium. In this case, instead of the concentration values, the activity of the species can be used to obtain standard thermodynamic equilibrium constant (K_c^0) of the adsorption system. This value can be obtained by calculating K_c' at different initial effluent concentrations and extrapolating data to zero. It will be also equal to the $1/\text{intercept}$ of C_{eq}/q_{eq} vs. C_{eq} graph ($=bQ^0$) at 25°C , which indicates the

linearized form of the Langmuir adsorption model equation.

According to the law of thermodynamics the relationship of ΔG^0 to ΔH^0 and ΔS^0 can be expressed as:

$$\Delta G^0 = \Delta H^0 - T \Delta S^0 \quad (8)$$

Moreover, the relationship between the K_c^0 and T is obtained by Equation (6) into Equation (8) and called as the van't Hoff equation:

$$\ln K_c^0 = \frac{\Delta S^0}{R} + \frac{\Delta H^0}{RT} \quad (9)$$

The enthalpy change and the entropy change of the system can be computed according to the linearized van't Hoff plot of $\ln K_c^0$ vs. $1/T$.

3. RESULTS AND DISCUSSIONS

3.1. Characterization of The Adsorbents

Figure 1a-b show that DOP exhibited irregular shape bulk-like carbon monoliths with a smooth surface where no cavities or holes detected. On the other hand, CMOP presented a well-developed porous and interconnected network with abundant micro and mesoporous structure (Figure 1c, and d) which may be attributed to etching effect of acidic treatment .

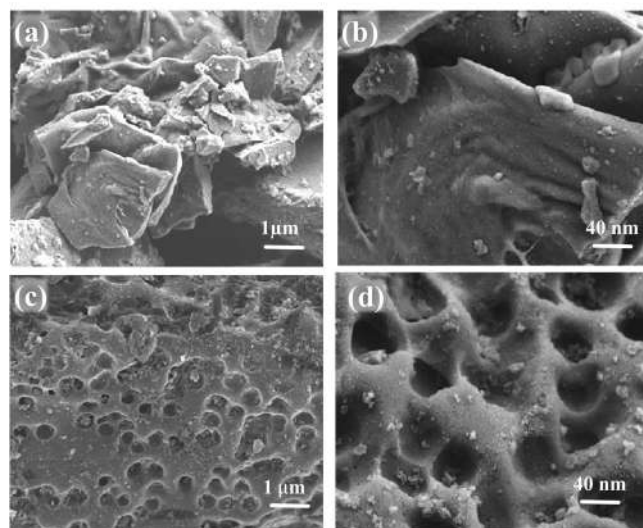


Figure 1 FE-SEM images of (a,b) DOP, and (c,d) CMOP at the same magnifications

The porous structure of the DOP, and CMOP was analyzed by the N_2 adsorption/desorption

isotherms. As shown in Figure 2a, DOP presented essentially a Type-I isotherm which confirms the presence of dominant microporous structure [20]. This was also confirmed by the pore size distribution curve (Figure 2b) calculated by the BJH method. On the other hand, CMOP exhibited type-IV isotherm with an H4 type hysteresis loop located between 0.40 and 0.99 of P/P^0 , according to the presence of mesoporous carbon structures [21]. Furthermore, a sharp increase of N_2 uptake at a relative pressure of <0.1 proves the existence of micropores. Chemical modification improved S_{BET} and porosity structure of DOP, as presented in Table 1. While S_{BET} value of DOP is merely $102.0 \text{ m}^2 \cdot \text{g}^{-1}$, consisting of very low pore volume, after chemical treatment, the surface area and pore volume was enhanced to $651.0 \text{ m}^2 \cdot \text{g}^{-1}$ and $0.625 \text{ cm}^3 \cdot \text{g}^{-1}$ (Table 1), respectively. These results proves that acidic treatment was an effective method for synthesis of well-ordered porous carbon structure with high porosity.

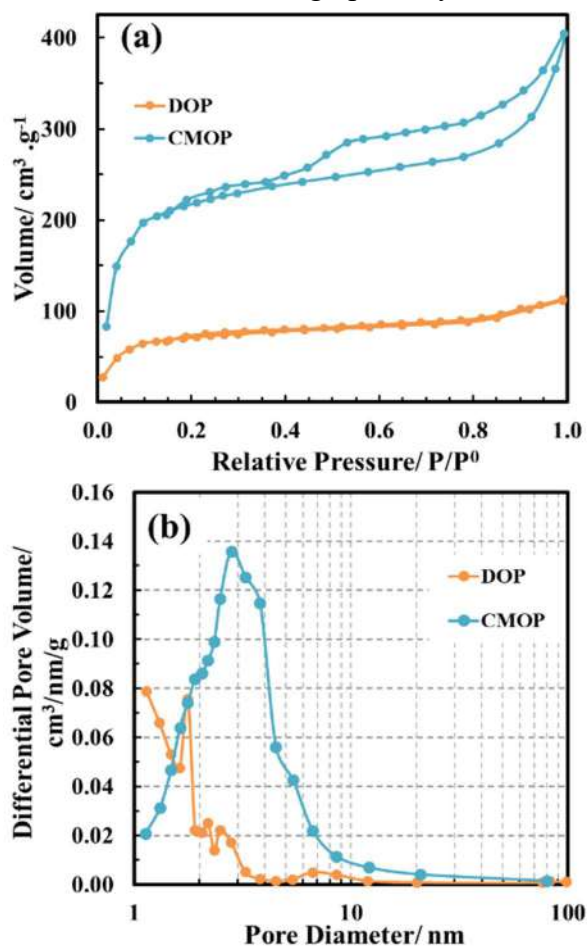


Figure 2 (a) N_2 adsorption/desorption isotherms, and (b) the BJH pore size distributions of DOP and CMOP

Table 1
Physicochemical parameters obtained from N_2 adsorption/desorption isotherms of DOP and CMOP samples

Sample ID	S_{BET} $\text{m}^2 \cdot \text{g}^{-1}$	V_{micro} cm^3/g	V_{meso} cm^3/g	V_{total} cm^3/g	% V_{micro}	% V_{meso}
DOP	102.0	0.095	0.046	0.141	67.38	32.62
CMOP	651.0	0.258	0.394	0.652	39.55	60.45

3.2. Evaluation of the Uptake Performance

3.2.1. Effects of initial pH

As shown in Figure 3, the pH dependence of the adsorption capacity of both DOP and CMOP were investigated at $100 \text{ mg} \cdot \text{L}^{-1}$ initial dye concentration between the pH range out from 2.0 to 10.0. It can be seen that the dye removal of each adsorbent was strongly depended on the initial pH. While the highest uptake of DOP was obtained at pH 2.0 as $19.4 \text{ mg} \cdot \text{g}^{-1}$, this value for CMOP was shifted to pH 8.0, almost neutral, as $30.4 \text{ mg} \cdot \text{g}^{-1}$ for the uptake of RBB (Figure 3). However, it should be taken into consideration that natural wastewaters generally have pH values higher than acidic values ($\text{pH} > 2$). The pH values close to the natural pH value are more relevant results due to easy and direct application to the system of interest. The results verified that the DOP mainly consists of negatively charged surface functional groups such as carboxyl groups, nitrogen-containing functional groups, and some weaker acidic groups. Just as the pH of the system decreases, the adsorbent surface charges more positively. Thus, the RBB adsorption capacity of the DOP turns out more favorable owing to the electrostatic attractions between RBB anions and positively charged adsorbent surface. DOP charged more positively for pH values lower than 3.5-4.0 because of the ionization of the surface functional groups and charged more negatively at higher pH values. At acidic medium, most of the potential active sites of the adsorbent are protonated so the maximum adsorption capacity of DOP was obtained at pH 2.0 [5]. This result is also supported by the other researchers that the surface functional groups of the adsorbent may become protonated under relatively acidic media [22-25]. According to some researchers, nitrogen containing functional

groups show significant potential for the removal of reactive dyes from aqueous solution due to the electrostatic interactions between amine groups of the adsorbate and sulfonate groups of the RBB [16, 26].

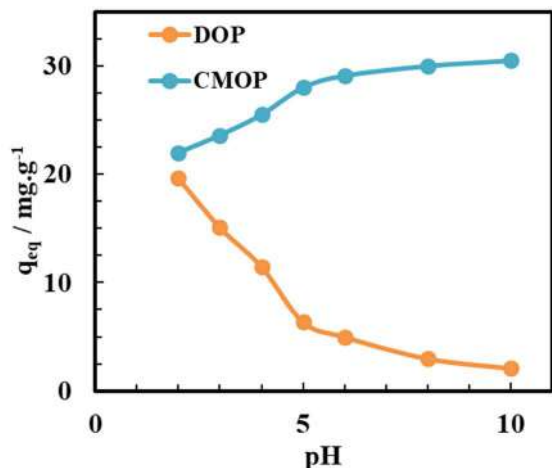


Figure 3 Effect of the initial pH of the solution on the equilibrium uptake of RBB (C_0 : 100 $\text{mg}\cdot\text{L}^{-1}$, T : 25 $^{\circ}\text{C}$, agitation rate: 100 rpm)

As the pH is shifted to the alkaline region, while the number of positive surface charges decreases, the increment is observed in the amount of negatively charged surface sites. As a result of the electrostatic repulsion, this situation does not favor the adsorption of RBB anions on the adsorbent dominated by negative sites. The competition between the OH^- ions increased by the higher pH value and the RBB anions for the adsorption onto the active sites leads to decrease of the adsorption capacity of the adsorbent. It is suggested that as a result of acidic treatment of DOP, the surface charge has been changed anionic to cationic. The chemical modification of DOP by acidic treatment leads to a change of surface charge negative to positive, which therefore indicates that CMOP added favorable electrostatic contribution to RBB around the natural pH range. These findings also support the results related to the pH dependence of RBB adsorption capacity of the adsorbent represented in Figure 3. In the light of these results it can be suggested that the adsorption process of the RBB onto each adsorbent probably consist of two steps; electrostatic interaction and then ion-exchange or complexation between adsorbent and adsorbate.

3.2.2. Effect of initial RBB concentration and operation temperature

For different initial RBB concentration and operation temperature, each adsorbent showed different behavior (Figure 4). At all temperatures, adsorption on each adsorbent was enhanced significantly by increasing the initial RBB concentration tending to saturation at higher dye concentrations. Increasing the dye concentration provides a considerable driving force to eliminate the effect of mass transfer resistances of the dye between solid-liquid interfaces. Moreover, the number of interactions between the adsorbent and the adsorbate relatively increase by the initial dye concentration, which enhances the RBB removal capacity of the adsorbent. However, the removal RBB efficiency of each adsorbent does not increase with the initial dye concentration. At all temperatures studied, RBB removal % was higher at lower dye concentrations for each adsorbent due to the availability of unoccupied active sites on the surface of the adsorbents. Increasing the dye concentration diminished the dye removal efficiency, due to almost filled active sites of the adsorbents.

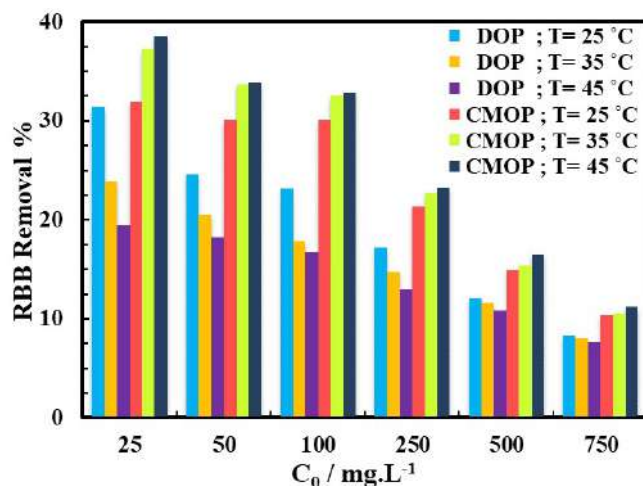


Figure 4 Effects of temperature and the initial dye concentration (C_0 ; $\text{mg}\cdot\text{L}^{-1}$) on RBB removal efficiency of DOP; at pH=2.0 and CMOP at pH=8.0

Temperature is another parameter which plays a crucial role in both the adsorption rate and the equilibrium dye uptake of adsorbents. The results obtained for DOP revealed that the adsorption behavior of DOP indicated an exothermic character and q_{eq} values diminished with the

increasing temperature. As adsorption generally is an exothermic process, this is expected due to the weakened physical bounding with increasing temperature. At 100 mg.L⁻¹ initial dye concentration with increasing temperature from 25 °C to 45 °C, while the equilibrium uptake capacity of DOP decreased from 23.3 mg.g⁻¹ to 16.7 mg.g⁻¹, that of CMOP increased from 30.4 mg.g⁻¹ to 36.6 mg.g⁻¹. The decrease in adsorption of DOP at higher temperature may be referred to the deactivation of the active sites on the adsorbent surface (Table 2). As listed in Table 2, the data obtained from adsorption of RBB on CMOP demonstrated that the adsorption performance of the adsorbent was favored by the increase of the temperature, so the results showed that the adsorption of RBB by CMOP was endothermic. The change of the adsorption characteristic from exothermic to endothermic behavior revealed that the chemical modification

by acidic treatment of the DOP led to change the surface charge and the structure. The enhancement of the adsorption capacity could be attributed to an increase in the number of active sites on the surface available for the adsorption, increase in the porosity and the total pore volume of the adsorbent (Figure 2). It may also be attributed to the decrease in the mass transfer resistance with decreasing the thickness of the boundary layer surrounding the adsorbent. Furthermore, the kinetic energy of the molecules, namely the mobility of the RBB molecules increases with the increasing of the temperature. Consequently, the dye molecules can easily transport from the bulk solution to the adsorbent-solution interface, so this may easily enhance the rate of intra-particle diffusion of adsorbate [19]. It can be concluded that the adsorption of RBB on the CMOP may involve not only the physical adsorption but also the chemical adsorption.

Table 2

Effect of temperature and initial dye concentration on adsorption rate (r_{ad}), equilibrium uptake of RBB (q_{eq}), and RBB removal % for DOP and CMOP (X : 1.0 g.L⁻¹, and agitation rate: 100 rpm)

T (°C)	C ₀ (mg.L ⁻¹)	DOP at pH= 2.0			CMOP at pH= 8.0		
		r _{ad} (mg.g ⁻¹ min ⁻¹)	q _{eq} (mg.g ⁻¹)	RBB Removal %	r _{ad} (mg.g ⁻¹ min ⁻¹)	q _{eq} (mg.g ⁻¹)	RBB Removal %
25	25	0.14	7.4	31.4	0.25	7.9	32.0
	50	0.24	12.4	24.6	0.46	14.6	30.1
	100	0.51	23.3	23.2	0.73	30.4	30.1
	250	0.87	43.3	17.2	1.13	54.1	21.4
	500	1.23	61.1	12.1	1.37	75.2	14.9
	750	1.45	62.4	8.3	1.48	78.5	10.4
35	25	0.12	6.1	23.9	0.26	8.3	37.3
	50	0.21	10.2	20.5	0.49	16.4	33.7
	100	0.43	18.1	17.9	0.79	33.1	32.5
	250	0.75	37.3	14.7	1.18	56.1	22.7
	500	1.12	59.2	11.6	1.44	77.1	15.4
	750	1.29	60.5	8.0	1.55	79.6	10.6
45	25	0.11	5.2	19.5	0.29	8.1	38.5
	50	0.19	9.3	18.2	0.52	17.1	33.9
	100	0.42	16.7	16.7	0.84	36.6	32.8
	250	0.72	33.1	13.0	1.24	58.3	23.3
	500	1.09	54.8	10.8	1.49	82.2	16.5
	750	1.27	57.3	7.6	1.59	84.4	11.2

Figure 5 demonstrated the adsorption kinetics of RBB, at all temperatures by plotting the uptake capacity (q) vs. time (t) for 25 mg.L⁻¹ and 750 mg.L⁻¹ initial RBB concentrations for the first 7 h of the adsorption.

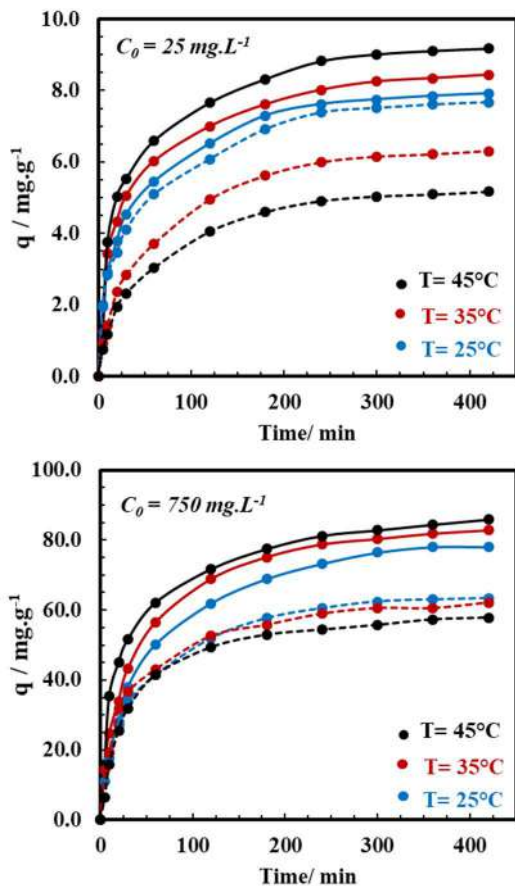


Figure 5 The adsorption equilibrium curves of RBB at different initial dye concentrations (C_0) and at different temperatures for DOP (dashed lines) and CMOP (Straight lines) at pH= 2.0 and pH=8.0, respectively

Table 3

Comparison of the experimental and calculated q_{eq} values for the pseudo-first order and pseudo-second order adsorption kinetics at different temperatures of RBB concentration of 100 mg.L⁻¹

	T (°C)	C_0 (mg.L ⁻¹)	$q_{eq.exp}$ (mg.g ⁻¹)	Pseudo-first order kinetic model			Pseudo-second order kinetic model		
				$q_{eq.cal}$ (mg.g ⁻¹)	$k_{1.ad}$ (min ⁻¹)	R ²	$q_{eq.cal}$ (mg.g ⁻¹)	$k_{2.ad} \times 10^3$ (g.mg ⁻¹ min ⁻¹)	R ²
DOP at pH=2.0	25	100.5	23.31	17.91	0.0143	0.962	23.81	2.03	0.998
	35	100.9	18.09	13.31	0.0127	0.939	17.92	1.82	0.993
	45	99.0	16.69	14.04	0.0124	0.989	16.89	1.75	0.999
CMOP at pH=8.0	25	101.0	30.4	25.9	0.0189	0.923	31.5	1.08	0.999
	35	101.9	33.1	25.4	0.0233	0.946	32.4	1.11	0.999
	45	105.4	36.6	33.5	0.0240	0.943	37.9	1.29	0.999

Figure 5 shows a contact time from 2 to 4 h depending on the temperature and the adsorbent was sufficient to reach equilibrium. The adsorption level did not change subsequently up to 24 h. At the beginning of the adsorption process, the RBB uptake capacity of the adsorbents increased with the contact time linearly, then non-linearly got to a slower rate and at the end, the adsorbent achieved the saturation called the equilibrium time and equilibrium uptake capacity (q_{eq}). Moreover, it was noticed that at all temperatures for all initial RBB concentrations, the majority of RBB adsorption onto each adsorbent (~ 60 - 70 %) took place within the first two hours of the whole process (Table 2). Both DOP and CMOP have an affinity for RBB and the uptake of RBB occurs mainly by surface binding. The number of available active sites of the surface is the limiting factor for the adsorption [19]. CMOP showed higher uptake of RBB than DOP at all temperatures due to its surface characteristics, especially specific surface area, number of active sites, surface charge, the total pore volume and pore size distribution (Table 1).

3.3. Modelling of The Adsorption

3.3.1. Modelling of adsorption kinetics: Application of simplified kinetic models

The adsorption rate constants ($k_{1.ad}$ and $k_{2.ad}$) and theoretical equilibrium uptake capacities ($q_{eq.cal}$) of each adsorbent were obtained for each adsorbent-dye system (Table 3).

As indicated in Table 3, for both of the adsorbents, the correlation coefficients (R^2) for pseudo-second-order kinetic were calculated much higher than those calculated for the pseudo-first-order kinetic. It was concluded that the pseudo-second order kinetic model fits better the experimental data obtained for RBB adsorption onto both adsorbents for the entire adsorption period suggesting chemisorption mechanism. Besides the pseudo-first order and pseudo-second order kinetic models, the saturation type kinetic model was also applied to experimental data to describe the batch adsorption kinetics over the entire concentration range of RBB and all temperatures studied as presented in Table 4. Table 4 shows that this kinetic model was also well fitted with the experimental data to express the adsorption kinetics of RBB on DOP and CMOP (plots not shown). It was observed that the adsorption rate constants were affected by the temperature. The change of the rate constants with the temperature indicated that adsorption reaction was one of the rate controlling steps of the whole process. All of these findings suggested that the adsorption of RBB at 25- 45 °C could be best described by the pseudo-second order kinetics and saturation type kinetic model, with high correlation coefficients.

Table 4

The saturation type kinetic rate constants obtained at different temperatures for different adsorbents

	T (°C)	$k_{ad} \times 10^2$ (L.g ⁻¹ min ⁻¹)	$k_{o,ad} \times 10^2$ (L.mg ⁻¹)	R ²
DOP at pH=2.0	25	6.22	0.30	0.998
	35	4.91	0.25	0.999
	45	4.46	0.21	0.998
CMOP at pH=8.0	25	1.24	0.72	1.000
	35	1.37	0.80	1.000
	45	1.42	0.82	0.999

3.3.2. Modelling of the adsorption Equilibrium: Application of adsorption equilibrium models

According to the linearized Langmuir model equation (Equation 4), the theoretical maximum adsorption capacity (Q^0) of RBB on DOP and CMOP were obtained as 63.30 mg.g⁻¹ at 25 °C, and 89.30 mg.g⁻¹ at 45 °C, respectively. At all temperatures, Q^0 values were calculated higher for the CMOP-RBB system in comparison with the DOP-RBB system. The higher b value indicates the higher affinity of the adsorbents for the adsorbate [18]. Similarly, the b values for CMOP were much higher than that of DOP at all temperatures investigated (Table 5).

Table 5 The Langmuir and the Freundlich adsorption isotherm parameters for RBB adsorption on DOP and CMOP at various temperatures

	T (°C)	The Langmuir Model Constants			The Freundlich Model Constants				
		Q^0 (mg.g ⁻¹)	b	R^2	ϵ (%)	K_F [(mg.g ⁻¹) (mg.L ⁻¹) ⁿ]	n	R^2	ϵ (%)
DOP at pH=2.0	25	63.30	0.0073	0.9987	2.2	1.67	1.5	0.9780	8.2
	35	61.70	0.0050	0.9989	2.2	1.49	0.9	0.9998	6.7
	45	57.80	0.0048	0.99991	1.9	1.41	0.7	0.9886	8.5
CMOP at pH=8.0	25	78.10	0.0713	0.99986	3.4	1.69	2.2	0.9947	16.5
	35	82.60	0.1122	0.99987	2.3	1.72	2.8	0.9958	15.5
	45	89.30	0.1894	0.99990	2.2	1.75	3.7	0.9977	13.2

K_F values calculated for each adsorbent showed that RBB adsorption capacity of CMOP relatively higher than DOP (Table 5). A higher value of K_F indicates that a higher adsorption capacity. Although the K_F increased with an increase in the temperature for CMOP, it decreased for DOP. It was also observed that while all n values obtained for CMOP were greater than unity, these values for DOP was greater only at 25 °C than unity (Table 5). These results indicated that RBB was

more favorably adsorbed by CMOP at all temperatures studied. The non-linearized adsorption isotherm models for the fitting of RBB adsorption on DOP and CMOP were plotted as graphs of q_{eq} vs. C_{eq} at different temperatures (Figure 6). The overlapping of the experimental and the non-linearized model curves was an evidence that the Langmuir adsorption model closely agreed with the equilibrium data for each adsorbent-dye system.

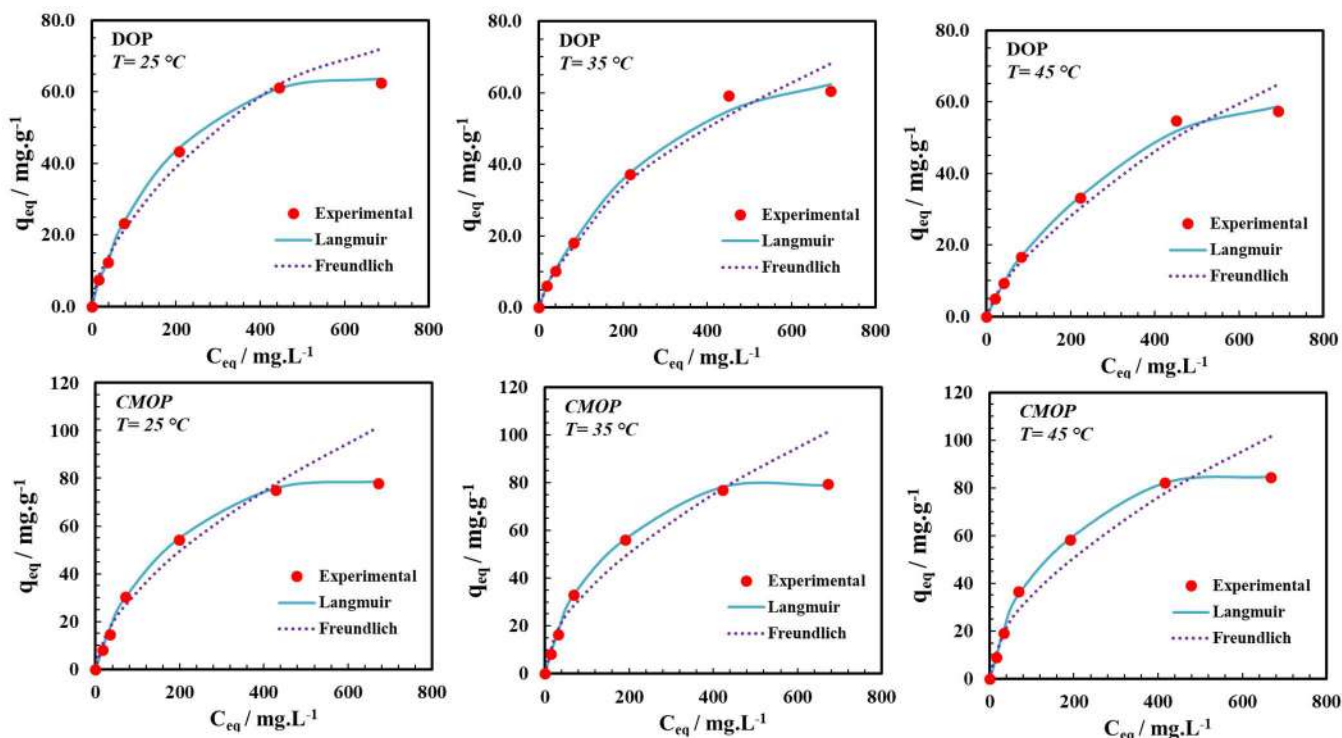


Figure 6 The experimental and estimated non-linearized adsorption isotherms of RBB on DOP, at pH= 2.0 and CMOP, at pH=8.0 at different temperature

In Table 5, the adsorption model parameters calculated by related model equations (Equation (4) and (5)), the linear regression coefficients (R^2) and average percentage error values (ε) were also presented. It was obvious that the Langmuir adsorption isotherm model well fitted the experimental data with much higher R^2 values, than that of the Freundlich model (Table 5 and Figure 6). On the other hand, the linear regression coefficients (>0.97) indicated that the Freundlich model was comparable to the Langmuir model. Another criterion for determination of the most applicable isotherm model is the magnitude of average percentage error values (ε) which show the deviation from the experimental q_{eq} values. On the basis of the ε values, it was proven the

adsorption equilibrium data of RBB fitted very well to the Langmuir model in the initial dye concentration and temperature ranges investigated for each adsorbent. With an average percentage error values more than 6.7%, it was concluded that the Freundlich model exhibited a relatively poor fit to the adsorption data of RBB onto each adsorbent. The applicability of the Langmuir model indicated that the adsorption process of RBB was monolayer and had constant adsorption energy.

Table 5 also demonstrated that both of the model constants of CMOP increased with the temperature rise, which means that the RBB adsorption phenomenon on CMOP is governed by

an endothermic process, whereas RBB adsorption onto DOP showed exothermic character. The typical physical adsorption shows exothermic character. The weak electrostatic forces between the opposite charged sites on the adsorbent and effluent species in the solution are responsible for the adsorption behavior [17].

3.3.3 Modelling of adsorption thermodynamics

All of the thermodynamic parameters of each adsorbent-dye system were obtained by using the thermodynamic relationships and represented in Table 6. Generally, increasing of the adsorption capacity with the increasing temperature reflects the exothermic character of the adsorption process. This situation leads to negative standard enthalpy change of the process. Notably, an exothermic process is because the total energy released in bond occurred between effluent and the adsorbent is higher than the bond breaking, leading to release of extra energy in the form of heat [1, 2].

The standard thermodynamic equilibrium constant (K_c^0) of the adsorption system was obtained with the help of the linearized form of the Langmuir adsorption model equation (for detail see Section 2.5.3). The K_c^0 values at 25 °C are calculated for DOP and CMOP as 4.2 and 5.5, respectively.

Table 6 shows that the signs of all thermodynamic parameters were in accordance with the experimental data of the adsorption isotherms. The negative value of enthalpy change reveals exothermic adsorption favorable at lower temperatures. It is demonstrated by a decrease in the maximum adsorption capacity of the adsorbent at higher temperatures. Meanwhile, the positive value of ΔH^0 for CMOP reflects that the endothermic nature of the adsorption process favorable at higher temperatures and possible relatively stronger bonding between the RBB and CMOP.

Table 6 Comparison of the thermodynamic parameters of RBB adsorption on DOP and CMOP

Adsorbent	ΔG^0 (kJ mol ⁻¹)	ΔH^0 (kJ mol ⁻¹)	ΔS^0 (kJ mol ⁻¹ K ⁻¹)
DOP (at pH=2.0)	-3.58	-19.79	-0.05
CMOP (at pH=8.0)	-4.24	43.77	0.16

Furthermore, both the magnitude and the sign of entropy change give the information about whether the adsorption process is occurred by an associative mechanism ($\Delta S^0 < 0$) or more randomly (a dissociative mechanism) ($\Delta S^0 > 0$). While the positive ΔS^0 value suggests that the high affinity of CMOP to RBB in solution and some structural changes or rearrangement in the dye-adsorption complex, the negative entropy change values confirm the decreased randomness and disorder at the solid-liquid interface during the adsorption of RBB onto CMOP. Furthermore, the positive entropy change indicated that the adsorption process was entropy-governed rather than enthalpy-governed. The negative ΔG^0 value implies that at all temperatures suggested that the adsorption process took place favorably and spontaneously.

4. CONCLUSIONS

This study has investigated the adsorption characteristics of the untreated waste orange peel-DOP and chemical pre-treated waste orange peel-CMOP adsorbents for the removal of RBB ions from the aqueous solutions. As a result of acidic treatment, the lignin, cellulose and hemicellulose structures in the DOP have been decomposed, the surface charge have changed negative to positive due to the acidic medium, and a highly porous structure has been obtained. The optimum pH value of the system has shifted from pH 2.0 to 8.0, almost natural, and the RBB uptake capacity of the adsorbent has been increased. The maximum adsorption capacity calculated according to the Langmuir model was determined as 62.4 mg/g at 25°C and pH 2.0 for DOP and this value was figured out for CMOP as 84.4 mg.g⁻¹ at 45°C and pH 8.0 (35.2% higher). The Langmuir adsorption model provided more realistic description of RBB

onto both adsorbent-dye systems and could be used to predict the uptake of RBB with more accuracy than the Freundlich model for each system. The acidic treatment of DOP change the adsorption characteristic from exothermic to endothermic. The acidic treatment had shifted the structure of the DOP to shift the mechanism of the adsorption process from physical adsorption to the chemical adsorption with higher ΔH^0 value ($>10 \text{ kJ kmol}^{-1}$).

The novel CMOP adsorbent, a widely available agricultural by-product, could be a promising candidate for practical applications as a low-cost and efficient agricultural waste adsorbent for anionic dye removal from the textile industry wastewater.

Funding

The authors received no financial support for the research, authorship, and/or publication of this paper.

The Declaration of Conflict of Interest/ Common Interest

No conflict of interest or common interest has been declared by the authors.

Authors' Contribution

CK: investigation, conceptualization, methodology, data curation, Writing- original draft preparation, Writing-reviewing and editing draft preparation, visualization ZA: Supervision, conceptualization, methodology, resources.

The Declaration of Ethics Committee Approval

The authors declare that this document does not require an ethics committee approval or any special permission.

The Declaration of Research and Publication Ethics

The authors of the paper declare that they comply with the scientific, ethical and quotation rules of SAUJS in all processes of the paper and that they

do not make any falsification on the data collected. In addition, they declare that Sakarya University Journal of Science and its editorial board have no responsibility for any ethical violations that may be encountered, and that this study has not been evaluated in any academic publication environment other than Sakarya University Journal of Science.

REFERENCES

- [1] S.P. Kodal and Z. Aksu, "Cationic surfactant-modified biosorption of anionic dyes by dried *Rhizopus arrhizus*." *Environmental technology*, vol. 38, no. 20, pp. 2551-2561, 2017.
- [2] Z. Aksu, "Application of biosorption for the removal of organic pollutants: a review." *Process Biochemistry*, vol. 40, pp. 997-1026, 2005.
- [3] E. Bayram and E. Ayranci, "Investigation of changes in properties of activated carbon cloth upon polarization and of electrosorption of the dye basic blue-7." *Carbon*, vol. 48, pp. 1718-1730, 2010.
- [4] S.P.D Monte Blanco, F.B. Scheufele, A.N. Modenes, F.R. Espinoza-Quinones, P. Marin, A.D. Kroumov and C.E. Borba, "Kinetic, equilibrium and thermodynamic phenomenological modeling of reactive dye adsorption onto polymeric adsorbent." *Chemical Engineering Journal*, vol. 307, pp. 466-475, 2017.
- [5] Z. Aksu and A. İsoğlu, "Use of agricultural waste sugar beet pulp for the removal of Gemazol turquoise blue-G reactive dye from aqueous solution." *Journal of Hazardous Materials B*, vol. 137, pp. 418-430, 2006.
- [6] A.A. Attia, B.S. Girgis, and N.A. Fathy, "Removal of methylene blue by carbons derived from peach stones by H_3PO_4 activation: batch and column studies." *Dyes and Pigments*, vol. 76, pp. 282-289, 2008.
- [7] M, Olivares-Marín, C. Fernández-González A. Macías-García, and V. Gómez-Serrano,

- “Preparation of activated carbons from cherry stones by activation with potassium hydroxide.” *Applied Surface Science*, vol. 252, pp. 5980–5983, 2006.
- [8] W. Li, K. Yang, J. Peng, L. Zhang, S. Guo, and H. Xia, “Effects of carbonization temperatures on characteristics of porosity in coconut shell chars and activated carbons derived from carbonized coconut shell chars.” *Industrial Crops and Products*, vol. 28, pp. 190–198, 2008.
- [9] I.A.W. Tan, A.L. Ahmad, and B.H. Hameed, “Adsorption of basic dye on high-surface-area activated carbon prepared from coconut husk: equilibrium, kinetic and thermodynamic studies.” *Journal of Hazardous Materials*, vol. 154, pp. 337–346, 2008.
- [10] F.S. Vieira, A.R. Cestari, I.F. Gimenez, N.L.V. Carreño, and L.S. Barreto, “Kinetic and calorimetric study of the adsorption of dyes on mesoporous activated carbon prepared from coconut coir dust.” *Journal of Colloid and Interface Science*, vol. 298, pp. 515–522, 2006.
- [11] M. Olivares-Marín, V. Del-Prete, E. Garcia-Moruno, C. Fernández-González, A. Macías-García, and V. Gómez-Serrano, “The development of 500 an activated carbon from cherry stones and its use in the removal of ochratoxin A from red wine.” *Food Control*, vol. 20, no. 3, pp. 298–303, 2009.
- [12] J.M. Dias, M.C.M. Alvim-Ferraz, M.F. Almeida, J. Rivera-Utrilla, and M. Sánchez-Polo. “Waste materials for activated carbon preparation and its use in aqueous-phase treatment: a review.” *Journal of Environmental Management*, vol. 85, no. 4, pp. 833–846, 2007.
- [13] S. Liang, X. Guo, N. Feng, and Q. Tian “Application of orange peel xanthate for the adsorption of Pb^{2+} from aqueous solutions.” *Journal of Hazardous Materials*, vol. 170, pp. 425–429, 2010.
- [14] D.D. Lu, Q.L. Cao, X.M. Li, X. Cao, F. Luo, and W. Shao, “Kinetics and equilibrium of Cu(II) adsorption onto chemically modified orange peel cellulose biosorbents.” *Hydrometallurgy*, vol. 95, no. 1-2, pp. 145–152, 2009.
- [15] P.D. Pathak, S.A. Mandavgane, and B.D. Kulkarni, “Characterizing fruit and vegetable peels as bioadsorbents.” *Current Science*, vol. 110, pp. 2114–2123, 2016.
- [16] J.J.M Órfão, A.I.M. Silva, J.C.V. Pereira, S. A. Barata, I. M. Fonseca, P. C. C. Faria, and M. F. R. Pereira. “Adsorption of a reactive dye on chemically modified activated carbons—influence of pH.” *Journal of Colloid and Interface Science*, vol. 296, no. 2, pp. 480–489, 2006.
- [17] N.H. Tran, S.J. You, and H.P. Chao, “Thermodynamic parameters of cadmium adsorption onto orange peel calculated from various methods: A comparison study.” *Journal of Environmental Chemical Engineering*, vol. 4, pp. 2671–2682, 2016.
- [18] I. Langmuir, “The adsorption of gases on plane surfaces of glass, mica, and platinum.” *Journal of the American Chemical Society*, vol. 40, pp. 1361–140, 1918.
- [19] Z. Aksu, A.I. Tatlı, and Ö. Tunç, “A comparative adsorption/biosorption study of Acid Blue 161: Effect of temperature on equilibrium and kinetic parameters.” *Chemical Engineering Journal*, vol. 142, pp. 23–39, 2008.
- [20] Q. Meng, Q. Kaiqiang, M. Liying, H. Chunnian, L. Enzo, H. Fang, S. Chunsheng, L. Qunying, L. Jiajun, and Z. Naiqin, “N-doped porous carbon nanofibers/porous silver network hybrid for high-rate supercapacitor electrode.” *ACS applied materials & interfaces*, vol. 9, no. 36, pp. 30832–30839, 2017.
- [21] Karaman C., Bayram E., Karaman O., Aktaş Z., “Preparation of high surface area nitrogen doped graphene for the assessment of

morphologic properties and nitrogen content impacts on supercapacitors", JOURNAL OF ELECTROANALYTICAL CHEMISTRY, vol.868, pp.114197-, 2020

- [22] E. Errais, J. Duplay, M. Elhabiri, M. Khodja, R. Ocampo, R. Baltenweck-Guyot, and F. Darragi "Anionic RR120 dye adsorption onto raw clay: surface properties and adsorption mechanism." Colloids and Surfaces A: Physicochemical and Engineering Aspects, vol. 403, 69–78, 2012.
- [23] J. Huang, D. Liu, J. Lu, H. Wang, X. Wei, and J. Liu "Biosorption of reactive black 5 by modified *Aspergillus versicolor* biomass: kinetics, capacity and mechanism studies." Colloids and Surfaces A: Physicochemical and Engineering Aspects, vol. 492, pp. 242–248, 2016.
- [24] A. Srinivasan, and T. Viraraghavan, "Decolorization of dye wastewaters by biosorbents: a review." Journal of Environmental Management, vol. 91, pp. 1915–1929, 2010.
- [25] Y.S. Al-Degs, M.I. El-Barghouthi, A.H. El-Sheikh, and G.M. Walker, "Effect of solution pH, ionic strength, and temperature on adsorption behavior of reactive dyes on activated carbon." Dyes and Pigments, vol. 77, pp.16–23, 2008.
- [26] A.R. Cestari, E.F.S. Vieira, A.G.P. Dos Santos, J.A. Mota, and V.P. De Almeida, "Adsorption of anionic dyes on chitosan beads. 1. The influence of the chemical structures of dyes and temperature on the adsorption kinetics." Journal of Colloid and Interface Science, 280, 380–386, 2004.

Appendices

Molecular Structure of RBB

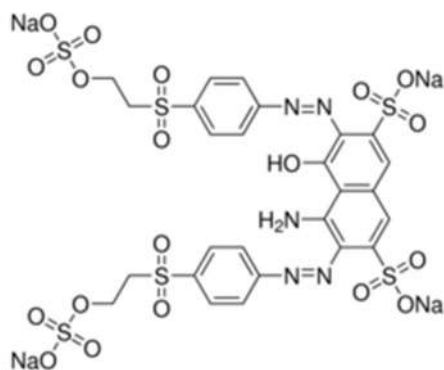


Figure 1 The Structural molecular formula of RBB [1]

Details for kinetic modelling of adsorption

In order to evaluate the adsorption kinetics, three simplified kinetic models including were applied to the experimental data: pseudo-first-order, pseudo-second-order, and saturation type. The related equations are given on Table A1. Principally, all of these three kinetic models include all of the mass transfer steps of the adsorption process, so they are called as pseudo-models.

Table A1
Simplified adsorption kinetic models

Kinetic Model	Non-Linear Function	Linearized Function
Pseudo-first order	$\frac{dq}{dt} = k_{1,ad} (q_{eq} - q)$	$\log(q_{eq} - q) = \log(q_{eq}) - \frac{k_{1,ad}}{2.303} t$
Pseudo-second order	$\frac{dq}{dt} = k_{2,ad} (q_{eq} - q)^2$	$\frac{t}{q} = \frac{1}{k_{2,ad} q_{eq}^2} + \frac{1}{q_{eq}} t$
Saturation type	$r_{ad} = \left. \frac{dq}{dt} \right _{t=0} = \frac{k_{ad} C_0}{1 + k_{0,ad} C_0}$	$\frac{1}{r_{ad}} = \frac{1}{k_{ad} C_0} + \frac{k_{0,ad}}{k_{ad}}$

$k_{1,ad}$ (min^{-1}); $k_{2,ad}$ ($\text{g.mg}^{-1}\text{min}^{-1}$); k_{ad} ($\text{L.g}^{-1}\text{min}^{-1}$) and $k_{0,ad}$ (L.mg^{-1}) are the of pseudo-first order, pseudo-second order and saturation type adsorption rate constants, respectively; r_{ad} is the initial adsorption rate at $t=0$; q_{eq} is the amount of adsorbed dye per gram of adsorbent at equilibrium (mg.g^{-1}).

Details for kinetic and equilibrium modelling of adsorption

To discover the maximum RBB adsorption capacity of the adsorbents, the experimental data were fitted to the Freundlich and Langmuir models which are most commonly used adsorption isotherms characterizing the non-linear equilibrium between adsorbed effluent on the active sites of the adsorbent (q_{eq}) and effluent in the bulk solution (C_{eq}) at a constant temperature, represented in Table A2.

Tabel A2
Adsorption isotherm models

Isotherm Model	Equation	Nomenclature
Langmuir Model	$q_{eq} = \frac{Q^0 b C_{eq}}{1 + b C_{eq}}$	Q^0 ; The maximum adsorption capacity b ; Bonding energy of adsorption C_{eq} ; Residual dye concentration at equilibrium (mg.L^{-1})
Freundlich Model	$q_{eq} = K_F C_{eq}^{1/n}$	K_F ; Freundlich adsorption constant about adsorption capacity [$(\text{mg.g}^{-1}).(\text{mg.L}^{-1})^n$] n ; Freundlich adsorption constant (about adsorption intensity)